

THE UNIVERSITY of ADELAIDE

Investigating the Contribution of Specific Cancer-Associated Fibroblast Subsets to Colorectal Tumourigenesis

A thesis submitted in fulfilment of

DOCTOR OF PHILOSOPHY

Adelaide Medical School

The University of Adelaide

By

Krystyna Anna Gieniec

December 2020

Table of Contents

Included Publications **5**
Abstract **6**
Declaration **7**
Acknowledgements **8**
List of Commonly Used Abbreviations **9**
Chapter 1: Introduction **11**
The colonic epithelium 12
Fibroblasts play important roles in promoting tumourigenesis 14
Knowledge gap and PhD project aims 16
MCAM as a potential CRC-promoting candidate 17
GREM1 as a CRC-promoting factor 19
The significance of identifying and targeting tumour-promoting CAFs 22
Chapter 2: Materials and Methods **23**
Cell culture 23
Generation of CMT93 M7 24
Generation of AP mono8 HP2.3 24
Generation of AKP mono7 HP1.7 25
Generation of AKP mono7 CAS9^{-}GFP^{-} 26
RNA-sequencing from FACS-purified mouse colonic cells 27
Analysis of the Cancer Genome Atlas (TCGA) data 28
Extraction of primary mouse colon myofbs 28
Confirmation of *Mcam* expression in mouse cell lines 28
Generation of pUltra_*Mcam* 29
Generation of *Mcam*-overexpressing YH2 cells and primary myofbs 30
Generation and validation of the *Mcam*$^{-/-}$ mouse 31
qPCR screen in primary mouse colon myofbs 32
Proliferation assays 33
Collagen contraction assays 34
Colony forming unit-fibroblast (CFU-F) assays 34
Wound healing assays 34
Mouse colon OU/tumouroid viability assays 35
Human tissues 35
Antibodies for use in immunohistochemistry (IHC) and immunofluorescence (IF) 35
IHC and IF 36
Hematoxylin and eosin (H&E) staining 37
Mouse experiments 37

AOM/DSS mouse model of primary CRC 37
Mouse models of primary CRC via colonoscopy-guided cell implantation 37
Mouse model of hepatic metastatic CRC 38
IVIS bioluminescence imaging 39
FOLFOX chemotherapy pilot 40
GREM1 NAb studies 40
Statistical analysis 40
Chapter 3: Animal Model Development 41
Orthotopic and hepatic metastatic mouse models of CRC 41
Orthotopic injection of traditional mouse CRC cell lines either failed to generate tumours in immunocompetent mice or produced tumours unrepresentative of human CRC 43
Colon tumouroids from transgenic mice failed to generate orthotopic tumours in immunocompetent mice 46
Engineered mouse colon tumouroids to generate orthotopic mouse models of CRC 48
Discussion 57
Chapter 4: MCAM in the Colorectal Tumour Stroma 61
Identification of MCAM as a candidate CRC-promoting stromal factor 61
$MCAM^+$ stroma arises from proliferative resident cells 65
$MCAM^+$ stroma marks both fibroblastic and endothelial populations in mouse CRC 66
Mcam is expressed in primary cultured mouse colon myofbs and CAFs 67
Induction of ectopic *Mcam* expression in YH2 and primary myofbs 68
Generation of $Mcam^{-/-}$ mice and colon myofbs 71
MCAM affects the expression of other tumour-promoting genes in primary myofbs 73
MCAM reduces the activity and stemness of myofbs, while improving migration 76
Colon myofb-produced MCAM does not directly affect neoplastic colon epithelial growth *ex vivo* 79
Discussion 82
Chapter 5: GREM1 Inhibition in Mouse Models of CRC 88
Piloting standard-of-care chemotherapy in our hepatic metastatic mouse model of CRC 89
Liver tumours generated from AP mono8 HP2.3 tumouroids do not respond to GREM1 inhibition 93
Pre-treatment with the GREM1 NAb impedes primary CRC growth but does not improve survival 97
Discussion 103
Chapter 6: Summary of Results and General Discussion 107
Chapter summaries 107
Future directions and clinical implications of MCAM 108
Future directions and clinical implications of GREM1 109
Other ways to therapeutically target CAFs 110
Appendix 1. 'Cancer-Associated Fibroblasts – Heroes or Villains?' 111

Appendix 2. Direct Binding Partners of MCAM 124
Appendix 3. Molecular Pathways Downstream of MCAM Activation 125
Appendix 4. 'The Origin and Contribution of the Tumor Stroma in Colorectal Carcinogenesis' 127
Appendix 5. 23 Genes Expressed More in the Stroma Than Epithelium of Colorectal Tumours 226
Appendix 6. Table of Results From the Scoring Matrix Used During RNA-Sequencing List Refinement 228
Appendix 7. The Expression of Other Genes Examined That are not Linked to *Mcam* Expression Levels 231
Appendix 8. 'The Balance of Stromal BMP Signaling Mediated by *GREM1* and *ISLR* Drives Colorectal Carcinogenesis' 235
Bibliography 362

Included Publications

APPENDIX 1

Gieniec, K. A., Butler, L. M., Worthley, D. L., Woods, S. L. (2019). Cancer-associated fibroblasts – heroes or villains? *The British Journal of Cancer*, 121(4), p.293-302. doi: https://doi.org/10.1038/s41416-019-0509-3.

APPENDIX 4

Kobayashi, H., Gieniec, K. A., Lannagan, T. R. M., Wang, T., Asai, N., Mizutani, Y., Ida, T., Ando, R., Suzuki, N., Ichinose, M., Wright, J. A., Vrbanac, L., Ng, J. Q., Lawrence, M. J., Sammour, T., Hayakawa, Y., Klebe, S., Shin, A. E., Asfaha, S., Bettington, M., Arpaia, N., Danino, T., Butler, L. M., Burt, A. D., Leedham, S. J., Rustgi, A. K., Mukherjee, S., Takahashi, M., Wang, T. C., Enomoto, A., Woods, S. L., Worthley, D. L. (Unpublished). The origin and contribution of the tumor stroma in colorectal carcinogenesis.

APPENDIX 8

Kobayashi, H., Gieniec, K. A., Wright, J. A., Wang, T., Asai, N., Mizutani, Y., Ida, T., Ando, R., Suzuki, N., Lannagan, T. R. M., Ng, J. Q., Hara, A., Shiraki, Y., Mii, S., Ichinose, M., Vrbanac, L., Lawrence, M. J., Sammour, T., Uehara, K., Davies, G., Lisowski, L., Alexander, I. E., Hayakawa, Y., Butler, L. M., Zannettino, A. C. W., Din, M. O., Hasty, J., Burt, A. D., Leedham, S. J., Rustgi, A. K., Mukherjee, S., Wang, T. C., Enomoto, A., Takahashi, M., Worthley, D. L., Woods, S. L. (2020). The balance of stromal BMP signaling mediated by GREM1 and ISLR drives colorectal carcinogenesis. *Gastroenterology*, doi: https://doi.org/10.1053/j.gastro.2020.11.011.

Abstract

Despite colorectal cancer (CRC) remaining a prominent cause of cancer death worldwide, there is little known about how the surrounding connective tissue 'stroma' specifically encourages poorer prognosis. While many studies have attempted to interrogate the molecular cross-talk between the tumour and stromal cancer-associated fibroblasts (CAFs), the most important tumour-promoting interactions remain ill-defined. We are yet to adequately exploit these pathways for the prevention and treatment of CRC. In this thesis I aimed to identify and test specific CAF subsets for their putative ability to promote CRC, both *in vitro* and *in vivo.* Through RNA-sequencing, prognostic analyses and immunohistochemistry, I identified Melanoma cell adhesion molecule (MCAM) as a candidate CRC-promoting stromal factor that was significantly associated with worse patient prognosis. MCAM expression was significantly upregulated in mouse and human CRC compared to normal colon tissue and marked proliferative tumour-associated stroma comprised of both endothelial and fibroblast cell populations *in vivo*. Upon overexpression in primary mouse colon fibroblasts *in vitro*, MCAM significantly reduced contractile activity and enhanced migration. I also developed immunocompetent mouse models of primary and metastatic CRC to examine the efficacy of an inhibitor of a known CRC-promoting stromal factor, Gremlin1 (GREM1). These mouse models involved the implantation of mouse colorectal tumour organoids directly into the colon wall via colonoscope or into the liver via the portal vein, and the tumours generated represented human disease both genetically and pathologically. If we can better understand CAF biology and heterogeneity, and identify specific tumour-promoting CAF subtypes, then we can develop more targeted therapeutic strategies that inhibit both the cancer and its enhancing stroma to ultimately improve CRC patient survival.

Declaration

I certify that this work contains no material which has been accepted for the award of any other degree or diploma in my name, in any university or other tertiary institution and, to the best of my knowledge and belief, contains no material previously published or written by another person, except where due reference has been made in the text. In addition, I certify that no part of this work will, in the future, be used in a submission in my name, for any other degree or diploma in any university or other tertiary institution without the prior approval of the University of Adelaide and where applicable, any partner institution responsible for the joint-award of this degree.

I acknowledge that copyright of published works contained within this thesis resides with the copyright holder(s) of those works.

I also give permission for the digital version of my thesis to be made available on the web, via the University's digital research repository, the Library Search and also through web search engines, unless permission has been granted by the University to restrict access for a period of time.

I acknowledge the support I have received for my research through the provision of an Australian Government Research Training Program Scholarship.

Krystyna Gieniec **07/12/2020**

Acknowledgements

I would like to thank members of the Gut Cancer group at SAHMRI for never failing to support me over the course of my candidature, both on personal and academic levels: Dan Worthley, Jo Wright, Tongtong Wang, Laura Vrbanac, Hiroki Kobayashi, Tammy Lannagan, Jia Ng, Nobu Suzuki and Mari Ichinose. In particular, I would like to thank my supervisor Susi Woods. With her leadership, nurturing feedback and emotional support, I have developed both as a person and as a researcher and the experience has been invaluable. I would also like to thank Lisa Butler for stepping in and being a fantastic primary supervisor with extremely valuable advice. I will miss everyone dearly and wish them all the best in the future.

I would also like to thank friends and family, particularly my parents, Slawek and Danusia, and my partner in life, Simon, for their continued love and support throughout these challenging years. I could not have done it without them and am incredibly lucky to have such amazing people in my life.

Lastly, I would like to thank the Australian Government and Lions Medical Research Foundation for financially supporting me and my research throughout my candidature. With their assistance, I was able to solely focus on my research and complete my candidature to the best of my abilities. I would also like to thank EMBL Australia for selecting me to attend their PhD course in 2017, and the Adelaide Graduate Centre for the Travel Scholarship that enabled me to attend a national conference in 2018.

List of Commonly Used Abbreviations

Ab	Antibody
ACTA2	Actin alpha 2
AKP tumouroid	*Apc*$^{\Delta/\Delta}$;*Kras*^{G12D};*Tp53*$^{\Delta/\Delta}$
AP tumouroid	*Apc*$^{\Delta/\Delta}$;*Tp53*$^{\Delta/\Delta}$
APC	Adenomatous polyposis coli
AOM	Azoxymethane
BMP	Bone morphogenetic protein
CAF	Cancer-associated fibroblast
CAS9	CRISPR associated protein 9
CFU-F	Colony forming unit-fibroblast
CRC	Colorectal cancer
CRISPR	Clustered Regularly Interspaced Short Palindromic Repeats
DSS	Dextran sulfate sodium
ECM	Extracellular matrix
EGF	Epidermal growth factor
eGFP	Enhanced GFP
EGFR	EGF receptor
EGFRi	EGFR inhibitor
EMT	Epithelial-to-mesenchymal transition
F	Forward primer
FACS	Fluorescence activated cell sorting
GFP	Green fluorescent protein
GFR	Growth factor-reduced
GREM1	Gremlin1
H&E	Haematoxylin and eosin
HMPS	Hereditary mixed polyposis syndrome
IF	Immunofluorescence
IHC	Immunohistochemistry
Indel	Insertion/deletion mutation
KRAS	Kirsten ras oncogene
MAPK	Mitogen-activated protein kinase
MCAM	Melanoma cell adhesion molecule
MSCs	Mesenchymal stem cells
Myofbs	Myofibroblasts
NAb	Neutralising antibody

NOG	Noggin
OUs	Organoid units
R	Reverse primer
RSPO	R-spondin
SAGE	South Australian Genome Editing Facility
SAHMRI	South Australian Health and Medical Research Institute
siRNA	Small interfering RNA
shRNA	Short hairpin RNA
TGF-β	Transforming growth factor beta
TP53	Tumour protein p53
VEGF	Vascular endothelial growth factor
VEGFR2	Vascular endothelial growth factor receptor 2
WT	Wild type
WNT	Wingless-related integration site

Chapter 1: Introduction

Colorectal cancer (CRC) affects 1 in 13 Australians. In 2020 it is estimated that approximately 15,500 people will be diagnosed and 5,300 will succumb to the disease, making it the fourth most common and second most lethal cancer in Australia [1] (Fig 1.1). CRC can develop by the accrual of sequential genetic and epigenetic changes, and sporadic disease develops with alterations to two main pathways: conventional or serrated. Colorectal tumours developed through the conventional pathway are characterised by chromosomal instability (CIN) with the stepwise loss of key tumour suppressors such as *Adenomatous polyposis coli* (*APC*) and activation of oncogenes such as the *Kirsten ras oncogene* G12D ($KRAS^{G12D}$) mutation [2]. Serrated pathway tumours account for approximately 25% of CRC cases [3] and do not have CIN. They are best differentiated from conventional pathway tumours by the presence of the *B-raf proto-oncogene* V600E ($BRAF^{V600E}$) mutation, which activates the Mitogen-activated protein kinase (MAPK) pathway, and the coincident coordinated epigenetic modification of specific target promoters termed the CpG Island Methylator Phenotype (CIMP) [4]. The incidence of sporadic CRC can be increased by chronic inflammation, such that patients with Inflammatory Bowel Disease have a 2.4-fold higher risk of developing CRC than the normal population [5]. Colitis-associated CRC contributes to only 1-2% of all colorectal cancers but these patients tend to have worse prognosis and decreased survival [6]. Despite the success of standard-of-care chemotherapies such as FOLFOX to treat CRC, only 50% of patients with advanced disease respond [7]. We are therefore in need of more effective treatments for CRC, and my thesis will add to the growing literature that provides rationale for targeting specific tumour-promoting cancer-associated fibroblast (CAF) subtypes as a novel therapeutic strategy.

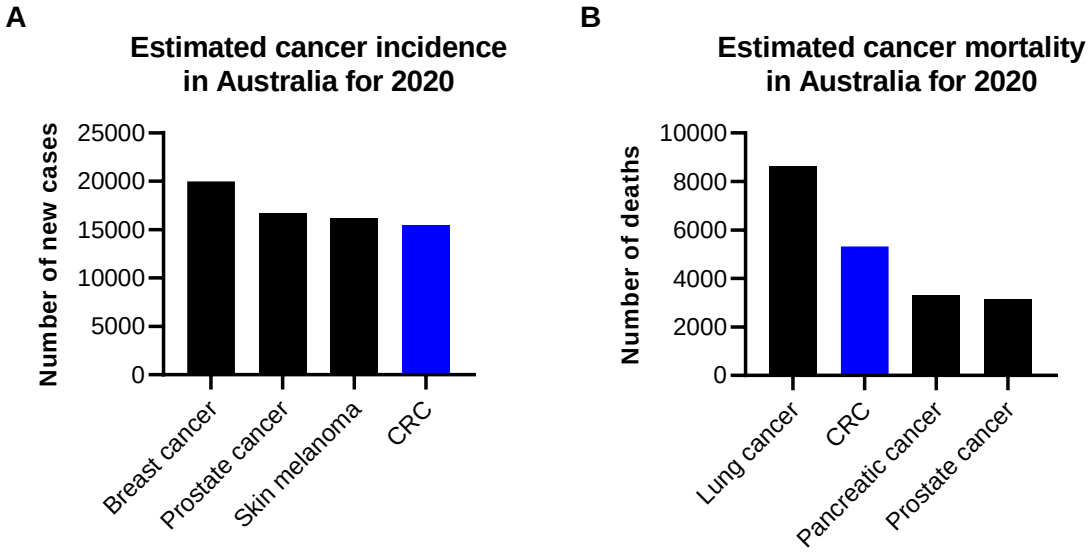


Figure 1.1. CRC is common and lethal. A–B, graphs showing estimated cancer incidence (**A**) and mortality (**B**) in Australia for 2020. Data was collected from the Australian Institute of Health and Welfare [1].

The colonic epithelium

CRC develops through the transformation of colon epithelial cells, which normally form U-shaped crypt structures. The primary intestinal epithelial stem cell niche resides at the base of the crypts and is regulated by extracellular niche factors. As the daughter 'transit-amplifying' (TA) cells migrate up and out of the niche, they are exposed to different factors and consequently differentiate into the many different epithelial cell types comprising the intestine, before ultimately shedding into the lumen [8] (Fig 1.2A). An estimated 10 billion cells are shed each day after exposure to the harsh luminal environment; thus, to maintain barrier function, the epithelium must undergo rapid renewal and the epithelial cells at the base of the crypts are highly proliferative as a consequence. This is demonstrated by Ki67 immunohistochemistry (IHC) staining, which is a marker of proliferation (Fig 1.2B). The colon epithelia can be modelled *ex vivo* using three-dimensional organoid technology, which was pioneered by the Clevers group [9]. Organoid units (OUs) are an epithelial cell culture and are generated via the differentiation of self-renewing epithelial stem cells into all the different epithelial cell types of the organ of interest (Fig 1.3A) [10]. Interestingly, small intestinal epithelial cell types are represented at normal ratios in OUs and their localisation and movement along the crypt-villus axis reflects the small intestine *in vivo* [9]. The different absorptive and digestive functions along the axis are also recapitulated [11]. Mouse colon OUs can form cystic or budded structures (Fig 1.3B-C) and are grown in media supplemented with key extracellular factors that recreate the epithelial stem cell niche – Wingless-related integration site (WNT), R-spondin (RSPO), Epidermal growth factor (EGF) and Noggin (NOG). While WNT and EGF promote self-renewal, RSPO potentiates WNT signalling and NOG maintains stemness by antagonising Bone morphogenetic protein (BMP) signalling and thus inhibiting differentiation [9]. As this media promotes stem cell renewal, OUs can be expanded indefinitely. OUs must also be grown as a suspension in Matrigel, an extracellular matrix (ECM) substituent, which is crucial as a scaffold and to prevent cell anoikis [9]. A diagram of how normal mouse colonic OUs are cultured is represented in Fig 1.3D.

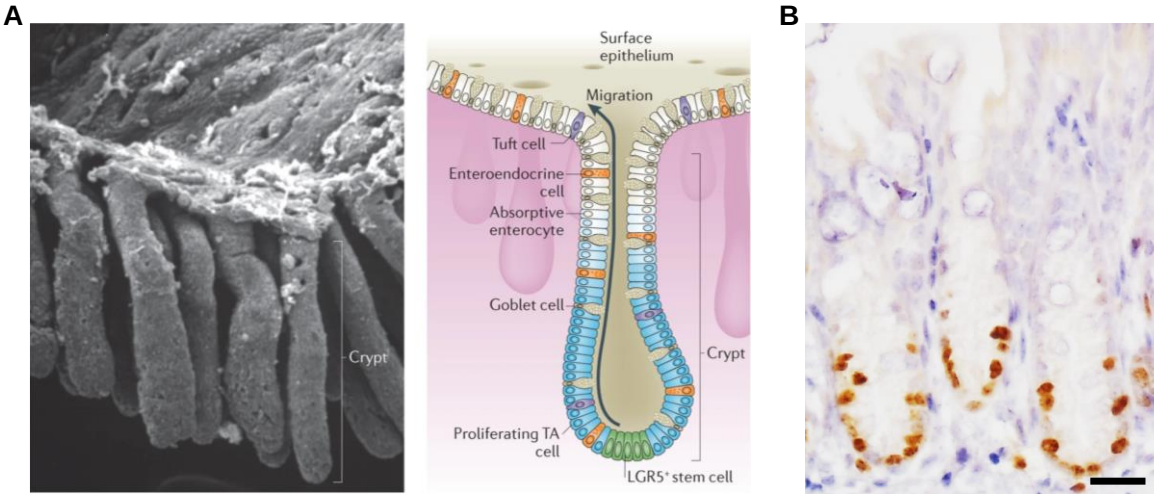


Figure 1.2. legend on next page.

Figure 1.2. Colon crypt organisation. A, scanning electron micrograph showing the structural organisation of the mouse colon (left picture), and the epithelial cell organisation in each crypt (right picture), taken from [8]. TA = transit amplifying cells, LGR5 = Leucine-rich repeat-containing G-coupled receptor 5. Reprinted by permission from RightsLink: Springer Nature, Nature Reviews Molecular Cell Biology, Adult intestinal stem cells: critical drivers of epithelial homeostasis and regeneration, Nick Barker, 2014. **B,** Ki67 staining in the adult mouse colon; scale = 20µm.

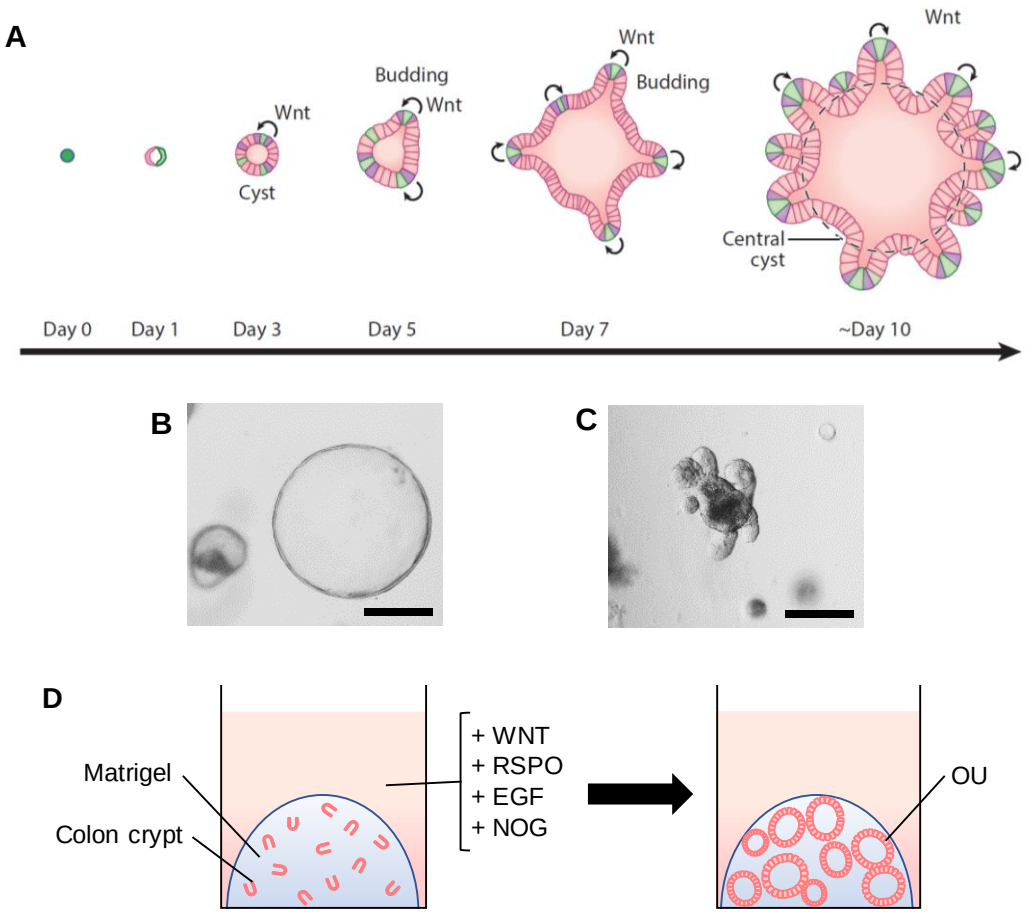


Figure 1.3. Culture of mouse colon OUs. A, schematic of small intestinal OU development taken from [10]. The cellular location of stem cells (green), WNT-producing Paneth cells (purple) and differentiated cells (pink) within the OUs are shown. Republished with permission of Annual Reviews, Inc., from Mini-gut organoids: reconstitution of the stem cell niche, Shoichi Date & Toshiro Sato, 31, 1, 2015; permission conveyed through Copyright Clearance Center, Inc. **B–C,** like small intestinal OUs, colon OUs can become cystic (**B**) or budded (**C**) in appearance; scale bar = 200um. **D,** schematic of mouse colon OU culture. Colonic crypts from mice are suspended in an extracellular matrix substitute (Matrigel) and grown in media containing WNT, RSPO, EGF and NOG to stimulate stem cell proliferation, generating three-dimensional OUs.

OUs can also be used to model cancer *in vitro*, with tumour OUs termed tumouroids. One striking study explored using CRC patient-derived tumouroids in personalised medicine, making associations between cancer mutations and sensitivity to different compounds such that they were subsequently able to retrospectively predict patient responses in the clinic [12]. In addition to using patient-derived tumouroids, tumouroids can also be generated by inducing mutations in normal OUs via Clustered Regularly Interspaced Short Palindromic Repeats (CRISPR)/CRISPR associated protein 9 (CAS9)-mediated genome engineering [13], as in the following examples [14-20]. These engineered tumouroids were subsequently able to generate tumours in mice. In this thesis, I use two different engineered tumouroid lines to model primary and hepatic metastatic CRC in mice.

Fibroblasts play important roles in promoting tumourigenesis

Fibroblasts are the heterogeneous, non-specialised cells of the connective tissue stroma that support tissue function and homeostasis by regulating the ECM, inflammation and epithelial cell proliferation and differentiation [21]. There is no overarching molecular marker that specifically defines all fibroblast populations, but one of the most commonly used markers is Actin alpha 2 (ACTA2). However, like all other fibroblast markers, ACTA2 expression is not unique to fibroblasts alone. In the colon, fibroblasts form a reticular sheath that intimately surrounds the overlying intestinal epithelial cells [22, 23] (Fig 1.4A-B). They are a predominantly quiescent cell type, only transiently acquiring activity during periods of tissue remodelling and repair. Activated fibroblasts, termed myofibroblasts (myofbs), either apoptose or revert back to a dormant state once their function becomes redundant; otherwise, pathological conditions such as tissue fibrosis and chronic inflammation can arise [24]. This chronic tissue repair response has been implicated in the progression to cancer [25], and tumours can therefore be considered as "wounds that do not heal" [26]. Distinct, constitutively activated fibroblasts that surround tumours are termed CAFs and they, along with other elements of the tumour microenvironment, can indulge in reciprocal dialogues with the neoplastic epithelium to maximise tumour fitness.

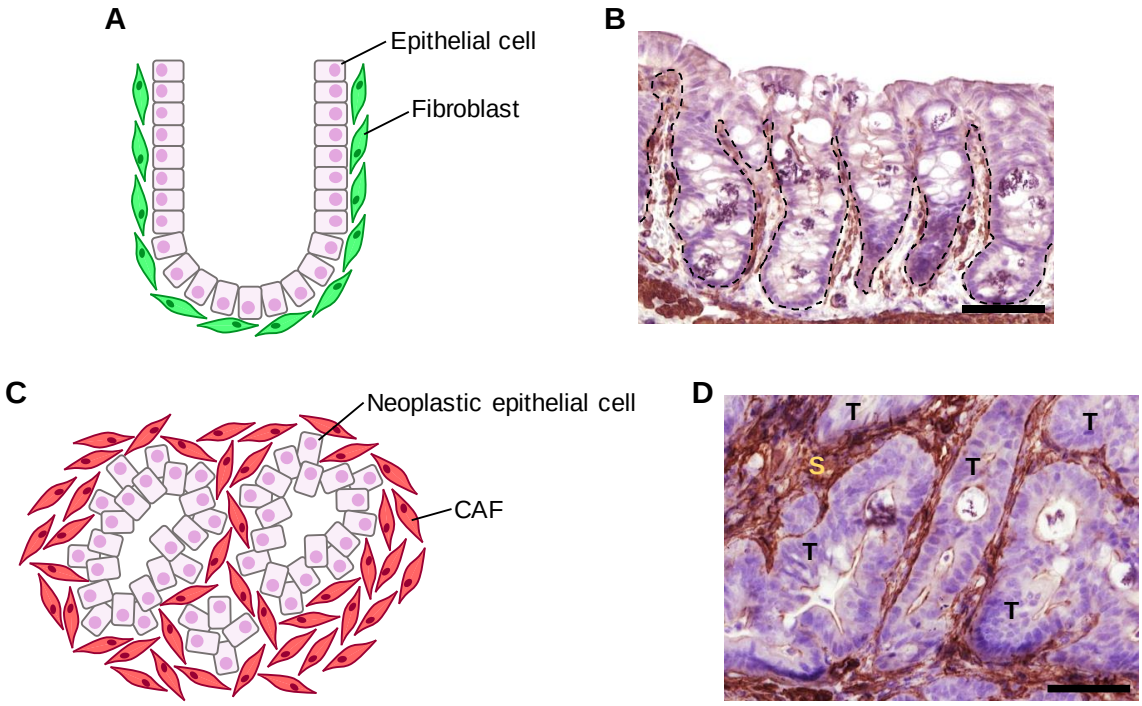


Figure 1.4. Localisation of colon fibroblasts and CAFs. A, schematic of the normal colon showing a thin layer of fibroblasts that intimately surround the crypt epithelium. **B,** ACTA2 expression in the adult mouse colon identifies subepithelial fibroblasts and the underlying muscularis mucosae. The edge of the crypt epithelia is shown with a dashed line. **C,** schematic of CRC showing an upregulated stromal infiltrate that is CAF-rich. **D,** ACTA2 expression in mouse CRC; S = stroma, T = tumour epithelium. Scale = 50µm.

CAFs play an active role in tumourigenesis. In 2015, it was discovered that genes positively associated with CRC recurrence and poor prognosis were predominantly upregulated within CAFs, not the tumour cells [27, 28]. Furthermore, when CRC was classified into four distinct consensus molecular subtypes (CMSs) it was revealed that CMS4, with upregulated stromal infiltrate (Fig 1.4C-D), was associated with more aggressive tumour stages and consequently worse overall survival [29]. CAFs have since been associated with all stages of cancer development, from primary growth to secondary colonisation at metastatic sites, in all solid cancer types. Their tumour-promoting functions include improving tumour energy synthesis, remodelling the ECM to further accelerate tumour invasion, inducing cancer cell stemness and epithelial-to-mesenchymal transition (EMT), and cultivating metastatic outgrowth, in addition to encouraging other cells to induce an oxygen-rich, immunosuppressive and pro-inflammatory environment [30-32]. The existence of CAF subsets with tumour-suppressing properties has also been acknowledged; for example, depletion of $ACTA2^+$ CAFs accelerated the progression of pancreatic cancer in mice and significantly reduced their survival [33]. This tumour-suppressing role, however, appears to be cancer type-specific, as depleting $ACTA2^+$ CAFs in mouse models of breast cancer significantly reduced primary tumour burden [34].

CAF heterogeneity and the tumour-promoting and –suppressing phenotypes are covered in greater detail in my published review [30] (Appendix 1).

Knowledge gap and PhD project aims

CAFs are a heterogeneous and somewhat poorly defined population that can have both tumour-promoting and -inhibiting properties. The composition of CAF subtypes within each cancer type can be different; for example, 43.5% of $ACTA2^+$ CAFs co-expressed Fibroblast-specific protein 1 (FSP1) in pancreatic cancer but this overlap was reduced to 10.9% in breast cancer [35]. CAFs are therefore likely to be regulated by unknown, tissue-specific factors. There are limited studies that have examined CAFs in CRC specifically. One group used single-cell RNA sequencing of human CRC samples to demonstrate that *ACTA2* was co-expressed with other fibroblast markers such as *Transgelin* (*TAGLN*) and *Platelet-derived growth factor subunit A* (*PDGFA*), while the other common fibroblast marker, *Fibroblast activation protein alpha* (*FAP*), was co-expressed with markers such as *Decorin* (*DCN*) and *Collagen type I alpha 2 chain* (*COL1A2*) [36]. Another group showed that $FSP1^+$ CAFs were significantly more frequent in the colorectal intratumoural stroma than at the invasive front [37]. While these studies are important in defining CAF composition and localisation in CRC, they do not define the markers of specific tumour-promoting subtypes. One recent study, however, identified *Biglycan* (*BGN*), *Reticulocalbin 3* (*RCN3*), *TAGLN*, *Myosin light chain 9* (*MYL9*) and *Tropomyosin 2* (*TPM2*) as independent fibroblast-specific biomarkers of poor prognosis CRC [38], but they did not specifically demonstrate that these CAFs promoted CRC. There are a handful of CAF-expressed factors shown to affect CRC cells *in vitro*, for example, Gremlin1 (GREM1) [39], and there are even fewer CAF-derived factors that have been proven to promote colorectal tumourigenesis *in vivo*. As current treatments fail many CRC patients with advanced disease, the need for novel strategies that also target the tumour stroma is clear. I broadly hypothesise that the development of these strategies will rely upon a more detailed understanding of CAF biology. As such, my PhD project was designed to explore putative CRC-promoting CAF subtypes both *in vitro* and *in vivo* through the following aims:

1. To develop immunocompetent mouse models of CRC that recapitulate the common genetic and pathological features of the human disease
2. To identify prognostically significant tumour-promoting factors produced by CAFs in CRC
3. To explore how the CAF factors identified in Aim 2 affect the expression profile and function of fibroblasts and the growth of epithelial cells *ex vivo*
4. To examine the putative tumourigenic role of CAF factors in mouse models of CRC

Aim 1 is explored in Chapter 3, where I successfully developed primary and metastatic models of CRC in immunocompetent mice. Aims 2 and 3 are explored in Chapter 4, where I identified and examined Melanoma cell adhesion molecule (MCAM) as a putative CRC-promoting CAF factor. I

hypothesise that MCAM$^+$ CAFs promote colorectal tumourigenesis. Aim 4 is explored in Chapter 5, where I therapeutically inhibited the known tumour-promoting CAF factor, GREM1, in both primary and metastatic CRC mouse models. I hypothesise that by inhibiting GREM1 we can improve the survival of mice with primary and metastatic CRC.

MCAM as a potential CRC-promoting candidate

MCAM was the top CAF-associated, CRC-promoting candidate from the discovery arm of my PhD project (Aim 2); please see Chapter 4 for how MCAM was identified. MCAM (also known as Cluster of differentiation 146, or CD146) is a transmembrane glycoprotein receptor belonging to the cell adhesion molecule (CAM), mucin and immunoglobulin superfamilies. A secreted form of MCAM (sMCAM) has also been discovered in endothelial cultures [40] and has additional roles in monocyte and endothelial cell chemotaxis [41, 42]. *Mcam*/*MCAM* is expressed in multipotent mesenchymal stem cells (MSCs), pericytes and endothelial cells in normal tissues [40, 43-48], in immune cells during inflammation [49, 50], and in cancer-associated pericytes, CAFs [51-53] and CAFs with a pericyte-like gene signature [54-56] across different cancer types. *Mcam*/*MCAM* is also expressed in melanoma, sarcoma, breast, liver and rhabdoid cancer cells [57-67]. *Mcam*/*MCAM* expression can be induced in: fibroblasts by Transforming growth factor beta 1 (TGF-β1), Bone morphogenetic protein 4 (BMP4) and Vascular endothelial growth factor (VEGF) [68]; CAFs by TGF-β1 [69]; endothelial cells by VEGF, Tumour necrosis factor (TNF) and Interleukin 1 beta (IL-1β) [41, 70, 71]; and cancer cells by Protein kinase B (AKT), Insulin like growth factor binding protein 4 (IGFBP4) and cyclic adenosine monophosphate (cAMP) [72-74].

In the normal setting, MCAM has a role in maintaining the multipotency of MSCs [45, 46] and MCAM$^+$ pericytes are thought to be MSC progenitors [75, 76]. In endothelial cells, *Mcam/MCAM* expression promotes proliferation, migration and angiogenesis [42, 61, 77-81] and MCAM$^+$ endothelium can induce neural stem cell differentiation [82]. Both MCAM$^+$ endothelial cells and pericytes are also essential for the development of the blood-brain barrier (BBB), and MCAM is essential for the Platelet-derived growth factor subunit B (PDGFB)-promoted proliferation, migration and recruitment of pericytes to the BBB [44]. MCAM also promotes fibroblast migration [68] and improves the ability of fibroblast-like cells to contract collagen [83].

In the inflammatory setting, MCAM defines circulatory Th17 cells [50] and is involved in the recruitment of T cells to inflamed sites. It has been shown that MCAM$^+$ lymphocytes adhere to and transmigrate across endothelial cells better than MCAM$^-$ lymphocytes, and this extravasation may require both endothelial and lymphocytic *Mcam* expression [49] or presence of the MCAM ligand Laminin-411 (LAMA4) in the endothelial basement membrane [50]. MCAM$^+$ endothelial cells can also promote immune cell extravasation and transmigration [71]. Two MCAM neutralising antibodies (NAbs) have successfully been used to reduce chronic inflammatory diseases in mice by significantly

reducing lymphocyte infiltration into inflamed tissues: AA98 and PRX003. The AA98 MCAM NAb specifically targets endothelial MCAM [84] and works by significantly impairing MCAM dimerisation to inhibit downstream signalling pathways [85, 86]. AA98 significantly reduced colitis in mice and was especially effective when combined with the anti-TNFα antibody V1q to downregulate endothelial *MCAM* expression [71]. Furthermore, AA98 significantly reduced disease severity in a mouse model of experimental autoimmune encephalomyelitis [87]. The PRX003 MCAM NAb is different from AA98 in that it targets $MCAM^+$ circulating T cells, inhibiting their interaction with LAMA4. This was shown to significantly alleviate the progression of experimental autoimmune encephalitis and psoriatic disease in mice [88, 89]. PRX003 was subsequently shown in Phase1a/1b clinical trials to be safe and well-tolerated, but while it reduced MCAM expression in circulating T cells it did not sufficiently decrease T cell infiltration into the skin and the patient group examined (psoriasis) derived no significant benefit [90] (ClinicalTrials.gov Identifier NCT02458677 and NCT02630901).

In the cancer setting, high *MCAM*/MCAM expression in colorectal, liver, breast, lung, gastric, ovarian and oesophageal squamous cell carcinoma is associated with worse patient survival [58, 66, 91-96]. $MCAM^+$ cancer cells have an enhanced ability to initiate tumours in mice [97, 98] and have significantly improved proliferation [57, 67, 98], stemness [61, 62, 64, 66], migration, EMT, invasion and metastasis [57, 58, 60-63, 65-68, 97, 99, 100]. One group attempted to prevent $MCAM^+$ melanoma colonisation by vaccinating mice with an alphavirus-based DNA vaccine encoding *Mcam* prior to tumour cell implantation; the vaccine was able to induce effective humoral and $CD8^+$ T cell responses that significantly reduced primary tumour incidence and lung metastasis [97]. The PRX003 MCAM NAb was also used to target established $MCAM^+$ prostate tumours *in vivo* and was shown to significantly reduce bone metastasis [100]. $MCAM^+$ cancer cells can also induce tumour angiogenesis [66, 86, 98]. $MCAM^+$ endothelial cells also play an important role in tumour angiogenesis, as their inhibition using the AA98 MCAM NAb significantly reduced blood vessel density and thus tumour growth in mouse models of hepatocarcinoma, leiomyosarcoma, melanoma, pancreatic cancer and colitis-induced CRC [71, 77, 84]. In these models AA98 may additionally block the interaction between MCAM and its co-receptor, Vascular endothelial growth factor receptor 2 (VEGFR2), and the co-administration of AA98 with the VEGF inhibitor bevacizumab had an additive inhibitory effect on melanoma and pancreatic cancer growth and angiogenesis *in vivo* [77]. Furthermore, the incidence and progression of colitis-induced CRC was significantly reduced in endothelial *Mcam* knock-out mice [71]. The binding of Galectin-3 (GAL-3) to endothelial MCAM has also been shown to induce the secretion of many metastasis-promoting cytokines, including Interleukin-6 (IL-6), by the endothelial cells [101, 102]. The MCAM NAb, ABX-MA1, targets both $MCAM^+$ cancer and endothelium and was shown to significantly inhibit tumour growth, angiogenesis and lung metastasis in a mouse model of melanoma [61]. Although, it did not affect the incidence of osteosarcoma but reduced its lung metastasis *in vivo* [99]. M2J-1 is a unique NAb that targets sMCAM specifically, which has effects on

cancer, endothelial and immune cells. In a pancreatic cancer mouse model, treatment with M2J-1 was shown to significantly reduce tumour cell colonisation, vascularisation and growth while inducing apoptosis [98]. Studies have also observed that MCAM can inhibit apoptosis in cancer cells [62, 72, 98] and endothelial cells [80, 103] in stress-induced environments. Overall, the stimulatory roles of MCAM in tumour growth, progression and angiogenesis place it as an ideal tumour-promoting candidate for further study.

As can be seen from the above, MCAM has predominantly been studied in endothelial and cancer cells. There are two studies to date that have examined the role of $MCAM^+$ CAFs in cancer; one showed that $MCAM^+$ breast CAFs maintained the oestrogen-dependent proliferation of oestrogen receptor $(ER)^+$ breast cancer cells, such that they maintained sensitivity to tamoxifen therapy [51], while the second showed that the reduction of *MCAM* expression in $MCAM^+$ pancreatic CAFs enhanced their activation and viability and improved the migration and invasion of pancreatic cancer cells, suggesting they are a tumour-suppressing subtype in pancreatic cancer [69]. I am the first to examine $MCAM^+$ myofbs and the role of $MCAM^+$ CAFs in CRC specifically.

There are multiple receptors and ligands that directly bind to and activate MCAM, although these have mostly been identified for $MCAM^+$ endothelial cells (Appendix 2). Homophilic MCAM-MCAM interactions have never been proven but have been suggested, for example, between $MCAM^+$ endothelium and $MCAM^+$ lymphocytes [104] and between $MCAM^+$ melanoma and $MCAM^+$ B cells [63]. When MCAM-activating ligands are unknown, researchers commonly culture their cell of interest in conditioned media from tumour cells to induce MCAM receptor dimerisation [86, 105], which is essential for signal transduction. MCAM dimerisation can also be synthetically forced by adding anti-MCAM antibody to the culture media [106, 107]. Upon MCAM activation there are many pathways induced, including AKT, MAPK, mechanistic target of rapamycin kinase (mTOR) complex 2 (mTORC2), Nuclear factor kappa B (NF-κB) and non-canonical WNT (Appendix 3). These pathways have again been examined in cells other than CAFs, particularly endothelial and cancer cells. I am the first to examine molecular pathways downstream of MCAM in *Mcam*-expressing colorectal myofbs.

GREM1 as a CRC-promoting factor

To examine potential therapeutic targets in CRC CAFs I also focussed on a previously identified candidate, GREM1. GREM1 is a secreted protein known for its ability to antagonise BMP signalling [108], inhibiting both the canonical and non-canonical pathways through SMAD and MAPK respectively [109]. The ability of GREM1 to regulate BMP signalling is critical during development, especially during limb and kidney embryogenesis, and *Grem1* knock-out mice die shortly after birth due to the absence of kidneys [110, 111]. GREM1 and BMP signalling also play an important role in colon crypt organisation, and thus in maintaining homeostatic colon function. At the crypt base, the

epithelial stem cell niche is maintained by high WNT and low BMP levels, and after the daughter cells exit this niche, low WNT/high BMP levels at the crypt top promote their differentiation and eventual apoptosis [112-114]. GREM1 is expressed and secreted by the myofbs that reside beneath the crypt base, acting locally to sequester BMP ligands and thus prevent BMP activity within the epithelial stem cell niche to ultimately promote epithelial stemness [115, 116] (Fig 1.5). These GREM1$^+$ sub-crypt myofbs are defined as intestinal reticular stem cells (iRSCs), and their myofibroblastic progeny form the reticular sheath that surrounds the entire crypt epithelium [23]. GREM1 can also bind to and activate VEGFR2 in a BMP-independent manner [117], leading to the formation of VEGFR2/αvβ3 integrin complexes and the promotion of angiogenesis [118]. Only GREM1 homodimers are VEGFR agonists, while GREM1 monomers are VEGFR antagonists that significantly reduce mammary and prostate tumour growth and vascularisation in mice [119]. *Grem1*/*GREM1* expression can be induced in CAFs by Sonic hedgehog (SHH) signalling [120] and in fibroblasts, CAFs and epithelial cells by TGF-β signalling [121, 122].

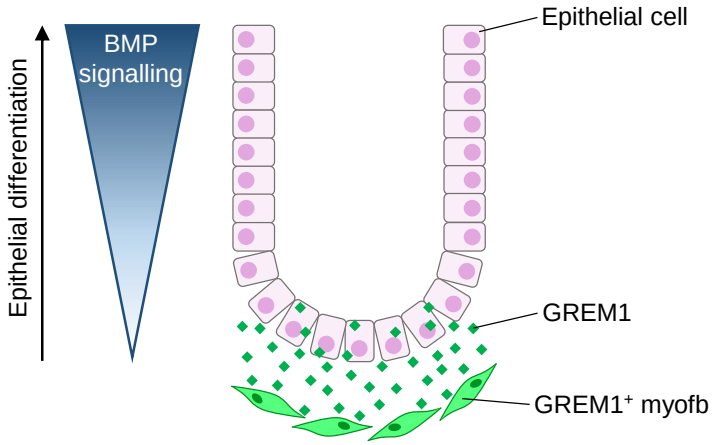


Figure 1.5. BMP signalling in the colon. Schematic displaying GREM1$^+$ fibroblasts localised at the base of the colonic crypt. GREM1 secreted by fibroblasts will locally antagonise BMP signalling and thus promote epithelial stemness only at the crypt base.

The dysregulation of the homeostatic BMP balance can promote intestinal tumourigenesis [109], and high *GREM1*/GREM1 expression in cancers including colorectal, pancreatic, breast and glioblastoma is associated with worse patient survival [112, 115, 120, 121, 123, 124]. GREM1 can be secreted by the tumour and/or tumour stroma, and one study demonstrated that widespread *Grem1* knock-out significantly reduced primary tumour burden and size in the APC$^{min/+}$ mouse model of spontaneous intestinal tumourigenesis [112]. Epithelial *GREM1* upregulation occurs in breast, pancreatic, glioblastoma and mesothelioma cancer cells [120, 123-127], and in colon cancer cell lines with a more mesenchymal than epithelial morphology [128]. The knock-down of *GREM1* in GREM1$^+$ mesothelioma, breast cancer, pancreatic cancer and mesenchymal-like colon cancer cells via small interfering RNA (siRNA) or short hairpin RNA (shRNA) was shown to significantly reduce

proliferation, EMT, and migration *in vitro* [120, 125, 126, 128]. *In vivo*, the CRISPR/CAS9-mediated knock-out of *Grem1* in metastatic GREM1$^+$ breast cancer cells significantly reduced tumour invasion and primary and metastatic tumour growth [123]. Furthermore, GREM1$^+$ glioma cancer stem cells (CSCs) and non-CSCs induced to overexpress *GREM1* via lentiviral transduction had significantly improved stemness and tumour initiation abilities [124], and *GREM1* overexpression in mesothelioma cells significantly enhanced tumour angiogenesis and had a tendency for improved metastasis [127]. In CRC, epithelial *GREM1* upregulation is usually only observed in patients with hereditary mixed polyposis syndrome (HMPS) [129]. These individuals are predisposed to CRC, as progenitor cells that have exited the stem cell niche reacquire stem cell properties and form ectopic crypts that proliferate and can accumulate somatic mutations [112]. In patients with sporadic CRC, GREM1 is commonly detected in the tumour stroma and *GREM1* stromal overexpression is observed in more than 50% of tumours [130].

GREM1 can be secreted by MSCs, fibroblasts and CAFs in the tumour stroma. One study showed that conditioned medium from a heterogeneous population of *GREM1*-expressing MSCs enhanced the proliferation, viability and expression of EMT markers in oesophageal cancer cells *in vitro*, while significantly improving tumour size, EMT and angiogenesis in a MSC/cancer cell co-injection mouse model. These *in vitro* and *in vivo* effects were reversed using MSCs with shRNA-mediated *GREM1* knock-down [131]. GREM1$^+$ bone marrow MSCs were also shown to promote the proliferation of multiple myeloma plasma cells *in vitro*, while GREM1 inhibition via a NAb significantly reduced primary tumour burden *in vivo* [132]. In fibroblasts, recombinant GREM1 was shown to upregulate the expression of pro-fibrotic genes and the production of ECM proteins [122] while *GREM1* knock-down via siRNA significantly reduced their proliferation and migration [120]. *GREM1* expression was also shown to increase the activity of breast CAFs, which then became enabled to significantly promote the stemness, EMT and invasion of breast cancer cells *in vitro* and in a zebrafish co-injection model [121]. Only one study has examined GREM1$^+$ colorectal CAFs, demonstrating that they triggered CRC cell motility and invasion *in vitro* and thus also hypothetically at the desmoplastic cancer invasion front using mathematical modelling [39]. GREM1$^+$ fibroblasts and CAFs also have a role in inducing a tumour-supportive immune system, with GREM1$^+$ pancreatic stellate cells shown to promote and suppress the activation of pro-tumour M2 and anti-tumour M1 macrophages, respectively [133].

As can be seen from the above studies, GREM1 is involved in promoting cancer cell proliferation, stemness, EMT, invasion and metastasis, and in activating pro-tumour macrophages. Not only have studies shown that GREM1 significantly promotes tumorigenesis in mouse models of glioma [124], mesothelioma [127], oesophageal cancer [131] and HMPS-driven CRC [112], but also that *GREM1*/GREM1 depletion significantly reduces the progression of oesophageal cancer [131], breast cancer [123], multiple myeloma [132] and HMPS-driven CRC [112] *in vivo*. I am the first to examine the

role of GREM1^{+} CAFs (and the efficacy of targeting them with a GREM1 NAb) in sporadic primary and metastatic mouse models of CRC.

The significance of identifying and targeting tumour-promoting CAFs

Solid cancers are a complex, dynamic and adaptive ecosystem reinforced by genetic diversity and epigenetic plasticity. As such, drug resistance can emerge and is problematic for many patients. Consequently, there is a need to investigate therapies that are not necessarily directed at the tumour cells themselves and, as such, CAFs provide an attractive target: they are relatively genetically stable and thus less likely than tumour cells to acquire therapeutic resistance, and their presence across different cancer types suggests possible broad applicability of effective therapies. I broadly hypothesise that the identification of specific tumour-promoting CAF subtypes in each cancer type will lead to targeted therapeutic strategies with less clinical variability and improved patient outcomes. Thus, in this thesis, I specifically test whether MCAM^{+} or GREM1^{+} CAFs promote colorectal tumourigenesis and whether inhibition of GREM1 improves the survival of mice with primary and metastatic CRC.

Chapter 2: Materials and Methods

Cell culture

The mouse colonic fibroblast cell line, YH2, was generously provided by Professor Tony Burgess from the Walter and Eliza Hall Institute of Medical Research. The original MC38 mouse colorectal adenocarcinoma cell line was generously provided by Professor John Mariadason from the Olivia Newton-John Cancer Research Institute and was modified to express tdTomato and firefly luciferase in my Honours year. The mouse rectal carcinoma cell line, CMT93, was generously provided by Associate Professor Atsushi Enomoto from the Nagoya University Graduate School of Medicine. The 293FT human embryonal kidney cell line was purchased from Thermo Fisher Scientific (R70007). The YH2, MC38-tdTomato^{+}luciferase^{+}, CMT93 and 293FT cell lines were cultured in Dulbecco's modified Eagle's medium (DMEM; Sigma-Aldrich, D5796) supplemented with 10% foetal bovine serum (FBS; Thermo Fisher Scientific, 10099141), 2mM L-glutamine (Sigma-Aldrich, G7513), and 1% penicillin/streptomycin solution (Sigma-Aldrich, P4333).

Primary mouse colon myofbs were cultured in RPMI-1640 medium (Sigma-Aldrich, R8758) supplemented with 5% FBS, 2mM L-glutamine, 1% penicillin/streptomycin solution, 10mM HEPES solution (Sigma-Aldrich, H0887)s, 1mM sodium pyruvate (Sigma-Aldrich, S8636), 10µM Y-27632 (Sigma Aldrich, Y0503) and 50µM 2-mercaptoethanol (Sigma-Aldrich, M-6250). This media is called "RPMI-5" [(134)].

Normal mouse colon OUs were grown in Advanced DMEM/F-12 media (Thermo Fisher Scientific, 12634-010) supplemented with 1X Antibiotic-Antimycotic (Thermo Fisher Scientific, 15240062), 50µg/mL gentamycin (Thermo Fisher Scientific, 15750-060), 10mM HEPES solution, 1X GlutaMAX Supplement (Thermo Fisher Scientific, 35050-061), 1X N-2 Supplement (Thermo Fisher Scientific, 17502-048), 1X B-27 Supplement (Thermo Fisher Scientific, 17504-001), 50ng/mL recombinant murine EGF (PeproTech, 315-09), 100ng/mL recombinant murine NOG (PeproTech, AF-250-38), 10µM Y-27632, 3µM GSK-3 Inhibitor (Merck Millipore, 361559), 3µM iPSC Induction Enhancer (Merck Millipore, 420220), 50% WNT3a conditioned medium and 20% RSPO-2 conditioned medium. The WNT3a and RSPO-2 conditioned mediums are shared laboratory resources and each new batch is tested for WNT reporter activity. AP mono8 and AKP mono7 colorectal tumouroid lines were grown in similar media, except WNT3a and RSPO-2 conditioned media as well as recombinant EGF were not added. Furthermore, 1X EGFRi (Merck Millipore, 324840) and 50nM Nutlin-3a (Sigma Aldrich, SML0580) were added every second passage to maintain the tumourigenic mutations. The *Braf*^{V600E}ΔTRZI colorectal tumouroids [(17)] and AKP colorectal tumouroids generously provided by A/Prof Jatin Roper [(20)] were grown in similar media to normal organoids, except WNT3a and RSPO-2 conditioned media as well as recombinant NOG

were not added to the media. Media for all OUs and tumouroids was changed 3 or 4 days post-plating. All OUs and tumouroids were grown in 100% growth factor-reduced (GFR) Matrigel (Life Sciences, 356231) domes. A schematic of normal OU and tumouroid cultures are shown in Fig 1.3D (Chapter 1) and 3.5A (Chapter 3), respectively.

Cells and OUs were grown in a 37℃ incubator with 5% CO_2 and were examined using brightfield and GFP settings on an inverted fluorescent microscope (Olympus, IX53). They were routinely screened for Mycoplasma contamination by the MycoAlert Mycoplasma Detection Kit (Lonza, LT07-118).

Immortal mouse cell lines and primary mouse colon myofbs were split using Trypsin-ethylenediaminetetraacetic acid (EDTA) solution (Sigma Aldrich, T3924) following a wash in 1X phosphate-buffered saline (PBS; Sigma-Aldrich, D8537). To split OUs and tumouroids set in GFR Matrigel, they were first collected in cold 1X PBS, spun down, and then resuspended in TrypLE Express (Thermo Fisher Scientific, 12605028) for digestion into cell clumps.

Generation of CMT93 M7

The 50X concentrated retrovirus encoding SFG-NES-TGL [135] was generated by Dr Josephine Wright and kept as frozen stocks at -80°C. The SFG-NES-TGL plasmid was generously provided by Dr Vasilios Panagopoulos from the South Australian Health and Medical Research Institute (SAHMRI). A 10X concentration of this retrovirus was added with 4µg/mL polybrene and DMEM media (no antibiotics) to one 6-well containing a 70% confluent monolayer of CMT93 cells, and the plate was spun at 1700 *rpm* for 1 hour at room temperature to induce cell infection. After 48 hours, the cells were dissociated from the well using Trypsin-EDTA solution and plated at less than 1 cell per 96-well in media containing 200µg/mL neomycin (Sigma Aldrich, N1876). 16 CMT93 monoclonal lines were expanded in total. To detect firefly luciferase activity, each monoclonal line was first collected and lysed with 2X Passive Lysis Buffer (Promega, E1941). The luminescence values of the cell lysates were then measured using Luciferase Assay Reagent II (LAR II; Promega, E1960) and the GloMax Discover Microplate Reader (Promega, GM3000) following the manufacturer's instruction. Monoclonal line 7 (M7) expressed the most luciferase and as such was chosen and tested for tumourigenicity *in vivo* (see 'Orthotopic mouse models of CRC' below).

Generation of AP mono8 HP2.3

Please refer to the methods in Appendix 8 [136] regarding the generation of the AP mono8 HP2.3 colorectal tumouroid line.

Generation of AKP mono7 HP1.7

The AKP mono7 tumouroid line was generated by Dr Susan Woods and the 50X concentrated retrovirus encoding SFG-NES-TGL was generated by Dr Josephine Wright; both are kept as frozen stocks at -80°C. AKP mono7 tumouroids were confirmed to have loss-of-function *Apc* and *Tp53* mutations using amplicon sequencing with the primers in Table 2.1. To examine *Kras* mutations, nested PCR was first performed to generate a *Kras*-containing amplicon using the primers in Table 2.2. Amplicon sequencing from the second PCR products was then performed to verify the $Kras^{G12D}$ mutation, using the primers in Table 2.3.

Table 2.1. Sequencing primers used to verify *Apc* and *Tp53* mutations in monoclonal AKP tumouroid lines

Primer	Sequence (5'→3')
Apc F	CTGAGACTTGCACATCGCAGCTTAATTCAGGCAAATCCTAAGAGAG
Apc R	GTGACCTATGAACTCAGGAGTCGGTCTGTTTGCCATGAGATTCC
Tp53 F	GTGACCTATGAACTCAGGAGTCTAGTGAGGTAGGGAGCGACTTC
Tp53 R	CTGAGACTTGCACATCGCAGCCCAAAGAGCGTTGGGCATGTG

F = forward primer, R = reverse primer. The overhang sequences are underlined.

Table 2.2. Primers to generate the *Kras*-containing amplicon from monoclonal AKP tumouroid lines

Primer	Sequence (5'→3')
(PCR) *Kras* F	CTTTATTGCAGAACTGCTCTGATGG
(PCR) *Kras* R	GGATGGCATCTTGGACCTTACTC

Table 2.3. Sequencing primers used to verify the $Kras^{G12D}$ mutation in monoclonal AKP tumouroid lines

Primer	Sequence (5'→3')
Kras F	GTGACCTATGAACTCAGGAGTCAGTTTTTGATAATCTTGTGTGAGAC
Kras R	CTGAGACTTGCACATCGCAGCAGCCTTGGAACTAAAGGACATC

The overhang sequences are underlined.

Prior to transduction, AKP mono7 tumouroids were first digested to single cells using TrypLE Express, filtered through a 40µm cell strainer (Merck, CLS431750) and plated at 20,000 cells/96-well in full selection AKP media (+EGFRi, +Nutlin-3a) minus antibiotics. 4µg/mL polybrene and 50µL of 10X concentrated SFG-NES-TGL retrovirus was then added per well and the plate was spin-infected at 600 *rcf* for 1 hour at room temperature. The plate was then incubated at 37°C for 4 hours. Tumouroid cells well then scratched off the bottom of the wells and plated in GFR Matrigel

(approximately 10,000 cells/dome) with full selection AKP media. The untransduced control was prepared in the same way as the transduced cells, except it was spin-infected with 50µL 1X PBS instead of virus. The tumouroids were then re-plated at low density and 15 tumouroids were handpicked using a P200 pipette, digested and then plated individually to generate 15 monoclonal lines. The firefly luciferase activity of each line (lysed in 2X Passive Lysis Buffer) was analysed using LARII and the GloMax Discover Microplate Reader. Monoclonal line 7 (HP1.7) expressed the most luciferase and as such was tested for tumourigenicity *in vivo* (see 'Orthotopic mouse models of CRC').

Generation of AKP mono7 CAS9^{-}GFP^{-}

The AKP mono7 and *Braf*^{V600E}ΔTRZI [17] colorectal tumouroid lines were first digested to single cells using TrypLE Express, washed in 1X PBS twice and resuspended in fluorescence activated cell sorting (FACS) buffer (2% FBS and 3% bovine serum albumin (BSA; Sigma-Aldrich, A9647) in 1X PBS) with 10µM Y-27632. Cells were then filtered through a 40µm cell strainer on top of a FACS tube (StemCell Technologies, 100-0087) and 1µL of 4'6-diamidino-2-phenylindole (DAPI) was added/tube. Single, live GFP^{high} AKP mono7 cells were then collected into 1mL Advanced DMEM/F-12 media with 10µM Y-27632 using the BD FACSAria Fusion Cell Sorter (BD Biosciences). Collected cells were washed in 1X PBS and plated in GFR Matrigel domes.

A midiprep of pCAG-Flpe (Addgene, 13787) clone #2 was made using the NucleoBond Xtra Midi kit (Takara, 740412). Prior to transfection, AKP mono7 GFP^{high} tumouroids were first digested to single cells using TrypLE Express, filtered through a 40µm cell strainer and plated at 40,000 cells/96-well in full selection AKP media minus antibiotics. The transfection mixture containing 50µL of OptiMEM (Thermo Fisher Scientific, 31985070), 1.4µL of LF2000 Transfection Reagent (Thermo Fisher Scientific, 11668019) and 0.5µg of pCAG-Flpe was then gently added to each well after incubation at room temperature for 20 minutes, and the plate was then incubated at 37°C for 4 hours. Tumouroid cells were then scratched off the bottom of the plates and plated in GFR Matrigel (approximately 8,000 cells/dome) with full selection AKP media. The untransfected control was prepared in the same way as the transfected cells except plasmid was not added to the transfection mixture. After 5 days, untransfected and transfected AKP mono7 GFP^{high} tumouroids were prepared for FACS as above and, using the untransfected cells to set the negative gate, single, live GFP^{-} cells were collected from the transfected population and plated in GFR Matrigel.

DNA was extracted from AKP mono7 GFP^{high} (CAS9^{+}) and AKP mono7 GFP^{-} (CAS9^{-}) tumouroids using the PureLink Genomic DNA Mini Kit (Thermo Fisher Scientific, K182002). Polymerase chain reaction (PCR) using the GoTaq Green Master Mix (Promega, M7122) was then run using the primers in Table 2.4 (Sigma-Aldrich) and the primer combinations in Table 3.2 (see Chapter 3) to amplify DNA across the *Cas9* sequence. PCR products were loaded onto a 1% agarose gel containing

0.4X GelRed (AdeLab Scientific, GTS41003) with the Quick-Load 100bp DNA Ladder (New England BioLabs, N0467S) and gel electrophoresis was run. PCR products were visualised using a Gel Doc XR+ Gel Documentation System (Bio-Rad).

Table 2.4. PCR primers used to validate *Cas9* excision in AKP mono7 GFP$^-$ tumouroids

Primer	Sequence (5'→3')
F1	CGTGCTGGTTATTGTGCTGTC
F2	ACCAGAGCAAGAACGGCTAC
R1	ACAGAGTTGGTGCCGATGTC
R2	GCAGTTCATTCAGGGCACCG
R3	ATCCGCTCGATGAAGCTCTG

AKP mono7 CAS9$^+$GFP^{high} and AKP mono7 CAS9$^-$GFP$^-$ tumouroids were also collected and lysed in RIPA buffer (150mM sodium chloride, 1% Triton X-100, 0.5% sodium deoxycholate, 0.1% sodium dodecyl sulfate (SDS) and 50mM Tris pH 8.0 in water) containing 1X cOmplete Protease Inhibitor Cocktail (Merck, 11697498001) and 1X PhosSTOP Phosphatase Inhibitor Cocktail (Merck, 4906845001). Sample protein concentrations were quantified via a Lowry Assay using the *DC* Protein Assay Kit II (Bio-Rad, 5000112) with BSA standards and was read on the VersaMax Microplate Reader (Molecular Devices). Samples of the same protein concentration and volume were loaded onto 4-20% Mini-PROTEAN TGX Stain-Free Protein Gels (Bio-Rad, 4568093) with Precision Plus Protein Dual Color Standards (Bio-Rad, 1610374) and SDS-PAGE was run. A Trans-Blot SD Semi-Dry Transfer Cell (Bio-Rad, 1703940) was then used to transfer the proteins from the gel to a Immun-Blot PVDF Membrane (Bio-Rad, 1620177). Ponceau S Stain (VWR, K793) was used to visualise transferred proteins. The blot was then blocked in 5% skim milk in PBST (1X PBS + 0.1% Tween20) and incubated with mouse monoclonal anti-CAS9 (1:1000; Cell Signaling Technology, 14697) or mouse monoclonal anti-β-actin (1:1000; Santa Cruz Biotechnology, sc-47778) antibodies overnight at 4℃. The blot was then washed in PBST and incubated with sheep anti-mouse horseradish peroxidase (HRP) secondary antibody (1:5000; Merck, NA9310) for an hour at room temperature, followed by more washes in PBST. The blot was then covered in Luminata Crescendo Western HRP substrate (Thermo Fisher Scientific, WBLUR0500) and CAS9 (163kDa) and β-actin (42kDa) bands were visualised using the Chemi-Doc MP Gel Imaging System (Bio-Rad).

RNA-sequencing from FACS-purified mouse colonic cells

Please refer to the methods in Appendix 4 regarding the extraction and running of RNA-sequencing samples.

Analysis of the Cancer Genome Atlas (TCGA) data

Please refer to the methods in Appendix 4 regarding the TCGA analysis of the top 342 RNA-sequencing candidates.

Extraction of primary mouse colon myofbs

Primary myofbs were extracted from mouse colons using a similar protocol previously described [134]. Briefly, mouse colons were longitudinally opened and left in 0.04% sodium hypochlorite solution in 1X PBS for 5 minutes at room temperature. Colons were then washed in 1X PBS and incubated in chelation buffer containing 3mM EDTA and 0.05mM 1,4-Dithiothreitol (DTT; Merck, 10708984001) in 1X PBS for 1 hour at room temperature. Colons were then serial-shaken in 1X PBS to release the crypts, until the PBS remained clear. Colons were then transferred to pre-warmed digestion mix containing 1mg/mL collagenase type IV (Thermo Fisher Scientific, 17104019), 125µg/mL dispase II (Thermo Fisher Scientific, 17105041), 25ng/mL DNase I (Merck, D4263) and 10µM Y-27632 in Advanced DMEM/F-12 media and incubated in a 37°C shaker for approximately 40 minutes. After further manual dissociation using a pipette controller, colons were spun and the pellet was resuspended in ACK Lysing Buffer (Thermo Fisher Scientific, A1049201) for a maximum of 10 minutes. During this time, the solution was passed through a 70µm cell strainer (Merck, CLS431751). Cells were then spun, resuspended in RPMI-5 and plated in 10cm cell culture plates (approximately $1x10^6$ cells/plate). The media was changed 24 hours later and approximately 1 week post-plating it is generally accepted that only myofbs continue to proliferate.

Confirmation of *Mcam* expression in mouse cell lines

Colon myofb samples were extracted and grown from mice as above (see 'Extraction of primary mouse colon myofbs'), while YH2, mouse colon CAF and mouse colon OU samples were grown from frozen laboratory stocks (NOTE: CAF samples contain epithelial contamination). Samples were collected in 1mL TRIzol Reagent (Thermo Fisher Scientific, 15596018) with 200µL of chloroform and spun at 13,000 *rcf* for 15 minutes at 4°C. Approximately 500µL of the clear aqueous phase was collected per sample, to which 500µL of cold propanol was added. 10ng/mL of glycogen (Thermo Fisher Scientific, 10814010) was then added to each sample and was precipitated overnight at -80°C. Defrosted samples were then spun at 13,000 *rcf* for 15 minutes at 4°C. The white RNA pellets were then washed twice with 80% ethanol, with a spin at 13,000 *rcf* for 5 minutes at 4°C between each wash. The RNA was dissolved in nuclease-free water once the ethanol had evaporated. Embryonic day 15 RNA was already made and kept in the -80°C freezer. cDNA was then made from each sample using the SuperScript IV First-Strand Synthesis System (Thermo Fisher Scientific, 18091200) and the Veriti 96-well Thermal Cycler (Thermo Fisher Scientific, 4375786). Primers binding *Gapdh* and *Mcam* (Table 2.5) were designed using the Primer-BLAST online program [137] and were ordered from IDT and Sigma-Aldrich respectively. These primers were then reconstituted to 100µM using 1X TE buffer (pH 8.0; IDT, 11-05-01-13). Using the KAPA SYBR FAST qPCR Master Mix Kit

with ROX Low Reference Dye (KAPA Biosystems, KK4602), samples were run in a QuantStudio 7 Real-Time PCR System (Thermo Fisher Scientific). The data was analysed using the 2-ΔΔCt method and normalised to *Gapdh* expression levels.

Table: 2.5: Sequences for *Mcam* and *Gapdh* SYBR Green qPCR primers

Gene name	F primer sequence (5'→3')	R primer sequence (5'→3')
Gapdh	CCTCGTCCCGTAGACAAAATG	TGTAGTTGAGGTCAATGAAGGG
Mcam	GCCCTTGCAAGAGGAGGAGAA	ACTAGGCGTGCACTCAGAACA

Generation of pUltra_*Mcam*

Midipreps of pUltra (Addgene, 24129) and pCMV3-mMCAM (Sino Biological, MG50794-UT) were made using the NucleoBond Xtra Midi kit. pUltra was verified via BbsI restriction enzyme digest (New England BioLabs, R0539) followed by gel electrophoresis on a 1% agarose gel with Quick-Load 1kb DNA ladder (New England BioLabs, N0468) to confirm the size of digested products, while the *Mcam* sequence in pCMV3-mMCAM was verified via Sanger sequencing by the Australian Genome Research Facility (AGFR) using the primers in Table 2.6. To generate pUltra_*Mcam*, pUltra was first linearised using BamHI-HF (New England BioLabs, R3136) and the pUltra_*Mcam* amplicon was amplified via PCR using the PrimeSTAR Max DNA Polymerase (Takara, R045B), primers in Table 2.7 and the Veriti 96-well Thermal Cycler. Linearised pUltra and the pUltra_*Mcam* amplicon were then loaded onto a 1% agarose gel and gel electrophoresis was run. DNA was purified from the gel bands using the NucleoSpin Gel and PCR Clean-up kit (Takara, 740609) and run again on a 1% agarose gel to confirm purity and determine DNA concentration. 30ng of linearised pUltra and 80ng of the pUltra_*Mcam* amplicon were then ligated using the In-Fusion HD Cloning Kit (Clontech, 639649) as per manufacturer's instructions. Stellar Competent Cells (Clontech, 636763) were then transformed with 5µL of the In-Fusion mix as per manufacturer's instruction and spread onto agar plates containing 1X ampicillin. Midipreps from 6 colonies were generated using the NucleoBond Xtra Midi kit. Each clone was digested with BsmBI (New England BioLabs, R0580) and SpeI-HF (New England BioLabs, R3133) restriction enzymes and run on a 1% agarose gel to confirm *Mcam* insertion into pUltra. pUltra_*Mcam* clones #1 and #4 were sent for Sanger sequencing by the AGFR using the primers in Table 2.8.

Table 2.6: Primers used for Sanger sequencing of pCMV3-mMCAM

Primer	Sequence (5'-3')
pCMV3-F	CAGGTGTCCACTCCCAGGTCCAAG
pcDNA3-R	GGCAACTAGAAGGCACAGTCGAGG
Mcam CDS primer 1	ACTATTCAAGCCAATGTCGTGGGCATC
Mcam CDS primer 2	TTGGAGCCTGCCGAAAAGCACCATAG
Mcam CDS primer 3	ATGGAACCCAGATCCACAGACAGTAGTGA

Table 2.7: Primers to generate the pUltra_*Mcam* amplicon

Primer	Sequence (5'-3')
pUltra_Mcam-F	GCCTTCTAGAGGATCCATGGGGCTGCCCAAACTGG
pUltra_Mcam-R	CGCCGGAGCCGGATCCCTAATGCCTCAGAT

Table 2.8: Primers used for Sanger sequencing of pUltra_*Mcam*

Primer	Sequence (5'-3')
pUltra-F(up)	GCCGACAAGCAGAAGAACGGCATC
pUltra-R	GTCGACGACTCCGGAACGAATTCTGA

Generation of *Mcam*-overexpressing YH2 cells and primary myofbs

A transfection mixture containing 1mL OptiMEM, 30µL LF2000 Transfection Reagent, 6µg psPAX2 (Addgene, 12260), 6µg pCMV-VSV-G (Addgene, 8454) and 5µg pUltra (control GFP) or pUltra_*Mcam* clone #1 was gently added to a 70-90% confluent monolayer of 293FT cells grown in DMEM media (no antibiotics), after incubation at room temperature for 20 minutes. After 48 hours, 10mL of the control or pUltra_*Mcam* lentivirus-containing media was filtered through a 0.45µm PVDF membrane (Merck Millipore, SLHV033R). The YH2 cells and primary myofbs to be transduced were grown in 6-well plates and were 90% confluent at the time of transduction. For YH2 cells, the DMEM media was replaced with 2mL of neat lentivirus-containing media/well. For primary myofbs, the neat virus was concentrated approximately 40X using an Amicon Ultra-4 Centrifugal Filter Unit (Merck, UFC800308) and added to 2mL of RPMI-5 media (no antibiotics)/well. For both cell types, 4µg/mL of polybrene was also added to each well and the plates were spin-infected at 1700 *rpm* for 1 hour at room temperature.

3 days post-transduction, YH2 cells were digested to single cells using Trypsin-EDTA solution and prepared for FACS extraction of GFP^+ cells as above (see 'Generation of AKP mono7 $CAS9^-GFP^-$'), except cells were collected into FACS buffer with 10µM Y-27632. Once the cells had recovered they were re-sorted for GFP^{Hi} cells. Western blot was then undertaken as above (see 'Generation of AKP mono7 $CAS9^-GFP^-$'), using the following antibodies: rabbit monoclonal anti-MCAM (1:1000;

Abcam, ab75769), mouse monoclonal anti-β-actin (1:1000; Santa Cruz Biotechnology, sc-47778), donkey anti-rabbit HRP (1:10,000; Merck, NA9340) and sheep anti-mouse HRP (1:5000; Merck, NA9310). MCAM (113kDa) overexpression was confirmed in the MCAM GFP^{Hi} YH2 line.

For primary myofbs, a western blot was first undertaken on transduced, unsorted cells as above. Cells were then prepared for FACS extraction of GFP^{+} cells as above, except the cells were collected into FACS buffer with 50% FBS and plated into 6-wells pre-coated with 100ug/ml PureCol Type I Collagen Solution (Advanced BioMatrix, 5005) for 1.5-2 hours and then washed with 1X PBS. Some cells were then collected and lysed using TRIzol Reagent and RNA extraction, cDNA generation and qPCR analysis for *Mcam* expression was undertaken as above (see 'Confirmation of *Mcam* expression in mouse cell lines'). The primary mouse colon myofbs were transduced at passage 3, FACS sorted at passage 6 and used in all the *in vitro* assays below from passages 8-18.

Generation and validation of the *Mcam*$^{-/-}$ mouse

The *Mcam*$^{-/-}$ mouse line was generated by the South Australian Genome Editing Facility (SAGE), where exons 2-4 of *Mcam* were excised (see Chapter 4). *Mcam*$^{+/-}$ males were backcrossed two generations to SAHMRI C57BL/6J females prior to use in *in vitro* and *in vivo* experiments. Breeding for *Mcam*$^{+/+}$ and *Mcam*$^{-/-}$ mice was consistently maintained through *Mcam*$^{+/-}$ x *Mcam*$^{+/-}$ crosses and expected genotype frequencies were observed. There was no embryonic lethality or abnormalities observed in *Mcam*$^{-/-}$ mice. For genotyping, Mr Tongtong Wang optimised the primers shown in Table 2.9 (generated through Sigma-Aldrich) and these are now used by the Garvan Institute of Medical Research to genotype our *Mcam* colony. For more information regarding animals, animal housing and ethics, see the 'Mouse experiments' section below.

Table 2.9. Genotyping primers used for the *Mcam* colony

Primer	Sequence (5'-3')
WT-R	TTACCCTCTCCTTACCCTCAACTTC
KO-F	GCACATGCCTTACATTCCCC
KO-R	TGACTTACTCAGCATCACCTGT

Kidney and spleen tissues were collected from *Mcam*$^{+/+}$ and *Mcam*$^{-/-}$ mice and either homogenised in TRIzol Reagent using a tissue homogeniser or formalin-fixed for analysis of MCAM protein expression (see 'IHC and IF'). Primary colon myofbs were also extracted from *Mcam*$^{+/+}$ and *Mcam*$^{-/-}$ mice (see 'Extraction of primary mouse colon myofbs') and some cells were also lysed in TRIzol Reagent. RNA extraction and cDNA generation from all TRIzol samples was undertaken as above (see 'Confirmation of *Mcam* expression in mouse cell lines'). For the qPCR analysis of *Mcam* expression, new *Mcam* primer-probes were designed to bind exons 3 and 4 of *Mcam* (generated

through IDT; Table 2.10). Using the KAPA PROBE FAST qPCR Master Mix Kit with ROX Low Reference Dye (KAPA Biosystems, KK4703), samples were run in a QuantStudio 7 Real-Time PCR System. The data was analysed using the 2-ΔΔCt method and normalised to *Gapdh* expression levels, where mouse *Gapdh* primer-probes were pre-designed by IDT (Mm.PT.39a.1). Primary myofbs from *Mcam*$^{+/+}$ and *Mcam*$^{-/-}$ mice were used in all the *in vitro* assays below from passages 8-18.

Table 2.10: Sequence for custom-designed *Mcam* primer-probes

***Mcam* primer-probe sequence (5'→3')**	F: GAGCGAATGTTCCTGTGTAAGA
	R: GGCTTGAATAGTTGGTTCCTCT

qPCR screen in primary mouse colon myofbs

RNA extraction, cDNA generation and SYBR Green qPCR analyses were undertaken on primary colon myofb samples as above (see 'Confirmation of *Mcam* expression in mouse cell lines') using the primers detailed in both Table 2.5 and Table 2.11. Dr Tamsin Lannagan and Mr Tongtong Wang designed and optimised 37 primers in Table 2.11 (generated through IDT). *Vcam1* primers (generated through Sigma-Aldrich) were generously provided by Dr Krzysztof Mrozik from SAHMRI. I designed the remaining 10 primers (generated through Sigma-Aldrich).

Table 2.11: Sequences for additional SYBR Green primers used in the qPCR screen

Gene name	F primer sequence (5'→3')	R primer sequence (5'→3')
Acta2	CTCTTCCAGCCATCTTTCATTG	AATGCCTGGGTACATGGTG
Bmp4	ATTGCAGCTTTCTAGAGGTCC	GGGAGCCAATCTTGAACAAAC
Ccl5	GTGCCCACGTCAAGGAGTAT	TCTGGGTTGGCACACACTTG
Col1α1	AGCCGCAAAGAGTCTACATG	CTTAGGCCATTGTGTATGCAG
Col3α1	CCACTCTTATTTTGGCACAGC	TCATCGCAAAGGACAGATCC
Cox2	CCTCTGCGATGCTCTTCCGA	TCCCCACGGTTTTGACATGGA
Cxcl1	AGCCACACTCAAGAATGGTCG	TTCTCCGTTACTTGGGGACACC
Cxcl12	CTCCAAACTGTGCCCTTCAGA	TGAGCCTCTTGTTTAAAGCTTTCTC
Dcn	ACATAACTGCGATCCCTCAAG	GATGCTGTTGAAGCTCAATCC
Des	AAGATGGCCTTGGATGTGG	ACTTCAGAACCCCTTTGCTC
Egf	AGAAACACCAAGACCCCAAG	TGTGCCCATTCCATCTATGTG
Fap	CCAAAGAACCAGGAGCATGTAG	GTTTGTAACCATCCTTGTCGC
Fn1	AGAGCTATCCATTTCACCTTCAG	ACCTGTTTTCTGCCTTCCC
Grem1	GCTCTCCTTCGTCTTCCTC	AGTGTATGCGGTGCGATTC
Grem2	AGGCTTCCATCTCGTCATTG	TCTTCCGTGTTTCAGCTACC
Gsk3β	CGACCGAGAACCACCTCCTT	ACTGTGGTTACCTTGCTGCC
Hgf	CTACACTCTTGACCCTGACAC	TAACCTTCTCCTTGGCCTTG
Hspg2	CTCGAGGTGGAAGAGTGTCG	GCCGTTGCATTCACACAACT

Il-6	CCACTTCACAAGTCGGAGGCTTA	GCAAGTGCATCATCGTTGTTCAT
LepR	GACTTGCAGATGGTCACCCA	TGGGCTCAGACGTAGGATGA
Mmp2	ACGATGATGACCGGAAGTGG	GTGTAGATCGGGGCCATCAG
Mmp9	CGCCACCACAGCCAACTATGA	ACGAAGGGGAAGACGCACAG
Myc	TGCTGCATGAGGAGACACCG	CGACCTCTTGGCAGGGGTTT
Nanog	CAGTGGTTGAAGACTAGCAATGGT	GGCTTCCAGATGCGTTCACC
Nes	AGGGTCTACAGAGTCAGATCG	TGTCTGCAAGCGAGAGTTC
Nfκb1	AGGCCATTGAAGTGATCCAG	CTGTCACTATCCCGGAGTTC
Nid1	GGATGAAGTAGAGGAAACAGGAG	GCAGAAGCCAGTAGCATAGTC
Pdgfb	CACTCCATCCGCTCCTTTG	AGATGAGCTTTCCAACTCGAC
Pdgfrα	TGAAGGTGGCTGTGAAGATG	TGTAAATGGGACCTGACTTGG
Pdgfrβ	CATGGGTGGAGATTCGCAGG	GGATCTCATAGCGTGGCTTCT
Pdpn	GGAGGGCTTAATGAATCTACTGG	GGTTGTACTCTCGTGTTCTCTG
Postn	CTGAAGCCAGATGGAGAGTAC	CCATTGTAGAGGTCGCTAAGG
Ptgs2	CCAGCACTTCACCCATCAG	GTCCAGAGTTTCACCATAAATGTG
Rspo1	CAACCCCGACATGAACAAATG	CACTTGGTGCAGAAGTTGTG
Rspo2	GCCAGCAAAAGACACAATACC	AATCAGCTTCCGCCTCTTC
Rspo3	CAACCAGCGAGACAAGAACT	TCCAAACCTTTGCTGTCAGAG
S100a4	CTCTATTCAGCACTTCCTCTCTC	TGAGCTCTGTCTTGTTCAGC
Sparc	CTTCAGACCGCCAGAACTC	GAAGATCCAGGCCCTCATG
Tagln	GGCCTTTAAACCCCTCACCCAG	TTGTTGGCCATGTTGAGGCA
Tgfβ1	CTATGCTAAAGAGGTCACCCG	ACTGCTTCCCGAATGTCTG
Tgfβ2	TCCCGAATAAAAGCGAAGAGC	AACATTAGCAGGAGATGTGGG
Tgfβ3	TCGGAGTCTGAGTACTATGCC	CACTGAGGACACATTGAAACG
Tnc	CAGAGAAAGGACAGCAGAAGAG	GTATCCAGTGACCGATGCTC
Vcam1	ATTTTCTGGGGCAGGAAGTT	ACGTCAGAACAACCGAATCC
Vegfa	TGGCTTTGTTCTGTCTTTCTTTGG	ATGCGGATCAAACCTCACCA
Vim	TCAGCTCACCAACGACAAG	ACATCCTGTCTGAATGACTGC
Wnt2	GTAGATGCCAAGGAGAGGAAAG	CCAGCATGTCCTCAGAGTAC
Wnt5a	AAAGGGAACGAATCCACGCT	GGAGCCAGACACTCCATGAC

Proliferation assays

Primary myofbs were plated at 1000 cells/well in 96-well white assay tissue culture plates. 1.5 hours post-plating, cells were examined for viability at time (t) = 0 hours via the CellTiter-Glo Luminescent Cell Viability Assay (Promega, G7571) and the GloMax Discover Microplate Reader. Viability readings were also taken at t = 24, 48 and 72 hours post-plating. Each reading was divided by the average of readings taken at t = 0 hours, to give a proliferation fold change. Cells at each time point were examined in quadruplicate, and in three independent experiments.

Collagen contraction assays

For YH2 cells, each collagen gel mix contained $3x10^5$ cells resuspended in 400µL DMEM media with 200µL of 3mg/mL PureCol Type I Collagen Solution and 3µL of 1M sodium hydroxide (Sigma-Aldrich, S2770). 500µL of this mix was plated per 24-well and was allowed to polymerise for 20 minutes at room temperature. 600µL of DMEM media supplemented with 10% FBS, L-glutamine and penicillin/streptomycin was added per well, and gels were released from the wells using a pipette tip. Gels were imaged at t = 0, 24, 48 and 72 hours post-plating and the gel area was measured with ImageJ software (National Institutes of Health). The proportion of gel contraction at each time point compared to the size at t = 0 hours was then calculated.

For primary myofbs the method was almost identical, except the collagen mix contained $1x10^5$ cells resuspended in 400µL RPMI-5 media with 200µL of 3mg/mL PureCol Type I Collagen Solution and 5µL of 1M sodium hydroxide. 600µL of RPMI-5 media was also added per well.

As a positive control for contraction, $1.5x10^5$ MSCs per gel were used; as a negative control, gels were made with media only (no cells). Four gels were made using each YH2/myofb line per experiment, and each line was examined in 3 independent experiments. All cells were 80-90% confluent at the time of collection for these experiments.

Colony forming unit-fibroblast (CFU-F) assays

For YH2 cells, 400 cells were grown in 10mL DMEM supplemented with 10% FBS, L-glutamine and penicillin/streptomycin (per 10cm cell culture plate) for 10 days; 3 plates per experiment, 3 independent experiments. For primary myofbs, the 10cm plates were first pre-coated in 100ug/ml PureCol Type I Collagen Solution for 1.5-2 hours and then washed with 1X PBS, prior to seeding 800 cells in 10mL RPMI-5 (per plate). The primary myofb cultures were then grown for 14-18 days; 4 plates per experiment, 3 independent experiments. Media was changed on all plates at 7 days post-plating. When the YH2 cells and myofbs were collected, they were gently washed with 1X PBS and then stained in toluidine blue solution (0.1% Toluidine Blue in 2.4% neutral buffered formalin and 1X PBS). Colonies greater than 1mm in diameter were counted.

Wound healing assays

Scratch assays were undertaken as previously described [138]. Briefly, primary myofbs in 6-wells were grown to 95% confluency before washing in 1X PBS and adding serum starve media (RPMI-5 with 0.5% FBS) for 24 hours. After 24 hours, 3 vertical scratches were made per well using a P200 pipette tip and 4 horizontal lines were drawn in permanent marker on the base of the plate. The media was also replaced with fresh serum starve media. The scratch above each horizontal line was imaged at t = 0 and 15 hours post-scratch, giving 12 images/well at each time point. However, the scratch width was only analysed using ImageJ software in 10 identical locations between the two time points (5

width measurements/image). The percentage of wound closure was then calculated by dividing each scratch width measurement at t = 15 hours with the average of its corresponding scratch width at t = 0 hours, multiplied by 100%. This answer was then subtracted from 100%. Each myofibroblast line was assessed in 3 independent experiments.

Mouse colon OU/tumouroid viability assays

Normal mouse colon OUs (tdTomato$^+$luciferase$^+$, made by Dr Mari Ichinose) and AP mono7 HP2.3 tumouroids were digested to cell clusters using TrypLE Express. 100 OU or 50 AP clusters were then resuspended with 15,000 YH2 cells or 12,000 primary myofbs in 100µL 50% GFR Matrigel (diluted in cold Advanced DMEM/F-12 media), per 96-well. 500uL of OU or AP media was gently added after the GFR Matrigel had set for 20 minutes. The co-culture set-up is shown in Fig 4.12C (Chapter 4). OU and AP co-cultures were cultured for 6 or 5 days post-plating, respectively, with a media change at day 3. Wells were collected in cold 1X PBS and briefly digested in TrypLE Express before lysing in 2X Passive Lysis Buffer. The luminescent viability readout was then quantified using LARII and the GloMax Discover Microplate Reader.

Human tissues

Please refer to Appendix 4 regarding human CRC sample collection and ethics. Paraffin-embedded sections with differing grades of CRC were generously provided by Dr Mark Bettington from Envoi Pathology and the paraffin-embedded tissue microarray with associated clinical data was generously provided by Sonja Klebe from SA Pathology. All samples were de-identified.

Antibodies for use in immunohistochemistry (IHC) and immunofluorescence (IF)

The following primary antibodies were used in this study: rabbit monoclonal anti-MCAM (1:500; Abcam, ab75769), mouse monoclonal anti-COX4i2 (1:100; Novus Biological, H00084701-M01), rabbit polyclonal anti-GJA4 (1:50; Thermo Fisher Scientific, 42-4400), rabbit polyclonal anti-NGFR (1:1500; Abcam, ab8874), rabbit polyclonal anti-NOTCH3 (1:2000; Abcam, ab23426), rabbit polyclonal anti-SOX2 (1:250; Abcam, ab97959), rat monoclonal anti-BrdU (1:600; Abcam, ab6326), rat monoclonal anti-CD31 (1:50; Dianova, DIA-310), mouse monoclonal anti-ACTA2 (1:500; Agilent, M0851), rat monoclonal anti-CD45-FITC (1:50; BioLegend, 103108), rat monoclonal anti-EPCAM (1:100; eBioscience, 14-5791-81), rabbit monoclonal anti-Ki67 (1:600; Abcam ab16667), rabbit polyclonal anti-γH2AX (1:3000; Abcam, ab11174), rabbit polyclonal anti-phospho SMAD1/SMAD5/SMAD8 (Ser463/465) (i.e. pSMAD1/5/8, 1:100: Merck Millipore, AB3848-I). The following secondary antibodies were used in this study: goat polyclonal anti-rabbit HRP (1:400; Thermo Fisher Scientific, A24537), goat polyclonal anti-rabbit HRP polymer (1:3; Abcam, ab214880), goat polyclonal anti-mouse HRP (1:400; Thermo Fisher Scientific, A24512), goat polyclonal anti-rabbit Alexa Fluor (AF)-488 (1:400; Thermo Fisher Scientific, A-11008), goat polyclonal anti-rabbit AF-594 (1:400; Thermo Fisher Scientific, A-11012), goat polyclonal anti-rat

AF-647 polyclonal secondary (1:400; Thermo Fisher Scientific, A-21247), goat polyclonal anti-rat AF-488 (1:400; Thermo Fisher Scientific, A-11006), polyclonal goat anti-mouse AF-647 (1:400; Thermo Fisher Scientific, A-21235).

IHC and IF

Mouse tissues were fixed in 10% neutral buffered formalin solution (Sigma-Aldrich, HT501128) overnight followed by dehydration with 70% ethanol and paraffin-embedding. Paraffin-embedded tissues were cut into 5µm sections using a rotary microtome (Thermo Fisher Scientific, HM 325) and adhered onto SuperFrost Ultra Plus glass slides (Thermo Fisher Scientific, J3800AMNZ). Cut sections of paraformaldehyde-fixed mouse tissues for use in IF were used from -80°C storage. Formalin-fixed and paraffin-embedded tissue sections were deparaffinised with xylene and rehydrated with water, followed by antigen retrieval by boiling samples in a decloaker either with pH 6.0 Antigen Unmasking Solution (Vector Laboratories, H-3300) or pH 9.0 Antigen Retrieval Solution (for pSMAD1/5/8 staining; Thermo Fisher Scientific, 00-4956-58).

For IHC, inactivation of endogenous peroxidase was performed with 0.5% H_2O_2 in methanol for 30 minutes, followed by washes with 1X PBS. Sections were then blocked in either 1:10 Serum-Free Protein Block (Agilent, X0909) in 1X PBS (for MCAM, COX4i2 and Ki67 staining), 1:10 Serum-Free Protein Block with 1% BSA in PBST (for NGFR staining), 1:10 Serum-Free Protein Block with 2% BSA in PBST (for NOTCH3 and γH2AX staining), 1:10 Serum-Free Protein Block with 3% BSA in PBST (for pSMAD1/5/8 staining), 1:10 Serum-Free Protein Block with 4% BSA in PBST (for GJA4 staining), or 1:10 Serum-Free Protein Block with 2% BSA and 0.1% Triton X-100 in PBST (for SOX2 staining). Sections were incubated with the indicated primary antibodies overnight at 4°C and washed with PBS or PBST. Sections were then incubated with HRP-conjugated secondary antibody for 1 hour (for Thermo Fisher Scientific A24537 and A24512) or 30 minutes (for Abcam ab214880) at room temperature, followed by further PBS/PBST washes and signal detection with diaminobenzidine (DAB) solution (Agilent, K346811-2). Sections were then stained with Mayer's Hematoxylin Solution (Sigma-Aldrich, MHS32) for 17 minutes, followed by dehydration in 100% ethanol and xylene and mounting using DPX Mountant for Histology (Sigma-Aldrich, 06522). Slides were then scanned by the Pannoramic 250 Flash II (3DHistech) and uploaded onto CaseViewer software, from which 40X images were saved. Positive (brown) cells were then either manually counted using ImageJ software or, in the case of the pSMAD1/5/8 IHC, counted in FIJI software (ImageJ) using a script designed by Dr Hiroki Kobayashi (please refer to the methods in Appendix 8 [136]).

For IF, sections were blocked in 1:10 Serum-Free Protein Block in 1X PBS (for MCAM, BrdU, CD31, ACTA2, CD45 and EPCAM staining). Sections were then incubated with the indicated primary antibodies overnight at 4°C and washed with PBS or PBST. Sections were then incubated

with fluorescent-conjugated secondary antibodies for 1 hour at room temperature. The sections were then mounted with ProLong Gold Antifade reagent containing DAPI (Thermo Fisher Scientific, P36931). Fluorescence was examined using a confocal laser-scanning microscope (TCS SP8 MP, Leica), with further colour optimisation of images using FIJI software. Fluorescence overlap was quantified manually.

In all histopathological quantification using the normal colorectal tissues in human and mouse, only lamina propria regions were evaluated.

Hematoxylin and eosin (H&E) staining

Slides containing mouse and human formalin-fixed tissue sections were stained with H&E by the pathology core in the Adelaide Health and Medical Sciences (AHMS) building. Slides were then scanned by the Pannoramic 250 Flash II and uploaded onto CaseViewer software, which was used to examine pathology and calculate tumour area.

Mouse experiments

Animals were obtained from the SAHMRI Bioresources facility and housed under pathogen-free conditions. The facility maintains NSG and C57BL/6J mice from The Jackson Laboratory. Rosa26-Cas9 knockin mice, referred to in this thesis as "Cas9" mice, were purchased from The Jackson Laboratory (stock #024858) and were re-derived into C57BL/6J mice in the SAHMRI facility. These mice have a mixed background of 129, C57BL/6N, FVB/N and C57BL/6J, making them more than 75% C57BL/6 background. Cas9 males were then backcrossed 5 generations to SAHMRI C57BL/6 females, producing "Cas9 BX" mice. *Mcam*$^{-/-}$ mice were generated as above (see 'Generation and validation of the *Mcam*$^{-/-}$ mouse') and maintained in the facility. A Clinical Record Sheet was used to determine humane end point. One point was given for the presence of each of the following observations: weight loss >15%, hunched/ruffled coat, dehydration, absence of movement, facial grimace, inability to pass stool (for primary CRC mice), lack of warmth/pale complexion (for hepatic metastatic CRC mice). Once a score of 3 was reached the mice were humanely euthanised via carbon dioxide asphyxiation. In all experiments, sample sizes were determined based on pilot experiments and sample availability. All animal studies were approved by the SAHMRI Animal Ethics Committee (SAM174, SAM322, SAM387.19).

AOM/DSS mouse model of primary CRC

Please refer to the methods in Appendix 4.

Mouse models of primary CRC via colonoscopy-guided cell implantation

CRC cell line monolayers were digested using Trypsin-EDTA solution. Cells were then washed twice in cold 1X PBS supplemented with 10μM Y-27632 and counted. The desired cell number was

then resuspended in 10% GFR Matrigel, 1:1000 Indian Ink (Royal Talens, 44727000) and 10µM Y-27632 in 1X PBS. Each animal received 2x20µL injections of the desired cell number. For the CMT93 M7 pilot, $1x10^6$, $2x10^6$ or $3.8x10^6$ cells were implanted/injection into C57BL/6 mice (n=2/group) and $1x10^6$ cells were implanted/injection into a NSG mouse (n=1). For the MC38 tdTomato$^+$luciferase$^+$ pilot, $1x10^5$, $2.5x10^5$ or $5x10^5$ cells were implanted/injection into C57BL/6 mice (n=3/group). For the MC38 tdTomato$^+$luciferase$^+$ experiment into *Mcam*$^{+/+}$ and *Mcam*$^{-/-}$ mice (n=2 mice/group), $5x10^5$ cells were implanted/injection.

Tumouroids were isolated from GFR Matrigel and dissociated into single cells and small clusters using TrypLE Express. Cell clusters (equivalent to approximately 150 whole tumouroids/injection) were then washed twice in cold 1X PBS supplemented with 10µM Y-27632 and clusters containing more than 3 cells were counted. The digested tumouroids were then resuspended in 10% GFR Matrigel, 1:1000 Indian Ink and 10µM Y-27632 in 1X PBS. Each animal received 2x20µL injections. For the pilot using AKP tumouroids from the Roper laboratory [20], approximately 2,300 clusters were implanted/injection into a NSG mouse (n=1) and C57BL/6 mice (n=5). For the pilot using AKP mono7 HP1.7 tumouroids, approximately 3,500 clusters were implanted/injection into NSG (n=3 males, n=2 females), Cas9 BX (n=3 males, n=2 females) and C57BL/6 (n=6 males, n=3 females) mice. For the pilot using AKP mono7 CAS9$^+$GFP^{high} and CAS9$^-$GFP$^-$ tumouroids, approximately 5,300-5,500 clusters were implanted/injection into NSG (n=1 male for the CAS9$^+$GFP$^+$ line, n=1 male and n=1 female for the CAS9$^-$GFP$^-$ line), Cas9 BX (n=3 males/group, n=2 females/group) and C57BL/6 (n=3 males/group, n=2 females/group) mice. All tumouroids were grown in full selection media prior to collection for injection.

The colonoscopy-guided orthotopic injection of CRC cell lines or tumouroids into the distal colon wall was undertaken in anaesthetised mice (8-24 weeks old) on a heat pad as previously described [17], except only two injections of 20µL were performed per animal. Either Mr Tongtong Wang or Dr Laura Vrbanac assisted with the injections. Tumour growth was monitored at the injection sites weekly via colonoscopy, with tumour scoring as previously described using the Becker scale [139]. Once animals reached a grade 4 tumour or above, they were given daily powdered food soaked in water with a few drops of Coloxyl Infant Drops diluted 1:10 (in water).

Mouse model of hepatic metastatic CRC

AP mono8 HP2.3 tumouroids grown in full selection media were digested to single cells using harsh TrypLE Express digestion with 10µM Y-27632. Single cells were then resuspended in 1X PBS, filtered through a 40µm cell strainer and counted. $5x10^5$ single cells were then resuspended in 100µL of 1X PBS with 10µM Y-27632, per injection. Each animal received 1x100µL injection.

Injection of single tumouroid cells into the liver via the portal vein was undertaken as previously described [(140)], with modifications. Briefly, mice were anaesthetised, placed onto a heat pad covered with sterile cloth and given 100µg/kg buprenorphine subcutaneously. The area between the sternum and the hips was then shaved and sterilised using alternating wipes with Betadine Antiseptic Solution and 80% ethanol (3 wipes each). A 2-3cm incision was then made from the sternum down, first through the skin layer and then through the peritoneal wall. The intestines were then gently pushed out through the incision onto sterile gauze swabs that had been pre-wet with 1X PBS, using a sterile cotton bud, until the portal vein was visible. The intestines were then covered with more wet gauze swabs to prevent drying. The TSK Low Dead Space Hub BoNT 33G Needle (Precise Medical Supplies, TSK LDS-33009) attached to a Hamilton syringe (Hamilton, CAL80630) was then inserted at a 5-10 degree angle into the portal vein and 100uL of the tumouroid suspension was slowly injected to prevent cell shearing. The needle was then swiftly replaced with a sterile cotton bud and pressure was applied at the injection site for 5-15 minutes to stop the bleeding. Once the bleeding had ceased, a 0.5x0.5cm piece of sterile Gelfoam absorbable gelatin sponge (McFarlane, 16227UP) was placed on the injection site to further seal the wound. A few drops of PBS was then added to the intestines, which were then gently pushed back into the cavity using a clean sterile cotton bud. The peritoneal wall was then closed using 4/0 vicryl-coated sutures (McFarlane, 15040ET) and the skin was closed using Wound Clips (Thermo Fisher Scientific, 01-804-5) with a Wound Clip Applier (Thermo Fisher Scientific, 01-804). Betadine Antiseptic Solution was applied to the closed incision after surgery and each day following for approximately 3 days. 100µg/kg buprenorphine was also administered subcutaneously 24 hours post-surgery. The wound clips were removed approximately 6-7 days later using a Wound Clip Remover (Thermo Fisher Scientific, 01-804-15). All surgical equipment used was autoclaved and sterilised with 80% ethanol between each animal. Cloth, cotton buds, gauze swabs and the Gelfoam sponge were also autoclaved prior to use.

IVIS bioluminescence imaging

D-luciferin (Biosynth, L-8220) was dissolved in cold 1X PBS to a concentration of 30mg/mL and filtered through a syringe filter unit with 0.22µm PVDF membrane (Merck Millipore, SLGV033RB) prior to aliquoting and freezing at -20°C. Prior to imaging, mice containing firefly luciferase^{+} tumours were shaved either from the sternum down to the anus (for primary CRC mice) or from the neck down to the hip on the right-hand side (for hepatic metastatic CRC mice) to allow luminescence signal to be detected. Shaved animals were given 100µL D-luciferin via intraperitoneal injection (approximately 150mg/kg per mouse). They were then anaesthetised and placed into a Xenogen IVIS Spectrum In Vivo Imaging System (Perkin Elmer Inc), either lying on their back with stomach facing upwards (for primary CRC mice) or on their left-hand side with right-hand side facing upwards (for hepatic metastatic CRC mice). Luminescence was detected using an automatic exposure setting and luciferase activity was quantified using Living Image software (Perkin Elmer Inc). The stage was

used as the background luminescence measurement and was subtracted from the measurements of all the mice.

FOLFOX chemotherapy pilot

AP mono8 HP2.3 single tumouroid cells were prepared and injected into the portal vein of 8-52-week old Cas9 mice as above (see 'Portal vein mouse model of hepatic metastatic CRC'). Mice either remained untreated or were administered a FOLFOX dosing regimen used previously [141-144] from 1 or 3 weeks post-tumouroid injection (n=3 males and n=3 females per group). This FOLFOX regimen was given once weekly via a single intraperitoneal injection and consisted of 50mg/kg 5-FU, 6mg/kg OX and 90mg/kg LV. 5-FU (Merck, F6627) was reconstituted in DMSO to a concentration of 100mg/mL, which was then further diluted to 10mg/mL in 1X PBS and aliquoted and stored at -80°C. 5mg/mL and 10mg/mL stocks of OX and LV respectively were obtained by Dr Susan Woods from a hospital pharmacy; they were kept at room temperature and 4°C, respectively. FOLFOX treatment was stopped at 8 weeks post-tumouroid injection.

GREM1 NAb studies

For the primary CRC model, 8-52-week old Cas9 mice were first treated for 2 weeks with either IgG control antibody (Ab; n=5 males, n=4 females) (Ab101.4) or GREM1 NAb (n=4 males, n=4 females) (Ab7326). These antibodies were generously provided by Dr Gareth Davies from UCB Pharma and were administered subcutaneously at 30mg/kg twice weekly as previously described [132], until humane end point. AP mono8 HP2.3 tumouroid clusters were then prepared and injected directly into the colon wall of these mice as above (see 'Orthotopic mouse models of primary CRC') with approximately 4,300 clusters per injection.

For the hepatic metastatic CRC model, AP mono8 HP2.3 single tumouroid cells were prepared and injected into the portal vein of 8-52-week old Cas9 mice as above (see 'Portal vein mouse model of hepatic metastatic CRC'). Twice weekly subcutaneous treatment with either 30mg/kg IgG Ab (n=8 males, n=11 females) or Grem1 NAb (n=9 males, n=10 females) begun 1 week post-tumouroid injection and continued until humane end point.

Statistical analysis

Statistical analyses were conducted using GraphPad Prism 8.00. *P*-values of less than 0.05 were considered statistically significant. When data was normally or not normally distributed, a student's t test or Mann-Whitney U test was undertaken, respectively. When comparing the means of two or more independent groups, a one-way ANOVA with Tukey's multiple comparisons was undertaken. When examining how two independent variables in combination affected the dependent variable, a two-way ANOVA with Tukey's multiple comparisons was undertaken. For survival analyses, a Mantel-Cox test was performed.

Chapter 3: Animal Model Development

In this chapter I detail the development of several immunocompetent mouse models of CRC (Aim 1). We have not only successfully replicated spontaneous, inflammation-induced CRC in mice, as may be seen in ulcerative colitis patients, but I have also induced orthotopic and hepatic metastatic tumours that have common genetic features of and pathology to the human disease. These models have enabled me to identify putative CRC-promoting stromal factors (Aim 2; see Chapter 4), and to examine the efficacy of standard-of-care chemotherapy and a novel drug targeting stromal GREM1 in primary and metastatic CRC (Aim 4; see Chapter 5).

Orthotopic and hepatic metastatic mouse models of CRC

There are three mouse tumour models used throughout this PhD thesis: two primary, orthotopic models of CRC and a secondary, late stage model of CRC that mimics metastasis to the liver.

The first orthotopic mouse model is a well described model of ulcerative colitis-induced CRC which has been in use for over two decades [145, 146]. Cyclic administration of the inflammatory agent dextran sulfate sodium (DSS) results in the establishment of chronic colitis and the development of colorectal dysplasia with pathological features that resemble those of human chronic inflammatory bowel disease. The incidence of neoplasia can be increased and its progression to cancer significantly accelerated by administering DSS in combination with a known colon carcinogen, azoxymethane (AOM) [145]. AOM is known to induce activating mutations in the common CRC drivers *KRAS* and *Catenin beta-1* (*CTNNB1)*, but is rarely observed to mutate the key CRC tumour suppressors *APC* or *Tumour protein p53* (*TP53*) [145, 147]. To this end, mice are given a single intraperitoneal injection of AOM (10mg/kg) followed 1 week later by the addition of 3% DSS to their drinking water. Mice are on DSS-containing water for 5 days followed by normal water for 16 days, for up to 3 cycles (Fig 3.1A). The inflammation then drives the spontaneous generation of colorectal tumours that can be visualised via colonoscopy approximately 3 months after the start of DSS treatment (Fig 3.1B). This model was established in the laboratory by Dr Tamsin Lannagan and used to identify MCAM as a putative CRC-promoting stromal factor in Chapter 4 (Aim 2).

The AOM/DSS model is an excellent pre-clinical system to characterise the molecular events required for spontaneous CRC formation in the presence of inflammation. However, the tumours generated are generally representative of early-stage CRC [145] and may give variable results in drug treatment studies due to the lack of mutational consistency within and across different animals that leads to the recruitment of slightly different local tumour microenvironments. To therefore examine MCAM and our other tumour-promoting stromal factor, GREM1, in more advanced mouse CRC (Aims 3 and 4; see Chapters 4 and 5), we developed another orthotopic model whereby CRC cells

are injected directly into the colon wall via a mouse colonoscope modified with a needle attachment [20, 148] (Fig 3.1C). I have injected both mouse CRC cell lines and primary mouse colorectal tumouroids using this technique (see below) and can comfortably inject at two different sites in the distal colon to give a maximum of two tumours per animal. Tumours can be monitored via colonoscopy, with qualitative grading according to the Becker scale [139] (Fig 3.1D). The CRC cells can additionally be modified to express firefly luciferase, allowing quantitative assessment of tumour growth via live bioluminescence imaging (Fig 3.1E) – another advantage of this model over AOM/DSS.

I also wanted to examine GREM1 in a metastatic mouse model of CRC, to see if it may be efficacious in late-stage CRC patients (Aim 4; see Chapter 5). As our orthotopic models do not commonly metastasise to distant sites, we needed to develop a metastatic model. The most common site for CRC metastasis is the liver, with 70% of metastatic lesions developing here [149]. We therefore chose to model hepatic metastasis by injecting luciferase-expressing mouse colorectal tumouroids into the liver via the portal vein (Fig 3.1F). The tumouroids successfully lodged in the liver from the bloodstream and resulted in large multifocal and multi-lobular liver tumours (Fig 3.1G) that could be monitored via live bioluminescence imaging (Fig 3.1H).

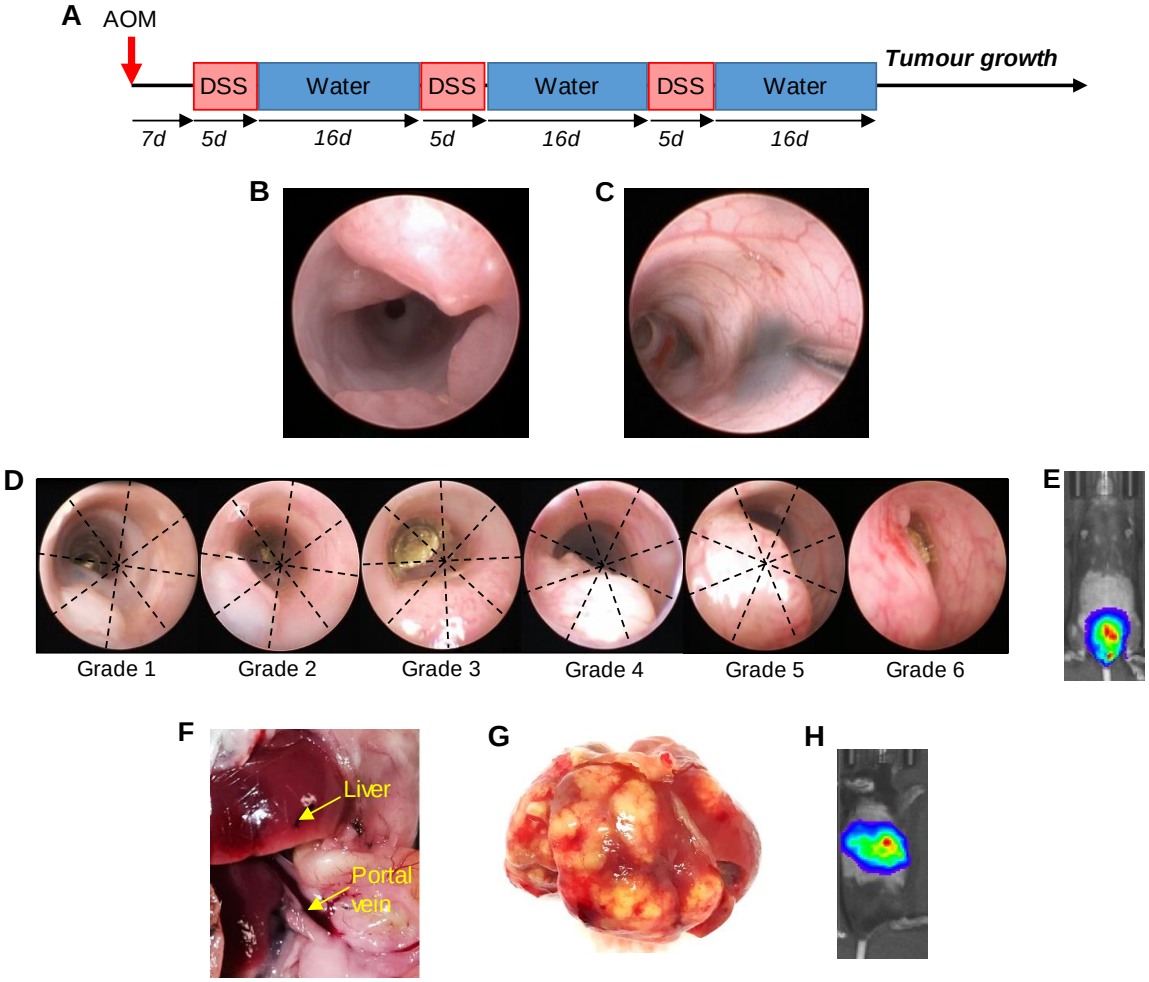


Figure 3.1 legend on next page.

Figure 3.1. Developed mouse models of primary and metastatic CRC. A–B, schematic of the AOM/DSS model of inflammation-induced CRC (**A**). Following injection of a carcinogen (AOM), mice are given the inflammatory agent DSS until tumour growth is detected via colonoscopy (**B**). **C,** injection of CRC cells into the colon wall via colonoscope with a needle attachment. Tattooing ink is added to the injection solution so that tumour growth can be monitored at the site of injection. **D,** colon tumour growth can be visualised via colonoscopy and is graded according to the Becker scale [(139)], where a grade 6 tumour is impassable. **E,** luciferase$^+$ colorectal tumours can also be monitored via live bioluminescence imaging. **F–H,** injection of luciferase$^+$ CRC cells through the portal vein (**F**) will generate a hepatic metastatic model of CRC, where mice develop liver tumours (**G**) that can be visualised and quantified via bioluminescence imaging (**H**).

Orthotopic injection of traditional mouse CRC cell lines either failed to generate tumours in immunocompetent mice or produced tumours unrepresentative of human CRC

Cancer cell lines are commonly used in mouse tumour models because they are easy to culture, flexible, scalable and reliable. As such, I initially trialled two different mouse CRC cell lines in our orthotopic model: CMT93 and MC38. The first line, CMT93, is a rectal cancer cell line generated by treatment of a C57BL/icrf male with the carcinogen methylazoxymethanol acetate [(150)]. These cells are epithelial in morphology and grow in tight clusters (Fig 3.2A). So that I could track tumour growth via bioluminescence imaging as well as colonoscopy, I first transduced these cells with a retrovirus encoding firefly luciferase, enhanced green fluorescent protein (eGFP) and neomycin resistance, as conferred by the SFG-NES-TGL plasmid [(135)]. Transduced cells were then plated at less than 1 cell per 96-well, generating 16 monoclonal lines that were expanded. A luciferase assay demonstrated that monoclonal line 7 had the greatest luminescence ("CMT93 M7"; Fig 3.2B), which was subsequently chosen for *in vivo* tumourigenic analysis. As the laboratory had never used even the parental line before, I undertook a pilot study to determine the optimal cell number per injection. Basing numbers on a prior report, which injected $2x10^6$ cells into the rectal submucosa [(151)], I chose to trial $1x10^6$, $2x10^6$ and $3.8x10^6$ cells per colonoscopic injection into C57BL/6 mice (n=2/group). As an immunocompromised control, I injected $1x10^6$ cells/injection into an NSG animal (n=1). Despite the NSG developing a grade 6 tumour by 4 weeks post-injection (Fig 3.2D), the bioluminescent signal remained close to background at 5 weeks post-injection (Fig 3.2C). This suggested that the level of luciferase activity in CMT93 M7 was too low to be detected *in vivo*, and consequently bioluminescence imaging of the remaining C57BL/6 animals ceased. Continued colonoscopic monitoring revealed that there was no tumour growth in C57BL/6 hosts up until the experiment was terminated at 12 weeks post-injection, regardless of the number of cells per injection (Fig 3.2D-E); this was supported at necropsy.

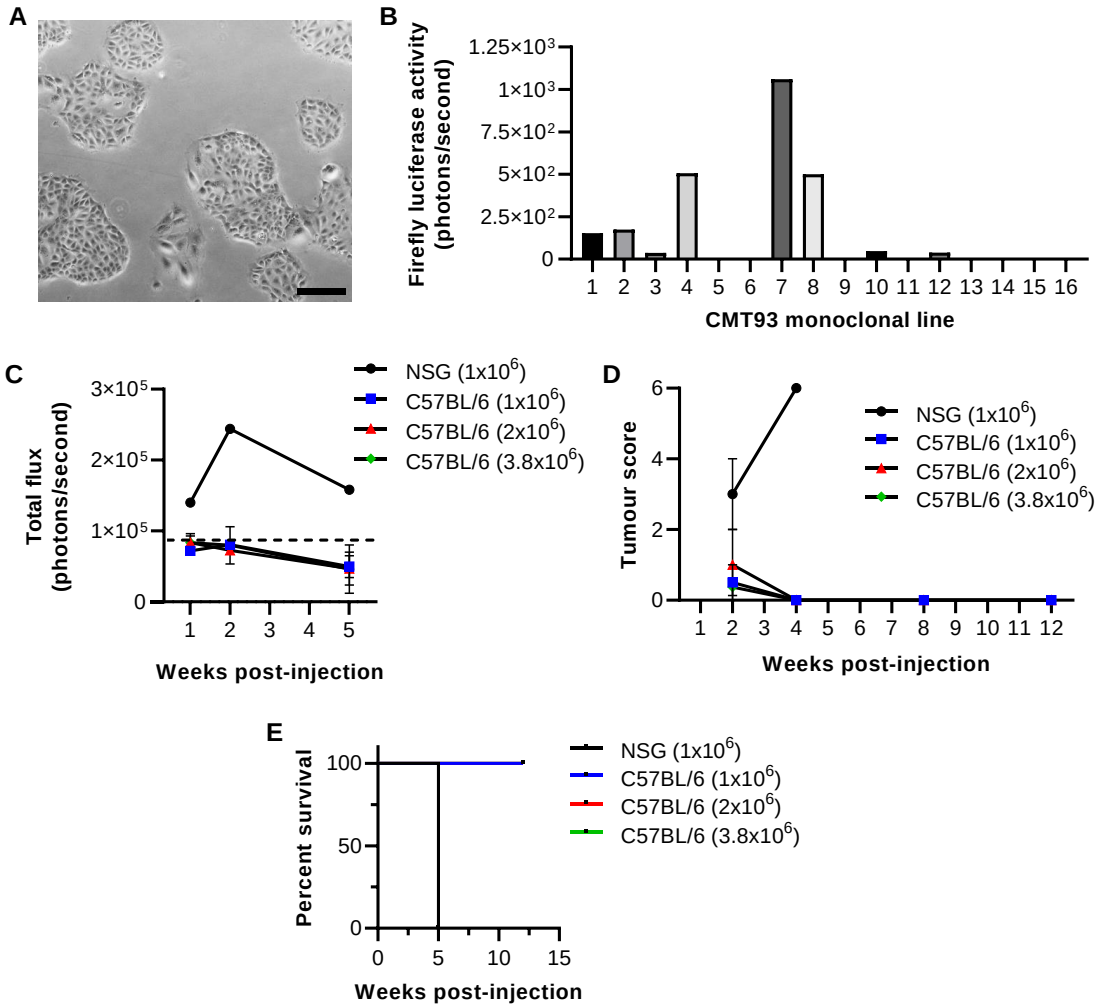


Figure 3.2. CMT93 M7 cells failed to generate colorectal tumours in C57BL/6 mice. **A,** representative brightfield image of the CMT93 mouse rectal cancer cell line; scale bar = 200µm. **B,** luciferase assay of 16 handpicked monoclonal lines of SFG-NES-TGL-transduced CMT93. **C–E,** CMT93 M7 was injected into the colon of NSG ($1x10^6$ cells/injection; n=1 mouse) and C57BL/6 ($1x10^6$, $2x10^6$ and $3.8x10^6$ cells/injection; n=2 mice/group), with tumour growth monitored via bioluminescence imaging (**C**) and colonoscopy (**D**). The dotted line in (**C**) represents background luminescence. The Kaplan-Meier survival curve is shown in (**E**). Two tumour cell injection sites/mouse. Mean +/- SEM.

The second mouse CRC cell line trialled in our orthotopic model was MC38, which is a colon adenocarcinoma line derived from a C57BL/6 female mouse treated with the carcinogen dimethylhydrazine [152, 153]. This line has a high mutational burden, is exceptionally aggressive, and consists of both epithelial and fibroblast-like cell morphologies (Fig 3.3A). During my Honours Degree, I successfully transduced MC38 cells to develop a tdTomato- and luciferase-expressing line which, with $1x10^6$ cells per orthotopic injection, generated aggressive tumours that caused C57BL/6 mice to reach humane end point by approximately 18 days post-injection. I aimed to prolong survival,

so that anything I manipulated in the experimental system (e.g. treating mice with a GREM1 NAb) had a chance to affect the outcome. As such, I piloted three different cell numbers per orthotopic injection in C57BL/6 mice: $1x10^5$, $2.5x10^5$ and $5x10^5$ (n=3 mice/group). Tumour growth was monitored via bioluminescence imaging and colonoscopy over 16 weeks, when the experiment was ended with one animal in each group failing to grow tumours; only data up until the first humane end point in each group is shown (Fig 3.3B-C). Over this period I observed that tumours developed more quickly in the $2.5x10^5$ cells/injection group, contrary to our expectation that the $5x10^5$ cells/injection group would grow the fastest. As a result, the $2.5x10^5$ cells/injection group was also the first to reach ethical end point (Fig 3.3D). As I found in my Honours Degree, the MC38 line is so aggressive that it also does not stay localised to the colon, developing large tumours studded throughout the mesenteries in most animals (Fig 3.3E-F). Consequently, the tumour score may remain low and bioluminescence imaging becomes the more dependable marker of a mouse reaching ethical end point. When Dr Hiroki Kobayashi (a qualified pathologist in our group) compared the pathology between the MC38-generated colon tumours and human colon adenocarcinoma, he observed a loss of epithelial structure and, more importantly, a lack of a desmoplastic reaction (Fig 3.3G). As the interest of my PhD lies within the tumour-promoting stroma, I could not use this MC38 orthotopic model for the accurate examination of stromal-expressed MCAM and GREM1.

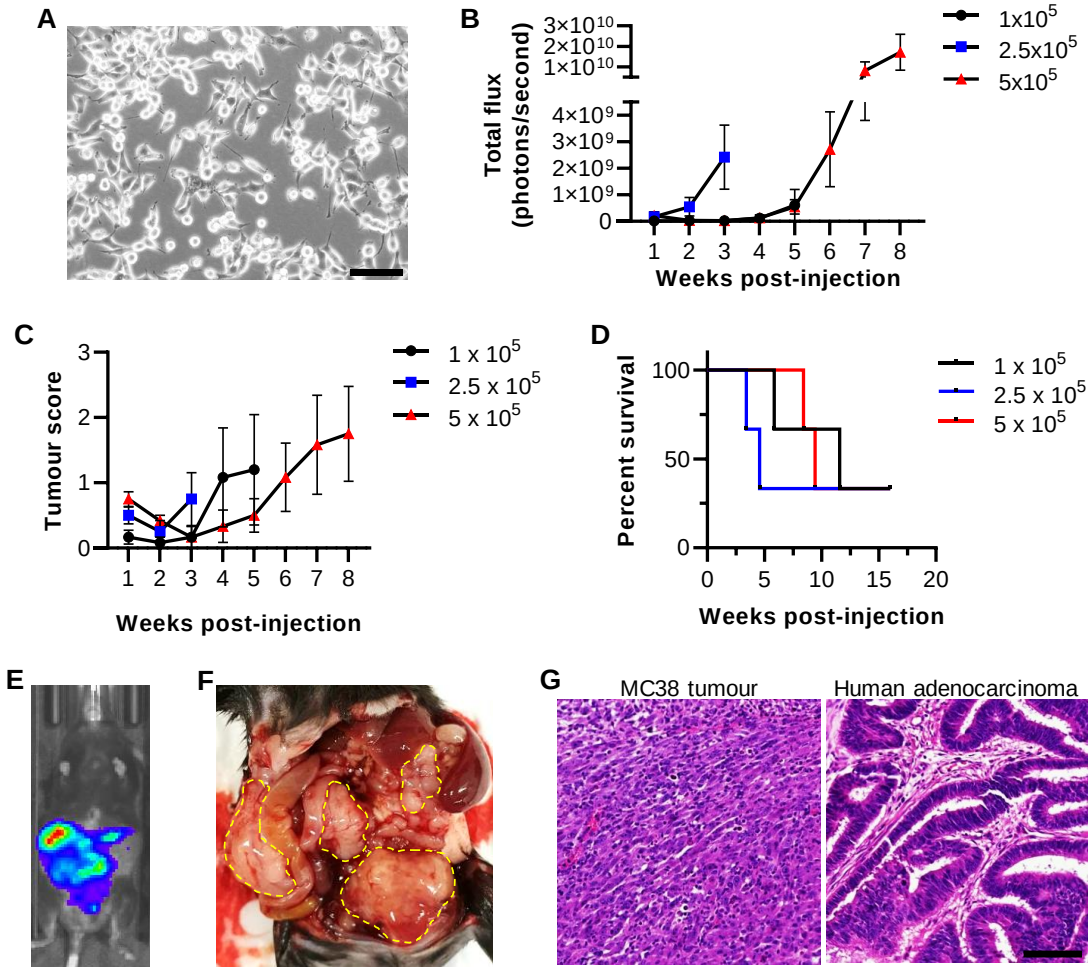


Figure 3.3. MC38 tdTomato$^+$luciferase$^+$ cells generate aggressive colorectal tumours with dissimilar pathology to human CRC. A, representative brightfield image of MC38 tdTomato$^+$luciferase$^+$ mouse CRC cells; scale bar = 100µm. **B–F,** MC38 tdTomato$^+$luciferase$^+$ cells were injected into the colon of C57BL/6 animals, with either 1x10^5, 2.5x10^5 or 5x10^5 cells/injection (n=3 mice/injection group). Tumour growth was monitored via bioluminescence imaging (**B**) and colonoscopy (**C**) until humane end point, although only data up until the first animal death in each group is shown. **D,** Kaplan-Meier curves showing survival of different injection groups. **E,** bioluminescent image showing peritoneal spread of MC38 cells, with matching necropsy image demonstrating multiple mesenteric tumours (yellow lines; **F**). **G,** representative H&E staining of MC38 colorectal tumours at humane end point compared to human colorectal adenocarcinoma; scale = 100µm. Mean +/- SEM. Two tumour cell injection sites/mouse.

Colon tumouroids from transgenic mice failed to generate orthotopic tumours in immunocompetent mice

As both CRC cell lines tested, CMT93 M7 and MC38 tdTomato$^+$luciferase$^+$, failed to sufficiently recapitulate features of human CRC in syngeneic mice, we turned to using a more complex form of epithelial cell culture – mouse colorectal tumouroids. As mentioned in the Introduction (see Chapter

1), OUs are not only naturally immortalised through the self-renewal of epithelial stem cells that generate them, but contain all the differentiated epithelial cell types of the parent organ that maintain their specific functions [9, 11]. Therefore, when compared to cell lines, tumouroids are likely to be more representative of the biological setting. As such, I next tested colorectal tumouroid lines to generate tumours in immunocompetent animals.

Colorectal tumouroids can be generated with specific CRC mutations. This enables testing of the contribution of specific alterations to tumourigenesis and can also help to inform treatment options for patients with those particular mutations. In our case, we are interested in genes commonly mutated in the conventional molecular pathway to CRC: *Apc* (A), *Kras* (K) and *Tp53* (P). A/Prof Jatin Roper and his colleagues successfully generated an AKP colon tumouroid line, by extracting colon OUs from the $Apc^{fl/fl}$;$Kras^{LSL\text{-}G12D/+}$;$Trp53^{fl/f}$ mouse and transducing them with Ad5CMV::Cre. Upon colonoscopic implantation into syngeneic C57BL/6 mice (40 tumouroids/injection), 42.5% of injection sites developed colorectal tumours [20]. A/Prof Roper had generously provided us with these tumouroids, of which I injected into NSG (n=1) and C57BL/6 (n=5) mice via colonoscope at approximately 150 tumouroids/injection. Tumour growth was monitored via colonoscopy over 16 weeks and unfortunately, in our hands, C57BL/6 mice failed to grow colonic tumours (Fig 3.4A-B). This is presumably due to differences in C57BL/6 strains at the two different institutes. Tumour growth failure was also evident at necropsy of the C57BL/6 animals.

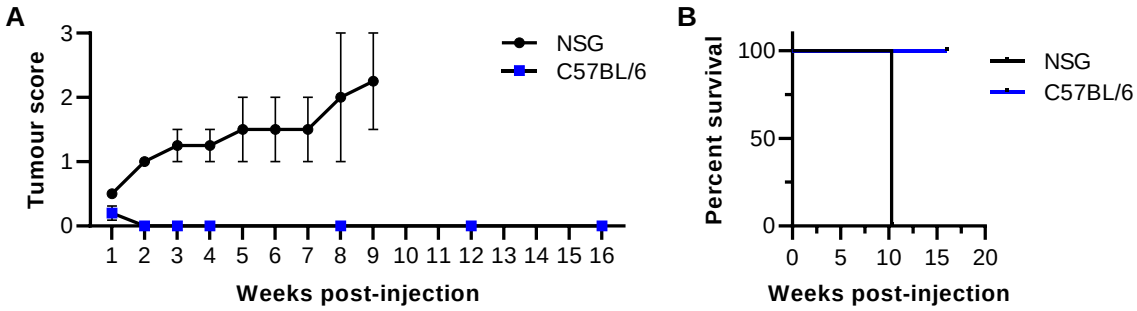


Figure 3.4. AKP colon tumouroids generated from transgenic mice failed to develop colorectal tumours in our C57BL/6 mice. A–B, AKP tumouroids (*Apc*, *Kras* and *Tp53* mutant) were generously provided by A/Prof Jatin Roper [20]. Approximately 150 of these AKPs were injected into the colons of NSG (n=1) and C57BL/6 (n=5) mice, per injection, with tumour growth monitored via colonoscopy (**A**; mean +/- SEM). **B,** Kaplan-Meier curves showing survival of different cohorts. Two tumouroid injection sites/mouse.

Engineered mouse colon tumouroids to generate orthotopic mouse models of CRC

Mouse colorectal tumouroids for use in our orthotopic CRC model can also be generated with *Apc*, *Kras* and *Tp53* mutations from normal OUs via CRISPR/CAS9-mediated genome engineering. Our first conventional molecular pathway tumouroid line was generated from colon OUs extracted from a male Rosa26-Cas9 knockin ("Cas9") mouse, which constitutively and ubiquitously expresses eGFP and CAS9 from *Streptococcus pyrogenes*. These OUs were transduced with a lentivirus containing guide RNAs (gRNAs) targeting *Apc*, *Kras* and *Tp53* and a *KrasG12D* homology directed repair (HDR) template. When *Apc* is mutated or deleted, β-catenin is stabilised and constitutive WNT signalling results [(154)]. When the oncogene KRAS is constitutively activated via transformation to *KrasG12D*, the EGF pathway is activated downstream of the EGF receptor (EGFR) [(155)]. To therefore select for tumouroids containing *Apc* and *Kras* mutations, WNT, RSPO and EGF are removed from the culture media and EGFR inhibitor (EGFRi) is added [(18)]. Nutlin-3a is also added to stabilise and activate p53 signalling [(156)]. Theoretically, only OUs containing oncogenic TP53 [(157)] expand, while OUs containing wild type (WT) P53 will apoptose and be lost from the culture. A diagram of how tumouroids are selected is represented in Fig 3.5A. The surviving polyclonal tumouroid population was then handpicked to monoclonal lines and CRISPR target site amplicons analysed via Sanger sequencing; unfortunately, no monoclonal lines had incorporation of the *KrasG12D* HDR template but four lines had bi-allelic insertion/deletion (indel) mutations generating premature stops in both *Apc* and *Tp53*. Tumouroid line 8, henceforth named "AP mono8", was then chosen and the DNA sequences highlighting the indel mutations generated are shown in Appendix 8 (Supplementary Fig 16B) [(136)]. AP mono8 tumouroids were then transduced with SFG-NES-TGL retrovirus and the highest luciferase-expressing handpicked monoclonal was chosen for *in vivo* analysis – "AP mono8 HP2.3". This tumouroid line was generated by Dr Susan Woods and Dr Tamsin Lannagan. To then test whether the AP mutations were tumourigenic, I assisted Dr Lannagan and Mr Tongtong Wang in the orthotopic injection of AP mono8 HP2.3 into NSG (n=1), Cas9 (n=2), and Cas9 mice backcrossed 5 generations to the SAHMRI C57BL/6 ("Cas9 BX"; n=2). Colorectal tumour growth was then tracked via bioluminescence imaging (Fig 3.5B); growth in the NSG and Cas9 mice suggested that AP mutations were indeed tumourigenic, as expected. The NSG mouse succumbed to colorectal tumour burden most quickly (Fig 3.5C). Cas9 BX animals, however, failed to support the implantation and growth of AP mono8 HP2.3 over the 12-week period examined (Fig 3.5B-C). Presumably, the Cas9 BX recipients (100% C57BL/6 background) were too genetically dissimilar to the OUs extracted from the original Cas9 mouse strain (more than 75% C57BL/6 background) and were immune-rejected. AP mono8 HP2.3 can therefore only be used in the original strain of Cas9 animals, where it successfully recapitulates human CRC pathology when injected orthotopically (Fig 3.5D); readily available C57BL/6 mice unfortunately cannot be used as hosts. This tumouroid line was used in Chapter 5 to assess the efficacy of a GREM1 NAb in original Cas9 mice with either primary or hepatic metastatic CRC.

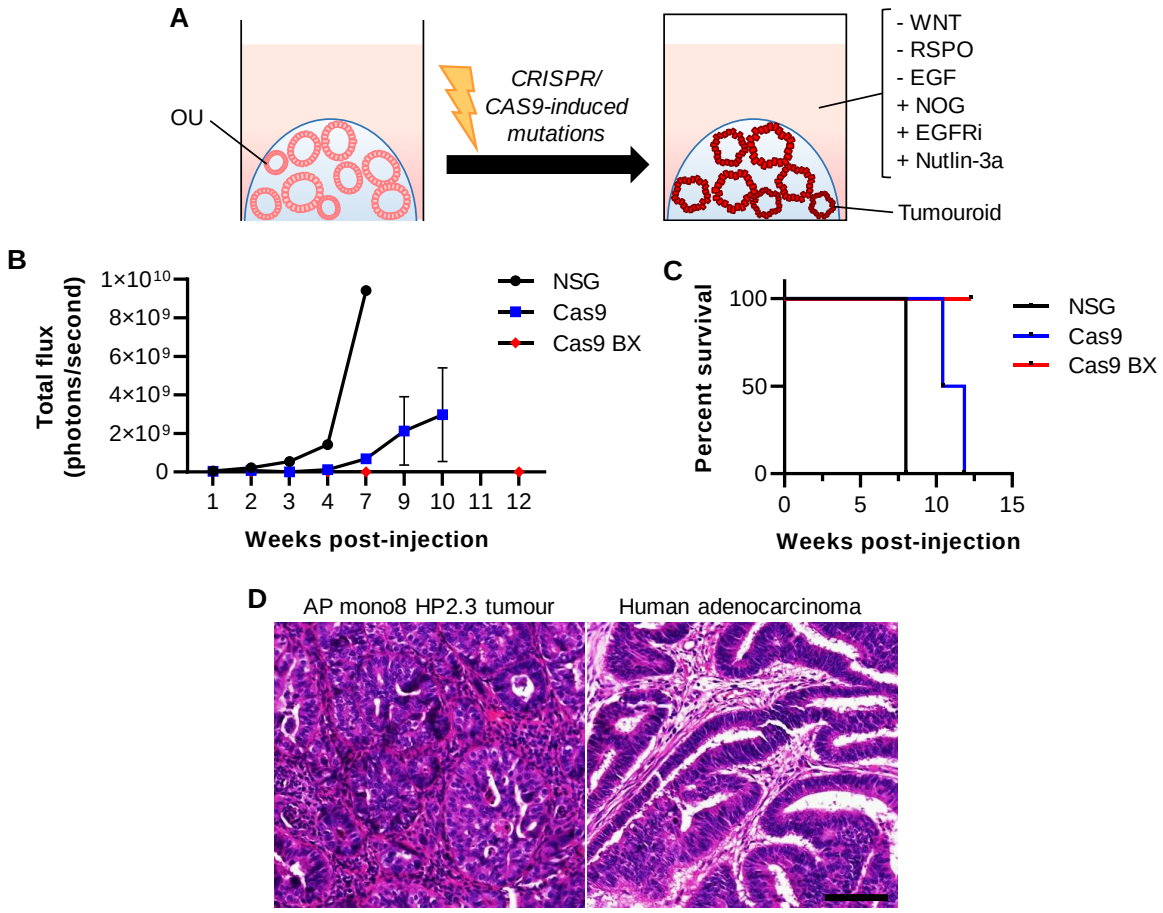


Figure 3.5. AP mono8 HP2.3 generated colorectal tumours in donor Cas9 but not Cas9 BX mice. A, schematic illustrating the positive selection of tumouroids with CRISPR/CAS9-induced mutations from normal, CAS9-expressing colonic OUs. These tumouroids no longer require WNT, RSPO and EGF and survive the addition of EGFRi and Nutlin-3a. This selection medium prevents the outgrowth of any untransformed, normal colonic stem cells. AP mono8 HP2.3 tumouroids are *Apc* and *Tp53* mutant. **B–C,** approximately 150 AP mono8 HP2.3 tumouroids were injected into the colon of NSG (n=1), Cas9 (n=2) and Cas9 BX (n=2) mice, per injection, with tumour growth monitored via bioluminescence imaging (**B**; mean +/- SEM). **C,** Kaplan-Meier curves showing survival of different cohorts. **D,** representative H&E staining of AP mono8 HP2.3 colorectal tumours in Cas9 mice at humane end point compared to human colorectal adenocarcinoma; scale = 100µm. Two tumouroid injection sites/mouse.

In an effort to generate an immunocompetent CRC model in C57BL/6 mice, Dr Susan Woods generated a monoclonal *Apc*$^{\Delta/\Delta}$;*Kras*^{G12D};*Tp53*$^{\Delta/\Delta}$ tumouroid line using the same protocol as above but with colon OUs extracted from a male Cas9 BX mouse – "AKP mono7". A C57BL/6-competent model was essential because I had planned to examine the role of MCAM in colorectal tumourigenesis by injecting tumouroids into *Mcam*$^{-/-}$ mice, which are 100% C57BL/6 background (see Chapter 4). Sequence verification of the *Apc* and *Tp53* bi-allelic indel mutations in AKP mono7

tumouroids are shown in Table 3.1. The *Kras*^{G12D} mutation was confirmed in one allele via sequencing, while the other allele had the following mutations: DNA changes = c.290T>C, c.300_304(deletion); protein change = p.Ile36Gly(frameshift)(stop codon)10. We did not examine the tumouroids for any potential off-target effects from the CRISPR-CAS9-induced DNA editing, which can be viewed as a limitation of this line. I then transduced the AKP mono7 tumouroids with SFG-NES-TGL retrovirus and confirmed luciferase expression in the transduced polyclonal line via a luciferase assay (Fig 3.6A). 15 transduced tumouroids were then handpicked to generate monoclonal lines and a luciferase assay revealed that line 7 expressed the most luciferase (Fig 3.6B). "AKP mono7 HP1.7" was subsequently orthotopically injected into NSG (n=3 males, n=2 females), Cas9 BX (n=3 males, n=2 females) and C57BL/6 (n=6 males, n=3 females) mice and colon tumour growth was monitored via bioluminescence imaging and colonoscopy for 23 weeks. The imaging and scope data up until the first animal death in each mouse strain and gender is displayed in Fig 3.6C-D. Similar to AP mono8 HP2.3, tumours formed in NSG mice and they succumbed approximately 5-6 weeks post-tumouroid injection. Although, dissimilarly, AKP mono7 HP1.7 was able to successfully generate tumours in Cas9 BX mice and lead to their humane end point by weeks 11 and 17 in males and females respectively (Fig 3.6E). Interestingly, there was no difference in tumour growth rate between male and female NSG mice, but tumours grew significantly slower in Cas9 BX females than males according to colonoscopy scoring from weeks 6 up until the first male death at week 11 (p<0.0001 at week 11, two-way ANOVA; Fig 3.6D). Colonoscopy revealed that tumours were present in Cas9 BX females for 2 weeks post-injection, but then begun receding and completely disappeared by 4 weeks only to resurface again from 10 weeks (Fig 3.6D). This phenomenon was also observed in C57BL/6 mice, although tumours did not re-develop over the 23 weeks monitored (Fig 3.6C-E). I hypothesised that the tumouroids were stimulating an immune reaction that was eventually overcome in Cas9 BX females but caused complete rejection in C57BL/6 animals. Assuming there are no significant off-target effects from the CRISPR/CAS9 generation of this tumouroid line or the retroviral integration site from SFG-NES-TGL transduction, then there are only a few proteins introduced into otherwise naïve C57BL/6 mice after injection that could potentially activate the immune system: the neomycin resistance cassette, firefly luciferase, eGFP and CAS9. Although luciferase has been shown to be immunogenic [158, 159], these tumouroids still grow in Cas9 BX animals which are luciferase (and neomycin resistance cassette) naïve. It is therefore more likely that eGFP and/or CAS9 are the immunogens in C57BL/6 mice.

Table 3.1. *Apc* and *Tp53* sequence verification in AKP mono7 tumouroids

Gene	Allele 1		Allele 2	
	DNA change	**Change to protein**	**DNA change**	**Change to protein**
Apc (WT protein, 2860 aa)	c.2206_2212del	p.Asp716GlyfsTer3	c.2209_2216del	p.Met717SerfsTer35
Tp53 (WT protein, 3900 aa)	c.871_876del insTTGGGCTTA	p.Cys239TrpfsTer3	c.875del	p.Met240TrpfsTer4

Note that these bi-allelic indel mutations result in prematurely truncated proteins. aa = amino acid; fs = frameshift mutation; Ter = translation termination (stop) codon.

To determine whether eGFP and CAS9 are causing immune rejection of AKP mono7-generated colorectal tumours in C57BL/6 mice, I sought to remove the *Cas9-P2A-eGFP* sequence present in these tumouroids (where P2A is the 2A self-cleaving peptide). This sequence is flanked by Flippase (FLP) recombinase recognition target (FRT) sites. Thus, in the presence of FLP recombinase, site-specific recombination will occur to excise this sequence. To remove false positive recombinants from the line (GFP^{low}), we first isolated GFP^{high} AKP mono7 cells using FACS (Fig 3.7A). Tumouroids with mutations in *B-raf*, *Transforming growth factor beta receptor 2* (*Tgfbr2*), *Ring finger protein 43* (*Rnf43*), *Zinc and ring finger 3* (*Znrf3*) and *Cyclin dependent kinase inhibitor 2A* (*p16Ink4a*), named $Braf^{V600E}$ΔTRZI, were generated in [17] and were used as a GFP^{-} control. Then, I transfected these AKP mono7 GFP^{high} tumouroids with a FLP recombinase expression plasmid (pCAG-Flpe) and selected for GFP^{-} cells via FACS 4 days later (Fig 3.7B-C). To determine CAS9 status in the AKP mono7 GFP^{-} tumouroids, primers were generated and used in three combinations to PCR amplify genomic DNA from control ($CAS9^{+}GFP^{high}$) and GFP^{-} tumouroids: forward #1 (F1) + reverse #1 (R1), F1 + R2, and F2 + R3 (Fig 3.7D, Table 3.2). The agarose gel electrophoresis of these PCR amplicons showed that the *Cas9-P2A-eGFP* sequence was indeed removed in AKP mono7 GFP^{-} at the genomic DNA level, with an approximately 300bp band produced with F1 + R2 primers and no band with F2 + R3 primers (Fig 3.7E). CAS9 excision was also confirmed at the protein level by western blot, as the 160kDa CAS9 band was absent in the GFP^{-} tumouroids compared to GFP^{high} (Fig 3.7F). This tumouroid line is henceforth called "AKP mono7 $CAS9^{-}GFP^{-}$".

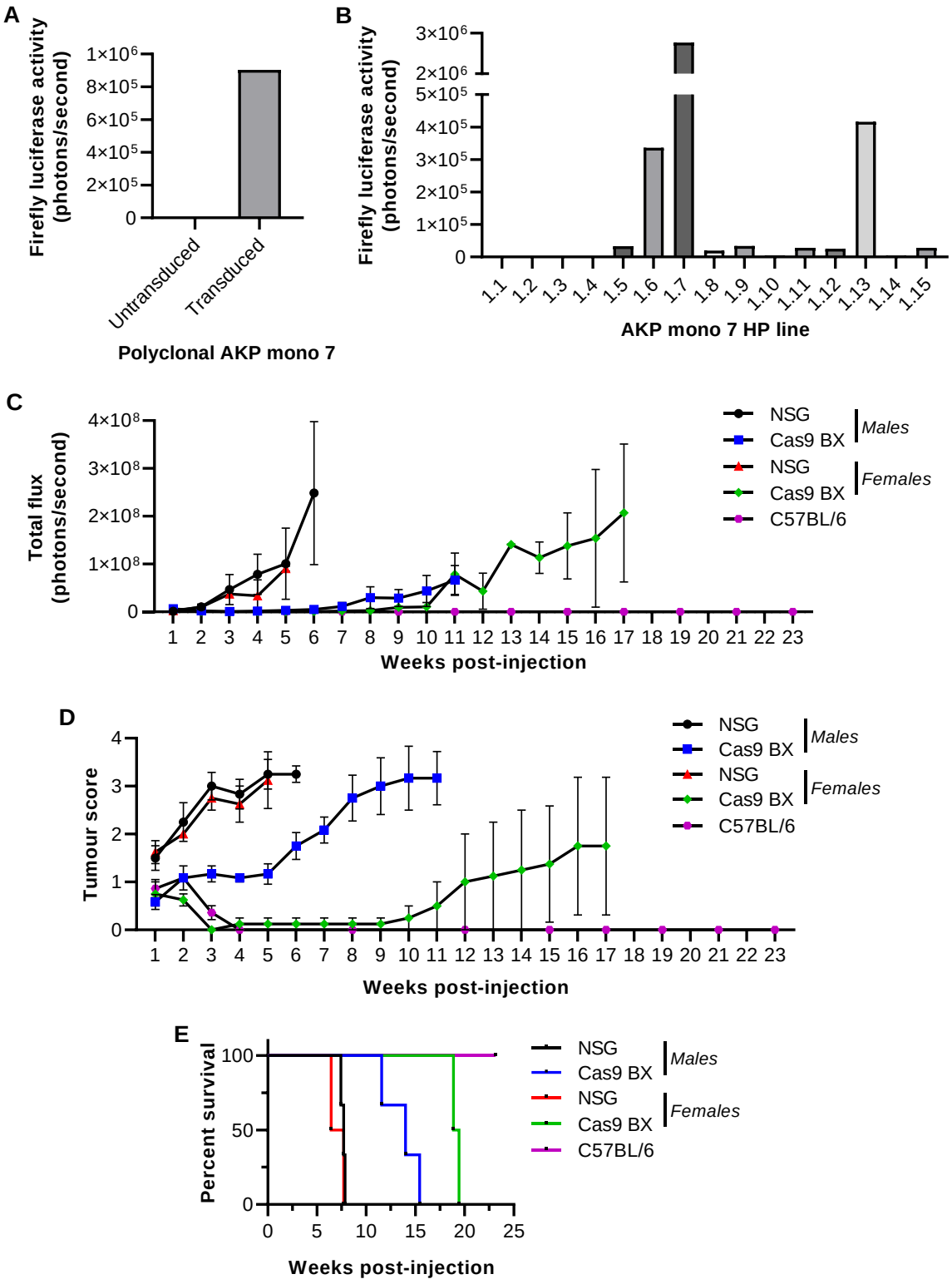


Figure 3.6 legend on next page.

Figure 3.6. AKP mono7 HP1.7 generated colorectal tumours in syngeneic Cas9 BX but not C57BL/6 mice. A, luciferase assay of AKP mono7 tumouroids (*Apc*, *Kras* and *Tp53* mutant) either untransduced or transduced with SFG-NES-TGL retrovirus. **B,** luciferase assay of 15 handpicked (HP) monoclonals from transduced AKP mono7 tumouroids. **C–E,** approximately 150 AKP mono7 HP1.7 tumouroids were injected into the colon of NSG (n=3 males, n=2 females), Cas9 BX (n=3 males, n=2 females) and C57BL/6 (n=9 mice), per injection. Tumour growth was monitored via bioluminescence imaging (**C**) and colonoscopy (**D**) until humane end point, although only data up until the first animal death in each group is shown. **E,** Kaplan-Meier curves showing survival of different cohorts. Mean +/-SEM. Two tumouroid injection sites/mouse.

Table 3.2. PCR primer combinations and product lengths used to validate *Cas9* excision in AKP mono7 GFP$^-$ tumouroids

Combination	Product length in:	
	CAS9$^+$ (bp)	CAS9$^-$ (bp)
F1 + R1	382	N/A
F1 + R2	6954	294
F2 + R3	427	N/A

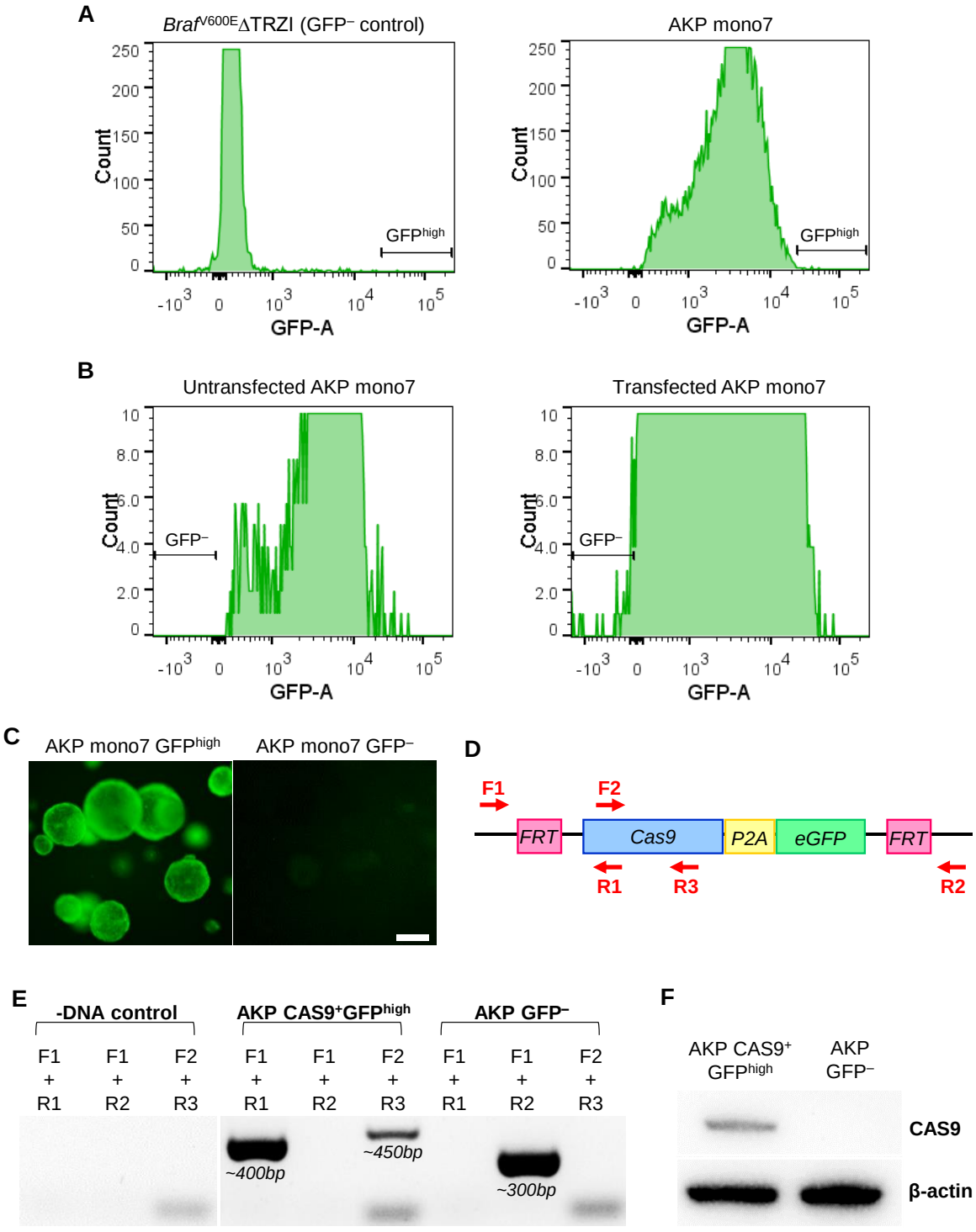


Figure 3.7 legend on next page.

Figure 3.7. Generation of AKP mono7 CAS9^{-}GFP^{-} tumouroids. A, Histogram displaying green fluorescence from *Braf*^{V600E}ΔTRZI organoids (GFP^{-} control; left) and AKP mono7 tumouroids (right). AKP mono7 GFP^{high} cells were collected via FACS. **B,** AKP mono7 GFP^{high} tumouroids were transfected with pCAG-Flpe, which contains an enhanced form of the FLP recombinase that will excise the *Cas9-P2A-eGFP* sequence flanked by FRT sites. AKP mono7 GFP^{-} cells were then isolated via FACS. **C,** representative green fluorescent images of AKP mono7 GFP^{high} and GFP^{-} tumouroids post-FACS; scale bar = 200um. **D,** genomic location of the *Cas9-P2A-eGFP* sequence in the Rosa26-Cas9 knockin mice, including the forward (F) and reverse (R) primer binding locations for validating *Cas9-P2A-eGFP* sequence loss after FLP-FRT site-specific recombination. **E,** image of PCR amplicons from AKP mono7 CAS9^{+}GFP^{high} and GFP^{-} tumouroids separated by size using a 1% agarose gel. **F,** whole cell lysates from AKP mono7 CAS9^{+}GFP^{high} and GFP^{-} tumouroids separated by SDS-PAGE and subjected to western blot for CAS9 (160kDa).

To test whether AKP mono7 CAS9^{-}GFP^{-} could generate tumours in immunocompetent, CAS9/eGFP naïve, C57BL/6 animals, AKP mono7 CAS9^{+}GFP^{high} and CAS9^{-}GFP^{-} tumouroids were orthotopically injected into NSG (n=1 male, n=1 female), Cas9 BX (n=3 males, n=2 females) and C57BL/6 (n=3 males, n=2 females) mice each. Colorectal tumours were monitored via colonoscopy over 16 weeks, but tumour score data is only displayed up until the first humane animal death in each tumouroid group and gender across the different mouse strains (Fig 3.8A-C). Kaplan-Meier survival curves are shown in Fig 3.8D-F. While both genders of NSG mice grew CAS9^{+}GFP^{high} and CAS9^{-}GFP^{-} tumours at a similar rate (Fig 3.8A, D), Cas9 BX and C57BL/6 females failed to develop tumours from either tumouroid line (Fig 3.8B-C, E-F). Furthermore, Cas9 BX males developed tumours from both tumouroid lines at similar rates (Fig 3.8B, E) whereas only CAS9^{-}GFP^{-} tumouroids grew in C57BL/6 males (Fig 3.8C, F). A summary of the tumour take rates are displayed in Table 3.3. These data demonstrate that tumours generated from orthotopically injected CAS9 and eGFP-expressing tumouroids are immune-rejected in C57BL/6 mice, supporting my hypothesis that CAS9 and/or eGFP are immunogenic in the C57BL/6 CRC model. Moreover, both CAS9^{+}GFP^{high} and CAS9^{-}GFP^{-} colorectal tumours pathologically resembled human CRC (Fig 3.8G). Therefore, AKP mono7 CAS9^{-}GFP^{-} tumouroids will be used by the laboratory in future studies examining MCAM tumourigenesis in male *Mcam*$^{+/+}$ and *Mcam*$^{-/-}$ hosts of C57BL/6 origin.

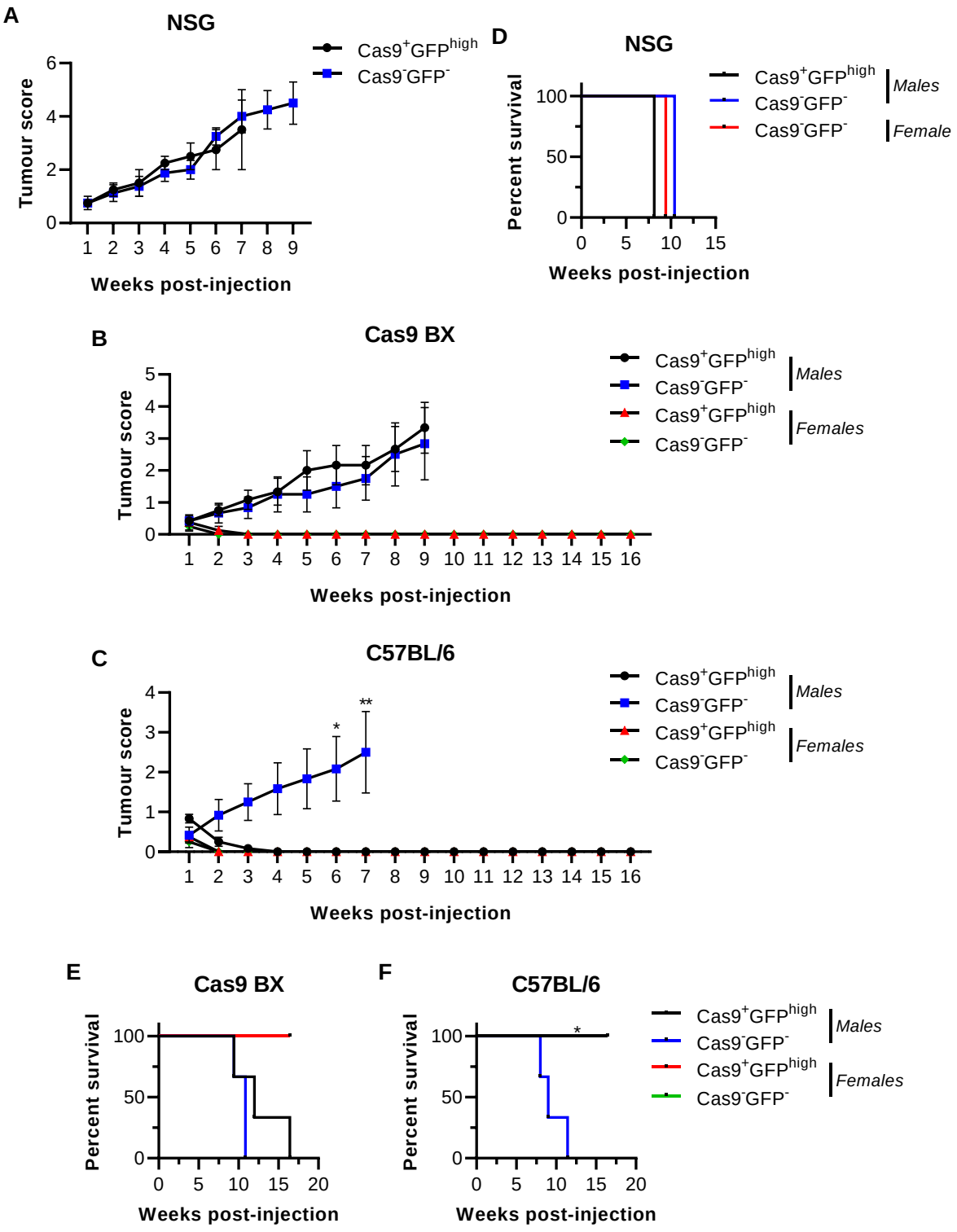


Figure 3.8 continued on next page.

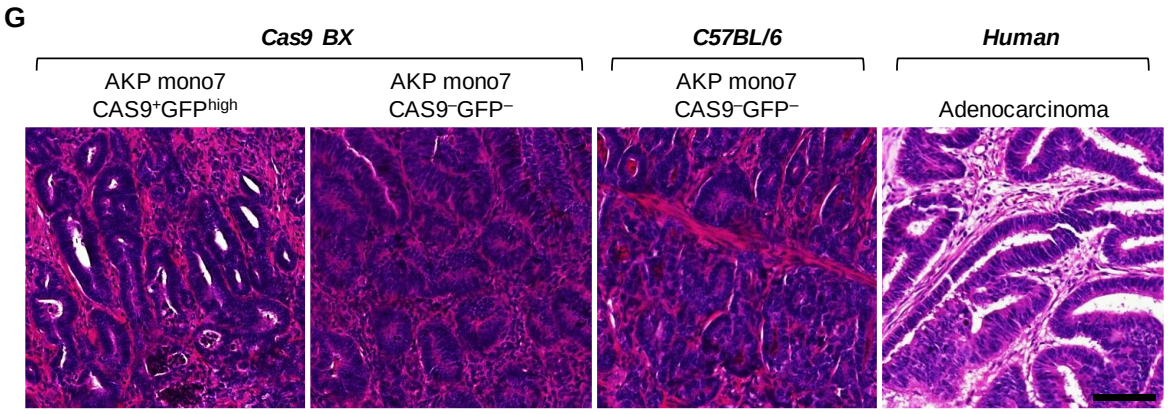


Figure 3.8. CAS9 and eGFP in AKP mono7 tumouroids are immunogenic. A–F, approximately 150 AKP mono7 CAS9^{+}GFP^{high} and CAS9^{-}GFP^{-} tumouroids were injected into the colon of NSG (n=1 male, n=1 female), Cas9 BX (n=3 males, n=2 females) and C57BL/6 (n=3 males, n=2 females) mice, per injection, each. The female NSG injected with CAS9^{+}GFP^{high} tumouroids was culled from a tumour-unrelated cause and therefore removed from the datasets. Tumour growth was monitored via colonoscopy in NSG (**A**), Cas9 BX (**B**) and C57BL/6 (**C**) animals until humane end point, although only data up until the first animal death in each tumouroid group and gender is shown. **D–F,** Kaplan-Meier curves showing survival of tumouroid groups and genders within NSG (**D**), Cas9 BX (**E**) and C57BL/6 (**F**) cohorts. **G,** representative H&E staining of end point CAS9^{+}GFP^{high} tumours in Cas9 BX males and CAS9^{-}GFP^{-} tumours in Cas9 BX and C57BL/6 males, compared to human colorectal adenocarcinoma; scale = 100µm. Mean +/- SEM. Tumour score was analysed using a two-way ANOVA and survival using a Mantel-Cox test. * = p<0.05, ** = p<0.01. Two tumouroid injection sites/mouse.

Table 3.3. Summary of AKP mono7 CAS9^{+}GFP^{high} and CAS9^{-}GFP^{-} orthotopic tumour take rate in NSG, Cas9 BX and C57BL/6 mice

Mouse strain	CAS9^{+}GFP^{high} tumour take rate		CAS9^{-}GFP^{-} tumour take rate	
	Males	Females	Males	Females
NSG	2/2 (100%)	N/A	2/2 (100%)	2/2 (100%)
Cas9 BX	5/6 (83%)	0/4 (0%)	4/6 (67%)	0/4 (0%)
C57BL/6	0/6 (0%)	0/4 (0%)	5/6 (83%)	0/4 (0%)

Two tumouroid injections/mouse.

Discussion

In this chapter I explored the development of immunocompetent mouse models of CRC (Fig 3.1; Aim 1). Each model will be used to answer different questions throughout my thesis, so that I can better understand how the tumour-associated stroma promotes colorectal tumourigenesis and

metastasis. Although the AOM/DSS and primary models both generate orthotopic colorectal tumours, AOM/DSS tumours arise from the spontaneous mutagenesis of colon epithelial cells driven by inflammation within the mouse while the primary model implants colorectal tumouroids taken from a donor mouse and specifically mutated *in vitro*, directly into the colon. Tumours generated from colonoscopy-guided CRC cell implantation will therefore give less variable and mutation-specific results. Additionally, AOM/DSS tumours are typically low-grade [145] whilst our tumouroid lines develop higher-grade tumours, due to the mutation of multiple key genetic CRC drivers (*Apc*, *Kras* and *Tp53*). The orthotopic implantation of CRC cells and colorectal tumour monitoring via mouse colonoscopy are relatively new techniques that require specialist skills [148]. As such, there are not many research groups in our field that are capable of doing this and only one other group to date has published results from colonoscopically-implanted tumouroids [20, 160]. Many other research groups use *Apc* mutant mice with multiple intestinal neoplasia (Min; $Apc^{Min/+}$ [161]) as their model of CRC, despite tumours more commonly developing in the small intestine than colon [162, 163]. There are more recently developed *Apc* mutant mouse models that have increased colonic tumour burden, but tumours are dispersed throughout the colon and are typically low-grade [163]. It is important that we study colorectal tumours in the distal colon, as this is where CRC commonly develops in people [164]. Thus, as our orthotopic AP and AKP tumouroid models developed high-grade tumours strictly in the distal colon, we can more accurately model human CRC and assess therapeutic options.

To develop an implantable, immunocompetent orthotopic model of primary CRC that recapitulates the common genetic and pathological features of the human disease, I had to test multiple mouse CRC lines. I first tried two luciferase-expressing immortalised cell lines, CMT93 M7 and MC38 $tdTomato^{+}luciferase^{+}$. Unfortunately, colorectal tumours from CMT93 M7 cell injections were rejected in C57BL/6 mice (Fig 3.2D-E). This suggested that either the M7 subclone had reduced tumourigenicity, or that perhaps our SAHMRI C57BL/6J strain was not a compatible syngeneic host to the C57BL/icrf or C57BL/6N strains previously shown to develop CMT93 tumours [150, 151]. It is unlikely that CMT93 M7 tumours were rejected due to the luciferase, as the level of luciferase expression could not be detected above the background level *in vivo* (Fig 3.2C). Moreover, the MC38 $tdTomato^{+}luciferase^{+}$ and tumouroid lines do express detectable luciferase levels *in vivo* and could develop tumours in immunocompetent animals (Fig 3.3B, 3.5B, 3.6C, 3.8A-C). Although MC38 tumours did grow in C57BL/6 hosts, the $1x10^5$ and $2.5x10^5$ cells/injection groups grew tumours faster than the $5x10^5$ cells/injection group (Fig 3.3B-D). As the $5x10^5$ cells/injection group was injected last from a single cell preparation for this dilution series, it is possible that the cells became less viable on ice over time. Then, as the MC38 cell line is relatively immunogenic [165], the increased dosage of low viability MC38 cells may have induced a substantial immune response in the $5x10^5$ cells/injection group and resulted in slower tumour growth. Regardless, the MC38 cells were so aggressive and fast-growing that the tumours lacked epithelial structure and stromal compartmentalisation (Fig 3.3G). Multiple tumour entities were also found attached to the

mesenteries (Fig 3.3E-F), developing either as part of metastasis or the accidental injection of cells through the colon and into the peritoneal cavity. As I wanted to study the stromal-induced promotion of colorectal tumours specifically in a model that closely resembles human CRC, I chose not to use MC38 cells in the orthotopic model. MC38 cells should therefore continue to be used only in examining anti-cancer immunity and immunotherapy [166-169], and not to investigate tumour-stroma interactions.

I next tested the ability of various colorectal tumouroid lines to develop orthotopic tumours in immunocompetent mice. The first AKP tumouroid line was generated from transgenic mice and reported to have a 42.5% take rate in C57BL/6 mice [20]. I, however, observed a 0% take rate in C57BL/6 mice despite increasing the number of tumouroids/injection from 40 to 150 (Fig 3.4). This suggested that our C57BL/6 mice may not be a compatible syngeneic host, resulting in tumour rejection. I next tested our AP mono8 HP2.3 tumouroid line, which only developed colorectal tumours in NSG and syngeneic Cas9 mice (Fig 3.5B-C). These tumouroids can also be used in Cas9 mice for the CRC hepatic metastasis model, which is further explored in Chapter 5. The luminescent AKP mono7 HP1.7 tumouroid line could not develop colorectal tumours in syngeneic C57BL/6 mice, but could in syngeneic Cas9 BX mice, although tumour growth was slower in females than males (Fig 3.6C-E). Our model may be replicating a phenomenon observed in humans, where CRC incidence is higher in men than women [1]. Men also have a higher prevalence of adenomas, advanced adenomas and colorectal carcinomas compared to age-matched females [170]. Although, this gender bias was absent in NSG mice and therefore suggests the involvement of the immune system. As the AKP tumouroids were generated from male colon OUs, it is conceivable that female mice initially rejected these foreign cells. It was observed very early that female mice frequently reject skin grafts, thymic grafts and lymph nodes from males of their own strain [171], and female patients who receive male kidney allografts are more likely than any other gender combination to reject the transplant [172]. This is because the female immune response is stimulated by the sex-linked histocompatibility gene located on the Y chromosome, and results in the generation of H-Y antibodies that reject the tissue [173, 174]. I then observed that, with time, the AKP mono7 HP1.7 line overcame this immune response to successfully, yet belatedly, generate tumours in Cas9 BX females. This may be something that the laboratory investigates further in the future, perhaps by monitoring the production of H-Y antibodies in females with male tumouroids and/or by making AKP tumouroids from female colon OUs and testing the gender bias again *in vivo*. Or, we could simply accept this phenomenon and limit the recipient mice to males to reduce experimental variability. AKP mono7 tumouroids could only develop colorectal tumours in C57BL/6 mice when *Cas9* and *eGFP* were genetically ablated (Fig 3.8C, F). CAS9 and eGFP have already been shown to activate the mouse immune system [175-177] and cause slower tumour growth or complete tumour rejection [178-181]. Even humans have an immune memory response to CAS9 [182-185], which complicates any endeavours to use CRISPR/CAS9 engineering in gene therapy. There are, however, some studies indicating that eGFP is not

immunogenic in C57BL/6 tumour models [186, 187]. Thus, CAS9 may be the stronger immunogen in our model but I am not interested in investigating this as my aim was simply to develop a CRC model in immunocompetent mice, which I have successfully done. Only male C57BL/6 mice can be injected with the AKP mono7 $CAS9^{-}GFP^{-}$ tumouroid line, as females completely reject the male-derived tissue (Fig 3.8C, F). It is important to note that the $CAS9^{-}GFP^{-}$ tumouroids were generated from a sub-selected population of $CAS9^{+}GFP^{high}$ tumouroids (Fig 3.7A), which may be a more H-Y antibody inducing population than the original, unsorted AKP mono7 line that was slowly able to grow in female mice (Fig 3.6C-E). Both AP mono8 HP2.3 and AKP mono7 $CAS9^{-}GFP^{-}$ colorectal tumours in Cas9 and C57BL/6 mice respectively are localised to the distal colon and closely recapitulate the pathology of human CRC (Fig 3.5D, 3.8G), making them a more preferable model over MC38 tumours for studying the tumour-promoting stroma. It should, however, be re-emphasised that our AP mono8 and AKP mono7 tumouroid lines are monoclonal. Monoclonal lines were chosen because we wanted to model cancer with specific mutations and with a predictable tumour growth pattern *in vivo*. While this deliberate decrease in heterogeneity could be viewed as a limitation to our models, the use of a polyclonal line may have promoted the outgrowth of different dominant clones between tumours that may have altered the growth kinetics, ultimately increasing variability between mice.

In conclusion, I have successfully generated tumouroid-induced mouse models of primary and hepatic metastatic CRC. These models successfully recapitulate the common genetic and pathological features of the human disease, in immunocompetent mice. Using these models, I was able to further explore the role of stromal MCAM and GREM1 in colorectal tumourigenesis *in vivo*.

Chapter 4: MCAM in the Colorectal Tumour Stroma

In this chapter I address Aims 2 and 3 of my PhD project; to identify prognostically significant tumour-promoting CAF factors in CRC, and to then examine the role of these factors in the growth and behaviour of colonic fibroblasts and epithelial cells. Through examination of our bulk RNA-sequencing data from mice, comparing sorted normal colon myofbs to developmental and tumour-associated colon myofbs, we identified MCAM as a putative, stromal-specific CRC-promoting factor. As high *MCAM*/MCAM expression is associated with worse CRC patient prognosis, I expand my analysis to include mechanistic studies of this novel therapeutic target. Some key findings of this chapter are included in our group's manuscript (see Appendix 4), with additional *in vitro* studies presented here only.

Identification of MCAM as a candidate CRC-promoting stromal factor

Interestingly, tumourigenesis and developmental biology share substantial similarities in many molecular processes and as such display related gene expression profiles and regulation of signalling pathways [188, 189]. For example, factors involved in CAF activation, such as TGF-β and BMPs, also play crucial roles in the early development of gastrointestinal organs [31, 190]. To therefore explore whether these shared mechanisms could be harnessed to develop a therapeutic approach targeting CRC stroma, we undertook a systemic approach to identify novel colonic stromal factors involved in both tumourigenesis and development.

To this end, we first needed to identify times of greatest epithelial proliferation in neoplastic and developmental mouse colon so that the 'activated stroma' in these settings could be compared to that of adult, homeostatic mouse colon. Members of our group Dr Tamsin Lannagan and Mr Tongtong Wang demonstrated that epithelial staining for the proliferative marker Ki67 was enhanced at postnatal day 14 (P14; data not shown), which became our developmental sample time point, and chose end point tumours generated from the AOM/DSS model (see Chapter 3) as our neoplastic samples. They then extracted fibroblasts/CAFs from adult colon, P14 colon and AOM/DSS tumours via FACS based on their lack of expression of markers for blood cells (CD45, TER119), endothelium (CD31) and epithelium (EPCAM) – a process termed 'trilineage depletion'. Mr Wang then analysed bulk RNA-sequencing from these FACS-purified fibroblasts/CAFs, revealing that 342 genes were upregulated in both the AOM/DSS tumours and developmental colon compared to adult colon (Figure 4.1, Step 1). The prognostic significance of these 342 genes was then assessed by bioinformatically performing survival analyses using the TCGA dataset; 46 genes were shown to be significantly associated with human CRC survival ($p<0.05$; Fig 4.1, Step 2). At this point I joined the research project and compared the RNA expression of each of these 46 genes in epithelia and fibroblasts in both normal and AOM/DSS tumour settings; I selected 23 genes of interest that were

expressed more highly in fibroblasts in comparison to epithelial cells in both settings (Fig 4.1, Step 3; Appendix 5). To further refine this gene list for detailed study these 23 genes were then subjected to a scoring matrix, whereby 1 point was awarded for each of the following: (1) log fold change ($logFC_2$) ≥ 2, (2) prognostic *p* value ≤ 0.01, (3) RNA upregulation in mice is consistent with protein upregulation in human CRC as assessed by the Human Protein Atlas [191], (4) upregulation is consistent with worse cancer outcome in published literature, (5) the availability of published and reliable anti-mouse IHC antibodies, (6) the availability of inhibitors for future therapeutic studies (Fig 4.1, Step 4; Appendix 6). Six candidates scored ≥ 4 out of a possible 6: *Cytochrome C oxidase subunit 4 isoform 2* (*Cox4i2*), *Gap junction alpha-4* (*Gja4*), *Mcam*, *Nerve growth factor receptor* (*Ngfr*), *Notch receptor 3* (*Notch3*) and *SRY-box transcription factor 2* (*Sox2*) (Fig 4.1, Step 5).

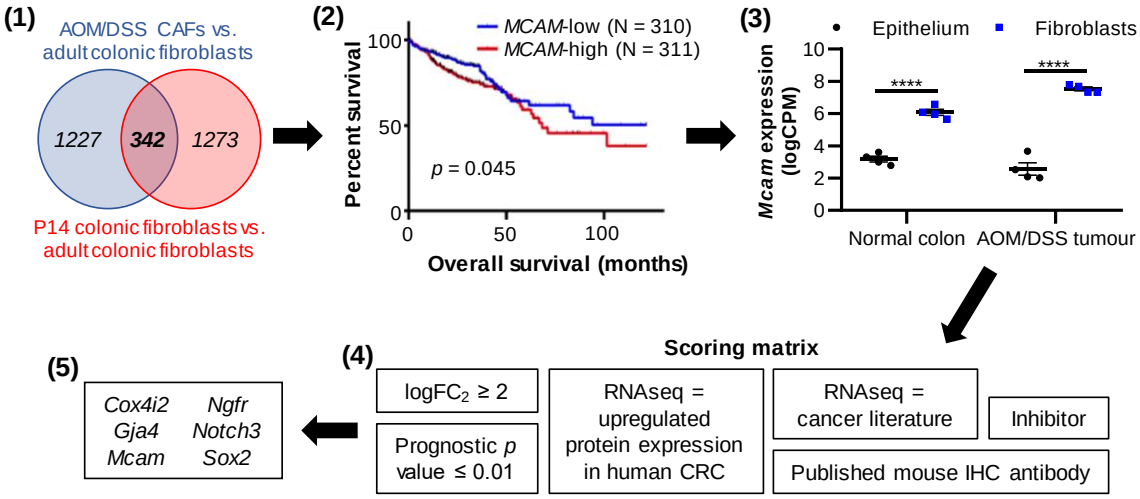


Figure 4.1. RNA-sequencing data refinement to identify the top putative CRC-promoting CAF markers. Step 1, bulk RNA-sequencing was used to determine the 342 genes upregulated in fibroblasts/CAFs extracted from both P14 developmental colon and AOM/DSS tumours compared to normal, adult colon (n=4 mice/group). **Step 2,** these 342 genes were examined for prognostic significance in the human CRC dataset, TCGA, to reveal 46 genes significantly associated with survival ($p<0.05$; n=621 patients). **Step 3,** of these 46 genes, 23 were expressed more in fibroblasts than epithelial cells in AOM/DSS tumours at the RNA level. CPM = counts per million. Mean +/-SEM, student's t tests; **** = $p<0.0001$. The mean and statistics were calculated using data from biological replicates. **Steps 4–5,** these 23 genes were subjected to a scoring matrix, receiving 1 point for each of the 6 criteria (**Step 4**). Only the 6 candidates scoring ≥ 4 out of a possible 6 were examined for protein expression in adult colon, P14 colon and AOM/DSS tumours (**Step 5**).

To validate upregulation of the top RNA-sequencing stromal candidates at the protein level, IHC staining of COX4I2, GJA4, MCAM, NGFR, NOTCH3 and SOX2 in mouse adult colon, P14 colon

and AOM/DSS tumours was undertaken and examined (Fig 4.2A). Of these candidates, only MCAM was stromal-specific and had significantly enhanced staining in developmental and neoplastic settings compared to the normal, adult colon (Fig 4.2A-B). To determine the relevance of this observation to human disease, I performed MCAM IHC on a small progression series of human CRC patient samples (n=4-5 samples/tumour grade); MCAM expression was also significantly upregulated in adenoma and adenocarcinoma samples compared to normal colon (Fig 4.3A-B). I then performed a more extensive MCAM IHC study using tissue microarrays from Australian CRC patients (n=101) with associated survival data. Quantification of this IHC staining by a pathologist in our group (Dr Hiroki Kobayashi) revealed that high MCAM expression was indeed an independent prognostic factor for poor overall survival in CRC patients (Fig 4.3C-D; Appendix 4, Supplementary Tables 2 and 3). These data suggest that MCAM has a role in tumour progression and may therefore potentially be a novel therapeutic target in CRC.

This refinement of candidate genes from our RNA-sequencing data was also included in our manuscript (Appendix 4), however, the process was simplified for publication with some differences in refinement. Despite these differences, MCAM remained the only candidate with stromal-specific expression significantly upregulated in developmental and neoplastic mouse colon compared to normal mouse colon.

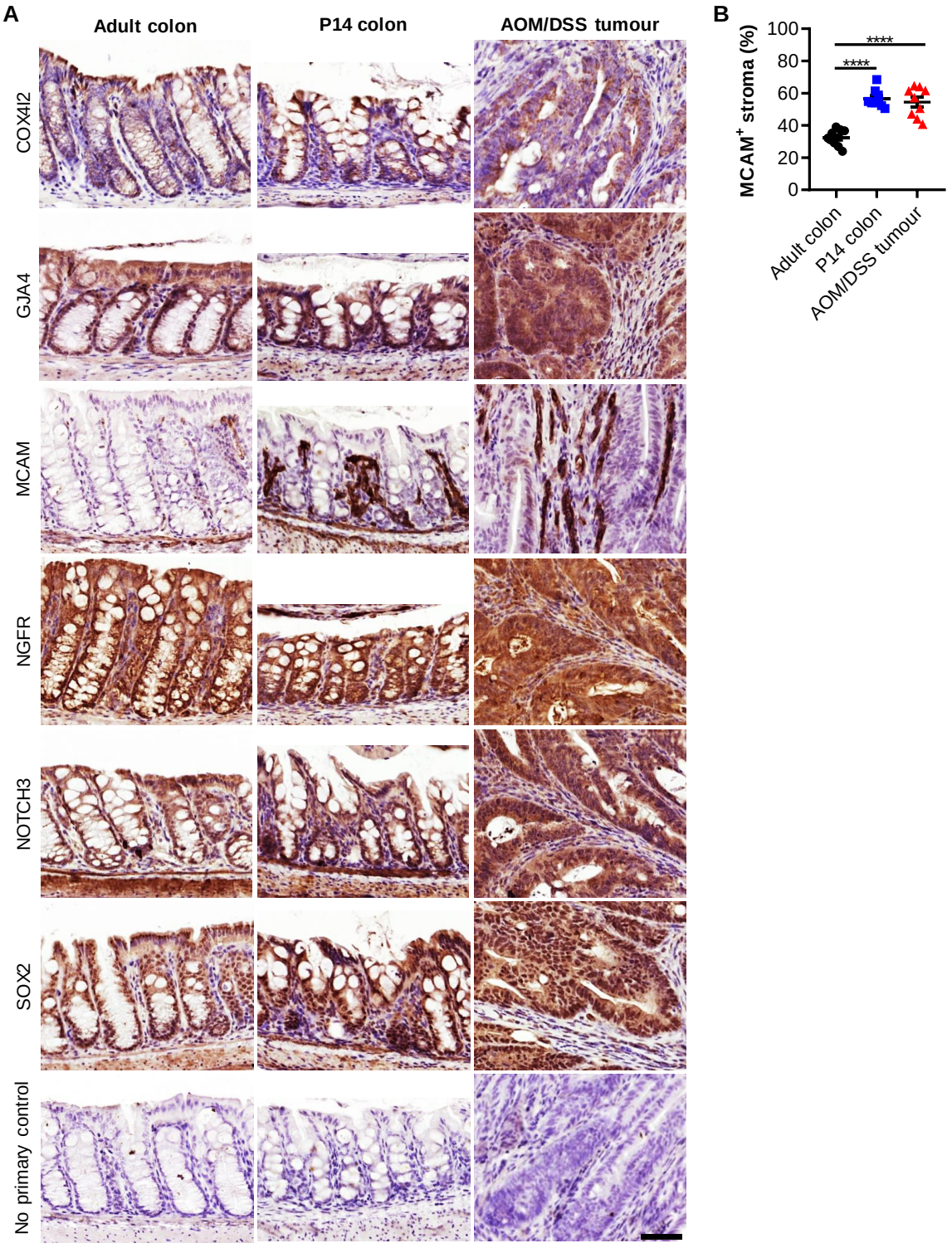


Figure 4.2. MCAM was immunohistochemically validated as having increased stromal-restricted expression in mouse CRC. A, IHC staining of the top 6 RNA-sequencing candidates in mouse adult colon, P14 colon and AOM/DSS tumours; scale bar = 50µm. Staining negative controls (lacking primary antibody) are included to show secondary antibody specificity. **B,** quantification of MCAM staining in the different mouse colon samples (n=3 animals/group, with 3 high powered images quantified/animal). Mean +/- SEM, student's t tests; **** = $p<0.0001$. The mean and statistics were calculated using data combined from both biological and technical replicates.

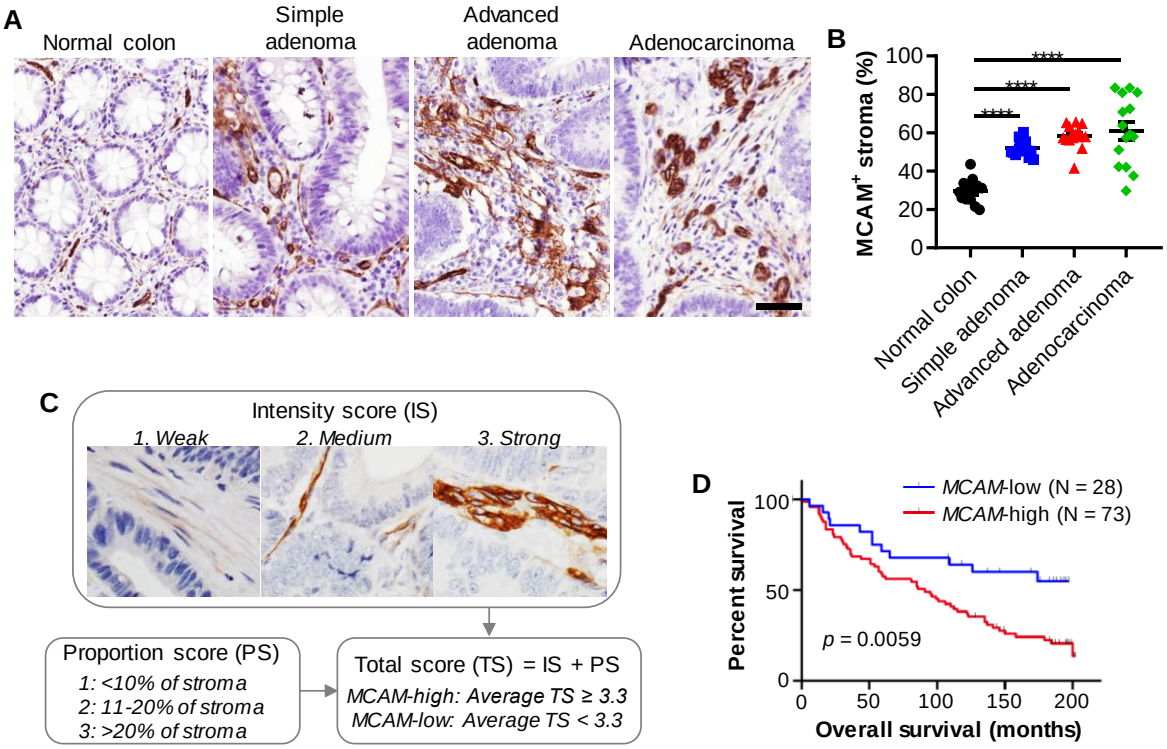


Figure 4.3. MCAM expression significantly increases with human CRC grade and is associated with worse patient survival. A–B, IHC staining of MCAM in normal colon and increasingly advanced stages of human CRC (**A**; scale bar = 50µm), with quantification in **B** (n=4-5 samples/group, with 3 high powered images quantified/sample). **C–D,** tissue microarray of Australian CRC patients (**C**; n=101 patients), with survival analysis in **D**. Mean +/- SEM, student's t tests, **** = p<0.0001. The mean and statistics were calculated using data combined from both biological and technical replicates.

MCAM$^+$ stroma arises from proliferative resident cells

To determine if MCAM$^+$ CRC-associated stromal cells arise from the transdifferentiation or proliferation of resident cells, I made use of mouse tumour samples previously collected in our group. Dr Tamsin Lannagan had continuously administered the DNA intercalating agent 5-bromodeoxyuridine (BrdU) to a cohort of animals as soon as AOM/DSS tumours became visible via colonoscopy, up until humane end point (Fig 4.4A). In this model, BrdU will incorporate into and label any cells that undergo proliferation during the course of tumourigenesis. I then co-stained these samples for MCAM and BrdU and discovered that approximately 60% of MCAM$^+$ cells were new (BrdU$^+$) in AOM/DSS tumours, compared to 10% in the adjacent, non-neoplastic colon (Fig 4.4B-C; Appendix 4). As such, it can be concluded that the MCAM$^+$ tumour stroma mostly arises from resident cells that have locally proliferated during colorectal tumourigenesis. This is useful mechanistic information to accrue as we search to uncover methods to target these cancer stromal cells.

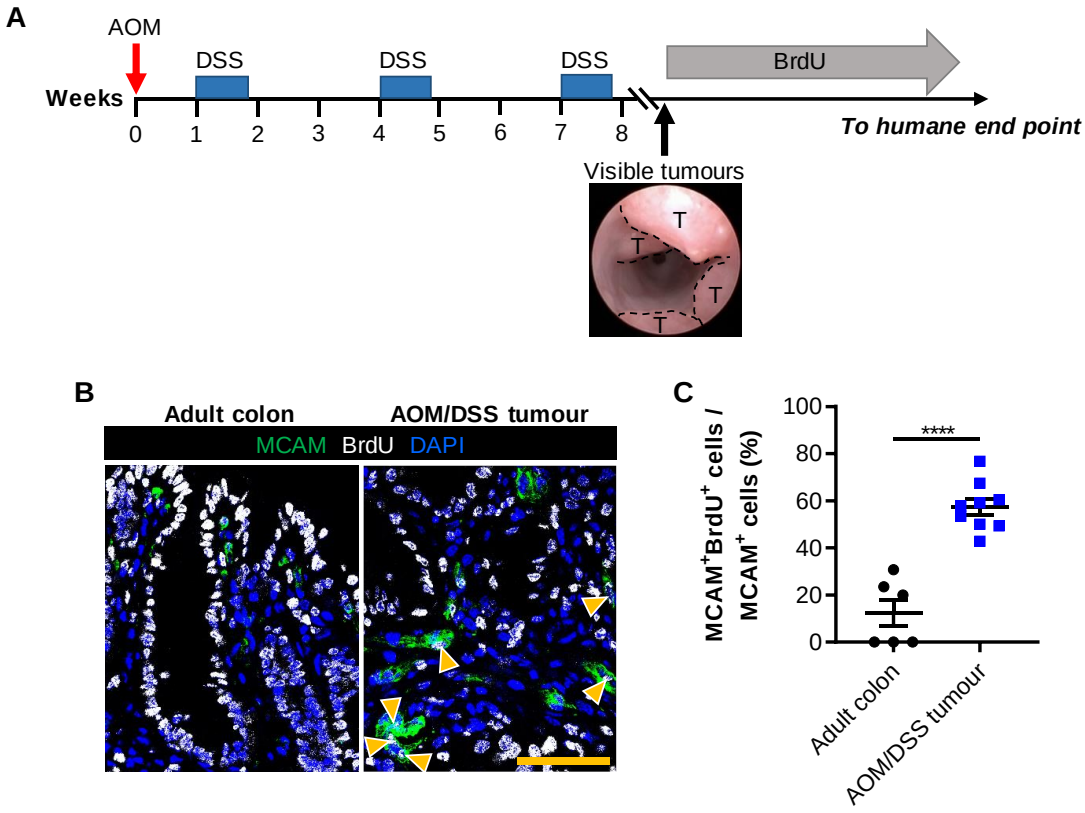


Figure 4.4. MCAM$^+$ stroma expands during mouse colorectal tumourigenesis. A, schematic of the AOM/DSS model combined with BrdU treatment to label all proliferating cells from the first sign of visible tumours. **B–C,** immunofluorescent (IF) co-staining of MCAM with BrdU in adult colon and AOM/DSS tumours (**B**; scale bar = 50μm), and the quantification of overlap in MCAM$^+$ cells in **C** (n=3 animals, with 3 high powered images quantified/animal). Mean +/- SEM, student's t tests, **** = p<0.0001. The mean and statistics were calculated using data combined from both biological and technical replicates.

MCAM$^+$ stroma marks both fibroblastic and endothelial populations in mouse CRC

The trilineage depletion strategy we used to generate our RNA-sequencing data results in a group of cells, primarily a fairly heterogeneous population of fibroblasts. To further validate this stromal restriction, I next investigated which cell types in mouse CRC expressed *Mcam*. To do this, I co-stained AOM/DSS tumours for MCAM and common markers of endothelial (CD31), fibroblast (ACTA2), immune (CD45) and epithelial (EPCAM) cells. As can be seen in Fig 4.5A-B (and Appendix 4), MCAM was expressed in both tumour-associated endothelium and fibroblasts (approximately 60% and 40% of all MCAM$^+$ cells respectively). Immune and epithelial cells were completely devoid of MCAM expression. This suggests that MCAM is highly stromal-specific in CRC, marking populations of tumour-associated fibroblasts, endothelial cells and/or pericytes (fibroblast-like cells closely associated with blood vessels).

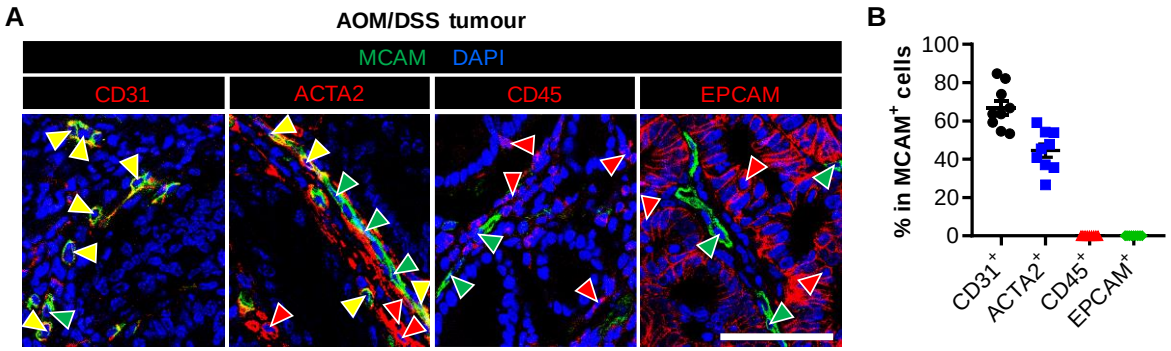


Figure 4.5. MCAM$^+$ mouse CRC stroma is composed of endothelial and fibroblastic populations. A–B, IF co-staining of MCAM with well-known endothelial (CD31), fibroblastic (ACTA2), immune (CD45) and epithelial (EPCAM) markers in AOM/DSS tumours (**A**; scale bar = 50µm), and the quantification of overlap in MCAM$^+$ cells in **B** (n=3 animals/group, with 3 high powered images quantified/animal). Mean +/- SEM. The mean was calculated using data combined from both biological and technical replicates.

***Mcam* is expressed in primary cultured mouse colon myofbs and CAFs**

As I first wanted to model and thus determine the molecular mechanism of MCAM function in mouse colorectal tumourigenesis using cell culture, I needed to examine the expression levels of *Mcam* in different cultured mouse colon myofb lines; thus, I quantified *Mcam* expression in primary myofbs (n=3), primary CAFs (n=2) and the immortalised myofb cell line, YH2 (n=3), relative to the expression in mouse embryonic tissue at embryonic day 15 (E15; n=1) (Fig 4.6A). The data shows that primary myofbs and YH2 cells do express *Mcam* in culture, although the levels are extremely low in YH2 cells, and confirms that *Mcam* is upregulated in primary CAFs (approximately 4-fold higher expression than in primary myofbs). Additionally, I examined *Mcam* in OUs (n=2) and confirmed extremely low expression (Fig 4.6A), validating our IHC data (Fig 4.5B).

Ideally for the *in vitro* cell culture experiments, I would use primary and YH2 myofbs as our *Mcam*^{low} lines and CAFs as our *Mcam*^{high} line and compare the differences in growth and function. However, the laboratory has unfortunately been unsuccessful in culturing a pure population of viable CAFs to date. Using standard isolation techniques [134] with digested mouse colon tumours plated on plastic to cultivate myofbs and CAFs, we discovered that red fluorescent protein$^+$ (RFP$^+$) AP tumouroid cells also survived and contaminated the RFP$^-$ culture (data not shown). The laboratory also tried FACS trilineage depletion of colon tumours to extract CAFs, but the subsequent viability of sorted CAFs in culture was dismal. Thus, to examine MCAM, I chose to enhance *Mcam* expression in the low-*Mcam* expressing YH2 (Fig 4.6B) and primary myofb (Fig 4.6C) lines.



Figure 4.6. *Mcam* is expressed in cultured mouse colon myofbs and CAFs. A, qPCR examination of *Mcam* expression in primary cultured mouse colon myofbs (n=3), primary cultured mouse colon CAFs (n=2), the YH2 mouse colon myofb cell line (n=3) and primary colon epithelial cells grown as organoids (OUs; n=2), compared to mouse E15 tissue (n=1). Samples were run in technical triplicate but only biological replicates are shown. Mean +/- SEM. **B–C,** representative images of the YH2 myofb cell line (**B**) and primary myofbs (**C**) at high confluency in culture; scale bar = 200µm.

Induction of ectopic *Mcam* expression in YH2 and primary myofbs

To examine the function of fibroblast-produced MCAM *in vitro*, I induced ectopic *Mcam* expression in the mouse colon YH2 and primary myofb lines via lentiviral transduction. The backbone lentiviral vector selected was pUltra, and I inserted the mouse *Mcam* coding sequence immediately downstream of *eGFP-P2A* via InFusion HD Cloning. This generated a bicistronic messenger RNA regulated by the strong promoter, UbC (Fig 4.7A). I then used restriction enzyme digests to check the potential pUltra_*Mcam* clones from the ligation and confirmed that clones #1 and #4 displayed the correct pattern and therefore contained DNA encoding *Mcam* (Fig 4.7B). Sanger sequencing verified that both clones had the correct DNA sequence, and clone #1 was used to produce pantropic pUltra_*Mcam* lentivirus using 293FT packaging cells.

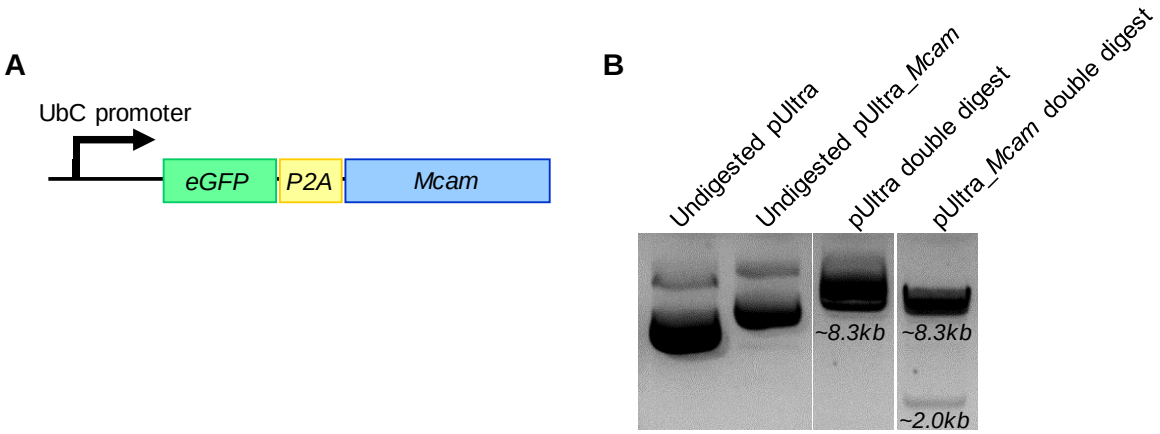


Figure 4.7 legend on next page.

Figure 4.7. Generation of pUltra_*Mcam*. A, linear map of pUltra_*Mcam*, where the mouse *Mcam* coding sequence is downstream of the P2A self-cleavage site in the pUltra lentiviral vector. **B,** pUltra_*Mcam* clones were digested with SpeI and BsmBI and run on a 1% agarose gel to validate successful insertion of the *Mcam* coding sequence into pUltra.

To then examine the effect of MCAM overexpression in an immortalised cell line, YH2 myofbs were transduced with pUltra or pUltra_*Mcam* lentivirus to generate control GFP- or MCAM/GFP-expressing cells, respectively. Single, live GFP^+ cells were extracted via FACS, where the gate was set to collect the top 5% of GFP-expressing control cells. This set threshold meant that only the top 2% of GFP-expressing MCAM cells was collected (Fig 4.8A, left panels). The sorted cells were then plated and allowed to recover before undergoing a second round of FACS to isolate GFP^{high} populations (Fig 4.8A, right panels). Whole cell lysates of the GFP^{Hi} cells were then separated via SDS-PAGE and subjected to western blot for MCAM protein, confirming successful overexpression in the MCAM YH2 line (Fig 4.8B).

To also examine the effect of MCAM overexpression in primary, non-immortal cells, I transduced low passage myofbs with pUltra or pUltra_*Mcam* lentivirus. A western blot of unsorted, transduced cells validated MCAM overexpression in the MCAM myofb line compared to the control (Fig 4.8C). After I successfully optimised the FACS conditions to maintain the viability of primary myofbs, I subsequently set FACS gates to exclude GFP^- cells and collected single, live, GFP-expressing MCAM myofbs. I did not sort the control myofbs, as 99.8% of the cells were already over the set GFP threshold (Fig 4.8D). *Mcam* overexpression at the RNA level was confirmed in MCAM GFP^+ myofbs (Fig 4.8E).

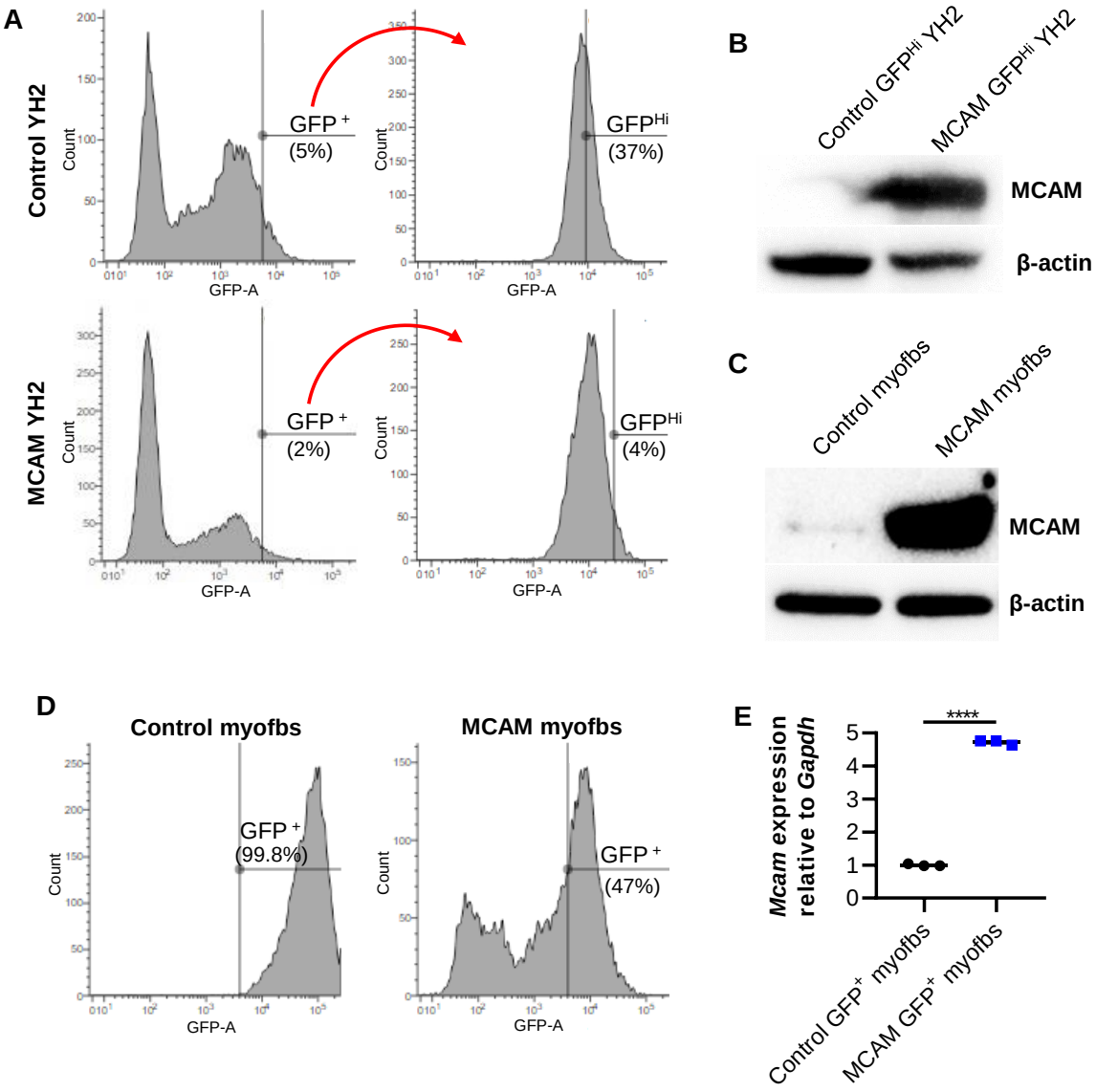


Figure 4.8. Generation of *Mcam*-overexpressing myofbs. A, YH2 cells transduced with GFP-expressing (control) or MCAM/GFP-expressing lentivirus underwent two rounds of FACS for GFP positivity to obtain GFP^{Hi} populations (left panels = first sort, right panels = second sort). Cells were sorted from single, live populations. **B,** whole cell lysates from control and MCAM GFP^{Hi} YH2 cells were separated by SDS-PAGE and subjected to western blot for MCAM. **C,** whole cell lysates from unsorted populations of primary colon myofbs transduced with GFP (control) or MCAM/GFP lentivirus were separated by SDS-PAGE and subjected to western blot for MCAM. **D,** control and MCAM myofbs underwent one round of FACS to extract GFP^{+} populations from single, live cells. **E,** qPCR examination of *Mcam* expression in control and MCAM GFP^{+} myofbs, analysed in technical triplicate. Mean +/- SEM, student's t tests, **** = p<0.0001.

Generation of *Mcam*$^{-/-}$ mice and colon myofbs

In addition to examining the effect of MCAM overexpression in myofbs *in vitro*, I also examined the effect of MCAM loss. To do this, we first generated a ubiquitous *Mcam*$^{-/-}$ C57BL/6 mouse line via CRISPR-CAS9 genetic engineering through SAGE. In these mice, there is a 935 base pair deletion that removes the coding region for exons 2 through 4 for *Mcam* (Fig 4.9A). Consequently, the first 22 amino acids of MCAM remain unaffected but the frameshift caused by the deletion generates a new sequence of 57 amino acids that results in an early stop codon. If aberrant protein is produced, it will only be 79 amino acids long compared to 649 amino acids in normal MCAM (Fig 4.9B). I confirmed the knock-out of *Mcam* in this mouse line by analysing *Mcam* gene expression at the RNA and protein levels in kidney and spleen tissues from *Mcam*$^{-/-}$ mice and *Mcam*$^{+/+}$ littermate controls; *Mcam*/MCAM expression was not detected in *Mcam*$^{-/-}$ tissue (Fig 4.9C-D). In the kidneys and spleens of *Mcam*$^{+/+}$ mice, MCAM appears to mark the endothelial cells of blood vessels and capillaries (Fig 4.9D), which is consistent with my previous data (Fig 4.5B). I next extracted and cultured primary myofbs from the colons of *Mcam*$^{+/+}$ (n=2) and *Mcam*$^{-/-}$ (n=3) mice and confirmed *Mcam* depletion in *Mcam*$^{-/-}$ myofbs via qPCR (Fig 4.9E). I then wanted to confirm that the loss of MCAM was maintained during tumourigenesis, when it is usually upregulated. As a tumouroid line capable of generating tumours in immunocompetent C57BL/6 mice had not been developed at this point, I chose to use the MC38 model. Thus, I orthotopically injected the MC38 tdTomato^{+}luciferase^{+} CRC cell line into *Mcam*$^{+/+}$ and *Mcam*$^{-/-}$ mice (n=2 mice/group). As expected, MCAM protein was lost in the colorectal tumours generated in *Mcam*$^{-/-}$ mice (Fig 4.9F). Interestingly, tumour CD31 staining was indifferent between the two animal groups, indicating that the *Mcam*$^{-/-}$ mice do not have a blood vessel defect (data not shown).

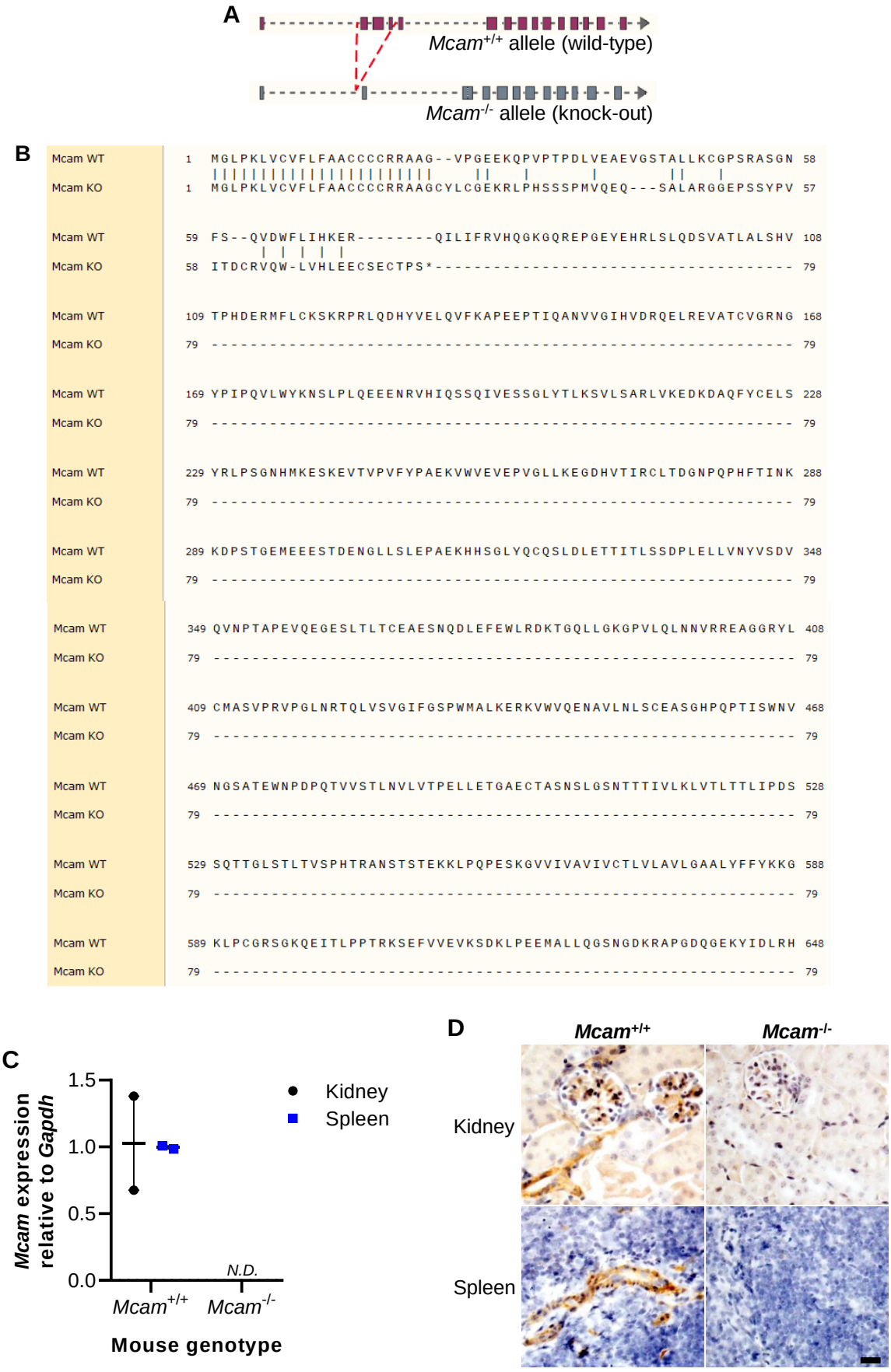


Figure 4.9 continued on next page.

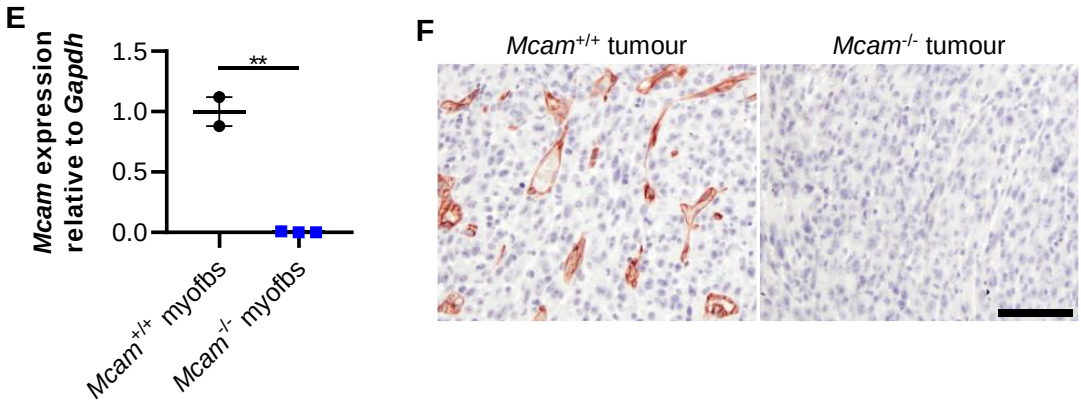


Figure 4.9. Generation of the *Mcam*$^{-/-}$ mouse line. A, exons 2-4 of *Mcam* were constitutively and ubiquitously deleted in C57BL/6 mice using CRISPR/CAS9 gene editing to generate the *Mcam*$^{-/-}$ mouse line. **B,** the frameshift generated from the deletion resulted in early post-translational termination. **C–D,** *Mcam* deletion was validated at the RNA (**C**) and protein (**D**) levels in kidney and spleen tissues (n=2 *Mcam*$^{+/+}$, n=3 *Mcam*$^{-/-}$ mice). N.D. = not detected. **E,** qPCR examination of *Mcam* expression in colon myofbs extracted from *Mcam*$^{+/+}$ (n=2) and *Mcam*$^{-/-}$ (n=3) mice. Each sample was analysed in technical triplicate. **F,** IHC staining of MCAM in colorectal tumours generated from the colonoscopy-guided injection of MC38 tdTomato^{+}luciferase^{+} cells into *Mcam*$^{+/+}$ and *Mcam*$^{-/-}$ mice (n=2 mice/group). Scale bar = 20μm. Mean +/- SEM, student's t tests, ** = p<0.01. The mean and statistics were calculated using data from biological replicates.

MCAM affects the expression of other tumour-promoting genes in primary myofbs

To first determine whether MCAM affected the transcriptional profile of mouse colon myofbs, I ran a qPCR screen of 48 known CAF-associated genes in MCAM GFP^{+} and *Mcam*$^{-/-}$ myofbs with their respective controls (control GFP^{+} and *Mcam*$^{+/+}$ myofbs). These genes were selected based on their association with proliferation, stemness, ECM organisation, inflammation, angiogenesis, migration, invasion and metastasis, and the protein products can either remain in the cell or be secreted. As I identified MCAM as a putative CRC-promoting factor, I hypothesised that myofbs expressing high levels of *Mcam* would exhibit a tumour-promoting expression profile. Of these 48 genes examined, only 6 were oppositely regulated between MCAM GFP^{+} and *Mcam*$^{-/-}$ myofbs – *Grem1*, *c-Myc*, *Nidogen 1* (*Nid1*), *Platelet derived growth factor receptor beta* (*Pdgfrβ*), *Periostin* (*Postn*), and *R-spondin 2* (*Rspo2*) (Fig 4.10). The other 42 genes examined were upregulated or downregulated in both MCAM GFP^{+} and *Mcam*$^{-/-}$ myofbs, and/or not significantly different from their respective controls (Appendix 7). Thus, it appears that MCAM reduces the expression of *Grem1*, *Nid1*, *Pdgfrβ*, *Postn*, and *Rspo2* while inducing *c-Myc* expression in mouse colon myofbs (Fig 4.10). However, worse prognosis in patients with different cancer types is associated with the high expression of each of these genes, except *Rspo2* (only in CRC specifically; Table 4.1), which would accordingly suggest that high levels of MCAM are associated with improved survival outcome. This is not consistent

with my previous data using patient samples, tumour grading and survival analyses (Fig 4.1, Step 2; Fig 4.3D). This qPCR data also suggests that high *Mcam* expression induces a less proliferative, stem cell-like, migratory and invasive phenotype in myofbs, with the downregulated secretion of factors known to promote angiogenesis, tumour growth and metastasis. To understand these results further, I next examined how MCAM affected the cellular functions of the different colon myofb lines.

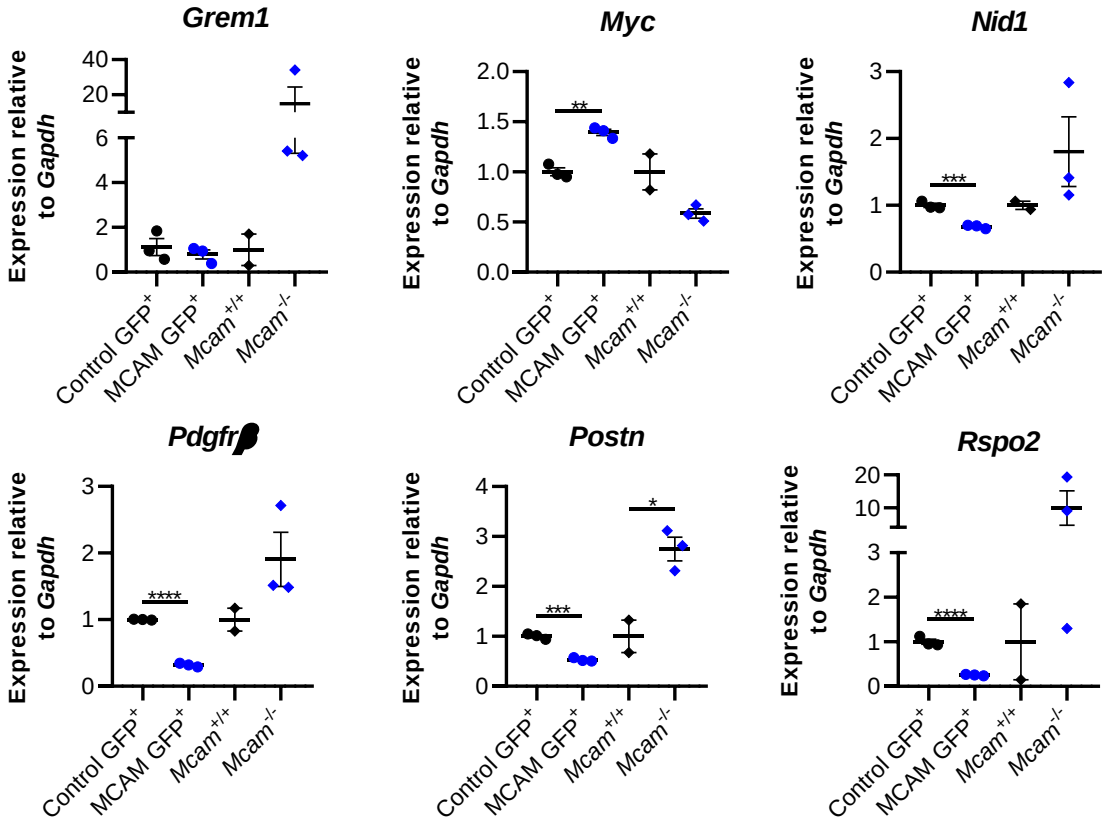


Figure 4.10. Possible downstream effectors of MCAM in mouse colon myofbs. qPCR examination of *Grem1*, *c-Myc*, *Nid1*, *Pdgfrβ*, *Postn*, and *Rspo2* in MCAM GFP^{+} and *Mcam*$^{-/-}$ myofbs, compared to their respective controls (control GFP^{+} and *Mcam*$^{+/+}$ myofbs). Control and MCAM GFP^{+} myofbs are displayed and analysed as a technical triplicate (n=1 experimental replicate), while *Mcam*$^{+/+}$ and *Mcam*$^{-/-}$ myofbs are displayed and analysed as experimental replicates (n=2 *Mcam*$^{+/+}$ and n=3 *Mcam*$^{-/-}$ lines). Mean +/- SEM, student's t test, * = p<0.05, ** = p<0.01, *** = p<0.001 and **** = p<0.0001.

Table 4.1. The function and prognosis of known tumour-promoting genes affected by MCAM in mouse colon myofbs

Gene	Normal function and role in cancer	Cancer prognosis with high expression	Effect of MCAM on expression	Predicted cancer prognosis with high MCAM expression
Grem1	BMP antagonist [108] and VEGFR2 agonist [117] that promotes cancer cell proliferation, stemness, EMT, invasion and metastasis, and activates pro-tumour macrophages (see Chapter 1 for more information).	Poor prognosis in CRC [112, 115], pancreatic cancer [120], breast cancer [121, 123] and glioblastoma [124].	Reduced.	Good*.
c-Myc	Master transcription factor that regulates downstream effectors involved in ribosome biogenesis, protein translation, cell-cycle progression and metabolism to ultimately control a plethora of biological functions such as cell proliferation, differentiation, survival, and adhesion. Frequently deregulated in cancer [192]. Associated with fuelling tumours [193], invasion and metastasis [194], and therapeutic resistance [195-197].	Poor prognosis in breast cancer [196, 198].	Increased.	Poor.
Nid1	Glycoprotein that stabilises the basement membrane structure and promotes wound healing. Associated with EMT, invasion, metastasis and therapeutic resistance [199-201]. However, it can be aberrantly methylated in colon and gastric cancers [202] and its degradation is associated with non-small cell lung cancer [203].	Poor prognosis in CRC [201], breast cancer and melanoma [200].	Reduced.	Good*.
Pdgfrβ	Receptor tyrosine kinase that plays an essential role in blood vessel development [204, 205]. Important for tumour angiogenesis [206]. Also associated with tumour proliferation, stemness, EMT, invasion, metastasis [207-209] and recurrence [210, 211].	Poor prognosis in CRC [209], renal cell carcinoma [212], ovarian cancer [213], glioblastoma [207] and prostate cancer [211].	Reduced.	Good*.

Postn	Secreted ECM protein regulated by several transcription factors and hormones. Promotes proliferation, angiogenesis, migration and metastasis of cancer cells, and counteracts hypoxia-induced apoptosis in cancer cells. Associated with therapeutic resistance. Effects on EMT are tumour cell type-dependent. [214].	Poor prognosis in CRC, prostate cancer, lung cancer, pancreatic cancer, ovarian cancer, breast cancer, hepatocellular cancer and osteosarcoma [214].	Reduced.	Good*.
Rspo2	Potentiates WNT/β-catenin signalling [215, 216] and antagonises fibroblast growth factor (FGF) signalling [217]. Essential regulator of tissue development and homeostasis [218]. Associated with tumour growth, stemness, EMT, invasion, migration, metastasis and therapeutic resistance [219-221]. In CRC, however, it adopts a more tumour-suppressive role and decreases cell proliferation, migration, invasion and metastasis [222, 223].	Poor prognosis in tongue squamous cell carcinoma [221] and breast cancer [224]. Good prognosis in CRC [222] and lung cancer [225].	Reduced.	Poor (in CRC).

* = disagrees with my data that high *Mcam* expression is associated with worse prognosis (Fig 4.1A, Step 2; Fig 4.3D).

MCAM reduces the activity and stemness of myofbs, while improving migration

To examine how *Mcam* expression affects the function of mouse colon myofbs, I undertook a series of *in vitro* assays examining proliferation, activity, stemness and migration. As I identified MCAM as a putative CRC-promoting factor, I hypothesised that high *Mcam*-expressing myofbs would be more proliferative and stem cell-like with improved abilities to contract a collagen matrix and migrate than low *Mcam*-expressing myofbs. To first determine whether altering *Mcam* expression affected proliferation, MCAM GFP^{+} and *Mcam*$^{-/-}$ myofbs were assessed for their replicative ability over a 72-hour period (Fig 4.11A) using CellTiter-Glo and compared to their respective controls. Myofbs expanded during this time but the growth rate was similar between experimental and control groups (Fig 4.11B-C). This suggests that MCAM does not have a role in colon myofb proliferation. Next, collagen contraction assays (Fig 4.11D) were undertaken in MCAM GFP^{Hi} YH2, MCAM GFP^{+} myofbs and *Mcam*$^{-/-}$ myofbs to test their activity relative to their respective controls. With the overexpression of *Mcam*, primary myofbs contracted the collagen significantly less than its control (Fig 4.11F). *Mcam*-overexpressing YH2 myofbs also exhibited a similar although not significant

decrease in contraction compared to its control (Fig 4.11E). There was also no statistically significant difference in contraction between *Mcam*$^{-/-}$ myofbs and its control, although there was a trend towards increased contractility with the loss of *Mcam* (Fig 4.11G). Together, these results suggest that MCAM reduces the ability of colon myofbs to contract ECM. I then tested the ability of myofbs to generate colonies from single cells in colony forming unit-fibroblast (CFU-F) assays, which are indicative of stemness. I saw a significant decrease in the number of colonies formed from MCAM GFP^{+} myofbs and a trend towards reduced colony number in MCAM GFP^{Hi} YH2 cells, compared to their respective controls (Fig 4.11H-I). Conversely, *Mcam*$^{-/-}$ myofbs produced slightly more colonies than their respective control although again this was not statistically significant (Fig 4.11J). These data suggest that MCAM reduces the stemness of colon myofbs. Finally, in scratch assays (Fig 4.11K), *Mcam*-overexpression and knock-out significantly increased and decreased myofb migration to bridge the inflicted scratch respectively, relative to their respective controls (Fig 4.11L-M). This suggests that MCAM improves the motility of colon myofbs. Overall, MCAM significantly reduces the stemness of primary myofbs and their capacity to contract ECM but improves their ability to migrate.

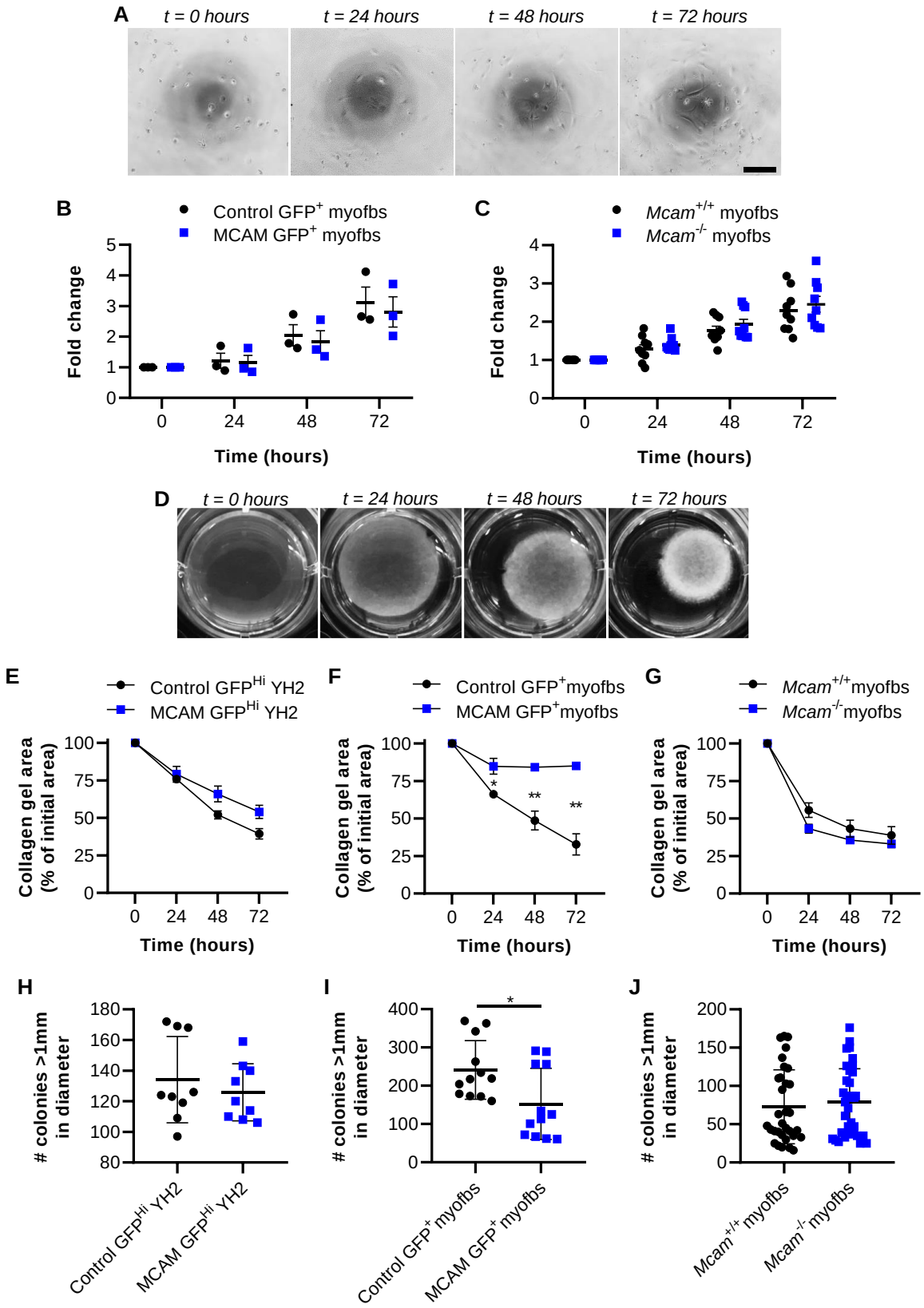


Figure 4.11 continued on next page.

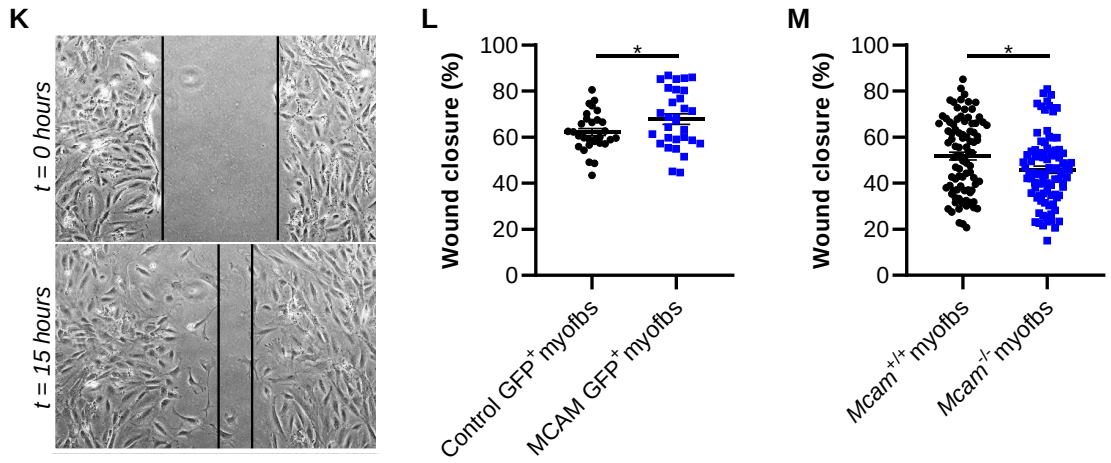


Figure 4.11. MCAM effects the collagen contraction, stemness and migration of primary mouse colon myofbs. The respective, appropriate controls in the following assays for MCAM GFP^{Hi} YH2 (n=1), MCAM GFP^{+} myofbs (n=1) and *Mcam*$^{-/-}$ myofbs (n=3) are control GFP^{Hi} YH2 (n=1), control GFP^{+} myofbs (n=1) and *Mcam*$^{+/+}$ myofbs (n=3). **A,** representative images of myofbs expanding over 72 hours in the proliferation assay; scale bar = 200µm. **B–C,** proliferation assays displaying the fold change in growth from 0 to 72 hours in MCAM GFP^{+} (**B**) and *Mcam*$^{-/-}$ (**C**) myofbs compared to their controls. **D,** representative images of primary myofbs contracting a collagen gel matrix over a 72-hour period. **E–G,** collagen contraction assays displaying the percentage gel contraction from 0 to 72 hours in MCAM GFP^{Hi} YH2 (**E**), MCAM GFP^{+} myofbs (**F**) and *Mcam*$^{-/-}$ myofbs (**G**) compared to their controls. **H–J,** CFU-F assays displaying the number of MCAM GFP^{Hi} YH2 (**H**), MCAM GFP^{+} myofb (**I**) and *Mcam*$^{-/-}$ myofb (**J**) colonies larger than 1mm in diameter that expanded from single cells, compared to their controls. **K,** representative images of primary myofbs in the scratch assay, where 24-hour serum-starved cells are given 15 hours to close the scratch "wound". **L–M,** scratch assays displaying the percentage of wound closure at 15 hours compared to 0 hours using MCAM GFP^{+} (**L**) and *Mcam*$^{-/-}$ (**M**) myofbs, and their controls. All assays were performed in experimental triplicate. The proliferation, collagen contraction and CFU-F assays were done with 3-4 technical replicates, while the scratch assays used 10 technical replicates (with the scratch width measured in 5 different places/technical replicate). Mean +/- SEM, student's t test, * = p<0.05 and ** = p<0.01. The mean and statistics were calculated using data combined from both biological and technical replicates.

Colon myofb-produced MCAM does not directly affect neoplastic colon epithelial growth *ex vivo*

CRC cells are derived from the epithelium and myofbs are known to induce changes in epithelial cells, especially in a cancer setting [30] (see Appendix 1). It is therefore important to examine whether *Mcam*-expressing colon myofbs have a direct effect on the growth of nearby colon epithelia. To

model this interaction *ex vivo*, I set-up a co-culture system between mouse colon OUs and myofbs with different expression levels of *Mcam*. Before attempting this co-culture, however, I first optimised the number of OUs to be plated per 96-well; I found that plating 100 OU fragments/well generated the desired density of readily quantifiable OUs. I did not see a dramatic difference in the size of OUs between the different densities trialled (Fig 4.12A), and a luminescent viability assay showed that OU cell viability approximately doubled between 50 and 100, and 100 and 200 OUs/well, as expected (Fig 4.12B). It is important to note that the OUs used for these assays were modified to express luciferase (by Dr Mari Ichinose), so that in a co-culture system I quantify the viability of OU cells and not co-cultured, viable myofbs. I also chose to use 50% Matrigel instead of 100%, which is not as viscous and can therefore form a thin, more even layer on the bottom of the wells instead of a concave dome. This reduces the number of different planes OUs can grow in, and therefore makes them easier to analyse under a microscope.

To model the crosstalk between the mouse colonic epithelium and nearby myofb support cells, I next optimised a myofb:OU co-culture system. As the MCAM I ectopically overexpressed in the YH2 and primary myofb lines is predicted to be localised to the cell membrane, the mechanism of action may require interaction with unknown receptors present on epithelial cell membranes. As such, I chose to grow the myofbs in close contact with the OUs rather than as a feeder layer, and thus suspended a mixture of myofbs and OUs in Matrigel for the experiments (Fig 4.12C-E). Interestingly, I found that primary myofbs spread much further within the Matrigel than YH2 myofbs (Fig 4.12E). I then set up co-culture assays, plating normal colonic OUs with MCAM GFP^{Hi} YH2 cells or MCAM GFP^{+} primary myofbs or their respective controls. The addition of control or *Mcam*-overexpressing YH2 myofbs to OUs did not significantly affect the number of OU cells, although there was a lot of variability in the OU signal alone which hampered this assay (Fig 4.12F). Co-culture with control primary myofbs, however, did significantly increase the OU-derived luciferase activity compared to OUs alone and the MCAM GFP^{+} myofb co-culture (Fig 4.12G). These data suggest that $MCAM^{+}$ myofbs significantly reduce the myofb-mediated growth induction of normal epithelial cells, contrary to my hypothesis. I decided not to pursue this result further as I was more interested in modelling the crosstalk between myofbs and neoplastic colonic epithelium. As such, I repeated the co-culture experiments except using luminescent AP mono8 HP2.3 tumouroids (50 fragments/well). This time, co-culture with either YH2 or primary myofbs significantly reduced the tumouroid-derived luciferase activity. However, there was no significant difference in OU cell viability between the control and *Mcam*-overexpressing YH2 and primary myofb co-cultures (Fig 4.12H-I). These data suggest a MCAM-independent mechanism of neoplastic epithelial growth modulation by myofbs.

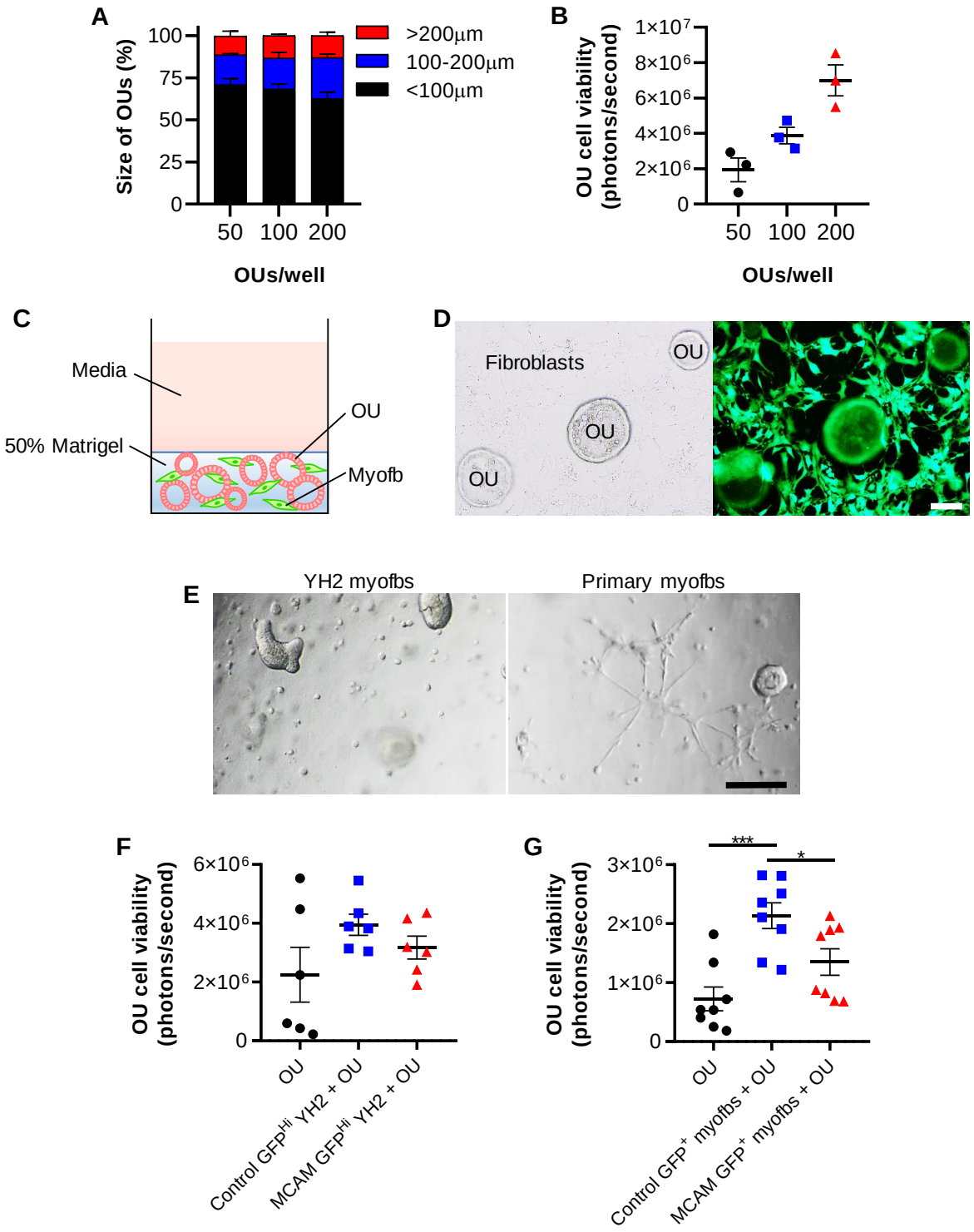


Figure 4.12 continued on next page.

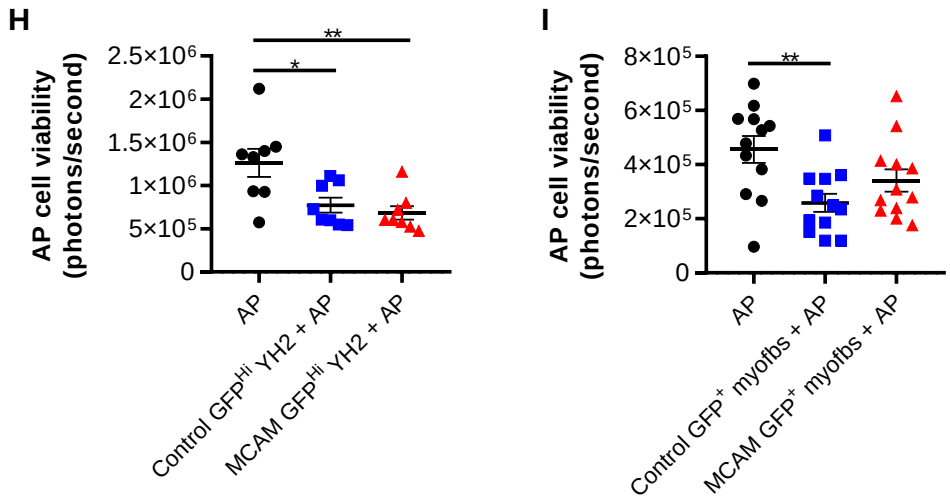


Figure 4.12. Colon myofb-produced MCAM reduces colon OU growth but does not affect mouse colon tumouroid growth. A, analysis of OU size across the different densities plated/well. **B,** luminescent viability assay of OUs plated at different densities. **C,** diagram of the myofb:OU co-culture system, where myofbs are mixed with 100 OU fragments in 50% Matrigel and plated in 96-well plates. **D,** in this co-culture system, myofbs are in close contact with the OUs; scale bar = 100µm. **E,** spreading of YH2 cells and myofbs within the Matrigel; scale bar = 200µm. **F–G,** luminescent viability assay of normal colon OUs alone or co-cultured with control and MCAM GFP^{Hi} YH2 (**F**) or control and MCAM GFP^{+} myofbs (**G**). **H–I,** luminescent viability assay of colon AP mono8 HP2.3 tumouroids alone or co-cultured with control and MCAM GFP^{Hi} YH2 (**H**) or control and MCAM GFP^{+} myofbs (**I**), with 50 AP tumouroid fragments plated/well. For all assays, OUs were analysed at day 6 and AP tumouroids at days 4-5 post-plating. **A–B** displays one experimental replicate done in technical triplicate/density. **F** and **G** were done in experimental duplicate with 3-4 technical replicates. **H** and **I** were done in experimental duplicate and triplicate respectively, in technical quadruplicate. **A** was analysed via a two-way ANOVA, **F–I** via a one-way ANOVA. Mean +/- SEM, * = p<0.05, ** = p<0.01 and *** = p<0.001. The mean and statistics were calculated using data combined from both biological and technical replicates.

Discussion

In this chapter I identified MCAM from our RNA-sequencing data as a putative CRC-promoting stromal protein upregulated during tumourigenesis and significantly associated with worse patient prognosis. I then attempted to determine how MCAM effects the phenotype of both immortal and primary mouse colon myofbs; firstly, by examining the expression of other pro-tumour genes, and secondly, by investigating differences in proliferation, stemness, activity and motility. I also examined the direct effect of MCAM^{+} myofbs on normal and neoplastic epithelial cell growth. As such, this chapter addressed Aims 2 and 3 of my PhD project.

I began this chapter by interrogating our bulk RNA-sequencing data, which identified genes in fibroblasts that were upregulated during mouse colorectal development and tumourigenesis compared to the homeostatic, adult colon, in order to identify putative CRC-promoting factors produced by CAFs. It should be noted, however, that we did not examine fibroblast-associated genes upregulated only in tumourigenesis, and therefore may have missed some novel tumour-promoting candidates though our approach. The laboratory chose to use tumours derived from the AOM/DSS model for this analysis instead of tumours with a defined set of mutations (e.g. those generated from AP and AKP tumouroids) because they spontaneously develop in the presence of inflammation and a carcinogen. As such, each tumour may have a slightly different mutational burden and recruit slightly different tumour-promoting stroma. The drawback of using the AOM/DSS model, however, is that only approximately 18% of tumours invade the surrounding tissue [145] and metastasis does not occur; thus, the tumours are representative of early-stage CRC. Inflammation-associated CRC also contributes to only 1-2% of all colorectal cancers [6]. Nonetheless, filtering the initial list of 342 upregulated stromal candidates through the TCGA dataset (Fig 4.1, Step 2) not only selected genes significantly associated with patient survival, but also indicated that these early stage, inflammation-associated candidates were also present in patients with advanced, sporadic CRC. This was confirmed when I demonstrated upregulated MCAM expression in all stages of sporadic human CRC (Fig 4.3A-B). The RNA-sequencing candidates should therefore theoretically be present in the stroma of most CRC subtypes, suggesting the broad applicability of any drug inhibitors of these candidates.

Refinement of the RNA-sequencing gene list identified COX4I2, GJA4, MCAM, NGFR, NOTCH3 and SOX2 as candidate CRC-promoting stromal factors (Fig 4.1, Step 5). IHC staining of these proteins in the same tissue types used for the RNA-sequencing revealed that only MCAM was stromal-specific and upregulated in CRC (Fig 4.2A-B). The other candidates appeared to have a similar expression pattern between normal mouse colon and AOM/DSS tumours, marking both stromal and epithelial populations at similar intensities and proportions (Fig 4.2A). These candidates will therefore not be examined further in our laboratory and mouse models, but this does not mean that they are not important in other cancer types. NOTCH3 and SOX2 are well-known oncogenic proteins, shown to promote many different cancers including colorectal, breast, ovarian, liver and prostate via various mechanisms [226, 227]. Interestingly, studies have demonstrated that NOTCH3 and SOX2 are significantly upregulated in CRC tissue compared to normal colon, although the tissues examined were of human and not murine origin which may explain why we did not see a significant difference in our IHC [228-230]. NGFR has contradictory roles in cancer, demonstrating tumour-suppression in CRC, prostate cancer and basal-like breast cancer [231-233] but tumour-promotion in cancers including glioblastoma, breast, melanoma and oral squamous cell carcinoma [234-236]. The functions of COX4I2 and GJA4 are not well known in cancer, but COX4I2 can be used as a marker

for tumour angiogenesis in adrenal pheochromocytoma [237] and for the early detection of lung cancer [238], while mutations in GJA4 predispose individuals to angiosarcomas [239].

In addition to demonstrating that MCAM was upregulated in the stroma of both mouse and human CRC (Fig 4.2, 4.3A-B), I also found that high *MCAM*/MCAM expression was associated with worse CRC patient survival (Fig 4.1, Step 2; Fig 4.3C-D). Other papers have also investigated the clinical association between *MCAM*/MCAM expression and survival in patients with cancers including colorectal, liver, lung, breast, gastric, ovarian and oesophageal squamous cell carcinoma [58, 66, 91-96], and are consistent with our work. I also discovered that MCAM$^+$ mouse colorectal tumour stroma was predominantly derived from proliferating resident cells that were induced during tumourigenesis (Fig 4.4C), and that cancer-associated endothelial cells, fibroblasts and/or pericytes produce MCAM (Fig 4.5). Other studies have also identified high *Mcam/MCAM* expression in endothelial cells and pericytes [43, 44, 48, 75, 76], as well as the pericytes and fibroblasts associated with breast cancer [51, 53]. There are also multiple, independent single cell RNA-sequencing datasets that show high *Mcam/MCAM* expression is detected in a specific subset of CAFs with a pericyte-like gene signature in breast and pancreatic cancers [54-56]. We are, however, the first group to investigate MCAM$^+$ CAFs in CRC, as mentioned in the Introduction chapter (Chapter 1).

A focus of this body of work was to uncover the role of colon fibroblast-produced MCAM. This is relatively unknown as the function, binding partners and molecular pathways downstream of MCAM have been studied predominantly in cells other than fibroblasts i.e. endothelial, epithelial and immune cells (Chapter 1, Appendix 2 and 3). Thus, to begin investigating MCAM in fibroblasts, I generated different lines with differing levels of *Mcam* expression. I induced ectopic *Mcam* overexpression in YH2 and primary myofbs via lentiviral transduction (Fig 4.8) and extracted colon myofbs from *Mcam*$^{-/-}$ mice to obtain a knock-out line (Fig 4.9). YH2 and primary myofbs transduced with control GFP lentivirus and colon myofbs extracted from *Mcam*$^{+/+}$ littermates were the appropriate, respective controls.

My functional investigation of MCAM in colon myofbs begun with identifying possible downstream effectors of MCAM, through assessing changes in the RNA expression of known CAF-associated, pro-tumour genes between MCAM GFP$^+$ and *Mcam*$^{-/-}$ myofbs compared to their respective controls. I discovered that MCAM reduced the expression of *Grem1*, *Nid1*, *Pdgfrβ*, *Postn*, and *Rspo2* and increased *c-Myc* expression (Fig 4.10). This not only suggested that low *Mcam* expression could be associated with worse survival (Table 4.1), which is not the case (Fig 4.1, Step 2; Fig 4.3D), but that high *Mcam*-expressing myofbs are less proliferative, stem cell-like, migratory and invasive and secrete less pro-angiogenic and pro-tumourigenic factors than low *Mcam*-expressing myofbs. This is contradictory to our tumour-promoting hypothesis developed through Figures 4.1-4.3. This also disagrees with literature examining MCAM primarily in cells of endothelial and neoplastic origin,

where it was shown to promote proliferation, stemness, migration, EMT, invasion, metastasis and angiogenesis and inhibit apoptosis (see Chapter 1). While I demonstrated that primary MCAM GFP$^+$ myofbs were indeed significantly less stem cell-like and active than their low *Mcam*-expressing control (Fig 4.11F, 4.11H), proliferation was indifferent between groups (Fig 4.11B-C) and migration was actually significantly improved (Fig 4.11L-M). I cannot indefinitely dismiss an effect on fibroblast proliferation, however, as one study showed that *MCAM*-silenced melanoma cells proliferated similarly to their *MCAM*-expressing control *in vitro* but generated significantly less Ki67$^+$ proliferative tumours *in vivo* [67]. The tumour microenvironment may therefore be important in regulating MCAM-mediated growth and this phenomenon may also occur in my *in vitro* studies, but we will not know until we examine MCAM$^+$ and MCAM$^-$ CAFs *in vivo*. The significantly reduced ability of MCAM GFP$^+$ myofbs to contract collagen compared to control myofbs may be attributable to significantly reduced *Acta2* expression in this line (Appendix 7), which is a marker of fibroblast activation. Interestingly, one group demonstrated that silencing *MCAM* in pancreatic CAFs significantly enhanced their activation, although this was not demonstrated using collagen contraction assays [69]. Another group did, however, show that MCAM improved the ability of annulus fibrosus cells to contract collagen [83]. The differences in results between my work and these two studies may be a result of different cell types examined. The significant decrease in stemness and activity was only observed in *Mcam*-overexpressing primary myofbs and not YH2 myofbs (Fig 4.11E, H). This may be due to differences between immortalised and primary cells, as YH2 myofbs are adapted to culture on plastic and display more stem cell-like behaviour and primary myofbs are more active than YH2 cells, so MCAM may have had a lesser and greater impact respectively. Activity and stemness were also not significantly different between *Mcam*$^{+/+}$ and *Mcam*$^{-/-}$ myofbs, although *Mcam*$^{-/-}$ myofbs had significantly reduced motility (Fig 4.11G, J, M). This decreased migratory ability has been demonstrated before, but in MCAM knock-out mouse embryonic fibroblasts [68]. In my assays, however, *Mcam*$^{+/+}$ myofbs were not the perfect control as they expressed low levels of *Mcam* (at least at the RNA level; Fig 4.6A). As such, knocking-out *Mcam* from these cells may not have generated a sizeable difference in myofb behaviour. Equally, use of myofbs from a constitutive knock-out animal may have led to the compensation of other fibroblast genes for the loss of *Mcam* function. In the future, better positive controls would have been *Mcam*$^{+/+}$ myofbs with enhanced endogenous *Mcam* expression or MCAM$^+$ CAFs.

Overall, our *in vitro* fibroblast assays have demonstrated that high *Mcam*-expressing primary myofbs have a reduced ability to contract collagen gels and an improved ability to migrate (Fig 4.11F, L). In the collagen contraction assays, the contractile forces generated by the activated myofbs propagate through the matrix and subsequently arrange the collagen fibres into high density structures, decreasing the matrix volume and thus shrinking the gel [240] (Fig 4.11D). Multiple studies have demonstrated that high density collagen is associated with tumourigenesis; not only is it a potent inducer of invadopedia in cancer cells and primary myofbs, which are cell protrusions that locally

degrade the ECM and mediate invasion [241], but it also enhances the formation, invasion and metastasis of mammary tumours in mice [242]. High density collagen has also been shown to decrease and increase cytotoxic T cell and regulatory T cell abundance, respectively [243, 244], and reduce T cell infiltration into tumours [245], decreasing anti-tumour immunity. These studies unfortunately suggest that low *Mcam*-expressing myofbs are more tumour-supportive than high *Mcam*-expressing myofbs. However, it has also been demonstrated that the formation of blood vessel networks is reduced in high density collagen [246]; so, the low density collagen induced by $MCAM^{+}$ myofbs may have a role in improving tumour angiogenesis. Regarding motility, researchers commonly examine how CAFs induce cancer cell motility rather than motility within the fibroblasts themselves. Although, one study did demonstrate that CAFs were more motile than myofbs in ECM and that these highly motile CAFs facilitated cancer cell invasion [247]. It has been shown that CAFs can directly adhere to skin and squamous cell carcinoma cells, inducing ECM tracks ahead to further accelerate invasion [248, 249]. Furthermore, lung cancer cells can acquire invasive potential by adhering to CAFs and migrating along their long protrusions [250]. It is therefore conceivable that highly motile $MCAM^{+}$ myofbs may drive collective myofb-CRC cell invasion more than $MCAM^{low}$ myofbs, but we are yet to investigate this. One study, however, concluded that collective CAF-melanoma cell invasion and ECM stiffness was reduced through inhibition of CAF motility and contraction [251], implying that for effective invasion the CAFs must be both highly motile and contractile. As our high *Mcam*-expressing myofbs have reduced contractility, we cannot predict the overall effect on tumour invasion and must therefore answer this through *in vivo* experimentation.

It is important to note that I have assumed the ectopically produced MCAM in the MCAM GFP^{Hi} YH2 and MCAM GFP^{+} primary myofb lines was both functional and active, and that the endogenously produced MCAM in $Mcam^{+/+}$ myofbs was active too. This is reasonable to assume as I observed significant differences between the experimental and control groups in the qPCR screen and fibroblast assays (Fig 4.10, 4.11). I have therefore assumed that the MCAM receptor has dimerised, either through homophilic MCAM-MCAM interactions between cells or interactions between MCAM and unidentified fibroblast co-receptors or secreted ligands. In hindsight, I perhaps should have ensured MCAM dimerisation and activation prior to performing my *in vitro* work, by culturing myofbs in tumour conditioned media or adding anti-MCAM antibody to the culture media as others have done [85, 86, 106, 107]. If I had improved my experiments in this way, then perhaps I would have observed more significant phenotypic differences between myofbs expressing high or low levels of *Mcam*.

I also investigated the direct role of $MCAM^{+}$ myofbs on OU and AP tumouroid growth. The results from the qPCR screen (Fig 4.10, Table 4.1) suggested that high *Mcam*-expressing myofbs produce less pro-tumourigenic factors than low *Mcam*-expressing myofbs, which may subsequently reduce OU/AP tumouroid growth. I found that *Mcam*-overexpressing primary myofbs did indeed

significantly reduce OU growth in myofb:OU *ex vivo* co-cultures, compared to co-cultures with its control (Fig 4.12G). Although we are the first group to examine the role of $MCAM^+$ myofbs on normal epithelial cell proliferation, this result was contrary to our hypothesis and was not replicated in *Mcam*-overexpressing YH2 cells (Fig 4.12F). *Mcam*-overexpressing YH2 and primary myofbs also did not significantly affect AP tumouroid growth compared to their respective co-culture controls (Fig 4.12H-I). Interestingly, the addition of control myofbs significantly enhanced normal OU growth but significantly reduced AP tumouroid growth (Fig 4.12F-I). One study has already demonstrated that YH2 cells stimulate colon OU formation [252], so it is unsurprising that primary myofbs can do the same. There is also literature demonstrating that normal myofbs can suppress transformed cells [253-258]; perhaps if I did a co-culture with $MCAM^+$ CAFs, which are modified by the tumour microenvironment, I would see enhanced growth in both OUs and AP tumouroids. $MCAM^+$ myofbs may still influence neoplastic epithelial growth, however, albeit indirectly via other cell types; for example, $MCAM^+$ myofbs could interact with cancer-associated endothelial cells to promote angiogenesis and thus tumour growth and survival. Or, perhaps $MCAM^+$ myofbs affect epithelial migration and invasion instead of growth.

It should be noted that colon myofbs were the chosen cell type for the examination of MCAM because they are a major source of CAFs in our AOM/DSS model (Appendix 4). However, *Mcam*/*MCAM* is also expressed in both normal [44, 48, 75, 76] and tumour-associated pericytes [52, 53], which are another potential source of CAFs [31, 54-56]. The unexpected results from this chapter may therefore be due to the use of the wrong cell type to mimic the effect of *Mcam* expression by CAFs, and the laboratory may choose to examine the putative tumour-promoting role of $MCAM^+$ pericytes in the future.

In conclusion, I have identified MCAM as a CAF-expressed, putative CRC-promoting factor that is associated with worse patient survival. By modulating the expression of *Mcam* in different colon myofb lines, I discovered that MCAM induced a tumour-suppressive gene expression profile in myofbs and significantly reduced their activity while improving motility. I also showed that $MCAM^+$ myofbs do not directly affect the growth of AP tumouroids. Unfortunately, more work needs to be done to identify the cell types and molecular pathways influenced by $MCAM^+$ myofbs and whether this results in the promotion of colorectal tumourigenesis.

Chapter 5: GREM1 Inhibition in Mouse Models of CRC

In this chapter I address Aim 4 of my PhD project; to examine the putative tumourigenic role of colon CAF factors *in vivo*. Specifically, I examined the function of GREM1 in our primary and hepatic metastatic models of CRC by treating mice with a GREM1 NAb or IgG1 isotype antibody (Ab) control from UCB Pharma. This GREM1 NAb has successfully been used in a mouse model of multiple myeloma where it was shown to significantly reduce tumour burden [132], and is currently in a Phase 1/2 clinical trial to examine safety and anti-tumour activity in patients with advanced solid tumours (ClinicalTrials.gov identifier: NCT04393298). In our manuscript [136] (Appendix 8), Dr Hiroki Kobayashi showed that high *GREM1* expression was associated with worse CRC patient survival (Appendix 8; Fig 2D-E). He also demonstrated that fibroblast-derived GREM1 improved the growth of mouse colorectal AP mono8 HP2.3 tumouroids, while the GREM1 NAb reduced their growth (Appendix 8; Fig 5C-D). Dr Kobayashi has additionally shown that *Grem1* expression is significantly upregulated in human colorectal tumours and liver metastases (Appendix 8; Fig 1C, Fig 2A-B and Supplementary Fig 8A-B), and that *Grem1* is expressed in colorectal and liver tumours generated by tumouroid injection into our orthotopic and hepatic metastatic CRC mouse models (Fig 5.1); thus, I hypothesised that GREM1 inhibition *in vivo* via the NAb would reduce primary and metastatic tumour growth and ultimately improve mouse survival. I also wanted to investigate whether combinational therapy of the GREM1 NAb with CRC standard-of-care chemotherapy (FOLFOX) was more efficacious than FOLFOX or the GREM1 NAb alone, and therefore conducted a FOLFOX pilot to determine the optimal dosing schedule in our hepatic metastatic CRC mouse model.

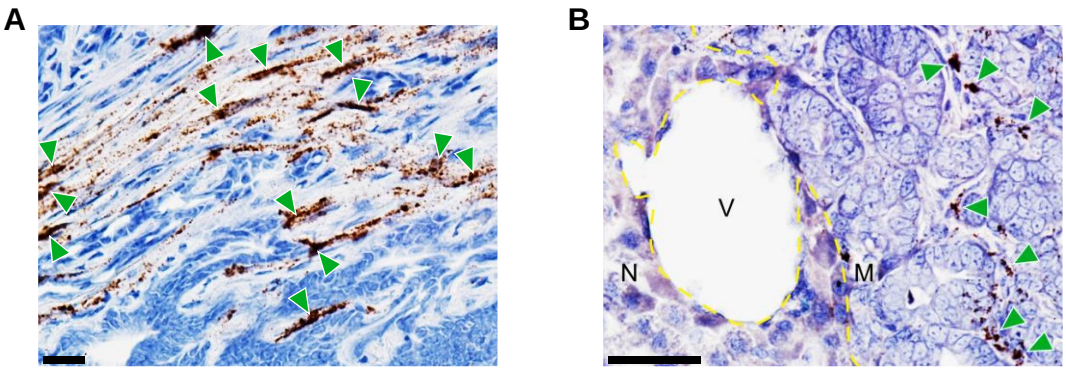


Figure 5.1 legend on next page.

Figure 5.1. *Grem1* is expressed in tumours from our primary and metastatic CRC mouse models. A–B, In-situ hybridisation (ISH) for *Grem1* in tumouroid-derived colorectal (**A**) and liver (**B**) tumours in the syngeneic mouse models of primary and metastatic CRC, respectively. The staining was done by Dr Hiroki Kobayashi. Green arrowheads indicate *Grem1* expression. **A,** *Grem1* was expressed by CAFs in the colorectal mesenchymal stroma; scale bar = 20μm. **B,** *Grem1* was expressed by CAFs in the liver mesenchymal stroma (M) of metastases, but not in the normal liver (N). The yellow dotted line demarcates the normal liver and CRC liver metastases. V = the portal vein, scale bar = 50μm.

Piloting standard-of-care chemotherapy in our hepatic metastatic mouse model of CRC

A standard path to the clinic for novel therapeutic agents begins with pre-clinical testing and a Phase 1 trial for safety. If the agent has pre-clinical efficacy in combination with standard-of-care chemotherapy, this may expedite uptake to Phase 2 efficacy studies as clinicians may be more comfortable adding novel agents to treatments they are familiar with, with proven efficacy, rather than trialling the single agent alone. As such, I aimed to develop a pre-clinical model of advanced CRC with the standard first-line chemotherapy used in patients with locally advanced or metastatic CRC, FOLFOX, and test in combination with the GREM1 NAb to determine if co-treatment further improved survival outcomes.

FOLFOX has three components: 5-fluorouracil (5-FU), leucovorin (LV) and oxaliplatin (OX). 5-FU has been used in CRC treatment for more than 40 years. *In vivo*, it is catabolised into many different metabolites that exert their anti-cancer effects by incorporating into DNA and RNA and by inhibiting thymidylate synthase, a key enzyme in the production of the essential DNA base thymidine [259, 260]. However, only 10-20% of colorectal tumours respond to 5-FU monotherapy as it has a very short plasma half-life and rapidly falls below the cytotoxic threshold. Significant toxicities are also associated with its use, such that 30-40% of patients require dose reduction [261]. To improve efficacy, 5-FU is combined with biochemical modulators such as LV to stabilise the binding of its metabolites to thymidylate synthase and subsequently improve the inhibition [260]. While 5-FU/LV dual therapy significantly improved response rates compared to 5-FU monotherapy (23% vs 11%), it did not improve the overall survival in advanced CRC patients [262]. Thus, to further improve response rates, other anti-cancer drugs such as OX have been tried with 5-FU/LV. OX is a platinum-based drug that generates DNA adducts, which cause double strand breaks that subsequently activate DNA repair mechanisms or even programmed cell death pathways if the damage is severe [263]. As a first-line treatment in Phase 3 trials compared to 5-FU/LV alone, 5-FU/LV/OX (FOLFOX) improved the median progression-free survival of patients with advanced CRC and improved the tumour response rate from 22% to 51% [7, 264].

Before I could examine whether GREM1 inhibition combined with FOLFOX was more efficacious than the GREM1 NAb or FOLFOX alone in our CRC mouse models, I needed to pilot a FOLFOX treatment regimen. As FOLFOX is commonly administered to patients with advanced disease, and more than 80% of administered 5-FU is catabolised in the liver [265], I chose the hepatic metastatic CRC model for the pilot. Thus, AP mono8 HP2.3 tumouroids were digested to single cells and injected into the liver of Cas9 mice (n=18) via the portal vein. This tumouroid line was chosen because the AKP mono7 $CAS9^{-}GFP^{-}$ tumouroid line had not yet been developed, and so I could not induce hepatic metastases in C57BL/6 mice. Bioluminescence imaging was then used 1 week post-surgery to allocate mice into untreated or treated groups, such that the average bioluminescent readout between groups was similar (data not shown). Animals in the treated groups were administered FOLFOX using the previously reported dosing of 50mg/kg 5-FU, 6mg/kg OX and 90mg/kg LV, once a week [141-144] via a single, intra-peritoneal injection, beginning either 1 (Fw1) or 3 (Fw3) weeks post-tumouroid injection. Treatment was stopped at 8 weeks post-injection. A schematic of the small pilot cohort is displayed in Fig 5.2A (n=3 male and n=3 female mice/group). Hepatic tumour growth was monitored via bioluminescence imaging over 17 weeks but only data up until the first humane animal end point in each group and gender is displayed to allow the comparison of all animals in each group (Fig 5.2B). Interestingly in this model, untreated males tended to develop liver tumours faster than untreated females and consequently reached ethical end point sooner, although this was not significant (Fig 5.2B-C). Untreated males also had a significantly higher tumour burden than Fw1 males at 5 weeks post-tumouroid injection (p=0.0253, two-way ANOVA), while Fw1 females had significantly higher tumour burden than Fw3 females at 6 weeks post-tumouroid injection (p=0.0334, two-way ANOVA) (Fig 5.2B). Overall, it appeared that there was a trend towards decreased tumour burden in treated mice compared to untreated controls when animals were separated into males and females (Fig 5.2B). Unfortunately, treated mice did not significantly outlive untreated animals regardless of how soon after tumour induction treatment was started (Fig 5.2D-E). Instead of improving the survival outcome, as I would expect, this FOLFOX regimen had toxic side effects that resulted in premature animal collection. Males were especially prone, reaching humane end point significantly sooner than untreated males (Fig 5.2D). Treated females were more resistant (Fig 5.2E) but also suffered from extreme weight loss that necessitated humane culling. Many mice developed a blood-filled abdomen, termed haemorrhagic ascites (Fig 5.2F), which is the result of severe liver damage caused by the tumours. Interestingly, no untreated males developed haemorrhagic ascites compared to 100% of males receiving FOLFOX. This difference is significant (Table 5.1) and suggests that treated males were reaching ethical end point due to a combination of FOLFOX-related toxicity and tumour burden. Untreated females, however, were just as likely as treated females to develop haemorrhagic ascites (Table 5.1). When I examined the pathology of livers collected at ethical end point and stained with H&E, I observed that the total tumour area per animal was not significantly different between untreated and treated groups and that this was independent of whether treated animals were euthanised during or after FOLFOX was stopped at 8-weeks post-

tumouroid injection (Fig 5.2G-H). This suggests that FOLFOX was ineffective in decreasing tumour burden in our model, despite being administered at a toxic dose. As 5-FU and OX reduce DNA synthesis and induce DNA damage [259, 260, 263], I hypothesised that treated animals would have decreased tumour proliferation and enhanced tumour DNA damage repair compared to untreated animals. However, I observed similar Ki67 and phosphorylated histone variant H2AX (γH2AX) staining between groups at ethical end point, regardless if treated animals were collected during or after FOLFOX was stopped (Fig 5.2I-L). This suggests that either the FOLFOX administered was not sufficiently active *in vivo* using this regimen or that the AP mono8 HP2.3-derived tumours were insensitive to this treatment. As this FOLFOX regimen was inefficacious and toxic, I did not combine FOLFOX with the GREM1 NAb and thus examined the efficacy of the GREM1 NAb alone in subsequent CRC mouse studies (see below).

Table 5.1. Contingency table of number of mice with haemorrhagic ascites in untreated and FOLFOX-treated groups

Males						
Treatment group	**No haemorrhagic ascites**		**Haemorrhagic ascites**		**Total number of male mice**	**Fisher's exact test**
	Number	**Percentage**	**Number**	**Percentage**		
Untreated	3	100.00	0	0.00	3	$p = 0.0119$
FOLFOX	0	0.00	6	100.00	6	
Females						
Treatment group	**No haemorrhagic ascites**		**Haemorrhagic ascites**		**Total number of female mice**	**Fisher's exact test**
	Number	**Percentage**	**Number**	**Percentage**		
Untreated	1	33.33	2	67.67	3	$p > 0.9999$
FOLFOX	1	16.67	5	83.33	6	

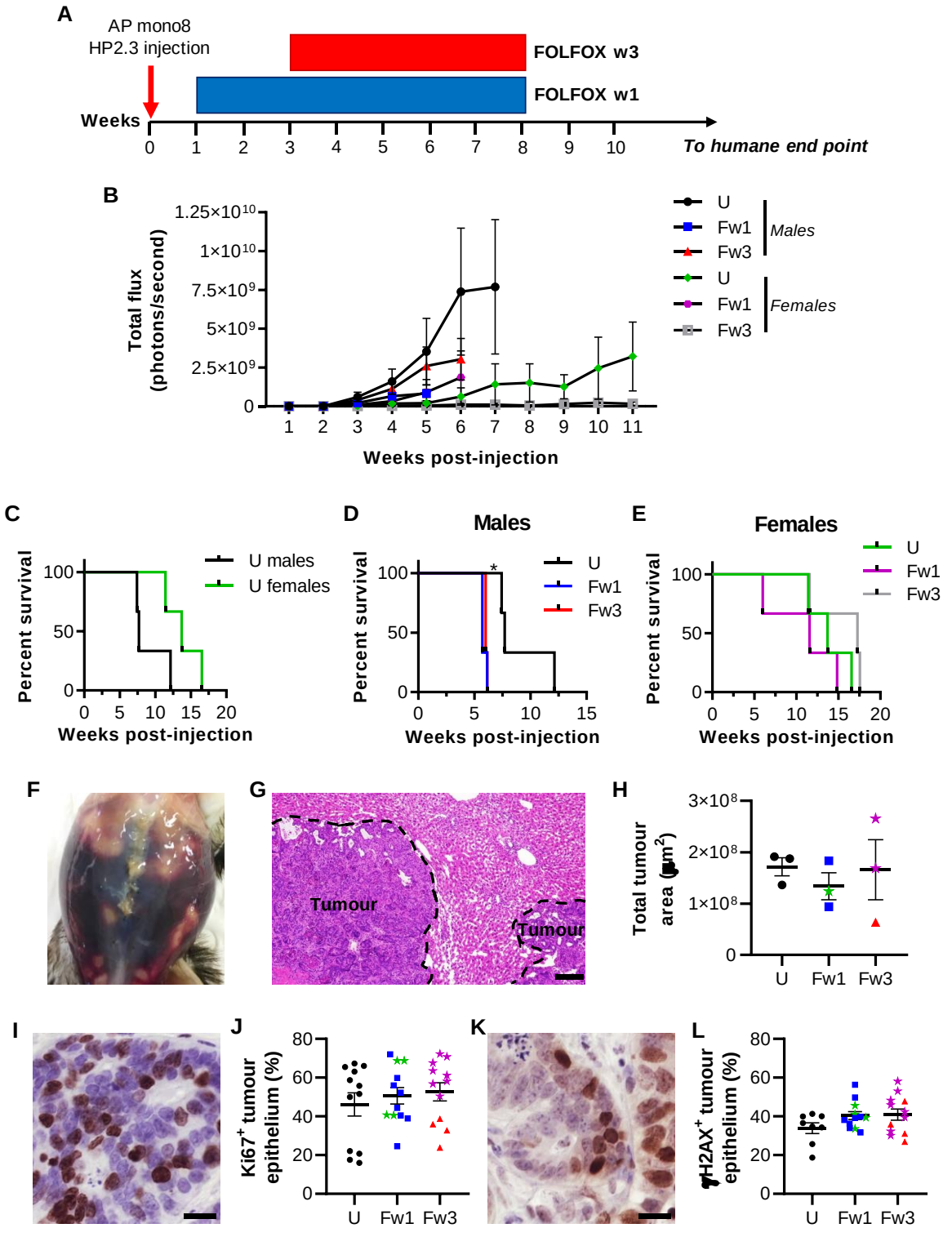


Figure 5.2 legend on next page.

Figure 5.2. The FOLFOX regimen caused severe toxicity and did not improve survival in a hepatic metastatic CRC mouse model. A–L, $5x10^5$ single AP mono8 HP2.3 tumouroid cells were injected into the liver of syngeneic Cas9 mice and FOLFOX (50mg/kg 5-FU + 6mg/kg OX + 90mg/kg LV) was administered as a single intra-peritoneal injection once weekly from either 1 or 3 weeks post-tumouroid injection, until 8 weeks post-injection (n=3 male and n=3 female mice/treatment group). **A,** schematic of FOLFOX administration. **B,** liver tumour growth in untreated (U), FOLFOX week 1 (Fw1) and FOLFOX week 3 (Fw3) mouse groups was monitored via bioluminescence imaging. Data up until the first animal death in each group and gender is shown. **C–E,** Kaplan-Meier survival curves of untreated males vs females (**C**), untreated vs treated males (**D**) and untreated vs treated females (**E**). **F,** image of a mouse abdomen at necropsy with the skin removed but peritoneum intact, showing haemorrhagic ascites underneath. **G,** H&E image of liver tumours; scale bar = 200µm. **H,** quantification of total liver tumour area/treatment group at humane end point (n=3 mice/group). Only biological replicates are displayed and analysed. **I–J,** representative image of Ki67 staining in end point liver tumours (**I**) and the quantification in **J**. **K–L,** representative image of γH2AX staining in end point liver tumours (**K**) and the quantification in **L**. In **H**, **J** and **L**, green and purple stars in the Fw1 and Fw3 groups respectively indicate animals that died within the weeks of FOLFOX treatment. For Ki67 and yH2AX quantification (**J**, **L**), liver tumours from n=2-3 mice/group were examined at humane end point with 4 high powered fields quantified/animal; scale bar = 20um. The mean and statistics were calculated using data combined from both biological and technical replicates. **B** was assessed for statistical significance via a two-way ANOVA, **C–E** via a Mantel-Cox test for survival, and **H** and **J–K** via student's t tests. Mean +/- SEM, * = $p<0.05$. The mean and statistics were calculated using data combined from both biological and technical replicates.

Liver tumours generated from AP mono8 HP2.3 tumouroids do not respond to GREM1 inhibition

I initially designed an experiment to examine the effect of GREM1 inhibition in the hepatic metastatic CRC mouse model using AP mono8 HP2.3 tumouroids, to match Dr Hiroki Kobayashi's examination of *Immunoglobulin superfamily containing leucine rich repeat* (*Islr*) overexpression in the same model (see Appendix 8; Fig 6). Exploring metastatic disease is also beneficial when considering that Phase 1 clinical trials often recruit patients with advanced, chemoresistant disease. I therefore injected single AP mono8 HP2.3 tumouroid cells into the liver of Cas9 mice (n=38), via the portal vein. 1 week post-surgery, mice underwent bioluminescence imaging and were randomly assigned to either the IgG Ab or GREM1 NAb treatment groups (n=8 males and n=11 females in the IgG group, n=9 males and n=10 females in the GREM1 group). Bi-weekly subcutaneous injection of either IgG Ab or GREM1 NAb, dosed at the previously reported 30mg/kg [(132)], began immediately

after the randomisation and continued until humane end point (Fig 5.3A). Tumour growth was tracked weekly via bioluminescence imaging over 26 weeks, after which I decided to end the experiment despite two GREM1 NAb-treated females remaining. These mice had still not developed tumours according to the imaging despite one having visible signal at the week 1 allocation, and it had been 6 weeks since the last signal-positive animal reached humane end point. The lack of liver tumour growth in these two animals was confirmed at necropsy. The number of animals that developed liver tumours in each treatment group, however, was not significantly different (Table 5.2).

Table 5.2. Contingency table of number of animals that developed liver tumours in the hepatic metastatic CRC model

Treatment group	No liver tumours		Liver tumours		Total number of animals	Fisher's exact test
	Number	Percentage	Number	Percentage		
IgG	0	0.00	19	100.00	19	$p = 0.4865$
GREM1	2	10.53	17	89.47	19	

Both male and female mice began reaching ethical end point from liver tumours approximately 9 weeks post-injection. The bioluminescence readings for these first 9 weeks revealed that there was no significant difference in liver tumour burden between the IgG Ab- and GREM1 NAb-treated groups (Fig 5.3B). This was supported by quantification of the mean tumour area as a percentage of the total liver area at humane end point, visualised by H&E staining (Fig 5.3C-D). Liver tumour proliferation, as quantified by Ki67 staining, was also not significantly different between the treatment groups at humane end point (Fig 5.3E-F). When I examined the incidence of macroscopic metastases at necropsy I found that the most common metastatic site was the lungs, with 58% and 63% of IgG Ab- and GREM1 NAb-treated mice presenting with visible lung lesions, respectively (Fig 5.3G). When the lungs were examined microscopically after H&E staining (Fig 5.3H), 83% of IgG Ab-treated animals had metastatic lung lesions; however, there was still no significant difference in the number of animals that developed lung metastases between treatment groups (Table 5.3). There was also no significant difference in the number of lung metastases per animal between groups (Fig 5.3I), but the average area of the lesions was significantly larger in GREM1 NAb-treated animals (Fig 5.3J). These data suggest that GREM1 downregulation promotes more efficient metastatic growth but not the establishment of lung metastases. Overall, use of the GREM1 NAb did not significantly improve survival when compared to the IgG Ab-treated group in either gender, despite two GREM1 NAb-treated females remaining tumourless after 26 weeks (Fig 5.3K-L). Due to the lack of efficacy of the GREM1 NAb, I tested whether the NAb was active *in vivo* at humane end point following continuous weekly dosing. Thus, liver sections were stained for phosphorylated SMAD1/5/8 (pSMAD1/5/8), a readout of BMP pathway activity, and Dr Hiroki Kobayashi and I

demonstrated that staining was enhanced in GREM1 NAb-treated tumours (Appendix 8; Supplementary Fig 20C-D). This indicated that BMP signalling was indeed induced in GREM1 NAb-treated mice, as expected. The GREM1 NAb was therefore simply not efficacious in our hepatic metastatic CRC model.

Table 5.3. Contingency table of number of animals with lung metastases in the hepatic metastatic CRC model

Treatment group	No lung metastases		Lung metastases		Total number of animals	Fisher's exact test
	Number	Percentage	Number	Percentage		
IgG	3	16.67	15	83.33	18	$p = 0.2691$
GREM1	7	36.84	12	63.16	19	

Lungs were not collected from one IgG Ab-treated mouse.

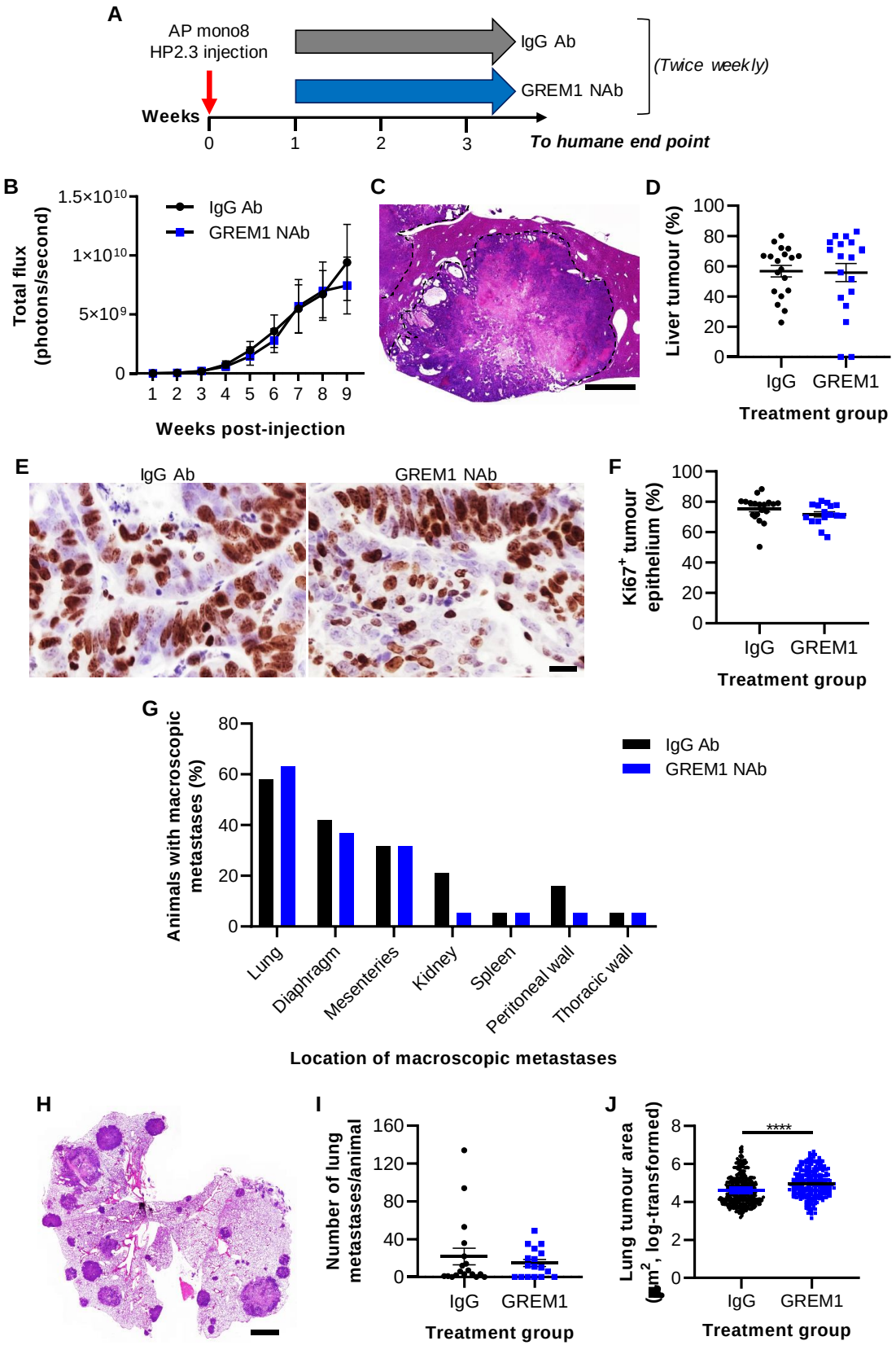


Figure 5.3 continued on next page.

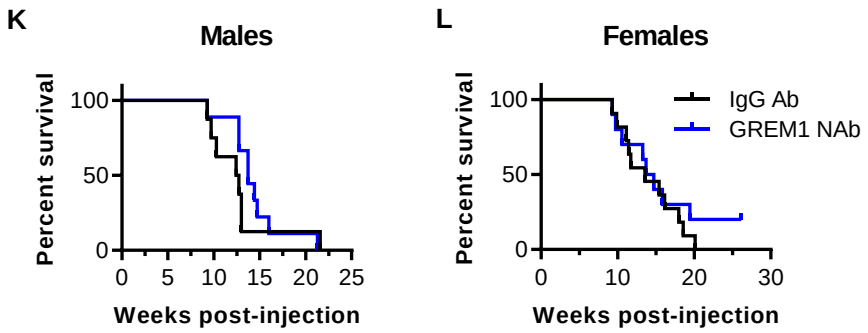


Figure 5.3. GREM1 inhibition does not affect tumour growth or survival in a hepatic metastatic mouse model of CRC. A–L, $5x10^5$ single AP mono8 HP2.3 tumouroid cells were injected into the liver of syngeneic Cas9 mice and treatment with either 30mg/kg IgG Ab or GREM1 NAb begun one week later and continued until humane end point (n=19 mice/group). **A,** schematic of IgG Ab and GREM1 NAb administration. **B,** Liver tumour growth was monitored via bioluminescence imaging. Data up until the first animal death in each treatment group is shown. **C,** H&E image of liver tumours; scale bar = 2000µm. **D,** quantification of the mean liver tumour area as a percentage of the total liver area at humane end point. **E–F,** representative images of Ki67 liver tumour staining in IgG Ab- and GREM1 NAb-treated mice at humane end point (**E**; scale bar = 20µm) and the quantification in **F**, where 4 high powered fields of liver tumours from each animal was examined. **G,** percentage of animals in each treatment group presenting with macroscopic metastases at different locations within the peritoneal and thoracic cavities. **H,** H&E image of lungs studded with metastatic lesions (dark purple); scale bar = 2000µm. **I,** quantification of the number of lung metastases per animal in each treatment group at humane end point. **J,** log-transformed data of the average area of lung metastases in each treatment group at humane end point. **K–L,** Kaplan-Meier curves showing survival of males (**K**) and females (**L**) in different treatment groups. Data in **F–G** and **I–J** excludes the two GREM1 NAb-treated females that were culled after 26 weeks of the experiment with no tumour burden. **B** and **G** were assessed for statistical significance via a two-way ANOVA, **D** and **I–J** via a Mann-Whitney U test, **F** via a student's t test, and **K–L** via a Mantel-Cox test for survival. Mean +/- SEM, **** = $p<0.0001$. The mean and statistics were calculated using data combined from both biological and technical replicates.

Pre-treatment with the GREM1 NAb impedes primary CRC growth but does not improve survival

I next wanted to investigate the role of GREM1 and efficacy of the GREM1 NAb in a pre-treated, orthotopic mouse model of primary CRC located within the colon microenvironment. In this way, I could explore the possible role of GREM1 in tumour initiation as well as progression. Thus, Cas9 mice were randomly assigned to treatment groups and pre-treated with IgG Ab or GREM1 NAb

(n=10/group) for 2 weeks prior to the colonoscopy-guided injection of AP mono8 HP2.3 tumouroids into the colon wall. Treatment with the IgG Ab and Grem1 NAb (30mg/kg each) was given bi-weekly until humane end point (Fig 5.4A), as in the hepatic metastatic model. Tumouroids were injected into two different locations along the distal colon which, with a 100% take rate, should generate two tumours per animal; I found the take rate to be 94% and 81% in IgG Ab- and GREM1 NAb-treated animals respectively (Table 5.4). As the take rate was not statistically different between groups, blocking GREM1 did not have a significant impact on colorectal tumour initiation in this model. Tumour growth was then monitored via weekly bioluminescence imaging and colonoscopy over 28 weeks, after which the experiment was stopped with one female in each treatment group remaining. At necropsy, this IgG Ab-treated female along with two GREM1 NAb-treated animals were excluded from our analyses as their tumours were incorrectly seeded to locations other than the colon. As GREM1 is a tumour microenvironment protein, it is important to examine the GREM1 NAb treatment in the context of the colon for this cohort. As such, the number of animals in each treatment group became n=5 males and n=4 females in the IgG Ab-treated group, and n=4 males and n=4 females in the GREM1 NAb-treated group.

Table 5.4. Contingency table of number of colon tumours that developed from tumouroid injections in the primary CRC model

Treatment group	No colon tumour		Colon tumour		Total number of tumouroid injections	Fisher's exact test
	Number	Percentage	Number	Percentage		
IgG	1	5.56	17	94.44	18	$p = 0.3226$
GREM1	3	18.75	13	81.25	16	

These data exclude the 1 IgG Ab- and 2 GREM1 NAb-treated animals that did not develop tumours in the colon.

The bioluminescence readings, shown only up until the first humane end point in each treatment group and gender, reveal that treatment with the GREM1 NAb reduced colorectal tumour growth compared to treatment with the IgG Ab placebo (Fig 5.4B). This was supported by colonoscopy, where the average tumour grade was consistently lower in GREM1 NAb-treated animals (Fig 5.4C). These data also support Dr Hiroki Kobayashi's *in vitro* work, where the GREM1 NAb reduced the size of AP tumouroids grown in GREM1-containing conditioned medium (Appendix 8; Fig 5C-D). Tumour growth reduction was particularly clear in female mice, where by 16 weeks post-tumouroid injection GREM1 NAb-treated females had significantly less tumour than IgG Ab-treated females (Fig 5.4B-C). Females also developed colorectal tumours significantly slower than males in each treatment group according to colonoscopy grading (Fig 5.4C). In the IgG Ab-treated group, females had significantly less tumour burden than males from 8 to 12 weeks post-tumouroid injection, when the males begun reaching ethical end point ($p<0.0001$ at week 12, two-way ANOVA); for the

GREM1 NAb-treated group, this significant difference was observed from weeks 5 to 6 and 8 to 13 (p<0.0001 at week 13, two-way ANOVA). This phenomenon is consistent with our previous data examining AP mono8 HP2.3-generated tumours (Fig 5.2B-C). By colonoscopy, I observed two ways that an animal would become impacted and reach ethical end point; either the tumour grew flat and spread across the entire colon wall, causing colon thickening and ultimately defunction, or the tumour grew into the colon lumen and physically blocked the passage of stool (Fig 5.4D). It appeared that more GREM1 NAb-treated animals had circumferential tumour spreading while more IgG Ab-treated animals had luminal tumour growth, although this difference was not statistically significant (Table 5.5). At necropsy, I confirmed that tumours grew both intra- and extra-luminally or predominantly extra-luminally with greater tumour mass (Fig 5.4E). These two tumour morphologies could be the result of tumouroid injection into different colonic layers and/or changes in the invasive ability of tumours due to different Ab treatments. During colonoscopy-guided injection, cells can be implanted either into the mucosa (the correct target layer) or the main muscle layer (the muscularis propria, or subserosa). When I evaluated the injected layer in IgG Ab-treated animals by examining colonoscopy records of each injection, I discovered that "mucosal" injections gave rise to both tumour types in equal proportion while all muscle injections generated predominantly extra-luminal tumours (Table 5.6). So that I could examine tumours generated from the same colon layer, I removed these 3 muscle layer-injected, IgG Ab-treated tumours from all subsequent analyses; there were no tumours derived from muscle injections in GREM1 NAb-treated mice. From mucosal injections, more GREM1 NAb-treated mice tended to develop both intra- and extra-luminal tumours by ethical end point (Table 5.7) and this tended to make them more susceptible to lethal colon defunction (Table 5.8), although these results were not statistically significant. Significance for these datasets may have been achieved if I used more animals and suggests that the GREM1 NAb may have decreased colon tumour invasiveness into outer layers. However, the pathology of H&E-stained end point colonic tumours revealed that GREM1 NAb treatment did not affect tumour grade, as tumours in both treatment groups invaded from the mucosa into the submucosa and subserosa layers, with some even penetrating the final colonic layer, the serosa (Fig 5.4F). All tumours were therefore high-grade T3 and T4, according to the American Joint Committee on Cancer (AJCC) tumour/node/metastasis (TNM) classification [(266)]. Thus, GREM1 NAb-treated tumours were just as aggressive as IgG Ab-treated tumours at end point despite differences in macroscopic morphology. GREM1 NAb-treatment also did not decrease the number of animals presenting with macroscopic metastases at necropsy (Fig 5.4G), although sites in the peritoneum may have been seeded when I occasionally injected a few microlitres of tumouroids through the colon during the injection procedure. Overall, the GREM1 NAb unfortunately did not significantly improve mouse survival in this model although females responded better than males (Fig 5.4H-I). This result, again, was not due to inactive GREM1 NAb at humane end point as colon tumours treated with the NAb had enhanced pSMAD1/5/8 staining (Fig 5.4J-K). Thus, the GREM1 NAb is not efficacious in our orthotopic CRC model.

Table 5.5. Contingency table of number of animals that died from either colon defunction or colorectal tumour blockage

Treatment group	Colon defunction		Tumour blockage		Total number of animals	Fisher's exact test
	Number	Percentage	Number	Percentage		
IgG	2	22.22	7	77.78	9	$p = 0.1534$
GREM1	5	62.5	3	37.5	8	

Table 5.6. Contingency table examining colorectal tumour injection site vs tumour morphology in IgG Ab-treated animals

Injection site	Intra- and extra-luminal		Predominantly extra-luminal		Total number of tumours	Fisher's exact test
	Number	Percentage	Number	Percentage		
Mucosa	7	50.00	7	50.00	14	$p = 0.2279$
Muscle	0	0.00	3	100.00	3	

Table 5.7. Contingency table of number of animals that had intra- and extra-luminal or predominantly extra-luminal colorectal tumours at end point

Treatment group	Intra- and extra-luminal		Predominantly extra-luminal		Total number of tumours	Fisher's exact test
	Number	Percentage	Number	Percentage		
IgG	7	50.00	7	50.00	14	$p = 0.4401$
GREM1	9	69.23	4	30.77	13	

These data exclude the 3 colon tumours grown from muscle-injected tumouroids in the IgG Ab-treated group.

Table 5.8. Contingency table examining cause of death vs colorectal tumour morphology

Cause of death	Intra- and extra-luminal		Predominantly extra-luminal		Total number of tumours	Fisher's exact test
	Number	Percentage	Number	Percentage		
Colon defunction	9	75.00	3	25.00	12	$p = 0.2388$
Tumour blockage	7	46.67	8	53.33	15	

These data exclude the 3 colon tumours grown from muscle-injected tumouroids in the IgG Ab-treated group.

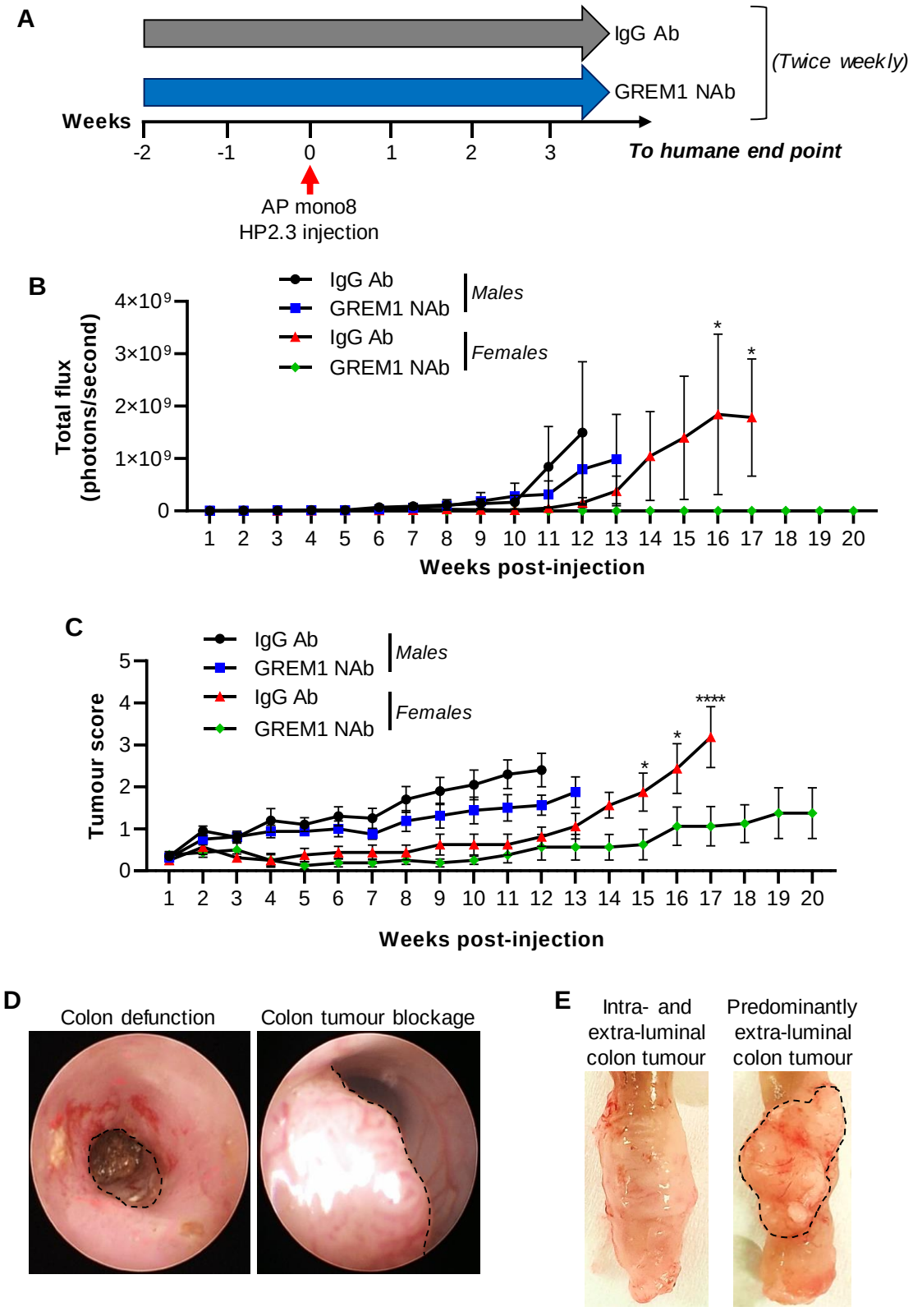


Figure 5.4 continued on next page.

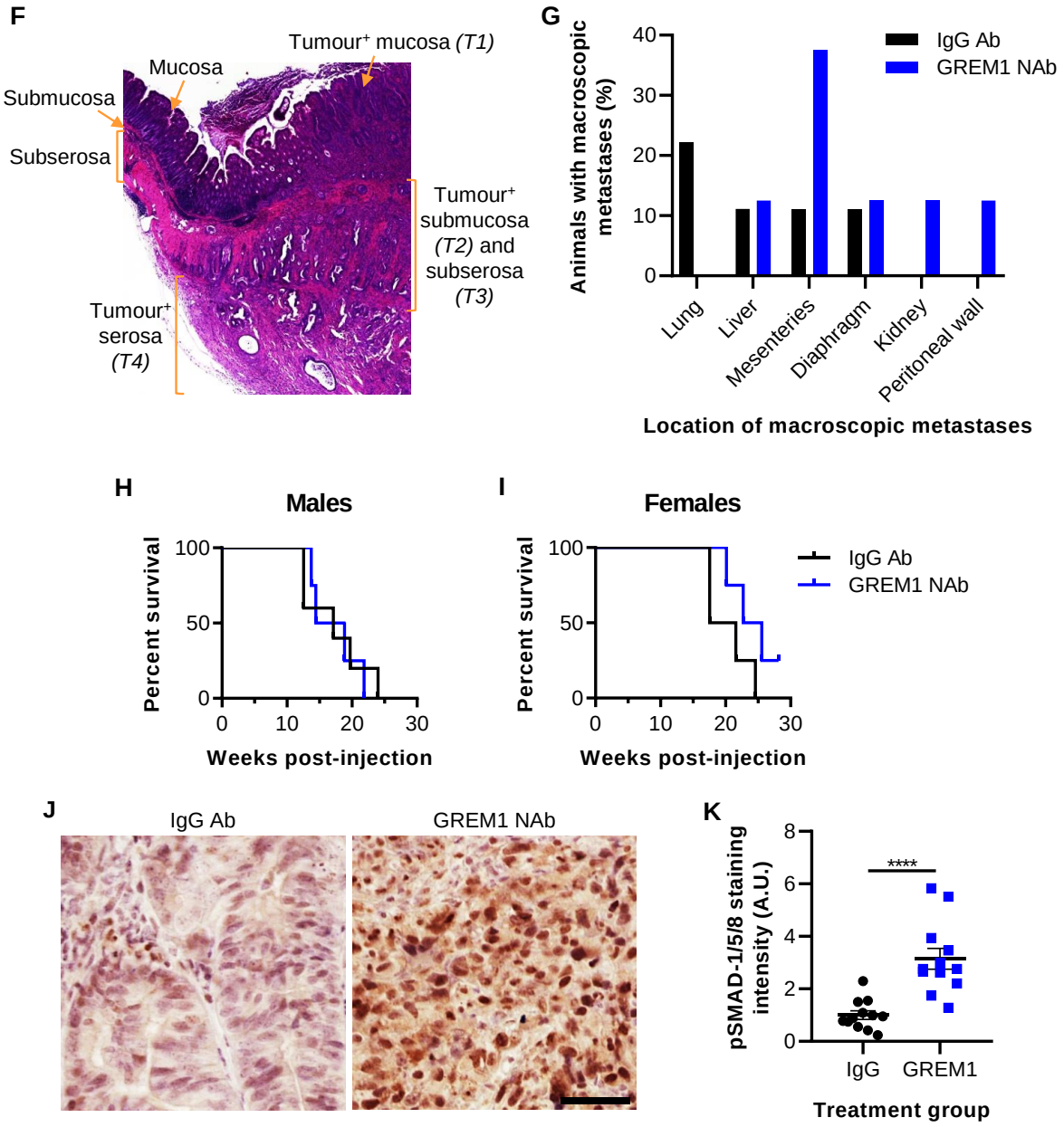


Figure 5.4. Pre-treatment with the GREM1 NAb delays orthotopic CRC growth but does not significantly improve survival. A, schematic of IgG Ab and GREM1 NAb administration in the syngeneic model of primary CRC. Treatment with either 30mg/kg IgG Ab (n=5 males, n=4 females) or GREM1 NAb (n=4 males, n=4 females) begun two weeks prior to AP mono8 HP2.3 injection into the colon wall of Cas9 mice and continued until humane end point. 150 tumouroids were injected/injection, with two injections/mouse. **B–C,** colon tumour growth was monitored via bioluminescence imaging (**B**) and colonoscopy (**C**). Data up until the first animal death in each treatment group and gender is shown. **D,** representative colonoscopy images showing flat luminal tumours that spread around the colon and caused defunction (left panel) or large tumours that grow into the lumen and cause blockage (right panel). **E,** representative images of two colon tumour morphologies; tumours that grow both intra- and extra-luminally (left panel), and tumours

that grow predominantly extra-luminally (right panel). **F,** H&E image of a T4 classified colon tumour, where the tumour has invaded from the mucosal layer into the submucosal, subserosal and serosal layers. **G,** percentage of animals in each treatment group presenting with macroscopic metastases at different locations within the peritoneal and thoracic cavities. **H–I,** Kaplan-Meier curves showing survival of males (**H**) and females (**I**) in different treatment groups. **J–K,** representative images of pSMAD1/5/8 liver tumour staining in IgG Ab- and GREM1 NAb-treated mice at humane end point (**J**; scale bar = 50μm) and the quantification (**K**), where 4 high powered fields of liver tumours from each animal was examined (n=3 animals/treatment group). The mean and statistics were calculated using data combined from both biological and technical replicates. **B–C** and **G** were assessed for statistical significance via a two-way ANOVA, **H–I** via a Mantel-Cox test for survival, and **K** via a student's t test. Mean +/- SEM, * = $p<0.05$, **** = $p<0.0001$.

Discussion

This thesis chapter investigated the putative tumourigenic role of stromal GREM1 in mouse models of primary and metastatic CRC (Aim 4), by treating mice with a GREM1 inhibitor (NAb), and examined the effect of the GREM1 NAb on tumour mouse survival.

I initially wanted to test FOLFOX in combination with the GREM1 NAb to investigate the effect on mouse survival, but found that the FOLFOX treatment regimen piloted did not significantly improve the survival of mice with hepatic metastatic CRC (Fig 5.2D-E). This is contrary to our expectations, considering its efficacious use in CRC patients [7, 264]. It did, however, significantly reduce tumour burden in male mice treated with FOLFOX from 1 week post-tumouroid injection compared to untreated males (Fig 5.2B), but the average total area of liver tumours was indifferent between treatment groups at ethical end point (Fig 5.2H). Treated mice also suffered from severe toxic side effects in the presentation of anaemia associated with haemorrhagic ascites (Fig 5.2F) and extreme weight loss, both conditions ethically requiring culling and resulting in the significantly early death of male mice (Fig 5.2D). Haemorrhagic ascites can occur in patients with advanced liver disease, where a consequential increase in liver blood pressure causes blood vessels to rupture, and chemotherapy is known to have a large range of side-effects in patients including lowering platelet counts; thus, it is conceivable that treated animals had decreased blood clotting efficiency and were consequently more prone to developing haemorrhagic ascites, especially males (Table 5.1). In the clinic, patients are constantly monitored for haematological toxicity, renal and hepatic impairment, peripheral neuropathy, mucositis and stomatitis, diarrhoea and hand foot syndrome, and doses of 5-FU, LV or OX are either decreased or stopped completely until the side effects dissipate. As such, a shortened treatment time or reduced dose of compounds may have allowed more animals to reach tumour burden end points rather than FOLFOX-related toxicity end points. The once-weekly dose of 50mg/kg 5-FU, 6mg/kg OX and 90mg/kg LV via intra-peritoneal injection was taken from

published papers administering FOLFOX to mice or rats [141-144], and those studying the effect on tumours successfully observed a reduction in growth [142, 144]. Most papers, however, do not provide specific details about the timing of 5-FU, LV and OX administration, but those that do specify that 5-FU and LV were given 2 hours after OX [141, 142, 267]. The most common FOLFOX regimens used clinically, FOLFOX4 and modified FOLFOX6, also split the drug administration, combining OX and LV and giving 5-FU afterwards [268, 269]. As such, the decision to administer all three drugs in one injection may have caused the problematic toxicity observed. Although, this toxic, high-dose FOLFOX regimen used in the pilot still appeared insufficiently active or was ineffective against our AP tumouroid-derived tumours, as the protein levels of two indicators of FOLFOX activity, Ki67 and γH2AX, were similar across untreated and treated groups (Fig 5.2I-L). In hindsight, I should have first tested the FOLFOX treatment on AP mono8 HP2.3 tumouroids and another sensitive line (as a positive control) *in vitro*. This would have indicated whether the FOLFOX preparation was adequate and active, and whether the tumouroid line was sensitive or resistant. One study also showed that stage II and III CRC patients with *KRAS*-mutant tumours responded better to FOLFOX than *KRAS* WT patients [270], and the AP tumouroid line has WT *Kras*; if I therefore used a *Kras*-mutant tumouroid line (such as AKP mono7 $CAS9^{-}GFP^{-}$), I may have seen a better response *in vivo*. If I were to repeat the pilot, I would begin FOLFOX treatment as soon as tumours were visible via colonoscope, potentially at a reduced dose, and I would give OX 2 hours after 5-FU and LV.

Using the GREM1 NAb alone, I demonstrated that established hepatic metastases generated from CRC tumouroids did not respond to stromal GREM1 inhibition and consequently GREM1 NAb-treated mice did not significantly outlive those treated with the IgG Ab control (Fig 5.3). I also discovered that GREM1 inhibition significantly enhanced the size of lung metastatic lesions (Fig 5.3J), contrary to our hypothesis. This also disagrees with publications examining GREM1 and metastasis *in vivo*, with one study demonstrating significantly decreased breast cancer metastasis upon *GREM1* knock-out [123] and another study demonstrating a tendency for enhanced mesothelioma cell metastasis upon *GREM1* overexpression [127]. Although, these studies examined *GREM1* expression in cancer cells, not CAFs, and used immunodeficient mice. It is therefore possible that CRC cells react differently to GREM1 inhibition in the microenvironment of other metastatic sites and that this may involve modulations in the immune system. The GREM1 NAb, however, may have prevented the growth of liver tumours in two female mice over the 26-week experiment, but the difference between the number of animals that developed liver tumours between treatment groups was not statistically significant (Table 5.2). As one of these females had measurable bioluminescent signal at the week 1 allocation (data not shown), it is unlikely that there was a technical error during surgery.

I next examined the possible role of GREM1 in tumour initiation and growth using a primary orthotopic CRC model, where mice were treated with the IgG Ab or GREM1 NAb for 2 weeks prior

to tumouroid implantation into the colon wall. I observed that the tumour take was not significantly different between treatment groups (Table 5.4), but that colon tumour growth was significantly reduced in GREM1 NAb-treated females (Fig 5.4B-C). Other studies have also observed significantly reduced primary tumour burden in mice when GREM1 was absent. One study depleted *Grem1* in a breast cancer cell line via CRISPR/CAS9 technology and demonstrated significantly reduced primary tumour size and weight compared to their *Grem1* WT line [(123)]. Another study depleted *GREM1* in MSCs using shRNA and showed that co-injection with oesophageal cancer cell lines significantly decreased primary tumour size compared to co-injections with *GREM1*-WT MSCs [(131)]. Lastly, GREM1 secreted from multiple myeloma cells was inhibited using the same GREM1 NAb as us and primary tumour burden was significantly decreased compared to IgG Ab-treated animals [(132)]. Prior mechanistic studies have shown that GREM1 promotes cancer cell proliferation *in vitro* while GREM1 depletion reduces cancer cell proliferation and induces apoptosis *in vitro*, and reduces angiogenesis *in vivo* [(120, 126-128, 131, 132)]. A role for GREM1 in immune modulation is less well defined. A mechanistic analysis of the role of GREM1 in the primary CRC model awaits repetition but with collection of the cohort at an earlier time point; survival benefit was the major priority of my work, but end point samples are unsuitable for many analyses. Overall, however, the GREM1 NAb did not improve survival in our pre-treated orthotopic CRC model though results were more promising in female mice (Fig 5.4H-I); perhaps if I had used more females I would have observed statistical significance.

It is unknown why female mice were more responsive to GREM1 NAb treatment than males in both of our CRC models, with two non-tumour-bearing females remaining in our hepatic metastatic model (Fig 5.3L) and all females in our pre-treated orthotopic model showing significantly reduced tumour growth (Fig 5.4B-C) and slightly (although not significantly) improved survival (Fig 5.4I) compared to IgG Ab-treated females. Gender variations could be due to differences in sex-hormone signalling or the immune system and gut microbiota [(271, 272)], or simply because tumours grew more slowly in female mice (Fig 5.2B-C, 5.4C). As discussed in Chapter 3, the most likely reason for reduced growth rate is because female mice may be producing H-Y antibodies [(173)] that initially reject the AP mono8 HP2.3 tumouroids, which were generated from normal colon OUs extracted from a male donor. We could therefore repeat the experiment using AP tumouroids generated from a female donor and, if tumour growth is still significantly slower in GREM1 NAb-treated females compared to IgG Ab-treated females, then perhaps use of the GREM1 NAb should be preferentially considered for female CRC patients as this agent moves into clinical trials.

I also observed that mice in the pre-treated primary CRC model, especially females, responded more to GREM1 NAb treatment than animals with established hepatic CRC metastases (Fig 5.3B, 5.4B-C). This suggests that either treatment was more effective at reducing tumour growth prior to tumour colonisation by inducing an unfavourable microenvironment, or GREM1 has a more essential

tumour-promoting role in colorectal rather than liver tumour microenvironments. *Grem1*/*GREM1* is also noticeably more highly expressed in mouse and human CRC than liver metastases (Fig 5.1, Appendix 8; Fig 1C, Fig 2A-B and Supplementary Fig 8A-B). Regardless, GREM1 NAb treatment did not significantly improve mouse survival in either model (Fig 5.3K-L, 5.4H-I). This was not due to inactivity of the drug, as BMP signalling was enhanced in GREM1 NAb-treated tumours compared to IgG Ab-treated tumours even at humane end point (Fig 5.4J-K, Appendix 8; Supplementary Fig 20C-D). Dr Hiroki Kobayashi has also shown that the GREM1 NAb is functional *in vitro*, as expression of the BMP target gene *Id1* was increased in AP mono8 HP2.3 tumouroids upon GREM1 NAb treatment (Appendix 8; Fig 5B). It is possible, however, that tumours became resistant to increased BMP signalling and as such no survival advantage was seen. It is also possible that GREM1 simply does not have an essential role in colon or liver tumour microenvironments, especially when liver tumours have already developed, as tumours can overcome its loss and continue to grow unhindered. Although the papers investigating GREM1 depletion *in vivo* observed significant tumour growth reduction compared to their GREM1 WT controls, they do not publish the impact of depletion on survival outcomes [112, 123, 131, 132]; perhaps, they also did not observe a significant survival advantage in their cancer models.

In conclusion, I found that GREM1 inhibition via a NAb did not significantly improve the survival of mice with primary or metastatic CRC, which was the primary outcome of my experiments. As such, GREM1 may not be a prominent enough promoter of cancer in these models despite promising preliminary data. Although, use of the NAb in female mice appears to more effective than in males and has given us hints that GREM1 may be involved in tumour growth in our models.

Chapter 6: Summary of Results and General Discussion

Specific tumour-promoting CAF subtypes have been minimally explored in CRC; as such, my PhD project was designed to investigate putative CRC-promoting subtypes both *in vitro* and *in vivo*. CAFs form an attractive therapeutic target because they are genetically stable in comparison to tumour cells, and if we can inhibit their tumour-promoting roles specifically then we may be able to improve patient outcomes with a reduced chance of drug resistance. The two CAF-associated candidates specifically tested in my PhD were MCAM and GREM1, and I hypothesised that $MCAM^+$ and/or $GREM1^+$ CAFs promote colorectal tumourigenesis. I also hypothesised that GREM1 inhibition via a NAb would improve the survival of mice with primary and metastatic CRC.

Chapter summaries

In Chapter 3 I successfully developed two immunocompetent mouse models of induced CRC (Aim 1). The AOM/DSS model, already established in our group by Dr Tamsin Lannagan, mimics colitis-associated CRC, where spontaneous, low-grade colorectal tumours develop in a chronic inflammatory colon environment induced by DSS after exposure to the carcinogen AOM (3.1A-B). In the primary CRC model, colorectal tumour cells are orthotopically injected directly into the colon wall via colonoscope with a needle attachment to induce colorectal tumours (Fig 3.1C-E). Finally, in the hepatic metastatic CRC model, colorectal tumour cells are injected into the liver via the portal vein to induce liver tumours representative of CRC metastasis (3.1F-H). I successfully generated tumours in immunocompetent mice using two colorectal tumouroid lines; AP mono8 HP2.3-derived tumours were *Apc* and *Tp53* mutant and grew in syngeneic, original Cas9 knock-in recipient mice (Fig 3.5B-C), while AKP mono7 $Cas9^{-}GFP^{-}$-derived tumours were *Apc*, *Kras* and *Tp53* mutant and grew in C57BL/6 mice (Fig 3.8C, F). These tumouroid-derived tumours not only modelled human disease genetically, but also pathologically (Fig 3.5D, 3.8G).

In Chapter 4 I identified MCAM as the top candidate tumour-promoting stromal factor in colorectal tumourigenesis from our laboratory's RNA-sequencing data (Aim 2) and examined its role in modulating fibroblast phenotypes (Aim 3). I discovered that MCAM is significantly upregulated in mouse and human CRC (Fig 4.2, 4.3A-B), and that high *MCAM*/MCAM expression is significantly associated with worse CRC patient survival (Fig 4.1 Step 2, Fig 4.3C-D). While both mouse colorectal tumour-associated endothelial cells and fibroblasts express MCAM (Fig 4.5), I focussed on the role of MCAM in fibroblasts which is relatively unknown. I found that MCAM effects the expression profile of primary mouse colon myofbs, inducing a more tumour-suppressive transcriptional profile that is contrary to our tumour-promoting hypothesis (Fig 4.10, Table 4.1). MCAM also significantly reduced the activity and stemness of these myofbs, but significantly improved their ability to migrate in scratch assays (Fig 4.11). I also discovered that high MCAM-

expressing myofbs significantly reduced the control myofb-mediated promotion of OU growth in an *ex vivo* co-culture system (Fig 4.12G), but that MCAM^{+} myofbs did not directly affect the growth of neoplastic tumouroids in the same system (Fig 4.12I). Fibroblast-derived MCAM may therefore exert its effects on tumourigenesis through other cell types in the tumour microenvironment, such as endothelial or immune cells, which was not tested in my thesis.

In Chapter 5 I examined the tumourigenic role of stromal GREM1 and the efficacy of a GREM1 NAb in *Grem1*-expressing mouse models of primary and metastatic CRC (Aim 4, Fig 5.1). I found that treatment with the GREM1 NAb did result in BMP pathway activation but did not improve the survival of mice with established liver tumours (Fig 5.3). However, pre-treatment with the GREM1 NAb in the primary CRC model significantly reduced colorectal tumour growth in female mice without significantly affecting invasion, metastasis or survival (Fig 5.4). Thus, in our model systems, blocking GREM1 does not appear to be an efficacious single-agent therapeutic approach for primary or metastatic CRC.

Future directions and clinical implications of MCAM

In the MCAM chapter (Chapter 4) there are some additional *in vitro* fibroblast assays that we could do to complement those already done to understand how high *Mcam* expression leads to worse prognosis for CRC patients. The migration assay I did was essentially a wound healing assay, which quantifies the ability of myofbs to move into a scratched space and effectively "heal" the wound (Fig 4.11K). This assay is performed under serum starvation to reduce proliferation into the scratch but does not actively enforce migration towards a chemoattractant as may occur *in vivo*. Thus, another type of migration assay that would provide additional insights involves the use of a transwell system, where MCAM GFP^{Hi} YH2, MCAM GFP^{+} myofbs and *Mcam*$^{-/-}$ myofbs (and their respective controls) are separately plated in the top chambers under serum starvation and the number of cells that move into the bottom chamber with 10% FBS (the chemoattractant) are quantified. If we then replaced the transwells with Matrigel invasion chambers, we could examine the ability of myofbs to invade through matrix before reaching the serum-rich media. To investigate the previously reported role for MCAM in angiogenesis, conditioned media from my different myofb lines could be added to endothelial cells in tube formation assays to examine downstream effects of MCAM^{+} myofbs on angiogenesis. We could also grow CRC cells in this myofb conditioned media prior to seeding in migration and invasion assays and examine how MCAM^{+} myofb-secreted factors influence epithelial motility and invasion. The literature also demonstrates that MCAM inhibits apoptosis in cancer and endothelial cells under stressful conditions [62, 72, 80, 98, 103]; however, this stress-survival mechanism has not been examined in fibroblasts. As such, a DNA damaging agent could be added to the myofb cultures to mimic chemotherapy, followed by Annexin V staining to observe whether MCAM^{+} myofbs are more resistant. One key limitation of my studies has been the inability to culture pure CAFs that have been transformed by the colorectal tumour microenvironment *in vivo*. In the future,

ectopic MCAM dimerisation and activation in myofbs could be investigated using tumour conditioned media [86, 105] or an anti-MCAM antibody [106, 107].

Ongoing studies in the laboratory are examining the role of MCAM in primary and metastatic colorectal tumourigenesis *in vivo* by injecting AKP mono7 CAS9^{-}GFP^{-} tumouroids into the colon or liver of *Mcam*$^{+/+}$ and *Mcam*$^{-/-}$ mice. These models allow an evaluation of the ability of the tumouroids to initiate tumours at these sites and investigate differences in tumour angiogenesis, immune infiltrate (e.g. pro-tumour macrophages, T cells), collagen density, invasion and metastasis *in vivo*. Based on my findings in Chapter 4 and in published literature (see Chapter 1), I would hypothesise that colorectal and liver tumour colonisation, growth, invasion, metastasis and angiogenesis is significantly reduced, and survival is significantly improved, in *Mcam*$^{-/-}$ compared to *Mcam*$^{+/+}$ mice. If this hypothesis is supported, then we could co-inject control GFP^{+} or MCAM GFP^{+} myofbs with the AKP tumouroid line into *Mcam*$^{-/-}$ mice and potentially show that MCAM, produced specifically by myofbs, is capable of restoring tumourigenicity. The next logical step to move this work towards the clinic would be testing MCAM inhibitors in our pre-clinical models. As explored in Chapter 1 there are four different MCAM NAbs that have been developed and successfully used to reduce tumourigenesis in mouse models of hepatocarcinoma, leiomyosarcoma, osteosarcoma, melanoma, pancreatic cancer, prostate cancer and colitis-induced CRC: AA98, PRX003, ABX-MA1 and M2J-1 [61, 71, 77, 84, 98-100]. AA98 recognises both mouse and human MCAM and preferentially targets intratumoural neovasculature over blood vessels from normal tissues [84]. PRX003 also recognises and targets mouse and human MCAM, but as expressed by immune and cancer cell populations [88, 89, 100]. ABX-MA1 targets both MCAM^{+} cancer and endothelium of mouse and human origin [61]. Lastly, M2J-1 specifically targets sMCAM expressed by MCAM^{+} cancer cells [98]. As AA98, PRX003 and ABX-MA1 bind membrane-bound murine MCAM, the next step would be to test whether they individually recognise MCAM^{+} CAFs in our tumour models and generate therapeutic efficacy. Unfortunately, AA98 is under patent and we are not able to obtain it from the group that developed it. It would be fantastic if PRX003 did indeed target MCAM^{+} CAFs and improve mouse survival as its safety for use in people has already been proven (ClinicalTrials.gov Identifier NCT02458677 and NCT02630901), so we could move straight into Phase 2 clinical trials in CRC patients in which it has never been tested.

Future directions and clinical implications of GREM1

There are only two prior studies investigating the pre-clinical targeting of GREM1 in cancer. The first study used the same GREM1 NAb as in this thesis and demonstrated significantly reduced primary tumour burden in a mouse model of multiple myeloma [132]. The GREM1 NAb, patented as UCB6114, is currently in an ongoing Phase 1/2 clinical trial examining its safety and anti-tumour activity in patients with advanced solid tumours (ClinicalTrials.gov Identifier NCT04393298). The second study used the omega-3 fatty acid, docosahexaenoic acid, to reduce *GREM1* expression in

breast cancer cells and this significantly inhibited GREM1-induced EMT [125]. The GREM1 chapter (see Chapter 5) generated one particularly intriguing and potentially impactful result – that GREM1 NAb treatment significantly reduced orthotopic colorectal tumour growth in pre-treated female mice. To understand this further, this experiment could be repeated with female mice collected at an earlier, defined time point to examine changes in tumour proliferation, apoptosis, angiogenesis [120, 126-128, 131, 132] and immune infiltrate between IgG Ab- and GREM1 NAb-treated groups. We would also need to determine why the GREM1 NAb works better in female mice, whether it is due to sex-hormone signalling or the immune system and gut microbiota [271, 272], or slower tumour growth rate. An understanding of the mechanism of action of the GREM1 NAb may suggest patient populations that might derive the most benefit from this agent as it moves into Phase 2/3 clinical trial.

Other ways to therapeutically target CAFs

In my thesis I have explored one way that CAFs can be therapeutically targeted – through inhibition of specific tumour-promoting proteins or pathways associated with tumour-promoting subtypes. Researchers have also been exploring other ways to prevent CAF activation during tumourigenesis [30] (Appendix 1). As an example, one group showed that the vitamin-D derivative, calcipotriol, blocked the TGF-β-mediated differentiation of pancreatic fibroblasts into CAFs. The subsequent reduction in fibrosis and inflammation then significantly enhanced the therapeutic responsiveness of pancreatic tumours in mice [273]. Likewise, the histone deacetylase inhibitor Sciptaid was used to significantly reduce the activity and content of fibroblasts, which impaired collective CAF-tumour cell invasion and delayed melanoma growth *in vivo* [251]. Researchers are additionally exploring ways to reprogram activated CAFs back into normal, quiescent fibroblasts [30] (Appendix 1). This has been shown using the miRNAs miR-145 and Let7b which, upon re-expression, deactivated TGF-β-activated normal oral fibroblasts and breast CAFs respectively *in vitro* [274, 275]. Let-7b re-expression also significantly reduced the ability of breast CAFs to promote the migration and invasion of breast cancer cells *in vitro* [274]. The long-term phenotypical and molecular reversion of activated CAFs to normal, resting fibroblasts was also achieved via the combined inhibition of DNA methyltransferase activity and JAK signalling in breast CAFs, and this significantly reduced breast cancer invasion *in vivo* [276]. Theoretically, tumour-promoting CAFs could also be skewed towards a tumour-suppressing phenotype to improve cancer prognosis, however, no studies have been able to demonstrate this to date. Ongoing research into this area will provide therapeutic options to target the tumour microenvironment together with standard tumour-targeting chemotherapies (or newer immunotherapies), to ultimately improve the outcomes for CRC patients.

Appendix 1. ‘Cancer-Associated Fibroblasts – Heroes or Villains?’

This manuscript is a review on CAF heterogeneity and the tumour-promoting and -suppressing phenotypes. It additionally explores CAF-directed cancer treatment strategies, which involves either targeting the CAFs directly or using them as a means for drug delivery.

Statement of Authorship

Title of Paper	Cancer-associated fibroblasts – heroes or villains?
Publication Status	Published
Publication Details	Gieniec, K. A., Butler, L. M., Worthley, D. L., Woods, S. L. (2019). Cancer-associated fibroblasts – heroes or villains? *The British Journal of Cancer*, 121(4), p.293-302.

Principal Author

Name of Principal Author	Krystyna Gieniec		
Contribution to the Paper	Discussed manuscript content, wrote the manuscript.		
Overall Percentage (%)	90%		
Certification:	This paper reports on original research I conducted during the period of my Higher Degree by Research candidature and is not subject to any obligations or contractual agreements with a third party that would constrain its inclusion in this thesis. I am the primary author of this paper.		
Signature		Date	*30/10/20*

Co-author contributions

By signing the Statement of Authorship, each author certifies that:

i. the candidate's stated contribution to the publication is accurate (as detailed above);
ii. permission is granted for the candidate to include the publication in the thesis; and
iii. the sum of all the co-author contributions is equal to 100% less the candidate's stated contribution.

Name of co-author	Lisa Butler		
Contribution to the paper	Discussed manuscript content.		
Signature		Date	*6/11/20*

Name of co-author	Daniel Worthley		
Contribution to the paper	Discussed manuscript content.		
Signature		Date	*6/11/20*

Name of co-author	Susan Woods		
Contribution to the paper	Discussed manuscript content, helped to evaluate and edit the manuscript, acted as corresponding author.		
Signature		Date	*6/11/20*

BJC British Journal of Cancer

www.nature.com/bjc

REVIEW ARTICLE

Cancer-associated fibroblasts—heroes or villains?

Krystyna A. Gieniec[1,2], Lisa M. Butler[1,2], Daniel L. Worthley[2] and Susan L. Woods[1,2]

Cancer-associated fibroblasts (CAFs) were originally presumed to represent a homogeneous population uniformly driving tumorigenesis, united by their morphology and peritumoural location. Our understanding of CAFs has since been shaped by sophisticated in vitro and in vivo experiments, pathological association and, more recently, ablation, and it is now widely appreciated that CAFs form a group of highly heterogeneous cells with no single overarching marker. Studies have demonstrated that the CAF population contains different subtypes based on the expression of marker proteins with the capacity to promote or inhibit cancer, with their biological role as accomplices or adversaries dependent on many factors, including the cancer stage. So, while CAFs have been endlessly shown to promote the growth, survival and spread of tumours via improvements in functionality and an altered secretome, they are also capable of retarding tumorigenesis via largely unknown mechanisms. It is important to reconcile these disparate results so that the functions of, or factors produced by, tumour-promoting subtypes can be specifically targeted to improve cancer patient outcomes. This review will dissect out CAF complexity and CAF-directed cancer treatment strategies in order to provide a case for future, rational therapies.

British Journal of Cancer (2019) 121:293–302; https://doi.org/10.1038/s41416-019-0509-3

BACKGROUND

Fibroblasts are non-specialised cells of the connective tissue stroma that support tissue function and homoeostasis by regulating the extracellular matrix (ECM), inflammation and epithelial cell proliferation and differentiation (reviewed in ref. [1]) They are predominantly quiescent, only transiently acquiring activity during periods of tissue remodelling and repair. Activated fibroblasts will then either apoptose or revert back to a dormant state once their function becomes redundant; otherwise, pathological conditions such as tissue fibrosis and chronic inflammation can arise.[2] This chronic tissue repair response has been implicated in the progression to cancer,[3] and tumours can therefore be considered as 'wounds that do not heal'.[4] Distinct, activated fibroblasts that surround tumours are termed cancer-associated fibroblasts (CAFs) and they, along with other elements of the tumour microenvironment, can indulge in reciprocal dialogues with the neoplastic epithelial cells to maximise tumour fitness.

The role of CAFs in cancer has risen to prominence, with genes positively associated with colorectal cancer (CRC) recurrence and poor prognosis predominantly found to be upregulated within the CAF population, not in tumour cells.[5,6] Furthermore, when CRC was classified into four distinct consensus molecular subtypes (CMSs), it was revealed that CMS4, with over-representation of the stromal signature, was associated with more aggressive tumour stages and worse overall survival than other subtypes.[7] CAFs have subsequently been implicated in different stages of cancer development, from primary growth to secondary colonisation at metastatic sites, in different cancer types. However, a number of contradictory studies have proposed an anti-tumour role for CAFs, as ablation of CAFs expressing specific markers, such as α-smooth muscle actin (α-SMA), or inhibition of signalling pathways proposed to be important in CAF-mediated tumorigenesis (such as hedgehog, Hh) actually resulted in more aggressive pancreatic ductal adenocarcinoma (PDAC).[8,9] While studies involving tumour-suppressive CAF populations are in the minority, they clearly demonstrate the need to more fully understand the role of discrete and possibly opposing CAF subpopulations in order to effectively target tumours.

The identification of markers that define CAF subsets is in its infancy, and this has hindered the study of specific CAFs. Two commonly used molecular CAF markers are α-SMA and fibroblast activation protein (FAP), but these markers do not perfectly demarcate precisely the same population of cells.[10] Many other markers for CAFs have been identified, such as vimentin, fibroblast-specific protein-1 (FSP1), and platelet-derived growth factor receptor-β (PDGFRβ),[11] which are discussed below. It has become apparent that CAFs form a large heterogeneous population of cells expressing a wide array of molecular markers, which are not necessarily unique to fibroblasts. It might be that particular CAF subsets have a tendency for tumour promotion or suppression, perhaps determined by tumour type and location, but the biological programmes influencing these phenotypes currently remain unknown. In order to successfully use CAFs as a form of cancer treatment, CAF complexity must be resolved such that specific pro-tumorigenic subtypes can be inhibited or converted back into a quiescent state.

This review will provide an overview of our current knowledge of the pro- and anti-tumour roles of CAFs in various tumour entities and the implications for these findings on cancer treatment.

THE TUMOUR-PROMOTING CAF PHENOTYPE

The primary role of activated fibroblasts is to remodel and regenerate tissues, which they do under normal circumstances in a highly regulated manner. However, this function can be hijacked

[1]School of Medicine, University of Adelaide, Adelaide, SA, Australia and [2]Precision Medicine, South Australian Health and Medical Research Institute, Adelaide, SA, Australia
Correspondence: Susan L. Woods (susan.woods@adelaide.edu.au)

Received: 13 June 2018 Revised: 19 May 2019 Accepted: 22 May 2019
Published online: 10 July 2019

© The Author(s), under exclusive licence to Cancer Research UK 2019

and enhanced in cancer, generating misregulated, tumour-promoting CAFs. As will be discussed below, CAFs can indirectly support tumorigenesis by encouraging an oxygen-rich, immunosuppressive and pro-inflammatory microenvironment. In addition, CAFs are capable of directly supporting tumour growth, invasion and metastasis.

CAFs encourage the development of a tumour-promoting stroma

Although CAFs are the predominant cell type in the tumour stroma, many other stromal cells contribute to carcinogenesis. These include pro-inflammatory, immunosuppressive and endothelial cells, which can be recruited or influenced by CAFs via a wide array of CAF-derived factors.

Multiple studies have emphasised the tumour-promoting role of inflammatory cells, from their production of many pro-tumour factors to their mutagenic involvement in tumour evolution.[12] CAFs can adopt a pro-inflammatory gene signature at an early stage in cancer development, induced by tumour-derived interleukin (IL)-1β and, as such, themselves mediate this tumour-enhancing inflammation.[13] CAFs can additionally be involved in tumour immune evasion, inducing an immune-suppressive microenvironment to facilitate tumour escape from anti-tumour immune surveillance. When FAP^+ stroma was specifically ablated using diphtheria toxin in genetically modified Lewis lung cancer (LCC) mice, cytotoxic T-cell activity was restored and rapid tumour necrosis resulted.[14] Combining this ablation with the chemotherapeutic agent, doxorubicin, resulted in a reduced infiltration of immune-suppressor cells such as T-regulatory (Treg) cells and further activated the anti-tumour immune response.[15] CAFs can directly deactivate the immune system, with some CAF subsets shown to express the negative co-regulatory immune signals, programmed death-ligand (PD-L)1 and PD-L2 or secrete immune-suppressive factors, such as prostaglandin E2 (PGE2), to directly reduce the activation of T and natural killer cells.[2,16] The CAF-rich peritumoural stroma can also physically prevent the immune system from effectively interacting with the tumour. This phenomenon of immune exclusion from tumours has been linked to the lack of patient response to PD-L1 blockade in many cancers, including metastatic urothelial cancer, and it is associated with a signature of transforming growth factor-β (TGF-β) signalling in fibroblasts,[17] which is known to activate fibroblasts and induce the dense stromal reaction. When mouse models of immune-excluded breast or metastatic CRC were co-treated with TGF-β and PD-L1 inhibitors, the expression of matrix-remodelling factors in CAFs was reduced and T cells were then able to penetrate both primary and metastatic tumour masses to cause regression.[17,18] However, the consequences of attempts to manipulate the immune system for cancer treatment are not always predictable due to the complex interplay between different cell types in the tumour microenvironment, including fibroblasts. For example, use of a colony-stimulating factor 1 receptor (CSF1R) inhibitor for targeting pro-tumour, tumour-associated macrophages in mouse models of LLC and melanoma resulted in the enhanced recruitment of polymorphonuclear myeloid-derived suppressor cells (PMN-MDSC). The block in CSF1 signalling caused CAFs to secrete the PMN-MDSC chemokine, C–X–C Motif Chemokine Ligand 1 (Cxc11); CAFs were therefore able to neutralise the anti-tumour effect of the CSF1R inhibitor. Tumours were reduced when tumour-bearing mice were treated with both the CSF1R inhibitor and a C–X–C Motif Chemokine Receptor 2 (CXCR2) antagonist (to prevent PMN-MDSC migration), and tumours were completely blocked when a PD-1 antibody was added to this combination.[19]

CAFs can respond to hypoxia by upregulating hypoxia-induced angiogenesis regulator (HIAR), which in turn increases CAF motility and secretion of vascular endothelial growth factor A (VEGFA).[20] This induces angiogenesis to improve tumour oxygenation, nutrient flow and waste removal, and the resultant decline in hypoxia stimulates further CAF activation.[21] CAFs can also be influenced to stimulate a vessel-rich environment by tumour cells. As an example, hepatocellular carcinoma (HCC)-derived exosomal miRNA-21 activates hepatic stellate cells into CAFs by blocking PTEN, causing the CAFs to upregulate angiogenic cytokines including VEGF and increasing vessel density in HCC patients.[22]

CAFs improve tumour energy synthesis

There are many ways in which CAFs can increase the net energy production of tumours, fuelling growth. The 'reverse Warburg effect' was recently termed[23] to define the phenomenon whereby CAFs undergo autophagy and mitophagy, resulting in aerobic glycolysis and the release of energy-rich metabolites that are then absorbed by cancer cells to enter the tricarboxylic acid (TCA) cycle. This upregulates tumour mitochondrial oxidative phosphorylation, improving ATP production.[24] In addition, the ketones and lactate produced as the end products of fibroblastic glycolysis have been shown to promote the growth and metastasis of breast cancer in an immunodeficient mouse model,[25] by increasing the transcriptional profile of genes associated with 'stemness' in cancer cell lines. This suggests a link between metabolism and cancer stem cells (CSCs, see below), which could potentially be severed using oxidative mitochondrial metabolism inhibitors, such as metformin.[24] Patient-derived lymphoma CAFs have also been shown to secrete significant amounts of pyruvate, fuelling lymphoma tumours via the reverse Warburg effect.[26] Patient-derived prostate cancer CAFs can assist nutrient-deprived prostate and pancreatic cancer cell lines, via secretion of exosomes containing intact metabolites, including amino acids and TCA-cycle intermediates, allowing the tumour cells to continue growing rapidly.[27] Interestingly, tumours can enhance their own survival by secreting exosomes that alter CAF metabolism. In one study, breast-cancer-secreted exosomes containing miR-105 reprogrammed CAFs by activating MYC signalling. This imbued the CAFs with the capacity to enhance glucose metabolism when nutrients were sufficient, or detoxify metabolic wastes into energy-rich metabolites when nutrients were scarce, thus ensuring the tumour remained sufficiently energised for sustained growth.[28]

ECM remodelling and tumour invasion

The ECM is a dynamic scaffold of glycosaminoglycans and proteins that functions as a cell-docking station and facilitates cell communication, differentiation, adhesion and movement. It is constantly being degraded and synthesised by fibroblasts in a regulated response to changing tissue conditions; degradation is facilitated by matrix metalloproteinases (MMPs) and synthesis is associated with the increased production of proteins, such as collagen.[29] The ECM also functions as a biological repository, sequestering a wide range of growth factors and cytokines.[30] CAFs perpetually remodel the ECM, and the degradation of ECM molecules by CAF-generated MMPs not only releases sequestered proteins to create a self-sustaining feed-forward loop of CAF activation and ECM remodelling but also creates new molecule fragments with potential pro-migratory and pro-angiogenic roles.[31,32] Moreover, ECM degradation physically frees up space for proliferating and migrating tumour cells. The net outcome is accelerated cancer progression. CAFs additionally stimulate constitutive collagen cross-linking; they are the primary source of the cross-linking inducer lysyl oxidase (LOX) in mouse mammary cancer,[33] and LOX inhibition in a mouse breast cancer model led to a decline in fibrosis, tumour invasion and metastasis.[34] CAF-derived FAP organises these cross-linked fibres into parallel orientations through its serine protease activity, forming stiff 'migration highways' that enhance the directionality and velocity of pancreatic cancer cells during invasion via activation of the β_1-integrin/FAK signalling pathway; without FAP, the ECM remains disorganised and invasion is impeded.[35] Lung cancer cells can also adhere to CAFs via integrin α5β1 and quickly migrate along the long fibroblast protrusions, acquiring

invasive potential in three-dimensional collagen matrix.[36] In addition, CAFs can directly adhere to the skin and squamous cell carcinoma (SCC) cells, inducing ECM tracks ahead to further accelerate invasion.[37,38]

CAFs, cancer stemness and metastasis

CAFs are suggested to play a role in the induction and maintenance of a small population of tumorigenic cells that are capable of self-renewal and multilineage differentiation. These cells, termed CSCs, have a crucial role in cancer initiation, with one CSC capable of giving rise to an entire tumour.[39] CSCs are predominantly dormant so they are naturally resistant to anti-proliferative chemotherapy and therefore difficult to eradicate, and might be responsible for relapse years after initial treatment.[40] CAF-derived chemokine (CC motif) ligand 2 (CCL2), IL-6, hepatocyte growth factor (HGF), osteopontin (OPN) and stromal cell-derived factor 1 (SDF-1) each independently induce the CSC phenotype in epithelial cells.[41–43]

CAFs can enhance cancer stemness by inducing an epithelial-to-mesenchymal transition (EMT) programme in cancer cells, as described in a mouse model of human prostate cancer.[44] EMT is associated with increased motility of cancer cells, with loss of cell–cell adhesion and polarity,[45] and increased resistance to therapy. IL-6 is one example of a CAF-derived factor that induces EMT in oesophageal cancer, and IL-6 inhibition restored sensitivity of patient-derived oesophageal cancer organoids to chemotherapy and radiotherapy.[46] During EMT, there is also evidence of a reversion to the epithelial phenotype (mesenchymal-to-epithelial transition, MET), allowing metastatic outgrowth (discussed in ref. [47]) CAFs are able to accompany disseminated tumour cells in the circulation, providing survival cues and an early growth advantage at the metastatic site; partial depletion of CAFs at this stage significantly decreases the number of successful lung metastases in a mouse model.[48] In serous ovarian cancer, this phenomenon is a feature of high-grade tumours, where ascetic tumour cells marked by integrin α-5 (ITGA5) expression are prone to forming spheroids with CAFs. When CAFs were pre-treated with imatinib to inhibit PDGFR signalling, mice with ovarian cancer had reduced peritoneal colonisation and improved survival.[49] Infiltrating tumour cells can also secrete extracellular vesicles containing TGF-β, educating the foreign niche to resemble the primary microenvironment. The activated tissue-resident fibroblasts then express factors to promote epithelial colonisation (MET) and proliferation, initiating secondary tumorigenesis.[50–52]

Tumour-promoting CAFs are therefore at least partly responsible for the acquisition of proliferative, pro-inflammatory, immune-suppressive, angiogenic, pro-invasive and pro-metastatic environments that are required for aggressive tumorigenesis (Fig. 1).

THE TUMOUR-SUPPRESSING CAF PHENOTYPE

Despite the overwhelming evidence indicating that CAFs have a tumour-promoting role, there are studies suggesting that these cells, along with normal fibroblasts, are involved in tumour suppression. Whether these fibroblast subtypes are normal fibroblasts that are resistant to conversion into CAFs, or distinct anti-tumour CAF subpopulations, remain unknown (Fig. 1).

The notion that normal cell types have tumour-suppressing properties was demonstrated by injecting a teratoma cell line into an early mouse embryo; the resulting postnatal animals were derived from both host and transplanted tumour cells, but the tumorigenic phenotype had somehow been suppressed so that normal development ensued.[53] Normal, resting fibroblasts were suggested to be the tumour-suppressing cell type, as they were shown to restrain the growth of transformed baby hamster kidney cells in vitro[54] and transformed keratinocytes in vivo.[55] Another in vivo study showed that PDGFRα$^+$ CAFs isolated from a PDAC mouse model stimulated subcutaneous PDAC tumour growth in mice by 76%, while normal pancreatic fibroblasts inhibited tumour growth by 65%.[56] Tumour growth-suppressive factors, such as whey acidic protein four-disulphide core domain 1 (WFDC1), were highly expressed in resting fibroblasts but downregulated in CAFs,[57] suggesting that dormant fibroblasts might indeed suppress tumorigenesis. Resting fibroblasts at metastatic sites can also impede colonisation, as normal bone marrow stroma was shown to induce quiescence in infiltrating breast cancer cells via the gap junction-mediated transfer of several miRNAs targeting CXCL12.[58]

Studies have also uncovered the presence of tumour-suppressing fibroblasts in established tumours. PDAC is notorious for its large fibrotic tumour response, with the majority of tumour volume being composed of α-SMA$^+$ fibroblasts.[8] Depleting these fibroblasts was hypothesised to reduce PDAC aggression, but clinical studies relying on this strategy revealed accelerated disease progression.[59] Upon further investigation in mice, it was confirmed that deletion of α-SMA$^+$ fibroblasts induced invasive tumours that showed enhanced EMT and increased numbers of CSCs, and resulted in reduced survival. This outcome was primarily due to a decline in immune surveillance and increased infiltration of Treg cells. The fibrotic response associated with PDAC is therefore a host defence mechanism against tumour invasion.[8] Unexpected results were also seen with alteration of Hh signalling in CAFs. It has been shown that tumour-derived sonic hedgehog (Shh) activates smoothened (SMO) in fibroblasts, which activates the fibroblasts and consequently promotes PDAC desmoplasia.[60] When Hh signalling was inhibited in CAFs in a PDAC mouse model using the drug IPI-926, the tumours became transiently vascularised and delivery of the chemotherapeutic agent gemcitabine was enhanced, increasing mouse survival. This study demonstrates another example of how CAFs can impact tumour chemoresistance, as the desmoplastic response causes poor intratumoural vascularity and consequently inefficient drug delivery.[61] Thus, naturally, it was hypothesised that continued research into Hh-signalling inhibition would be therapeutically advantageous. This was not always the case, as deletion of Shh enhanced disease progression and reduced CAF content in a PDAC model,[9] and activating Hh signalling in fibroblasts markedly reduced tumour load and disease progression in a colon cancer model.[62] Hh-signalling CAFs therefore appear to act as both tumour promoters and tumour suppressors, with the specific factors that predict this behaviour across multiple cancer types remaining unknown. Interest surrounding serum amyloid A (Saa3) expression in mouse Pdgfrα$^+$ CAFs has also recently come into light, as Pdgfrα$^+$Saa3$^+$ CAFs were shown to stimulate PDAC growth in an orthotopic mouse model while Pdgfrα$^+$Saa3$^-$ CAFs inhibited growth.[56] Inhibiting Saa3 could therefore result in an abundance of anti-tumour CAFs, but the initial findings of this study await further validation as to their suitability as a therapeutic target for PDAC. Interestingly, the phenomenon of CAF-induced cancer regression was demonstrated in a recent study, whereby CAFs were shown to restore lung SCC spheroids from a dysplastic to hyperplastic state through the suppression of high epithelial Sox2 activity. As such, CAFs may have the ability to override cell intrinsic oncogenic changes and determine the extent of disease progression.[63]

There is a growing body of evidence suggesting that cancer cells influence whether or not fibroblasts suppress tumour growth. In the normal setting, stromal cells express TGF-β inhibitors (reviewed in ref. [64]) and low expression of one such fibroblast-derived inhibitor, asporin, is correlated with poor survival in breast cancer patients. However, asporin expression appears to be influenced by the tumour's genetic subtype, suggesting that the level of fibroblast-induced tumour suppression can be partly determined by the tumour itself.[65] Likewise, breast tumours can downregulate the roundabout homologue 1 (Robo1) receptor to

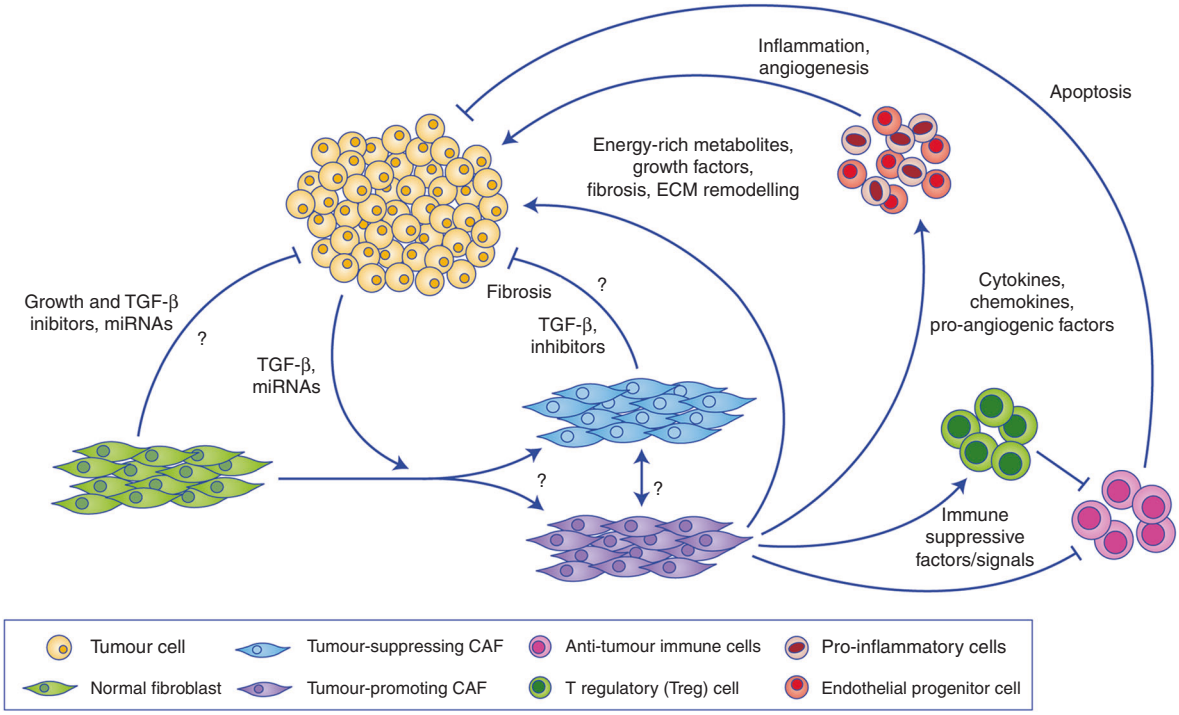


Fig. 1 Roles of CAFs in tumorigenesis. Tumour cells and the surrounding fibroblasts or CAFs communicate to generate a microenvironment that either promotes or suppresses tumorigenesis. Normal fibroblasts can be stimulated to become CAFs by the tumour, however, the biological programmes that determine their skew towards a tumour-promoting or tumour-suppressing subtype remain unknown. The tumour-promoting subtypes aid tumour growth, survival and spread both directly and indirectly, through other tumour-associated stromal cell types. Both normal fibroblasts and CAFs have been shown to inhibit or retard tumorigenesis, but the mechanisms are relatively unknown

stop the tumour-suppressive effects of its fibroblast-derived ligand, slit homologue 2 (SLIT2), which inhibits proliferative β-catenin signalling. This change in expression is associated with poor prognosis.[66,67]

The tumour-suppressive phenotype of fibroblasts and CAFs is therefore dependent on the factors they produce, which remain largely uncharacterised. Successful tumours must then be able to evolve mechanisms to control, evade or overcome fibroblast-induced suppression.

THERAPEUTIC IMPLICATIONS

Because cancer is a complex, dynamic and adaptive ecosystem reinforced by genetic diversity and epigenetic plasticity, the rapid emergence of drug resistance is problematic for many patients. Consequently, there is a need to investigate therapies that are not necessarily directed at the tumour cells themselves and, as such, CAFs provide an attractive target: they are genetically stable and consequently less likely than tumour cells to acquire therapeutic resistance, and their presence across different cancer types entices a broad applicability of effective therapies. Some studies have examined the effect of ablating the prominent CAF subtypes on carcinogenesis: deletion of FAP-expressing fibroblasts induced rapid tumour necrosis in LLC[14] and impeded metastasis in PDAC,[68] whereas elimination of α-SMA fibroblasts enhanced tumorigenesis in both mouse and clinical models.[8,59] CAF-directed therapy should therefore be designed against specific pro-tumour factors or functions with the aim of preventing CAF function or activation, or reprogramming CAFs back into a normal, resting phenotype.

Targeting CAFs as a method of cancer therapy

FAP has been the focus of many CAF-directed preclinical and clinical cancer studies. A DNA vaccine directed against FAP was shown to significantly suppress primary and secondary tumours in a murine colon cancer model by upregulating cytotoxic T-cell-mediated killing, increasing animal survival.[69] Tumour angiogenesis was also suppressed following depletion of FAP^+ CAFs via FAP-targeted chimeric antigen receptor (CAR) T cells, with resultant murine pancreatic tumour retardation.[70] The enzymatic activity of FAP has also been inhibited using the drug PT-100, which attenuated tumour growth in many mouse models,[71] but showed minimal activity in phase 2 trials of patients with metastatic CRC.[72] The humanised anti-FAP antibody, sibrotuzumab, also showed no beneficial effect in phase 2 trials for metastatic CRC.[73] In both of these trials, the patients were heavily pre-treated and could therefore represent a refractory patient population. It is also hypothesised that the biological effects of FAP may be more prominent in smaller tumours or earlier stages of CRC, not in late-stage metastasis. Other CAF subtypes, namely $CD10^+GPR77^+$ and $IL\text{-}7^+$ CAFs, have been targeted pre-clinically, resulting in impaired tumour stemness and growth with restored chemosensitivity in breast cancer patient-derived xenografts (PDXs) and cell lines, respectively.[74,75] Intriguingly, $CD10^+GPR77^+$ CAFs directly conveyed a chemo-resistant phenotype on breast cancer cells in co-culture, co-transplant and PDX models through the secretion of factors such as IL-6 and the upregulation of the multidrug-resistance transporter ABCG2.[74] The SOM230 analogue, Pasireotide, has been used in mouse models of PDAC to prevent IL-6 synthesis (amongst other proteins) through activation of the somatostatin (sst1) receptor, which then inhibits the mammalian target of the rapamycin (mTOR)/4E-BP1 pathway. This pathway is highly activated in $\alpha\text{-SMA}^+$ CAFs isolated from human PDAC resections, and when SOM-230 was administered to mice engrafted with human PDAC there was a reduction in tumour growth and chemoresistance to gemcitabine. This drug targets the pathway in CAFs specifically, as the sst1 receptor is not present in the epithelium.[76] CAF-mediated secretion of IL-6 has also been inhibited by resveratrol, inducing a switch in expression from

N-cadherin to E-cadherin in migrating mouse cholangiocarcinoma cells to diminish their invasion and induce autophagy.[77]

Additional targets for cancer treatment are MMPs, even though they are not solely expressed by CAFs, and many different MMP inhibitors have been developed and tested in phase 1, 2 and 3 clinical trials. Unfortunately, all clinical trials testing small molecule, broad-spectrum MMP inhibitors in a range of cancer types and stages, to date, have failed to improve clinical outcomes and resulted in major musculoskeletal toxicity in many cases. This field is advancing tremendously, however, with the development of many small molecule inhibitors and antibodies targeting specific domains of particular tumour-promoting MMPs, and improved targeting of natural MMP inhibitors, such as the tissue inhibitors of metalloproteinases (TIMPs). This topic is extensively reviewed in ref. [78] Recent clinical trials combining gemcitabine with the SMO inhibitor, vismodegib, have also been underway in patients with metastatic PDAC, despite the preclinical evidence suggesting Hh-driven PDAC CAFs are also tumour suppressors;[9] fibrosis was reduced in 45.4% of patients in a pilot trial, and no toxicity was observed in a phase 1b/2 trial, but there was no improved overall response rate or survival with dual therapy in either trial.[79,80] Perhaps these disappointments are due to the non-selective ablation of Hh-driven, tumour-suppressing CAF subtypes amongst the tumour-promoting subtypes. However, 3 of 12 patients with metastatic triple-negative breast cancer treated with docetaxel and the SMO inhibitor Sonidegib in a recent phase 1 clinical trial showed clinical benefit, with one experiencing a complete response. The accompanying preclinical data suggest that mechanistically these outcomes were due to the downregulation of CSC markers.[81] As more is learnt about the heterogeneity of Hh-signalling CAFs, the aim is to target only the pro-tumour subsets and ultimately lead to improved cancer therapies.

Methods to inhibit CAF activation are also in development as novel cancer therapeutics. The downregulation of the androgen receptor (AR) in dermal fibroblasts was shown to induce early CAF activation and enhance tumorigenicity of SCC and melanoma cells. As such, this study suggested the use of bromodomain (BET) inhibitors, such as JQ1, to restore AR expression. This resulted in reduced CAF activity and prevented tumour growth in a melanoma mouse model.[82] Compounds such as the synthetic vitamin-D derivative, calcipotriol, have also been used to block the TGF-β-mediated differentiation of pancreatic fibroblasts into CAFs, decreasing inflammation and fibrosis and improving chemotherapeutic responsiveness in mice with spontaneous PDAC.[83] Similarly, the endogenous bioactive lipid lipoxin A4 (LXA4) was used to inhibit Smad2/3 signalling in pancreatic fibroblasts to ultimately retard murine pancreatic tumour growth.[84] In other approaches, the epigenetic machinery inducing CAF activation has been targeted. Firstly, TGF-β-mediated CAF differentiation was targeted by using Scriptaid to inhibit histone deacetylase. Reduced fibroblast content and activity, impaired collective CAF-tumour cell invasion and delayed melanoma growth in vivo resulted.[85] Secondly, targeting the RNA editor, Adenosine Deaminase family acting on RNA (ADAR1), appears warranted in CRC; ADAR1 is overexpressed in human CRC and leads to elevated antizyme inhibitor 1 (*AZIN1*) RNA editing levels, which is correlated with increased CAF marker expression and aggressive tumours.[86]

Reprogramming activated fibroblasts or CAFs back into their dormant state is another strategy for impairing tumorigenesis. miRNAs have attracted interest in this context, and in the case of lung fibrosis, upregulation of the miR-19a-19b-20a sub-cluster was observed during disease progression. This sub-cluster suppressed TGF-β-induced fibroblast activation, suggesting that normal fibroblasts attempt to stop their own activation.[87] Upregulation of the TGF-β pathway inhibitor, miR-145, was also observed in TGF-β-induced and primary oral cancer CAFs. When normal oral fibroblasts were transfected with miR-145 prior to TGF-β treatment, their in vitro activation was impaired, and when transfected following treatment, their quiescent phenotype was rescued. Thus, it is again seen that normal fibroblasts may inherently contain a negative feedback loop to protect against CAF conversion.[88] Another study demonstrated that CAFs within human breast tumours had decreased levels of the tumour suppressor miRNA, Let-7b, compared with their normal fibroblast counterparts. Inhibition of Let-7b in these normal breast fibroblasts increased their activation and capacity to induce breast cancer cell EMT in vitro, and enhanced tumour growth in a murine breast cancer model. The opposite was observed upon re-expression of Let-7b in human breast CAFs, and the cancer-promoting abilities of breast myofibroblasts were reduced.[89] Pancreatic CAFs have also been reprogrammed towards quiescence via activation of the tumour-suppressor p53 by the Nutlin-3a derivative RG7112, resulting in a reduction of murine pancreatic desmoplasia.[90] The combined inhibition of DNA methyltransferase activity and Janus kinase (JAK) signalling also resulted in the long-term phenotypical and molecular reversion of activated CAFs to normal, resting fibroblasts, causing murine breast tumours to become less invasive.[91]

Although some preclinical studies have demonstrated the benefits of targeting CAFs alone, presumably the simultaneous targeting of both the tumour and CAF compartments will ultimately improve efficacy in clinical trials. Some preclinical studies have targeted both the tumour and CAFs with one therapeutic agent. One group designed a novel dendrimer conjugated to the mTOR inhibitor rapamycin to successfully inhibit mTOR signalling and VEGF expression in prostate cancer cells and fibroblasts, and reduce fibroblast-mediated prostate tumour progression and metastasis.[92] Another group targeted neuregulin (NRG1), which is highly expressed in the cancer cells and CAFs of PDAC. Their NRG1 inhibitory antibody, 7E3, was able to promote apoptosis in the pancreatic tumour cells and CAFs, and inhibit the growth of the tumour.[93] Other studies have combined different CAF-targeting and tumour-targeting drugs to investigate their dual anti-tumour efficacy. For example, compromising the integrity of collagen fibres using nab-paclitaxel, combined with gemcitabine, reduced the number of CAFs and improved overall survival in a phase 3 clinical trial of pancreatic cancer, compared with either agent alone.[94,95] Similarly, in the preclinical setting, only the dual administration of the chemotherapeutic oxaliplatin with PT-100 increased mouse survival by decreasing CAF content, colon tumour growth, angiogenesis and pro-tumour immune cell recruitment.[96] This is not always the outcome, however, as PT-100 combined with cisplatin for stage IV melanoma or with docetaxel for non-small-cell lung carcinoma (NSCLC) did not show a therapeutic advantage in phase 2 human trials.[97,98] Other trials have attempted to reduce tumorigenesis by disrupting the cross-talk between the cancer and CAFs. As an example, HGF is predominantly produced by CAFs and activates its cognate receptor, c-Met kinase, on tumour cells, promoting tumorigenesis and chemoresistance via a variety of mechanisms (reviewed in ref. [99]). HGF and c-Met have both been targeted in many preclinical and clinical trials; for example, inhibition of HGF via a neutralising antibody or siRNA knockdown impaired gastric tumour growth in mice,[100] and the combination of gemcitabine with the c-Met inhibitor, tivantinib, demonstrated early signs of anti-tumour activity in various solid tumours in a phase 1 trial, warranting a phase 2 trial.[101] In recent times, many c-Met small molecule inhibitors have been in development and they are reviewed in ref. [102]

There are many tumour-CAF co-targeting clinical trials currently recruiting patients: for example, RO6874281 is a recombinant fusion protein that targets an engineered, variant form of IL-2 to human FAP^+ cells, to stimulate a local immune response and therefore improve anti-tumour immunity. It is currently being combined with trastuzumab (for $HER2^+$ breast cancers) or with the

epidermal growth factor receptor (EGFR) inhibitor cetuximab (for head and neck cancers) in phase 1 trials (NCT02627274), or with the anti-PD-L1 antibody atezolizumab in a phase 2 trial investigating advanced and/or metastatic solid tumours (NCT03386721). The scientific community awaits the outcomes of these, and other, tumour-CAF-targeted trials.

Using CAFs as a means of drug delivery

Another strategy for CAF-directed anti-cancer therapy involves the skewing of CAFs towards a suppressive phenotype. However, to the best of our knowledge, no studies have directly explored this approach; the lack of specific biomarkers for CAFs and for their tumour-promoting and tumour-suppressing phenotypes has become a hindrance. However, one way to evade the issues surrounding CAF heterogeneity (for now) involves the use of the general CAF population as a drug delivery tool. A prodrug has been designed to be cleaved, using the protease activity of FAP, into the cytotoxic drug thapsigargin, and it produced a local therapeutic response in mouse models of breast and prostate cancer.[103] MMPs have also been used to cleave MMP-sensitive micelles encapsulating the chemotherapeutic drug docetaxel, releasing it locally to reduce cervical cancer growth in mice.[104] Moreover, nanoparticles containing plasmids encoding a secreted form of the pro-apoptotic factor TRAIL (sTRAIL) have been non-specifically targeted to CAFs, modifying them to express sTRAIL. This approach killed nearly all of the local bladder and pancreatic tumour cells and diminished CAF numbers, prolonging survival and efficiently ameliorating metastasis in preclinical models.[105] Leucine-rich-repeat-containing 15 (LRRC15)$^+$ CAFs have also been targeted using a LRRC15-antibody drug conjugate (ABBV-085) to deliver the potent anti-mitotic drug monomethyl auristatin E (MMAE) in PDX models of NSCLC-adenocarcinoma, osteocarcinoma, breast cancer and glioblastoma, significantly reducing tumour volume. Nevertheless, complete responses in these models were only seen when combined with various types of chemotherapy, radiation and immune therapy agents.[106]

Another approach still in its infancy uses CAFs and CAF-derived factors as ecological traps, designed to mimic the normal niche to attract disseminated cancer cells that are subsequently killed via methods, such as TRAIL-induced apoptosis and trap-targeted stereotactic radiation.[107] However, this method involves surgical implantation, creating a wound site that in itself was observed to activate tissue-resident fibroblasts and attract more cancer cells.[107] One group was able to encapsulate live CAFs in microparticles that could then be intraperitoneally injected, without wounding. The CAF-derived ECM surface of the beads selectively captured disseminated cells from different tumour origins, and the iron oxide nanoparticles incorporated into the bead surface allowed for magnetic retrieval of the microparticles. This technique was able to prolong mouse survival by delaying peritoneal metastasis.[107]

CAFs as prognostic tools

The differential expression of specific genes in the tumour stroma, compared with the normal stroma of the same tissue, generates expression signatures that can offer prognostic clues in many different types of cancers. One of the first studies to recognise the prognostic relevance of the tumour stroma to survival and recurrence, in breast cancer patients, identified a 26-gene 'stroma-derived prognostic predictor'.[108] This signature, however, was not specific to CAFs but to all cells in the tumour stroma. Other studies have since derived prognostic gene signatures from the CAF population specifically, for example in CRC,[5] NSCLC[109] and hepatocellular carcinoma.[110] However, the CAF-associated signatures identified in these studies do not overlap; for example, the CRC 4-gene signature includes *FAP* and *CALD1* (the gene encoding caldesmon 1),[5] the 11-gene NSCLC signature includes *THBS2* (the gene encoding thrombospondin 2) and *CLU* (the gene encoding clusterin),[109] and the 12-marker liver cancer panel includes fibroblast growth factor 5 (FGF5) and MMP1.[110] Again, heterogeneity is to blame for the lack of a uniform CAF-associated prognostic gene signature, and it may be that every different type of cancer has its own specific predictor. One group has also found a CAF-associated gene signature that predicts chemotherapy resistance in the neoadjuvant setting for breast cancer, based on the differential expression of 50 genes, including *DCN* (the gene encoding decorin), *COL1A2* (the gene encoding collagen type 1α2), *FAP*, *CALD1* and *THBS2*.[111] In addition, the presence of CD146-expressing CAFs predicts tamoxifen sensitivity and better treatment outcome in patients with oestrogen receptor-positive (ER$^+$) breast cancer, as they maintain ER expression (unlike CD146-null CAFs).[112]

Tumour and CAF data can be obtained from the blood and peritoneal fluid, and sequential liquid biopsy samples allow the dynamic monitoring of these cells during cancer progression. This technique was originally used to detect disseminated cancer cells, which were indicative of increased recurrence and poorer survival and therefore served as prognostic, metastatic markers.[107] However, this technology was subsequently enriched to detect circulating CAFs, demonstrating that CAFs were present in 88% of breast cancer patients with metastases, 23% of patients with localised disease and 0% of healthy donors.[113] Moreover, in oesophageal cancer, ADAM12 is the serum-borne marker for IL-6$^+$ CAFs, and its presence predicts poor response to neoadjuvant chemoradiation.[46]

CAF MARKERS AND HETEROGENEITY

Historically, research has underestimated the complexity of CAF heterogeneity and studies have used the entire, mixed, CAF population to draw general conclusions, an approach that is likely to have resulted in observational variability and ultimately enhanced confusion in the field. As we come to appreciate the complexity of CAFs, studies are now attempting to single out specific CAF subtypes, predominantly targeting the two most common types— either α-SMA$^+$ or FAP$^+$ CAFs. But, even this approach has had variable results, and their co-expression is also debatable. One study demonstrated that they define completely different CAF subsets, at least in CRC, with α-SMA associating with other activated fibroblast markers such as transgelin (TAGLN) and platelet-derived growth factor subunit A (PDGFA), whilst FAP associated with other markers, including DCN and COL1A2.[10] It is worth noting that this was the first comprehensive study that attempted to define human CAF subsets, using single-cell sequencing. Another study defined α-SMA^{High}FAP$^+$ pancreatic CAFs as a myofibroblastic, active subtype responsive to TGF-β, while the remaining α-SMA^{Low} CAFs were shown to secrete inflammatory mediators such as IL-6 that promoted the growth and proliferation of patient-derived PDAC organoids. These two CAF subtypes were mutually exclusive, but reversible in different culture conditions.[114] Furthermore, another study that defined four breast CAF subsets, based on their expression of α-SMA, FAP, FSP1, PDGFRβ and CD29, demonstrated that α-SMA^{High}FAP^{High} CAFs were associated with an immune-suppressive environment, enhancing Treg cells via CXCL12 secretion. The α-SMA^{High}FAP^{Neg} CAF subset was devoid of these properties.[115] These last two studies are some of the first to examine the potential functional roles of different CAF populations in pancreatic and breast cancer, respectively, yet the α-SMA$^+$FAP$^+$ CAF subset they both identified had slightly different properties. Similar CAF subtypes may therefore have unique roles in each tissue type, adding an extra layer of complexity. There are also differences in CAF marker expression between tissues; for example, 43.5% of α-SMA$^+$ fibroblasts co-expressed FSP1 in pancreatic cancer, but this overlap was reduced to 10.9% in breast cancer.[11] CAFs may therefore be further regulated by other unknown, tissue-specific factors.

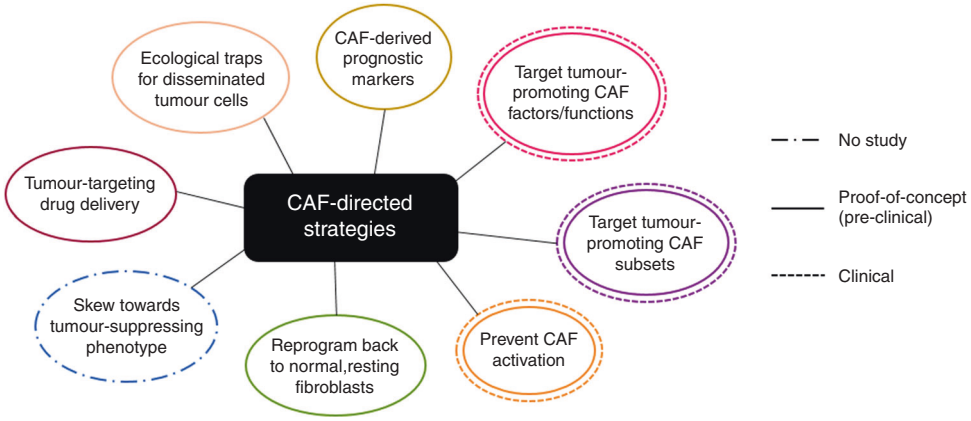


Fig. 2 CAF-directed cancer therapies. Outlined are several preclinical and clinical approaches aimed at targeting CAFs in an attempt to impede tumorigenesis. Ideally, for full efficacy, these strategies will be used in conjunction with drugs that target tumours

Other studies have attempted to define CAF heterogeneity, not based on α-SMA and FAP expression. Bartoschek et al.[116] were able to define three distinct populations of breast cancer CAFs from a mouse model, which was confirmed in patients; vascular CAFs (vCAFs) were Nidogen2^{+}, matrix-related CAFs (mCAFs) were Pdgfrα^{+} and developmental CAFs (dCAFs) were Pdgfrβ^{-}Scrg1^{+}. αSMA and FAP expression did not segregate with these populations. The presence of vCAFs and mCAFs correlated with metastatic dissemination, and the mCAF signature additionally correlated to a treatment-predictive stromal signature in breast cancer. Each subset could be spatially separated and this was linked to different origins; vCAFs from perivascular cells, mCAFs from resident fibroblasts and dCAFs from tumour cells that had undergone EMT.[116] The heterogeneity of CAFs is understandable given different source populations in different locations. Another example of spatially demarcated CAFs was demonstrated by Cremasco et al.[117] in a mouse model of immune-excluded breast cancer, where FAP^{+}PDPN^{+} CAFs were localised around the tumour edge and in close contact with T cells, while FAP^{+}PDPN^{-} 'cancer-associated pericytes' (CAPs) surrounded vessels. Interestingly, CAFs were enriched in TGF-β signalling and fibrosis and produced nitric oxide to suppress T-cell proliferation; CAPs were not immunosuppressive.[117] Moreover, Biffi et al.[118] demonstrated that myofibroblastic CAFs (myCAFs) were found adjacent to PDAC tumours, while inflammatory CAFs (iCAFs) were preferentially localised in the dense PDAC stroma. This study demonstrated another concept alluded to above, that tumours can influence CAF activation and as a result also CAF heterogeneity; PDAC tumour-derived IL-1 steered CAFs towards an iCAF phenotype, while TGF-β biased towards myCAFs. CAFs in different locations could therefore have been exposed to different tumour ligands, influencing their phenotype. TGF-β was also shown to convert iCAFs into myCAFs, via antagonism of the JAK/STAT pathway and down-regulation of IL-1R1 expression.[118] The presence of interconvertible myCAFs and iCAFs in PDAC is supported by Ohlund et al.[114] Biffi et al.[118] therefore suggest drug combinations targeting both iCAFs and myCAFs, to decrease tumour-promoting inflammation and deplete the dense stroma impeding drug delivery. In another study, Neuzillet et al.[119] proposed the 'pCAFassigner' classification system to segregate their three defined human-derived PDAC CAF subtypes based on the expression of periostin (POSTN), myosin-11 (MYH11) and PDPN. Tumour-conditioned medium was shown to induce two of the three CAF subtypes in pancreatic stellate cells in vitro, suggesting tumours can influence dynamic CAF states.[119] It also appears that the cancer stage can influence the dominating CAF phenotype, via cancer-derived exosomes, particularly in CRC; early-stage CRC exosomes promoted highly proliferative and angiogenic CAFs, while late-stage exosomes from metastatic CRC lines induced highly invasive CAFs.[120]

CONCLUSION

Tumours and their local microenvironment form a complex ecosystem that can ultimately promote cancer progression. It has now become widely accepted that CAFs can have a dual role in tumorigenesis, owing to their heterogeneity; they can either promote cancer via induction of an inflammatory, immune-suppressive, angiogenic, energy-rich, invasive and metastatic environment, or suppress cancer via predominantly unknown mechanisms (Fig. 1). It might be that fibroblasts begin as a tumour-suppressive cell type, but as the tumour develops it begins to influence the environment and transforms these fibroblasts into pro-tumoural factories. It is therefore conceivable that fibroblasts act as both heroes and villains.

As different CAF expression profiles may define their role in tumorigenesis, CAF molecular marker combinations must be further refined to assist in the classification of pro- and anti-tumour subsets in different tissues. This will provide us with better prognostic CAF biomarkers and more specific avenues for CAF-directed cancer treatments, allowing us to precisely target the tumour-promoting subtypes and CAF-derived factors or skew the CAF phenotype away from tumour promotion, or prevent CAF activation altogether (Fig. 2). These novel strategies can then be combined with other tumour-targeting drugs to ultimately improve treatment efficacy and patient survival.

AUTHOR CONTRIBUTIONS

All authors contributed substantially to the discussion of article content and reviewed the paper before submission. K.A.G. wrote the paper.

ADDITIONAL INFORMATION

Competing interests: The authors declare no competing interests.

Ethics approval and consent to participate: Not applicable.

Funding: This work was supported by Cure Cancer Australia/Cancer Australia (APP1102534), the Cancer Council SA Beat Cancer Project on behalf of its donors and the State Government of South Australia through the Department of Health SA and by the Australian National Health and Medical Research Council (NHMRC) (through APP1140236, APP1143414). K.A.G. is supported by the Australian Government's Research Training Program Stipend and the Lions Medical Research Foundation Inc. Scholarship, L.M.B. by a Principal Cancer Research Fellowship and D.L.W. by a NHMRC Career Development Fellowship.

Data availability: Not applicable.

Note: This work is published under the standard license to publish agreement. After 12 months the work will become freely available and the license terms will switch to a Creative Commons Attribution 4.0 International (CC BY 4.0).

Publisher's note: Springer Nature remains neutral with regard to jurisdictional claims in published maps and institutional affiliations.

REFERENCES

1. Koliaraki, V., Pallangyo, C. K., Greten, F. R. & Kollias, G. Mesenchymal cells in colon cancer. *Gastroenterology* **152**, 964–979 (2017).
2. Kalluri, R. The biology and function of fibroblasts in cancer. *Nat. Rev. Cancer* **16**, 582–598 (2016).
3. Coussens, L. M. & Werb, Z. Inflammation and cancer. *Nature* **420**, 860–867 (2001).
4. Dvorak, H. F. Tumors: wounds that do not heal. Similarities between tumor stroma generation and wound healing. *N. Engl. J. Med.* **315**, 1650–1659 (1986).
5. Calon, A., Lonardo, E., Berenguer-Llergo, A., Espinet, E., Hernando-Momblona, X., Iglesias, M. et al. Stromal gene expression defines poor-prognosis subtypes in colorectal cancer. *Nat. Genet.* **47**, 320–329 (2015).
6. Isella, C., Terrasi, A., Bellomo, S. E., Petti, C., Galatola, G., Muratore, A. et al. Stromal contribution to the colorectal cancer transcriptome. *Nat. Genet.* **47**, 312–319 (2015).
7. Guinney, J., Dienstmann, R., Wang, X., de Reynies, A., Schlicker, A., Soneson, C. et al. The consensus molecular subtypes of colorectal cancer. *Nat. Med.* **21**, 1350–1356 (2015).
8. Ozdemir, B. C., Pentcheva-Hoang, T., Carstens, J. L., Zheng, X., Wu, C. C., Simpson, T. R. et al. Depletion of carcinoma-associated fibroblasts and fibrosis induces immunosuppression and accelerates pancreas cancer with reduced survival. *Cancer Cell* **25**, 719–734 (2014).
9. Rhim, A. D., Oberstein, P. E., Thomas, D. H., Mirek, E. T., Palermo, C. F., Sastra, S. A. et al. Stromal elements act to restrain, rather than support, pancreatic ductal adenocarcinoma. *Cancer Cell* **25**, 735–747 (2014).
10. Li, H., Courtois, E. T., Sengupta, D., Tan, Y., Chen, K. H., Goh, J. J. et al. Reference component analysis of single-cell transcriptomes elucidates cellular heterogeneity in human colorectal tumors. *Nat. Genet.* **49**, 708–718 (2017).
11. Sugimoto, H., Mundel, T. M., Kieran, M. W. & Kalluri, R. Identification of fibroblast heterogeneity in the tumor microenvironment. *Cancer Biol, Ther,* **5**, 1640–1646 (2014).
12. Hanahan, D. & Weinberg, R. A. Hallmarks of cancer: the next generation. *Cell* **144**, 646–674 (2011).
13. Erez, N., Truitt, M., Olson, P., Arron, S. T. & Hanahan, D. Cancer-associated fibroblasts are activated in incipient neoplasia to orchestrate tumor-promoting inflammation in an NF-kB-dependent manner. *Cancer Cell* **17**, 135–147 (2010).
14. Kraman, M., Bambrough, P. J., Arnold, J. N., Roberts, E. W., Magiera, L., Jones, J. O. et al. Suppression of antitumor immunity by stromal cells expressing fibroblast activation protein-α. *Science* **330**, 827–830 (2010).
15. Liao, D., Luo, Y., Markowitz, D., Xiang, R. & Reisfeld, R. A. Cancer associated fibroblasts promote tumor growth and metastasis by modulating the tumor immune microenvironment in a 4T1 murine breast cancer model. *PLoS One* **4**, https://doi.org/10.1371/journal.pone.0007965 (2009).
16. Li, T., Yang, Y., Hua, X., Wang, G., Liu, W., Jia, C. et al. Hepatocellular carcinoma-associated fibroblasts trigger NK cell dysfunction via PGE2 and IDO. *Cancer Lett* **318**, 154–161 (2012).
17. Mariathasan, S., Turley, S. J., Nickles, D., Castiglioni, A., Yuen, K., Wang, Y. et al. TGFbeta attenuates tumour response to PD-L1 blockade by contributing to exclusion of T cells. *Nature* **554**, 544–548 (2018).
18. Tauriello, D. V. F., Palomo-Ponce, S., Stork, D., Berenguer-Llergo, A., Badia-Ramentol, J., Iglesias, M. et al. TGF beta drives immune evasion in genetically reconstituted colon cancer metastasis. *Nature* **554**, 538–543 (2018).
19. Kumar, V., Donthireddy, L., Marvel, D., Condamine, T., Wang, F., Lavilla-Alonso, S. et al. Cancer-associated fibroblasts neutralize the anti-tumor effect of CSF1 receptor blockade by inducing PMN-MDSC infiltration of tumors. *Cancer Cell* **32**, 654–668 (2017).
20. Kugeratski, F. G., Atkinson, S. J., Neilson, L. J., Lilla, S., Knight, J. R. P., Serneels, J. et al. Hypoxic cancer-associated fibroblasts increase NCBP2-AS2/HIAR to promote endothelial sprouting through enhanced VEGF signaling. *Sci. Signal.* **12**, https://doi.org/10.1126/scisignal.aan8247 (2019).
21. Madsen, C. D., Pedersen, J. T., Venning, F. A., Singh, L. B., Moeendarbary, E., Charras, G. et al. Hypoxia and loss of PHD2 inactivate stromal fibroblasts to decrease tumour stiffness and metastasis. *EMBO Rep.* **16**, 1394–1408 (2015).
22. Zhou, Y., Ren, H., Dai, B., Li, J., Shang, L., Huang, J. et al. Hepatocellular carcinoma-derived exosomal miRNA-21 contributes to tumor progression by converting hepatocyte stellate cells to cancer-associated fibroblasts. *J. Exp. Clin. Cancer Res.* **37**, https://doi.org/10.1186/s13046-018-0965-2 (2018).
23. Pavlides, S., Whitaker-Menezes, D., Castello-Cros, R., Flomenberg, N., Witkiewicz, A. K., Frank, P. G. et al. The reverse Warburg effect: aerobic glycolysis in cancer associated fibroblasts and the tumor stroma. *Cell Cycle* **8**, 3984–4001 (2009).
24. Martinez-Outschoorn, U. E., Prisco, M., Ertel, A., Tsirigos, A., Lin, Z., Pavlides, S. et al. Ketones and lactate increase cancer cell "stemness," driving recurrence, metastasis and poor clinical outcome in breast cancer: achieving personalized medicine via Metabolo-Genomics. *Cell Cycle* **10**, 1271–1286 (2011).
25. Bonuccelli, G., Tsirigos, A., Whitaker-Menezes, D., Pavlides, S., Pestell, R. G., Chiavarina, B. et al. Ketones and lactate "fuel" tumor growth and metastasis: evidence that epithelial cancer cells use oxidative mitochondrial metabolism. *Cell Cycle* **9**, 3506–3514 (2010).
26. Sakamoto, A., Kunou, S., Shimada, K., Tsunoda, M., Aoki, T., Iriyama, C. et al. Pyruvate secreted from patient-derived cancer-associated fibroblasts supports survival of primary lymphoma cells. *Cancer Sci.* **110**, 269–278 (2019).
27. Zhao, H., Yang, L., Baddour, J., Achreja, A., Bernard, V., Moss, T. et al. Tumor microenvironment derived exosomes pleiotropically modulate cancer cell metabolism. *Elife* **5**, https://doi.org/10.7554/eLife.10250 (2016).
28. Yan, W., Wu, X., Zhou, W., Fong, M. Y., Cao, M., Liu, J. et al. Cancer-cell-secreted exosomal miR-105 promotes tumour growth through the MYC-dependent metabolic reprogramming of stromal cells. *Nat Cell Biol.* **20**, 597–609 (2018).
29. Kalluri, R. & Zeisberg, M. Fibroblasts in cancer. *Nat. Rev. Cancer* **6**, 392–401 (2006).
30. De Wever, O. & Mareel, M. Role of tissue stroma in cancer cell invasion. *J. Pathol.* **200**, 429–447 (2003).
31. Kalluri, R. Basement membranes: structure, assembly and role in tumour angiogenesis. *Nat. Rev. Cancer* **3**, 422–433 (2003).
32. Kuchnio, A., Moens, S., Bruning, U., Kuchnio, K., Cruys, B., Thienpont, B. et al. The cancer cell oxygen sensor PHD2 promotes metastasis via activation of cancer-associated fibroblasts. *Cell Rep.* **12**, 992–1005 (2015).
33. Pickup, M. W., Laklai, H., Acerbi, I., Owens, P., Gorska, A. E., Chytil, A. et al. Stromally derived lysyl oxidase promotes metastasis of transforming growth factor-beta-deficient mouse mammary carcinomas. *Cancer Res.* **73**, 5336–5346 (2013).
34. Levental, K. R., Yu, H., Kass, L., Lakins, J. N., Egeblad, M., Erler, J. T. et al. Matrix crosslinking forces tumor progression by enhancing integrin signaling. *Cell* **139**, 891–906 (2009).
35. Lee, H. O., Mullins, S. R., Franco-Barraza, J., Valianou, M., Cukierman, E. & Cheng, J. D. FAP-overexpressing fibroblasts produce an extracellular matrix that enhances invasive velocity and directionality of pancreatic cancer cells. *BMC Cancer* **11**, https://doi.org/10.1186/1471-2407-11-245 (2011).
36. Miyazaki, K., Oyanagi, J., Hoshino, D., Togo, S., Kumagai, H. & Miyagi, Y. Cancer cell migration on elongate protrusions of fibroblasts in collagen matrix. *Sci. Rep.* **9**, https://doi.org/10.1038/s41598-018-36646-z (2019).
37. Gaggioli, C., Hooper, S., Hidalgo-Carcedo, C., Grosse, R., Marshall, J. F., Harrington, K. et al. Fibroblast-led collective invasion of carcinoma cells with differing roles for RhoGTPases in leading and following cells. *Nat. Cell Biol.* **9**, 1392–1400 (2007).
38. Labernadie, A., Kato, T., Brugues, A., Serra-Picamal, X., Derzsi, S., Arwert, E. et al. A mechanically active heterotypic E-cadherin/N-cadherin adhesion enables fibroblasts to drive cancer cell invasion. *Nat. Cell Biol.* **19**, 224–237 (2017).
39. Vermeulen, L., Todaro, M., De Sousa Mello, F., Sprick, M. R., Kemper, K., Perez Alea, M. et al. Single-cell cloning of colon cancer stem cells reveals a multi-lineage differentiation capacity. *Proc. Natl Acad. Sci. USA* **106**, 13427–13432 (2008).
40. Clevers, H. The cancer stem cell: premises, promises and challenges. *Nat. Med.* **17**, 313–319 (2011).
41. Tsuyada, A., Chow, A., Wu, J., Somlo, G., Chu, P., Loera, S. et al. CCL2 mediates cross-talk between cancer cells and stromal fibroblasts that regulates breast cancer stem cells. *Cancer Res.* **72**, 2768–2779 (2012).
42. Todaro, M., Gaggianesi, M., Catalano, V., Benfante, A., Iovino, F., Biffoni, M. et al. CD44v6 is a marker of constitutive and reprogrammed cancer stem cells driving colon cancer metastasis. *Cell Stem Cell* **14**, 342–356 (2014).
43. Xiong, S., Wang, R., Chen, Q., Luo, J., Wang, J., Zhao, Z. et al. Cancer-associated fibroblasts promote stem cell-like properties of hepatocellular carcinoma cells through IL-6/STAT3/Notch signalling. *Am. J. Cancer Res.* **8**, 302–316 (2018).
44. Giannoni, E., Bianchini, F., Masieri, L., Serni, S., Torre, E., Calorini, L. et al. Reciprocal activation of prostate cancer cells and cancer-associated fibroblasts stimulates epithelial-mesenchymal transition and cancer stemness. *Cancer Res.* **70**, 6945–6956 (2010).
45. Kalluri, R. & Weinberg, R. A. The basics of epithelial-mesenchymal transition. *J. Clin. Invest.* **119**, 1420–1428 (2009).

46. Ebbing, E. A., van der Zalm, A. P., Steins, A., Creemers, A., Hermsen, S., Rentenaar, R. et al. Stromal-derived interleukin 6 drives epithelial-to-mesenchymal transition and therapy resistance in esophageal adenocarcinoma. *Proc. Natl Acad. Sci. USA* **116**, 2237–2242 (2019).
47. Brabletz, T. EMT and MET in metastasis: where are the cancer stem cells? *Cancer Cell* **22**, 699–701 (2012).
48. Duda, D. G., Duyverman, A. M., Kohno, M., Snuderl, M., Steller, E. J., Fukumura, D. et al. Malignant cells facilitate lung metastasis by bringing their own soil. *Proc. Natl Acad. Sci. USA* **107**, 21677–21682 (2010).
49. Gao, Q., Yang, Z., Xu, S., Li, X., Yang, X., Jin, P. et al. Heterotypic CAF-tumor spheroids promote early peritoneal metastatis of ovarian cancer. *J. Exp. Med.* **216**, 688–703 (2019).
50. De Wever, O., Van Bockstal, M., Mareel, M., Hendrix, A. & Bracke, M. Carcinoma-associated fibroblasts provide operational flexibility in metastasis. *Semin Cancer Biol.* **25**, 33–46 (2014).
51. Del Pozo Martin, Y., Park, D., Ramachandran, A., Ombrato, L., Calvo, F., Chakravarty, P. et al. Mesenchymal cancer cell-stroma crosstalk promotes niche activation, epithelial reversion, and metastatic colonization. *Cell Rep.* **13**, 2456–2469 (2015).
52. Malanchi, I., Santamaria-Martinez, A., Susanto, E., Peng, H., Lehr, H. A., Delaloye, J. F. et al. Interactions between cancer stem cells and their niche govern metastatic colonization. *Nature* **481**, 85–89 (2011).
53. Mintz, B. & Illmensee, K. Normal genetically mosaic mice produced from malignant teratocarcinoma cells. *Proc. Natl Acad. Sci. USA* **72**, 3585–3589 (1975).
54. Stoker, M. G., Shearer, M. & O'Neill, C. Growth inhibition of polyoma-transformed cells by contact with static normal fibroblasts. *J. Cell Sci.* **1**, 297–310 (1966).
55. Dotto, G. P., Weinberg, R. A. & Ariza, A. Malignant transformation of mouse primary keratinocytes by Harvey sarcoma virus and its modulation by surrounding normal cells. *Proc. Natl Acad. Sci. USA* **85**, 6389–6393 (1988).
56. Djurec, M., Grana, O., Lee, A., Troule, K., Espinet, E., Cabras, L. et al. Saa3 is a key mediator of the protumorigenic properties of cancer-associated fibroblasts in pancreatic tumors. *Proc. Natl Acad. Sci. USA* **115**, E1147–E1156 (2018).
57. Madar, S., Brosh, R., Buganim, Y., Ezra, O., Goldstein, I., Solomon, H. et al. Modulated expression of WFDC1 during carcinogenesis and cellular senescence. *Carcinogenesis* **30**, 20–27 (2009).
58. Lim, P. K., Bliss, S. A., Patel, S. A., Taborga, M., Dave, M. A., Gregory, L. A. et al. Gap junction-mediated import of microRNA from bone marrow stromal cells can elicit cell cycle quiescence in breast cancer cells. *Cancer Res.* **71**, 1550–1560 (2011).
59. Amakye, D., Jagani, Z. & Dorsch, M. Unraveling the therapeutic potential of the Hedgehog pathway in cancer. *Nat. Med.* **19**, 1410–1422 (2013).
60. Bailey, J. M., Swanson, B. J., Hamada, T., Eggers, J. P., Singh, P. K., Caffery, T. et al. Sonic hedgehog promotes desmoplasia in pancreatic cancer. *Clin. Cancer Res.* **14**, 5995–6004 (2008).
61. Olive, K. P., Jacobetz, M. A., Davidson, C. J., Gopinathan, A., McIntyre, D., Honess, D. et al. Inhibition of hedgehog signaling enhances delivery of chemotherapy in a mouse model of pancreatic cancer. *Science* **324**, 1457–1461 (2009).
62. Gerling, M., Buller, N. V., Kirn, L. M., Joost, S., Frings, O., Englert, B. et al. Stromal Hedgehog signalling is downregulated in colon cancer and its restoration restrains tumour growth. *Nat. Commun.* **7**, https://doi.org/10.1038/ncomms12321 (2016).
63. Chen, S., Giannakou, A., Wyman, S., Gruzas, J., Golas, J., Zhong, W. et al. Cancer-associated fibroblasts suppress SOX2-induced dysplasia in a lung squamous cancer coculture. *Proc. Natl Acad. Sci. USA* **115**, E11671–E11680 (2018).
64. Costanza, B., Umelo, I. A., Bellier, J., Castronovo, V. & Turtoi, A. Stromal modulators of TGF-beta in cancer. *J. Clin. Med.* **6**, https://doi.org/10.3390/jcm6010007 (2017).
65. Maris, P., Blomme, A., Palacios, A. P., Costanza, B., Bellahcene, A., Bianchi, E. et al. Asporin is a fibroblast-derived TGF-beta1 inhibitor and a tumor suppressor associated with good prognosis in breast cancer. *PLoS Med.* **12**, https://doi.org/10.1371/journal.pmed.1001871 (2015).
66. Chang, P. H., Hwang-Verslues, W. W., Chang, Y. C., Chen, C. C., Hsiao, M., Jeng, Y. M. et al. Activation of Robo1 signaling of breast cancer cells by Slit2 from stromal fibroblast restrains tumorigenesis via blocking PI3K/Akt/beta-catenin pathway. *Cancer Res.* **72**, 4652–4661 (2012).
67. Marlow, R., Strickland, P., Lee, J. S., Wu, X., Pebenito, M., Binnewies, M. et al. SLITs suppress tumor growth in vivo by silencing Sdf1/Cxcr4 within breast epithelium. *Cancer Res.* **68**, 7819–7827 (2008).
68. Lo, A., Li, C. P., Buza, E. L., Blomberg, R., Govindaraju, P., Avery, D. et al. Fibroblast activation protein augments progression and metastasis of pancreatic ductal adenocarcinoma. *JCI Insight* **2**, https://doi.org/10.1172/jci.insight.92232 (2017).
69. Wen, Y., Wang, C. T., Ma, T. T., Li, Z. Y., Zhou, L. N., Mu, B. et al. Immunotherapy targeting fibroblast activation protein inhibits tumor growth and increases survival in a murine colon cancer model. *Cancer Sci.* **101**, 2325–2332 (2010).
70. Lo, A., Wang, L. S., Scholler, J., Monslow, J., Avery, D., Newick, K. et al. Tumor-promoting desmoplasia is disrupted by depleting FAP-expressing stromal cells. *Cancer Res.* **75**, 2800–2810 (2015).
71. Adams, S., Miller, G. T., Jesson, M. I., Watanabe, T., Jones, B. & Wallner, B. P. PT-100, a small molecule dipeptidyl peptidase inhibitor, has potent antitumor effects and augments antibody-mediated cytotoxicity via a novel immune mechanism. *Cancer Res.* **64**, 5471–5480 (2004).
72. Narra, K., Mullins, S. R., Lee, H.-O., Strzemkowski-Brun, B., Magalong, K., Christiansen, V. J. et al. Phase II trial of single agent Val-boroPro (talabostat) inhibiting fibroblast activation protein in patients with metastatic colorectal cancer. *Cancer Biol. Ther.* **6**, 1691–1699 (2007).
73. Hofheinz, R. D., al-Batran, S. E., Hartmann, F., Hartung, G., Jäger, D., Renner, C. et al. Stromal antigen targeting by a humanised monoclonal antibody: an early phase II trial of sibrotuzumab in patients with metastatic colorectal cancer. *Onkologie* **26**, 44–48 (2003).
74. Su, S., Chen, J., Yao, H., Liu, J., Yu, S., Lao, L. et al. CD10(+)GPR77(+) cancer-associated fibroblasts promote cancer formation and chemoresistance by sustaining cancer stemness. *Cell* **172**, 841–856 (2018).
75. Boesch, M., Onder, L., Cheng, H. W., Novkovic, M., Morbe, U., Sopper, S. et al. Interleukin 7-expressing fibroblasts promote breast cancer growth through sustenance of tumor cell stemness. *Oncoimmunology* **7**, https://doi.org/10.1080/2162402X.2017.1414129 (2018).
76. Duluc, C., Moatassim-Billah, S., Chalabi-Dchar, M., Perraud, A., Samain, R., Breibach, F. et al. Pharmacological targeting of the protein synthesis mTOR/4E-BP1 pathway in cancer-associated fibroblasts abrogates pancreatic tumour chemoresistance. *EMBO Mol. Med.* **7**, 735–753 (2015).
77. Thongchot, S., Ferraresi, A., Vidoni, C., Loilome, W., Yongvanit, P., Namwat, N. et al. Resveratrol interrupts the pro-invasive communication between cancer associated fibroblasts and cholangiocarcinoma cells. *Cancer Lett.* **430**, 160–171 (2018).
78. Radisky, E. S., Raeeszadeh-Sarmazdeh, M. & Radisky, D. C. Therapeutic potential of matrix metalloproteinase inhibition in breast cancer. *J. Cell Biochem.* **118**, 3531–3548 (2017).
79. Catenacci, D. V., Junttila, M. R., Karrison, T., Bahary, N., Horiba, M. N., Nattam, S. R. et al. Randomized phase Ib/II study of gemcitabine plus placebo or vismodegib, a hedgehog pathway inhibitor, in patients with metastatic pancreatic cancer. *J. Clin. Oncol.* **33**, 4284–4292 (2015).
80. Kim, E. J., Sahai, V., Abel, E. V., Griffith, K. A., Greenson, J. K., Takebe, N. et al. Pilot clinical trial of hedgehog pathway inhibitor GDC-0449 (vismodegib) in combination with gemcitabine in patients with metastatic pancreatic adenocarcinoma. *Clin. Cancer Res.* **20**, 5937–5945 (2014).
81. Cazet, A. S., Hui, M. N., Elsworth, B. L., Wu, S. Z., Roden, D., Chan, C. L. et al. Targeting stromal remodeling and cancer stem cell plasticity overcomes chemoresistance in triple negative breast cancer. *Nat. Commun.* **9**, https://doi.org/10.1038/s41467-018-05220-6 (2018).
82. Clocchiatti, A., Ghosh, S., Procopio, M. G., Mazzeo, L., Bordignon, P., Ostano, P. et al. Androgen receptor functions as transcriptional repressor of cancer-associated fibroblast activation. *J. Clin. Invest.* **128**, 5531–5548 (2018).
83. Sherman, M. H., Yu, R. T., Engle, D. D., Ding, N., Atkins, A. R., Tiriac, H. et al. Vitamin D receptor-mediated stromal reprogramming suppresses pancreatitis and enhances pancreatic cancer therapy. *Cell* **159**, 80–93 (2014).
84. Schnittert, J., Heinrich, M. A., Kuninty, P. R., Storm, G. & Prakash, J. Reprogramming tumor stroma using an endogenous lipid lipoxin A4 to treat pancreatic cancer. *Cancer Lett.* **420**, 247–258 (2018).
85. Kim, D. J., Dunleavey, J. M., Xiao, L., Ollila, D. W., Troester, M. A., Otey, C. A. et al. Suppression of TGFbeta-mediated conversion of endothelial cells and fibroblasts into cancer associated (myo)fibroblasts via HDAC inhibition. *Br. J. Cancer* **118**, 1359–1368 (2018).
86. Takeda, S., Shigeyasu, K., Okugawa, Y., Yoshida, K., Mori, Y., Yano, S. et al. Activation of AZIN1 RNA editing is a novel mechanism that promotes invasive potential of cancer-associated fibroblasts in colorectal cancer. *Cancer Lett.* **444**, 127–135 (2019).
87. Souma, K., Shichino, S., Hashimoto, S., Ueha, S., Tsukui, T., Nakajima, T. et al. Lung fibroblasts express a miR-19a-19b-20a sub-cluster to suppress TGF-beta-associated fibroblast activation in murine pulmonary fibrosis. *Sci. Rep.* **8**, https://doi.org/10.1038/s41598-018-34839-0 (2018).
88. Melling, G. E., Flannery, S. E., Abidin, S. A., Clemmens, H., Prajapati, P., Hinsley, E. E. et al. A miRNA-145/TGF-beta1 negative feedback loop regulates the cancer-associated fibroblast phenotype. *Carcinogenesis* **39**, 798–807 (2018).
89. Al-Harbi, B., Hendrayani, S. F., Silva, G. & Aboussekhra, A. Let-7b inhibits cancer-promoting effects of breast cancer-associated fibroblasts through IL-8 repression. *Oncotarget* **9**, 17825–17838 (2018).
90. Saison-Ridinger, M., DelGiorno, K. E., Zhang, T., Kraus, A., French, R., Jaquish, D. et al. Reprogramming pancreatic stellate cells via p53 activation: a putative

target for pancreatic cancer therapy. *PLoS One* **12**, https://doi.org/10.1371/journal.pone.0189051 (2017).
91. Albrengues, J., Bertero, T., Grasset, E., Bonan, S., Maiel, M., Bourget, I. et al. Epigenetic switch drives the conversion of fibroblasts into proinvasive cancer-associated fibroblasts. *Nat. Commun.* **6**, https://doi.org/10.1038/ncomms10204 (2015).
92. Hill, E. E., Kim, J. K., Jung, Y., Neeley, C. K., Pienta, K. J., Taichman, R. S. et al. Integrin alpha V beta 3 targeted dendrimer-rapamycin conjugate reduces fibroblast-mediated prostate tumor progression and metastasis. *J. Cell Biochem.* **119**, 8074–8083 (2018).
93. Ogier, C., Colombo, P. E., Bousquet, C., Canterel-Thouennon, L., Sicard, P., Garambois, V. et al. Targeting the NRG1/HER3 pathway in tumor cells and cancer-associated fibroblasts with an anti-neuregulin 1 antibody inhibits tumor growth in pre-clinical models of pancreatic cancer. *Cancer Lett*. **432**, 227–236 (2018).
94. Von Hoff, D. D., Ervin, T., Arena, F. P., Chiorean, E. G., Infante, J., Moore, M. et al. Increased survival in pancreatic cancer with nab-paclitaxel plus gemcitabine. *N. Engl. J. Med.* **369**, 1691–1703 (2013).
95. Alvarez, R., Musteanu, M., Garcia-Garcia, E., Lopez-Casas, P. P., Megias, D., Guerra, C. et al. Stromal disrupting effects of nab-paclitaxel in pancreatic cancer. *Br. J. Cancer* **109**, 926–933 (2013).
96. Li, M., Li, M., Yin, T., Shi, H., Wen, Y., Zhang, B. et al. Targeting of cancer-associated fibroblasts enhances the efficacy of cancer chemotherapy by regulating the tumor microenvironment. *Mol. Med. Report* **13**, 2476–2484 (2016).
97. Eager, R. M., Cunningham, C. C., Senzer, N. N., Stephenson, J. Jr., Anthony, S. P., O'Day, S. J. et al. Phase II assessment of talabostat and cisplatin in second-line stage IV melanoma. *BMC Cancer* **9**, https://doi.org/10.1186/1471-2407-9-263 (2009).
98. Eager, R. M., Cunningham, C. C., Senzer, N., Richards, D. A., Raju, R. N., Jones, B. et al. Phase II trial of talabostat and docetaxel in advanced non-small cell lung cancer. *Clin. Oncol. (R Coll Radiol)* **21**, 464–472 (2009).
99. Owusu, B. Y., Galemmo, R., Janetka, J. & Klampfer, L. Hepatocyte growth factor, a key tumor-promoting factor in the tumor microenvironment. *Cancers (Basel)* **9**, https://doi.org/10.3390/cancers9040035 (2017).
100. Wu, X., Chen, X., Zhou, Q., Li, P., Yu, B., Li, J. et al. Hepatocyte growth factor activates tumor stromal fibroblasts to promote tumorigenesis in gastric cancer. *Cancer Lett.* **335**, 128–135 (2013).
101. Pant, S., Saleh, M., Bendell, J., Infante, J. R., Jones, S., Kurkjian, C. D. et al. A phase I dose escalation study of oral c-MET inhibitor tivantinib (ARQ 197) in combination with gemcitabine in patients with solid tumors. *Ann. Oncol.* **25**, 1416–1421 (2014).
102. Parikh, P. K. & Ghate, M. D. Recent advances in the discovery of small molecule c-Met Kinase inhibitors. *Eur. J. Med. Chem.* **143**, 1103–1138 (2018).
103. Brennen, W. N., Rosen, D. M., Wang, H., Isaacs, J. T. & Denmeade, S. R. Targeting carcinoma-associated fibroblasts within the tumor stroma with a fibroblast activation protein-activated prodrug. *J. Natl Cancer Inst.* **104**, 1320–1334 (2012).
104. Gao, W., Xiang, B., Meng, T. T., Liu, F. & Qi, X. R. Chemotherapeutic drug delivery to cancer cells using a combination of folate targeting and tumor microenvironment-sensitive polypeptides. *Biomaterials* **34**, 4137–4149 (2013).
105. Miao, L., Liu, Q., Lin, C. M., Luo, C., Wang, Y., Liu, L. et al. Targeting tumor-associated fibroblasts for therapeutic delivery in desmoplastic tumors. *Cancer Res.* **77**, 719–731 (2017).
106. Purcell, J. W., Tanlimco, S. G., Hickson, J. A., Fox, M., Sho, M., Durkin, L. et al. LRRC15 is a novel mesenchymal protein and stromal target for antibody-drug conjugates. *Cancer Res*. **78**, 4059–4072 (2018).
107. De Vlieghere, E., Gremonprez, F., Verset, L., Marien, L., Jones, C. J., De Craene, B. et al. Tumor-environment biomimetics delay peritoneal metastasis formation by deceiving and redirecting disseminated cancer cells. *Biomaterials* **54**, 148–157 (2015).
108. Finak, G., Bertos, N., Pepin, F., Sadekova, S., Souleimanova, M., Zhao, H. et al. Stromal gene expression predicts clinical outcome in breast cancer. *Nat. Med.* **14**, 518–527 (2008).
109. Navab, R., Strumpf, D., Bandarchi, B., Zhu, C., Pintilie, M., Ramnarine, V. R. et al. Prognostic gene-expression signature of carcinoma-associated fibroblasts in non-small cell lung cancer. *Proc. Natl Acad. Sci. USA* **108**, 7160–7165 (2011).
110. Zou, B., Liu, X., Gong, Y., Cai, C., Li, P., Xing, S. et al. A novel 12-marker panel of cancer-associated fibroblasts involved in progression of hepatocellular carcinoma. *Cancer Manag. Res.* **10**, 5303–5311 (2018).
111. Farmer, P., Bonnefoi, H., Anderle, P., Cameron, D., Wirapati, P., Becette, V. et al. A stroma-related gene signature predicts resistance to neoadjuvant chemotherapy in breast cancer. *Nat. Med.* **15**, 68–74 (2009).
112. Brechbuhl, H. M., Finlay-Schultz, J., Yamamoto, T. M., Gillen, A. E., Cittelly, D. M., Tan, A. C. et al. Fibroblast subtypes regulate responsiveness of luminal breast cancer to estrogen. *Clin. Cancer Res.* **23**, 1710–1721 (2017).
113. Ao, Z., Shah, S. H., Machlin, L. M., Parajuli, R., Miller, P. C., Rawal, S. et al. Identification of cancer-associated fibroblasts in circulating blood from patients with metastatic breast cancer. *Cancer Res.* **75**, 4681–4687 (2015).
114. Ohlund, D., Handly-Santana, A., Biffi, G., Elyada, E., Almeida, A. S., Ponz-Sarvise, M. et al. Distinct populations of inflammatory fibroblasts and myofibroblasts in pancreatic cancer. *J. Exp. Med.* **214**, 579–596 (2017).
115. Costa, A., Kieffer, Y., Scholer-Dahirel, A., Pelon, F., Bourachot, B., Cardon, M. et al. Fibroblast heterogeneity and immunosuppressive environment in human breast cancer. *Cancer Cell* **33**, 463–479 (2018).
116. Bartoschek, M., Oskolkov, N., Bocci, M., Lovrot, J., Larsson, C., Sommarin, M. et al. Spatially and functionally distinct subclasses of breast cancer-associated fibroblasts revealed by single cell RNA sequencing. *Nat. Commun.* **9**, https://doi.org/10.1038/s41467-018-07582-3 (2018).
117. Cremasco, V., Astarita, J. L., Grauel, A. L., Keerthivasan, S., MacIsaac, K., Woodruff, M. C. et al. FAP delineates heterogeneous and functionally divergent stromal cells in immune-excluded breast tumors. *Cancer Immunol Res.* **6**, 1472–1485 (2018).
118. Biffi, G., Oni, T. E., Spielman, B., Hao, Y., Elyada, E., Park, Y. et al. IL1-Induced JAK/STAT signaling is antagonized by TGFbeta to shape CAF heterogeneity in pancreatic ductal adenocarcinoma. *Cancer Discov.* **9**, 282–301 (2019).
119. Neuzillet, C., Tijeras-Raballand, A., Ragulan, C., Cros, J., Patil, Y., Martinet, M. et al. Inter- and intra-tumoural heterogeneity in cancer-associated fibroblasts of human pancreatic ductal adenocarcinoma. *J. Pathol.* **248**, 51–65 (2018).
120. Rai, A., Greening, D. W., Chen, M., Xu, R., Ji, H., Simpson, R. J. Exosomes derived from human primary and metastatic colorectal cancer cells contribute to functional heterogeneity of activated fibroblasts by reprogramming their proteome. *Proteomics* **19**, https://doi.org/10.1002/pmic.201800148 (2018).

Appendix 2. Direct Binding Partners of MCAM

Partner type	Partner name	MCAM$^+$ cell examined	Result of binding	Additional requirements	References
Co-receptor	VEGFR2	Endothelial cells	Migration and angiogenesis	VEGF	(77)
	PDGFRβ	Pericytes	Proliferation and migration	PDGFB	(44)
Ligand (secreted)	WNT5a	Epithelial and endothelial cells	Migration		(81)
	GAL-1	Endothelial cells	Protection from apoptosis		(103)
	GAL-3	Endothelial cells	Expression of metastasis-promoting cytokines		(102)
	NTN1	Endothelial cells	Proliferation, migration and angiogenesis		(79)
	S100A8/ A9	Cancer cells	Proliferation, EMT, invasion and metastasis		(57)
Ligand (membrane-bound)	MTP	Endothelial cells	Differentiation of neural stem cells to neurons		(82)
Ligand (present in endothelial basement membrane)	LAMA4	Th17 cells	Adhesion to endothelial basement membrane. Cells can then transmigrate into the tissue and promote inflammation		(50)
Internal complex	MSN (as part of the ERM complex)	Endothelial cells, pericytes and cancer cells	MCAM is linked to the cytoskeleton, allowing local cytoskeletal rearrangements and cell migration (60). MCAM-ERM also participates in signal transduction (77, 277)	MCAM binds phosphorylated MSN	(60, 77, 277)

GAL-1 = Galectin-1; PDGFRβ = Platelet-derived growth factor receptor beta; NTN1 = Netrin-1; S100A8/A9 = S100 calcium binding protein A8/A9; MTP = Matriptase; MSN = Moesin; ERM = Ezrin-Radixin-Moesin.

Appendix 3. Molecular Pathways Downstream of MCAM Activation

MCAM$^+$ cell examined	**MCAM inducer**	**Pathway induced**	**Result of pathway activation**	**References**
Pericytes	PDGFB + PDGRFβ + ERM complex	AKT/JNK/ERK/p38 MAPK	Proliferation and migration	(277)
Smooth muscle cells	Hypoxia + HIF-1α	NF-κB/HIF-1α	Proliferation, migration, anti-apoptosis, loss of contractile markers	(278)
Endothelial cells	VEGF + VEGFR2	AKT/p38 MAPK/NF-κB	Migration and angiogenesis	(77)
	Unknown, cancer cell-produced	AKT/p38 MAPK/NF-κB	Migration and angiogenesis	(85, 86)
	NTN1 (low concentrations)	ERK/p38 MAPK	Proliferation, migration and angiogenesis	(79)
	VEGF/Insulin/IGF1/ FGF2 + RTK	Stabilisation of RICTOR = mTORC2 activation	Proliferation and survival	(80)
	MTP	p38 MAPK/β-Catenin/IL-6	Differentiation of neural stem cells to neurons	(82)
Endothelial and cancer cells	WNT5A	DVL2/JNK = activation of non-canonical Wnt signalling	Migration	(81)
Cancer cells	WNT5A, CXCL12	Recruitment of W-RAMP structure (contains MCAM)	Migration towards CXCL12	(279)
	Unknown	NF-κB-induced expression of GSK3β = inactivation of canonical Wnt signalling	Decreased stemness	(280)
	Unknown, cancer- or tumour microenvironment-produced	Notch	Stemness	(64)

	Unknown	RHOA/SLUG	Expression of EMT genes	[66]
	Unknown, but requires ERM complex	RHOA	Migration	[60]
	S100A8/A9	ETV4/ZEB1	Expression of EMT genes, migration, invasion and metastasis	[57]
	Unknown	ATF3/ID1/MMP2	Proliferation, invasion and metastasis	[67]
	AKT + DNA damage	Activation of AKT and inhibition of BAD	Anti-apoptosis	[72]

In cancer cells, the "unknown" pathway inducer may be produced by themselves or possibly be a result of MCAM-MCAM homophilic interactions. JNK = c-Jun n-terminal kinase; ERK = Extracellular-signal-regulated kinase; HIF-1α = Hypoxia inducible factor 1 subunit alpha; IGF1 = Insulin like growth factor 1; FGF2 = Fibroblast growth factor 2; RTK = Receptor tyrosine kinase; RICTOR = Rapamycin-insensitive companion of mTOR; DVL2 = Dishevelled segment polarity protein 2; CXCL12 = C-X-C motif chemokine ligand 12; W-RAMP = WNT-mediated receptor-actin-myosin polarity; GSK3β = Glycogen synthase kinase 3 beta; RHOA = Ras homolog family member A; SLUG = Snail family transcriptional repressor 2; ETV4 = ETS variant transcription factor 4; ZEB1 = Zinc finger E-box binding homeobox 1; ATF3 = Activating transcription factor 3; ID1 = Inhibitor of DNA binding 1; MMP2 = Matrix metallopeptidase 2; BAD = BCL2 associated agonist of cell death.

Appendix 4. ‘The Origin and Contribution of the Tumor Stroma in Colorectal Carcinogenesis’

This manuscript examines the origin of CAFs in CRC and identifies MCAM as a stromal marker significantly associated with worse CRC patient prognosis. This is not the final version of the manuscript and it will be subject to further alteration prior to submission to Nature Cancer (in the first instance) to include data from the colonoscopy-guided implantation of AKP mono7 $CAS9^{-}GFP^{-}$ tumouroids into the colons of $Mcam^{+/+}$ and $Mcam^{-/-}$ mice. This additional data will provide further survival and mechanistic analyses of stromal-derived MCAM *in vivo*.

Statement of Authorship

Title of Paper	The origin and contribution of the tumor stroma in colorectal carcinogenesis
Publication Status	Unpublished and Unsubmitted work written in a manuscript style
Publication Details	Kobayashi, H., Gieniec, K. A., Lannagan, T. R. M., Wang, T., Asai, N., Mizutani, Y., Ida, T., Ando, R., Suzuki, N., Ichinose, M., Wright, J. A., Vrbanac, L., Ng, J. Q., Lawrence, M. J., Sammour, T., Hayakawa, Y., Klebe, S., Shin, A. E., Asfaha, S., Bettington, M., Arpaia, N., Danino, T., Butler, L. M., Burt, A. D., Leedham, S. J., Rustgi, A. K., Mukherjee, S., Takahashi, M., Wang, T. C., Enomoto, A., Woods, S. L., Worthley, D. L. (Unpublished). The origin and contribution of the tumor stroma in colorectal carcinogenesis.

Principal Author

Name of Principal Author	Krystyna Gieniec		
Contribution to the Paper	I discussed manuscript content, performed data interpretation and monitored animals. Experimentally, I performed histopathological analyses of ACTA2 expression in mouse and human tissues, refined the RNA-sequencing data to MCAM, and performed histopathological analyses of MCAM expression in mouse and human tissue. These experiments took approximately one year. I then spent a year and a half optimising and conducting *in vitro* assays to examine the effect of MCAM in fibroblasts; this work is not included in the current version of the manuscript but is detailed in Chapter 4 of my thesis. This current version will be amended prior to submission to Nature Cancer to include data from *Mcam*$^{-/-}$ tumour mice, of which I validated the knock-out, wrote the animal ethics and modified an existing tumouroid line such that we could implant it into immunocompetent mice (one year of work; please see Chapter 3 and 4 of my thesis). I am the primary co-author.		
Overall Percentage (%)	20%		
Certification:	This paper reports on original research I conducted during the period of my Higher Degree by Research candidature and is not subject to any obligations or contractual agreements with a third party that would constrain its inclusion in this thesis. I am the primary co-author of this paper.		
Signature		Date	*30/10/20*

Co-author contributions

By signing the Statement of Authorship, each author certifies that:

i. the candidate's stated contribution to the publication is accurate (as detailed above);
ii. permission is granted for the candidate to include the publication in the thesis; and
iii. the sum of all the co-author contributions is equal to 100% less the candidate's stated contribution.

Name of co-author	Hiroki Kobayashi		
Contribution to the paper	Discussed manuscript content, interpreted data, analysed colorectal cancer tissue microarray, performed histopathological analyses, performed statistical analyses, wrote manuscript. Primary co-author.		
Signature		Date	*6/11/20*

Name of co-author	Tamsin Lannagan		
Contribution to the paper	Discussed manuscript content, helped in data interpretation, extracted samples for RNA-sequencing, developed the AOM/DSS colorectal cancer mouse model in the laboratory, performed animal experiments using *Lepr*-Cre, *Grem1*-CreERT2 and Acta2-RFP (bone marrow transplant) mice, performed histopathological analyses. Primary co-author.		
Signature		Date	*17/11/20*

Name of co-author	Tongtong Wang		
Contribution to the paper	Discussed manuscript content, helped in data interpretation, extracted samples for RNA-sequencing, analysed RNA-sequencing and microarray datasets, performed statistical analyses, assisted in animal monitoring.		
Signature		Date	*6/11/20*

Name of co-author	Naoya Asai		
Contribution to the paper	Supervised development of work, performed animal experiments using *Islr*-CreERT2 mice, helped in data interpretation.		
Signature		Date	*9/11/20*

Name of co-author	Yasuyuki Mizutani		
Contribution to the paper	Performed smFISH, helped in data interpretation.		
Signature		Date	*17/11/20*

Name of co-author	Tadashi Ida		
Contribution to the paper	Performed smFISH, helped in data interpretation.		
Signature		Date	*18/11/20*

Name of co-author	Ryota Ando		
Contribution to the paper	Performed smFISH, helped in data interpretation.		
Signature		Date	*17/11/20*

Name of co-author	Nobumi Suzuki		
Contribution to the paper	Discussed manuscript content, helped in data interpretation.		
Signature		Date	*9/11/20*

Name of co-author	Mari Ichinose		
Contribution to the paper	Discussed manuscript content, helped in data interpretation.		
Signature		Date	*9/11/20*

Name of co-author	Josephine Wright		
Contribution to the paper	Discussed manuscript content, helped in data interpretation.		
Signature		Date	*6/11/20*

Name of co-author	Laura Vrbanac		
Contribution to the paper	Discussed manuscript content, helped in data interpretation.		
Signature		Date	*6/11/20*

Name of co-author	Jia Ng		
Contribution to the paper	Discussed manuscript content, helped in data interpretation.		
Signature		Date	*6/11/20*

Name of co-author	Matthew Lawrence		
Contribution to the paper	Discussed manuscript content, helped in data interpretation.		
Signature		Date	*9/11/20*

Name of co-author	Tarik Sammour		
Contribution to the paper	Discussed manuscript content, helped in data interpretation.		
Signature		Date	*10/11/20*

Name of co-author	Yoku Hayakawa		
Contribution to the paper	Discussed manuscript content, helped in data interpretation.		
Signature		Date	11/18/2020

Name of co-author	Sonja Klebe		
Contribution to the paper	Discussed manuscript content, helped in data interpretation, collected and provided human colorectal cancer clinical data and samples for the MCAM tissue microarray.		
Signature		Date	*9/11/20*

Name of co-author	Alice Eunjung Shin		
Contribution to the paper	Performed animal experiments using *Krt19*-Cre mice, helped in data interpretation.		
Signature		Date	*9/11/20*

Name of co-author	Samuel Asfaha		
Contribution to the paper	Supervised development of work, discussed manuscript content.		
Signature		Date	*9/11/20*

Name of co-author	Mark Bettington		
Contribution to the paper	Discussed manuscript content, helped in data interpretation, collected and provided human colorectal cancer samples of different grades.		
Signature		Date	18.11.2020

Name of co-author	Nicholas Arpaia		
Contribution to the paper	Discussed manuscript content, helped in data interpretation.		
Signature		Date	*1/12/20*

Name of co-author	Tal Danino		
Contribution to the paper	Discussed manuscript content, helped in data interpretation.		
Signature		Date	*17/11/20*

Name of co-author	Lisa Butler		
Contribution to the paper	Supervised development of work, discussed manuscript content.		
Signature		Date	*6/11/20*

Name of co-author	Alastair Burt		
Contribution to the paper	Supervised development of work, discussed manuscript content.		
Signature		Date	*9/11/20*

Name of co-author	Simon Leedham		
Contribution to the paper	Discussed manuscript content, helped in data interpretation, provided *Apc*$^{Min/+}$ samples.		
Signature		Date	*9/11/20*

Name of co-author	Anil Rustgi		
Contribution to the paper	Discussed manuscript content, helped in data interpretation.		
Signature		Date	*1/12/20*

Name of co-author	Siddhartha Mukherjee		
Contribution to the paper	Discussed manuscript content, helped in data interpretation.		
Signature		Date	*9/11/20*

Name of co-author	Masahide Takahashi		
Contribution to the paper	Supervised development of work, discussed manuscript content, helped in data interpretation.		
Signature		Date	*9/11/20*

Name of co-author	Timothy Wang		
Contribution to the paper	Discussed manuscript content, helped in data interpretation.		
Signature		Date	*9/11/20*

Name of co-author	Atsushi Enomoto		
Contribution to the paper	Supervised development of work, discussed manuscript content, helped in data interpretation and manuscript evaluation, wrote the manuscript. Will act as corresponding author.		
Signature		Date	*9/11/20*

Name of co-author	Susan Woods		
Contribution to the paper	Supervised development of work, discussed manuscript content, helped in data interpretation and manuscript evaluation, wrote the manuscript. Will act as corresponding author.		
Signature		Date	*6/11/20*

Name of co-author	Daniel Worthley		
Contribution to the paper	Supervised development of work, discussed manuscript content, helped in data interpretation and manuscript evaluation, wrote the manuscript. Will act as corresponding author.		
Signature		Date	*6/11/20*

The origin and contribution of the tumor stroma in colorectal carcinogenesis

Short title: The origin of the CRC mesenchyme

(32/45 characters with spaces)

Hiroki Kobayashi[1,2,3,4]*, Krystyna A. Gieniec[1,2]*, Tamsin RM. Lannagan[1,2]*, Tongtong Wang[1,2], Naoya Asai[5], Yasuyuki Mizutani[3,6], Tadashi Iida[3,6], Ryota Ando[3], Nobumi Suzuki[1,2,7], Mari Ichinose[1,2], Josephine A Wright[2], Laura Vrbanac[1,2], Jia Q Ng[1,2], Matthew J. Lawrence[8], Tarik Sammour[1,2,8], Yoku Hayakawa[7], Sonja Klebe[9], Alice Eunjung Shin[10], Samuel Asfaha[10], Mark L. Bettington[11,12,13], Nicholas Arpaia[14,15], Tal Danino[15], Lisa M. Butler[1,2], Alastair D. Burt[1,16], Simon J. Leedham[17], Anil K. Rustgi[18], Siddhartha Mukherjee[19], Masahide Takahashi[3,4,20], Timothy C. Wang[19], Atsushi Enomoto[3, 21], Susan L. Woods[1,2,21], and Daniel L. Worthley[2,21]

[1] Adelaide Medical School, University of Adelaide, Adelaide, SA, 5000, Australia

[2]South Australian Health and Medical Research Institute, Adelaide, SA, 5000, Australia

[3]Department of Pathology, [4]Division of Molecular Pathology, Center for Neurological Disease and Cancer, Nagoya University Graduate School of Medicine, Nagoya, Aichi, 466-8550, Japan

[5]Department of Molecular Pathology, Graduate School of Medicine, Fujita Health University, Toyoake, Aichi, 470-1192, Japan

[6]Department of Gastroenterology and Hepatology, Nagoya University Graduate School of Medicine, Nagoya, Aichi, 466-8550, Japan

[7]Department of Gastroenterology, Graduate School of Medicine, The University of Tokyo, Tokyo, 113-0033, Japan

[8]Colorectal Unit, Department of Surgery, Royal Adelaide Hospital, Adelaide, SA, 5000, Australia.

[9]Department of Anatomical Pathology, Flinders Medical Centre, Bedford Park, Adelaide, SA, 5001, Australia

[10]Department of Medicine, University of Western Ontario, London, ON, Canada

[11]Envoi Specialist Pathologists, Kelvin Grove 4059, Queensland, Australia

[12]Faculty of Medicine, University of Queensland, Herston 4006, Queensland, Australia

[13]QIMR Berghofer Medical Research Institute, Herston 4006, Queensland, Australia

[14]Department of Microbiology and Immunology, Vagelos College of Physicians and Surgeons, Columbia University, New York, NY, USA.

[15]Herbert Irving Comprehensive Cancer Center, Columbia University, New York, NY, USA.

[16]Precision and Molecular Pathology, Newcastle University, Newcastle upon Tyne NE2 4HH, UK

[17]Intestinal Stem Cell Biology Lab, Wellcome Trust Centre Human Genetics, University of Oxford, Oxford, UK

[18]Herbert Irving Comprehensive Cancer Center, Division of Digestive and Liver Diseases, Department of Medicine, Columbia University, New York, NY, USA

[19]Department of Medicine and Irving Cancer Research Center, Columbia University, New York, NY, USA

[20]International Center for Cell and Gene Therapy, Fujita Health University, Toyoake, Aichi, 470-1192, Japan

[21]Co-corresponding authors

*These authors contributed equally.

Abbreviations

ANOVA, analysis of variance; AOM, azoxymethane; CAFs, cancer-associated fibroblasts; CMS, consensus molecular subtype; CRC, colorectal cancer; DSS, dextran sodium sulfate; FACS, fluorescence-activated cell sorting; IF, immunofluorescence; IHC, immunohistochemistry; ISH, *in situ* hybridization; PC, principal component; MSCs, mesenchymal stem/stromal cells; qRT-PCR, quantitative reverse-transcription polymerase chain reaction; scRNA-seq, single-cell RNA-sequencing; smFISH, single-molecule fluorescent *in situ* hybridization; TGFβ, transforming growth factor β

Correspondence

D.L.W.; Dan.Worthley@sahmri.com, Group Leader, Gut Health, SAHMRI

Address: SAHMRI (5 South), North Terrace, Adelaide SA 5000, AUSTRALIA, 08-8128-4386

S.L.W.; susan.woods@adelaide.edu.au, Group Leader, Gut Cancer, the University of Adelaide,

Address: SAHMRI (5 South), North Terrace, Adelaide SA 5000, AUSTRALIA, 08-8128-4386

A.E.; enomoto@iar.nagoya-u.ac.jp, Professor, Department of Pathology, Nagoya University School of Medicine

Address: 65 Tsurumai-Cho, Showa-Ku, Nagoya, 466-8550, JAPAN, 05-2744-2093

Conflict of interest statement

All authors declare no conflicts of interest related to the work.

Transcript Profiling: GSE162508

Writing Assistance: N/A

Author Contributions

H.K., K.A.G., T.R.L., S.A., A.E., M.T., T.C.W., S.L.W., and D.L.W. conceived and designed the study. H.K., K.A.G., and T.R.L. performed most of the experiments. H.K. and T.W. (Tongtong Wang) performed statistical analyses. T.W. and H.K. analyzed RNA-seq and microarray datasets. Y.M., T.I, and R.A. performed smFISH. N.A. and A.E.S. performed animal experiments using *Islr*-CreERT2 and *Krt19*-Cre mice, respectively. S.K. and M.L.B. collected and provided human CRC clinical data and the samples. S.J.L. provided *Apc*$^{Min/+}$ mouse samples. H.K., K.G.W., and T.R.L. performed histopathological analyses. N.A., S.A., A.D.B., M.T., A.E., S.L.W., and D.L.W. supervised the project. H.K., A.E., S.L.W., and D.L.W. wrote the manuscript. All authors contributed substantially to the discussion of content for the article, reviewed and/or edited the manuscript before submission.

Word count:

Abstract; 256 words/260 words

The main manuscript including abstract, methods, figure legends and references; 7400/7000 words

Total number of figures and tables: 5 figures

Abstract

Background and aims

Cancer-associated fibroblasts (CAFs) play a critical role in colorectal cancer (CRC) progression. However, the precise cellular origins of the tumor stroma remain unknown, making it challenging to therapeutically target the tumor mesenchyme. Here, we aimed to identify key cellular contributors to and components of the CRC mesenchyme associated with poor prognosis.

Methods

We used a mouse model of inflammation-associated CRC in 5 different genetic fate-mapping transgenic mouse lines to characterize the origins of the CRC stroma. To identify a potential therapeutic target expressed by the CRC stroma, RNA-sequencing of fluorescence-activated cell sorting (FACS)-purified CRC stromal cells was performed. CRC patient RNA-sequencing data (n=621) and tissue microarray (n=101) were used to examine the prognostic significance of marker expression.

Results

We found that approximately half of the CRC CAFs marked by α-smooth muscle actin (αSMA) in a mouse model of CRC emerge through proliferation. Lineage tracing experiments revealed that intestinal leptin receptor (*Lepr*)-lineage stromal cells expanded and contributed to 75% of the αSMA^+ proliferating CAFs. Notably, no αSMA^+ CAFs arose from *Krt19*-lineage epithelial cells or bone marrow-derived cells. Moreover, RNA-sequencing of FACS-purified CRC mesenchymal cells identified MCAM as a CRC stroma-specific marker, which is expressed by *Lepr*-lineage cells. Analysis of human CRC samples showed that high MCAM expression driven, in part, by TGF-β was independently prognostic of poor overall survival.

Conclusion

Our data identify intestinal *Lepr*-lineage cells as a major source of the tumor stroma in CRC and suggest that targeting $MCAM^+$ cells may serve as an attractive therapeutic approach to restrain CRC progression.

(255/260 words)

4-5 Keywords: colorectal cancer, tumor microenvironment, cancer-associated fibroblasts, Acta2

Introduction

Colorectal cancer (CRC) is one of the leading causes of cancer-related deaths worldwide. One hallmark of CRC is a prominent fibrotic stroma (also termed desmoplasia), composed of cancer-associated fibroblasts (CAFs), extracellular matrix (ECM), endothelial cells and immune cells, which can account for up to 90% of the tumor[1].

Previous studies have demonstrated that CAFs play a critical role in cancer progression via secretion of growth factors, cytokines, pro-angiogenic factors, and ECM[2-4]. Remarkably, recent studies using immunophenotyping and transcriptome analyses such as single-cell RNA-sequencing (scRNA-seq), have revealed that CAFs are comprised of heterogeneous subpopulations on the basis of both functions and markers[5, 6]. Notwithstanding our emerging understanding of the heterogeneous CAFs acting on either promotion or restraint of cancer progression through their interaction with other components of the tumor microenvironment, the cellular origins of CAFs remain elusive. Consequently, our limited understanding of the origins of the tumor stroma has hampered the development of efficacious therapeutics that selectively target stromal cell lineages that drive cancer progression[2].

It has been postulated that CAFs could arise through at least four non-mutually exclusive mechanisms: ***proliferation (A)***, ***activation (B)***, ***transdifferentiation (C),*** and ***recruitment (D)***[2, 7]. Although studies using autochthonous mouse models of cancers have indicated that some CAFs undergo proliferation ***(A; Proliferation)***[8-10], the relative contribution of proliferating and non-proliferating CAFs to the entire pool remains to be fully elucidated in CRC. In addition, quiescent fibroblasts undergo phenotypic conversion into activated myofibroblasts via stimuli from the TME, such as transforming growth factor β (TGF-β) ***(B; Activation)***[2, 11]. Interestingly, several fate-mapping studies have indicated that non-fibroblast lineage cells such as epithelial cells, can transdifferentiate into CAFs through epithelial-to-mesenchymal transition (EMT) ***(C; Transdifferentiation)***[12, 13]. Moreover, bone marrow transplantation experiments have revealed that more than 20% of ACTA2 (Protein name, alpha-smooth muscle actin; αSMA)$^{+}$ CAFs were recruited

from the bone marrow-derived mesenchymal stem/stromal cells (MSCs) in a mouse model of gastric cancer ***(D; Recruitment)***[14]. A more recent paper, however, has suggested that local precursors were a predominant contributor to ACTA2^{+} CAFs[15]. Thus far, the cellular sources of CAFs remain highly controversial. In striking contrast to organ fibrosis such as liver, kidney, and skin fibrosis in which the origins of myofibroblasts have been extensively investigated[16-22], to our knowledge, no previous CAF studies have comprehensively performed lineage-tracing experiments to track the aforementioned four possible CAF sources. This has resulted in our incomplete understanding of cancer stromagenesis and contribution of cellular lineages with fibrogenic potential.

Here, to unequivocally determine the cellular origins and contribution of CAFs in CRC, we conducted fate-mapping studies using 5 genetically engineered mouse strains. We identified intestinal *Lepr* (Leptin receptor)-lineage cells as a major contributor to the CRC mesenchyme. Furthermore, RNA-sequencing of the CRC tumor stroma revealed that *Mcam* (melanoma cell adhesion molecule; also known as CD146 or MUC18) could be a potential therapeutic target expressed by the CRC stroma, which is derived from *Lepr*-lineage cells.

Lepr is a well-established marker for perivascular mesenchymal cells, which play a crucial role in bone marrow hematopoietic stem cell maintenance[23, 24]. Previous fate-mapping studies have demonstrated that *Lepr*-expressing cells give rise to most bone and adipocytes formed in the adult normal bone marrow[25] as well as myofibroblasts in primary myelofibrosis, a disease characterized by bone marrow fibrosis[18]. However, the significance of *Lepr*-lineage cells in the development of cancer mesenchyme remains largely unexplored.

Similarly to *Lepr*, MCAM is highly expressed by perivascular stromal cells in the bone marrow[26-28], but also by endothelial cells, pericytes, and CAFs[29, 30]. Numerous publications have illustrated that MCAM contributes to cancer progression by promoting cancer cell growth, angiogenesis, and metastasis[29-35]. Interestingly, multiple independent scRNA-seq datasets have recently provided consistent evidence that high *MCAM/Mcam* expression was detected in a specific subset of CAFs with a pericyte-like or microvascular gene signature[9, 34, 36, 37]. Nevertheless, the progenitors of

MCAM$^+$ cells in the cancer stroma have been poorly defined to date.

In this study, using human CRC samples and a mouse model of CRC, we first investigated the relative contribution of proliferating and non-proliferating ACTA2$^+$ CAFs to the CRC stroma. Then, we examined the cellular sources of proliferating CAFs by employing 5 different genetic fate-mapping mouse models, and found that *Lepr*-lineage cells are a major cellular source of the CRC mesenchyme. Next, by combining fluorescence-activated cell sorting (FACS), RNA-sequencing, and immunohistochemistry, we identified MCAM as a potential therapeutic target derived from *Lepr*-lineage cells. Finally, we investigated the clinical significance of MCAM expression using human CRC RNA-sequencing data and tissue microarray samples.

Materials and Methods

Human and animal Ethics

Human CRC samples were obtained at the time of surgery for routine pathological analysis. A waiver of consent was granted in line with the Australian National Statement on Ethical Conduct in Human Research section 2.3, to generate a tissue microarray from stored, de-identified FFPE CRC samples and associated clinical data. This study was approved by the Southern Adelaide Clinical Human Research Ethics Committee (HREC/19/SAC/70, OFR62.19). All animal protocols were approved by the Animal Ethics committees of SAHMRI and Nagoya University Graduate School of Medicine (SAM205, SAM236, SAM303, SAM387.19 and 31434).

Detailed methodological information is described in **Supplementary Methods**.

Results

Desmoplasia is increased during CRC carcinogenesis in human and mice.

Initially, to explore whether desmoplasia is increased during CRC carcinogenesis, we performed immunohistochemistry (IHC) for ACTA2, a well-established marker for myofibroblasts and CAFs[2], using human normal colorectal mucosa, adenoma, and adenocarcinoma samples. The ratio of $ACTA2^+$ myofibroblastic CAFs in the total stromal cell population was increased stepwise from normal mucosa to adenocarcinoma, suggesting that the desmoplastic reaction is promoted throughout multistage colorectal carcinogenesis[38] **(Figure 1A and B)**. The elevated ACTA2 expression level during colorectal carcinogenesis was corroborated by analysis of transcript expression microarray data from human normal colon and colon cancer specimens[39] **(Figure 1C)**.

Next, with the aim of investigating the prognostic significance of increased *ACTA2* expression in CRC, we analyzed *ACTA2* transcript levels in The Cancer Genome Atlas (TCGA) data. Consistent with prior reports showing that stromal gene expression predicts dismal prognosis in CRC[40, 41], high *ACTA2* transcript levels were inversely associated with overall survival in patients with CRC **(Figure**

1D). Moreover, high *ACTA2* expression, as well as high expression of *FAP*, an activated fibroblast marker[2], was consistently associated with poor overall survival across multiple expression datasets from CRC patients **(Supplementary Figure 1)**. Notably, the highest expression of *ACTA2* was observed in the poor-prognosis stroma-rich molecular subtype of CRC (Consensus Molecular Subtype 4; CMS4)[42] **(Figure 1E)**.

We then sought to examine whether a similar desmoplastic tumor stroma could be developed in mouse models of CRC. To this end, we studied the commonly used azoxymethane (AOM)/ dextran sulfate sodium (DSS) mouse model of inflammation-associated CRC **(Figure 1F and G)** and performed ACTA2 immunostaining. In line with a previous study[43], ACTA2 expression was significantly elevated in the stroma of AOM/DSS tumors compared with the adjacent normal mucosa **(Figure 1H and I)**. Similarly, small intestinal tumors that form in *Apc*$^{Min/+}$ mice showed an increase in stromal ACTA2 expression in comparison with the adjacent normal tissue, but to a lesser extent than the AOM/DSS mouse model (**Supplementary Figure 2A and 2B**). Taken together, these data suggest that a myofibroblastic stromal reaction intensifies through CRC carcinogenesis in humans and that this feature of stromal activation of the human disease is faithfully recapitulated in the AOM/DSS mouse model of CRC.

A subpopulation of CRC CAFs arises through proliferation in human and mice.

Proliferating *Acta2*$^{+}$ CAFs are known to influence cancer progression and are key drivers of stromagenesis[3, 7, 8]. As such, we evaluated the proliferation status of myofibroblasts in human and mouse CRC. Co-staining of ACTA2 and Ki67 using human colorectal samples revealed that the ratio of proliferating myofibroblasts was increased in high-grade adenoma and adenocarcinoma compared with the normal mucosa, suggesting that myofibroblasts acquire proliferative capabilities during malignant progression **(Figure 2A and B)**. Notably, on average, 10% of ACTA2^{+} CAFs were positive for Ki67 in human CRC adenocarcinoma tissues **(Figure 2B)**. In keeping with this, analysis of scRNA-seq data from human CRC and normal mucosa[44] revealed that a minor subcluster of

ACTA2^{+} CAFs highly expressed *MKI67*, when compared to fibroblasts in the normal mucosa **(Supplementary Figure 3A-C).**

We then investigated whether a similar CAF proliferation could be observed in the AOM/DSS mouse model of CRC. To this end, we analyzed the proportion of fibroblasts that underwent proliferation during carcinogenesis by taking advantage of continuous 5-bromodeoxyuridine (BrdU) labeling **(Figure 2C)**. The ratio of ACTA2^{+} fibroblasts that incorporated BrdU was significantly elevated in AOM/DSS CRC, compared to the adjacent non-neoplastic colon, with approximately 45% of ACTA2^{+} CAFs marked by BrdU **(Figure 2D and E)**. In addition to BrdU, we performed immunofluorescence for Ki67 to evaluate the ratio of CAFs, which were in the active phases of the cell cycle at the time of humane endpoint. Contrasting with the BrdU incorporation ratio, the ratio of actively proliferating CAFs (Ki67^{+}ACTA2^{+} CAFs) in a total pool of ACTA2^{+} CAFs was only 2.88 ± 1.27% (Mean ± s.e.m.) and was not significantly different from the ratio of proliferating fibroblasts in the normal mucosa (1.80 ± 0.93%; **Figure 2D and E**). These data indicate that, in AOM/DSS tumors, the majority of ACTA2^{+} CAFs at humane endpoint were in quiescent G0 phase as evaluated by Ki67 negativity, but had undergone cell division and incorporated BrdU at an earlier stage of cancer development. Overall, our analyses of human and mouse CRC suggest that a subset of ACTA2^{+} CAFs emerge through proliferation, providing a potential mechanism for generating CRC CAFs.

Lepr-lineage stromal cells are a major contributor to the proliferating CAF population in AOM/DSS CRC.

Having observed that CAFs undergo proliferation in the CRC mesenchyme, we then examined the cellular sources of the proliferating ACTA2^{+} CAFs in AOM/DSS tumors by genetic fate-mapping. To this end, we took advantage of three mesenchymal cell-specific lineage-tracing mouse lines (*Lepr*-Cre; Rosa26-LSL-tdtomato[23-25], *Grem1*-CreERT2; Rosa26-LSL-ZsGreen[45] and *Islr*-CreERT2; Rosa26-LSL-tdtomato[46, 47]) and an epithelial lineage-specific mouse line (*Krt19*-Cre; Rosa26-

mt/mG[48]) as well as a bone-marrow transplantation model, coupled with BrdU labelling (**Figure 2C and 3A-E**). Given that adult tamoxifen induction before AOM/DSS administration yielded low tracing efficiency in AOM/DSS CRC mesenchyme in *Grem1*-CreERT2 mice (data not shown), we administered tamoxifen to *Grem1*-CreERT2, as well as *Islr*-CreERT2 mice, at postnatal day 6.

Immunofluorescence for EPCAM, a pan-epithelial cell marker, showed that all *Lepr*-, *Grem1*-, and *Islr*-lineage cells were observed only within the $EPCAM^-$ stroma, confirming their mesenchymal identity **(Figure 3A)**. Remarkably, approximately half of $ACTA2^+$ CAFs and 80% of proliferating $BrdU^+ACTA2^+$ CAFs were *Lepr*-lineage-positive in AOM/DSS tumors**,** with a minor fraction of $ACTA2^+$ CAFs derived from the *Grem1*-lineage (12.48 ± 1.09% of $ACTA2^+$ CAFs; Mean ± s.e.m.) and *Islr*-lineage (4.85 ± 3.42%; **Figure 3A and C-E)**. Similarly, immunofluorescence for another CAF marker, PDGFRA, demonstrated that *Lepr*-lineage cells represented a predominant contributor to $PDGFRA^+$ CAFs in the AOM/DSS model **(Supplementary Figure 4A and B)**. Together, these results suggest that *Lepr*-lineage stromal cells are a major, if not exclusive, source of proliferating $ACTA2^+$ CAFs in the AOM/DSS tumor.

EMT or recruitment from the bone marrow did not contribute to $ACTA2^+$ CAFs in the AOM/DSS mouse model of CRC.

EMT has been shown to be a potential mechanism to generate CAFs in mouse models of pancreatic and breast cancers[2, 12, 13]. Therefore, we explored whether colonic epithelial cells could undergo transdifferentiation into CRC CAFs. For this purpose, we utilized constitutive *Krt19*-Cre; Rosa26-mt/mG mice to track the fate of *Krt19*-lineage colonic epithelial cells[48]. Although the majority of colonic cells with epithelial morphology were marked following reporter recombination by Cre recombinase driven by the *Krt19* promoter, no *Krt19*-lineage cells were positive for ACTA2 in either normal colon or AOM/DSS tumors. This suggests that, at least in this mouse model of CRC, EMT of epithelial cells to $ACTA2^+$ fibroblasts does not occur **(Figure 3B and D)**.

Recruitment of cells from the bone marrow has also been proposed to be a potential source of CAFs[14, 49, 50]. To assess the relative contribution of bone marrow-derived cells and tissue-resident cells to the AOM/DSS CRC stroma, we performed a bone marrow transplantation experiment using an *Acta2*-RFP (red fluorescent protein) reporter mouse[51]. Initially, we validated that, in mice that did not undergo bone marrow transplantation, RFP was expressed by fibroblastic cells in AOM/DSS tumors in *Acta2*-RFP mice, confirming that the *Acta2* promoter is active in this CRC mouse model **(Supplementary Figure 5A and B)**. To perform bone marrow transplantation from *Acta2*-RFP mice, following total body irradiation, wild-type recipient mice were transplanted with bone marrow cells from *Acta2*-RFP donor mice and then treated with AOM/DSS to induce CRC **(Supplementary Figure 6A)**. Quantitative polymerase chain reaction (qPCR) for RFP using genomic DNA isolated from the bone marrow of the recipient mice confirmed engraftment of RFP^+ cells in the recipient bone marrow **(Supplementary Figure 6B)**. However, no bone marrow-transplanted RFP^+ cells were observed in AOM/DSS tumors in wild-type recipient mice **(Figure 3B and D).** This indicates that, at least in this experimental CRC model, CAFs did not arise via recruitment from the bone marrow, but only from local precursors.

Collectively, our data with 5 distinct genetically engineered mouse models **(Figure 3A)** pointed to tissue-resident *Lepr*-lineage stromal cells being a key contributor to the $ACTA2^+$ CAFs in the AOM/DSS mouse model of CRC.

Lepr-lineage intestinal stromal cells undergo proliferation and myofibroblastic differentiation during AOM/DSS CRC carcinogenesis.

Having identified intestinal *Lepr*-lineage stromal cells as a predominant contributor to the CRC mesenchyme, we next sought to characterize *Lepr*-lineage cells in the normal colon and AOM/DSS tumors. In the normal colon mucosa, pericryptal *Lepr*-lineage cells were preferentially located near the base of the crypts **(Figure 3F and G)**. *Lepr*-lineage cancer-associated stromal cells in AOM/DSS tumors exhibited higher ACTA2 positivity than *Lepr*-lineage stromal cells in the normal

mucosa, indicating that *Lepr*-lineage cells could undergo phenotypic conversion into myofibroblasts during cancer progression **(Supplementary Figure 7A and B)**. BrdU labeling in AOM/DSS-treated mice revealed that *Lepr*-lineage cells showed a higher proliferation capability in AOM/DSS tumors, in comparison with the adjacent normal mucosa **(Supplementary Figure 7C and D)**. Consistent with a previous report demonstrating that *Lepr* transcript levels were downregulated during bone marrow fibrosis[18], single-molecule fluorescent RNA *in situ* hybridization (smFISH) for *Lepr* revealed that active expression of *Lepr* in *Lepr*-lineage cells was significantly reduced in the AOM/DSS tumor compared with the normal colon **(Supplementary Figure 7E and F)**. Together, these findings indicate that intestinal *Lepr*-lineage stromal cells undergo expansion and myofibroblastic differentiation at the expense of *Lepr* expression during AOM/DSS colorectal carcinogenesis.

Identification of MCAM as a CRC stroma-specific marker that defines a subset of Lepr-lineage cells.

Lower *Lepr* expression in the CRC mesenchyme could potentially make it challenging to therapeutically target *Lepr*-lineage CAFs based on active *Lepr* expression. Therefore, we next aimed to identify a stromal factor that is actively expressed in the CRC mesenchyme as a potential therapeutic target to restrain CRC progression.

Interestingly, cancer biology and developmental biology share substantial similarities in many molecular processes and as such display related gene expression profiles and regulation of signaling pathways[52, 53]. For example, factors involved in CAF activation, such as TGF-β and bone morphogenetic proteins (BMPs), also play a crucial role in the early development of gastrointestinal organs[2, 54]. Therefore, to explore whether these shared mechanisms could be harnessed to develop a therapeutic approach targeting CRC stroma, we undertook a systematic approach to identify novel colonic stromal factors involved in both tumorigenesis and development.

To this end, we first flow-sorted fibroblasts using a negative selection strategy. Fibroblasts were selected based on their lack of expression of blood cell markers (CD45 and Ter119), an endothelial

marker (CD31) and an epithelial marker (EPCAM), from AOM/DSS tumors and developmental colon at postnatal day 14, as well as the normal adult colon **(Figure 4A)**. Fibroblast markers such as *Grem1*, *Acta2*, and *Fap* were highly expressed in the FACS-sorted mesenchymal cells ($CD45^-$, $Ter119^-$, $CD31^-$ and $EPCAM^-$), validating their enrichment for fibroblasts **(Supplementary Figure 8)**. Bulk RNA-sequencing from the FACS-purified fibroblasts revealed that 342 genes were differentially upregulated in both the AOM/DSS tumors and the developmental colon, compared with the normal adult colon **(Figure 4B; Step 1)**. We then analyzed the prognostic significance of the 342 genes by bioinformatically performing survival analysis using the TCGA data, resulting in the selection of 46 genes that were significantly associated with human CRC survival **(Figure 4B; Step 2, Supplementary Table 1)**. Furthermore, analysis of our RNA-seq data from normal adult colon and AOM/DSS tumors enabled the selection of 18 stroma-specific genes that were upregulated in fibroblasts compared to epithelial cells **(Figure 4B; Step 3, Supplementary Table 1)**. Then, to examine for genes that are expressed at the protein level in human CRC stroma, we interrogated human CRC immunohistochemistry data in the Human Protein Atlas database[55] and selected 6 proteins that are highly expressed in the CRC stroma **(Figure 4B; Step 4, and Supplementary Figure 9)**. Finally, our immunohistochemistry data for candidate genes showed that MCAM was consistently upregulated in the stroma of AOM/DSS tumors and the developmental colon, compared to the normal adult colon **(Figure 4C and D; Supplementary Figure 10)**. This systematic approach allowed us to identify MCAM as a colonic mesenchyme-specific gene, which is upregulated in both tumorigenesis and development and is associated with human CRC survival.

Next, we further validated the stromal specific expression pattern of MCAM by performing co-immunofluorescence for CD31, ACTA2, CD45, and EPCAM in AOM/DSS CRCs **(Supplementary Figure 11A and B)**. This immunostaining data revealed that MCAM was expressed by $CD31^+$ endothelial cells and $ACTA2^+$ CAFs, but not $CD45^+$ immune cells or $EPCAM^+$ epithelial cells, confirming that MCAM expression was restricted to the stroma. Consistent with this mouse data, expression microarray data from FACS-purified cells from human primary CRC tissues[56], as well as

scRNA-seq data from human primary CRC tissues[5], demonstrated that high *MCAM* transcripts were detected in endothelial cells and CAFs in human CRC **(Supplementary Figure 11C and D)**. In line with this, analysis of scRNA-seq data from colonic stromal cells from healthy individuals and ulcerative colitis patients[57] revealed that *MCAM* was highly expressed by myofibroblasts and endothelial cells as well as pericytes **(Supplementary Figure 12)**.

To characterize the cellular sources of MCAM$^+$ cancer-associated stromal cells in CRC, we first co-stained for MCAM and BrdU in AOM/DSS-treated mice that were administered BrdU during carcinogenesis. In keeping with previous scRNA-seq data showing that *Mcam* was highly expressed by a proliferative subpopulation of CAFs[9], more than half of the MCAM$^+$ stromal cells were positive for BrdU, indicating that the majority of MCAM$^+$ cancer-associated stromal cells arise through proliferation **(Figure 4E and F)**. Remarkably, immunofluorescence for MCAM in three genetic fate-mapping mouse models (*Lepr*-Cre, *Grem1*-CreERT2, and *Islr*-CreERT2 mice) revealed that about 75% of MCAM$^+$ cancer-associated stromal cells were derived from the *Lepr*-lineage in AOM/DSS tumors **(Figure 4G; Supplementary Figure 13A and B)**. Together, these data indicate that MCAM is a CRC-stroma specific marker that identifies a subset of proliferating *Lepr*-lineage stromal cells in mice.

Increased MCAM expression is associated with Consensus Molecular Subtype (CMS) 4 and predicts poor survival in patients with CRC.

Finally, we investigated the clinical significance of MCAM expression in CRC patients. Consistent with the observed upregulation of MCAM during mouse colorectal tumorigenesis, MCAM expression was increased in human colorectal adenocarcinoma and adenoma, compared with the normal mucosa **(Figure 5A and B).** In agreement with this, analysis of publicly available expression microarray data from human colorectal tissues showed that *MCAM* transcript levels were elevated during colorectal carcinogenesis **(Supplementary Figure 14A and B)**.

Furthermore, analyses of the TCGA dataset showed that the highest expression of *MCAM* was observed in a poor-prognosis stroma-rich molecular subtype of CRC (Consensus Molecular Subtype 4; CMS4)[42] **(Figure 5C)**. Given that TGF-β signaling activation is a defining characteristic of CMS4 CRC[42], we reasoned that TGF-β might be involved in the upregulation of *MCAM*. In keeping with our hypothesis, stimulation of a mouse colonic fibroblast cell line, YH2 cells[58], with recombinant TGF-β1 enhanced *Mcam* transcript levels as well as a TGF-β target gene, *Acta2*. This was rescued by co-treatment with Galunisertib, a specific inhibitor for TGF-β receptor 1 **(Figure 5D)** In support of this, analysis of the TCGA data showed that transcript levels of *MCAM* were positively correlated with expression levels of TGF-β target genes such as *ACTA2, SERPINE1*, and *CTGF*[11] in human CRC **(Figure 5E and Supplementary Figure 15)**.

Next, we investigated the clinical association between MCAM expression and survival by performing MCAM immunohistochemistry, using tissue microarrays from 101 CRC patients. Consistent with previous papers[59, 60], high MCAM expression was an independent prognostic factor for poor overall survival in CRC patients **(Figure 5F and G; Supplementary Table 2 and 3)**. Moreover, analyses of three independent CRC datasets[39, 61, 62] confirmed that high *MCAM* expression was inversely associated with survival **(Supplementary Figure 16)**. Taken together, these data indicate that high MCAM expression driven, at least in part, by TGF-β could be a biomarker to predict poor prognosis in human CRC and that MCAM is an attractive therapeutic target to restrain CRC progression.

Discussion

The long-held notion of tumors as “wounds that never heal” was postulated more than 30 years ago based on the similarities between cancer stromagenesis and wound healing[63]. Although numerous subsequent studies have deciphered the origins of myofibroblasts in multiple models of wound healing and fibrosis[16-22], the origins and contribution of the tumor stroma are still largely unknown. In the CAF research field, whilst our understanding of function and heterogeneity of CAFs has advanced quickly over the last decade[2], no previous studies have addressed the precise nature of tumor stromagenesis by comprehensive genetic fate-mapping. In the present study, as summarized in **Supplementary Figure 17**, we have shown that about 50% of ACTA2$^+$ CAFs are new cells generated through proliferation in an AOM/DSS mouse model of CRC, with the remaining 50% simply acquire ACTA2 expression without proliferation. Notably, 75% of the proliferating ACTA2$^+$ CAFs were derived from intestinal *Lepr*-lineage stromal cells. Using RNA-sequencing of FACS-purified colonic stromal cells, we identified MCAM as a marker for CRC stromal cells that represent a subset of the *Lepr*-lineage proliferating stromal cells. Our data show that high MCAM expression was associated with poor clinical outcomes in patients with CRC, suggesting that targeting MCAM may represent an attractive therapeutic strategy to retard CRC progression.

Several previous studies have indicated that recruitment from the bone marrow could contribute to CAFs in mouse models of cancers such as pancreatic, gastric, and breast cancer. In contrast, one paper demonstrated that no *Acta2*-RFP$^+$ CAFs were detected in intestinal tumors developed in an *Apc*$^{Min/+}$ mouse parabiosed with an *Acta2*-RFP mouse. In agreement with this, we found that no *Acta2*-RFP$^+$ stromal cells were derived from transplanted bone marrow cells in an AOM/DSS model of CRC. Similarly, we found that the EMT program in *Krt19*-lineage cells did not contribute to ACTA2$^+$ CAFs, at least, in the AOM/DSS CRC model, despite several papers indicating EMT as a potential source of pancreatic and breast tumor stroma[12, 13]. Therefore, it is plausible that the origins and contributions of CAFs are highly dependent on contexts such as tumor type and local

microenvironment. It would be intriguing, in future studies, to investigate whether different local precursors could give rise to functionally distinct CAFs in primary and metastatic cancer models.

Intestinal epithelial cells and cancer cells can develop from dedicated stem cell-progenitor cell hierarchies[64, 65]. Analogous to this, we have previously shown that *Grem1*$^+$ intestinal reticular stromal cells identify connective tissue stem cells in the normal small intestine[45]. Here, our data indicate that the majority of CRC CAFs arise through a particular mesenchymal lineage, *Lepr*-lineage intestinal stromal cells. Our findings that quiescent *Lepr*-lineage intestinal stromal cells can differentiate into mature ACTA2$^+$ myofibroblastic CAFs, presents one mesenchymal lineage hierarchy found in the CRC tumor microenvironment. Similarly, a recent paper has shown that *Gli1*$^+$ pancreatic stellate cells could contribute to approximately half of ACTA2$^+$ CAFs in a mouse model of pancreatic cancer[66]. Further research is required to determine the hierarchical relationship between *Lepr*-lineage and *Gli1*-lineage CAFs in the development of the tumor stroma.

One limitation of the present study is that we have not determined whether *Lepr*-lineage CAFs show extensive cellular plasticity during cancer development as has been shown to occur in cancer stem cells[64], or simply undergo an irreversible “lineage-restricted” differentiation. Given that CAFs are considered to exhibit tumor stage-dependent phenotypes[2, 67], it is conceivable that *Lepr*-lineage CAFs could adapt to dynamic phenotypic shifts during colorectal carcinogenesis.

We propose MCAM as an attractive therapeutic target that predicts CRC prognosis. Excitingly, MCAM-neutralizing antibodies show promising results in restraining cancer progression in preclinical models, including a model of CRC[29, 31, 68-71]. Future work should focus on elucidating the mechanism by which *Lepr*-lineage MCAM$^+$ cancer-associated stromal cells contribute to CRC progression, as well as whether the MCAM$^+$ stromal cells contribute to shaping an immunosuppressive tumor microenvironment.

In conclusion, our data show that *Lepr*-lineage intestinal stromal cells are key contributors to the CRC stroma and suggest that MCAM could be an attractive therapeutic target to restrain CRC progression. Our findings involving the origins and contribution of the tumor stroma pave the way for

a better understanding of the biological mechanisms underlying cancer stromagenesis, as well as for the development of novel therapeutic strategies that selectively target desmoplasia-driving CAFs.

Figure 1: ACTA2 expression is increased during colorectal carcinogenesis in humans and mice.

(A, B) Immunohistochemistry (IHC) for ACTA2 in human colorectal samples. **(A)** Representative pictures. **(B)** Quantification of ACTA2 positivity in total stromal cells (visualized by hematoxylin counterstaining). 3 high power fields (HPFs, 400x)/patient, n = 4-5 patients each.

(C) Violin plots depicting *ACTA2* expression in transcript expression microarray data from human normal colon mucosa and primary colon adenocarcinoma (GSE39582). n = 19 (normal colon mucosa) and 566 patients (primary colon adenocarcinoma).

(D) Kaplan-Meier survival curves showing overall survival rates of 621 primary colorectal cancer patients classified according to the expression level of *ACTA2* in The Cancer Genome Atlas (TCGA) dataset.

(E) Violin plots showing *ACTA2* expression level in four consensus molecular subtypes (CMS). n = 76 (CMS1), 220 (CMS2), 72 (CMS3), and 143 patients (CMS4).

(F) Scheme for the experimental course of azoxymethane (AOM)/ dextran sulfate sodium (DSS)-induced colorectal carcinogenesis.

(G) Representative endoscopic images of the normal colon mucosa and AOM/DSS tumors. T, tumors.

(H, I) Immunohistochemistry for ACTA2 in the normal mucosa and AOM/DSS tumors. **(H)** Representative pictures. **(I)** Quantification of ACTA2 positivity in total stromal cells. 3 HPFs/mouse, n = 3 mice each.

Note that only lamina propria regions were evaluated for the quantification of the normal mucosa (B and I).

One-way ANOVA followed by Tukey's post-hoc multiple comparison test (B), Log-rank test (D), Kruskal-Wallis test followed by Dunn's multiple comparisons test (E), and two-tailed unpaired Student's t-test (I), False delivery rate (FDR)-adjusted P-value is shown (C).

****, $P < 0.0001$; **, $P = 0.00299$; *, $P = 0.0451$.

Scale bars, 50 um.

Box plots have whiskers of maximum and minimum values; the boxes represent first, second (median), and third quartiles (B and I).

Solid black lines, median; Dotted black lines, quartiles (C and E).

Figure 2: A subset of ACTA2$^+$ CAFs undergo proliferation during colorectal carcinogenesis in humans and mice.

(A, B) Co-immunofluorescence for ACTA2 and Ki67 in human colorectal samples. **(A)** Representative pictures. Yellow arrowheads denote proliferating CAFs (ACTA2$^+$Ki67$^+$ cells). **(B)** Quantification of Ki67 positivity in total ACTA2$^+$ cells. 3 HPFs (400x)/patient, n = 4-5 patients each. **(C)** Scheme for the experimental course of AOM/ DSS-induced colon carcinogenesis and 5-bromodeoxyuridine (BrdU) administration. Note that continuous BrdU administration was commenced after a visible tumor was observed via mouse colonoscopy. T, tumor.

(D, E) Co-immunofluorescence for ACTA2 and Ki67 in the normal colon mucosa and AOM/DSS tumors. **(D)** Representative images. Yellow and red arrowheads denote ACTA2$^+$BrdU$^+$Ki67$^-$ cells and ACTA2$^+$BrdU$^+$Ki67$^+$ cells, respectively. Note that Ki67$^+$ACTA2$^+$ cells mark a rare subpopulation of ACTA2$^+$ cells. **(E)** Quantification of BrdU positivity (left) and Ki67 positivity (right) in total ACTA2$^+$ cells.

****, P < 0.0001; **, P = 0.0077; n.s., P = 0.5049.

Kruskal-Wallis test followed by Dunn's multiple comparisons test (B) and two-tailed unpaired Student's t-test (E)

Scale bars, 50 um.

Box plots have whiskers of maximum and minimum values; the boxes represent first, second (median), and third quartiles.

Figure 3: Proliferating ACTA2$^+$ CAFs derive predominantly from *Lepr*-lineage cells in an AOM/DSS mouse model of CRC.

(A) Immunofluorescence for ACTA2 and EPCAM in the normal colon mucosa and AOM/DSS tumors using genetic fate-mapping mouse models. Yellow arrowheads denote lineage-marker$^+$ACTA2$^+$ cells. All lineage markers are shown in red pseudocolor. See Figure 3D for quantification. R26, Rosa26-loxP-stop-loxP; BM, bone marrow; BMT, bone marrow transplantation; TAM, tamoxifen.

(B) Immunofluorescence for ACTA2 in the normal mucosa and AOM/DSS tumors using *Krt19*-Cre mice, showing that no ACTA2$^+$ cells were recombined (left). Immunofluorescence for ACTA2 and EPCAM in the normal mucosa and AOM/DSS tumor, using a wild-type recipient mouse transplanted with bone marrow cells from an *Acta2*-RFP mouse (right). No ACTA2$^+$ cells were positive for RFP. See Figure 3D for quantification.

(C) Immunofluorescence for ACTA2 and BrdU in AOM/DSS tumors using the BrdU-treated genetic fate-mapping mouse models. Yellow arrowheads denote proliferating CAFs that were derived from each cellular lineage (lineage-marker$^+$ACTA2$^+$BrdU$^+$ cells). See Figure 3E for quantification.

(D) Quantification of the ratio of lineage-marker$^+$ cells in total ACTA2$^+$ cells in the normal mucosa and AOM/DSS tumors. 4 HPFs/mouse. n = 3 (*Lepr*-Cre, *Grem1*-CreET2, *Islr*-CreERT2, *Acta2*-RFP) and 2 mice (*Krt19*-Cre).

(E) Quantification of the ratio of lineage marker$^+$ cells in total proliferating CAFs (ACTA2$^+$BrdU$^+$ cells). 4 HPFs/mouse. n = 3 mice each.

(F, G) Cellular position of *Lepr*$^+$ stromal cells in the normal adult mouse colon. **(F)** Representative pictures. White arrowheads denote *Lepr*-lineage tdtomato$^+$ cells. **(G)** Violin plots showing the positions of pericryptal *Lepr*$^+$ stromal cells relative to the adjacent epithelial position. n = 81 *Lepr*$^+$ cells from 3 mice. Only well-oriented crypts were evaluated. Solid black lines, median; Dotted black lines, quartiles.

Scale bars, 50 um.

Two-tailed unpaired t-test with Welch's correction (D) and Kruskal-Wallis test followed by Dunn's multiple comparisons test (E).

****, P < 0.0001; **, P = 0.0030 (D); **, P = 0.0043 (E).

Box plots have whiskers of maximum and minimum values; the boxes represent first, second (median), and third quartiles.

Figure 4: Identification of MCAM as a CRC mesenchyme-specific marker that represents a subset of *Lepr*-lineage proliferating cells.

(A) Experimental schematic for isolating colonic fibroblasts from the normal adult colon, AOM/DSS tumors, and postnatal day 14 colon. Gating strategy to isolate $CD45^-Ter119^-CD31^-EPCAM^-$ fibroblasts by fluorescence-activated cell-sorting (FACS) is shown for one mouse adult normal colon. Bulk RNA-sequencing from FACS-purified cells was performed using the normal adult colon, AOM/DSS tumors, and postnatal day 14 colon. n = 4 mice each.

(B) Strategy to identify colonic mesenchymal gene upregulated in development and carcinogenesis, which is associated with human CRC survival. **(1)** Venn diagram showing 342 upregulated genes shared between postnatal day 14 colon and AOM/DSS tumors, compared with the normal adult colon. **(2)** Survival analysis using the TCGA dataset was performed to select genes significantly associated with worse human CRC outcomes. **(3)** To examine for mesenchyme-specific genes, genes upregulated in $EPCAM^-CD31^-CD45^-Ter119^-$ fibroblasts compared with $EPCAM^+$ epithelial cells, both in the normal adult colon and AOM/DSS tumors, were selected using our RNA-seq data. Mean ± s.e.m. **(4)** Human CRC immunohistochemistry data from The Human protein atlas were used to further select genes whose protein expression was restricted to the CRC stroma. *Mcam* is highlighted in red.

(C, D) Validation of increased MCAM expression in AOM/DSS tumors and postnatal day 14 colon. Immunohistochemistry (IHC) for MCAM was performed. **(C)** Representative images. Blue, red, and green arrowheads denote MCAM expression in the normal adult colon, AOM/DSS tumor, and postnatal day 14 colon, respectively. **(D)** Quantification of the ratio of $MCAM^+$ cells in total stromal cells (visualized by hematoxylin counterstaining). 3 HPFs/mouse, n = 3 mice each.

(E, F) Co-immunofluorescence for MCAM and BrdU. **(E)** Representative images. Yellow arrowheads denote proliferating $MCAM^+$ cells. **(F)** Quantification of the ratio of $MCAM^+BrdU^+$ cells in total $MCAM^+$ cells.

(G) Immunofluorescence for MCAM using AOM/DSS tumors from *Lepr*-Cre; Rosa26-tdtomato mice showing the contribution of *Lepr*-lineage cells to $MCAM^+$ cells. Yellow arrowheads denote *Lepr*-$lineage^+MCAM^+$ cells.

****, $P < 0.0001$.

Log-rank test (B(2)), one-way ANOVA followed by Tukey's post-hoc multiple comparison test (B(3) and D), and two-tailed unpaired Student's t-test (F)

Box plots have whiskers of maximum and minimum values; the boxes represent first, second (median), and third quartiles.

Figure 5: High MCAM expression driven, in part, by TGF-β, is associated with poor survival in patients with CRC.

(A, B) Immunohistochemistry (IHC) for MCAM in human colorectal samples. **(A)** Representative pictures. **(B)** Quantification of MCAM positivity in total stromal cells (visualized by hematoxylin counterstaining). 3 high power fields (HPFs, 400x)/patient, n = 4-5 patients each.

(C) Violin plots showing *MCAM* expression levels in four consensus molecular subtypes (CMS). n = 76 (CMS1), 220 (CMS2), 72 (CMS3), and 143 patients (CMS4). Solid black lines, median; Dotted black lines, quartiles.

(D) A mouse colonic fibroblast cell line, YH2, was incubated with vehicle, recombinant TGFβ1, or recombinant TGFβ1 + TGFβ1-receptor inhibitor (Galunisertib) for 24 hours, followed by qRT-PCR. Mean ± s.e.m. n = 3.

(E) *MCAM* transcript levels positively correlate with *ACTA2* expression levels in the TCGA dataset. n = 511 patients with CMS1-4 CRC. Solid line, linear regression; dotted lines, 95% confidence interval.

(F, G) MCAM immunostaining in a CRC tissue microarray reveals that high MCAM expression levels are associated with poor survival in patients with CRC. **(F)** Representative images of MCAM immunostaining showing each intensity score. Cases with total scores (the sum of intensity and proportion scores) of ≥ 3.3 were defined as MCAM-high cancer. Each patient has 3-4 replicate tumor samples obtained from different locations within the tumor. **(G)** Kaplan-Meier survival curves showing overall survival rates of 101 primary colorectal cancer patients.

****, $P < 0.0001$; *, $P = 0.0124$.

Kruskal-Wallis test followed by Dunn's multiple comparisons test (B and C), one-way ANOVA followed by Tukey's post-hoc multiple comparison test (D), Spearman correlation (E), and Log-rank test (G).

Box plots have whiskers of maximum and minimum values; the boxes represent first, second (median), and third quartiles (B).

References

1. van Pelt GW, Sandberg TP, Morreau H, et al. The tumour-stroma ratio in colon cancer: the biological role and its prognostic impact. Histopathology 2018;73:197-206.
2. Kobayashi H, Enomoto A, Woods SL, et al. Cancer-associated fibroblasts in gastrointestinal cancer. Nat Rev Gastroenterol Hepatol 2019;16:282-295.
3. Kalluri R. The biology and function of fibroblasts in cancer. Nat Rev Cancer 2016;16:582-98.
4. Gieniec KA, Butler LM, Worthley DL, et al. Cancer-associated fibroblasts—heroes or villains? British Journal of Cancer 2019.
5. Li H, Courtois ET, Sengupta D, et al. Reference component analysis of single-cell transcriptomes elucidates cellular heterogeneity in human colorectal tumors. Nat Genet 2017;49:708-718.
6. Elyada E, Bolisetty M, Laise P, et al. Cross-species single-cell analysis of pancreatic ductal adenocarcinoma reveals antigen-presenting cancer-associated fibroblasts. Cancer Discov 2019.
7. Sahai E, Astsaturov I, Cukierman E, et al. A framework for advancing our understanding of cancer-associated fibroblasts. Nat Rev Cancer 2020.
8. Ozdemir BC, Pentcheva-Hoang T, Carstens JL, et al. Depletion of carcinoma-associated fibroblasts and fibrosis induces immunosuppression and accelerates pancreas cancer with reduced survival. Cancer Cell 2014;25:719-34.
9. Bartoschek M, Oskolkov N, Bocci M, et al. Spatially and functionally distinct subclasses of breast cancer-associated fibroblasts revealed by single cell RNA sequencing. Nature Communications 2018;9:5150.
10. Ohlund D, Handly-Santana A, Biffi G, et al. Distinct populations of inflammatory fibroblasts and myofibroblasts in pancreatic cancer. J Exp Med 2017;214:579-596.
11. Biffi G, Oni TE, Spielman B, et al. IL-1-induced JAK/STAT signaling is antagonized by TGF-beta to shape CAF heterogeneity in pancreatic ductal adenocarcinoma. Cancer Discov

2018.

12. Fischer KR, Durrans A, Lee S, et al. Epithelial-to-mesenchymal transition is not required for lung metastasis but contributes to chemoresistance. Nature 2015;527:472-6.

13. Rhim AD, Mirek ET, Aiello NM, et al. EMT and dissemination precede pancreatic tumor formation. Cell 2012;148:349-61.

14. Quante M, Tu SP, Tomita H, et al. Bone marrow-derived myofibroblasts contribute to the mesenchymal stem cell niche and promote tumor growth. Cancer Cell 2011;19:257-72.

15. Arina A, Idel C, Hyjek EM, et al. Tumor-associated fibroblasts predominantly come from local and not circulating precursors. Proc Natl Acad Sci U S A 2016;113:7551-6.

16. El Agha E, Kramann R, Schneider RK, et al. Mesenchymal Stem Cells in Fibrotic Disease. Cell Stem Cell 2017;21:166-177.

17. LeBleu VS, Taduri G, O'Connell J, et al. Origin and function of myofibroblasts in kidney fibrosis. Nat Med 2013;19:1047-53.

18. Decker M, Martinez-Morentin L, Wang G, et al. Leptin-receptor-expressing bone marrow stromal cells are myofibroblasts in primary myelofibrosis. Nat Cell Biol 2017;19:677-688.

19. Kramann R, Schneider RK, DiRocco DP, et al. Perivascular Gli1+ progenitors are key contributors to injury-induced organ fibrosis. Cell Stem Cell 2015;16:51-66.

20. Gupta V, Gupta I, Park J, et al. Hedgehog Signaling Demarcates a Niche of Fibrogenic Peribiliary Mesenchymal Cells. Gastroenterology 2020.

21. Rinkevich Y, Walmsley GG, Hu MS, et al. Skin fibrosis. Identification and isolation of a dermal lineage with intrinsic fibrogenic potential. Science 2015;348:aaa2151.

22. Driskell RR, Lichtenberger BM, Hoste E, et al. Distinct fibroblast lineages determine dermal architecture in skin development and repair. Nature 2013;504:277-281.

23. Ding L, Saunders TL, Enikolopov G, et al. Endothelial and perivascular cells maintain haematopoietic stem cells. Nature 2012;481:457-62.

24. Ding L, Morrison SJ. Haematopoietic stem cells and early lymphoid progenitors occupy

distinct bone marrow niches. Nature 2013;495:231-5.

25. Zhou BO, Yue R, Murphy MM, et al. Leptin-receptor-expressing mesenchymal stromal cells represent the main source of bone formed by adult bone marrow. Cell Stem Cell 2014;15:154-68.

26. Crisan M, Yap S, Casteilla L, et al. A perivascular origin for mesenchymal stem cells in multiple human organs. Cell Stem Cell 2008;3:301-13.

27. Sacchetti B, Funari A, Michienzi S, et al. Self-renewing osteoprogenitors in bone marrow sinusoids can organize a hematopoietic microenvironment. Cell 2007;131:324-36.

28. Corselli M, Chin CJ, Parekh C, et al. Perivascular support of human hematopoietic stem/progenitor cells. Blood 2013;121:2891-901.

29. Wang Z, Yan X. CD146, a multi-functional molecule beyond adhesion. Cancer Lett 2013;330:150-62.

30. Brechbuhl HM, Finlay-Schultz J, Yamamoto TM, et al. Fibroblast Subtypes Regulate Responsiveness of Luminal Breast Cancer to Estrogen. Clin Cancer Res 2017;23:1710-1721.

31. Xing S, Luo Y, Liu Z, et al. Targeting endothelial CD146 attenuates colitis and prevents colitis-associated carcinogenesis. Am J Pathol 2014;184:1604-16.

32. Wragg JW, Finnity JP, Anderson JA, et al. MCAM and LAMA4 Are Highly Enriched in Tumor Blood Vessels of Renal Cell Carcinoma and Predict Patient Outcome. Cancer Res 2016;76:2314-26.

33. Jiang T, Zhuang J, Duan H, et al. CD146 is a coreceptor for VEGFR-2 in tumor angiogenesis. Blood 2012;120:2330-9.

34. Zhang M, Yang H, Wan L, et al. Single cell transcriptomic architecture and intercellular crosstalk of human intrahepatic cholangiocarcinoma. J Hepatol 2020.

35. Wang Z, Xu Q, Zhang N, et al. CD146, from a melanoma cell adhesion molecule to a signaling receptor. Signal Transduction and Targeted Therapy 2020;5.

36. Costa A, Kieffer Y, Scholer-Dahirel A, et al. Fibroblast Heterogeneity and Immunosuppressive Environment in Human Breast Cancer. Cancer Cell 2018.
37. Dominguez CX, Muller S, Keerthivasan S, et al. Single-cell RNA sequencing reveals stromal evolution into LRRC15+ myofibroblasts as a determinant of patient response to cancer immunotherapy. Cancer Discov 2019.
38. Testa U, Pelosi E, Castelli G. Colorectal cancer: genetic abnormalities, tumor progression, tumor heterogeneity, clonal evolution and tumor-initiating cells. Med Sci (Basel) 2018;6.
39. Marisa L, de Reynies A, Duval A, et al. Gene expression classification of colon cancer into molecular subtypes: characterization, validation, and prognostic value. PLoS Med 2013;10:e1001453.
40. Calon A, Lonardo E, Berenguer-Llergo A, et al. Stromal gene expression defines poor-prognosis subtypes in colorectal cancer. Nat Genet 2015;47:320-9.
41. Isella C, Terrasi A, Bellomo SE, et al. Stromal contribution to the colorectal cancer transcriptome. Nat Genet 2015;47:312-9.
42. Guinney J, Dienstmann R, Wang X, et al. The consensus molecular subtypes of colorectal cancer. Nat Med 2015;21:1350-6.
43. Torres S, Bartolome RA, Mendes M, et al. Proteome profiling of cancer-associated fibroblasts identifies novel proinflammatory signatures and prognostic markers for colorectal cancer. Clin Cancer Res 2013;19:6006-19.
44. Lee HO, Hong Y, Etlioglu HE, et al. Lineage-dependent gene expression programs influence the immune landscape of colorectal cancer. Nat Genet 2020.
45. Worthley DL, Churchill M, Compton JT, et al. Gremlin 1 identifies a skeletal stem cell with bone, cartilage, and reticular stromal potential. Cell 2015;160:269-84.
46. Mizutani Y, Kobayashi H, Iida T, et al. Meflin-positive cancer-associated fibroblasts inhibit pancreatic carcinogenesis. Cancer Res 2019.
47. Hara A, Kobayashi H, Asai N, et al. Roles of the Mesenchymal Stromal/Stem Cell Marker

Meflin in Cardiac Tissue Repair and the Development of Diastolic Dysfunction. Circ Res 2019;125:414-430.

48. Asfaha S, Hayakawa Y, Muley A, et al. Krt19(+)/Lgr5(-) Cells Are Radioresistant Cancer-Initiating Stem Cells in the Colon and Intestine. Cell Stem Cell 2015;16:627-38.

49. Worthley DL, Si Y, Quante M, et al. Bone marrow cells as precursors of the tumor stroma. Exp Cell Res 2013;319:1650-6.

50. Raz Y, Cohen N, Shani O, et al. Bone marrow-derived fibroblasts are a functionally distinct stromal cell population in breast cancer. J Exp Med 2018.

51. Magness ST, Bataller R, Yang L, et al. A dual reporter gene transgenic mouse demonstrates heterogeneity in hepatic fibrogenic cell populations. Hepatology 2004;40:1151-9.

52. Reichert M, Takano S, von Burstin J, et al. The Prrx1 homeodomain transcription factor plays a central role in pancreatic regeneration and carcinogenesis. Genes Dev 2013;27:288-300.

53. Ma Y, Zhang P, Wang F, et al. The relationship between early embryo development and tumourigenesis. J Cell Mol Med 2010;14:2697-701.

54. Sancho E, Batlle E, Clevers H. Signaling pathways in intestinal development and cancer. Annu Rev Cell Dev Biol 2004;20:695-723.

55. Uhlen M, Fagerberg L, Hallstrom BM, et al. Proteomics. Tissue-based map of the human proteome. Science 2015;347:1260419.

56. Calon A, Espinet E, Palomo-Ponce S, et al. Dependency of colorectal cancer on a TGF-beta-driven program in stromal cells for metastasis initiation. Cancer Cell 2012;22:571-84.

57. Kinchen J, Chen HH, Parikh K, et al. Structural Remodeling of the Human Colonic Mesenchyme in Inflammatory Bowel Disease. Cell 2018;175:372-386.e17.

58. Hirokawa Y, Yip KH, Tan CW, et al. Colonic myofibroblast cell line stimulates colonoid formation. Am J Physiol Gastrointest Liver Physiol 2014;306:G547-56.

59. Tian B, Zhang Y, Li N. CD146 protein as a marker to predict postoperative liver metastasis in colorectal cancer. Cancer Biother Radiopharm 2013;28:466-70.

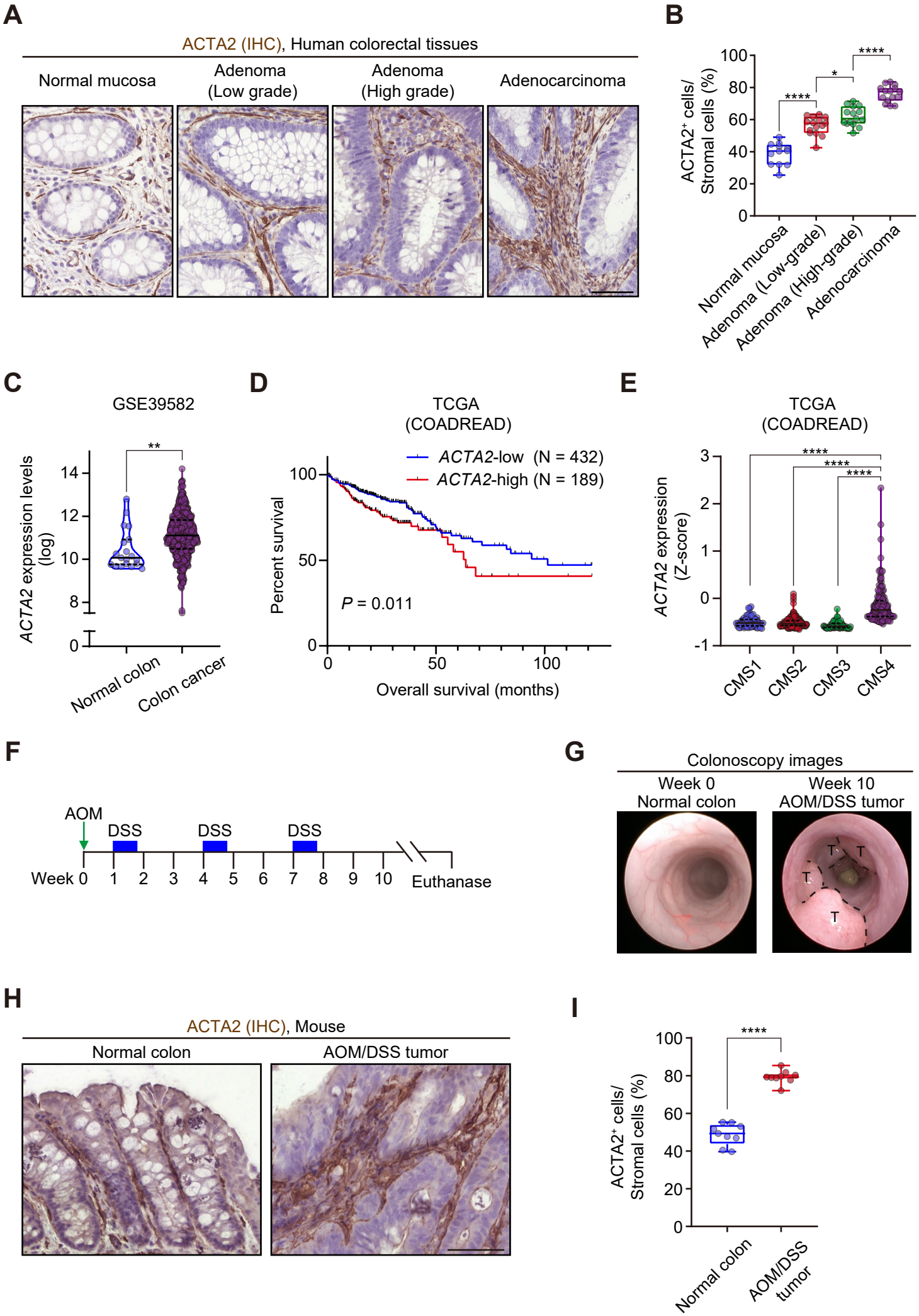
60. Zeng P, Li H, Lu PH, et al. Prognostic value of CD146 in solid tumor: A Systematic Review and Meta-analysis. Sci Rep 2017;7:4223.
61. Sheffer M, Bacolod MD, Zuk O, et al. Association of survival and disease progression with chromosomal instability: a genomic exploration of colorectal cancer. Proc Natl Acad Sci U S A 2009;106:7131-6.
62. de Sousa EMF, Colak S, Buikhuisen J, et al. Methylation of cancer-stem-cell-associated Wnt target genes predicts poor prognosis in colorectal cancer patients. Cell Stem Cell 2011;9:476-85.
63. Dvorak HF. Tumors: wounds that do not heal. Similarities between tumor stroma generation and wound healing. N Engl J Med 1986;315:1650-9.
64. Batlle E, Clevers H. Cancer stem cells revisited. Nat Med 2017;23:1124-1134.
65. Gehart H, Clevers H. Tales from the crypt: new insights into intestinal stem cells. Nat Rev Gastroenterol Hepatol 2018.
66. Garcia PE, Adoumie M, Kim EC, et al. Differential contribution of pancreatic fibroblast subsets to the pancreatic cancer stroma. Cellular and Molecular Gastroenterology and Hepatology 2020.
67. Friedman G, Levi-Galibov O, David E, et al. Cancer-associated fibroblast compositions change with breast cancer progression linking the ratio of S100A4+ and PDPN+ CAFs to clinical outcome. Nature Cancer 2020.
68. Yan X, Lin Y, Yang D, et al. A novel anti-CD146 monoclonal antibody, AA98, inhibits angiogenesis and tumor growth. Blood 2003;102:184-91.
69. Stalin J, Nollet M, Dignat-George F, et al. Therapeutic and Diagnostic Antibodies to CD146: Thirty Years of Research on Its Potential for Detection and Treatment of Tumors. Antibodies 2017;6.
70. Zoni E, Astrologo L, Ng CKY, et al. Therapeutic targeting of CD146/MCAM reduces bone metastasis in prostate cancer. Mol Cancer Res 2019.

71. Stalin J, Nollet M, Garigue P, et al. Targeting soluble CD146 with a neutralizing antibody inhibits vascularization, growth and survival of CD146-positive tumors. Oncogene 2016;35:5489-5500.

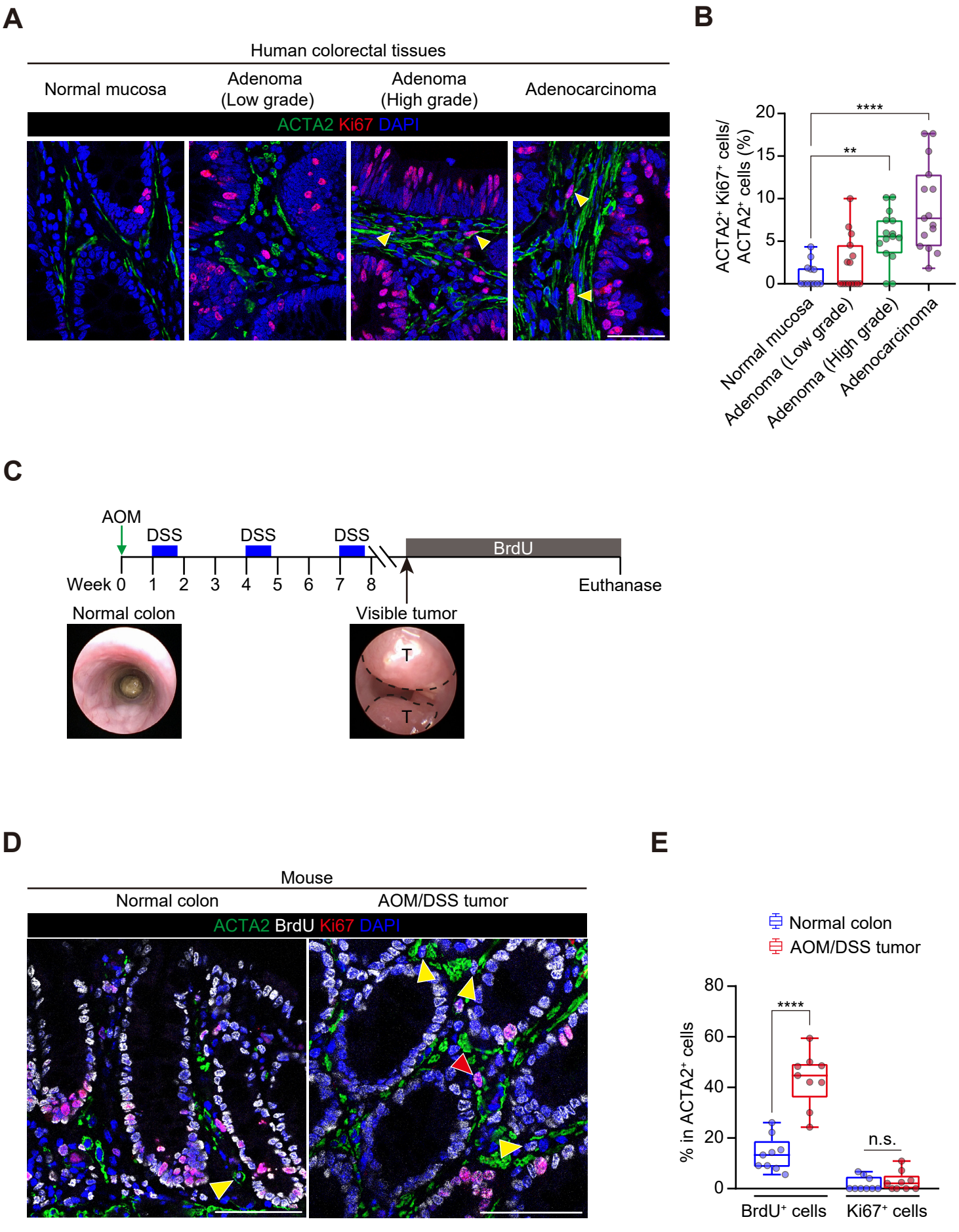
-Acknowledgments

This study was supported by grants from the National Health and Medical Research Council (APP1156391 to D.L.W., S.L.W.) (APP1081852 to D.L.W., APP1140236 to SLW, APP1099283 to DLW,); Cancer Council SA Beat Cancer Project on behalf of its donors and the State Government of South Australia through the Department of Health (MCF0418 to S.L.W., D.L.W., and PRF1117 to L.M.B.); a Grant-in-Aid for Scientific Research (S) (26221304 to M.T.) commissioned by the Ministry of Education, Culture, Sports, Science and Technology of Japan; AMED-CREST (Japan Agency for Medical Research and Development, Core Research for Evolutional Science and Technology (19gm0810007h0104 and 19gm1210008s0101 to A.E.); the Project for Cancer Research and Therapeutic Evolution (P-CREATE) from AMED (19cm0106332h0002 to A.E.); Japan Society for the Promotion of Science Overseas Challenge Program for Young Researchers (to H.K.), Takeda Science Foundation Fellowship (to H.K.), Greaton International Ph.D. Scholarship (to H.K.), Lions Medical Research Foundation Scholarship (to K.G.).

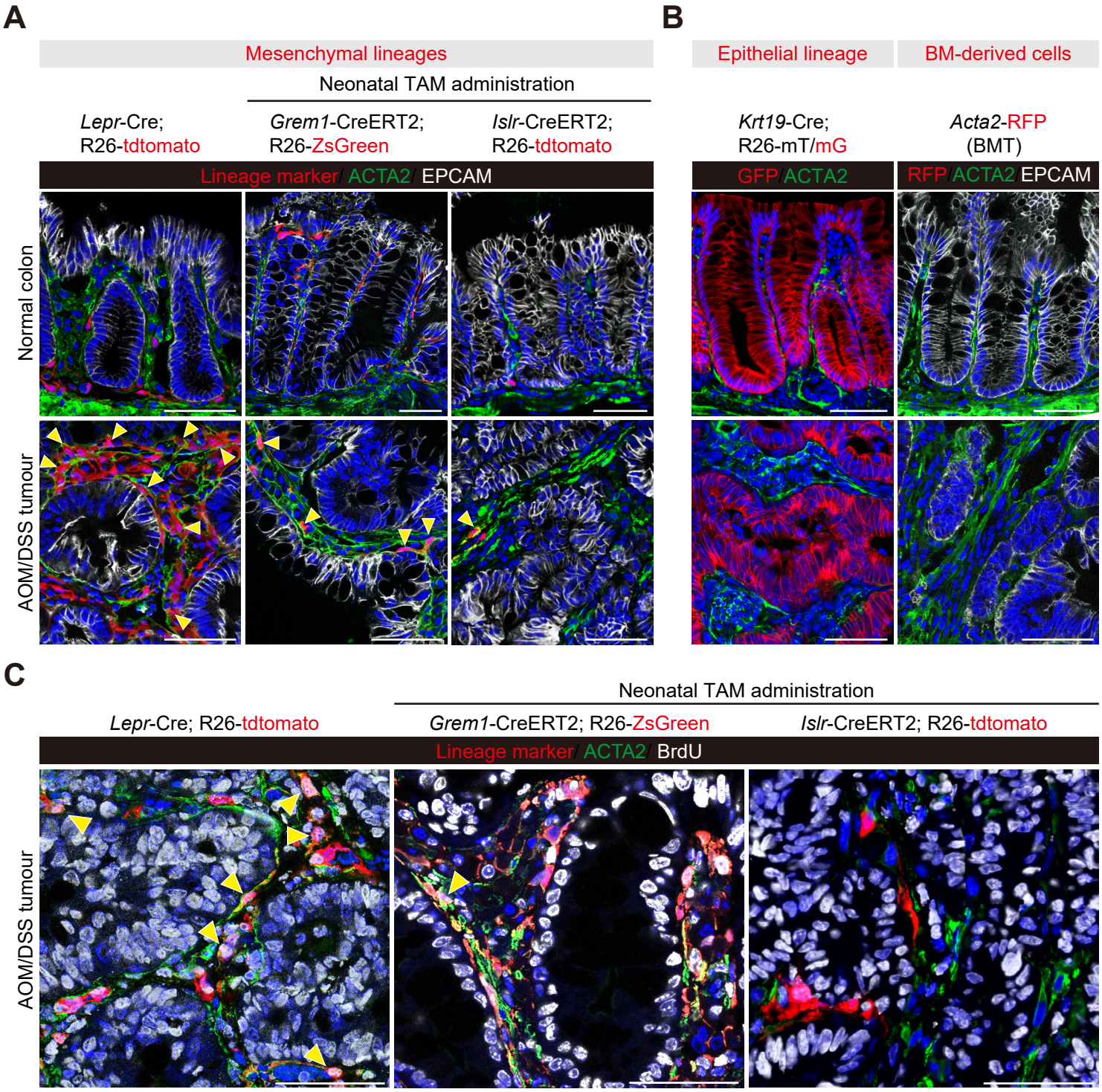
We thank Kaori Ushida, Kozo Uchiyama (Nagoya University, JAPAN) for technical assistance. The mouse colonic fibroblast cell line, YH2, was a kind gift from Professor Antony Burgess (Walter and Eliza Hall Institute of Medical Research, Australia). We acknowledge the facilities and the scientific and technical assistance of the South Australian Genome Editing (SAGE) Facility, the University of Adelaide, and the South Australian Health and Medical Research Institute. SAGE is supported by Phenomics Australia. Phenomics Australia is supported by the Australian Government through the National Collaborative Research Infrastructure Strategy (NCRIS) program.



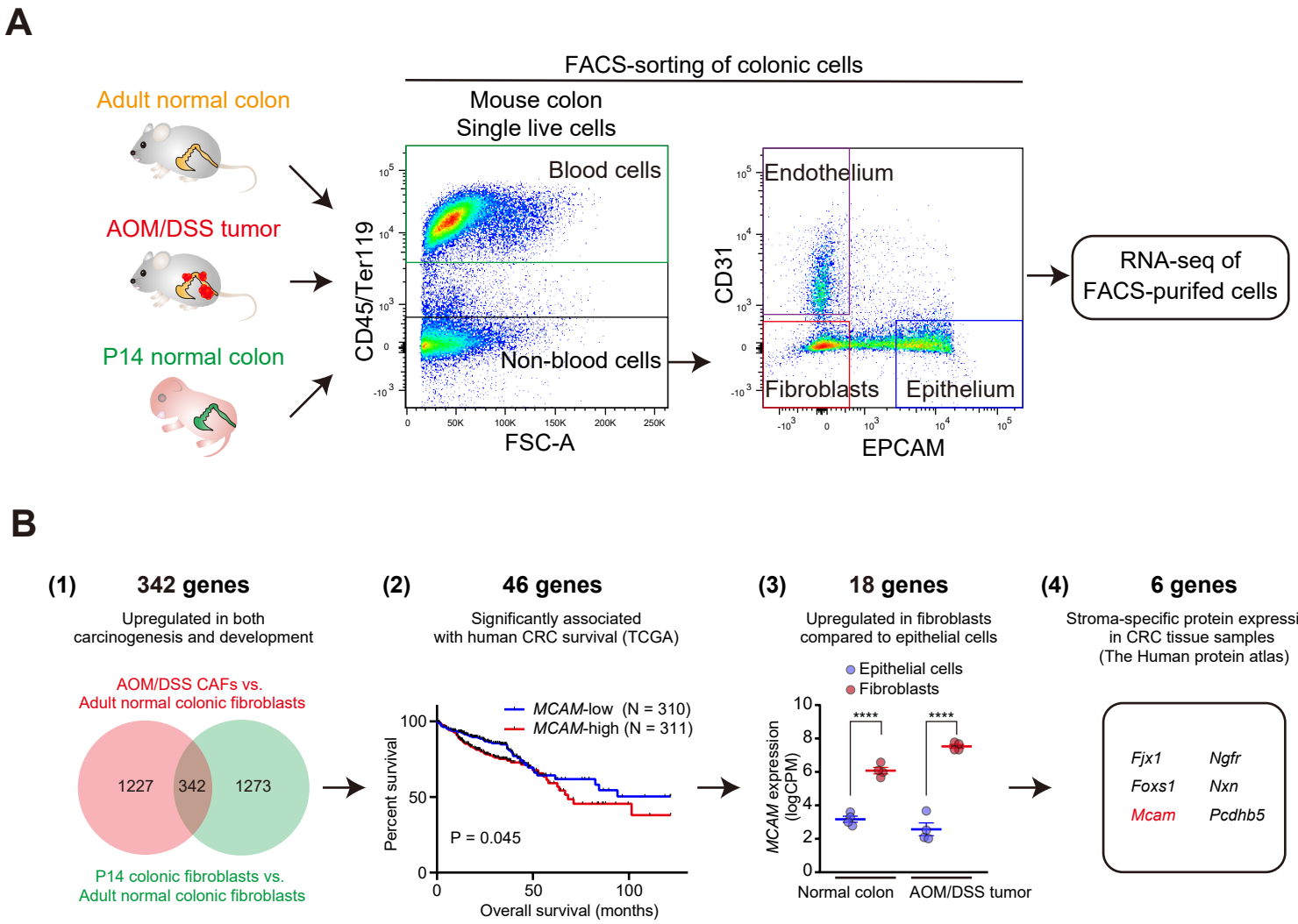
Kobayashi *et al.*, Figure 1.



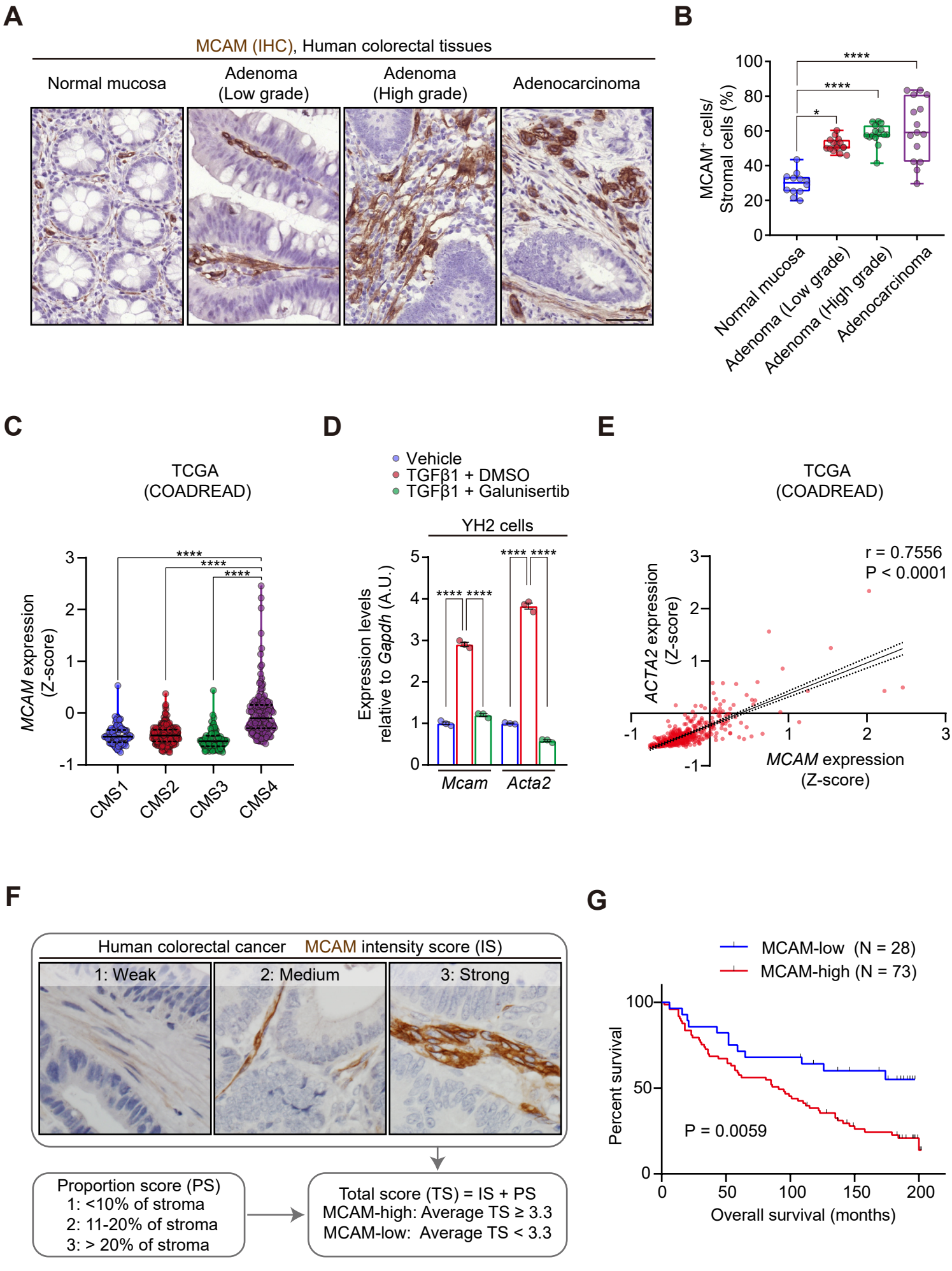
Kobayashi *et al.*, Figure 2.



Kobayashi *et al.*, Figure 3.



Kobayashi *et al.*, Figure 4.



Kobayashi *et al.*, Figure 5.

The origin and contribution of the tumor stroma in colorectal carcinogenesis

Kobayashi *et al.*

Supplemental Information

1. Supplementary Figures 1-17 and figure legends

2. Supplementary Table 1-3

3. Supplementary Methods

Supplementary Figure 1: Analyses of multiple human CRC expression datasets reveal that high *ACTA2* and *FAP* expression are associated with poor survival.

Associations between survival and transcript levels of intestinal fibroblast markers were assessed using 4 independent human CRC expression datasets[1-4].

Log-rank test. P-values less than 0.05 are shown in green.

Note that the same survival analysis of the TCGA dataset using *ACTA2* expression levels is shown in Figure 1D as well.

Supplementary Figure 2:ACTA2 expression is increased in intestinal tumors in *Apc*$^{Min/+}$ mice, compared with the adjacent normal intestine.

(A, B) Immunohistochemistry (IHC) for ACTA2 using the normal small intestine and small intestinal tumors in *Apc*$^{Min/+}$ mice. **(A)** Representative pictures. **(B)** Quantification of the ratio of ACTA2^{+} cells in total stroma cells (as visualized by hematoxylin counterstaining). 3 HPFs/mouse, n = 4 mice each.

Scale bar, 50 um. Mann-Whitney U-test (B)

Box plots have whiskers of maximum and minimum values; the boxes represent first, second (median), and third quartiles.

Supplementary Figure 3: Single-cell RNA-sequencing data from human CRC tissues reveal that a minor subpopulation of myofibroblastic CAFs are positive for *MKI67*.

(A-C) t-distributed stochastic neighbor embedding (t-SNE) plot showing human colorectal stromal cell subpopulations. 5933 stromal cells from 23 CRC patients were analyzed using single-cell RNA-sequencing (scRNA-seq) from unsorted colorectal cells (GSE132465).

Cluster annotations **(A).** Sample origins (CRC tissues or normal mucosa tissues) **(B)**. The intensity of the red represents the expression levels of *ACTA2* (left) or *MKI67* (right) **(C)**.

Green circles denote a myofibroblast subcluster characterized by expression of *ACTA2* and *MKI67* (proliferating CAFs).

A black dotted line in (A) encircles clusters of endothelial cells.

Supplementary Figure 4: *Lepr*-lineage cells are a major contributor to PDGFRA$^+$ CAFs in AOM/DSS tumors.

(A, B) Immunofluorescence for PDGFRA in the normal colon mucosa and AOM/DSS tumor in genetic fate-mapping mouse models. **(A)** Representative pictures. Yellow arrowheads denote lineage-marker$^+$ PDGFRA$^+$ cells. R26, Rosa26-loxP-stop-loxP. **(B)** Quantification of the ratio of lineage-marker$^+$ cells in total PDGFRA cells. 3-4 HPFs/mouse, n = 3 mice each.

Two-tailed unpaired t-test with Welch's correction (B)

Scale bars, 50 um.

Supplementary Figure 5: RFP reporter protein is expressed in AOM/DSS tumors in *Acta2*-RFP mice.

(A) Scheme for the experimental course of azoxymethane (AOM)/ dextran sulfate sodium (DSS)-induced colorectal carcinogenesis, using *Acta2*-RFP mice. RFP, Red Fluorescent Protein.

(B) Representative picture showing RFP fluorescence in colorectal tumors from AOM/DSS-treated *Acta2*-RFP mice. White arrowheads denote RFP expression. Note that RFP was expressed by spindle-shaped fibroblastic cells in the tumor. n ≥ 5 mice. Scale bar, 50 um.

Supplementary Figure 6: Validation of bone marrow-derived cell engraftment in the bone marrow of recipient mice.

(A) Experimental schematic depicting the bone marrow transplantation experiment and the following AOM/DSS treatment. Lethally irradiated C57B/6 wild-type (WT) recipient mice were transplanted with bone marrow cells from the *Acta2*-RFP donor mice. Before AOM/DSS administration was commenced, recipient mice were given 12-19 weeks for recovery and engraftment post bone marrow transplantation. Gy, Gray.

(B) qPCR for RFP using genomic DNA isolated from the recipient mice. To prepare a negative control for RFP genomic DNA from the bone marrow, wild-type recipient mice were transplanted with bone marrow cells from wild-type mice (WT→WT).

n = 3 (WT→WT) and 11 mice (Acta2-RFP→WT). A.U., Arbitrary Unit.

Mean ± s.e.m. Mann-Whitney U-test (B).

Supplementary Figure 7: *Lepr*-lineage stromal cells undergo proliferation and myofibroblastic differentiation at the expense of *Lepr* expression during colorectal carcinogenesis.

(A) Representative low-power magnification picture of an AOM/DSS tumor in a *Lepr*-Cre; Rosa26-tdtomato mouse immunostained with ACTA2. The number of $ACTA2^+$ cells and *Lepr*-lineage cells are increased in the tumor (T) compared with the normal colon (N). White dotted lines denote a border between the tumor and normal colon.

(B) Quantification of the ratio of $ACTA2^+$ cells in *Lepr*-$lineage^+$ cells ($tdtomato^+$ cells). 4 HPFs/mouse. n = 3 mice.

(C, D) Immunofluorescence for tdtomato and BrdU using the normal mucosa and AOM/DSS tumors in BrdU-treated *Lepr*-Cre; Rosa26-tdtomato mice. **(C)** Representative pictures. Yellow arrowheads denote *Lepr*-lineage proliferating cells ($tdtomato^+BrdU^+$ cells). **(D)** Quantification of *Lepr*-lineage proliferating cells in total *Lepr*-lineage cells. 4 HPFs/mouse. n = 3 mice.

(E, F) Combined *Lepr* single-molecule fluorescent *in situ* hybridization (smFISH) and tdtomato immunofluorescence (IF), showing that active expression of *Lepr* is decreased in *Lepr*-lineage cells in AOM/DSS tumors. **(E)** Representative pictures. Yellow arrowheads denote *Lepr*-lineage cells that actively express *Lepr* transcripts (*Lepr* $smFISH^+$ tdtomato IF^+ cells). Red arrowheads denote *Lepr*-lineage cells that do not actively express Lepr transcripts (*Lepr* $smFISH^-$ tdtomato IF^+ cells). Boxed areas are magnified in the insets. **(F)** Quantification of the ratio of *Lepr*-expressing cells in *Lepr*-lineage cells. 4 HPFs/mouse. n = 3 mice.

Two-tailed unpaired t-test with Welch's correction (B, D, and F).

Scale bars, 100 um (A), and 50 um (C and E).

Box plots have whiskers of maximum and minimum values; the boxes represent first, second (median), and third quartiles.

Supplementary Figure 8: Fibroblast maker genes are highly expressed in a FACS-purified CD45$^-$, Ter119$^-$, CD31$^-$ and EPCAM$^-$ colonic mesenchymal cell population.

Quantitative reverse-transcription polymerase chain reaction (qRT-PCR) for known marker genes in the fluorescence-activated cell sorting (FACS)-purified normal colonic cell populations was performed, followed by hierarchical clustering. n = 3 mice.

Ptprc, the gene name for CD45.

Supplementary Figure 9: Immunohistochemistry data in the Human Protein Atlas show that six candidate proteins are highly expressed in the human CRC stroma compared with cancer cells.

Histopathological analysis was performed for genes selected in Figure 4B(3) to examine whether the protein expression was observed in human CRC tissue sections. Immunohistochemistry pictures for human CRC samples were obtained from the Human Protein Atlas. Red arrowheads denote protein expression in the stroma. Yellow dotted lines indicate borders between epithelial cells and the stroma.

IHC, immunohistochemistry; E, epithelial cells (cancer cells) as visualized by hematoxylin counterstaining; S, stroma.

Supplementary Figure 10: Immunohistochemistry for several candidate genes in mouse colonic tissues did not confirm their stroma-specific protein expression, except for MCAM.

Representative immunohistochemistry (IHC) images for several candidate genes listed in **Figure 4B(4)**. Immunohistochemistry data for MCAM is shown in **Figure 4C**.

Note that immunohistochemistry for FOXS1, NXN, and PCDHB5 was not performed because of the lack of published immunohistochemistry-grade anti-mouse antibodies that could selectively stain the stroma. P14, postnatal day 14.

Scale bar, 50 um.

Supplementary Figure 11: *MCAM* is highly expressed in endothelial cells and CAFs in mouse and human CRC.

(A, B) MCAM is expressed by $CD31^+$ endothelial cells and $ACTA2^+$ CAFs in AOM/DSS tumors. Co-immunofluorescence for MCAM and lineage-marker proteins was performed. **(A)** Representative images. Yellow, green, and red arrowheads denote double-positive cells, MCAM single-positive cells, and lineage-marker single-positive cells, respectively. **(B)** Quantification of MCAM positivity in each lineage. 3 HPFs/mouse, n = 3 mice each.

(C) *MCAM* transcript levels in a cDNA (complementary DNA) expression microarray from fluorescence-activated cell sorting (FACS)-purified cells from human primary CRC tissues (GSE39396). n = 6 patients each. One-way ANOVA followed by Tukey's post-hoc multiple comparisons. **, P = 0.0017; ***, P = 0.0005; ****, P < 0.0001.

(D) Principle component (PC) analysis of *MCAM* expression levels using single-cell RNA-seq data from human normal colorectal mucosa and primary CRC (GSE81861). Dotted white lines encircle a cluster of endothelial cells or fibroblasts.

n = 375 cells from CRC tissues obtained from 11 patients, and 215 normal mucosa cells from 7 of the patients.

CPM, Counts Per Million.

Box plots have whiskers of maximum and minimum values; the boxes represent first, second (median), and third quartiles.

Supplementary Figure 12: Analysis of single-cell RNA-seq data from human colonic mesenchymal cells reveal that *MCAM* is highly expressed by myofibroblasts, pericytes, and endothelial cells as well as glial cells.

(A-E) t-distributed stochastic neighbor embedding (t-SNE) plot showing human colonic mesenchymal cell subpopulations. ScRNA-seq data from magnetic-activated cell sorting (MACS)-purified colonic mesenchymal cells ($EPCAM^-$, $CD45^-$, and $CD235a^-$ cells) from healthy donors and ulcerative colitis patients were analyzed (GSE114374). n = 4341 cells from 5 healthy donors and 4898 cells from 5 ulcerative colitis patients.

Cluster annotations **(A).** Expression levels of *MCAM* **(B)**, myofibroblastic marker genes, *ACTA2* and *MYH11* **(C),** *PDGFRB* **(D)**, and *PECAM1* **(E)** are shown.

Supplementary Figure 13: *Lepr*-lineage intestinal stromal cells, but not *Grem1*-lineage cells or *Islr*-lineage cells, are a major contributor to MCAM$^+$ cancer-associated stromal cells in AOM/DSS tumors.

(A, B) Immunofluorescence for MCAM was performed in AOM/DSS tumors from *Lepr*-Cre; Rosa26-tdtomato mice, *Grem1*-CreERT2; Rosa26-ZsGreen mice, and *Islr*-CreERT2; Rosa26-tdtomato mice. **(A)** Representative pictures. Note that a representative image for *Lepr*-Cre; Rosa26-tdtomato mice is shown in **Figure 4J**. **(B)** Quantification of the lineage-marker$^+$ cells in total MCAM$^+$ cells. 4 HPFs/mouse, n = 3 mice each.

Scale bars, 50 um.

Kruskal-Wallis test followed by Dunn's multiple comparisons test.

Box plots have whiskers of maximum and minimum values; the boxes represent first, second (median), and third quartiles.

Supplementary Figure 14: *MCAM* expression is increased during human CRC carcinogenesis.

(A) Violin plots depicting *MCAM* expression in cDNA expression microarray data from human normal colon mucosa and primary colon adenocarcinoma (GSE39582)[2]. n = 19 (normal colon mucosa) and 566 patients (primary colon adenocarcinoma).

(B) Violin plots depicting *MCAM* expression in cDNA expression microarray data from human colorectal adenoma and primary colorectal adenocarcinoma (GSE17538)[5]. n = 6 (colorectal adenoma) and 232 patients (primary colorectal adenocarcinoma).

False delivery rate (FDR)-adjusted P-values are shown.

Solid black lines, median; Dotted black lines, quartiles.

Supplementary Figure 15: *MCAM* transcript levels positively correlate with expression levels of TGF-β target genes in the TCGA dataset of human CRC.

MCAM transcript levels positively correlate with expression levels with TGF-β target genes**,** *SERPINE1* (left) and *CTGF* (right), in the TCGA dataset. n = 511 patients with CMS1-4 CRC.

Solid line, linear regression; dotted lines, 95% confidence interval.

Spearman correlation.

Supplementary Figure 16:High *MCAM* expression is associated with poor survival in patients with CRC.

Kaplan-Meier survival curves showing survival rates of CRC patients classified according to *MCAM* expression levels. Three independent expression microarray datasets from human CRC patients were analyzed.

Log-rank test.

Supplementary Figure 17: A working hypothesis for the origins and contribution of the CRC stroma.

Our work suggests that *Lepr*-lineage intestinal stromal cells are a major contributor to ACTA2^{+} and MCAM^{+} stromal cells in AOM/DSS tumors. The *Lepr*-lineage intestinal stromal cells undergo proliferation and myofibroblastic activation at the expense of *Lepr* expression during CRC carcinogenesis. Remarkably, no ACTA2^{+} CAFs arose through epithelial-mesenchymal transition (EMT) of *Krt19*-lineage cells or recruitment from the bone marrow, at least, in the AOM/DSS model of CRC. Approximately half of ACTA2^{+} CAFs and 75% of MCAM^{+} cancer-associated stromal cells are new cells generated through proliferation. Whether distinct CAFs could undergo phenotypic interconversion during CRC progression warrants further investigation.

Supplementary Methods

Antibodies

The following antibodies were used in this study. Rabbit monoclonal anti-MCAM (1:500 for immunohistochemistry(IHC) and immunofluorescence(IF), ab75769, Abcam), Rabbit polyclonal anti-RFP (1:500 for IF, 600-401-379, Rockland), Goat polyclonal anti-mouse PDGFRA (1:50 for IF,AF1062, R&D systems), Mouse monoclonal anti-αSMA (1:500 for IHC and IF, clone 1A4, Dako), Rabbit polyclonal anti-αSMA (1:500 for IF, ab5694, Abcam), Rat monoclonal anti-BrdU (1:600 for IF, ab6326, Abcam), Rat monoclonal anti-EPCAM (1:100 for IF, 14-5791-81, eBioscience), Rabbit monoclonal anti-Ki67 (1:200 for IF, ab16667, Abcam), Mouse monoclonal ZsGreen (1:1000 for IF, TA180002, OriGene), Rat monoclonal anti-CD31 (1:50 for IF, DIA-310, Dianova), Rat monoclonal anti-CD45-FITC (1:50 for IF,103108, BioLegend), Rabbit polyclonal anti-FJX1 (1:800 for IHC, PA5-63687, Invitrogen), and Rabbit polyclonal anti-NGFR (1:1500 for IHC, ab8874, Abcam).

Immunohistochemistry (IHC) and immunofluorescence (IF)

Tissues were either fixed with formalin overnight followed by dehydration with 70% ethanol and paraffin-embedding, or fixed with 4% paraformaldehyde overnight followed by dehydration with 30% sucrose and embedding with optimal cutting temperature (O.C.T.) compound. Formalin-fixed and paraffin-embedded tissue sections were deparaffinized with xylene and rehydrated with phosphate-buffered saline (PBS), followed by antigen retrieval by boiling samples in antigen retrieval buffer (pH 6, H-3300; Vector Laboratories) for 30 min.

For IHC, inactivation of endogenous peroxidase was performed with 0.5% H_2O_2 in methanol for 15 min, followed by washing with PBS. Then, sections were treated with blocking buffer (X0909, Dako) for 30 min, incubated with the indicated primary antibodies overnight at 4°C and washed with PBS. Sections were incubated with horseradish peroxidase (HRP)-polymer secondary antibody (ab214879 or ab214880, both from Abcam) for 30 min, followed by signal detection with diaminobenzidine (DAB) solution (K3468, DAKO).

For IF studies, sections were treated with blocking buffer (X0909, Dako) for 30 min, incubated with the indicated primary antibodies overnight at 4°C and washed with PBS. Sections were then incubated with Alexa Fluor 488/594/647-conjugated secondary antibodies (All from Thermo Fisher Scientific) for 1 h at room temperature. The sections were then mounted with ProLong Gold antifade reagent containing 4'6-diamidino-2-phenylindole (DAPI; Thermo Fisher Scientific), and fluorescence was examined using a confocal laser-scanning microscope (TCS SP8 MP, Leica) or an inverse immunofluorescence microscope BZ-X710 (Keyence) with optical sectioning.

Combined single-molecule fluorescent *in situ* hybridization (smFISH) and immunofluorescence (IF)

Combined smFISH and IF were implemented by first performing smFISH, followed by IF.

ISH analyses were performed on formalin-fixed and paraffin-embedded mouse tissue samples using RNAscope technology (RNAscope Multiplex Fluorescent Reagent Kit v2, Advanced Cell Diagnostics; ACD) following the manufacturer's instructions. Paraffin blocks were cut into 4-5 um sections. Briefly, tissue sections were baked in a dry oven (HybEZ II Hybridization System, ACD) at 60°C for 1 h and deparaffinized, followed by incubation with Pretreat 1, 2, and 3 (ACD). Slides were incubated with relevant probes for 1 h at 40°C, followed by successive incubations with Amp1 to 6 reagents. Staining was visualized with DAB or TSA Plus Cyanine 5 (NEL745001KT, PerkinElmer). For quantification, cells with no ISH staining were defined as "negative," and cells that show 1 dot/cell or more were defined as "positive." *In situ* hybridization (RNAscope) probe used in the study was mouse *Lepr* (Entrez Gene ID: 16847, target region 1361 - 2317, catalog number 402731).

After smFISH, the sections were blocked with blocking buffer (X0909, Dako) and then incubated with a primary antibody overnight at 4 °C. The sections were washed in 1x T-PBS 3 times and then incubated with Alexa Fluor 555-conjugated secondary antibody (Thermo Fisher Scientific) for 60 min at room temperature. The sections were then mounted with ProLong Gold antifade reagent containing 4'6-diamidino-2-phenylindole (DAPI; Thermo Fisher Scientific), and fluorescence was examined using

an inverse immunofluorescence microscope BZ-X710 (Keyence, Japan) with optical sectioning.

The Human Protein Atlas data

All immunohistochemistry images in Supplementary Figure 9 were obtained from the Human Protein Atlas[6] (https://www.proteinatlas.org/). Genes that were highly expressed in the CRC stroma compared to cancer cells (as visualized by DAB staining and hematoxylin counterstaining) were selected by a clinical pathologists. Immunohistochemistry data for COX4I2, NDUFA4L2, and SHC4 were not available in the Human Protein Atlas (website accessed in April, 2020), and thus were not included in the analysis.

Quantitative image analysis

In all histopathological quantification using the normal colorectal tissues in human and mouse, only lamina propria regions were evaluated. Quantification of fluorescent images was performed using consistent brightness and contrast levels in ImageJ[7]. In Figure 5F, a total score (the sum of intensity score and proportion score) was given to each of the 3-4 replicates/patient by a clinical pathologist. A patient with an average total score of ≥ 3.3 was defined as MCAM-high. The optimal cutoff was determined using the X-tile software[8].

Cell Culture

A mouse colonic fibroblast cell line, YH2 cells, was generously provided by Professor Tony Burgess (The Walter and Eliza Hall Institute of Medical Research). YH2 cells were cultured in Dulbecco's modified Eagle's medium (DMEM; Sigma) supplemented with 10% fetal bovine serum (FBS; Gibco). YH2 cells were stimulated with 10 ng/ml of recombinant human TGF-beta 1 (240-B-002, R&D systems), DMSO, and/or 10 uM of Galunisertib (ADV465749242; AChemBlock) in DMEM containing 1%FBS for 24 hours, as described[9].

All cell lines used were routinely screened for Mycoplasma contamination by MycoAlert Mycoplasma Detection Kit (LT07-118, Lonza).

Mouse model of genetic fate-mapping

Lepr-Cre (JAX Stock No. 008320); Rosa26-LSL (LoxP-stop-LoxP)-tdtomato (JAX Stock No. 007909), *Grem1*-CreERT2 (JAX Stock No. 027039); Rosa26-LSL (LoxP-stop-LoxP)-ZsGreen (JAX Stock No. 007906), *Islr*-CreERT2[10]; Rosa26-LSL-tdtomato, *Acta2*-RFP[11], and *Krt19*-Cre[12]; Rosa26-mT/mG (JAX Stock No. 007676) were used for lineage tracing experiments. *Grem1*-CreERT2 and *Islr*-CreERT2 mice were subcutaneously injected with 2 mg of tamoxifen (T5648, Sigma) dissolved in peanut oil on postnatal day 6.

An azoxymethane (AOM)/ dextran sulfate sodium (DSS) mouse model of CRC

A colitis-associated AOM/DSS mouse model of CRC was generated as described[13]. Briefly, AOM (Sigma, A5486; 10mg/kg) was administered by intraperitoneal injection to 6-12 week old mice. One week later, the mice commenced the first of three cycles of DSS to induce inflammation (MP Biomedicals, 160110; Molecular Weight 36,000-50,000 Da). Each cycle was comprised of 5 days 2 - 3% DSS (weight/volume) then 16 days of normal drinking water. To monitor tumor burden, mice were routinely colonoscoped, as previously described[14]. Once mice showed endoscopically visible tumors (for *Lepr*-Cre and *Grem1*-CreERT2 mice) or were finished with the last cycle of DSS administration (for *Islr*-CreERT2 mice), mice were started on BrdU (10280879001, Sigma). Mice received one intraperitoneal injection of BrdU (50 mg/kg) and then were administered continuous BrdU in drinking water (1 mg/ml). 10 weeks after AOM injection, mice were euthanized, and colons were removed, opened longitudinally. Colon tumor tissues were used for RNA isolation, followed by RNA-sequencing. For histopathological analysis, colon tumors and adjacent non-neoplastic tissues were fixed in 10% formalin or 4% paraformaldehyde overnight.

Bone marrow transplantation

Male and female C57BL/6 wild-type (WT) mice and *Acta2*-RFP mice were maintained in pathogen-free conditions in the SAHMRI Bioresources Animal Facility. The C57BL/6 WT mice were used at 8-12 weeks of age, and the *Acta2*-RFP mice were used at 14-21 weeks of age. Mice were irradiated in a filter top cage in a RS 2000 X-Ray Irradiator (Rad Source). The mice were exposed to a single lethal dose of 10 grays. On the day of irradiation, donor mice (C57BL/6 WT or *Acta2*-RFP) were culled, and bone marrow cells were harvested from femurs and tibia and were resuspended in PBS. 5 - 7.9 x 10^6 bone marrow cells were injected into the tail vein of recipient C57BL/6 WT mice using a 30G needle. Bone marrow recipient mice were placed on a prophylactic course of antibiotics commencing three days prior to irradiation. Mice received an initial subcutaneous injection of Baytril (10mg/kg), followed by Baytril Oral Solution administered in drinking water (0.28mg/ml) for 5-6 weeks. Fresh antibiotics were prepared weekly.

To confirm engraftment of bone marrow-derived cells in the bone marrow of the recipient mice, genomic DNA was extracted from harvested bone marrow samples using the QIAamp Mini DNA Blood kit before qPCR for RFP and *Bcl2*. *Bcl2* was used as a reference gene to normalize the total DNA amount, as described[15]. To determine the percentage of engraftment, a standard curve was prepared from known concentrations of DsRed/wild-type DNA (from 0.26%-100%). The mean values of delta-Ct (CtDsRed-CtBcl2) were plotted against the known concentrations of DNA using linear regression fitting. The percentage of DsRed expression in bone marrow samples from the experimental animals was then calculated against the curve. The following primers were used for qPCR. *Bcl2* forward, 5'- AAGCTGTCACAGAGGGGCTA -3'; *Bcl2* reverse, 5'- CAGGCTGGAAGGAGAAGATG -3'; RFP forward, 5'- CCCGACTACAAGAAGCTGTCCTTC -3'; RFP reverse, 5'- CGATGAACTTCACCTTGTAGATGAAGCAG -3'.

Mouse genotyping

Genomic DNA extracted from mouse ear or tails was used for PCR genotyping. The sequences of the primers were as follows:

Lepr-Cre forward, 5'-TTAATCCATATTGGCAGAACGAAAACG-3'; *Lepr*-Cre reverse, 5'-CAGGCTAAGTGCCTTCTCTACA-3'.

Lepr-Wild-Type (WT) forward, 5'-CGCACAGTCACAAGATAATGG -3'; *Lepr*-WT reverse, 5'-GCTCTACTGGAATGGAACCTT-3'.

Acta2-RFP forward, 5'-AGATCCACCAGGCCCTGAA-3'; *Acta2*-RFP reverse, 5'-GTCTTGAACTCCACCAGGTAG-3'

Islr-CreERT2 forward, 5'-ACACACGACCTTGGCAAGTCCCAGC-3'; *Islr*-CreERT2 reverse, 5'-CGATCCCTGAACATGTCCATCAGG-3';

Islr-WT forward, 5'-ACACACGACCTTGGCAAGTCCCAGC-3'; *Islr*-WT reverse,5'-GTCTGCAATCTGGAAGCCATACTTCTCC-3';

Grem1-CreERT2 forward, 5'-TTAATCCATATTGGCAGAACGAAAACG-3'; *Grem1*-CreERT2 reverse, 5'-CAGGCTAAGTGCCTTCTCTACA-3'.

Rosa26-LSL-tdtomato forward, 5'-AGATCCACCAGGCCCTGAA-3'; Rosa26-LSL-tdtomato reverse, 5'-GTCTTGAACTCCACCAGGTAG-3';

Rosa26-LSL-ZsGreen forward, 5'- GCGCCGTGTGCATCTG-3'; Rosa26-LSL-ZsGreen reverse, 5'-ACTCGTGGTACATGCAGTTCTC-3';

Rosa26-WT forward, 5'-TTCCCTCGTGATCTGCAACTC-3'; Rosa26-WT reverse, 5'-CTTTAAGCCTGCCCAGAAGACT-3' (used for Rosa26-LSL-tdtomato and Rosa26-LSL-ZsGreen genotyping)

RNA-sequencing from fluorescence-activated cell sorting (FACS)-purified mouse colonic cells

Four 8-week-old adult mice (2 males and 2 females), four postnatal day 14 mice (2 males and 2 females), and four AOM/DSS-treated mice (2 males and 2 females) were used to isolate colonic

cells. Colons were washed three times in Hank's Balanced Salt Solution (H9394, Sigma) and cut into 0.5 mm pieces with a pair of scissors. Colonic tissue pieces were spun at 450 g for 4 minutes. After discarding the supernatant, the colonic tissues were enzymatically digested with 35.5 mg of type IV collagenase (17104019, Life Technologies) and 1 mg of dispase (17105041, Life Technoogies) in 10 ml of HBSS, at 37 °C for 45 minutes. The digested colonic cells were then filtered through a 40-µm-nylon strainer to remove cell clumps. Cells were stained with the following antibodies: anti-EPCAM-Alexa Fluor 488 (118210, Biolegend), anti-CD31-Alexa Fluor 594 (102520, Biolegend), anti-CD45-APC (103112, Biolegend), and anti-TER119-APC (116212, Biolegend). Dead cells were excluded based on their positive staining for DAPI. FACS-sorting of $CD45^+$ immune cells ,$EPCAM^+$ epithelial cells, $CD31^+$ endothelial cells, and $EPCAM^-CD31^-CD45^-TER119^-$ stromal cells was performed using FACSAria Fusion (BD Bioscience). Data analysis was performed using FlowJo version 10.5.3 (LLC, USA).

Collected cells were spun at 800 g for 5 minutes.Cells were lysed with 1 ml of trizol, and RNA was isolated using PicoPure™ RNA Isolation Kit (KIT0204, Life Technologies) according to the manufacture's protocol. DNase treatment were performed with RNase-Free DNase Set (79254, Qiagen) on PicoPure spin columns.

The purity of the isolated RNA was assessed using Bioanalyzer (Agilent, US) to ensure high quality RNA (RNA integrity number > 7). 200-250 ng of RNA was used for stranded library preparation with RiboZero ribosomal RNA depletion (Kapa). Whole transcriptome 1 x 75 bp read sequencing was performed on a NextSeq 500 (Illumina) by the Australian Cancer Research Facility (ACRF). The RNA-sequencing reads were were trimmed for adaptor sequence, low-quality sequence removed and remaining reads aligned to a mouse reference genome (GRCm38 or UCSC mm10), using STAR aligner 2.4.2a allowing 2 mismatches. Gene expression levels were quantified using STAR with quantmode option. For differential expression (DE) analysis, read counts were normalised by the trimmed mean of M values (TTM) method implemented in R package edgeR (version 3.28.0). Differentially upregulated genes were defined as genes that

showed log2 fold change greater than or equal to 1 and false discovery rate less than 0.10. The RNA-seq data are available at the Gene Expression Omnibus (GEO) under accession code GSE162508.

Analyses of the Cancer Genome Atlas (TCGA) data

10-year-survival analyses of the the Cancer Genome Atlas (TCGA) data were performed on the R program with survival and survminer packages (https://CRAN.R-project.org/package=survminer) using the GDC colorectal cancer patient RNAseq data (https://portal.gdc.cancer.gov/). Gene expression levels analyzed by RSEM (RNA-Seq by Expectation-Maximization) were downloaded from the website and then normalized using the voom function[16]. Optimal cutoff levels for survival analyses were determined using survminer packages (https://CRAN.R-project.org/package=survminer). Log-rank tests were performed using the R survival package (https://cran.r-project.org/web/packages/survival/index.html). In Figure 4B(2), a median expression level were used as a cutoff value.

The Consensus Molecular Subtypes (CMS) labels were downloaded from the supplementary materials of previous publications (n = 511 patients with CMS1-4 CRC)[1, 17]. Then, expression Z-scores for tumor samples were calculated based on the standard deviation and mean value for the normal colorectal tissues. Violin plots were then generated using the ggplot2 package (version 3.2.1). Spearman correlation coeffient analyses between MCAM and TGF-β target genes were perfomed using the Z-scores of each gene (n = 511 patients with CMS1-4 CRC).

Analyses of publicly available cDNA gene expression microarray datasets

Expression microarray data (GSE17538[5], 33113[4], 39396[18], 39582[2], and 41258[3]) and patient information were obtained from Gene Expression Omnibus (GEO; https://www.ncbi.nlm.nih.gov/geo/). Normalized gene expression levels for the following probes were used. P_200974_at, *ACTA2*; P_209955_s_at, *FAP*; P_215305_at, *PDGFRA*; P_216572_at,

FOXL1; P_209087_x_at, *MCAM* (GSE17538, 33113, 39582, and 41258); 209087_PM_x_at, *MCAM* (GSE39396). In GSE41258, primary colorectal cancer samples included in a previous analysis[3] were analyzed by choosing samples with a label of “Included in analysis; Yes” on the GEO website. Optimal cutoff levels for survival analyses were determined using survminer packages (https://CRAN.R-project.org/package=survminer).Survival analyses (Log-rank test) were performed using a R program with survival (https://cran.r-project.org/web/packages/survival/index.html). For differential expression analyses, false delivery rate (FDR)-adjusted P-values were calculated by GEO2R (https://www.ncbi.nlm.nih.gov/geo/geo2r).

Analyses of publicly available single-cell RNA-seq (scRNA-seq) data

ScRNA-seq data (GSE81861)[19] were directly downloaded from the GEO website (GEO; https://www.ncbi.nlm.nih.gov/geo/). Reference component analyses[19] was performed according to the description on the Github repository (https://github.com/GIS-SP-Group/RCA). FPKM values for *MCAM* were scaled by size and plotted to aid visualization of their expression levels. ScRNAseq data from GSE114374[20] were analysed using BBrowser2 (Version 2.4.10; BioTuring, US; https://bioturing.com/) using the default cell type annotations. ScRNAseq data from GSE132465[21] were analyzed on the User-friendly InteRface tool to Explore Cell Atlas (URECA) website (http://ureca-singlecell.kr).

Quantitative PCR

Total RNA was extracted using TRIzol reagent (Invitrogen) and an RNeasy Mini Kit (Qiagen). Purified RNA samples were reverse-transcribed using Transcriptor Universal cDNA Master (Roche) according to the manufacturer’s instruction, followed by the dilution of cDNA at 1:5. Quantitative reverse-transcription PCR (qRT-PCR) of the complementary DNAs (cDNAs) was performed with KAPA PROBE or SYBER FAST qPCR Master Mix (KAPABiosystems) and was run on a

QuantStudio 7 Flex Real-Time PCR System (Thermo Scientific). The data were analyzed using the 2-ΔΔCt method and normalized to *Gapdh* expression levels.

Probes or primers (generated by IDT) used in this study are as follows. Primers and *Ccl8* probes were designed using the Primer-BLAST online program[22].

Primers used in Figure 5D:

Mouse *Mcam* (Forward: 5'-GCCCTTGCAAGAGGAGGAGAA-3' , Reverse: 5'-ACTAGGCGTGCACTCAGAACA-3'), mouse *Acta2* (Forward: 5'- CTCTTCCAGCCATCTTTCATTG-3' , Reverse: 5'-AATGCCTGGGTACATGGTG-3'), and mouse *Gapdh* (Forward: 5'-CCTCGTCCCGTAGACAAAATG-3' , Reverse: 5'- TGTAGTTGAGGTCAATGAAGGG-3').

Probes used in Supplementary Figure 7:

Mouse *Cd2* (Mm.PT.58.42401764), mouse *Ptprc* (Mm.PT.58.7583849), mouse *Cdh5* (Mm.PT.58.8747496), mouse *Vwf* (Mm.PT.58.32874548), mouse *Grem1* (Mm.PT.58.11631114), mouse *Acta2* (Mm.PT.58.16320644), mouse *Fap* (Mm.PT.58.31960536), mouse *Epcam* (Mm.PT.58.11851150), mouse *Cdh1* (Mm.PT.58.41847659), and mouse *Gapdh* (Mm.PT.39a.1)

Statistical analysis

Comparison of 2 groups was performed using two-tailed unpaired t-tests or Mann–Whitney U tests. For multiple comparisons, we used analysis of variance (ANOVA) or Kruskal-Wallis test. For survival analyses, Kaplan-Meier survival estimation with a Log-rank (Mantel-cox) test was performed. Statistical analyses were conducted using GraphPad Prism 8.00 (GraphPad) or SPSS Statistics ver. 25 (IBM). P-values of less than 0.05 were considered statistically significant.

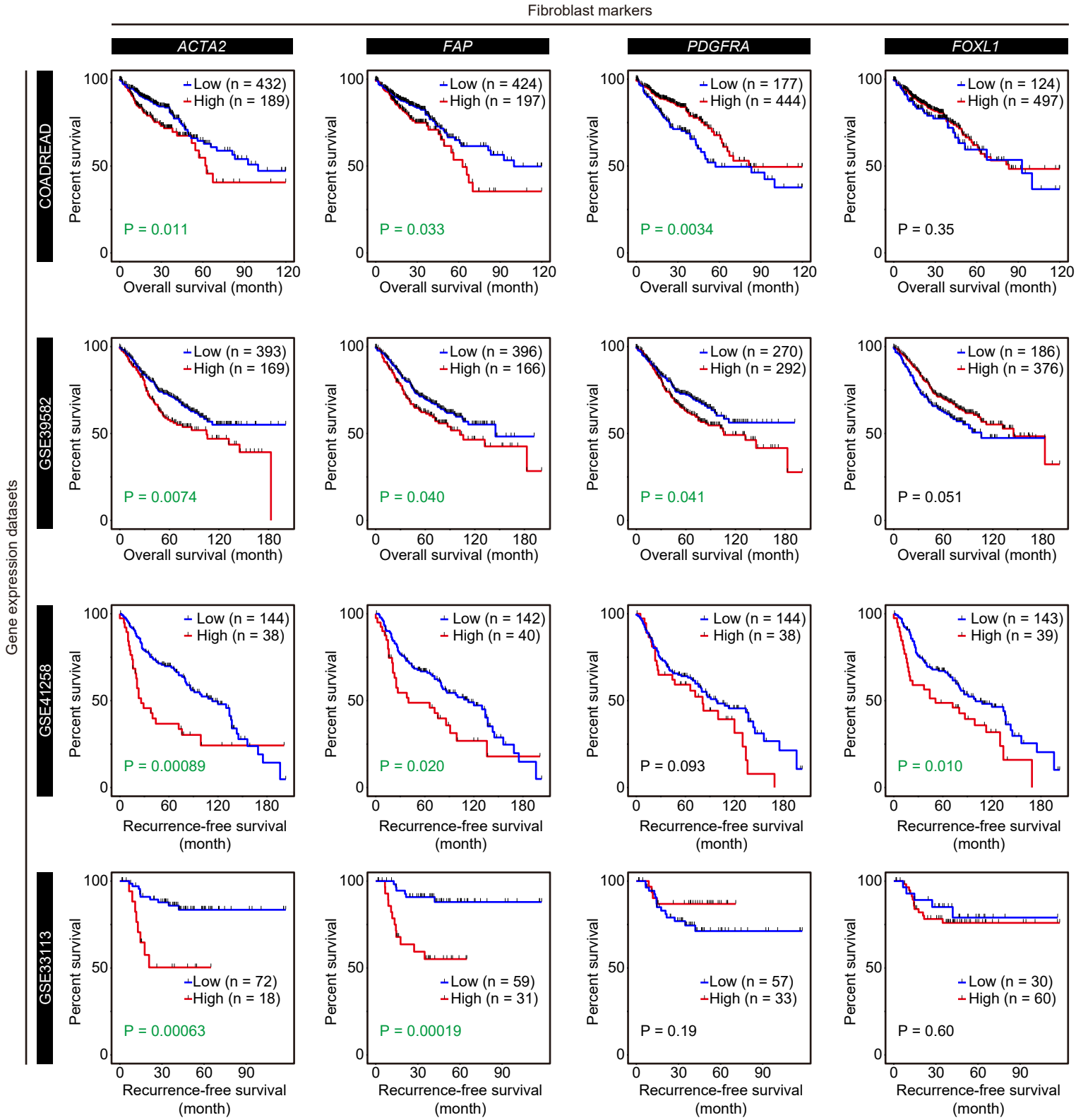
Data and materials availability

Data that support the findings of this study are available from the corresponding authors upon reasonable request. Noncommercially available materials described in this study may be obtained with a material transfer agreement (MTA). Requests for materials should be addressed to S.W.

Supplemental references

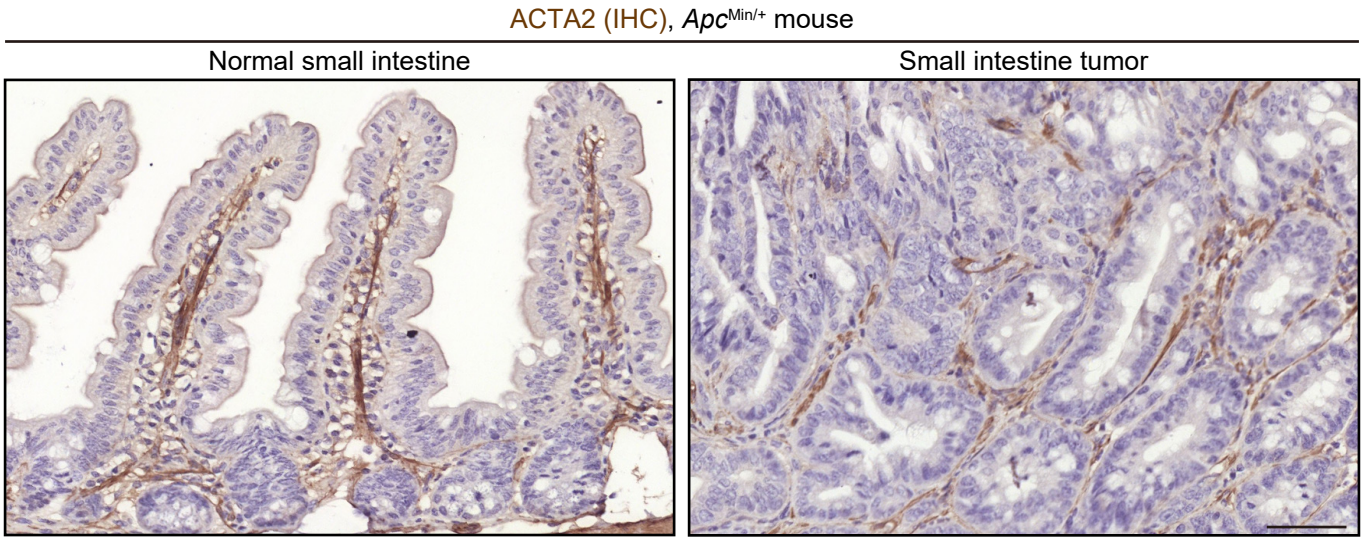
1. Cancer Genome Atlas N. Comprehensive molecular characterization of human colon and rectal cancer. Nature 2012;487:330-7.
2. Marisa L, de Reynies A, Duval A, et al. Gene expression classification of colon cancer into molecular subtypes: characterization, validation, and prognostic value. PLoS Med 2013;10:e1001453.
3. Sheffer M, Bacolod MD, Zuk O, et al. Association of survival and disease progression with chromosomal instability: a genomic exploration of colorectal cancer. Proc Natl Acad Sci U S A 2009;106:7131-6.
4. de Sousa EMF, Colak S, Buikhuisen J, et al. Methylation of cancer-stem-cell-associated Wnt target genes predicts poor prognosis in colorectal cancer patients. Cell Stem Cell 2011;9:476-85.
5. Smith JJ, Deane NG, Wu F, et al. Experimentally derived metastasis gene expression profile predicts recurrence and death in patients with colon cancer. Gastroenterology 2010;138:958-68.
6. Uhlen M, Fagerberg L, Hallstrom BM, et al. Proteomics. Tissue-based map of the human proteome. Science 2015;347:1260419.
7. Schneider CA, Rasband WS, Eliceiri KW. NIH Image to ImageJ: 25 years of image analysis. Nat Methods 2012;9:671-5.
8. Camp RL, Dolled-Filhart M, Rimm DL. X-tile: a new bio-informatics tool for biomarker assessment and outcome-based cut-point optimization. Clin Cancer Res 2004;10:7252-9.
9. Kobayashi H, Gieniec KA, Wright JA, et al. The balance of stromal BMP signaling mediated by GREM1 and ISLR drives colorectal carcinogenesis. Gastroenterology 2020.
10. Mizutani Y, Kobayashi H, Iida T, et al. Meflin-Positive Cancer-Associated Fibroblasts Inhibit Pancreatic Carcinogenesis. Cancer Res 2019;79:5367-5381.
11. Magness ST, Bataller R, Yang L, et al. A dual reporter gene transgenic mouse demonstrates heterogeneity in hepatic fibrogenic cell populations. Hepatology 2004;40:1151-9.

12. Asfaha S, Hayakawa Y, Muley A, et al. Krt19(+)/Lgr5(-) Cells Are Radioresistant Cancer-Initiating Stem Cells in the Colon and Intestine. Cell Stem Cell 2015;16:627-38.
13. Neufert C, Becker C, Neurath MF. An inducible mouse model of colon carcinogenesis for the analysis of sporadic and inflammation-driven tumor progression. Nat Protoc 2007;2:1998-2004.
14. Lannagan TRM, Lee YK, Wang T, et al. Genetic editing of colonic organoids provides a molecularly distinct and orthotopic preclinical model of serrated carcinogenesis. Gut 2019;68:684-692.
15. An N, Kang Y. Using quantitative real-time PCR to determine donor cell engraftment in a competitive murine bone marrow transplantation model. J Vis Exp 2013:e50193.
16. Ritchie ME, Phipson B, Wu D, et al. limma powers differential expression analyses for RNA-sequencing and microarray studies. Nucleic Acids Res 2015;43:e47.
17. Guinney J, Dienstmann R, Wang X, et al. The consensus molecular subtypes of colorectal cancer. Nat Med 2015;21:1350-6.
18. Calon A, Espinet E, Palomo-Ponce S, et al. Dependency of colorectal cancer on a TGF-beta-driven program in stromal cells for metastasis initiation. Cancer Cell 2012;22:571-84.
19. Li H, Courtois ET, Sengupta D, et al. Reference component analysis of single-cell transcriptomes elucidates cellular heterogeneity in human colorectal tumors. Nat Genet 2017;49:708-718.
20. Kinchen J, Chen HH, Parikh K, et al. Structural Remodeling of the Human Colonic Mesenchyme in Inflammatory Bowel Disease. Cell 2018;175:372-386.e17.
21. Lee HO, Hong Y, Etlioglu HE, et al. Lineage-dependent gene expression programs influence the immune landscape of colorectal cancer. Nat Genet 2020.
22. Ye J, Coulouris G, Zaretskaya I, et al. Primer-BLAST: a tool to design target-specific primers for polymerase chain reaction. BMC Bioinformatics 2012;13:134.

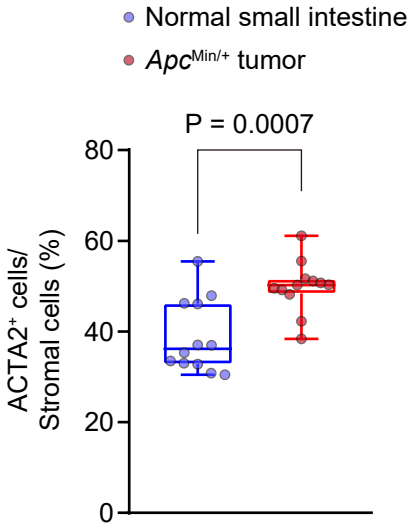


Kobayashi *et al.*, Supplementary Figure 1.

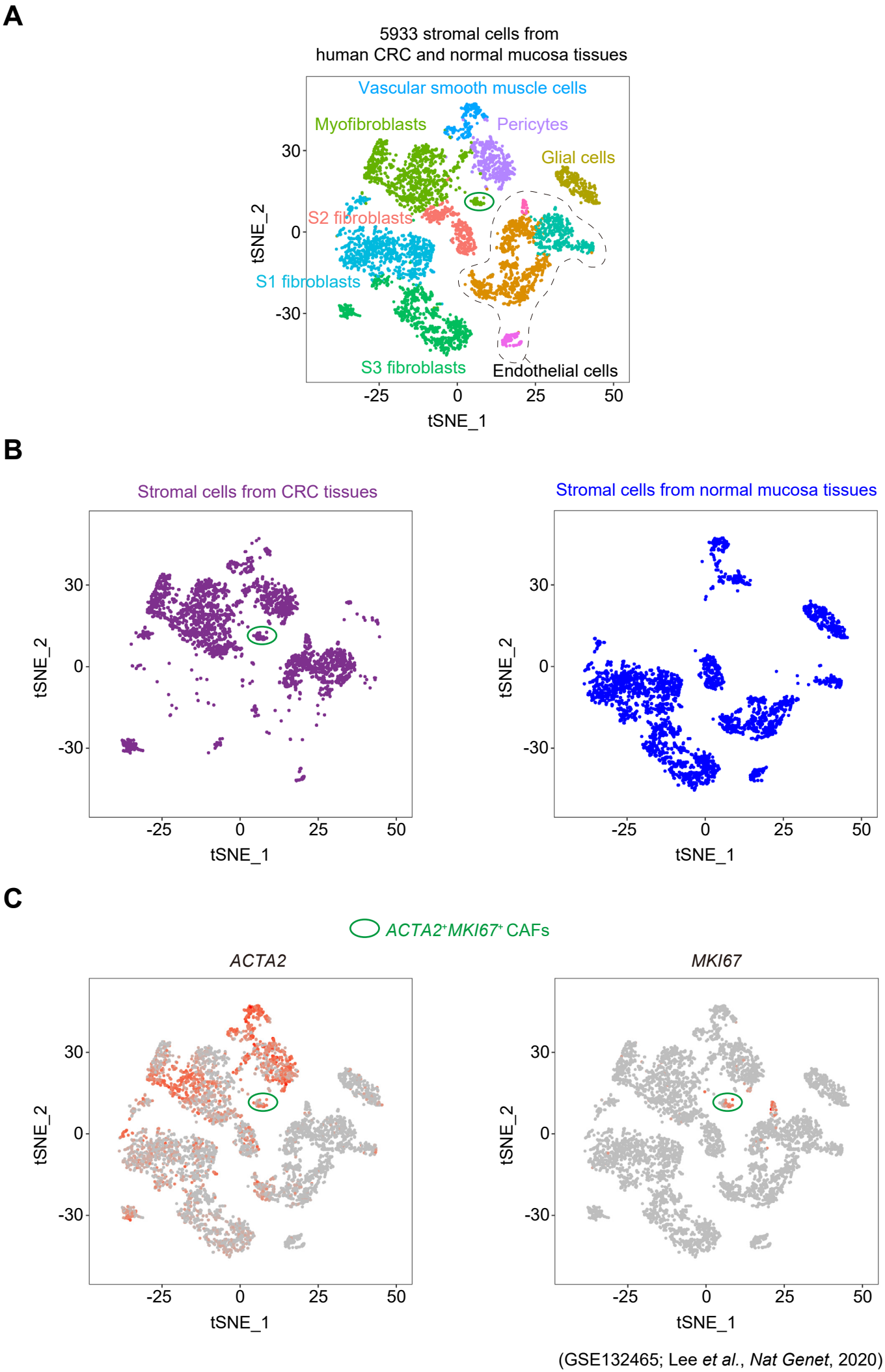
A



B

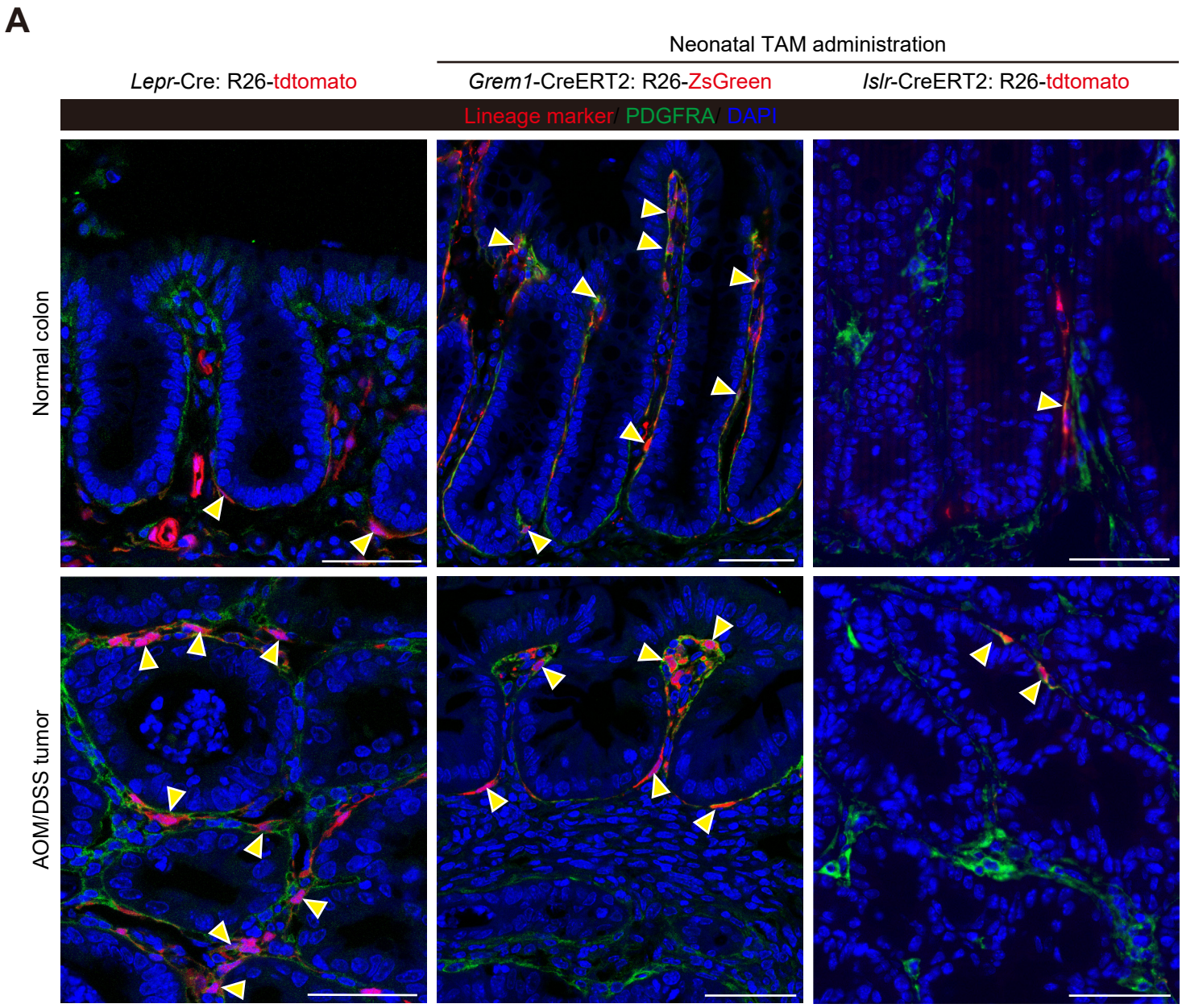


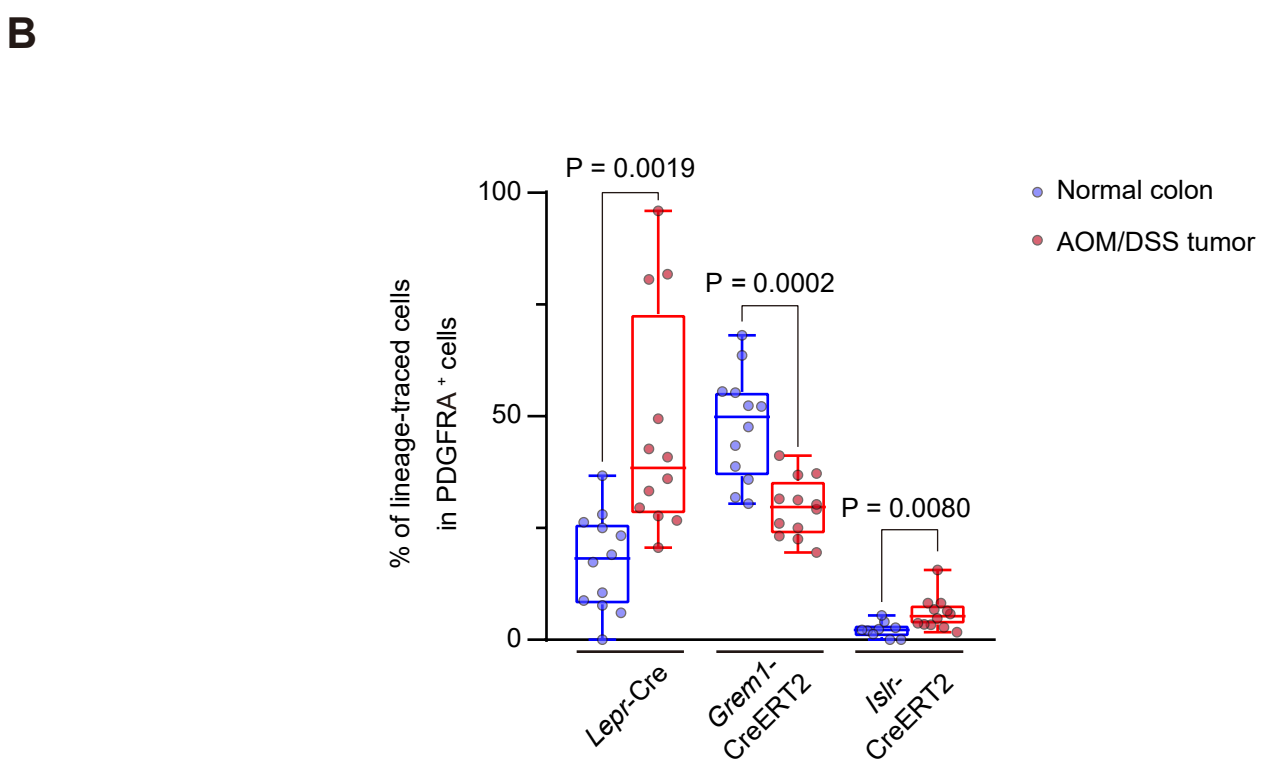
Kobayashi *et al.*, Supplementary Figure 2.



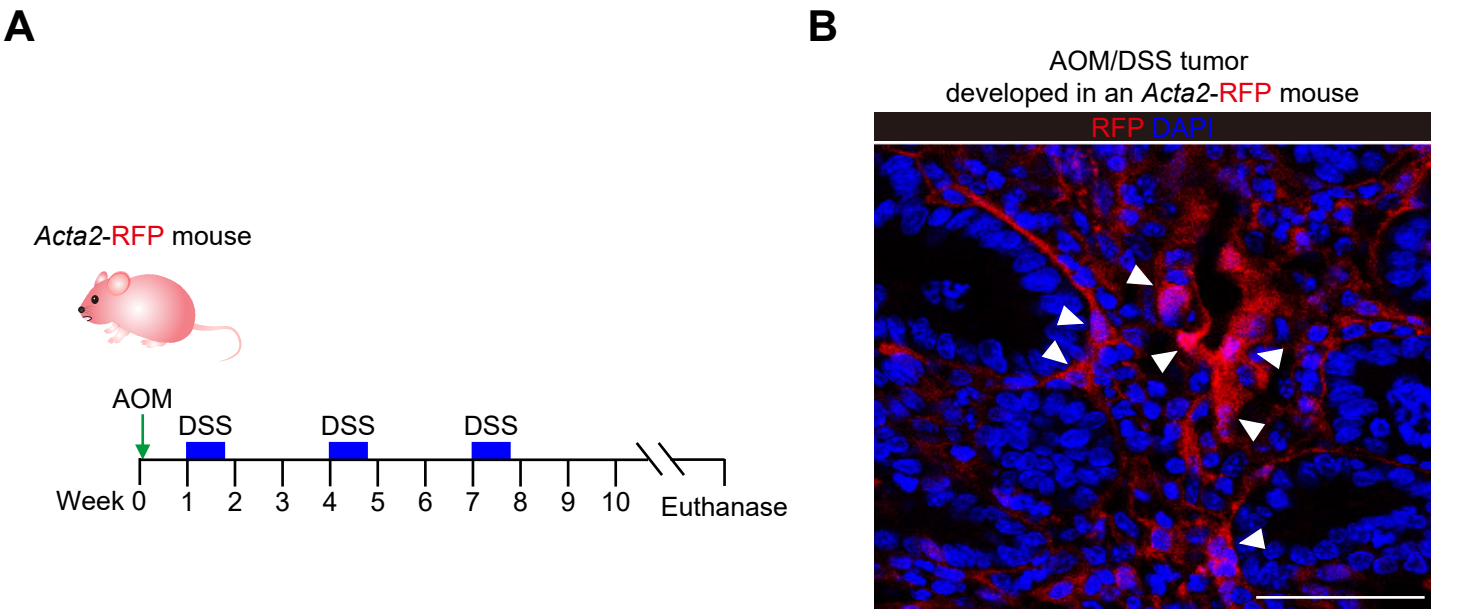
(GSE132465; Lee *et al.*, *Nat Genet*, 2020)

Kobayashi *et al.*, Supplementary Figure 3.

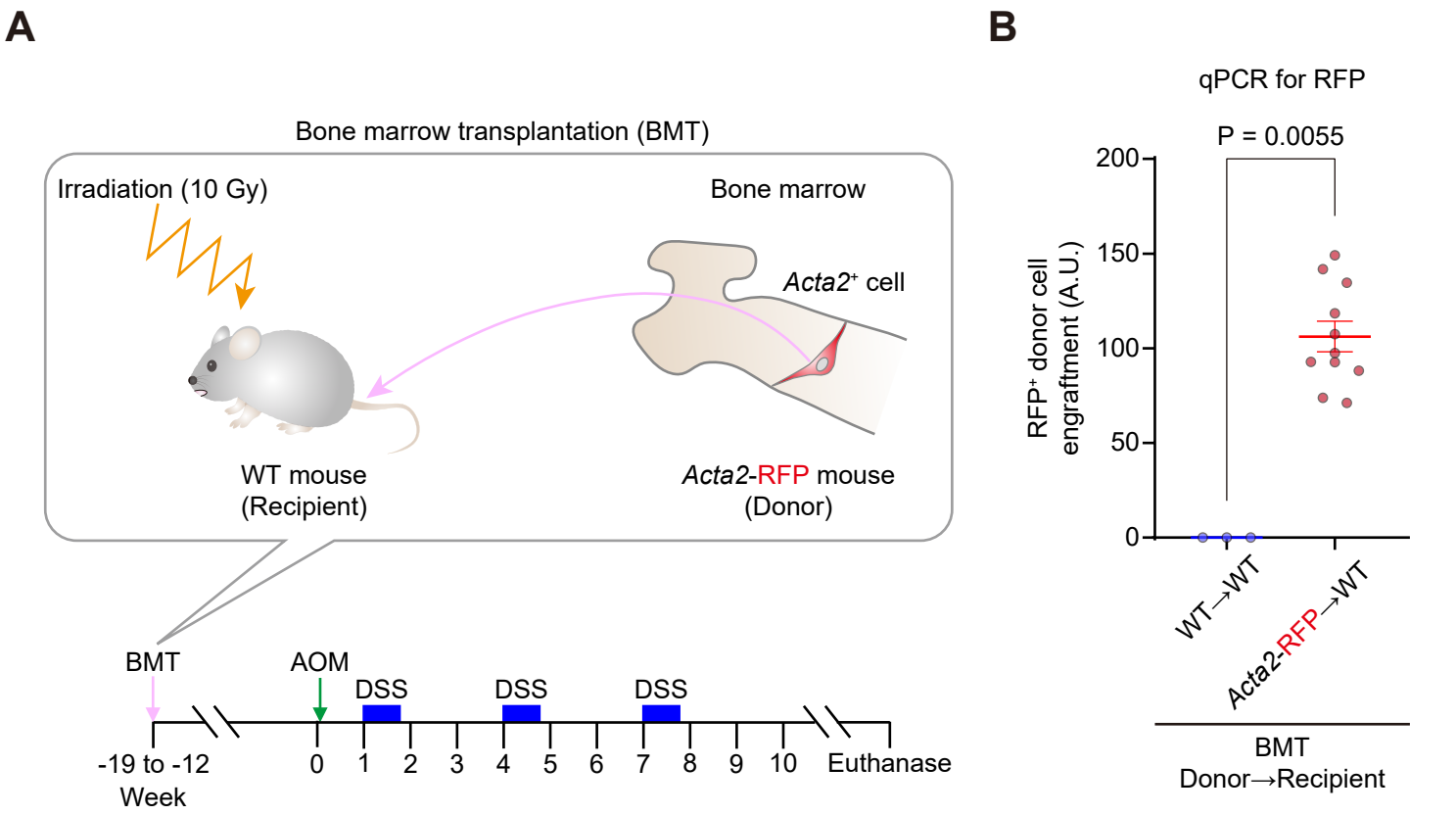




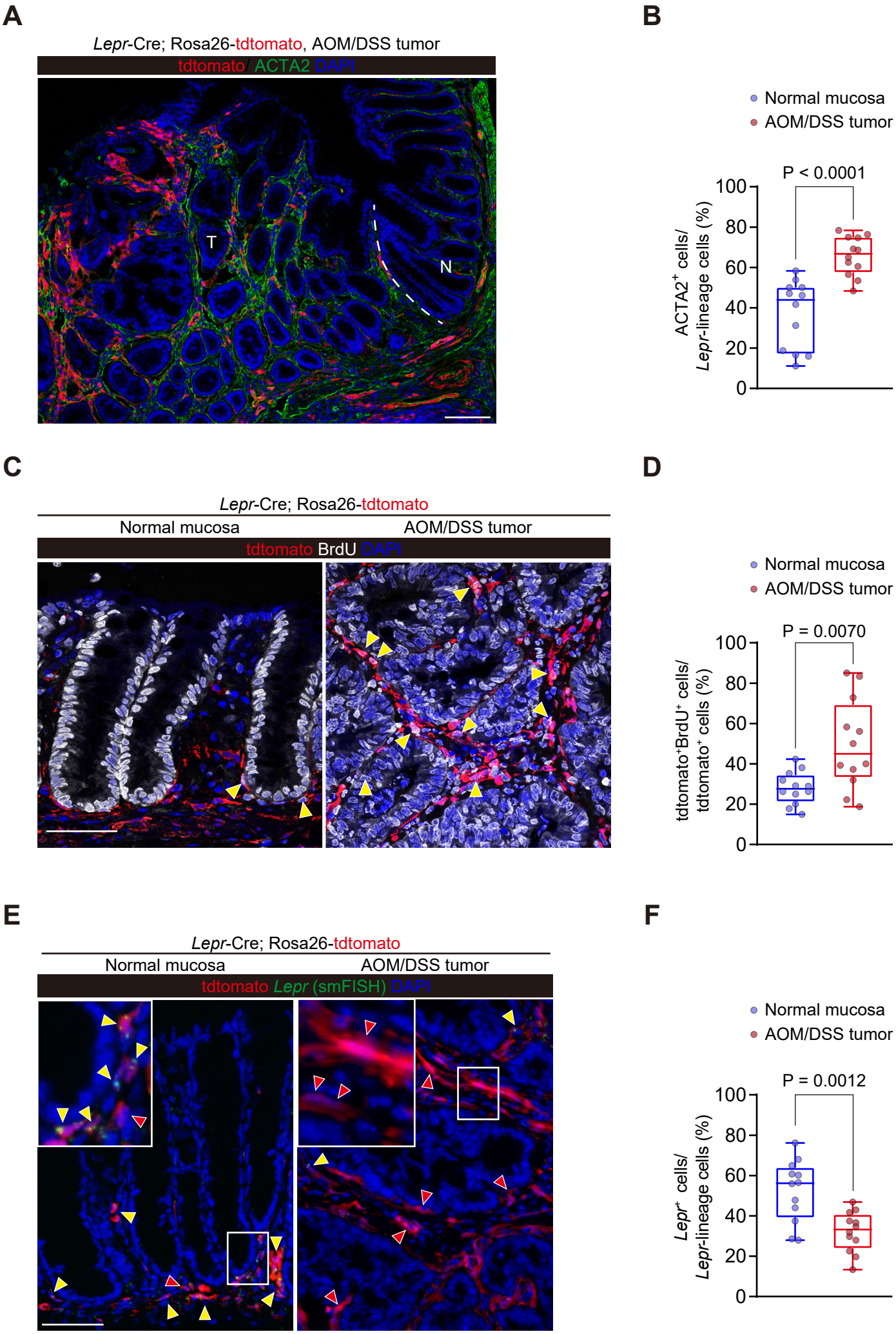
Kobayashi *et al.*, Supplementary Figure 4.



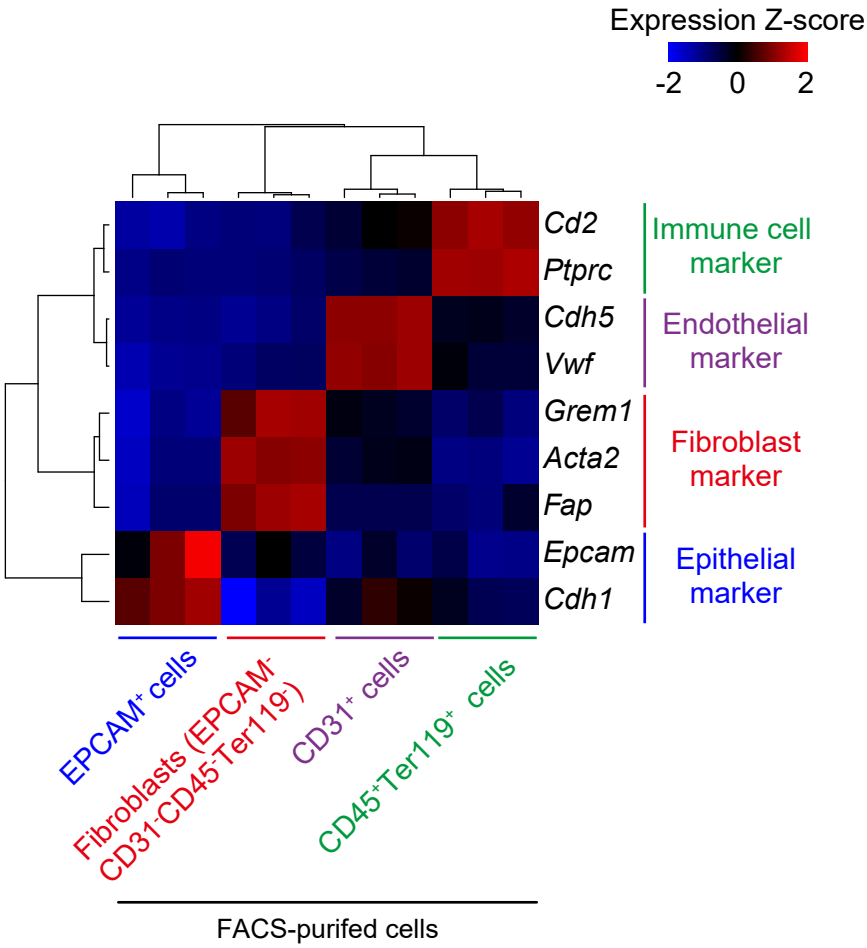
Kobayashi *et al.*, Supplementary Figure 5.



Kobayashi *et al.*, Supplementary Figure 6.

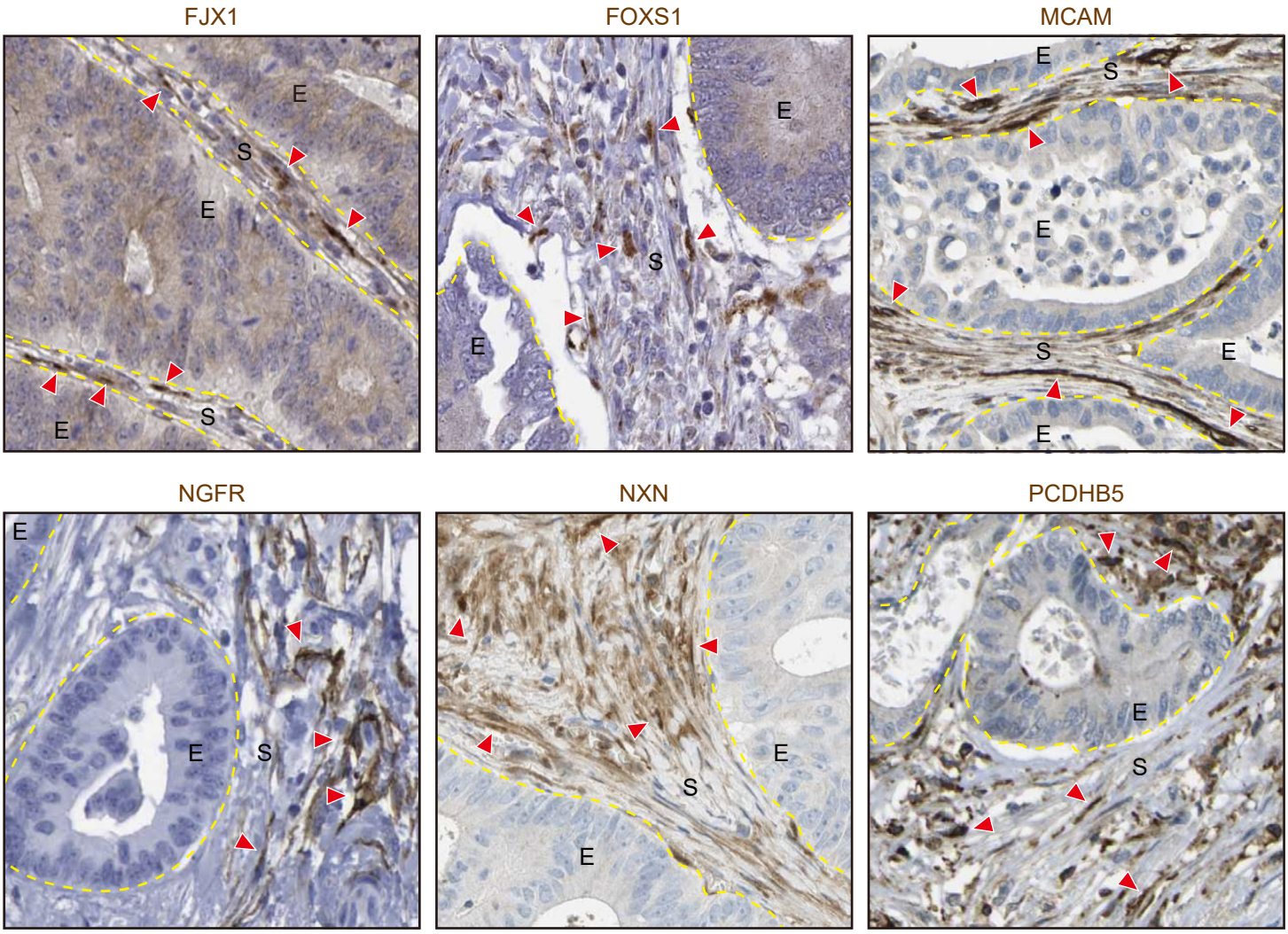


Kobayashi *et al.*, Supplementary Figure 7.



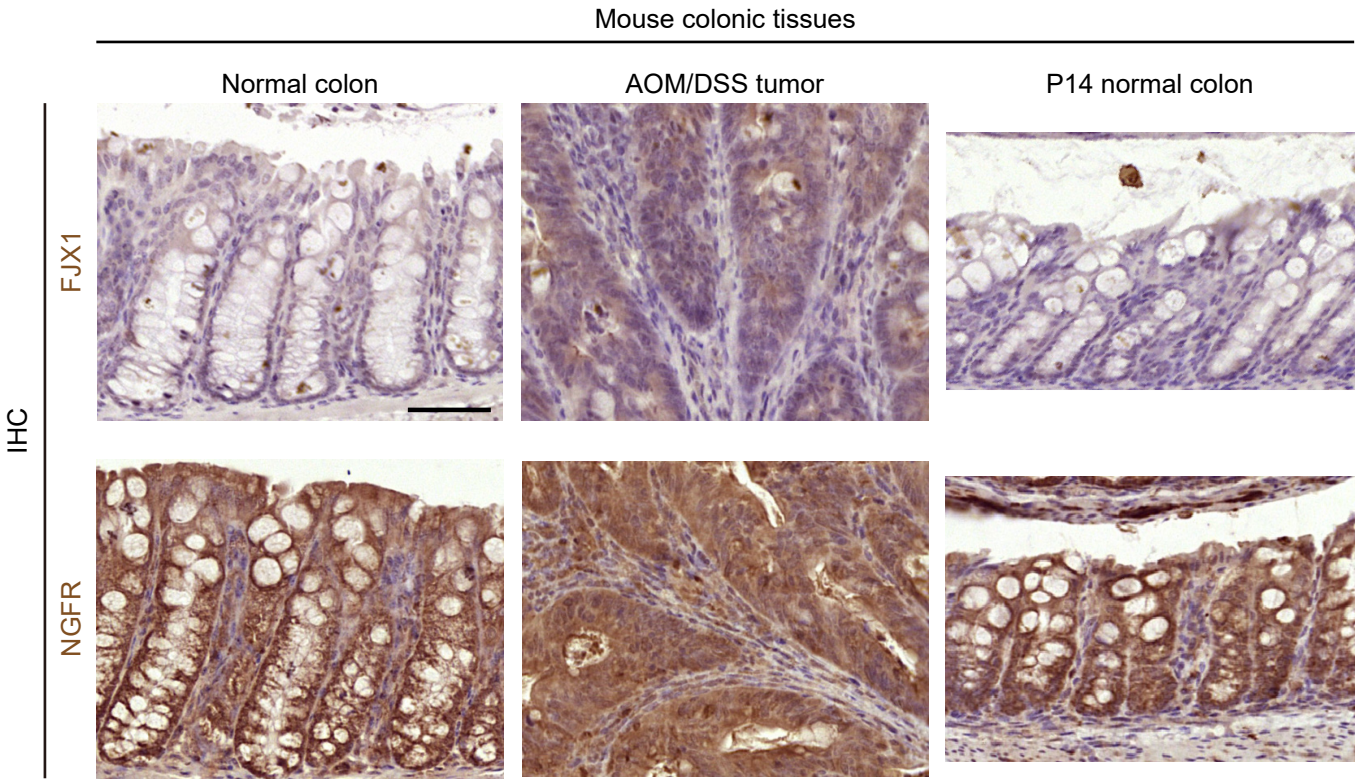
Kobayashi *et al.*, Supplementary Figure 8.

IHC, human CRC samples

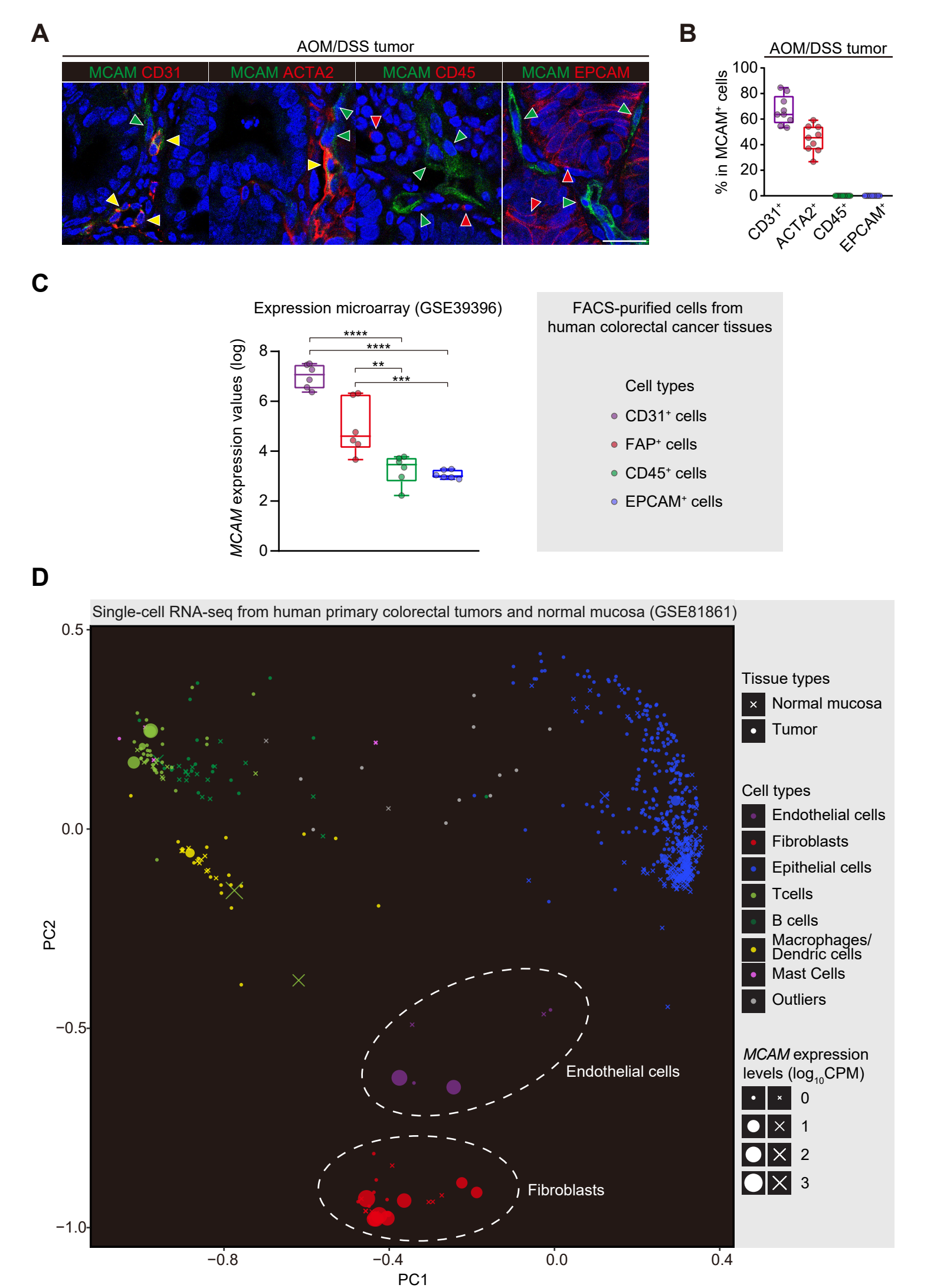


(The Human Protein Atlas)

Kobayashi *et al.*, Supplementary Figure 9.

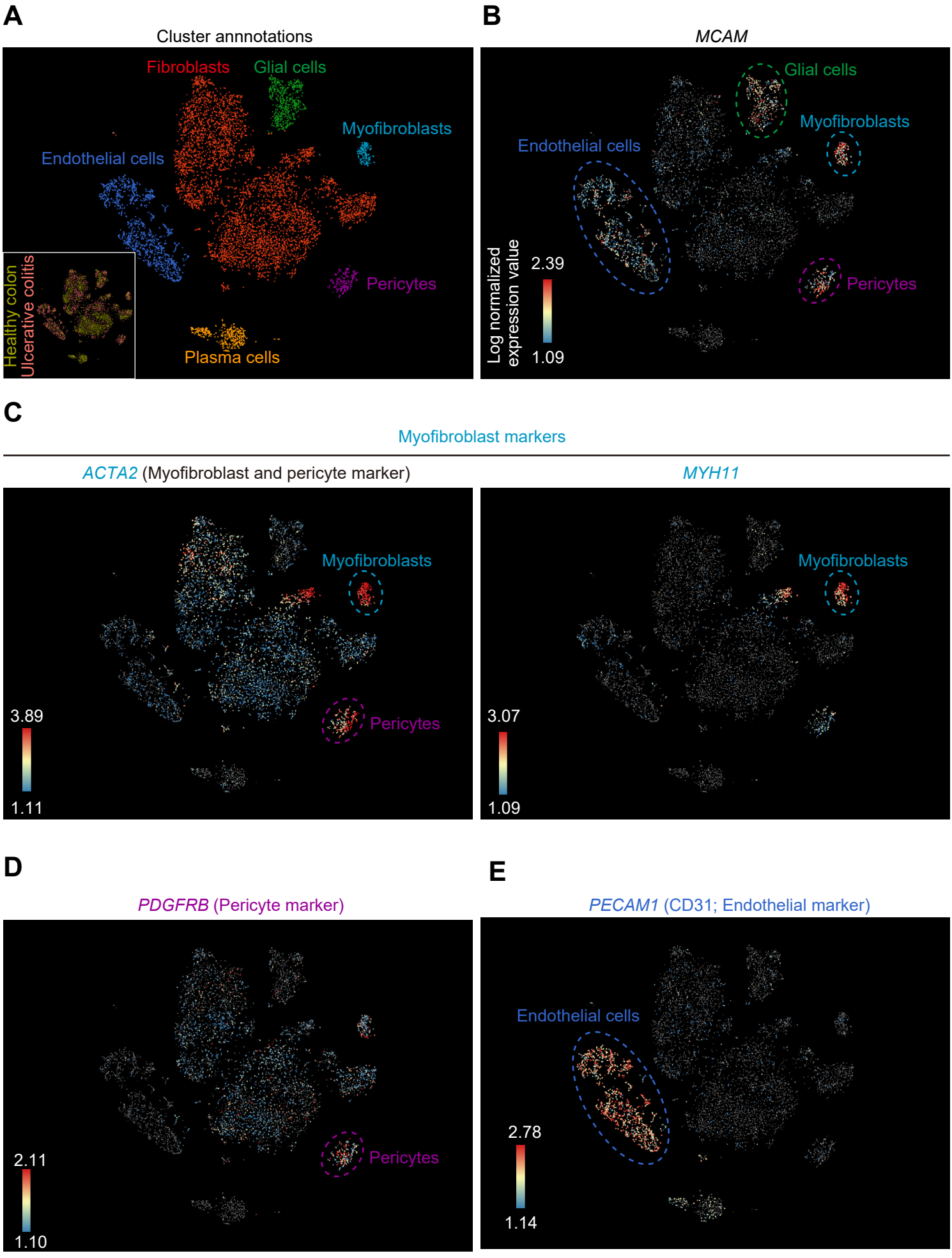


Kobayashi *et al.*, Supplementary Figure 10.



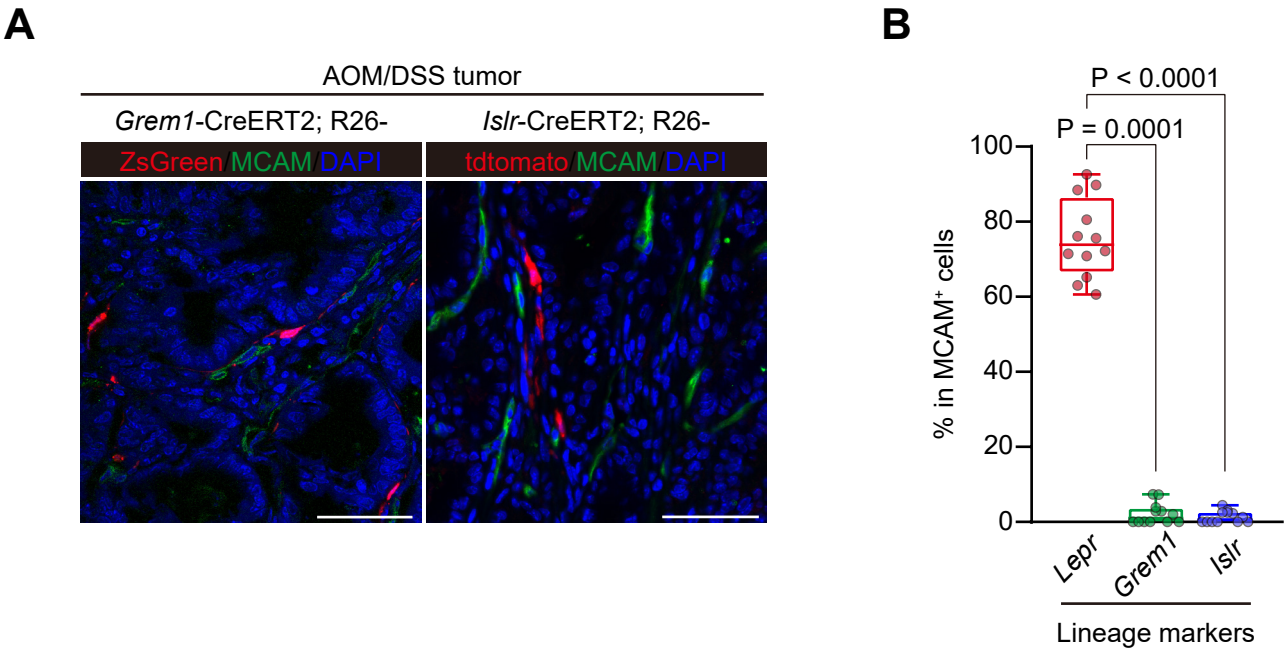
Kobayashi *et al.*, Supplementary Figure 11.

Single-cell RNA-sequencing from colonic stromal cells from healthy donars and ulcerative colitis patients



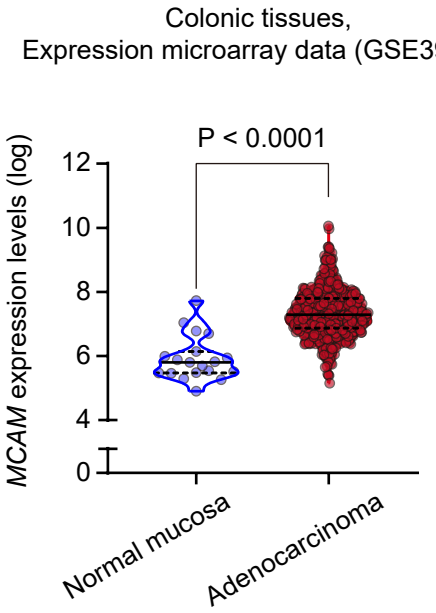
(GSE114374; Kinchen *et al.*, *Cell*, 2018)

Kobayashi *et al.*, Supplementary Figure 12.

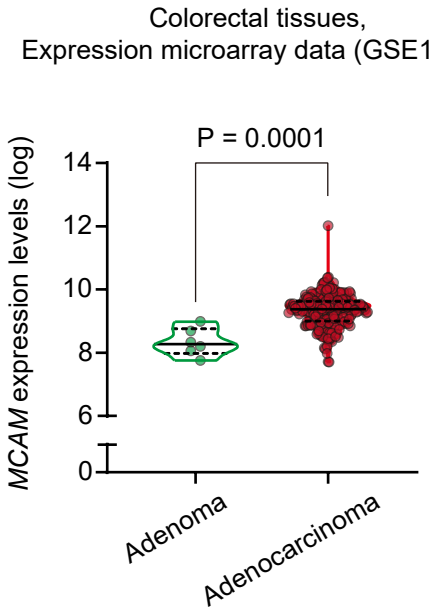


Kobayashi *et al.*, Supplementary Figure 13.

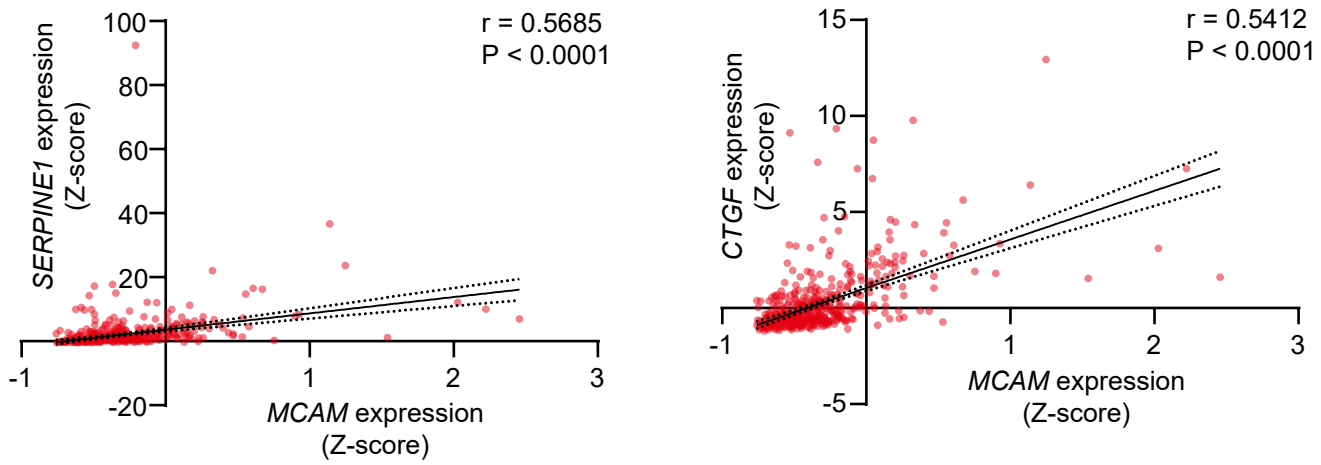
A



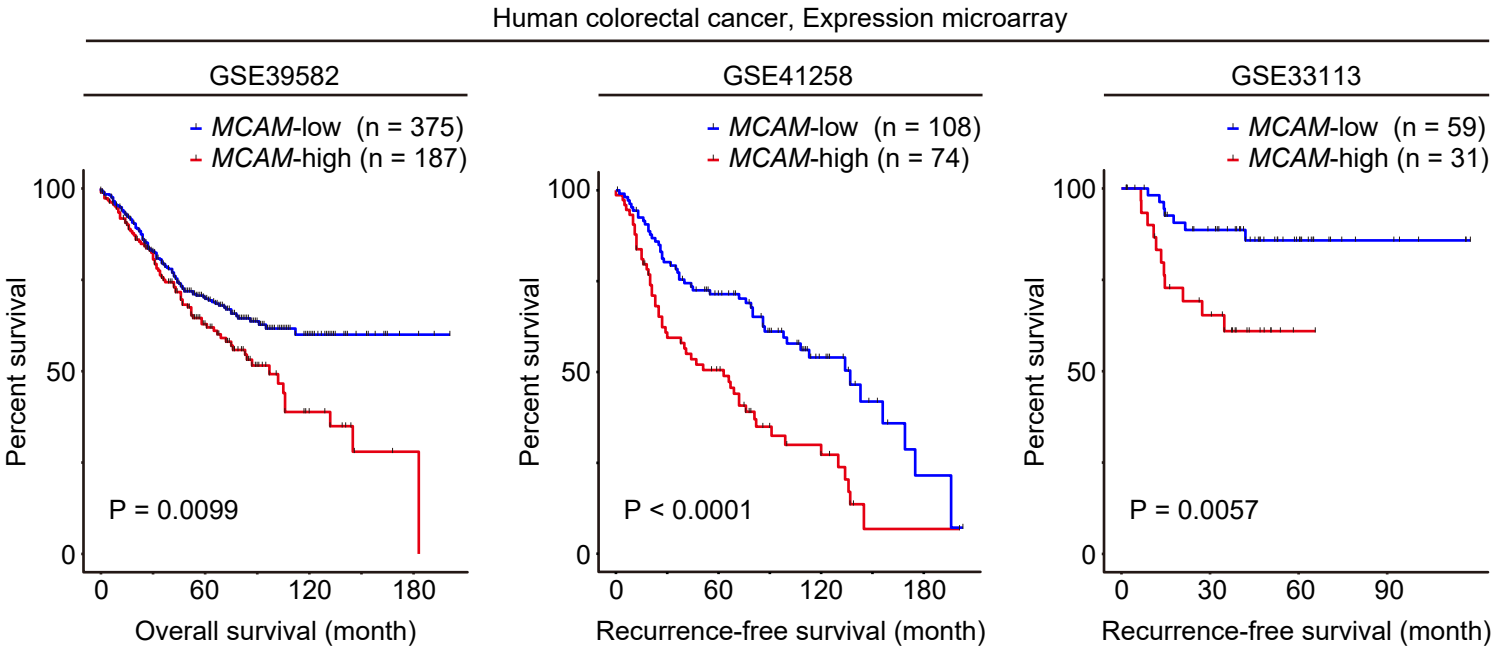
B



Kobayashi *et al.*, Supplementary Figure 14.

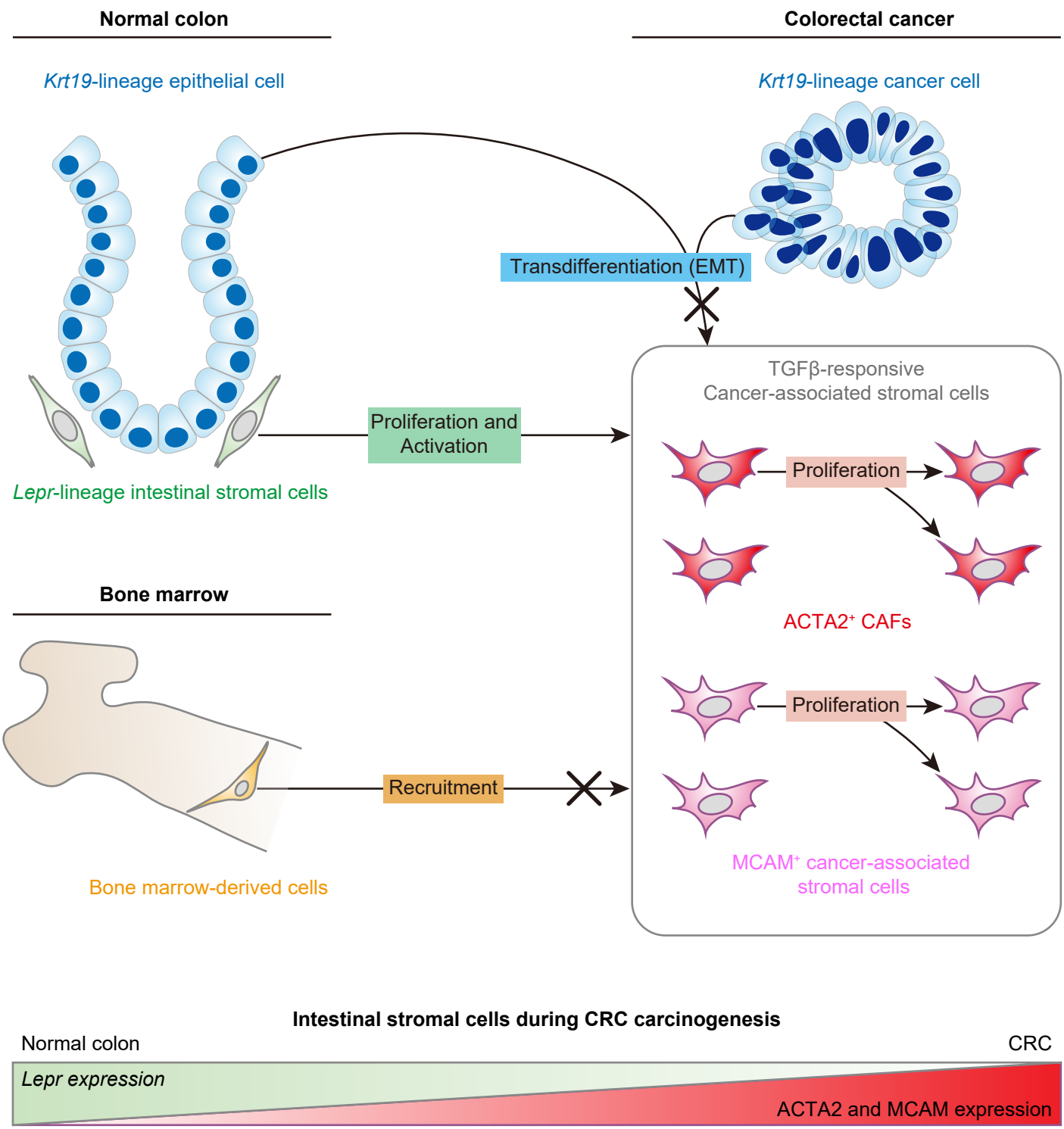


Kobayashi *et al.*, Supplementary Figure 15.



(GSE41258, Sheffer *et al.*, *Proc Natl Acad Sci USA*, 2009;
GSE39582, Marisa *et al.*, *PloS Med*, 2013;
GSE33113, de Sousa *et al.*, *Cell Stem Cell*, 2011)

Kobayashi *et al.*, Supplementary Figure 16.



Kobayashi *et al.*, Supplementary Figure 17.

Supplementary Table 1

List of 46 genes upregulated in both tumorigenesis and development
, which are associated with human CRC survival

ABCC9	*COX4I2*	*MEOX2*	*PCDHB7*	*TLX2*
AGER	*FJX1*	*MPP2*	*PLCG2*	*TMEM40*
ARL4C	*FOXS1*	*NAT8L*	*PLCH2*	*TNNT2*
AVPI1	*FUT1*	*NDUFA4L2*	*RHOV*	*TREX2*
BNIPL	*GJA4*	*NGFR*	*SEMA5B*	*TUBA8*
CCBE1	*GSTO1*	*NOTCH3*	*SHC4*	*UPK3BL*
CDH4	*HIST1H2AE*	*NRXN1*	*SIX4*	
CDKN2A	*HIST1H3D*	*NXN*	*SLC6A17*	
CELF4	*MACC1*	*OLFM2*	*SOX2*	
CHST3	*MCAM*	*PCDHB5*	*TGFA*	

The list above represents 46 genes selected in **Figure 4B (2)**.
The 18 genes that are upregulated in fibroblasts compared to epithelial cells,
in both normal adult colon and AOM/DSS tumor, are highlighted in red **(Figure 4B (3))**.

Supplementary Table 2

Clinicopathological characteristics of colorectal cancer patients analysed by MCAM immunohistochemistry

	All (n = 101)	**MCAM low (n = 28)**	**MCAM high (n = 73)**	***P* value (Fisher's exact test)**
Median age at diagnosis (range), years	72 (39-82)	67.5 (39-79)	74 (40-82)	
Median survival months (range)	106 (2-202)	142 (6-197)	91 (2-202)	
Median primary tumour diameter (range), mm	45 (15-110)	45 (15-110)	43 (15-100)	
Age, n (%)				0.091
≤ 65		12 (42.9%)	18 (24.7%)	
> 65		16 (57.1%)	55 (75.3%)	
Gender, n (%)				0.508
Male		13 (46.4%)	40 (54.8%)	
Female		15 (53.6%)	33 (45.2%)	
T status, n (%)				0.480
T3		27 (96.4%)	72 (98.6%)	
T4		1 (3.6%)	1 (1.4%)	
N status, n (%)				1.000
N0		15 (53.6%)	40 (54.8%)	
N1		9 (32.1%)	22 (30.1%)	
N2		4 (14.3%)	11 (15.1%)	
M status, n (%)				**0.032**
M0		28 (100.0%)	62 (84.9%)	
M1		0 (0.0%)	11 (15.1%)	
TNM stage, n (%)				0.051
Stage II		15 (53.6%)	38 (52.1%)	
Stage III		13 (46.4%)	24 (32.9%)	
Stage IV		0 (0.0%)	11 (15.1%)	
Tumour localization, n (%)				0.647
Left		19 (67.9%)	44 (60.3%)	
Right		9 (32.1%)	29 (39.7%)	
Differentiation, n (%)				0.251
Moderate		15 (53.6%)	49 (67.1%)	
Poor		13 (46.4%)	24 (32.9%)	
Treatment, n (%)				0.699
No		21 (75.0%)	56 (76.7%)	
Chemotherapy		6 (21.4%)	16 (21.9%)	
Radiotherapy		1 (3.6%)	1 (1.4%)	

P value less than 0.05 is shown in bold characters.

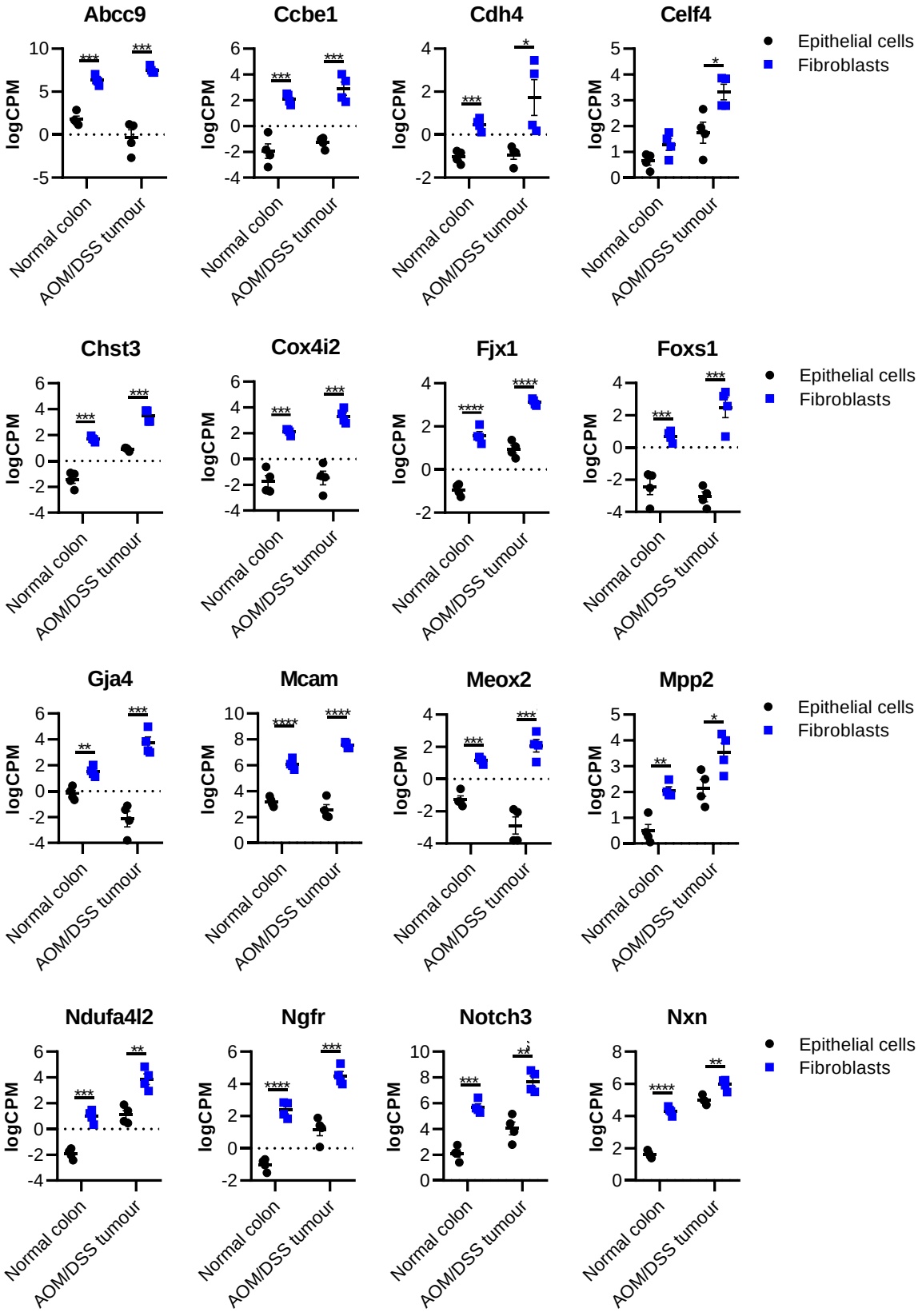
Supplementary Table 3

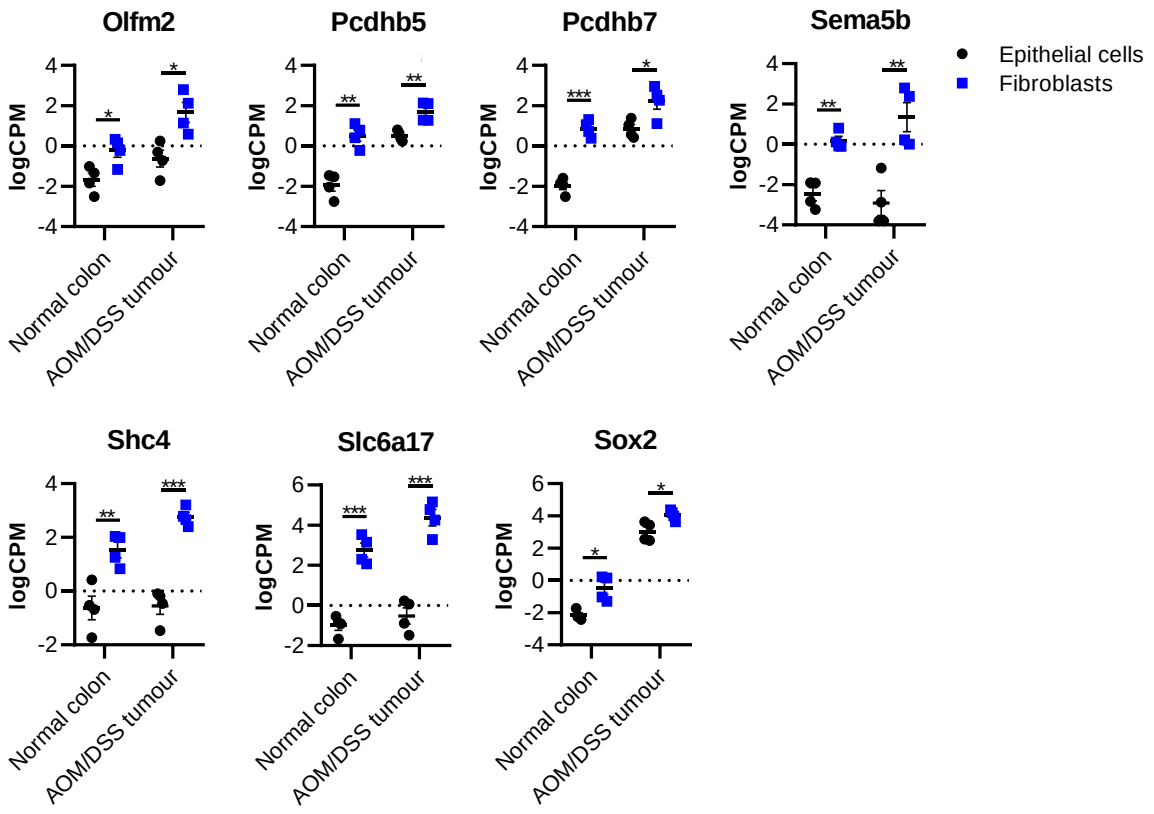
Univariate and multivariate Cox regression analysis of MCAM protein expression levels and overall surivival of colorectal cancer patients

	Overall survival			
	Univariate analysis		Multivariate analysis	
Variable	**HR (95% CI)**	***P* Value**	**HR (95% CI)**	***P* Value**
MCAM		**0.008**		**0.041**
Low	1.000		1.000	
High	2.341 (1.252-4.377)		1.974 (1.030-3.786)	
Age		**0.007**		**0.018**
≤ 65	1.000		1.000	
> 65	2.294 (1.251-4.206)		2.105 (1.137-3.896)	
Gender		0.205		
Female	1.000			
Male	1.363 (0.844-2.201)			
N status		0.260		0.410
N0	1.000		1.000	
N1 and N2	1.316 (0.817-2.119)		1.253 (0.733-2.141)	
M status		**0.002**		**0.031**
M0	1.000		1.000	
M1	3.022 (1.488-6.138)		2.393 (1.082-5.289)	
Tumour localization		**0.046**		0.101
Left	1.000		1.000	
Right	1.631 (1.008-2.641)		1.514 (0.922-2.487)	
Differentiation		0.825		
Moderate	1.000			
Poor	1.057 (0.646-1.731)			
Treatment		0.716		
No	1.000			
Yes (Chemotherapy or Radiotherapy)	0.901 (0.514-1.579)			

P values less than 0.05 are shown in bold characters.

Appendix 5. 23 Genes Expressed More in the Stroma Than Epithelium of Colorectal Tumours





Appendix 5. 23 genes expressed more in the stroma than epithelium of colorectal tumours. RNA-sequencing reads from fibroblast and epithelial populations in normal colon and AOM/DSS settings. These 23 genes were significantly more upregulated in tumour fibroblasts than tumour epithelium. CPM = counts per million. Mean +/- SEM, student's t test, * = $p<0.05$, ** = $p<0.01$, *** = $p<0.001$ and **** = $p<0.0001$. The mean and statistics were calculated using data from biological replicates.

Appendix 6. Table of Results From the Scoring Matrix Used During RNA-Sequencing List Refinement

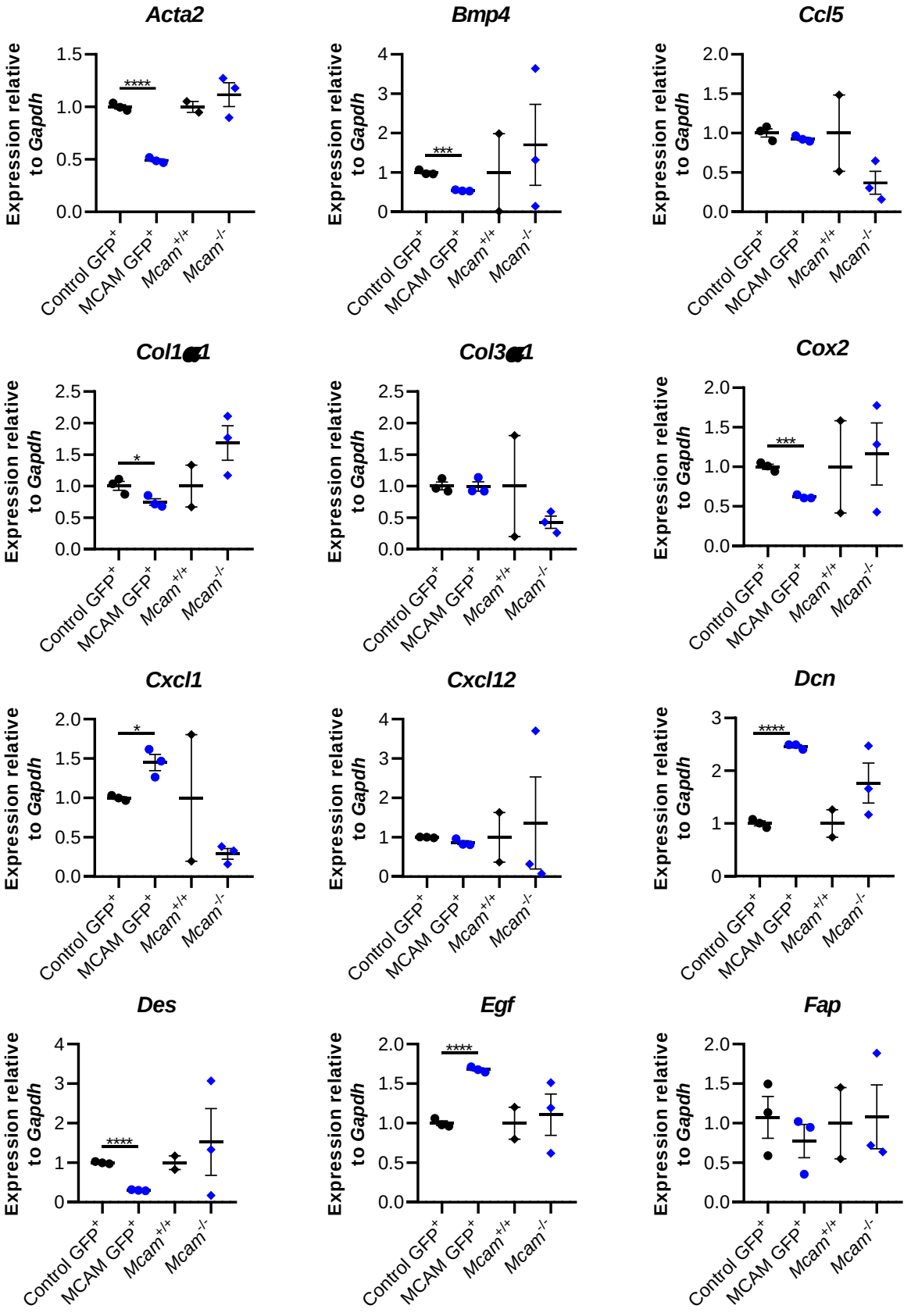
Gene	Log fold change ($logFC_2$)	Prognostic *p* value	Score out of 1						Tally (/6)	Pathways/Functions/ Processes
			$logFC_2 \geq 2$	Prog. *p* value ≤ 0.01	RNAseq = human protein expression	RNAseq = cancer literature	Published mouse IHC Ab	Inhibitors		
Abcc9	1.155	0.0002	0	1	1 – HPA	0	0	0	2	ATP-binding cassette (ABC) transporter, potassium ion import
Ccbe1	1.020	0.025	0	0	1	1	0 (human only)	1 (miR-330-3p)	3	Collagen, protease and calcium ion binding. Angiogenesis
Cdh4	1.917	0.040	0	0	0 (N/A) – HPA	0	0	0	0	Cell adhesion, calcium-dependent
Celf4	2.103	0.049	1	0	1 – HPA	1	0	0	3	Binds RNA, regulates splicing
Chst3	1.835	0.014	0	0	1 – HPA	1	0	0	2	Chondroitin sulfate biosynthesis
Cox4i2	1.279	0.008	0	1	1 – HPA	1	0	1	4	Activated by Protein Kinase C (PKC). Regulates cytochrome-c oxidase activity i.e. adenosine 5'-triphosphate (ATP) synthesis
Fjx1	1.529	0.010	0	1	1 – HPA	1	0	0	3	Cell-cell signalling. Downstream of NOTCH signalling. Promotes angiogenesis. Relatively unknown function
Foxs1	2.106	0.037	1	0	1 – HPA	1	0 (human only)	0	3	Angiogenesis, cell differentiation, EMT, transcriptional repressor
Gja4	2.442	0.022	1	0	1 – HPA	1	1	0	4	Cell-cell signalling, calcium ion transport, angiogenesis, lymphatic development/remodelling/function
Mcam	1.430	0.045	0	0	1 – HPA	1	1	1	4	Cell adhesion. Promotes cell migration, angiogenesis and intracellular calcium concentration. Cell protection from anoikis and activates NF-κB signalling

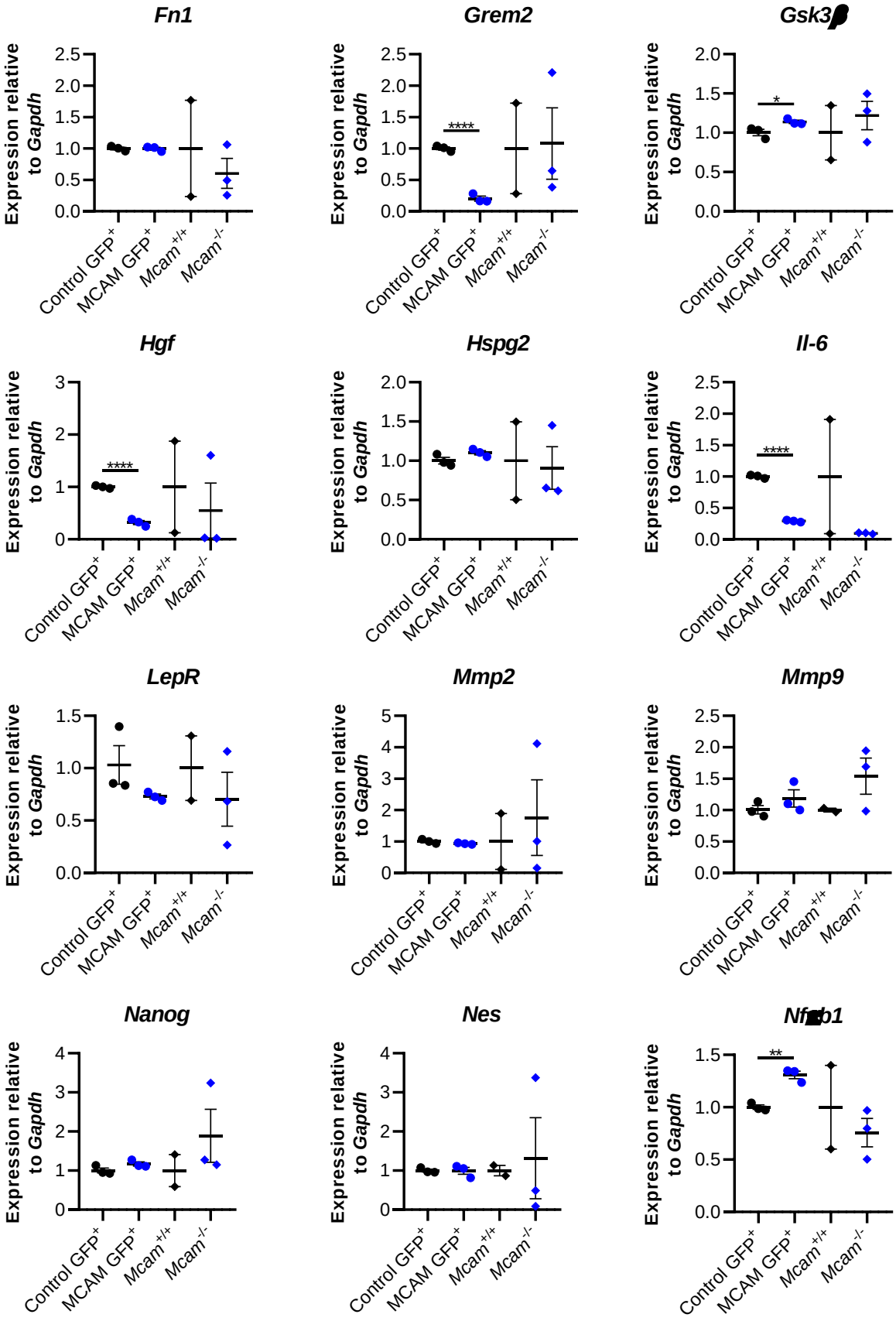
Meox2	1.069	0.026	0	0	0 (not in colon or CRC) – HPA	1	0	0	1	Transcriptional activator, inhibits PI3K/AKT pathway, binds Hedgehog-GLI1 promoter sequence, angiogenesis
Mpp2	1.589	4.2 E-05	0	1	1 – HPA	0 (N/A)	0	0	2	Binds PDZ domains and ion channels. Excitatory postsynaptic potential and protein homo-oligomerization
Ndufa4l2	3.038	0.011	1	0	0 (N/A) – HPA	1	0	0	2	Cytochrome-c oxidase activity i.e. ATP synthesis. Induced by hypoxia
Ngfr	2.129	0.020	1	0	1	1	1	1 (hsa-miR-939)	5	Involved in: Rho protein signal transduction, cell differentiation, cellular response to oxidative stress, glucose homeostasis, inflammatory response. Negative regulator of apoptosis, angiogenesis and Fibroblast growth factor receptor (FGFR) signalling pathway
Notch3	2.093	0.041	1	0	1 – HPA	1	1	1 (protein = evodiamine; pathway = GSI, BMS-906024**)**	5	NOTCH signalling pathway. Negative regulation of cell differentiation. Positive regulation of transcription and smooth muscle cell proliferation
Nxn	1.666	0.0273	0	0	1 – HPA	1	0	0	2	Catalyses disulphide bond formation and isomerisation. Redox-dependent regulator of WNT signalling pathway, involved in cell growth and differentiation
Olfm2	2.113	0.010	1	1	1 – HPA	1	0	0	4	Protein secretion, positive regulation of smooth muscle cell differentiation. Induced by TGF-β
Pcdhb5	1.190	0.003	0	1	1 – HPA	0 (N/A)	0 (human only)	0	2	Cell adhesion, chemical synaptic transmission
Pcdhb7	1.477	0.002	0	1	1 – HPA	0 (N/A)	0 (human only)	0	2	Cell adhesion, chemical synaptic transmission
Sema5b	1.669	0.003	0	1	0 (not in colon or CRC) – HPA	1	0 (no Ab available)	0	2	Cell differentiation, neuron projection extension and guidance, negative chemotaxis

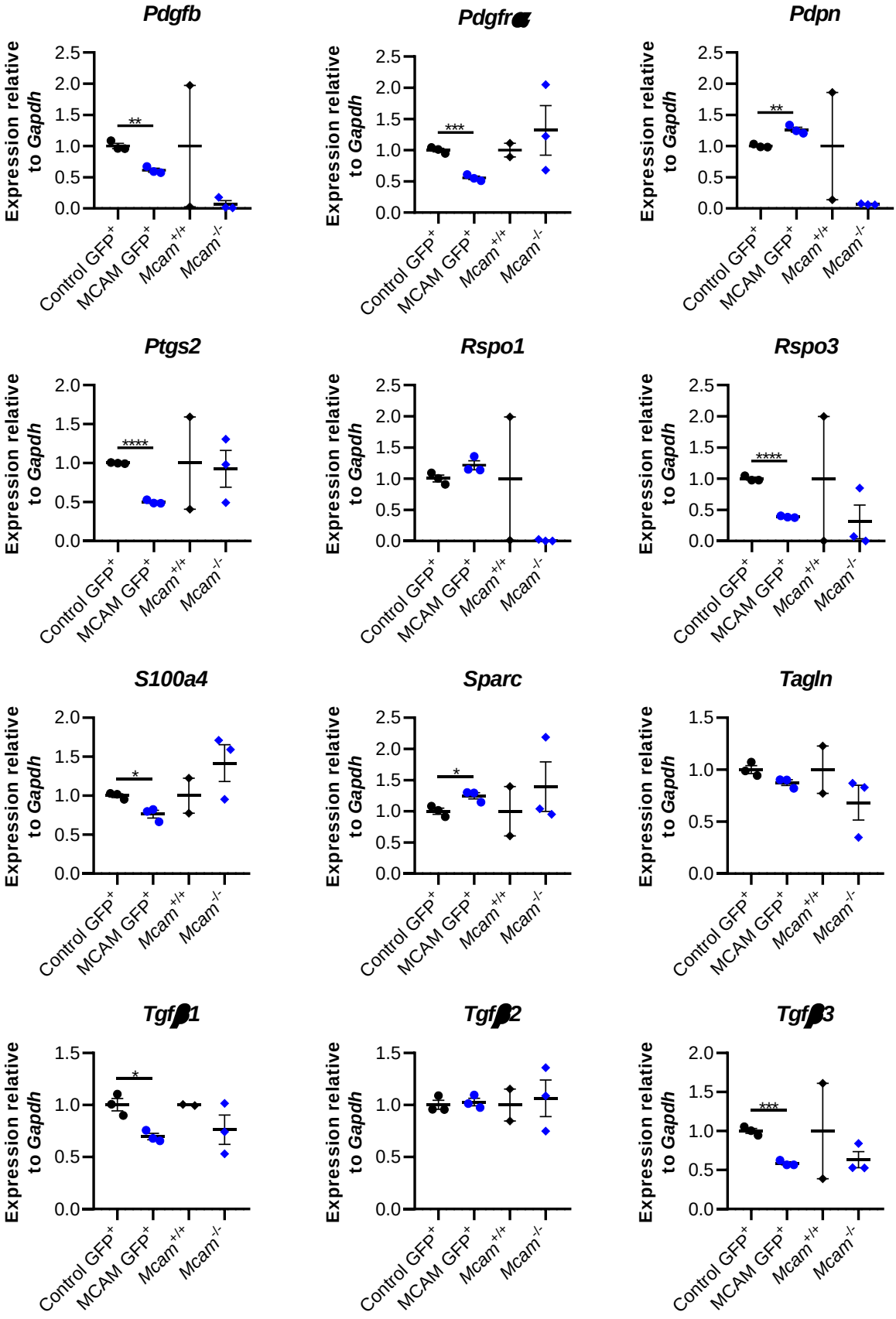
Shc4	1.193	0.049	0	0	0 (N/A) – HPA	1	0	1 (actinomycin D)	2	Positive regulation of cell proliferation. Involved in stem cell differentiation, intracellular signal transduction, apoptosis and tyrosine kinase signalling pathway
Slc6a17	1.647	0.035	0	0	0 (not in colon or CRC) – HPA	0 (N/A)	0 (human only)	0	0	Amino acid transmembrane transporter and neurotransmitter:sodium symporter activity
Sox2	4.538	0.041	1	0	1 – HPA	1	1	0	4	Protein heterodimerisation activity, transcriptional activator and repressor, cell cycle arrest/commitment/specification, stem cell maintenance and differentiation. Negative regulation of canonical WNT pathway, cell differentiation/proliferation. Positive regulation of MAPK cascade, NOTCH signalling, cell differentiation/ proliferation, cell-cell adhesion

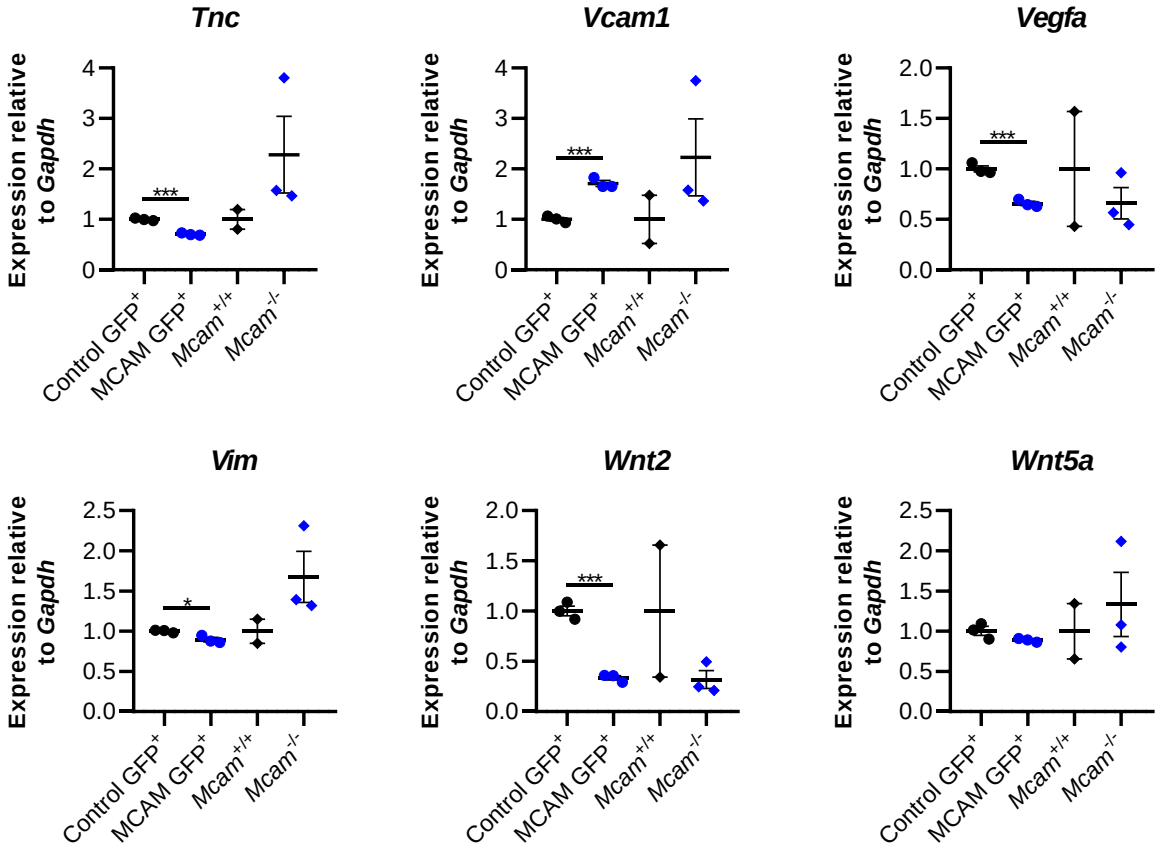
This table displays the information collected and used to score the 23 genes more highly expressed in the fibroblasts than epithelium of AOM/DSS tumours. There are 6 categories, with one point awarded per category. The 23 genes include *ATP-binding cassette, sub-family C member 9* (*Abcc9*), *Collagen and calcium binding EGF domains 1* (*Ccbe1*), *Cadherin-4* (*Cdh4*), *CUGBP elav-like family member 4* (*Celf4*), *Carbohydrate sulfotransferase 3* (*Chst3*), *Cox4i2*, *Four-jointed box kinase 1* (*Fjx1*), *Forkhead box S1* (*Foxs1*), *Gja4, Mcam, Mesenchyme homeobox 2* (*Meox2*), *Membrane palmitoylated protein 2* (*Mpp2*), *NADH dehydrogenase 1 alpha subcomplex subunit 4-like-2* (*Ndufa4l2*), *Ngfr, Notch3, Nucleoredoxin* (*Nxn*), *Olfactomedin 2* (*Olfm2*), *Protocadherin beta 5* (*Pcdhb5*), *Protocadherin beta 7* (*Pcdhb7*), *Semaphorin 5B* (*Sema5b*), *SHC adaptor protein 4* (*Shc4*), *Solute carrier family 6 member 17* (*Slc6a17*), and *Sox2*. 6 candidates, highlighted in blue, scored ≥ 4 out of a possible 6 and progressed to the next stage of RNA-sequencing list refinement – mouse IHC (see Fig 4.2). Although *Olfm2* scored 4/6, it was not chosen because there was no validated mouse IHC antibody available for purchase at the time. This data was collated from 31/08/2017 – 07/09/2017. HPA = Human Protein Atlas [(191)].

Appendix 7. The Expression of Other Genes Examined That are not Linked to *Mcam* Expression Levels




Fn1
Grem2
Gsk3β
Hgf
Hspg2
Il-6
LepR
Mmp2
Mmp9
Nanog
Nes
Nfκb1
Expression relative to Gapdh
Control GFP+
MCAM GFP+
Mcam+/+
Mcam-/-
****
*
**


Pdgfb
Pdgfrα
Pdpn
Ptgs2
Rspo1
Rspo3
S100a4
Sparc
Tagln
Tgfβ1
Tgfβ2
Tgfβ3
Expression relative to Gapdh
Control GFP+
MCAM GFP+
Mcam+/+
Mcam-/-



Appendix 7. The expression of other genes examined that are not linked to *Mcam* expression levels. qPCR examination of the other 42 genes associated with growth, stemness, fibrosis, angiogenesis, migration, inflammation and the immune response in MCAM GFP^{+} and *Mcam*$^{-/-}$ myofbs, compared to their respective controls (control GFP^{+} and *Mcam*$^{+/+}$ myofbs). Control and MCAM GFP^{+} myofbs are displayed and analysed as a technical triplicate (n=1 experimental replicate), while *Mcam*$^{+/+}$ and *Mcam*$^{-/-}$ myofbs are displayed and analysed as experimental replicates (n=2 *Mcam*$^{+/+}$ and n=3 *Mcam*$^{-/-}$ lines). *Ccl5 = C-C motif chemokine ligand 5*; *Col1α1 = Collagen type I alpha 1 chain*; *Col3α1 = Collagen type III alpha 1 chain*; *Cox2 = Cytochrome C oxidase subunit 2*; *Cxcl1 = C-X-C motif chemokine ligand 1*; *Des = Desmin*; *Fn1 = Fibronectin 1*; *Grem2 = Gremlin 2*; *Hgf* = H*epatocyte growth factor*; *Hspg2 = Heparan sulfate proteoglycan*; *LepR = Leptin receptor*; *Mmp9 = Matrix metalloproteinase 9*; *Nanog = Nanog homoebox*; *Nes = Nestin*; *Pdgfrα = Platelet derived growth factor receptor alpha*; *Pdpn = Podoplanin*; *Ptgs2 = Prostaglandin-endoperoxide synthase 2*; *S100A4 = S100 calcium binding protein A4*; *Sparc = Secreted protein acidic and cysteine rich*; *Tnc = Tenascin C*; *Vcam1 = Vascular cell adhesion molecule 1*; *Vim = Vimentin*. Mean +/- SEM, student's t test, * = p<0.05, ** = p<0.01, *** = p<0.001 and **** = p<0.0001.

Appendix 8. ‘The Balance of Stromal BMP Signaling Mediated by *GREM1* and *ISLR* Drives Colorectal Carcinogenesis’

This manuscript examines the stromal BMP balance and how the BMP signalling pathway can be downregulated by GREM1^{+} CAFs or upregulated by ISLR^{+} CAFs to promote and inhibit colorectal tumourigenesis, respectively. Thus, *Grem1* and *Islr* mark distinct CRC-promoting and -suppressing CAF subtypes, respectively. The final part of this manuscript explores GREM1 inhibition and *Islr* upregulation in the CRC mouse model of hepatic metastasis. This copy is a journal pre-proof.

Statement of Authorship

Title of Paper	The balance of stromal BMP signalling mediated by GREM1 and ISLR drives colorectal carcinogenesis.
Publication Status	Published
Publication Details	Kobayashi, H., Gieniec, K. A., Wright, J. A., Wang, T., Asai, N., Mizutani, Y., Ida, T., Ando, R., Suzuki, N., Lannagan, T. R. M., Ng, J. Q., Hara, A., Shiraki, Y., Mii, S., Ichinose, M., Vrbanac, L., Lawrence, M. J., Sammour, T., Uehara, K., Davies, G., Lisowski, L., Alexander, I. E., Hayakawa, Y., Butler, L. M., Zannettino, A. C. W., Din, M. O., Hasty, J., Burt, A. D., Leedham, S. J., Rustgi, A. K., Mukherjee, S., Wang, T. C., Enomoto, A., Takahashi, M., Worthley, D. L., Woods, S. L. (2020). The balance of stromal BMP signalling mediated by GREM1 and ISLR drives colorectal carcinogenesis. *Gastroenterology*, doi: https://doi.org/10.1053/j.gastro.2020.11.011

Candidate

Name of Candidate	Krystyna Gieniec		
Contribution to the Paper	I discussed manuscript content and helped in data interpretation. I performed the experiment examining the effect of the GREM1 neutralising antibody on the survival of mice with hepatic colorectal metastases and analysed the associated data. This experimental work took approximately one year. I also performed a similar experiment on mice with primary colorectal cancer (approximately 9 months of work) but this was not included in the submitted version of the manuscript (please see Chapter 5 of my thesis).		
Overall Percentage (%)	10%		
Certification:	This paper reports on original research I conducted during the period of my Higher Degree by Research candidature and is not subject to any obligations or contractual agreements with a third party that would constrain its inclusion in this thesis. I am the second author of this paper.		
Signature		Date	*30/10/20*

Co-author contributions

By signing the Statement of Authorship, each author certifies that:

i. the candidate's stated contribution to the publication is accurate (as detailed above);
ii. permission is granted for the candidate to include the publication in the thesis; and
iii. the sum of all the co-author contributions is equal to 100% less the candidate's stated contribution.

Name of principal author	Hiroki Kobayashi		
Contribution to the paper	Performed most of the experiments, data interpretation and statistical analyses, performed animal experiments with reporter mice and wrote the manuscript. Principal author.		
Signature		Date	*6/11/20*

Name of co-author	Josephine Wright		
Contribution to the paper	Discussed manuscript content, helped in data interpretation, generated genetically engineered colorectal tumouroids, performed an *in vitro* tumouroid experiment using *Islr*-YH2 cells.		
Signature		Date	*6/11/20*

Name of co-author	Tongtong Wang		
Contribution to the paper	Discussed manuscript content, helped in data interpretation, analysed RNA-sequencing datasets.		
Signature		Date	*6/11/20*

Name of co-author	Naoya Asai		
Contribution to the paper	Supervised development of work, discussed manuscript content, helped in data interpretation, performed animal experiments with reporter mice.		
Signature		Date	*9/11/20*

Name of co-author	Yasuyuki Mizutani		
Contribution to the paper	Discussed manuscript content, helped in data interpretation, performed smFISH.		
Signature		Date	*17/11/20*

Name of co-author	Tadashi Ida		
Contribution to the paper	Discussed manuscript content, helped in data interpretation, performed smFISH.		
Signature		Date	*18/11/20*

Name of co-author	Ryota Ando		
Contribution to the paper	Discussed manuscript content, helped in data interpretation, performed smFISH.		
Signature		Date	*17/11/20*

Name of co-author	Nobumi Suzuki		
Contribution to the paper	Discussed manuscript content, helped in data interpretation, generated genetically engineered colorectal tumouroids.		
Signature		Date	*9/11/20*

Name of co-author	Tamsin Lannagan		
Contribution to the paper	Discussed manuscript content, helped in data interpretation, generated genetically engineered colorectal tumouroids.		
Signature		Date	*17/11/20*

Name of co-author	Jia Ng		
Contribution to the paper	Discussed manuscript content, helped in data interpretation, performed animal experiments with reporter mice.		
Signature		Date	*6/11/20*

Name of co-author	Akitoshi Hara		
Contribution to the paper	Discussed manuscript content, helped in data interpretation.		
Signature		Date	*8/11/20*

Name of co-author	Yukihiro Shiraki		
Contribution to the paper	Discussed manuscript content, helped in data interpretation.		
Signature		Date	*9/11/20*

Name of co-author	Shinji Mii		
Contribution to the paper	Discussed manuscript content, helped in data interpretation.		
Signature		Date	*9/11/20*

Name of co-author	Mari Ichinose		
Contribution to the paper	Discussed manuscript content, helped in data interpretation.		
Signature		Date	*9/11/20*

Name of co-author	Laura Vrbanac		
Contribution to the paper	Discussed manuscript content, helped in data interpretation.		
Signature		Date	*6/11/20*

Name of co-author	Matthew Lawrence		
Contribution to the paper	Discussed manuscript content, helped in data interpretation.		
Signature		Date	*9/11/20*

Name of co-author	Tarik Sammour		
Contribution to the paper	Discussed manuscript content, helped in data interpretation.		
Signature		Date	*10/11/20*

Name of co-author	Kay Uehara		
Contribution to the paper	Discussed manuscript content, helped in data interpretation, collected human colorectal cancer clinical data and provided samples.		
Signature		Date	*10/11/20*

Name of co-author	Gareth Davies		
Contribution to the paper	Discussed manuscript content, helped in data interpretation, provided the GREM1 neutralising antibody and intellectual input.		
Signature		Date	10th Nov 2020

Name of co-author	Leszek Lisowski		
Contribution to the paper	Discussed manuscript content, helped in data interpretation, produced and tittered AAV vectors.		
Signature		Date	*9 Nov 2020*

Name of co-author	Ian Alexander		
Contribution to the paper	Discussed manuscript content, helped in data interpretation.		
Signature		Date	*9 Nov 2020*

Name of co-author	Yoku Hayakawa		
Contribution to the paper	Discussed manuscript content, helped in data interpretation.		
Signature		Date	11/18/2020

Name of co-author	Lisa Butler		
Contribution to the paper	Discussed manuscript content, helped in data interpretation.		
Signature		Date	*6/11/20*

Name of co-author	Andrew Zannettino		
Contribution to the paper	Discussed manuscript content, helped in data interpretation.		
Signature		Date	*11/11/20*

Name of co-author	M. Omar Din		
Contribution to the paper	Discussed manuscript content, helped in data interpretation.		
Signature		Date	*2020-11-09*

Name of co-author	Jeff Hasty		
Contribution to the paper	Discussed manuscript content, helped in data interpretation.		
Signature		Date	*19/11/20*

Name of co-author	Alastair Burt		
Contribution to the paper	Supervised development of work, discussed manuscript content, helped in data interpretation, wrote the manuscript.		
Signature		Date	*9/11/20*

Name of co-author	Simon Leedham		
Contribution to the paper	Discussed manuscript content, helped in data interpretation.		
Signature		Date	*9/11/20*

Name of co-author	Anil Rustgi		
Contribution to the paper	Discussed manuscript content, helped in data interpretation.		
Signature		Date	*1/12/10*

Name of co-author	Siddhartha Mukherjee		
Contribution to the paper	Discussed manuscript content, helped in data interpretation.		
Signature		Date	*9/11/20*

Name of co-author	Timothy Wang		
Contribution to the paper	Discussed manuscript content, helped in data interpretation.		
Signature		Date	*9/11/20*

Name of co-author	Atsushi Enomoto		
Contribution to the paper	Supervised development of work, discussed manuscript content, helped in data interpretation and manuscript evaluation, wrote the manuscript. Will act as corresponding author.		
Signature		Date	*9/11/20*

Name of co-author	Masahide Takahashi		
Contribution to the paper	Supervised development of work, discussed manuscript content, helped in data interpretation and manuscript evaluation. Will act as corresponding author.		
Signature		Date	*9/11/20*

Name of co-author	Daniel Worthley		
Contribution to the paper	Supervised development of work, discussed manuscript content, helped in data interpretation and manuscript evaluation, wrote the manuscript. Will act as corresponding author.		
Signature		Date	*6/11/20*

Name of co-author	Susan Woods		
Contribution to the paper	Supervised development of work, discussed manuscript content, helped in data interpretation and manuscript evaluation, generated genetically engineered colorectal tumouroids, wrote the manuscript. Will act as corresponding author.		
Signature		Date	*6/11/20*

Downloaded for Anonymous User (n/a) at The University of Adelaide from ClinicalKey.com.au by Elsevier on February 01, 2021.
For personal use only. No other uses without permission. Copyright ©2021. Elsevier Inc. All rights reserved.

Journal Pre-proof



The balance of stromal BMP signaling mediated by *GREM1* and *ISLR* drives colorectal carcinogenesis.

Hiroki Kobayashi, Krystyna A. Gieniec, Josephine A. Wright, Tongtong Wang, Naoya Asai, Yasuyuki Mizutani, Tadashi Ida, Ryota Ando, Nobumi Suzuki, Tamsin RM. Lannagan, Jia Q. Ng, Akitoshi Hara, Yukihiro Shiraki, Shinji Mii, Mari Ichinose, Laura Vrbanac, Matthew J. Lawrence, Tarik Sammour, Kay Uehara, Gareth Davies, Leszek Lisowski, Ian E. Alexander, Yoku Hayakawa, Lisa M. Butler, Andrew C.W. Zannettino, M. Omar Din, Jeff Hasty, Alastair D. Burt, Simon J. Leedham, Anil K. Rustgi, Siddhartha Mukherjee, Timothy C. Wang, Atsushi Enomoto, Masahide Takahashi, Daniel L. Worthley, Susan L. Woods

PII: S0016-5085(20)35400-7
DOI: https://doi.org/10.1053/j.gastro.2020.11.011
Reference: YGAST 63869

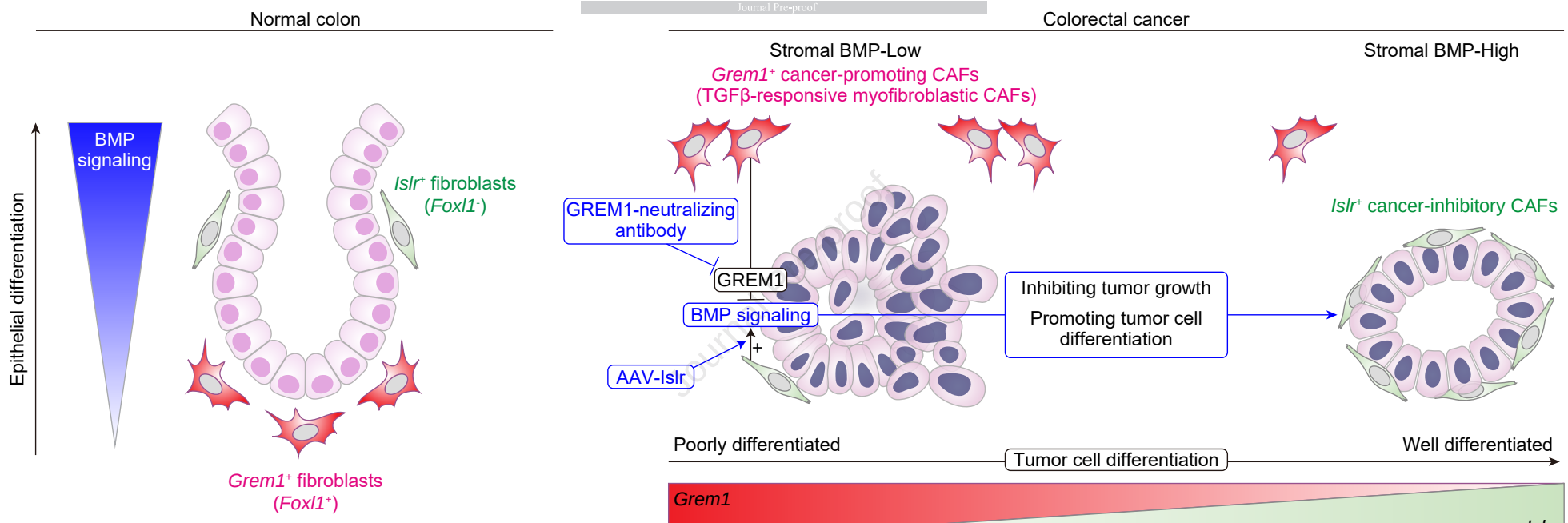
To appear in: *Gastroenterology*
Accepted Date: 9 November 2020

Please cite this article as: Kobayashi H, Gieniec KA, Wright JA, Wang T, Asai N, Mizutani Y, Ida T, Ando R, Suzuki N, Lannagan TR, Ng JQ, Hara A, Shiraki Y, Mii S, Ichinose M, Vrbanac L, Lawrence MJ, Sammour T, Uehara K, Davies G, Lisowski L, Alexander IE, Hayakawa Y, Butler LM, Zannettino ACW, Din MO, Hasty J, Burt AD, Leedham SJ, Rustgi AK, Mukherjee S, Wang TC, Enomoto A, Takahashi M, Worthley DL, Woods SL, The balance of stromal BMP signaling mediated by *GREM1* and *ISLR* drives colorectal carcinogenesis., *Gastroenterology* (2020), doi: https://doi.org/10.1053/j.gastro.2020.11.011.

This is a PDF file of an article that has undergone enhancements after acceptance, such as the addition of a cover page and metadata, and formatting for readability, but it is not yet the definitive version of record. This version will undergo additional copyediting, typesetting and review before it is published in its final form, but we are providing this version to give early visibility of the article. Please note that, during the production process, errors may be discovered which could affect the content, and all legal disclaimers that apply to the journal pertain.

© 2020 by the AGA Institute

Journal Pre-proof



Downloaded for Anonymous User (n/a) at The University of Adelaide from ClinicalKey.com.au by Elsevier on February 19, 2021. For personal use only. No other uses without permission. Copyright ©2021. Elsevier Inc. All rights reserved.

Kobayashi *et al.*, Graphical abstracts

Journal Pre-proof

The balance of stromal BMP signaling mediated by *GREM1* and *ISLR* drives colorectal carcinogenesis.

Short title: The role of BMP signaling in the CRC stroma

Hiroki Kobayashi[1, 2, 3, 4], Krystyna A. Gieniec[1,2], Josephine A. Wright[2], Tongtong Wang[1,2], Naoya Asai[5], Yasuyuki Mizutani[3, 6], Tadashi Ida[3, 6], Ryota Ando[3], Nobumi Suzuki[1,2,7], Tamsin RM. Lannagan[1,2], Jia Q Ng[1,2], Akitoshi Hara[8], Yukihiro Shiraki[3], Shinji Mii[3,4], Mari Ichinose[1,2], Laura Vrbanac[1,2], Matthew J. Lawrence[9], Tarik Sammour[1,2,9], Kay Uehara[10], Gareth Davies[11], Leszek Lisowski[12,13,14], Ian E. Alexander[15,16], Yoku Hayakawa[7], Lisa M. Butler[1,2], Andrew C. W. Zannettino[1,2], M. Omar Din[17], Jeff Hasty[18], Alastair D. Burt[1,19], Simon J. Leedham[20], Anil K. Rustgi[21], Siddhartha Mukherjee[22], Timothy C. Wang[22], Atsushi Enomoto[3]*, Masahide Takahashi[3,4,23]*, Daniel L. Worthley[2]*, and Susan L. Woods[1,2, 24]*

[1]Adelaide Medical School, University of Adelaide, Adelaide, SA, 5000, Australia.

[2]South Australian Health and Medical Research Institute, Adelaide, SA, 5000, Australia.

[3]Department of Pathology, [4]Division of Molecular Pathology, Center for Neurological Disease and Cancer, Nagoya University Graduate School of Medicine, Nagoya, Aichi, 466-8550, Japan.

[5]Department of Molecular Pathology, Graduate School of Medicine, Fujita Health University, Toyoake, Aichi, 470-1192, Japan.

[6]Department of Gastroenterology and Hepatology, Nagoya University Graduate School of Medicine, Nagoya, Aichi, 466-8550, Japan.

[7]Department of Gastroenterology, Graduate School of Medicine, The University of Tokyo, Tokyo, 113-0033, Japan.

[8]Department of Cardiology, Nagoya University Graduate School of Medicine, Nagoya, Aichi, 466-8550, Japan.

Downloaded for Anonymous User (n/a) at The University of Adelaide from ClinicalKey.com.au by Elsevier on February 19, 2021.
For personal use only. No other uses without permission. Copyright ©2021. Elsevier Inc. All rights reserved.

[9]Colorectal Unit, Department of Surgery, Royal Adelaide Hospital, Adelaide, SA, 5000, Australia.

[10]Division of Surgical Oncology, Department of Surgery, Nagoya University Graduate School of Medicine, Nagoya, Aichi, 466-8550, Japan.

[11]UCB Pharma, Slough, Berkshire, UK.

[12]Translational Vectorology Research Unit, Children's Medical Research Institute, Faculty of Medicine and Health, The University of Sydney, Sydney, NSW, Australia.

[13]Vector and Genome Engineering Facility, Children's Medical Research Institute, Faculty of Medicine and Health, The University of Sydney, Westmead, NSW 2145, Australia.

[14]Military Institute of Hygiene and Epidemiology, The Biological Threats Identification and Countermeasure Centre, 24-100 Puławy, Poland.

[15]Gene Therapy Research Unit, Sydney Children's Hospitals Network and Children's Medical Research Institute, Faculty of Medicine and Health, The University of Sydney, Sydney, NSW, Australia.

[16]Discipline of Child and Adolescent Health, Faculty of Medicine and Health, The University of Sydney, NSW, Australia.

[17]GenCirq, Inc., San Diego, CA, USA.

[18]Department of Bioengineering, University of California, San Diego, La Jolla, CA USA.

[19]Precision and Molecular Pathology, Newcastle University, Newcastle upon Tyne NE2 4HH, UK.

[20]Intestinal Stem Cell Biology Lab, Wellcome Trust Centre Human Genetics, University of Oxford, Oxford, UK.

[21]Herbert Irving Comprehensive Cancer Center, Division of Digestive and Liver Diseases, Department of Medicine, Columbia University, New York, NY, USA.

[22]Department of Medicine and Irving Cancer Research Center, Columbia University, New York, NY, USA.

Downloaded for Anonymous User (n/a) at The University of Adelaide from ClinicalKey.com.au by Elsevier on February 19, 2021.
For personal use only. No other uses without permission. Copyright ©2021. Elsevier Inc. All rights reserved.

[23]International Center for Cell and Gene Therapy, Fujita Health University, Toyoake, Aichi, 470-1192, Japan.

[24]Lead contact.

*Co-corresponding authors.

Grant Support

This study was supported by grants from the National Health and Medical Research Council (APP1156391 to D.L.W., S.L.W.; APP1108311 and APP1161583 to L.L.); Cancer Council SA Beat Cancer Project on behalf of its donors and the State Government of South Australia through the Department of Health (MCF0418 to S.L.W., D.L.W., and PRF1117 to L.M.B.); a Grant-in-Aid for Scientific Research (S) (26221304 to M.T.) commissioned by the Ministry of Education, Culture, Sports, Science and Technology of Japan; AMED-CREST (Japan Agency for Medical Research and Development, Core Research for Evolutional Science and Technology (19gm0810007h0104 and 19gm1210008s0101 to A.E.); the Project for Cancer Research and Therapeutic Evolution (P-CREATE) from AMED (19cm0106332h0002 to A.E.); Japan Society for the Promotion of Science Overseas Challenge Program for Young Researchers (to H.K.), Takeda Science Foundation Fellowship (to H.K.), Greaton International Ph.D. Scholarship (to H.K.).

Abbreviations

AAV, adeno-associated virus; ANOVA, analysis of variance; AOM, azoxymethane; BMP, bone morphogenetic protein; CAFs, cancer-associated fibroblasts; CRISPR, clustered regularly interspaced short palindromic repeats; CM, conditioned medium; CMS, consensus molecular subtype; CRC, colorectal cancer; DSS, dextran sodium sulfate; FACS, fluorescence-activated cell sorting; GFP, green fluorescent protein; IF, immunofluorescence; IHC, immunohistochemistry; ISH, in-situ hybridization; IVIS, *in vivo* imaging system; PC, principal component; MSCs, mesenchymal stem/stromal cells; qRT-PCR, quantitative reverse-transcription polymerase chain reaction;

Downloaded for Anonymous User (n/a) at The University of Adelaide from ClinicalKey.com.au by Elsevier on February 19, 2021.
For personal use only. No other uses without permission. Copyright ©2021. Elsevier Inc. All rights reserved.

scRNA-seq, single-cell RNA-sequencing; smFISH, single-molecule fluorescent in-situ hybridization; TGFβ, transforming growth factor β; TSS, transcriptional start site

Correspondence

Lead contact; S.L.W.

S.L.W.; susan.woods@adelaide.edu.au, Group Leader, Gut Cancer, the University of Adelaide,

D.L.W.; Dan.Worthley@sahmri.com, Group Leader, Gut Health, SAHMRI

Address: SAHMRI (5 South), North Terrace, Adelaide SA 5000, AUSTRALIA, 08-8128-4386

M.T.; mtakaha@med.nagoya-u.ac.jp, Professor, International Center for Cell and Gene Therapy, Fujita Health University

Address: 1-98 Dengakugakubo, Kutsukake-Cho, Toyoake, Aichi, 470-1192, JAPAN. 05-6293-2884

A.E.; enomoto@iar.nagoya-u.ac.jp, Professor, Department of Pathology, Nagoya University School of Medicine

Address: 65 Tsurumai-Cho, Showa-Ku, Nagoya, Aichi, 466-8550, JAPAN, 05-2744-2093

Disclosures

These authors disclose the following: Gareth Davies is a researcher at UCB Pharma (Slough, Berkshire, UK). A GREM1-neutralizing antibody was generated by the UCB Pharma and provided to researchers at the Gut Cancer Group, the University of Adelaide (Australia), at no cost. L.L. has consulted on technologies addressed in this paper and has stock and/or equity in companies with technology broadly related to this paper. M.O.D. and J.H. have financial interest in GenCirq Inc. (San Diego, CA, USA). All other authors declare no conflicts of interest.

Transcript Profiling: N/A

Writing Assistance: N/A

Downloaded for Anonymous User (n/a) at The University of Adelaide from ClinicalKey.com.au by Elsevier on February 19, 2021.
For personal use only. No other uses without permission. Copyright ©2021. Elsevier Inc. All rights reserved.

Author Contributions

H.K., K.A.G., A.E., M.T., D.L.W., and S.L.W. conceived and designed the study. H.K. performed most of the experiments and statistical analyses. K.A.G. conducted an *in vivo* GREM1-neutralizing antibody experiment. J.A.W. performed an *in vitro* tumoroid experiment using *Islr*-YH2 cells. T.W. (Tongtong Wang) analyzed RNA-seq datasets. J.A.W., T.R.M, N.S., and S.L.W. generated genetically engineered CRC organoids. Y.M., T.I., and R.A. performed smFISH. H.K., N.A., and J.Q.N. performed animal experiments with reporter mice. K.U. collected human CRC clinical data and provided the samples. L.L. produced and titered AAV vectors. G.D. provided a GREM1-neutralizing antibody and intellectual input. N.A., A.D.B., A.E., M.T., D.L.W., and S.L.W. supervised the project. H.K., A.D.B., A.E., M.T., D.L.W., and S.L.W. wrote the manuscript. All authors contributed substantially to the discussion of content for the article, reviewed and/or edited the manuscript before submission.

Word count:

Abstract; 259 words

Main manuscript characters; 6997 words

(inclusive of main text; references; figure legends)

Total number of figures and tables: 6 figures

Acknowledgments

We thank Kaori Ushida, Kozo Uchiyama, and Riku Takeuchi (Nagoya University, JAPAN) for technical assistance, Vector and Genome Engineering Facility (VGEF), Children's Medical Research Institute (CMRI) (NSW, AUSTRALIA) for producing recombinant AAV vectors, Dr. Andrew Kueh and Dr. Marco Herold (The Walter and Eliza Hall Institute of Medical Research, Victoria, AUSTRALIA) for amplicon sequencing of genetically engineered tumoroids. The Rspo-2 expression plasmid and a mouse colonic fibroblast cell line, YH2, were kind gifts from Professor Antony Burgess (Walter and

Downloaded for Anonymous User (n/a) at The University of Adelaide from ClinicalKey.com.au by Elsevier on February 19, 2021.
For personal use only. No other uses without permission. Copyright ©2021. Elsevier Inc. All rights reserved.

Eliza Hall Institute of Medical Research, Australia). L-Wnt3a cells were a kind gift from Professor Hans Clevers (Hubrecht Institute, The Netherlands).

Journal Pre-proof

Downloaded for Anonymous User (n/a) at The University of Adelaide from ClinicalKey.com.au by Elsevier on February 19, 2021.
For personal use only. No other uses without permission. Copyright ©2021. Elsevier Inc. All rights reserved.

Abstract

Background and aims

Cancer-associated fibroblasts (CAF), key constituents of the tumor microenvironment, either promote or restrain tumor growth. Attempts to therapeutically target CAFs have been hampered by our incomplete understanding of these functionally heterogeneous cells. Key growth factors in the intestinal epithelial niche, bone morphogenetic proteins (BMPs), also play a critical role in colorectal cancer (CRC) progression. However, the crucial proteins regulating stromal BMP balance and the potential application of BMP signaling to manage CRC remain largely unexplored.

Methods

Using human CRC RNA expression data, we identified CAF-specific factors involved in BMP signaling, then verified and characterized their expression in the CRC stroma by *in situ* hybridization. CRC tumoroids and a mouse model of CRC hepatic metastasis were used to test approaches to modify BMP signaling and treat CRC.

Results

We identified *Grem1* and *Islr* as CAF-specific genes involved in BMP signaling. Functionally, GREM1 and ISLR acted to inhibit and promote BMP signaling, respectively. *Grem1* and *Islr* marked distinct fibroblast subpopulations, and were differentially regulated by TGFβ and FOXL1, providing an underlying mechanism to explain fibroblast biological dichotomy. In CRC patients, high *GREM1* and *ISLR* expression were associated with poor and favorable survival, respectively. A GREM1-neutralizing antibody or fibroblast *Islr* overexpression reduced CRC tumoroid growth and promoted *Lgr5*$^{+}$ intestinal stem cell differentiation. Finally, adeno-associated virus 8 (AAV8)-mediated delivery of *Islr* to hepatocytes increased BMP signaling and improved survival in our mouse model of hepatic metastasis.

Conclusions

Stromal BMP signaling predicts and modifies CRC progression and survival, and can be therapeutically targeted by novel AAV-directed gene delivery to the liver.

Downloaded for Anonymous User (n/a) at The University of Adelaide from ClinicalKey.com.au by Elsevier on February 19, 2021.
For personal use only. No other uses without permission. Copyright ©2021. Elsevier Inc. All rights reserved.

Keywords:

colorectal cancer; cancer-associated fibroblasts; tumor microenvironment; Bone morphogenetic protein

Journal Pre-proof

Downloaded for Anonymous User (n/a) at The University of Adelaide from ClinicalKey.com.au by Elsevier on February 19, 2021.
For personal use only. No other uses without permission. Copyright ©2021. Elsevier Inc. All rights reserved.

Introduction

Colorectal cancer (CRC) is a major cause of cancer mortality[1]. Despite advances in surgical techniques and medical therapies targeting tumor cells, endothelial cells, and immune cells, the majority of metastatic CRC patients still die from their disease[1].

Cancer-associated fibroblasts (CAFs), a key constituent of the tumor microenvironment, influence CRC initiation, progression, and dissemination, and can promote drug resistance via secretion of growth factors, chemokines, extracellular matrix, and pro-angiogenic factors[2]. CAFs are not a uniformly pro-tumorigenic entity; rather, CAFs are composed of functionally heterogeneous subpopulations including tumor-promoting CAFs and tumor-retarding CAFs[2]. However, the markers and mechanisms underlying this CAF biological dichotomy are largely unknown, which has hampered therapeutic attempts to exploit these differences[2].

One key family of growth factors secreted by CAFs, as well as cancer cells, are the BMPs (bone morphogenetic proteins)[3]. BMPs belong to the TGFβ (transforming growth factor-β) superfamily. Binding of BMP ligands such as BMP 2, 4, and 7, to type I and II BMP receptors, induces phosphorylation of SMAD1/5/8, which in turn binds SMAD4 to increase target gene expression such as *ID1, 2, 3* and *4*[3]. BMP gradients partly define the intestinal epithelial stem cell niche in the normal colon and serve to promote or retard cancer progression in a context-dependent manner[3]. In the normal colon, the epithelial stem cell niche is maintained by low BMP and high Wnt at the crypt base, whereas epithelial cell differentiation is driven by increasing BMP and low Wnt towards the luminal surface[4]. The BMP gradient is finely tuned by BMP inhibitors, such as GREM1 and NOGGIN, which are secreted by fibroblasts near the crypt base[4-6]. In CRC, inactivation of BMP signaling through germline or sporadic mutations in BMP receptors and *SMAD4* contributes to CRC predisposition and progression[4]. Numerous studies have demonstrated the tumor-retarding role of BMP signaling in CRC cells themselves[3, 7, 8]. BMP signaling has been shown to reduce stemness of intestinal stem cells (ISCs) such as *Lgr5*$^{+}$ ISCs, leading to epithelial differentiation[7, 8]. Most CRC studies, however, have failed to address the function of stromal BMP signaling in CRC progression.

Downloaded for Anonymous User (n/a) at The University of Adelaide from ClinicalKey.com.au by Elsevier on February 19, 2021.
For personal use only. No other uses without permission. Copyright ©2021. Elsevier Inc. All rights reserved.

Here, we identified gremlin 1 (*GREM1)* and immunoglobulin superfamily containing leucine-rich repeat (*ISLR),* specifically and distinctly expressed by different types of CRC CAFs, as important regulators of BMP signaling within the tumor microenvironment.

GREM1, a ligand-sequestering antagonist for BMP2, 4, and 7, is expressed by mesenchymal stem/stromal cells (MSCs) in the bone marrow and intestinal fibroblasts[6]. *GREM1* expressed by CAFs can accelerate tumor cell proliferation via inhibition of BMP signaling[9]. In patients with CRC or breast cancer, high *GREM1* expression is associated with poor prognosis[10-12]. GREM1 secreted by glioma cancer stem cells blocks BMP2-induced differentiation of glioma cells, thereby maintaining their proliferation and stemness[13]. Furthermore, overexpression of *GREM1* in intestinal epithelial cells initiates colonic tumorigenesis, supporting the pro-tumorigenic role of *GREM1*[14, 15].

ISLR (also known as Meflin), a GPI (glycosylphosphatidylinositol)-anchored membrane protein, that is also secreted, was recently identified as a specific marker for MSCs and fibroblasts in various organs including the bone marrow, heart, and pancreas[16, 17]. In contrast to the tumor-promoting role of *GREM1*, our recent study found that *ISLR* defines a subset of tumor-retarding CAFs, which are distinct from α-smooth muscle actin $(\alpha SMA)^+$ CAFs in pancreatic cancer[16]. ISLR interacts with BMP7 to augment BMP7-Smad1/5 signaling[17]. Although a recent report has indicated that *ISLR* is highly expressed by fibroblasts in the inflamed colon and CRC[18], the biological role of ISLR in CRC related to BMP signaling remains unknown.

In this study, following the identification and validation of *GREM1* and *ISLR* as two functionally opposing BMP-related genes specifically expressed by CRC CAFs, we examined the prognostic significance of *GREM1* and *ISLR* expression levels in human CRC. Then, we characterized distinct expression patterns of *GREM1* and *ISLR* in both normal colon and CRC and the potential mechanism by which this CAF polarization occurs. Next, we explored whether a GREM1-neutralizing antibody or conditioned medium transfer from *Islr*-overexpressing colonic fibroblasts could restrain CRC organoid growth. Finally, we investigated whether AAV (adeno-associated virus) 8-mediated ectopic overexpression of *Islr* in hepatocytes could retard CRC liver metastasis progression in mice,

Downloaded for Anonymous User (n/a) at The University of Adelaide from ClinicalKey.com.au by Elsevier on February 19, 2021.
For personal use only. No other uses without permission. Copyright ©2021. Elsevier Inc. All rights reserved.

as a novel therapeutic approach to restrain CRC metastasis progression.

Materials and Methods

Statistical analysis

A comparison of 2 groups was performed using two-tailed unpaired t-tests or Mann–Whitney U tests. For multiple comparisons, we used analysis of variance (ANOVA) with subsequent Tukey or Sidak's post-hoc analysis (for parametric tests), or Kruskal-Wallis test followed by Dunn's post-hoc multiple comparisons (for non-parametric tests). For survival analyses, Kaplan-Meier survival estimation with a Log-rank (Mantel-cox) test was performed. Statistical analyses were conducted using GraphPad Prism 8.00 (GraphPad) or SPSS Statistics ver. 25 (IBM). P-values of less than 0.05 were considered statistically significant.

For all other Materials and Methods, see **Supplementary Materials**.

Results

Identification of CAF-specific expression of the BMP antagonist GREM1 and the BMP potentiator ISLR in CRC

To identify which BMP-related genes are specifically expressed by CAFs, we first analyzed expression microarray data from a study of fluorescence-activated cell sorting (FACS)-purified cells from human primary CRC tissues[19]. The top 150 differentially expressed gene probes upregulated in CAFs in each group (FAP^+ CAFs vs. $EpCAM^+$ cancer cells, FAP^+ CAFs vs. $CD31^+$ endothelial cells, and FAP^+ CAFs vs. $CD45^+$ immune cells) were selected for our analysis, resulting in the identification of 34 genes specifically expressed in human CRC CAFs **(Figure 1A; Supplementary Figure 1A and B; Supplementary Table 1)**. Next, to examine for genes involved in BMP signaling, we compared the 34 CAF-specific genes, with BMP-relevant genes listed in Gene Ontology and identified by literature review (BMP signaling pathway; GO0030509)[17] **(Figure 1B)**. This analysis

Downloaded for Anonymous User (n/a) at The University of Adelaide from ClinicalKey.com.au by Elsevier on February 19, 2021.
For personal use only. No other uses without permission. Copyright ©2021. Elsevier Inc. All rights reserved.

identified two genes, *GREM1* and *ISLR*, as human CRC CAF-specific genes relevant to BMP signaling.

To validate *GREM1* and *ISLR* expression in human CRC CAFs, we performed RNA *in situ* hybridization (ISH) on CRC patient samples and confirmed that both *GREM1* and *ISLR* are highly expressed by fibroblastic cells in the human CRC stroma compared to the normal colorectal stroma **(Figure 1C; Supplementary Figure 2)**. Consistent with the microarray data, single-molecule fluorescent ISH (smFISH) for *GREM1* and *ISLR* followed by FAP immunofluorescence showed that *GREM1* and *ISLR* were expressed by FAP^+ CAFs in human CRC sections **(Supplementary Figure 3)**. Moreover, the fibroblast-specific expression pattern of *GREM1* and *ISLR* was corroborated by analyses of publicly available single-cell RNA-seq (scRNA-seq) data from human normal colon mucosa and primary CRC[20] **(Supplementary Figure 4A and B)**.

We next sought to verify the functional roles of GREM1 and ISLR in the regulation of BMP signaling, using lentivirus-mediated overexpression of *Grem1* or *Islr* in a mouse colonic fibroblast cell line, YH2 cells. GREM1 and ISLR overexpression were detected in the conditioned medium from *Grem1*-overexpressing and *Islr*-overexpressing YH2 cells, respectively, suggesting that GREM1 and ISLR were secreted into the medium **(Figure 1D)**. Luciferase assays of BMP-responsive elements revealed that GREM1 overexpression suppressed, whereas ISLR overexpression augmented, BMP signaling **(Figure 1E)**. Furthermore, GREM1 overexpression inhibited BMP7-mediated phosphorylation of Smad1/5, a downstream effector of BMP signaling, thereby preventing the BMP7-induced increase in expression of BMP target genes, *Id2* and *Id4* **(Figure 1F and G)**. Conversely, these surrogates for the BMP signaling pathway were increased by ISLR overexpression. When *Grem1*-overexpressing YH2 cells were admixed with *Islr*-overexpressing YH2 cells, GREM1 and ISLR counteracted each other's effect on BMP7 signaling **(Supplementary Figure 5)**. Similar to the GREM1 antagonism of BMP7 signaling, GREM1 overexpression also prevented the BMP2-induced increase in *Id2* and *Id4*. In contrast, ISLR overexpression promoted the BMP2-mediated increase in *Id4*, but not *Id2* **(Supplementary Figure 6)**. Collectively, these data

Downloaded for Anonymous User (n/a) at The University of Adelaide from ClinicalKey.com.au by Elsevier on February 19, 2021.
For personal use only. No other uses without permission. Copyright ©2021. Elsevier Inc. All rights reserved.

indicate that two functionally opposing stromal regulators of BMP signaling, *GREM1* and *ISLR*, are upregulated in CRC CAFs and may contribute to fine-tuning of BMP signaling within the CRC stroma.

GREM1 and ISLR expression are upregulated during colorectal carcinogenesis in humans

Next, we investigated whether expression of *GREM1* and *ISLR* is upregulated during CRC progression. ISH for *GREM1* and *ISLR*, as well as scRNA-seq and expression microarray analyses, revealed that *GREM1* and *ISLR* expression were increased during human colorectal carcinogenesis **(Figure 2A and B; Supplementary Figure 4A and 7A-C)**. *GREM1* and *ISLR* upregulation was also observed in the stroma of liver metastases of human CRC compared to the normal liver tissues **(Supplementary Figure 8A-C)**. Furthermore, in line with the fibroblast-specific expression of *GREM1* and *ISLR*, analyses of The Cancer Genome Atlas (TCGA) and expression microarray data showed that the highest expression of *GREM1* and *ISLR* was observed in a stroma-rich molecular subtype of CRC (Consensus Molecular Subtype 4; CMS4) **(Supplementary Figure 9A and B)**. This is consistent with a recent paper showing that CMS4 tumors displayed the highest *GREM1* transcript levels[10]. Overall, these data suggest that *GREM1* and *ISLR* expression are upregulated in the CRC stroma during colorectal carcinogenesis.

GREM1 and ISLR expression levels are associated with poor and favorable clinical outcomes in patients with CRC, respectively

To investigate the clinical significance of *GREM1* and *ISLR* expression in CRC CAFs, we evaluated *GREM1* and *ISLR* expression by ISH in 53 rectal cancer surgical samples **(Figure 2C; Supplementary Table 2)**. Survival analyses demonstrated that high *GREM1* expression (Score ≥ 3) and high *ISLR* expression (Score ≥ 2) were independent prognostic factors for poor and favorable disease-free survival, respectively, in patients with rectal cancer **(Figure 2D: Supplementary Table 2 and 3)**.

Downloaded for Anonymous User (n/a) at The University of Adelaide from ClinicalKey.com.au by Elsevier on February 19, 2021.
For personal use only. No other uses without permission. Copyright ©2021. Elsevier Inc. All rights reserved.

Furthermore, analysis of expression microarray data from 556 primary colon cancer patient confirmed that the *GREM1*-high and *ISLR*-low groups each independently exhibited poor overall survival **(Figure 2E and Supplementary Table 4)**. No patients in this cohort had both *GREM1*-high and *ISLR*-low, suggesting that *GREM1*-high patients and *ISLR*-low patients were two separate patient subgroups **(Supplementary Table 5)**. Together, these data indicate that *GREM1* and *ISLR* expression levels may serve as prognostic biomarkers in human CRC with *GREM1* expression associated with poorer and *ISLR* expression associated with improved survival.

Grem1$^+$ *fibroblasts are distinct from Islr*$^+$ *fibroblasts in the normal mouse colon, with the majority of Grem1*$^+$ *fibroblasts marked by Foxl1*

We next sought to characterize the specific stromal cell types expressing *Grem1* and *Islr* in the normal colon. To this end, we performed *Grem1* and *Islr* ISH using normal mouse colons **(Figure 3A and B)**. As shown elsewhere[14], our ISH data confirmed that *Grem1* expression was observed in fibroblastic cells near the base of the colonic crypts in the lamina propria, as well as in muscularis mucosae cells. Interestingly, however, *Islr*$^+$ fibroblasts were located near the middle of the colonic crypts, suggesting that *Grem1*$^+$ intestinal fibroblasts were topographically distinct from *Islr*$^+$ intestinal fibroblasts in the normal colonic crypts.

To further define the fibroblast subpopulations expressing *Grem1* and *Islr*, we studied *Grem1*-CreERT2[6]; Rosa26-LSL-tdtomato mice and *Islr*-CreERT2[17]; Rosa26-LSL-tdtomato mice and co-stained with intestinal fibroblast markers **(Figure 3C and D)**. A recent report has illustrated that subepithelial telocytes identified by expression of *Foxl1* and platelet-derived growth factor receptor alpha (*Pdgfra*), provide key intestinal stem cell niche signaling molecules such as Wnts and *Grem1*[21]. Indeed, analysis of RNA-seq data from FACS-purified *Foxl1*-lineage intestinal telocytes and non-*Foxl1*-lineage intestinal mesenchymal cells[21] suggested that *Grem1* expression was observed in *Foxl1*-lineage$^+$ telocytes, but not in *Foxl1*-lineage$^-$ cells **(Supplementary Figure 10)**. Consistent with this, *Foxl1* smFISH or PDGFRα immunofluorescence (IF) using *Grem1*-CreERT2 mice showed that

Downloaded for Anonymous User (n/a) at The University of Adelaide from ClinicalKey.com.au by Elsevier on February 19, 2021.
For personal use only. No other uses without permission. Copyright ©2021. Elsevier Inc. All rights reserved.

the majority of the *Grem1*$^+$ fibroblasts, also known as *Grem1*$^+$ intestinal reticular stem cells (iRSCs)[6], expressed the telocyte markers, *Foxl1* and PDGFRα, in the lamina propria of the normal colon **(Figure 3C and D)**. In contrast, *Islr*$^+$ fibroblasts exhibited lower positivity for *Foxl1* and PDGFRα than *Grem1*$^+$ iRSCs. These data implied a high degree of overlap between *Grem1*$^+$ iRSCs and *Foxl1*$^+$ telocytes. This prompted us to investigate whether *Foxl1* might drive *Grem1* expression at the expense of *Islr* expression.

FOXL1 directly upregulates Grem1 transcription while repressing Islr expression in mouse colonic fibroblasts

To assess the effect of FOXL1 on the regulation of *Grem1* and *Islr* expression, human *FOXL1*-overexpressing YH2 cells were generated by lentiviral transduction **(Figure 3E)**. Consistent with our earlier co-localization analyses, FOXL1 overexpression in YH2 cells induced *Grem1* upregulation at the expense of *Islr* expression, accompanied by decreased *Id2* expression **(Figure 3F)**. Similarly, luciferase reporter assays showed that FOXL1 overexpression increased the activity of the *GREM1*-promoter reporter and reduced the activity of the *ISLR*-promoter reporter in comparison to control empty YH2 lines **(Supplementary Figure 11)**. Conversely, CRISPR/Cas9-mediated *Foxl1*-knockdown in mouse primary colonic fibroblasts attenuated *Grem1* expression while inducing upregulation of *Islr* and BMP target genes **(Figure 3G and Supplementary Figure 12)**.

To explore whether FOXL1 is directly involved in regulating *Grem1* expression, we generated *FOXL1*-Hemagglutinin (HA) tag-overexpressing YH2 cells **(Figure 3H)** and performed chromatin immunoprecipitation (CHIP) using an anti-HA antibody. CHIP-qPCR showed enrichment of FOXL1-HA binding to the *Grem1* promoter (transcriptional start site +2008 to +2014 bps; an intronic region) compared to immunoglobulin controls **(Figure 3I and J)**. Consistent herewith, a luciferase assay using the human *GREM1* promoter region in YH2 cells confirmed that FOXL1-mediated augmentation of *GREM1* expression was abrogated by truncation of the *GREM1* promoter to remove

Downloaded for Anonymous User (n/a) at The University of Adelaide from ClinicalKey.com.au by Elsevier on February 19, 2021.
For personal use only. No other uses without permission. Copyright ©2021. Elsevier Inc. All rights reserved.

the FOXL1-binding region **(Figure 3K)**. Collectively, these data indicate that FOXL1 is recruited to the *Grem1/GREM1* promoter to drive *Grem1* expression, providing mechanistic insight into the overlap between *Grem1*$^+$ iRSCs and *Foxl1*$^+$ telocytes.

GREM1$^+$ CAFs are myofibroblastic CAFs, which are distinct from *ISLR*$^+$ CAFs, in mouse and human CRC

Next, we sought to characterize *GREM1*$^+$ CAFs and *ISLR*$^+$ CAFs in the CRC mesenchyme. Using azoxymethane (AOM)/ dextran sulfate sodium (DSS) mouse CRC and human CRC samples, we carried out *Grem1/GREM1* and *Islr /ISLR* smFISH as well as IF for αSMA, a well-established marker of myofibroblastic CAFs. We found that, both in mouse and human CRC, *Grem1/GREM1*$^+$ CAFs were distinct from *Islr/ISLR*$^+$ CAFs and that αSMA positivity was higher in *Grem1/GREM1*$^+$ CAFs than *Islr/ISLR*$^+$ CAFs **(Figure 4A-G)**. A collagen gel contraction assay also revealed that *Grem1*-overexpressing YH2 cells exhibited increased contraction, a hallmark of activated myofibroblasts[2] **(Supplementary Figure 13A and B)**. Consistent with our smFISH data, scRNA-seq data from human CRC tissues[20] confirmed that *GREM1* expression levels were inversely correlated with *ISLR* expression **(Supplementary Figure 14A)** and that *GREM1*, but not *ISLR*, transcripts were positively correlated with *ACTA2* expression in CRC CAFs **(Supplementary Figure 14B)**. Furthermore, the scRNA-seq dataset revealed that *GREM1* was predominantly expressed by myofibroblasts. High *ISLR* transcripts were observed not only in myofibroblasts but also in Stromal 2 fibroblasts that are characterized by spatial proximity to epithelial cells and high expression of BMP ligands including BMP7[20] **(Supplementary Figure 14C and D)**. Interestingly, *GREM1*$^+$ CAFs were spatially distinct from *ISLR*$^+$ CAFs in desmoplastic human CRC, with *ISLR*$^+$ CAFs located in closer proximity to cancer cells than *GREM1*$^+$ CAFs **(Figure 4H and I)**.

As TGF-β1 has well-characterized functions in inducing myofibroblastic differentiation of CAFs[2], we examined whether TGF-β1 is involved in controlling the differential expression of *Grem1* and *Islr*. Stimulation of YH2 cells with recombinant TGF-β1 increased transcript levels of TGF-β target genes,

Downloaded for Anonymous User (n/a) at The University of Adelaide from ClinicalKey.com.au by Elsevier on February 19, 2021.
For personal use only. No other uses without permission. Copyright ©2021. Elsevier Inc. All rights reserved.

Serpine1 and *Acta2*, but also *Foxl1* and *Grem*1, while decreasing *Islr* expression. This was rescued by co-treatment with Galunisertib, a specific inhibitor for TGF-β receptor 1 **(Figure 4J)**. In keeping with the TGFβ-induced upregulation of *Foxl1* and *Grem1 in vitro*, *GREM1*$^{+}$ CAFs showed a higher degree of co-localization with *FOXL1* in human CRC sections than *ISLR*$^{+}$ CAFs did **(Supplementary Figure 15)**. Together, our data suggest that TGF-β1 upregulates *Foxl1* in fibroblasts that, in turn, binds to the *Grem1* promoter to upregulate *Grem1* expression. TGF-β1 and Foxl1 also reduce the expression of *Islr.* This signaling pathway may be involved in the selective development or differentiation of αSMA^{+}*Grem1*$^{+}$ myofibroblastic CAFs, which are distinct from *Islr*$^{+}$ αSMA^{-} CAFs, in mouse and human CRC.

Blocking BMP antagonism using a GREM1-neutralizing antibody promotes CRC organoid differentiation and restrains growth

What relevance do these stromal changes have on the cancer? We investigated whether augmenting BMP signaling either by *Grem1* inhibition or *Islr* overexpression could retard CRC progression. To this end, we took advantage of CRISPR/Cas9 genome engineering and generated luciferase-expressing *Apc*$^{\Delta/\Delta}$, *Trp53*$^{\Delta/\Delta}$ mouse CRC organoids (henceforth referred to as AP tumoroids) **(Supplementary Figure 16A and B)**. To disrupt BMP signaling, we sequentially mutated *Smad4*, a downstream effector of BMP signaling, to generate *Smad4*-mutant AP tumoroids (hereafter termed APS tumoroids) **(Supplementary Figure 16C and D)**.

Firstly, to test the role of GREM1 in CRC organoid growth, conditioned medium (CM) from *Grem1*-YH2 cells or control GFP-YH2 cells was transferred to either AP or APS tumoroids **(Supplementary Figure 17A)**. As expected, the expression of BMP target genes was repressed by CM transfer from *Grem1*-YH2 cells only in AP tumoroids, but not in APS tumoroids **(Supplementary Figure 17B)**. Luciferase activity was used to assess an effect of the treatment on viable cell number in luciferase-expressing AP or APS tumoroid cultures. CM from *Grem1*-YH2 cells increased the tumoroid-derived luciferase signals in AP tumoroids **(Supplementary Figure 17C)**. This was

Downloaded for Anonymous User (n/a) at The University of Adelaide from ClinicalKey.com.au by Elsevier on February 19, 2021.
For personal use only. No other uses without permission. Copyright ©2021. Elsevier Inc. All rights reserved.

ameliorated by the loss of *Smad4* in APS tumoroids, indicating that the pro-proliferation effect of GREM1 occurred via antagonism of BMP signaling. Consistent with the role of BMP signaling in promoting epithelial cell differentiation[4, 22], CM from *Grem1*-YH2 cells decreased the expression of *Krt20*, a marker for differentiated CRC cells, in AP tumoroids, but not in APS tumoroids **(Supplementary Figure 17D)**.

We next examined whether restoring BMP signaling with a GREM1-neutralizing antibody could repress CRC organoid growth. For this purpose, either a GREM1-neutralizing antibody or an IgG isotype was added to the AP and APS tumoroids incubated in CM from *Grem1*-YH2 cells **(Figure 5A)**. The effect of the GREM1-neutralizing antibody to abolish GREM1-mediated BMP antagonism was validated by quantitative reverse-transcription PCR (qRT-PCR) of *Id2* in YH2 cells **(Supplementary Figure 18A and B)**. Blocking the antagonism of BMP signaling by GREM1 using the GREM1-neutralizing antibody restored BMP target gene expression **(Figure 5B)** and reduced tumoroid-derived luciferase signals and tumoroid size in AP tumoroids, but not in APS tumoroids **(Figure 5C and D; Supplementary Figure 19A)**. Moreover, treatment with the GREM1-neutralizing antibody decreased *Lgr5* expression with a concomitant increase in *Krt20* expression in AP tumoroids. This effect was abrogated in APS tumoroids **(Figure 5E)**. Collectively, our *in vitro* data suggest that restoring BMP signaling with the GREM1-neutralizing antibody promoted differentiation of *Lgr5*$^{+}$ intestinal stem cells and attenuated tumoroid growth of *Smad4*-wild-type, but not *Smad4*-mutant CRC.

Conditioned medium from Islr-overexpressing intestinal fibroblasts increases BMP signaling, facilitates CRC organoid differentiation, and attenuates growth

Next, we tested whether CM from *Islr*-overexpressing YH2 cells could augment BMP signaling in CRC tumoroids and thus inhibit CRC tumoroid growth. Given that ISLR overexpression promoted BMP signaling in the presence of recombinant BMP7 **(Figure 1F and G)**, we collected CM from *Islr*- or GFP-overexpressing YH2 cells incubated with recombinant BMP7 and transferred the CM to AP

Downloaded for Anonymous User (n/a) at The University of Adelaide from ClinicalKey.com.au by Elsevier on February 19, 2021.
For personal use only. No other uses without permission. Copyright ©2021. Elsevier Inc. All rights reserved.

tumoroids **(Figure 5F)**. In keeping with our hypothesis of the opposing roles of GREM1 and ISLR, CM from *Islr*-YH2 cells increased *Id1* expression in AP tumoroids, suggesting that ISLR overexpression in fibroblasts enhanced BMP signaling in CRC tumoroids in a paracrine manner **(Figure 5G)**. Moreover, medium conditioned by *Islr*-YH2 cells decreased AP tumoroid-derived luciferase signals and tumoroid size **(Figure 5H and I; Supplementary Figure 19B)**. Similar to the GREM1-neutralizing antibody, this tumoroid growth inhibition by *Islr*-YH2 cell media was accompanied by a reduction in *Lgr5* transcripts and increased *Krt20* expression in AP tumoroids **(Figure 5J)**. Taken together, our *in vitro* studies indicate that modulating stromal, secreted BMP regulators of BMP signaling through either GREM1-neutralizing antibody or *Islr*-overexpression facilitates *Lgr5*$^{+}$ intestinal stem cell differentiation and diminishes CRC tumoroid growth.

Modifying the metastatic niche by AAV8-mediated in vivo overexpression of Islr in hepatocytes retards CRC hepatic metastasis

Hepatic metastasis is the major cause of CRC death[1], and, through portal vein dissemination, complicates most advanced gastrointestinal adenocarcinomas. Therefore, we explored whether enhancing BMP signaling either by the GREM1-neutralizing antibody or *Islr* overexpression could impair hepatic metastagenesis of CRC *in vivo*. For this purpose, we generated a mouse model of CRC hepatic metastasis using intraportal injection of AP tumoroids **(Figure 6A)**.

Initially, we examined whether treatment with the GREM1-neutralizing antibody could retard CRC hepatic metastasis and improve survival in comparison to an IgG isotype-treated control group **(Supplementary Figure 20A)**. Consistent with our earlier observation in human CRC liver metastases **(Supplementary Figure 8A and B)**, ISH for *Grem1* confirmed that *Grem1* was expressed by fibroblastic cells in the stroma of mouse CRC hepatic metastases **(Supplementary Figure 20B)**. Immunohistochemistry for pSmad1/5/8 demonstrated that the treatment with GREM1-neutralizing antibody restored BMP signaling in metastatic CRC **(Supplementary Figure 20C and D)**. The GREM1-neutralizing antibody-treated group showed a trend towards prolonged

Downloaded for Anonymous User (n/a) at The University of Adelaide from ClinicalKey.com.au by Elsevier on February 19, 2021.
For personal use only. No other uses without permission. Copyright ©2021. Elsevier Inc. All rights reserved.

overall survival and a trend towards decreased tumor growth, albeit that the groups, as dosed in this study, did not show significant differences in survival **(Supplementary Figure 20E and F)**.

Thus, we then focused on the other key stromal BMP signaling regulator, *Islr*. Inspired by recent advances in AAV-mediated gene therapy in human diseases[23, 24], we reasoned that augmenting BMP signaling, via ectopic overexpression of *Islr* in hepatocytes, a liver cell type shown to contribute to a metastatic niche[25], could potentially ameliorate the progression of CRC hepatic metastasis. We injected AAV8 (an AAV serotype with tropism for murine hepatocytes[26]) encoding either *Islr* or, as a control, a red fluorescent protein (mRuby2), via mouse tail vein **(Figure 6A)** to generate ectopic *Islr* overexpression in hepatocytes *in vivo* **(Figure 6B and C)**. Two weeks after the tail vein injection, AP tumoroid cells were injected directly into the portal vein to generate CRC hepatic metastases. The liver-directed delivery of *Islr* enhanced BMP signaling in CRC hepatic metastasis as well as in normal hepatocytes **(Figure 6D and E; Supplementary Figure 21A-C)**, and significantly prolonged mouse survival compared to the AAV8-mRuby2 control group **(Figure 6F)**. Notably, there was no histological evidence of liver injury induced by AAV8-*Islr* **(Supplementary Figure 22A and B)**.

To evaluate alterations in growth kinetics and histopathology by AAV8-*Islr*, we next monitored the growth of CRC hepatic metastases with an *in vivo* imaging system (IVIS) and harvested all mice 3 to 4 weeks after tumor injection **(Figure 6A)**. In line with improved survival, the AAV8-*Islr* group showed reduced tumor-derived luminescence signal, histological tumor area, and Ki-67 cell proliferation index **(Figure 6G-L)**. Consistent with our earlier *in vitro* data showing that stromal *Islr* overexpression promoted CRC tumoroid differentiation, *Islr*-overexpression in hepatocytes yielded more differentiated CRC histology **(Figure 6M and N)**. Furthermore, in agreement with anti-fibrotic roles of BMP7 signaling[17], αSMA immunostaining and Picro-Sirius red staining revealed that fibrosis was reduced in the AAV8-*Islr* group **(Supplementary Figure 23A-D)**. Taken together, these data suggest that BMP modulation could be an attractive target in CRC metastasis and that leveraging hepatocytes to augment BMP signaling by AAV8-*Islr* could represent an exciting, novel therapeutic opportunity in metastatic CRC.

Downloaded for Anonymous User (n/a) at The University of Adelaide from ClinicalKey.com.au by Elsevier on February 19, 2021.
For personal use only. No other uses without permission. Copyright ©2021. Elsevier Inc. All rights reserved.

Discussion

Initially identified more than 50 years ago[27], BMP is now known to be important in regulating intestinal epithelial homeostasis and cancer cell proliferation[3, 4]. The regulation of BMP in the tumor microenvironment and the role of BMP in tumor management, however, are still largely unknown. In the present study, we have shown that *GREM1* and *ISLR* are CAF-specific factors that exert opposing effects on BMP signaling in colonic fibroblasts and define distinct subpopulations of fibroblasts in the normal colon and CRC. FOXL1 and TGFβ may explain, at least in part, the polarization of CAFs into tumor-promoting *GREM1*$^+$ CAFs and tumor-retarding *ISLR*$^+$ CAFs. Moreover, *GREM1* and *ISLR* expression levels were associated with poor and favorable outcomes in patients with CRC. Using organoid culture and a preclinical mouse model, our data support that BMP signaling imbalance, regulated by *Grem1* and *Islr*, drives CRC progression and is a key target for cancer treatment. We provided the therapeutic proof-of-principle that augmenting BMP signaling, either by using a GREM1-neutralizing antibody or AAV8-*Islr*, represents an attractive future approach to treat CRC.

Previous studies have shown that stromal deletion of BMPR2 could facilitate carcinogenesis in CRC and breast cancer, suggesting tumor-suppressive functions of mesenchymal BMP signaling[28, 29]. Moreover, augmentation of BMP signaling mediated either by increased BMP ligand or decreased BMP antagonist secretion from the tumor mesenchyme, which occurs as a consequence of stromal Hedgehog signaling activation, restrains bladder or colorectal cancer progression[22, 30]. Our work supports these findings and provides novel insights into regulatory mechanisms of BMP signaling in the CRC tumor microenvironment. Given that loss of stromal BMPR2 expression increases cytokine production in a mouse model of breast cancer[28], further studies are warranted to investigate whether mesenchymal BMP signaling modulated by *GREM1* and *ISLR*, could also be involved in shaping the immunosuppressive tumor microenvironment.

High stromal TGFβ signaling is associated with worse outcomes for CRC patients[19]. Here, we provide a potential mechanism underlying CAF heterogeneity, initiated by TGFβ and FOXL1, that

Downloaded for Anonymous User (n/a) at The University of Adelaide from ClinicalKey.com.au by Elsevier on February 19, 2021.
For personal use only. No other uses without permission. Copyright ©2021. Elsevier Inc. All rights reserved.

polarizes fibroblasts towards *Grem1*^{high}*Islr*^{low} CAFs or *Islr*^{high}*Grem1*^{low} CAFs. TGFβ drives *Foxl1* expression in CAFs **(Figure 4J)**. FOXL1, in turn, directly upregulates *Grem1* expression to antagonize BMP signaling **(Figure 3E-K)** and promote cancer progression by suppressing differentiation of *Lgr5*$^{+}$ stem cells while inducing epithelial proliferation. In contrast, relatively low levels of TGFβ in the microenvironment of some tumors results in lower levels of FOXL1 that permits higher *Islr* expression and a relative tumor-suppressive and higher BMP signaling milieu **(Figure 3E-G and 4J)**. This potential TGFβ-FOXL1-*Grem1/Islr*-axis that modulates BMP signaling in the colon provides a novel mechanism to help understand the polarization of CAFs within the tumor microenvironment and presents a promising target for future cancer treatment.

Using scRNA-seq from normal mouse small intestines, one recent paper suggested that *Grem1* is expressed mainly by *Pdgfra*$^{low+}$*Cd81*$^{+}$ trophocytes that are distinct from *Foxl1*$^{+}$ telocytes[5]. Consistent with this, our *Foxl1* smFISH in *Grem1*-CreERT2 mice showed that there were less *Foxl1* and *Grem1* double-positive fibroblasts in the small intestine than the colon **(Supplementary Figure 24)**. This observation raises the possibility of organ-dependent *Foxl1* expression patterns within the context of gastrointestinal fibroblast heterogeneity, which warrants further research.

One limitation of the present study is that we have not unraveled the origins and lineage hierarchy of *Grem1*$^{+}$ iRSCs and *Islr*$^{+}$ fibroblasts despite presenting a potential mechanism for fibroblast polarization. Whether *Grem1*$^{+}$ CAFs and *Islr*$^{+}$ CAFs arise from their local progenitors, are recruited from the bone marrow, or are simply new expression profiles within existing cells, requires further investigation. Considering the possible plasticity of CAFs[2], it is plausible that *Grem1*$^{+}$ CAFs and *Islr*$^{+}$ CAFs could undergo phenotypic interconversion during tumor development, a state of dynamic flux between a relatively polarized cancer-retarding or cancer-promoting microenvironment.

We also provided the first experimental evidence that the GREM1-neutralizing antibody promoted differentiation of *Lgr5*$^{+}$ intestinal stem cells and retarded CRC tumoroid growth only in a *Smad4*-wild-type setting, but not in *Smad4*-mutant tumoroids. Our data reinforce the importance of stratifying patients that may benefit from the GREM1-neutralizing antibody according to the mutation

Downloaded for Anonymous User (n/a) at The University of Adelaide from ClinicalKey.com.au by Elsevier on February 19, 2021.
For personal use only. No other uses without permission. Copyright ©2021. Elsevier Inc. All rights reserved.

status of BMP-related genes such as *SMAD4* and BMP receptors in future preclinical and clinical trials. Our preliminary data with an *in vivo* experimental model of CRC hepatic metastases implied that the GREM1-neutralizing antibody still requires further optimization of therapeutic setting (metastatic prevention vs. treatment), dosage regimens, route of administration, and in combination with other agents. However, the combined *in vitro* and *in vivo* findings are encouraging.

To our knowledge, our study is the first to use AAV8 to target hepatocytes to treat hepatic metastasis[23, 31]. Clinical trials have demonstrated that *in vivo* gene delivery by AAV holds great promise in patients with non-neoplastic diseases such as inherited genetic diseases and degenerative neuromuscular disorders[23]. Excitingly, recent clinical trials have shown that hepatocyte-directed gene transfer of coagulation factors by AAV substantially improved clinical symptoms in patients with hemophilia[23, 24]. In light of new human liver-tropic bioengineered AAVs[26], our work suggests that AAV-mediated hepatocyte-directed therapy could, in the future, serve as a novel and well-tolerated cancer therapy. Furthermore, our findings pave the way for AAV-mediated delivery of payloads to modulate not only BMP signaling, but any other number of the relevant biological hallmarks of cancer[32].

In conclusion, our data show that stromal BMP signaling, inhibited by *GREM1* and promoted by *ISLR,* is biologically relevant in CRC growth, spread, and survival. By targeting the upstream determinants of mesenchymal expression, such as TGFβ and FOXL1, or by targeting the downstream drivers of BMP signaling, such as GREM1 and ISLR, one may identify new approaches to prevent and to treat cancer.

Downloaded for Anonymous User (n/a) at The University of Adelaide from ClinicalKey.com.au by Elsevier on February 19, 2021.
For personal use only. No other uses without permission. Copyright ©2021. Elsevier Inc. All rights reserved.

Figure 1: Identification of *GREM1* and *ISLR* as a BMP antagonist and potentiator, respectively, specifically expressed by CRC CAFs.

(A, B) Analysis of expression microarray data from FACS-purified cells from human primary CRC tissues. **(A)** Venn diagram depicting the overlap of top 150 differentially upregulated transcripts in the three groups as indicated. **(B)** Venn diagram showing the overlap of 34 CAF-specific genes and 157 BMP-related genes identified by Gene ontology of the BMP signaling pathway (GO: 0030509) and Hara *et al*., *Circ Res*, 2019[17].

(C) *In situ* hybridization (ISH) for *GREM1* and *ISLR* in the human normal colorectal mucosa and CRC. Dotted lines indicate the borders between epithelial cells (E) and the stroma (S). Red arrowheads denote *GREM1* or *ISLR* expression. Scale bar, 50 μm.

(D-G) Lentivirus-mediated overexpression of *Grem1* and *Islr* in a mouse colonic fibroblast cell line, YH2 cells, represses and augments BMP signaling, respectively. **(D)** Western blotting (WB) showing *Grem1* and *Islr* overexpression in the total cell lysates and conditioned medium. **(E)** Luciferase assays of BMP-responsive elements. n = 6. **(F, G)** YH2 cells were stimulated with recombinant BMP7, followed by WB **(F)** and quantitative reverse-transcription PCR (qRT-PCR). n = 3. **(G)**. A.U., arbitrary unit.

Mean ± s.e.m.. One-way ANOVA (E) or two-way ANOVA (G) with post-hoc Tukey's multiple comparisons.

Downloaded for Anonymous User (n/a) at The University of Adelaide from ClinicalKey.com.au by Elsevier on February 19, 2021.
For personal use only. No other uses without permission. Copyright ©2021. Elsevier Inc. All rights reserved.

Figure 2: *GREM1* and *ISLR* expression levels are associated with poor and favorable prognosis in patients with CRC, respectively.

(A, B) ISH for *GREM1* and *ISLR* using human rectal samples. **(A)** Representative images. Yellow dotted lines indicate the borders between the lamina propria (LP) and muscularis mucosa (MM). Green, blue, and red arrowheads denote *GREM1* or *ISLR* expression in the normal mucosa, adenoma, and adenocarcinoma, respectively. **(B)** Violin plots depicting *GREM1* and *ISLR* ISH signal^{+} areas in the stroma. 3 high-power fields (HPFs; 400x)/patient; 11 (normal mucosa), 3 (adenoma), 11 patients (adenocarcinoma).

Solid black lines, median; Dotted black lines, quartiles.

(C, D) ISH analysis of 53 human primary rectal cancer surgical samples. **(C)** Representative images. Cases with Score ≥ 3 and Score ≥ 2 were defined as *GREM1*-high and *ISLR*-high, respectively. **(D)** Kaplan-Meier survival curves.

(E) Kaplan-Meier survival curves in expression microarray data from 556 primary colon cancer patients.

Kruskal-Wallis test followed by Dunn's post-hoc multiple comparisons (B) and Log-rank test (D and E).

Scale bars, 50 μm.

Downloaded for Anonymous User (n/a) at The University of Adelaide from ClinicalKey.com.au by Elsevier on February 19, 2021.
For personal use only. No other uses without permission. Copyright ©2021. Elsevier Inc. All rights reserved.

Figure 3: *Grem1* and *Islr* identify distinct subpopulations of intestinal fibroblasts in the normal mouse colon and are differentially regulated by FOXL1.

(A, B) ISH for *Grem1* and *Islr* in the adult normal mouse colon. **(A)** Representative images. Red and green arrowheads denote *Grem1*$^+$ cells and *Islr*$^+$ cells, respectively. Yellow dotted lines delineate the boundaries between epithelial cells (E) and stromal cells (S). White dotted lines indicate the borders between the lamina propria (LP) and muscularis mucosa (MM). V, blood vessels. **(B)** Violin plots depicting the positions of mesenchymal cells expressing *Grem1* or *Islr* relative to the adjacent epithelial position. 344 *Grem1*$^+$ cells and 512 *Islr*$^+$ cells from 20 well-oriented crypts/mouse, 4 mice each. Black solid lines, median; Black dotted lines, quartiles.

(C, D) Single-molecule fluorescent ISH (smFISH) for *Foxl1* and immunofluorescence (IF) for PDGFRα in *Grem1*-CreERT2 mice and *Islr*-CreERT2 mice. **(C)** Representative pictures. Yellow arrowheads indicate double-positive cells (*Grem1*$^+$*Foxl1*$^+$ cells or *Grem1*$^+$PDGFRα$^+$ cells). Red arrowheads denote *Islr*-single-positive cells. **(D)** *Foxl1* positivity and PDGFRα positivity in the *Grem1*$^+$ cells and *Islr*$^+$ cels. 4 HPFs (400x)/mouse, 3 mice each.

(E, F) Lentivirus-mediated human *FOXL1* (h*FOXL1*) overexpression in YH2 cells induces *Grem1* upregulation and decreases *Islr* expression. **(E)** WB. **(F)** qRT-PCR (n = 3).

(G) CRISPR/Cas9-mediated knockdown of *Foxl1* reduces *Grem1* expression while upregulating *Islr* expression in primary mouse colonic fibroblasts as assessed by qRT-PCR (n = 3 mice each).

(H-K) FOXL1 interacts with a *Grem1* intron region. **(H)** WB showing hFOXL1-HA overexpression in YH2 cells. **(I)** Schematic representation of a FOXL1-binding site in the mouse *Grem1* intron (highlighted with yellow) and corresponding human *GREM1* promoter regions used in luciferase assays. TSS, transcriptional start site; ORF, open reading frame. **(J)** CHIP-qPCR in YH2 cells (n = 3).

(K) Luciferase assays of a human *GREM1* promoter (4.3 kbps) and a truncated Human *GREM1* promoter (3.6 kbps) that lacks the FOXL1-binding site (n = 4).

Mean ± s.e.m.. Mann-Whitney U-test (B), two-tailed unpaired Student's t-test (D, F, G, and J) and two-way ANOVA with Tukey's post-hoc multiple comparisons (K). Scale bars, 50 μm.

Downloaded for Anonymous User (n/a) at The University of Adelaide from ClinicalKey.com.au by Elsevier on February 19, 2021.
For personal use only. No other uses without permission. Copyright ©2021. Elsevier Inc. All rights reserved.

Figure 4: *GREM1*$^+$ CAFs are myofibroblastic CAFs, which are distinct from *ISLR*$^+$ CAFs in human and mouse CRC.

(A, B) Dual smFISH for *Grem1* and *Islr* in an AOM/DSS mouse model of CRC. **(A)** Representative pictures. Red, green, and yellow arrowheads denote *Grem1*$^+$*Islr*$^-$ CAFs, *Grem1*$^-$*Islr*$^+$, and *Grem1*$^+$*Islr*$^+$ CAFs, respectively. **(B)** Semi-quantification of the ratio of double-positive (*Grem1*$^+$*Islr*$^+$) cells in *Grem1*$^+$ cells and *Islr*$^+$ cells. 4 HPFs (400x)/mouse, 4 mice.

(C, D) *Grem1* smFISH or *Islr* smFISH followed by αSMA IF in AOM/DSS tumors. **(C)** Representative pictures. Yellow and green arrowheads indicate double-positive cells (*Grem1*$^+$αSMA$^+$ cells or *Islr*$^+$αSMA$^+$ cells) and *Islr*$^+$αSMA$^-$cells, respectively. **(D)** αSMA positivity in *Grem1*$^+$cells and *Islr*$^+$ cells. 4 HPFs/mouse, 4 mice each.

(E-G) Dual smFISH for *GREM1* and *ISLR* followed by αSMA IF in human CRC. **(E)** Representative pictures. Red and green arrowheads denote *GREM1*$^+$αSMA$^+$ cells and *ISLR*$^+$αSMA$^-$ cells, respectively. **(F)** Semi-quantification of the ratio of double-positive (*GREM1*$^+$*ISLR*$^+$) cells in *GREM1*$^+$ cells and *ISLR*$^+$ cells. **(G)** αSMA positivity in *GREM1*$^+$cells and *ISLR*$^+$ cells.
4-6 HPFs/patient, 5 patients.

(H, I) *GREM1*$^+$ CAFs are spatially distinct from *ISLR*$^+$ CAFs in human desmoplastic rectal cancer. **(H)** Representative pictures of *GREM1* and *ISLR* ISH on human desmoplastic rectal cancer samples. Red and green arrowheads denote *GREM1* and *ISLR* expression, respectively. **(I)** Quantification of the minimum distance between *GREM1* or *ISLR* ISH signals and the closest tumor cells. n = 38396 (*GREM1*) and 18028 DAB$^+$ signals (*ISLR*) from 3 low-power fields (100x)/patient, 7 patients each.

(J) YH2 cells were stimulated with a vehicle, recombinant TGFβ1, or recombinant TGFβ1 + Galunisertib for 24 hours, followed by qRT-PCR (n = 3).

Mean ± s.e.m.. Mann-Whitney U-test (D, G, and I) and one-way ANOVA with Tukey's post-hoc multiple comparisons (J). The boxed areas are magnified in the adjacent panels (A, C, and E). Scale bars, 50 μm (A, C, and E) and 250 μm (H). ****, P < 0.0001; **, P = 0.0013; *, P = 0.0122.

Downloaded for Anonymous User (n/a) at The University of Adelaide from ClinicalKey.com.au by Elsevier on February 19, 2021.
For personal use only. No other uses without permission. Copyright ©2021. Elsevier Inc. All rights reserved.

Figure 5: A GREM1-neutralizing antibody or conditioned medium from *Islr*-overexpressing intestinal fibroblasts restrains CRC tumoroid growth and promotes *Lgr5*$^{+}$ stem cell differentiation via increased BMP signaling in tumoroids.

(A) Experimental schematic depicting conditioned medium (CM) transfer from *Grem1*-overexpressing YH2 cells to AP (*Apc*$^{\Delta/\Delta}$ and *Trp53*$^{\Delta/\Delta}$) tumoroids or APS (*Apc*$^{\Delta/\Delta}$, *Trp53*$^{\Delta/\Delta}$, and *Smad4*$^{\Delta/\Delta}$) tumoroids. Either an IgG isotype or a GREM1-neutralizing antibody was added to the tumoroids.

(B) qRT-PCR for *Id1* in AP and APS tumoroids (n = 3).

(C) Representative pictures of AP tumoroids and APS tumoroids.

(D) Luciferase signals from AP tumoroids and APS tumoroids (n ≥ 8).

(E) qRT-PCR for *Lgr5* and *Krt20* in AP and APS tumoroids (n = 3).

(F) Experimental schematic depicting CM transfer from *Islr*-overexpressing YH2 cells to AP tumoroids. CM was collected from *Islr*- or GFP-overexpressing YH2 cells incubated with 10 ng/ml of recombinant BMP7 (rBMP7).

(G) qRT-PCR for *Id1* in AP tumoroids (n = 3).

(H) Representative pictures of AP tumoroids.

(I) Luciferase signals from AP tumoroids (n = 14).

(J) qRT-PCR for *Lgr5* and *Krt20* in AP tumoroids (n = 3).

Scale bars, 500 µm. Mean ± s.e.m.. Two-tailed unpaired Student's t-test (B, D, E, G, I, and J).

Note that data normalization was performed within the AP and APS tumoroid groups separately **(B, D, and E)**.

Downloaded for Anonymous User (n/a) at The University of Adelaide from ClinicalKey.com.au by Elsevier on February 19, 2021.
For personal use only. No other uses without permission. Copyright ©2021. Elsevier Inc. All rights reserved.

Figure 6: Adeno-associated virus 8-mediated *Islr* overexpression in hepatocytes augments BMP signaling and retards CRC hepatic metastasis growth.

(A) Experimental scheme. Yellow dotted lines outline the portal vein.

(B, C) ISH for *Islr* in the liver two weeks after tail vein injection of AAV8-*Islr* or AAV8-mRuby2. **(B)** Representative images. Red and blue arrowheads denote the endogenous expression of *Islr* in fibroblastic cells in the portal area and ectopic overexpression of *Islr* in hepatocytes, respectively. The yellow dotted line indicates the border between the portal area (P) and hepatocytes (H) **(C)** Semi-quantification. 5 HPFs (400x)/mouse, 3 mice each.

(D, E) Immunohistochemistry (IHC) for pSmad1/5/8 in liver metastases. **(D)** Representative pictures. **(E)** Quantification of 3,3'-Diaminobenzidine (DAB) intensity. 5 HPFs/mouse, 4 mice each. A.U., arbitrary unit.

(F) Kaplan-Meier survival curves.

(G, H) Luciferase signals from AP tumoroids were assessed by an *in vivo* imaging system (IVIS). **(G)** Representative images. **(H)** Growth kinetics. Signals within red rectangles in (F) were quantified. n = 5 (AAV-mRuby2) and 8 (AAV-*Islr*) mice.

(I, J) (I) Representative macroscopic pictures and hematoxylin and eosin (H&E)-stained sections of liver metastases. Dotted lines indicate borders between tumors (T) and the normal liver (N). **(J)** Quantification of tumor areas using H&E stained sections. 3 liver pieces/mouse, 5 (AAV-mRuby2) and 8 (AAV-*Islr*) mice.

(K, L) IHC for Ki-67. **(K)** Representative pictures. **(L)** Ki-67 positivity in total epithelial cells. 4 HPFs/mouse, 4 mice each.

(M, N) Evaluation of tumor cell differentiation status. **(M)** Representative pictures of IHC for EpCAM. Green dotted lines indicate tumor budding. diff, differentiated. **(N)** The ratio of poorly differentiated tumor areas in the total tumor areas. 11 liver pieces each group from 5 (AAV-mRuby2) and 8 (AAV-*Islr*) mice.

Downloaded for Anonymous User (n/a) at The University of Adelaide from ClinicalKey.com.au by Elsevier on February 19, 2021.
For personal use only. No other uses without permission. Copyright ©2021. Elsevier Inc. All rights reserved.

Scale bars represent 200 µm (A, B), 1 cm (macroscopic pictures in I), 1 mm (H&E staining in I), and 50 µm (D, K, and M).

Mean ± s.e.m.. Mann-Whitney U-test (C, E, J, L, and N), Log-rank test (F), and two-way repeated-measures ANOVA with post-hoc Sidak's multiple comparison test at Week 3 (H).

Journal Pre-proof

Downloaded for Anonymous User (n/a) at The University of Adelaide from ClinicalKey.com.au by Elsevier on February 19, 2021.
For personal use only. No other uses without permission. Copyright ©2021. Elsevier Inc. All rights reserved.

References

1. Ganesh K, Stadler ZK, Cercek A, et al. Immunotherapy in colorectal cancer: rationale, challenges and potential. Nature Reviews Gastroenterology & Hepatology 2019.
2. Kobayashi H, Enomoto A, Woods SL, et al. Cancer-associated fibroblasts in gastrointestinal cancer. Nat Rev Gastroenterol Hepatol 2019;16:282-295.
3. Bach DH, Park HJ, Lee SK. The Dual Role of Bone Morphogenetic Proteins in Cancer. Mol Ther Oncolytics 2018;8:1-13.
4. Jung B, Staudacher JJ, Beauchamp D. Transforming Growth Factor beta Superfamily Signaling in Development of Colorectal Cancer. Gastroenterology 2017;152:36-52.
5. McCarthy N, Manieri E, Storm EE, et al. Distinct Mesenchymal Cell Populations Generate the Essential Intestinal BMP Signaling Gradient. Cell Stem Cell 2020.
6. Worthley DL, Churchill M, Compton JT, et al. Gremlin 1 identifies a skeletal stem cell with bone, cartilage, and reticular stromal potential. Cell 2015;160:269-84.
7. **He XC**, **Zhang J**, Tong WG, et al. BMP signaling inhibits intestinal stem cell self-renewal through suppression of Wnt-beta-catenin signaling. Nat Genet 2004;36:1117-21.
8. **Qi Z**, **Li Y**, Zhao B, et al. BMP restricts stemness of intestinal Lgr5(+) stem cells by directly suppressing their signature genes. Nat Commun 2017;8:13824.
9. Sneddon JB, Zhen HH, Montgomery K, et al. Bone morphogenetic protein antagonist gremlin 1 is widely expressed by cancer-associated stromal cells and can promote tumor cell proliferation. Proc Natl Acad Sci U S A 2006;103:14842-7.
10. **Dutton LR**, **Hoare OP**, **McCorry AMB**, et al. Fibroblast-derived Gremlin1 localises to epithelial cells at the base of the intestinal crypt. Oncotarget 2019;10:4630-4639.
11. Ren J, Smid M, Iaria J, et al. Cancer-associated fibroblast-derived Gremlin 1 promotes breast cancer progression. Breast Cancer Res 2019;21:109.
12. **Neckmann U**, **Wolowczyk C**, Hall M, et al. GREM1 is associated with metastasis and predicts poor prognosis in ER-negative breast cancer patients. Cell Communication and

Downloaded for Anonymous User (n/a) at The University of Adelaide from ClinicalKey.com.au by Elsevier on February 19, 2021.
For personal use only. No other uses without permission. Copyright ©2021. Elsevier Inc. All rights reserved.

Signaling 2019;17.

13. Yan K, Wu Q, Yan DH, et al. Glioma cancer stem cells secrete Gremlin1 to promote their maintenance within the tumor hierarchy. Genes Dev 2014;28:1085-100.
14. **Davis H**, **Irshad S**, Bansal M, et al. Aberrant epithelial GREM1 expression initiates colonic tumorigenesis from cells outside the stem cell niche. Nat Med 2015;21:62-70.
15. Kawasaki K, Fujii M, Sugimoto S, et al. Chromosome Engineering of Human Colon-Derived Organoids to Develop a Model of Traditional Serrated Adenoma. Gastroenterology 2019.
16. **Mizutani Y**, **Kobayashi H**, **Iida T**, et al. Meflin-Positive Cancer-Associated Fibroblasts Inhibit Pancreatic Carcinogenesis. Cancer Res 2019;79:5367-5381.
17. **Hara A**, **Kobayashi H**, Asai N, et al. Roles of the Mesenchymal Stromal/Stem Cell Marker Meflin in Cardiac Tissue Repair and the Development of Diastolic Dysfunction. Circ Res 2019;125:414-430.
18. **Xu J**, **Tang Y**, Sheng X, et al. Secreted stromal protein ISLR promotes intestinal regeneration by suppressing epithelial Hippo signaling. The EMBO Journal 2020.
19. **Calon A**, **Espinet E**, Palomo-Ponce S, et al. Dependency of colorectal cancer on a TGF-beta-driven program in stromal cells for metastasis initiation. Cancer Cell 2012;22:571-84.
20. **Lee HO**, **Hong Y**, **Etlioglu HE**, , **Cho YB**, et al. Lineage-dependent gene expression programs influence the immune landscape of colorectal cancer. Nat Genet 2020.
21. Shoshkes-Carmel M, Wang YJ, Wangensteen KJ, et al. Subepithelial telocytes are an important source of Wnts that supports intestinal crypts. Nature 2018.
22. **Shin K**, **Lim A**, Zhao C, et al. Hedgehog signaling restrains bladder cancer progression by eliciting stromal production of urothelial differentiation factors. Cancer Cell 2014;26:521-33.
23. Dunbar CE, High KA, Joung JK, et al. Gene therapy comes of age. Science 2018;359.
24. George LA, Sullivan SK, Giermasz A, et al. Hemophilia B Gene Therapy with a High-Specific-Activity Factor IX Variant. N Engl J Med 2017;377:2215-2227.

Downloaded for Anonymous User (n/a) at The University of Adelaide from ClinicalKey.com.au by Elsevier on February 19, 2021.
For personal use only. No other uses without permission. Copyright ©2021. Elsevier Inc. All rights reserved.

25. Lee JW, Stone ML, Porrett PM, et al. Hepatocytes direct the formation of a pro-metastatic niche in the liver. Nature 2019;567:249-252.

26. Lisowski L, Dane AP, Chu K, et al. Selection and evaluation of clinically relevant AAV variants in a xenograft liver model. Nature 2014;506:382-6.

27. Urist MR. Bone: formation by autoinduction. Science 1965;150:893-9.

28. Pickup MW, Hover LD, Polikowsky ER, et al. BMPR2 loss in fibroblasts promotes mammary carcinoma metastasis via increased inflammation. Mol Oncol 2015;9:179-91.

29. Beppu H, Mwizerwa ON, Beppu Y, et al. Stromal inactivation of BMPRII leads to colorectal epithelial overgrowth and polyp formation. Oncogene 2008;27:1063-70.

30. Gerling M, Buller NV, Kirn LM, et al. Stromal Hedgehog signalling is downregulated in colon cancer and its restoration restrains tumour growth. Nat Commun 2016;7:12321.

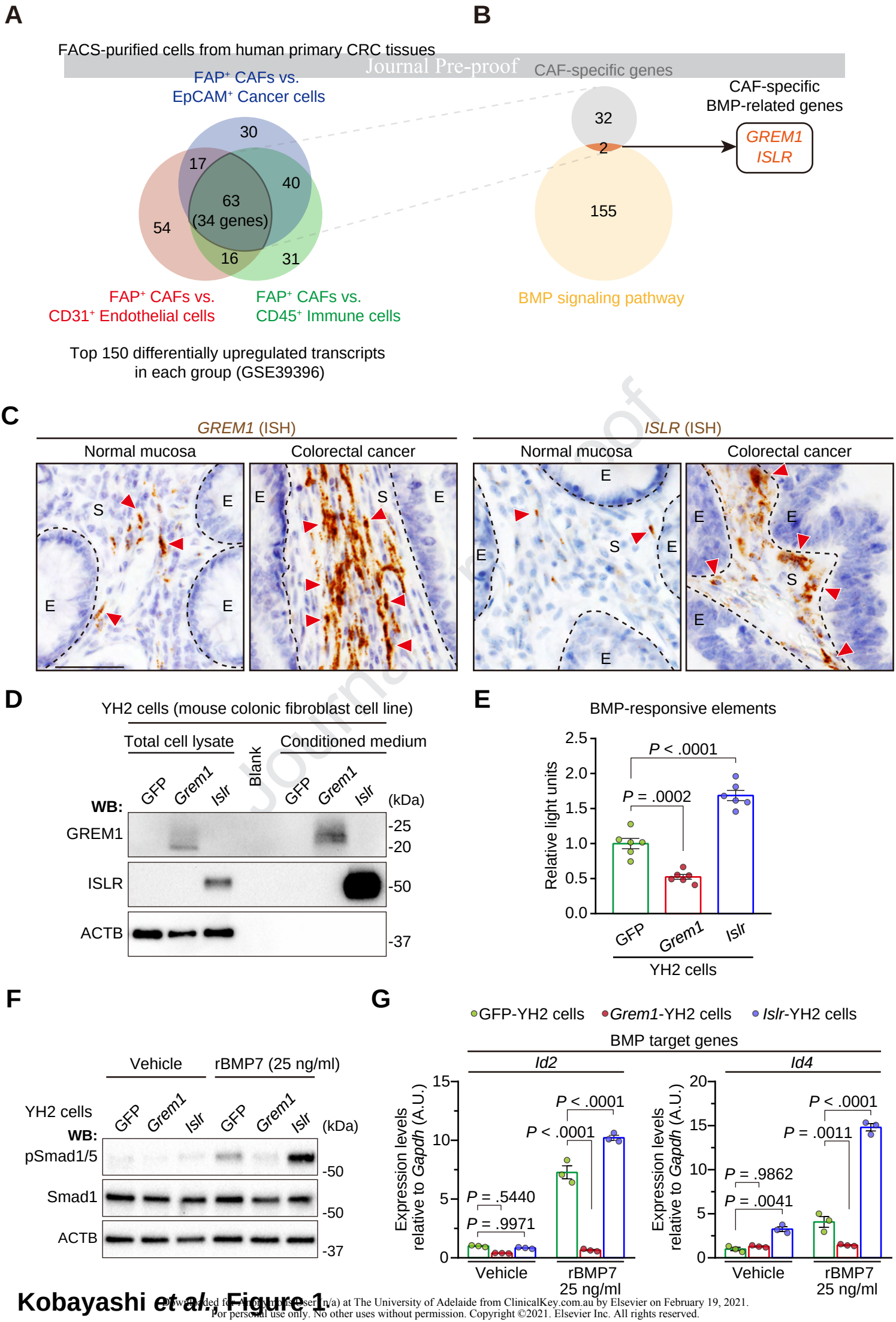
31. Xu R, Sun X, Tse LY, et al. Long-term expression of angiostatin suppresses metastatic liver cancer in mice. Hepatology 2003;37:1451-60.

32. Hanahan D, Weinberg RA. Hallmarks of cancer: the next generation. Cell 2011;144:646-74.

Author names in bold designate shared co-first authorship.

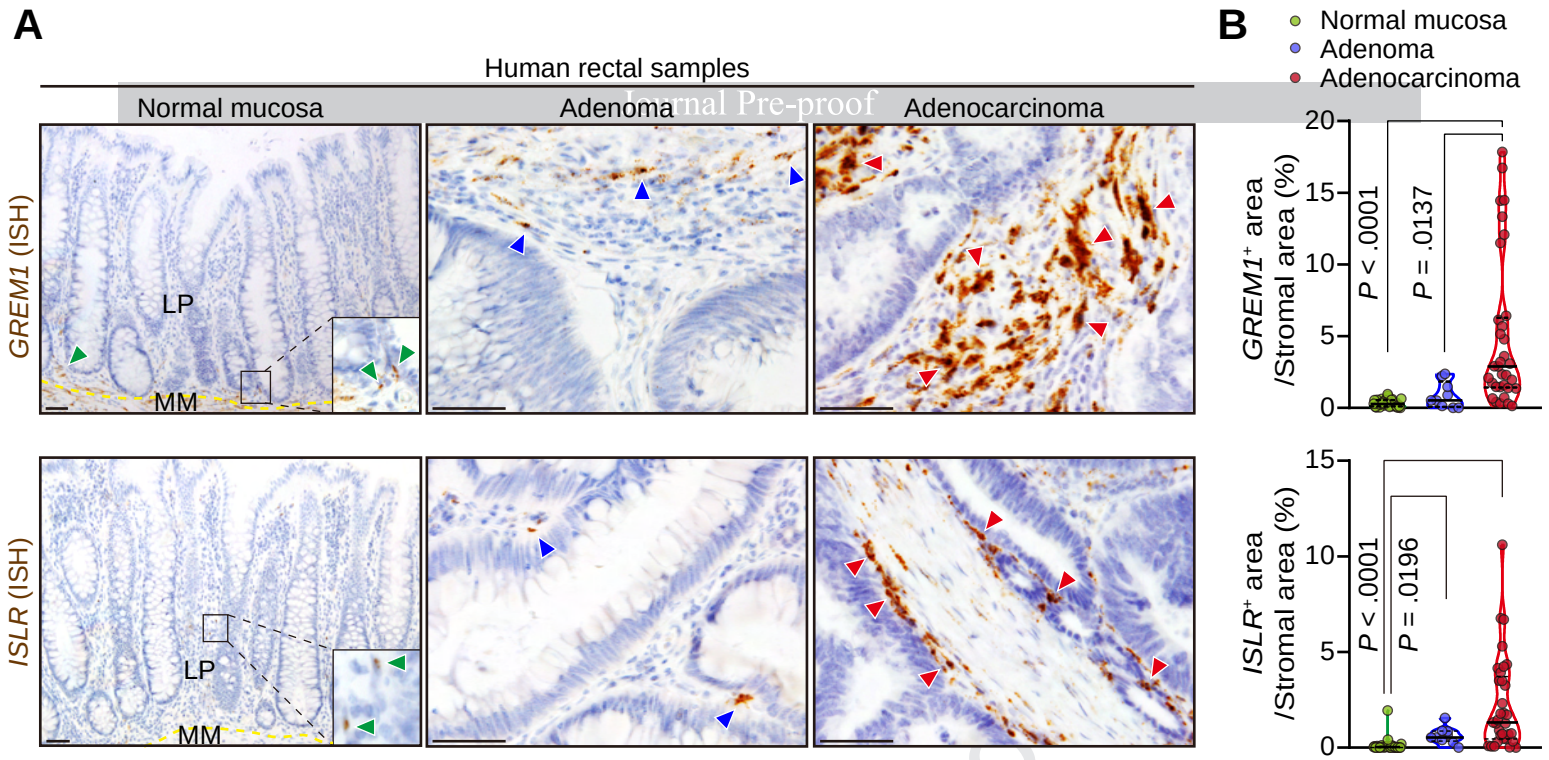
Downloaded for Anonymous User (n/a) at The University of Adelaide from ClinicalKey.com.au by Elsevier on February 19, 2021.
For personal use only. No other uses without permission. Copyright ©2021. Elsevier Inc. All rights reserved.

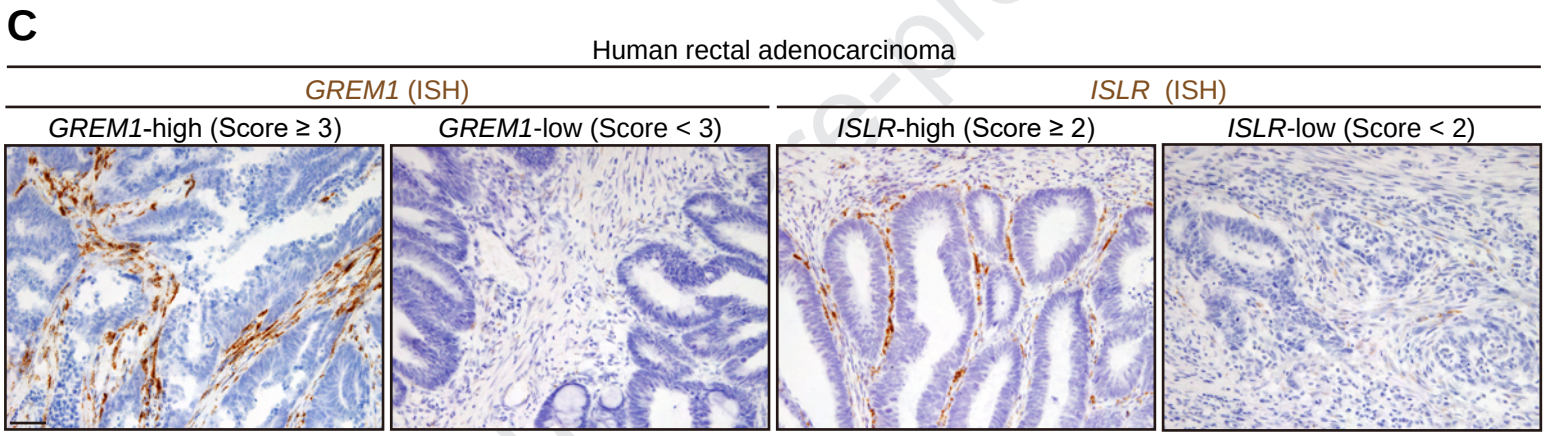
Journal Pre-proof

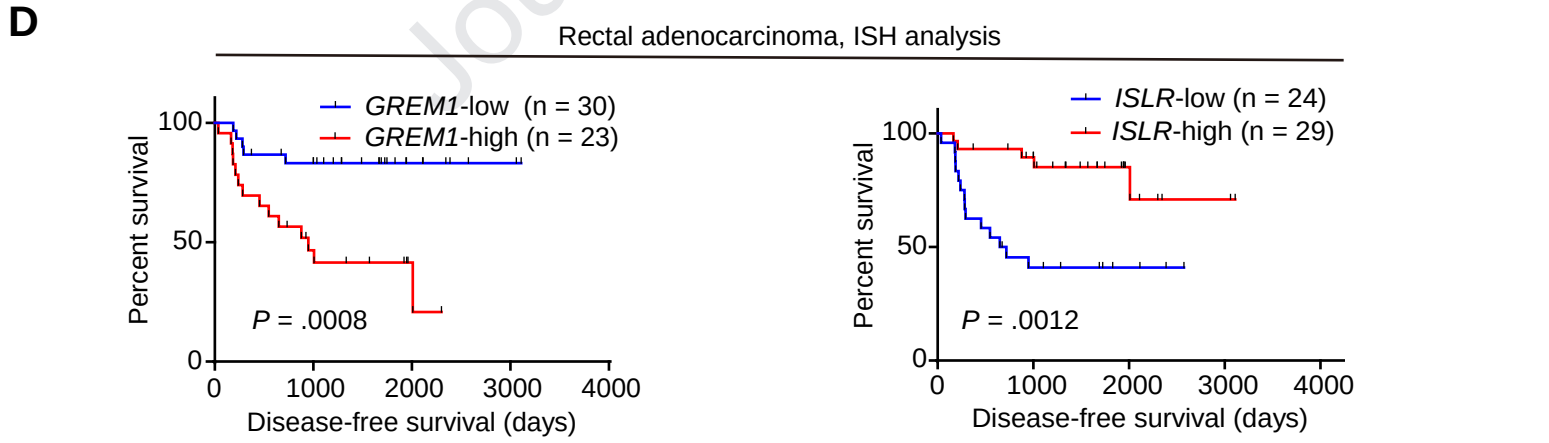


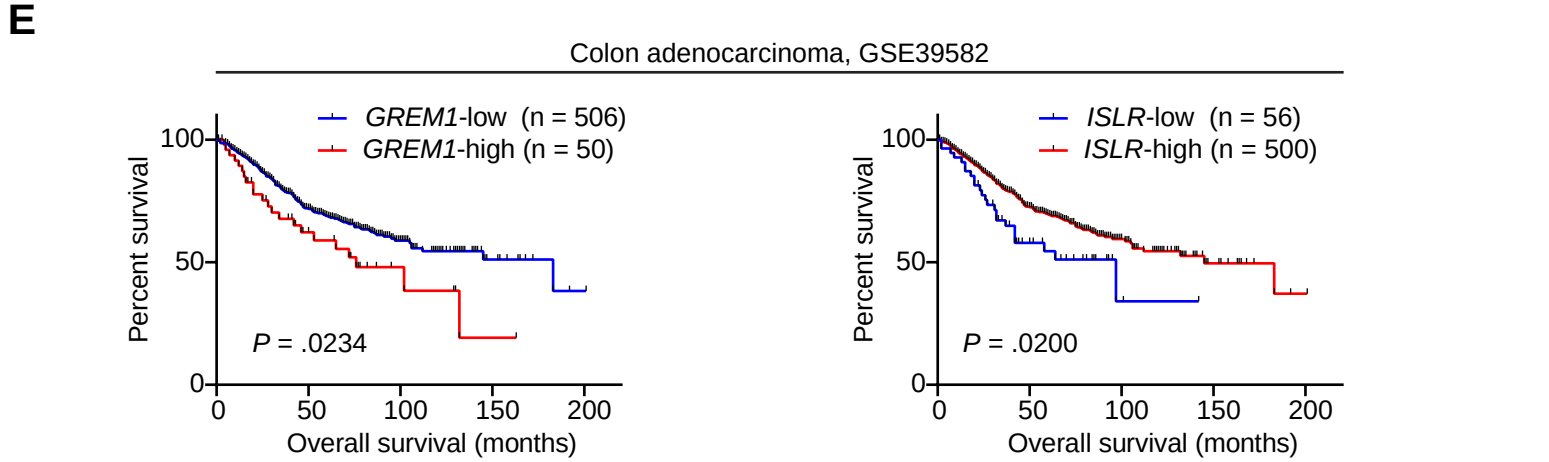
Kobayashi *et al.*, Figure 1.

Downloaded for Anonymous User (n/a) at The University of Adelaide from ClinicalKey.com.au by Elsevier on February 19, 2021.
For personal use only. No other uses without permission. Copyright ©2021. Elsevier Inc. All rights reserved.



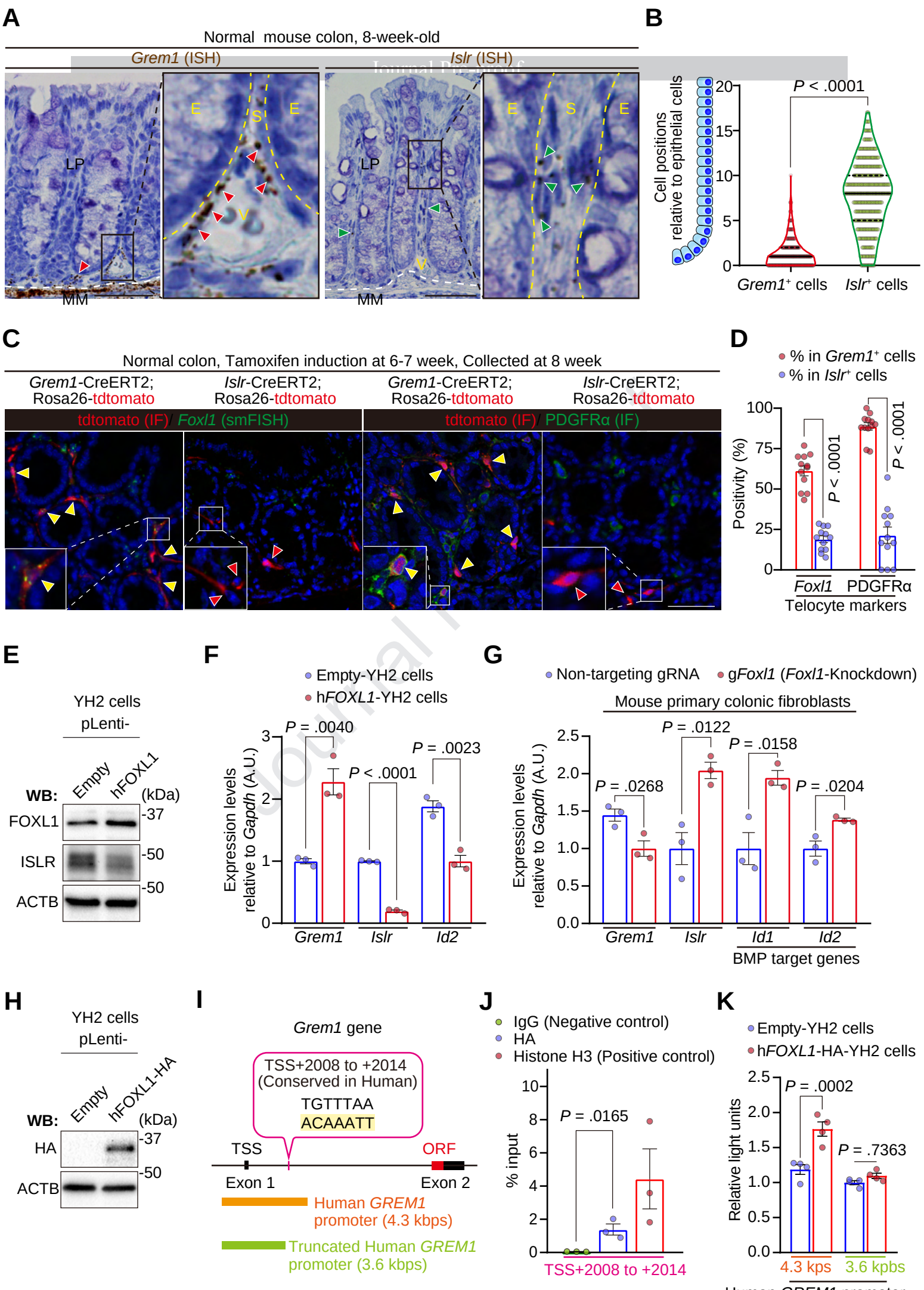






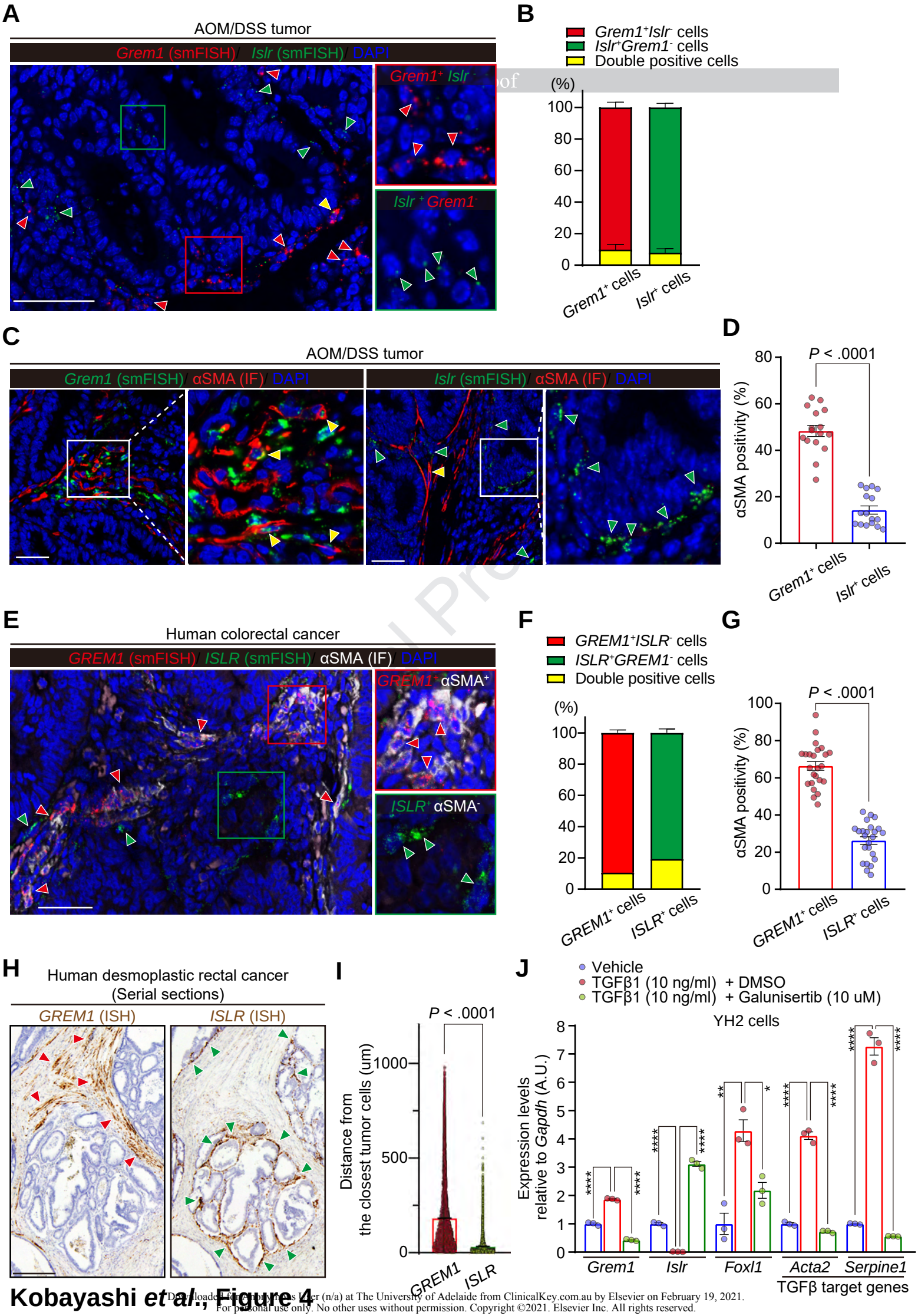
Kobayashi *et al.*, Figure 2.

Journal Pre-proof
Downloaded for Anonymous User (n/a) at The University of Adelaide from ClinicalKey.com.au by Elsevier on February 19, 2021.
For personal use only. No other uses without permission. Copyright ©2021. Elsevier Inc. All rights reserved.



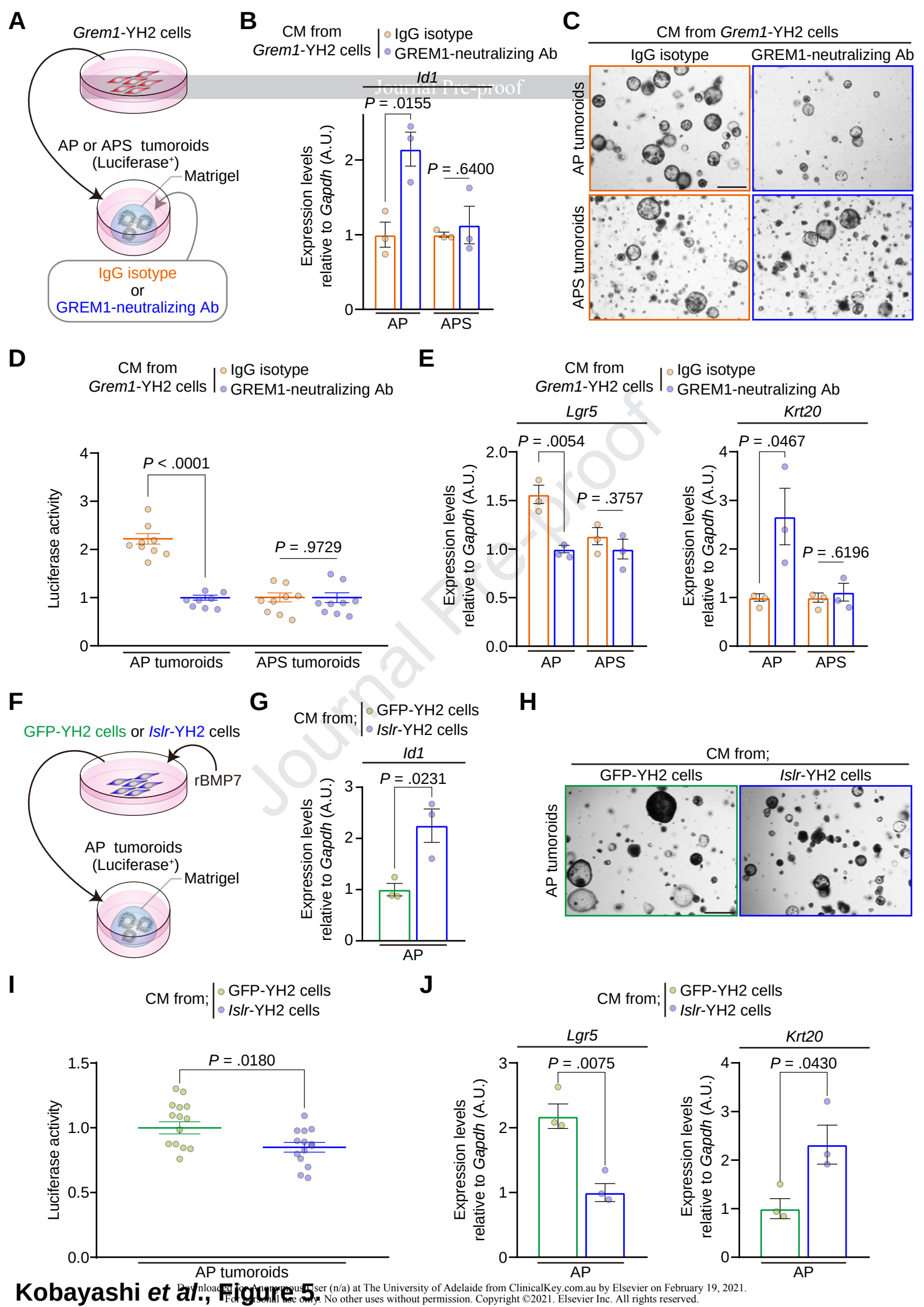
Kobayashi *et al.*, Figure 3.

Downloaded for Anonymous User (n/a) at The University of Adelaide from ClinicalKey.com.au by Elsevier on February 19, 2021.
For personal use only. No other uses without permission. Copyright ©2021. Elsevier Inc. All rights reserved.



Kobayashi *et al.*, Figure 4

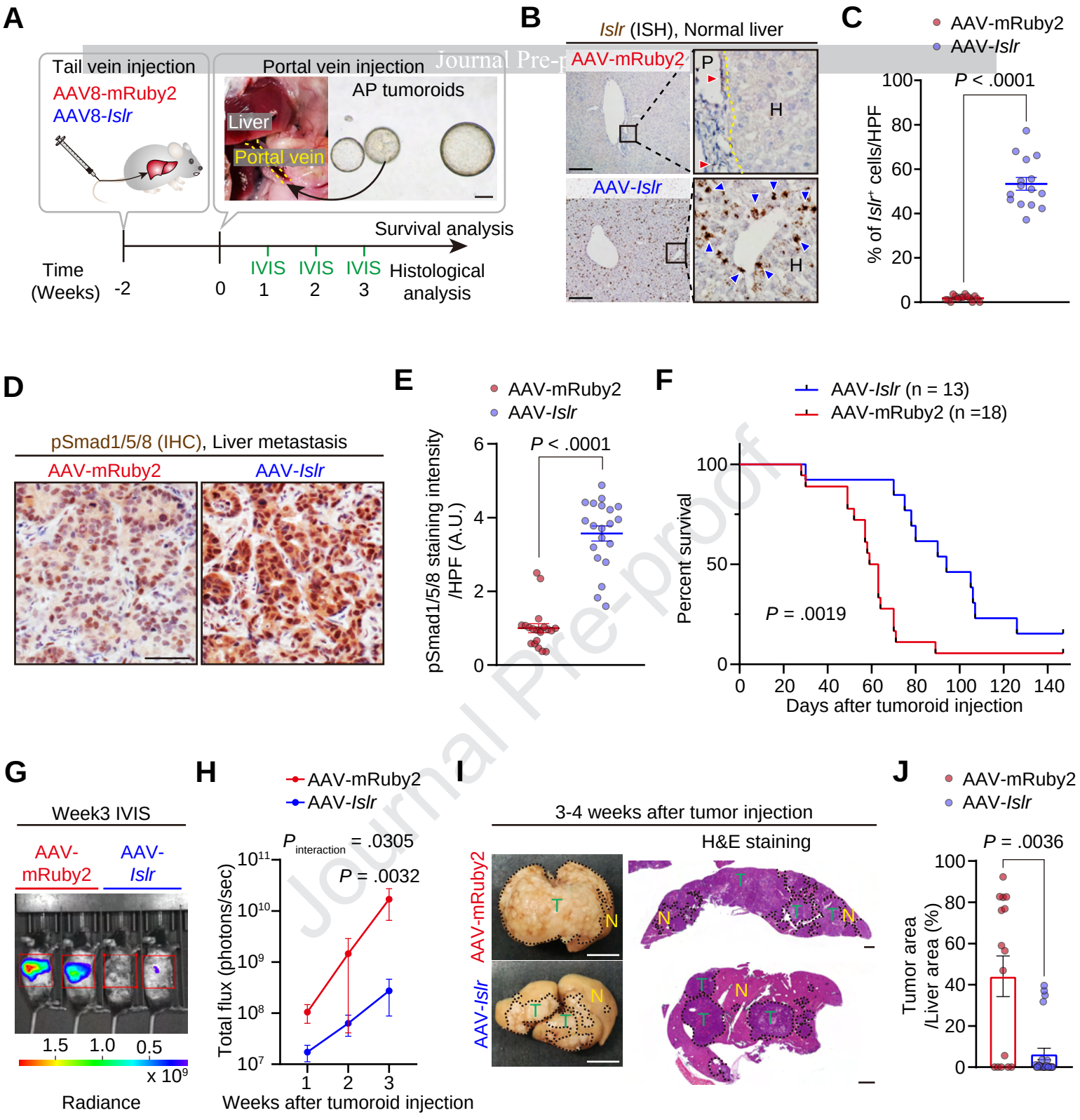
Downloaded for Anonymous User (n/a) at The University of Adelaide from ClinicalKey.com.au by Elsevier on February 19, 2021.
For personal use only. No other uses without permission. Copyright ©2021. Elsevier Inc. All rights reserved.



Journal Pre-proof

Kobayashi *et al.*, Figure 5.

Downloaded for Anonymous User (n/a) at The University of Adelaide from ClinicalKey.com.au by Elsevier on February 19, 2021.
For personal use only. No other uses without permission. Copyright ©2021. Elsevier Inc. All rights reserved.



Kobayashi *et al.*, Figure 6.

Downloaded for Anonymous User (n/a) at The University of Adelaide from ClinicalKey.com.au by Elsevier on February 19, 2021.
For personal use only. No other uses without permission. Copyright ©2021. Elsevier Inc. All rights reserved.

What you need to know

Background and context

Colorectal cancer (CRC) progression is promoted or restrained by cancer-associated fibroblasts (CAFs). However, the biological mechanisms underlying CAF heterogeneity and therapeutic strategies to target the CRC stroma remain largely unexplored.

New findings

Mesenchymal BMP signaling increased by ISLR and decreased by GREM1 regulates CRC progression. Augmenting BMP signaling by adeno-associated virus (AAV)-mediated delivery of *Islr* to hepatocytes inhibited CRC hepatic metastasis growth.

Limitations

This study was performed using mouse models and human tissue samples. Future studies are necessary to determine the therapeutic efficacy of modulating stromal BMP signaling in patients with CRC.

Impact

Targeting BMP signaling in the mesenchyme by novel approaches such as AAV-directed gene delivery to the liver, could prove effective adjuvant approaches to treat CRC.

Lay Summary

BMP signaling regulated by two CAF-specific factors, *GREM1* and *ISLR*, defines CAF biology, contributes to CRC progression, and can be therapeutically targeted using a novel hepatocyte-directed AAV gene therapy.

Downloaded for Anonymous User (n/a) at The University of Adelaide from ClinicalKey.com.au by Elsevier on February 19, 2021.
For personal use only. No other uses without permission. Copyright ©2021. Elsevier Inc. All rights reserved.

Journal Pre-proof

The balance of stromal BMP signaling mediated by *GREM1* and *ISLR* drives colorectal carcinogenesis.

Kobayashi *et al.*

Supplementary Materials

1. Supplementary Materials and Methods
2. Supplementary Figures 1-24 and Figure Legends
3. Supplementary Tables 1-5
4. Supplementary References

Journal Pre-proof

Downloaded for Anonymous User (n/a) at The University of Adelaide from ClinicalKey.com.au by Elsevier on February 19, 2021.
For personal use only. No other uses without permission. Copyright ©2021. Elsevier Inc. All rights reserved.

Journal Pre-proof

Supplementary Materials and Methods

Human and animal Ethics

Human CRC samples were obtained at the time of surgery from patients who had provided informed consent. This study was approved by the Ethics Committee of Nagoya University Graduate School of Medicine (2017-0127). All animal protocols were approved by the Animal Ethics committees of SAHMRI and Nagoya University Graduate School of Medicine (SAM322, SAM189, and 31434).

Antibodies

The following antibodies were used in this study. Goat polyclonal anti-GREM1 antibody (1:1000 for Western blotting; WB, AF956, R&D systems), Rabbit polyclonal anti-ISLR antibody (1:1000 for WB, HPA050811, Atlas Antibodies), Mouse monoclonal anti-ACTB (1:5000 for WB, sc-47778, Santa Cruz), Rabbit polyclonal anti-RFP (1:500 for IF, 600-401-379, Rockland), Rabbit monoclonal anti-Phospho-Smad1/5 (1:1000 for WB, clone 41D10, #9516, Cell signaling Technology), Rabbit polyclonal anti-Smad1 (1:1000 for WB, Cell Signaling Technology, #9743), Goat polyclonal anti-mouse PDGFRA (1:50 for immunofluorescence; IF,AF1062, R&D systems), Rabbit polyclonal anti-HA antibody (1:7500 for WB, ab9110, Abcam), Rabbit polyclonal anti-FOXL1 (1:1000 for WB, ABC937, Merck Millipore), Mouse monoclonal anti-αSMA (1:500 for IHC, clone 1A4, Dako), Rabbit monoclonal anti-Smad4 (1:5000 for WB, ab40759, Abcam), Rabbit monoclonal anti-Ki67 (1:200 for IHC, ab16667, Abcam), Rabbit polyclonal anti-EpCAM (1:150 for IHC, abcam71916, Abcam), Sheep polyclonal anti-FAP (1:100 for immunofluorescence, AF3715, R&D systems), and Rabbit polyclonal anti-Phospho-Smad1/5/8 (1:100 for IHC, AB3848-I, Merck Millipore). Mouse monoclonal GREM1-neutralizing antibody (Ab7326) and mouse monoclonal IgG1 isotype (Ab101.4) were provided by UCB Pharma.

Downloaded for Anonymous User (n/a) at The University of Adelaide from ClinicalKey.com.au by Elsevier on February 19, 2021.
For personal use only. No other uses without permission. Copyright ©2021. Elsevier Inc. All rights reserved.

RNA *in situ* hybridization (ISH)

All ISH analyses were performed on formalin-fixed and paraffin-embedded human and mouse tissue samples using RNAscope technology (RNAscope 2.5 HD Detection Kit or RNAscope Multiplex Fluorescent Reagent Kit v2, Advanced Cell Diagnostics; ACD) following the manufacturer's instructions. Briefly, tissue sections were baked in a dry oven (HybEZ II Hybridization System, ACD) at 60°C for 1 h and deparaffinized, followed by incubation with Pretreat 1, 2, and 3 (ACD). Slides were incubated with relevant probes for 1 h at 40°C, followed by successive incubations with Amp1 to 6 reagents. Staining was visualized with DAB or TSA Plus Cyanine 5 (NEL745001KT, PerkinElmer). For survival analysis with human CRC samples, ISH samples were quantified by a clinical pathologist in a blinded manner, following a semi-quantitative scoring method recommended by the manufacturer (ACD), where each signal was evaluated as 0 (no staining or < 1 dot/cell), 1 (1-3 dots/cell), 2 (4-9 dots/cell with no or very few dot clusters), 3 (10-15 dots/cell and < 10% dots are in clusters) or 4 (> 15 dots/cell and > 10% dots are in clusters). For other ISH analyses, cells with Score 0 were defined as "negative," and cells with Score 1 or more were defined as "positive." In normal colorectal samples, only lamina propria areas were quantified (Figure 2B; Figure 3B and D),

Probes used for *in situ* hybridization (ISH)

In situ hybridization (RNAscope) probes used in the study were human *PPIB* (a positive control probe, NM_000942.4, region 139 - 989, catalogue number 313901), bacterial *DapB* (a negative control probe, EF191515, regions 414 - 862, catalogue number 310043), human *ISLR* (NM_005545.3, region 275 - 1322, catalogue number 455481 or 455481-C2), mouse *Islr* (NM_012043.4, region 763 - 1690, catalogue number 450041 or NM_012043.4, region 277 - 2225, catalogue number 453321-C2), human *GREM1* (NM_013372.6, region 175 - 1472, catalogue number 312831 or 312831-C2), mouse *Grem1* (NM_011824.4, region 398 - 1359, catalogue number 314741), human *FOXL1* (NM_005250.2, region 1610 – 2981, catalogue number 558081), and mouse *Foxl1* (NM_008024.2, region 954 - 1931, catalogue number 407401).

Downloaded for Anonymous User (n/a) at The University of Adelaide from ClinicalKey.com.au by Elsevier on February 19, 2021.
For personal use only. No other uses without permission. Copyright ©2021. Elsevier Inc. All rights reserved.

Luciferase reporter assay

DNA fragments of 4.3 kbp (-1524 to +2841; +1 is the TSS of exon 1 of human *GREM1*) spanning human *GREM1* promoter and intron regions were generated by custom gene synthesis by Gene Universal (New Jersey, US) and inserted into the upstream of the luciferase (NanoLuc) reporter gene in the pNL2.1 vector (Promega). This region contained a putative hFOXL1-binding site at TSS+2103 to +2109 (corresponding to TSS+2008 to +2014 in mouse *Grem1*), as analyzed by the JASPAR database[1]. Sequences from TSS+2103 to +2841, which contains the putative hFOXL1-binding site, was deleted from the *GREM1* promoter (4.3 kbps)-Nanoluc plasmid, resulting in the generation of the truncated *GREM1* promoter (3.6 kbps)-Nanoluc vector.

3.5 kbp human *ISLR* promoter and intron regions (-2321 to +1179; +1 is the TSS of exon 1 of human *ISLR*) were inserted upstream of the luciferase (NanoLuc) reporter gene in the vector pNL2.1 (Promega), as described previously[2].

The pNL2.1 vectors containing the *GREM1* or *ISLR* promoter regions were co-transfected with pEF1a (Human elongation factor-1 alpha promoter)-Firefly into YH2 cells, using Lipofectamine 2000 (11668019, Thermo Fisher). Cell lysates were collected 48 hours after transfection using a passive lysis buffer (E1941, Promega). Luminescence values of cell lysates were measured using a Nano-Glo Dual-Luciferase Reporter Assay System (N1610, Promega) and a GloMax microplate reader (GM3000, Promega) following the manufacturer's instruction. The Nanoluc luminescence levels were normalized to the Firefly luminescence levels.

To evaluate BMP signaling activation in GFP-, *Islr*-, and *Grem1*-overexpressing YH2 cells, YH2 cells were co-transfected with pGL3 BMP-responsive element-Firefly (Addgene; Plasmid #45126) and pTK-Renilla (E2241, Promega). Cells were grown in DMEM containing 1% FBS, and cell lysates were collected 48 hours after transfection using passive lysis buffer (E1941, Promega). Luminescence values of cell lysates were measured using a Dual-Luciferase Reporter Assay System (E1960, Promega) and a GloMax microplate reader (GM3000, Promega). The Firefly luminescence

Downloaded for Anonymous User (n/a) at The University of Adelaide from ClinicalKey.com.au by Elsevier on February 19, 2021.
For personal use only. No other uses without permission. Copyright ©2021. Elsevier Inc. All rights reserved.

levels were normalized to the Renilla luminescence levels. Each assay was performed with at least two technical replicates.

Promoter analyses and chromatin immunoprecipitation (CHIP)

Promoter analyses were performed using the JASPAR database[1]. Promoter analyses of the genomic area around the *Grem1* transcriptional start site (TSS) for putative FOXL1-binding sites identified a binding motif for FOXL1 at TSS + 2008 to +2014 bps, an intronic region of the mouse *Grem1* gene, which was conserved in human.

Chromatin was prepared from three independent replicates of *FOXL1*- Hemagglutinin (HA)-overexpressing YH2 cells using a truChIP Chromatin Shearing Kit with Formaldehyde (520154, Covaris) according to the manufacturer's instruction. Chromatin shearing was performed using a Covaris M220 focused ultrasonicator. CHIP assay was performed using EpiQuik Chromatin Immunoprecipitation Kit (P-2002, Epigentek) and IgG isotype (ab171870, Abcam), anti-HA antibody (ab9110, Abcam), anti-Histone H3 antibody (ab1791, Abcam) as per manufacturer's protocol. Prepared DNA samples were analyzed by quantitative polymerase chain reaction (qPCR) using the following primers. Mouse *Grem1* promoter (Forward: 5'-gcaccgttggattaaggctc-3', Reverse: 5'-tgaagatcataggaaagctgtgaag-3')

Histopathological examination

All histopathological examination was performed using formalin-fixed and paraffin-embedded tissues. Paraffin blocks were cut into 4-5 µm sections. Hematoxylin and eosin (H&E) staining and Picro-Sirius red staining were performed by Histology Services (the University of Adelaide) or Sept Sapie (Tokyo, Japan).

Immunohistochemistry (IHC) and immunofluorescence (IF)

Downloaded for Anonymous User (n/a) at The University of Adelaide from ClinicalKey.com.au by Elsevier on February 19, 2021.
For personal use only. No other uses without permission. Copyright ©2021. Elsevier Inc. All rights reserved.

Formalin-fixed and paraffin-embedded tissue sections were deparaffinized with xylene and rehydrated with phosphate-buffered saline (PBS), followed by antigen retrieval by boiling samples in antigen retrieval buffer (pH 6 or pH 9, H-3300; Vector Laboratories, S1699; Dako, or S2367; Dako) for 30 min. Inactivation of endogenous peroxidase was performed with 0.5% H_2O_2 in methanol for 15 min, followed by washing with PBS. Then, sections were treated with blocking buffer (X0909, Dako) for 30 min, incubated with the indicated primary antibodies overnight at 4°C and washed with PBS. Sections were incubated with horseradish peroxidase (HRP)-polymer secondary antibody (ab214879 or ab214880, both from Abcam) for 30 min, followed by signal detection with diaminobenzidine (DAB) solution (K3468, DAKO).

For IF studies, deparaffinized sections were treated with blocking buffer (X0909, Dako) for 30 min, incubated with the indicated primary antibodies overnight at 4°C and washed with PBS. Sections were then incubated with Alexa Fluor 488/594/647-conjugated secondary antibodies (All from Thermo Fisher Scientific) for 1 h at room temperature. The sections were then mounted with ProLong Gold antifade reagent containing 4'6-diamidino-2-phenylindole (DAPI; Thermo Fisher Scientific), and fluorescence was examined using a confocal laser-scanning microscope (TCS SP8 MP, Leica) or an inverse immunofluorescence microscope BZ-X710 (Keyence) with optical sectioning.

Combined single-molecule fluorescent *in situ* hybridization (smFISH) and immunofluorescence (IF)

Combined smFISH and IF were implemented by first performing smFISH, followed by IF. After smFISH, the sections were blocked with blocking buffer (X0909, Dako) and then incubated with a primary antibody overnight at 4 °C. The sections were washed in 1x T-PBS 3 times and then incubated with Alexa Fluor 555-conjugated secondary antibody (Thermo Fisher Scientific) for 60 min at room temperature. The sections were then mounted with ProLong Gold antifade reagent containing 4'6-diamidino-2-phenylindole (DAPI; Thermo Fisher Scientific). Fluorescence was

Downloaded for Anonymous User (n/a) at The University of Adelaide from ClinicalKey.com.au by Elsevier on February 19, 2021.
For personal use only. No other uses without permission. Copyright ©2021. Elsevier Inc. All rights reserved.

examined using an inverse immunofluorescence microscope BZ-X710 (Keyence, Japan) with optical sectioning.

Western blot analysis

Cells were lysed in a lysis buffer (78501, Thermo Fisher) supplemented with cOmplete Protease Inhibitor (Roche) and PhosSTOP Phosphatase Inhibitor cocktails (4906845001, Roche). Lysates were clarified by centrifugation at 12,000 × g for 10 min at 4 °C. Then, sodium dodecyl sulfate (SDS) sample buffer (10 mM Tris-HCl, 2% SDS, 2 mM EDTA, 0.02% bromophenol blue, 6% glycerol; pH 6.8) was added. To prepare conditioned medium and total cell lysates for western blotting, YH2 cells were incubated for 72 hours in protein-free and FBS-free medium (Freestyle 293 expression medium; 12338018, Gibco). The medium was collected, centrifuged at 400 g for 5 minutes, and filtered through a 0.45 µm filter (16533, Sartorius) to remove cell debris. The medium was concentrated 10-fold using Amicon Ultra 3KDa centrifugal filters (UFC500396, Millipore).

The separation was performed by SDS-polyacrylamide gel electrophoresis using a precast gel (4568094, Bio-rad). Proteins were then transferred to Polyvinylidene Difluoride (PVDF) membranes (1620177, Bio-rad) using a semi-dry transfer system (1703940, Bio-rad). The membranes were blocked in 5% milk in PBS containing 0.05% Tween 20, and then incubated with primary antibodies. Proteins were detected by horseradish peroxidase (HRP)-conjugated secondary antibodies (NA9310V, GE Healthcare; N934VS, GE Healthcare; ab97120, Abcam), followed by signal development using an HRP substrate (WBLUR0500, Millipore). The blots were imaged using ChemiDoc MP (Bio-Rad) and quantified using the Image Lab software (Version 6.0.1, Bio-rad).

Plasmids

The cloning of mouse *Islr* cDNA was described previously[3]. A DNA fragment for the codon-optimized mouse *Grem1* gene was generated using a custom gene synthesis service by Gene Universal (New Jersey, USA). These genes were subcloned into bidirectional pLenti-EF1a

Downloaded for Anonymous User (n/a) at The University of Adelaide from ClinicalKey.com.au by Elsevier on February 19, 2021.
For personal use only. No other uses without permission. Copyright ©2021. Elsevier Inc. All rights reserved.

(Human elongation factor-1 alpha promoter)-MCS (multiple cloning site)-PGK-Puro vectors, resulting in the generation of pLenti-EF1a-*Islr*-PGK-Puro and pLenti-EF1a-*Grem1*-PGK-Puro.

To overexpress FOXL1 using a lentiviral expression system, DNA fragments for mouse codon-optimized human *FOXL1* gene with either no epitope tags or 3 x Hemagglutinin (HA) tags at the amino-terminus were generated using custom gene synthesis service by Gene Universal. These genes were subcloned into unidirectional pLenti-EF1a-GFP-p2A-Puro-EF1a-MCS vectors, resulting in the generation of pLenti-EF1a-GFP-p2A-Puro-EF1a-*FOXL1 and* pLenti-EF1a-GFP-p2A-Puro-EF1a-*FOXL1*-3 x HA.

To enable CRISPR/Cas9-mediated mouse *Foxl1* knockdown, the following mouse non-targeting gRNA (guide RNA) sequence or gRNA sequence targeting mouse *Foxl1* was subcloned into pLentiCRISPR v2 eSpCas9 plasmid by GenScript (New Jersey, USA).
Non-targeting gRNA: 5'- AAAAAGTCCGCGATTACGTC -3'
g*Foxl1*: 5'-GGGCTGTACACGTACAACAG -3'

To overexpress *Islr* using adeno-associated virus (AAV) expression system, mouse *Islr* cDNA was subcloned into a self-complementary AAV plasmid (VPK-430; Cell Biolabs), and a pAAV-CMV-*Islr* vector was generated. As a control, a self-complementary AAV plasmid expressing a red fluorescence protein, mRuby2 (pAAV-CAG-mRuby2; Addgene Plasmid #99123) was used.

Lentivirus production and transduction

293T cells were co-transfected with psPAX2 (Addgene; plasmid #12260) and pMD2.G (Addgene; plasmid #12259), and a lentivirus vector plasmid. At 48 and 72 h after transfection, viral supernatants were harvested, filtered through a 0.45-μm filter, and concentrated using Amicon Ultra Centrifugal Filters (Merck Millipore; UFC910024). Concentrated lentivirus particles were used for transduction. 48 h after transduction, positively transduced cells were selected with 2-4 μg/mL puromycin if the lentivirus vectors contain a puromycin resistance gene.

Downloaded for Anonymous User (n/a) at The University of Adelaide from ClinicalKey.com.au by Elsevier on February 19, 2021.
For personal use only. No other uses without permission. Copyright ©2021. Elsevier Inc. All rights reserved.

Journal Pre-proof

Retrovirus production and transduction

293T cells were co-transfected with the pEQ ecotropic-packaging vector[4] and a retrovirus vector plasmid. At 48 and 72 h after transfection, viral supernatants were harvested, filtered through a 0.45-µm filter, and concentrated using ultracentrifuge (Optima XPN, Beckman Coulter). Concentrated retrovirus particles were used for transduction.

Cell Culture

A mouse colonic fibroblast cell line, YH2 cells[5], was generously provided by Professor Tony Burgess (The Walter and Eliza Hall Institute of Medical Research). Normal mouse colonic organoids were isolated from a Rosa26-Cas9 mouse (JAX Stock Number 024858; C57BL/6 x 129 genetic background) housed under pathogen-free conditions in the SAHMRI Bioresources facility. YH2 cells were cultured in Dulbecco's modified Eagle's medium (DMEM; Sigma) supplemented with 10% fetal bovine serum (FBS; Gibco).

All cell lines used were routinely screened for Mycoplasma contamination by MycoAlert Mycoplasma Detection Kit (LT07-118, Lonza).

In Figure 1F, G, and Supplementary Figure 5, 6, YH2 cells were serum-starved in DMEM containing 1% FBS for 48 hours before stimulation with recombinant human BMP7 (PHC9541, Thermo Fisher) or BMP2 (cyt-261, Prospec) at the concentration indicated in figure legends. Proteins and RNAs were collected 30 minutes and 24 hours, respectively, after the addition of the recombinant BMP7 or BMP2. In Figure 4J, YH2 cells were stimulated with a vehicle, 10 ng/ml of recombinant human TGF-beta 1 (240-B-002, R&D systems) + DMSO, or 10 ng/ml of recombinant human TGF-beta 1 + 10 uM of Galunisertib (ADV465749242; AChemBlock), in DMEM containing 1% FBS for 24 hours. In Supplementary Figure 18A and B, recombinant human BMP2 (cyt-261, Prospec), recombinant human GREM1 (provided by UCB pharma), GREM1-neutralizing antibody (Ab7326), and mouse monoclonal IgG1 isotype (Ab101.4) were used for the experiment.

Downloaded for Anonymous User (n/a) at The University of Adelaide from ClinicalKey.com.au by Elsevier on February 19, 2021.
For personal use only. No other uses without permission. Copyright ©2021. Elsevier Inc. All rights reserved.

Isolation of primary mouse colonic fibroblasts

Isolation and culture of primary mouse colonic fibroblasts was performed using the protocol described elsewhere[6] with modifications. Briefly, colons were harvested from 8-16-week-old C57BL/6J mice and thoroughly washed with cold PBS. The colon tissues were incubated in PBS supplemented with 3 mM EDTA and 0.05 mM DTT for 60 minutes at room temperature to remove epithelial cells. After washing the colon three times with PBS, the colons were digested in 1 mg of collagenase type IV (17104-019, Gibco), 1 mg of dispase (17105-041, Gibco), and 2000 units of DNase I (D4527, Sigma) in 15 ml of RPMI-5 media (described below) at 37 °C for 30 minutes. The supernatant was filtered through a 70-µm cell strainer, and the cell suspension was plated on T75 flasks. Cells were cultured in RPMI-5 media; Roswell Park Memorial Institute media (R8756, Sigma) supplemented with 5% FBS (Gibco), 2 mM L-Glutamine, 1% Penicillin/Streptomycin, 10 mM HEPES, 1 mM sodium pyruvate, and 0.05 mM 2-mercaptoethanol[6]. At passage 2, cells were transduced with lentivirus encoding Cas9 protein and non-targeting guide RNA (gRNA) or gRNA targeting *Foxl1*. RNA and protein collection was performed at passage 4.

Organoid culture and organoid genome editing

The basal culture medium for mouse colon organoids was Advanced Dulbecco's modified Eagle medium/F12 (Life Technologies) supplemented with 1x gentamicin/antimycotic/antibiotic (Life Technologies), 10mM HEPES, 2mM GlutaMAX, 1 x B27 (Life Technologies), 1 x N2 (Life Technologies). The following niche factors were used: 50 ng/ml mouse recombinant EGF (Peprotech), 100 ng/ml mouse recombinant noggin (Peprotech), 20% R-spondin-2 conditioned medium, 50% Wnt-3A conditioned medium. Organoids were plated in 50 ul growth factor-reduced Matrigel (356231, Corning) on a 24-well dish, and 500 ul of the medium was added to organoids

Guide RNAs (gRNAs) specific for each target gene were either previously published or designed de novo using the CRISPR design Tool[7]. *Apc* and *p53* gRNA oligos were cloned into

Downloaded for Anonymous User (n/a) at The University of Adelaide from ClinicalKey.com.au by Elsevier on February 19, 2021.
For personal use only. No other uses without permission. Copyright ©2021. Elsevier Inc. All rights reserved.

pLentiGuide-CMV-dtomato (Modified from; Addgene Plasmid #17452). *Smad4* gRNA oligos were cloned into plentiGuide-Puro (Addgene Plasmid #52963).

gRNA sequences

Apc: 5'- GGAAGCCTTGTGGGACATGG -3'

Trp53: 5'- GTGTAATAGCTCCTGCATGG -3' [8]

Smad4: 5'- CAAAAGCGATCTCCTCCCGA -3' [9]

Normal colon organoids isolated from a Rosa26-Cas9 mouse (JAX Stock Number 024858)[8] were transduced with lentivirus expressing sg*Apc* and sg*Trp53*. 3 days later, media was changed to ADMEM (no Wnt, no Rspo, + Nutlin-3a; SML0580 Sigma) to enrich for correctly targeted clones (Supplementary Figure 16). Following the confirmation of correctly targeted monoclonal lines by amplicon sequence, retrovirus expressing Firefly (Retro-SFG-NES-HSV1-tk-GFP-Luciferase)[10] was transduced to the AP (*Apc*$^{\Delta/\Delta}$, *Trp53*$^{\Delta/\Delta}$) tumoroid line. Then, a monoclonal line that showed high luciferase signals was selected by evaluating the luciferase signals by a luminometer. The luciferase-expressing AP monoclonal tumoroid was further transduced with lentivirus expressing sg*Smad4* and a puromycin resistance gene. 3 days later, media was changed to ADMEM (no Wnt, no Rspo, no Noggin, + Puromycin + Nutlin-3a; SML0580 Sigma) to enrich for correctly targeted clones, followed by handpicking monoclonal lines.

Handpicked monoclonal organoid lines were screened for loss of function insertions/deletions using amplicon sequence using the following primers, as described[11]. Overhang sequences are underlined.

Apc forward: 5'- CTGAGACTTGCACATCGCAGCTTAATTCAGGCAAATCCTAAGAGAG -3'

Apc reverse: 5'- GTGACCTATGAACTCAGGAGTCGGTCTGTTTGCCATGAGATTCC -3'

Trp53 forward: 5'- GTGACCTATGAACTCAGGAGTCTAGTGAGGTAGGGAGCGACTTC -3'

Trp53 reverse: 5'- CTGAGACTTGCACATCGCAGCCCAAAGAGCGTTGGGCATGTG -3'

Smad4 forward: 5'- CTGAGACTTGCACATCGCAGCCTGGTGCTCCATTGCTTACT -3'

Downloaded for Anonymous User (n/a) at The University of Adelaide from ClinicalKey.com.au by Elsevier on February 19, 2021.
For personal use only. No other uses without permission. Copyright ©2021. Elsevier Inc. All rights reserved.

Journal Pre-proof

Smad4 reverse: 5'- GTGACCTATGAACTCAGGAGTCACTTAATTCCTCGATATTTAAGCTC -3'

To detect a large deletion in *Smad4* in APS tumoroids, PCR was performed using the following primers. *Smad4* forward, 5'- TTGTGTCAGCTCAGAGTGGGTC -3', *Smad4* reverse: 5'- GCAAACCACACGACGATGC -3'. After gel electrophoresis and purification of PCR products, Sanger sequencing for the PCR products was performed to examine mutations.

Conditioned medium (CM) experiments

In Figure 5A-E and Supplementary Figure 17A-D, monolayer GFP-overexpressing or *Grem1*-overexpressing YH2 cells were cultured for 72 hours in Dulbecco's Modified Eagle Medium (DMEM; Gibco) containing 1% fetal bovine serum (FBS; Gibco), 1% l-glutamine, and 1% Penicillin/Streptomycin. In Figure 5F-J, monolayer GFP-overexpressing or *Islr*-overexpressing YH2 cells were cultured for 72 hours in DMEM containing 1% FBS, 1% l-glutamine, and 1% Penicillin/Streptomycin with 10 ng/ml recombinant human BMP7 (PHC9541, Thermo Fisher). The medium was collected and filtered through a 0.45 µm filter (16533, Sartorius) to remove cell debris. 30 minutes after trypsinized tumoroid fragments equivalent to 2500 cells were plated in 50 ul growth factor-reduced Matrigel (356231, Corning) on a 24-well dish, 500 ul of the CM was added to tumoroids. The medium was changed to new CM every three days. In Figure 5A-E, a mouse GREM1-neutralizing antibody (Ab7326; 100 ug/ml) or a mouse IgG1 isotype (Ab101.4; 100 ug/ml) was added to each well every time CM was added to the tumoroids throughout the course of experiments.

Organoid area measurements, luciferase assays, and qRT-PCR were performed 8 days and 12 days after plating AP tumoroids and APS tumoroids, respectively, in experiments using *Grem1*-overexpressing YH2 cells. In experiments using *Islr*-overexpressing YH2 cells, organoid area measurements, luciferase assays, and qRT-PCR were performed 7 days after plating AP tumoroids

Downloaded for Anonymous User (n/a) at The University of Adelaide from ClinicalKey.com.au by Elsevier on February 19, 2021.
For personal use only. No other uses without permission. Copyright ©2021. Elsevier Inc. All rights reserved.

Luciferase assays for Firefly-expressing tumoroids

For luciferase assays using Firefly-expressing tumoroids (AP tumoroids and APS tumoroids), following the removal of medium, tumoroids and Matrigel were lysed with 200 ul of 2 x passive lysis buffer (E1941, Promega). Firefly luminescence values of cell lysates were measured using Luciferase Assay Reagent II (E1960, Promega) and a GloMax microplate reader (GM3000, Promega) following the manufacturer's instruction.

Tumoroid area quantification

The images of each well (one picture/independent replicate) were captured using an inverted microscope (IX53, Olympus; a 2 x objective lens). Each Organoid was quantified using the ImageJ software[12] to outline an organoid shape and measure an organoid area.

Quantitative PCR

Total RNA was extracted using TRIzol reagent (Invitrogen) and an RNeasy Mini Kit (Qiagen). Purified RNA samples were reverse-transcribed using Transcriptor Universal cDNA Master (Roche) according to the manufacturer's instruction, followed by the dilution of cDNA at 1:5. Quantitative reverse-transcription PCR (qRT-PCR) of the complementary DNAs (cDNAs) was performed with KAPA PROBE or SYBER FAST qPCR Master Mix (KAPABiosystems) and was run on a QuantStudio 7 Flex Real-Time PCR System (Thermo Scientific). The data were analyzed using the 2-ΔΔCt method and normalized to *Gapdh* expression levels.

Probes or primers (generated by IDT) used in this study are as follows. Primers were designed using the Primer-BLAST online program[13].

Probes:

Mouse *Grem1* (Mm.PT.58.11631114), Mouse *Islr* (Mm.PT.58.12037488), Mouse *Id1* (Mm.PT.58.6622645.g), Mouse *Id2* (Mm.PT.58.13116812.g), Mouse *Id3* (Mm.PT.58.29482466.g), Mouse *Id4* (Mm.PT.58.6851535), Mouse *Acta2* (Mm.PT.58.16320644), and Mouse *Serpine1*

Downloaded for Anonymous User (n/a) at The University of Adelaide from ClinicalKey.com.au by Elsevier on February 19, 2021.
For personal use only. No other uses without permission. Copyright ©2021. Elsevier Inc. All rights reserved.

(Mm.PT.58.6413525), Mouse *Gapdh* (Mm.PT.39a.1), Mouse *Lgr5* (Mm.PT.58.12492947), Mouse *Krt20* (Mm.PT.58.43092140).

Primers:

Mouse *Grem1* (Forward: 5'- GCTCTCCTTCGTCTTCCTC-3' , Reverse: 5'-AGTGTATGCGGTGCGATTC-3'), Mouse *Islr* (Forward: 5'-TGCGAGCAATCCAGTCCTTAGATG-3' , Reverse: 5'-AGCCCAACAAAGCAGGCACAG-3'), Mouse *Foxl1* (Forward: 5'-GTCGCTCAACGAGTGCTTCG-3' , Reverse: 5'-TGCGCCGATAATTGCCGTTC-3'), and Mouse *Gapdh* (Forward: 5'-CCTCGTCCCGTAGACAAAATG-3' , Reverse: 5'-TGTAGTTGAGGTCAATGAAGGG-3')

Analyses of publicly available cDNA gene expression microarray and RNA-seq datasets

For GSE39396 [14], microarray data were downloaded using GEOquery R package version 2.54.1. Differential gene expression was analyzed as described in the limma software manual[15]. Briefly, a linear modeling approach was employed by the function lmFit, followed by the empirical Bayes estimation through functions eBayes and topTable. Differentially upregulated genes were defined as genes that showed $\log_2$ fold change greater than or equal to 2 and false discovery rate less than 0.05. The top 150 differentially upregulated gene probes in FAP^+CAFs, in each group (FAP^+ CAFs vs. $EpCAM^+$ cancer cells, FAP^+ CAFs vs. $CD31^+$ endothelial cells, and FAP^+ CAFs vs. $CD45^+$ immune cells), were selected based on $\log_2$ fold change. Volcano plots were generated using the ggplot2 package (version 3.2.1). A human gene list in a Gene Ontology (BMP signaling pathway; GO0030509) was downloaded from AmiGO 2 (http://amigo.geneontology.org/amigo/search/ontology).

Expression microarray data (GSE17538, 39582, and 41258) and RNA-seq data (GSE94072) were obtained from Gene Expression Omnibus (GEO; https://www.ncbi.nlm.nih.gov/geo/). For survival analyses, gene expression levels for the following probes were used. 218469_PM_s_at for *GREM1* and 207191_PM_s_at for *ISLR*. Patient information in GSE41258 [16], GSE39582 [17], and GSE17538 [18]

Downloaded for Anonymous User (n/a) at The University of Adelaide from ClinicalKey.com.au by Elsevier on February 19, 2021.
For personal use only. No other uses without permission. Copyright ©2021. Elsevier Inc. All rights reserved.

were also obtained from GEO. False delivery rate (FDR)-adjusted P-values were calculated by GEO2R (https://www.ncbi.nlm.nih.gov/geo/geo2r). In GSE41258, normal colon samples, polyp (adenoma) samples, primary colon tumor samples, and liver metastasis samples included in a previous analysis[16] were analyzed by choosing samples with a label of "Included in analysis; Yes" on the GEO website. Optimal cutoff levels for survival analyses were determined using the X-tile software[19]. Patients with survival time zero (Events at the time of patient enrolment) were not included in survival analysis by a Prism 8 software (Graphpad; https://www.graphpad.com/guides/prism/8/statistics/stat_qa_survival_analysis.htm).In GSE94072, fragments per kilobase of exon per million fragments (FPKM) data were directly downloaded from the GEO website (https://www.ncbi.nlm.nih.gov/geo/query/acc.cgi?acc=GSE94072).

The analyses of *GREM1* and *ISLR* expression levels in the Consensus Molecular Subtypes (CMS) of CRC.

For TCGA data, the CMS labels were downloaded from the supplementary materials of previous publication[20, 21]. Expression values and sample IDs were downloaded from the GDC data portal (https://portal.gdc.cancer.gov/). Expression Z-scores for tumor samples were calculated based on the standard deviation and mean value for the normal colorectal tissues. Violin plots were then generated using the ggplot2 package (version 3.2.1).

The CMS classifier[20] was applied to the downloaded GSE39582 expression microarray data to classify the colon cancer patients into consensus molecular subtypes (CMSs). This allowed us to classify 566 colon cancer samples into 70 CMS1 tumors, 177 CMS2 tumors, 97 CMS3 tumors, 107 CMS4 tumors, and 115 unclassified tumors.

Analyses of publicly available single-cell RNA-seq data

ScRNA-seq data (GSE132465)[22] were analyzed using BBrowser2 (Version 2.6.4; BioTuring, US). Unique molecular identifier (UMI) counts available on the GEO website (GEO;

Downloaded for Anonymous User (n/a) at The University of Adelaide from ClinicalKey.com.au by Elsevier on February 19, 2021.
For personal use only. No other uses without permission. Copyright ©2021. Elsevier Inc. All rights reserved.

https://www.ncbi.nlm.nih.gov/geo/) were used for normalization by the software. Processed scRNA-seq data (GSE81861)[23] were directly downloaded from the GEO website, and Log_2 (FPKM + 1) values were used to plot *GREM1* and *ISLR* expression.

In Supplementary Figure 4A, fibroblasts include myofibroblasts, stromal 1, stromal 2, and stromal 3 fibroblasts[22]. Endothelial cells include tip-like endothelial cells, stalk-like endothelial cells, proliferative endothelial cells, and lymphatic endothelial cells[22]. In Supplementary Figure 4A and B, immune cells comprise T cells, B cells, myeloid cells, and mast cells[22, 23]. In spearman correlation analyses, given our focus on *GREM1*- or *ISLR*-expressing CAFs, 1156 CRC CAFs that show detectable *GREM1* or *ISLR* transcripts (log normalized *GREM1* expression > 0 or log normalized *ISLR* expression > 0) were analyzed among all CRC CAFs (1501 cells; myofibroblasts, Stromal1, Stromal 2, and Stromal 3 fibroblasts from CRC tissues). Log normalized expression values in the 1156 CRC CAFs were transformed to Z-scores in the Spearman correlation analyses.

Tamoxifen administration to mice

Grem1-CreERT2 (JAX Stock No. 027039); Rosa26-LSL (LoxP-stop-LoxP)-tdtomato (JAX Stock No. 007909) and *Islr*-CreERT2 [2]; Rosa26-LSL-tdtomato were subjected to tamoxifen administration. 6mg of tamoxifen (T5648, Sigma) dissolved in peanut oil was administered by oral gavage 4 times every other day to 6-week-old adult mice to sufficiently induce CreERT2-mediated recombination, followed by harvest of the 8-week-old mice. The colons and small intestines were removed, opened longitudinally, and fixed in 10% formalin overnight at room temperature. Tissues were subsequently dehydrated and paraffin-embedded. 4 μm sections were used for histological analysis (ISH/IF and IF).

Mouse genotyping

Genomic DNA extracted from mouse ear or tails was used for PCR genotyping. The sequences of the primers were as follows:

Downloaded for Anonymous User (n/a) at The University of Adelaide from ClinicalKey.com.au by Elsevier on February 19, 2021.
For personal use only. No other uses without permission. Copyright ©2021. Elsevier Inc. All rights reserved.

Islr-Wild-Type (WT) forward, 5'-ACACACGACCTTGGCAAGTCCCAGC-3'; *Islr*-WT reverse,5'-GTCTGCAATCTGGAAGCCATACTTCTCC-3';

Islr-CreERT2 forward, 5'-ACACACGACCTTGGCAAGTCCCAGC-3'; *Islr*-CreERT2 reverse, 5'-CGATCCCTGAACATGTCCATCAGG-3';

Grem1-CreERT2 forward, 5'-TTAATCCATATTGGCAGAACGAAAACG-3'; *Grem1*-CreERT2 reverse, 5'-CAGGCTAAGTGCCTTCTCTACA-3'.

Rosa26-LSL-tdtomato forward, 5'-AGATCCACCAGGCCCTGAA-3'; Rosa26-LSL-tdtomato reverse, 5'-GTCTTGAACTCCACCAGGTAG-3';

Rosa26-Cas9 forward, 5'-CGTCGTCCTTGAAGAAGATGGT-3'; Rosa26-Cas9 reverse, 5'-CACATGAAGCAGCACGACTT-3';

Rosa26-WT forward, 5'-TTCCCTCGTGATCTGCAACTC-3'; Rosa26-WT reverse, 5'-CTTTAAGCCTGCCCAGAAGACT-3'

An azoxymethane (AOM)/ dextran sulfate sodium (DSS) mouse model of CRC

A colitis-associated AOM/DSS mouse model of CRC was generated as described[24]. Briefly, AOM (Sigma, A5486; 10mg/kg) was administered by intraperitoneal injection to C57BL/6J mice obtained from Charles River Laboratories Japan. One week later, the mice commenced the first of three cycles of DSS to induce inflammation (MP Biomedicals, 160110; Molecular Weight 36,000-50,000 Da). Each cycle was comprised of 5 days 3% DSS (weight/volume) then 16 days of normal drinking water. 10 weeks after AOM injection, mice were euthanized, and colons were removed, opened longitudinally, and fixed in 10% formalin overnight at room temperature. Tissues were subsequently dehydrated and paraffin-embedded. 4 μm sections were used for histological analysis.

Mouse models of CRC liver metastasis

Tumoroids were isolated from Matrigel and dissociated to single cells using TrypLE. The cells were filtered through 40-μm meshes to remove cell clumps and suspended in cold PBS containing 10 μM

Downloaded for Anonymous User (n/a) at The University of Adelaide from ClinicalKey.com.au by Elsevier on February 19, 2021.
For personal use only. No other uses without permission. Copyright ©2021. Elsevier Inc. All rights reserved.

Y-27632 (In Vitro Technologies). 5.0 x 10^5 cells in 100 ul were injected directly into the portal vein using a 33G syringe.

Male and female Rosa26-Cas9 mice (JAX Stock Number 024858; C57BL/6 x 129 genetic background; 6 to 24-week-old), housed under pathogen-free conditions in the SAHMRI Bioresources facility, were used for portal vein injection.

In all animal experiments, mice were allocated randomly to different treatment groups. Sample sizes were determined based on pilot experiments and sample availability.

AAV packaging

AAV8 preparation was performed by Vector & Genome Engineering Facility, Children's Medical Research Institute (NSW, AUSTRALIA). The AAV vectors used in this study were packaged using a standard transient transfection as described previously[25]. In short, pAAV transfer vector, pAd5 helper plasmid[26], and AAV-helper plasmid encoding rep2 and cap8 (pR2C8) were transfected using PEI (Polysciences; Cat No. 239662) into HEK293 cell. Assembled vector particles were purified using iodixanol- density gradients as described[27]. Vector genomes were quantified using real-time quantitative PCR (RT-qPCR) as previously described[28].

Intravenous AAV8 injection

Male and female Rosa26-Cas9 mice (JAX Stock Number 024858; C57BL/6 x 129 genetic background; 6 to 24-week-old) were administered intravenously via the tail vein, with a 150-ul injection of 1.0 x 10^{11} viral genomes of AAV8-mRuby2 or AAV8-*Islr* per mouse. A 2-week interval after AAV injection was allowed for protein expression to occur before portal vein injection of tumoroids. In Figure, 6D, E, and I-N, AAV8-treated mice were harvested for histopathological analyses 3-4 weeks after tumor injection, before prominent necrosis complicated histological assessment.

Downloaded for Anonymous User (n/a) at The University of Adelaide from ClinicalKey.com.au by Elsevier on February 19, 2021.
For personal use only. No other uses without permission. Copyright ©2021. Elsevier Inc. All rights reserved.

Subcutaneous injection of the GREM1-neutralizing antibody

Subcutaneous injection of the GREM1-neutralizing antibody or IgG isotype was commenced 1 week after tumoroid injection. A 30 mg/kg dose of the GREM1-neutralizing antibody (Ab7326) or IgG isotype (Ab101.4) was subcutaneously administered to a mouse twice a week until endpoint criteria were met.

***In vivo* imaging system (IVIS)**

Liver metastasis tumor growth kinetics was assessed by an *in vivo* imaging system (IVIS) by using a Xenogen IVIS Spectrum Imaging System (Perkin Elmer Inc) 10 minutes after intraperitoneal injection of 150 mg/kg of D-Luciferin (L-8220, Biosynth Carbosynth). Luciferase activity was quantified using Living Image software (Perkin Elmer Inc).

A humane endpoint in animal experiments

In survival analyses, to determine the humane endpoint in animal experiments, a clinical record score was used. Scores were obtained by one point being given for the presence of each of the following observations: weight loss > 15%; hunched/ruffled coat; dehydrated; absence of movement; or facial grimace. Once a score of 3 was reached, the mice were euthanased.

Collagen gel contraction assay

Collagen gels were prepared by mixing YH2 cells with PureCol bovine type I collagen (Advanced Biomatrix), 1× PBS, 1 M NaOH (final concentration: 1.0 mg/mL PureCol). The mixture containing 3.0×10^5 cells/mL was seeded in 24-well cell culture plates and allowed to polymerize for 20 min. DMEM supplemented with 10% FBS and 1% penicillin/streptomycin was added, and gels were released from the wells. The gel area was measured with ImageJ (National Institutes of Health). Representative images were processed using Adobe Photoshop CC (Adobe).

Downloaded for Anonymous User (n/a) at The University of Adelaide from ClinicalKey.com.au by Elsevier on February 19, 2021.
For personal use only. No other uses without permission. Copyright ©2021. Elsevier Inc. All rights reserved.

Human CRC samples

All ISH was performed using surgery samples of CRC patients who were diagnosed with adenocarcinoma of the colon or rectum at Nagoya University Hospital (Nagoya, Japan). This study was conducted in accordance with the Helsinki Declaration for Human Research and approved by the Ethics Committee of Nagoya University Graduate School of Medicine (approval number: 2017-0127).

Quantitative image analysis

IHC or ISH images were processed into separate channels representing nuclei staining (Hematoxylin) and IHC or ISH staining (DAB) using a color deconvolution function in a Fiji software (ImageJ; National Institutes of Health). Then, binary images were generated by intensity thresholds, and DAB^+ areas were calculated by ImageJ. To evaluate pSmad1/5/8 staining intensity, following an application of the lower threshold, the DAB staining intensity per high power field was calculated by ImageJ.

In Figure 2B, (1) normal rectal mucosa adjacent to adenocarcinoma, (2) adenoma in carcinoma, and (3) adenocarcinoma were randomly selected from ISH samples, and were used for quantification. Stromal areas (total areas excluding epithelial cells) visualized by hematoxylin counterstaining were outlined and measured by a clinical pathologist, using Adobe Photoshop CC (Adobe). In the normal mucosa, only lamina propria regions were quantified.

Ki-67 labeling index was calculated as the percentage of $Ki\text{-}67^+$ cells in the total epithelial cells as visualized by hematoxylin counterstaining.

The MRI fibrosis tool (http://dev.mri.cnrs.fr/projects/imagej-macros/wiki/Fibrosis_Tool) was used to quantify the percentage of fibrosis areas (Picro-Sirius red^+ areas) at default settings.

Downloaded for Anonymous User (n/a) at The University of Adelaide from ClinicalKey.com.au by Elsevier on February 19, 2021.
For personal use only. No other uses without permission. Copyright ©2021. Elsevier Inc. All rights reserved.

Distance analysis using ISH samples

In Figure 4H and I, serial sections of human desmoplastic rectal cancer samples, in which the stroma accounted for more than 40% of the total tumor area, were evaluated. The minimum edge-to-edge distance between ISH signals and the closest tumor glands was calculated by DiAna plugin[29] for ImageJ. Briefly, tumor glands in ISH images were outlined by a clinical pathologist. Then, to identify ISH signals (DAB^+ signals), the ISH images were subjected to color deconvolution before applying intensity thresholding and a watershed algorism in a Fiji software. ISH signals were segmented using a minimum size threshold by DiAna plugin. Then, the smallest edge-to-edge distance between each ISH signal and the closest tumor gland was computed by DiAna plugin.

Evaluation of tumor differentiation and tumor budding

Evaluation of tumor differentiation and tumor budding was performed by a clinical pathologist. Poorly differentiated adenocarcinomas were defined as cancers that exhibit glandular differentiation in 5-50% of the tumor, as described[30].

Tumor budding was defined as a single tumor cell or a cell cluster of up to 4 tumor cells, as described[31].

Data and materials availability

Data that support the findings of this study are available from the corresponding authors upon reasonable request. Noncommercially available materials described in this study may be obtained with a material transfer agreement (MTA). Requests for materials should be addressed to S.W.

Downloaded for Anonymous User (n/a) at The University of Adelaide from ClinicalKey.com.au by Elsevier on February 19, 2021.
For personal use only. No other uses without permission. Copyright ©2021. Elsevier Inc. All rights reserved.

Supplementary Figure 1: Analyses of a human CRC expression microarray dataset reveal that *GREM1* and *ISLR* are highly expressed in FAP$^+$ CAFs compared to EpCAM$^+$ epithelial cells, CD45$^+$ immune cells, and CD31$^+$ endothelial cells.

(A) *GREM1* and *ISLR* expression levels in a cDNA (complementary DNA) expression microarray from fluorescence-activated cell sorting (FACS)-purified cells from human primary CRC tissues (GSE39396).

n = 6 patients each. One-way ANOVA followed by Tukey's post-hoc multiple comparisons.

****, P < 0.0001. Box plots have whiskers of maximum and minimum values; the boxes represent first, second (median), and third quartiles.

(B) Volcano plots showing differentially expressed transcripts between FAP$^+$ CAFs and EpCAM$^+$ epithelial cells **(a)**, between FAP$^+$ CAFs and CD45$^+$ immune cells **(b)** and between FAP$^+$CAFs and CD31$^+$ endothelial cells **(c)** (GSE39396).

n = 6 patients each. The adjusted P-value cutoffs and the $\log_2$ fold change cutoffs for differentially expressed genes were 0.05 and 2, respectively.

Semi-transparent purple, blue, green, and red dots denote differentially expressed transcripts, which are upregulated in FAP$^+$ CAFs, EpCAM$^+$ epithelial cells, CD45$^+$ immune cells, and CD31$^+$ endothelial cells, respectively. Gray dots represent transcripts that are not differentially expressed.

GREM1 and *ISLR* gene probes used for the analyses are as follows; 218468_PM_s_at (*GREM1*) and 207191_PM_s_at (*ISLR*).

Downloaded for Anonymous User (n/a) at The University of Adelaide from ClinicalKey.com.au by Elsevier on February 19, 2021.
For personal use only. No other uses without permission. Copyright ©2021. Elsevier Inc. All rights reserved.

Supplementary Figure 2: Validation of *in situ* hybridization staining using positive and negative control probes.

Representative *in situ* hybridization (ISH) pictures using serial sections from human colorectal cancer. ISH for *GREM1* and *ISLR* shows 3,3'-Diaminobenzidine $(DAB)^+$ staining specifically in the stroma, whereas positive control probe (*PPIB*, a ubiquitously expressed gene) staining is observed both in the epithelial cells and stroma. No apparent background staining is seen in ISH for a negative control probe that targets the bacterial *DapB* gene.

Dotted lines indicate the borders between epithelial cells (E) and the stroma (S). Red and green arrowheads denote DAB^+ staining in the stroma and epithelial cells, respectively. The boxed areas are magnified in the insets. Scale bar, 100 μm.

Journal Pre-proof

Downloaded for Anonymous User (n/a) at The University of Adelaide from ClinicalKey.com.au by Elsevier on February 19, 2021.
For personal use only. No other uses without permission. Copyright ©2021. Elsevier Inc. All rights reserved.

Supplementary Figure 3: *GREM1* and *ISLR* transcripts are detected in FAP$^+$ CAFs in single-molecule fluorescent *in situ* hybridization on human CRC sections.

Representative picture of *GREM1* and *ISLR* dual single-molecule fluorescent hybridization (smFISH) followed by FAP immunofluorescence (IF), using human CRC tissue sections. Red and green arrowheads denote *GREM1*$^+$FAP$^+$ cells and *ISLR*$^+$FAP$^+$ cells, respectively. Blue arrowheads indicate FAP$^-$ cells that do not express *GREM1* or *ISLR*. n = 3 patients. Scale bar, 50 µm.

Journal Pre-proof

Downloaded for Anonymous User (n/a) at The University of Adelaide from ClinicalKey.com.au by Elsevier on February 19, 2021.
For personal use only. No other uses without permission. Copyright ©2021. Elsevier Inc. All rights reserved.

Supplementary Figure 4: *GREM1* and *ISLR* are highly expressed in fibroblasts in single-cell RNA-seq data from human normal colorectal mucosa and primary CRC.

(A) Violin plots depicting *GREM1* and *ISLR* expression levels in single-cell RNA-seq (scRNA-seq) of unsorted cells from human primary CRC tissues and normal colorectal tissues (GSE132465)[22]. In fibroblasts, *GREM1* and *ISLR* transcripts are differentially upregulated in tumors compared with normal samples (Wilcoxon tests, red asterisks).

n = 1501, 1961, 17469, 1070, 27080, 12137, 768, 739, 353, 92, 91, 123, 23, and 282 cells (left to right). Tumor samples from 23 patients. Normal samples from 10 of the patients.

T, Tumor samples; N, Normal samples.

(B) Violin plots showing *GREM1* and *ISLR* expression levels in scRNA-seq of unsorted cells from human primary CRC tissues and normal colorectal tissues (GSE81861)[23].

n = 17, 9, 272, 160, 71, 42, 4, and 2 cells (left to right). Tumor samples from 11 patients. Normal samples from 7 of the patients.

Kruskal-Wallis tests followed by Dunn's post-hoc multiple comparisons were used to compare *GREM1* or *ISLR* expression levels in fibroblasts from tumor and normal samples with those in other cell populations (black asterisks).

****, P < 0.0001; *, P = 0.0132. Solid black lines, median; Dotted black lines, quartiles.

Journal Pre-proof

Downloaded for Anonymous User (n/a) at The University of Adelaide from ClinicalKey.com.au by Elsevier on February 19, 2021.
For personal use only. No other uses without permission. Copyright ©2021. Elsevier Inc. All rights reserved.

Supplementary Figure 5: GREM1 and ISLR overexpression counteract each other's effect on BMP7-*Id2/4* signaling *in vitro*.

Quantitative reverse-transcription PCR (qRT-PCR) for BMP target genes, *Id2* and *Id4*.

YH2 cells that overexpress GREM1, GFP, or ISLR were admixed at a 1:1 ratio and stimulated with 40 ng/ml of recombinant BMP7 for 24 hours (orange, purple, and aqua). *Grem1*-YH2 cells, GFP-YH2 cells, or *Islr*-YH2 cells alone were used as controls (red, green, and blue, respectively). The same number of cells (a total of 5.0×10^4 cells/well) were seeded in a 6-well plate in each condition.

n = 3 each. A.U., arbitrary unit. Mean ± s.e.m.. Two-way ANOVA with post-hoc Tukey's multiple comparisons.

Journal Pre-proof

Downloaded for Anonymous User (n/a) at The University of Adelaide from ClinicalKey.com.au by Elsevier on February 19, 2021.
For personal use only. No other uses without permission. Copyright ©2021. Elsevier Inc. All rights reserved.

Supplementary Figure 6: BMP2-induced increase in *Id4* is prevented by GREM1 and augmented by ISLR in YH2 cells.

qRT-PCR for *Id2* and *Id4* in YH2 cells. GFP-, *Grem1*-, or *Islr*-overexpressing YH2 cells were treated with 25 ng/ml of recombinant BMP2 for 24 hours. Note that GREM1 prevented the BMP2-induced increase in *Id2* whereas ISLR did not significantly promote the BMP2-mediated increase in *Id2* in YH2 cells.

n = 3 each. A.U., arbitrary unit. Mean ± s.e.m.. Two-way ANOVA with post-hoc Tukey's multiple comparisons.

Journal Pre-proof

Downloaded for Anonymous User (n/a) at The University of Adelaide from ClinicalKey.com.au by Elsevier on February 19, 2021.
For personal use only. No other uses without permission. Copyright ©2021. Elsevier Inc. All rights reserved.

Journal Pre-proof

Supplementary Figure 7: *GREM1* and *ISLR* expression levels are upregulated during human CRC carcinogenesis.

(A) Violin plots depicting *GREM1* and *ISLR* expression in cDNA expression microarray data from human normal colorectal mucosa, colorectal adenoma, and primary colorectal adenocarcinoma (GSE41258)[16].

n = 53 (normal mucosa), 46 (adenoma) and 182 patients (adenocarcinoma).

(B) Violin plots depicting *GREM1* and *ISLR* expression in cDNA expression microarray data from human normal colon mucosa and primary colon adenocarcinoma (GSE39582)[17]. n = 19 (normal colon mucosa) and 566 patients (primary colon adenocarcinoma).

(C) Violin plots depicting *GREM1* and *ISLR* expression in cDNA expression microarray data from human colorectal adenoma and primary colorectal adenocarcinoma (GSE17538)[18]. n = 6 (colorectal adenoma) and 232 patients (primary colorectal adenocarcinoma).

One-way ANOVA followed by Tukey's post-hoc multiple comparisons (A). False delivery rate (FDR)-adjusted P-values are shown (B and C). Solid black lines, median; Dotted black lines, quartiles.

Journal Pre-proof

Downloaded for Anonymous User (n/a) at The University of Adelaide from ClinicalKey.com.au by Elsevier on February 19, 2021.
For personal use only. No other uses without permission. Copyright ©2021. Elsevier Inc. All rights reserved.

Supplementary Figure 8: *GREM1* and *ISLR* are expressed in the stroma of human CRC hepatic metastases.

(A, B) ISH for *GREM1* and *ISLR* in the hepatic metastases of human CRC. **(A)** Representative images. *GREM1* and *ISLR* are expressed by fibroblastic cells in the stroma of the liver metastases. Dotted yellow lines indicate the borders between the normal liver (N) and CRC liver metastases (M). Red arrowheads denote *GREM1* or *ISLR* expression. The boxed areas are magnified in the insets. Scale bars, 100 µm. **(B)** Violin plots showing quantification of 3,3'-Diaminobenzidine $(DAB)^+$ areas by ImageJ. 5 HPFs/patient, 3 patients each. Solid black lines, median; Dotted black lines, quartiles. **(C)** Violin plots depicting *GREM1* and *ISLR* expression in cDNA expression microarray data from human normal liver and liver metastasis of CRC (GSE41258). n = 13 (normal liver) and 21 patients (CRC liver metastasis). Solid black lines, median; Dotted black lines, quartiles.

Mann-Whitney U-test (B). False delivery rate (FDR)-adjusted P-values are shown in (C).

Journal Pre-proof

Downloaded for Anonymous User (n/a) at The University of Adelaide from ClinicalKey.com.au by Elsevier on February 19, 2021.
For personal use only. No other uses without permission. Copyright ©2021. Elsevier Inc. All rights reserved.

Supplementary Figure 9: *GREM1* and *ISLR* are highly expressed in consensus molecular subtype 4 CRC.

(A) Violin plots showing expression levels of *GREM1* and *ISLR* in four consensus molecular subtypes (CMSs)[20]. Primary colon and rectal adenocarcinoma samples in The Cancer Genome Atlas (TCGA) data were analyzed. n = 76 (CMS1), 220 (CMS2), 72 (CMS3), and 143 patients (CMS4).

(B) Violin plots depicting *GREM1* and *ISLR* expression levels in four CMSs. Primary colon adenocarcinoma samples were analyzed using cDNA expression microarray data (GSE39582)[17]. n = 70 (CMS1), 177 (CMS2), 97 (CMS3), and 107 patients (CMS4).

Kruskal-Wallis test followed by Dunn's post-hoc multiple comparisons. Solid black lines, median; Dotted black lines, quartiles. ****, $P < 0.0001$.

Journal Pre-proof

Downloaded for Anonymous User (n/a) at The University of Adelaide from ClinicalKey.com.au by Elsevier on February 19, 2021.
For personal use only. No other uses without permission. Copyright ©2021. Elsevier Inc. All rights reserved.

Journal Pre-proof

Supplementary Figure 10: *Grem1* is highly expressed in *Foxl1*-lineage telocytes in the mouse small intestine.

Expression levels of *Grem1*, *Islr*, and *Foxl1* in RNA-sequence data from FACS-purified non-*Foxl1*-lineage mesenchymal cells, *Foxl1*-lineage mesenchymal cells (sorted from *Fox1*-Cre; Rosa26-YFP or *Foxl1*-Cre; Rosa26-mT/mG), *Lgr5*$^{+}$ intestinal stem cells (sorted by *Lgr5*-eGFP^{high} expression), and differentiated enterocytes (GSE94072).

Note that fragments per kilobase of exon per million fragments (FPKM) for *Grem1* and *Foxl1* were zero in all three biological replicates of non-*Foxl1* lineage mesenchymal cells.

n = 3 (non-*Foxl1*-lineage mesenchymal cells), 3 (*Foxl1*-lineage mesenchymal cells), 2 (*Lgr5*$^{+}$ intestinal stem cells) and 2 (Differentiated enterocytes) mice.

All data are represented as mean ± s.e.m.. Statistical analyses were performed using the Kruskal-Wallis test.

Journal Pre-proof

Downloaded for Anonymous User (n/a) at The University of Adelaide from ClinicalKey.com.au by Elsevier on February 19, 2021.
For personal use only. No other uses without permission. Copyright ©2021. Elsevier Inc. All rights reserved.

Supplementary Figure 11: Lentivirus-mediated FOXL1 overexpression increases *GREM1*-promoter activity while decreasing *ISLR*-promoter activity.

Luciferase assays of Human *GREM1*- or *ISLR*-promoter regions using human FOXL1-overexpressing YH2 cells and control empty YH2 cells.

n = 6 each. Data are represented as mean ± s.e.m.. Statistical analysis was performed using two-tailed unpaired Student's t-test.

Journal Pre-proof

Downloaded for Anonymous User (n/a) at The University of Adelaide from ClinicalKey.com.au by Elsevier on February 19, 2021.
For personal use only. No other uses without permission. Copyright ©2021. Elsevier Inc. All rights reserved.

Supplementary Figure 12: Validation of CRISPR/Cas9-mediated FOXL1-knockdown in mouse primary colonic fibroblasts by Western blot.

(A) Western blotting (WB) showing FOXL1-Knockdown by lentiviral transduction.

CRISPR, clustered regularly interspaced short palindromic repeats; gRNA, guide RNA.

(B) Densitometry of Western blotting (A) showing decreased FOXL1 protein expression by lentiviral transduction. A.U., arbitrary unit.

n = 3 mice each. Data are represented as mean ± s.e.m.. Statistical analysis was performed using two-tailed unpaired Student's t-test.

Journal Pre-proof

Downloaded for Anonymous User (n/a) at The University of Adelaide from ClinicalKey.com.au by Elsevier on February 19, 2021.
For personal use only. No other uses without permission. Copyright ©2021. Elsevier Inc. All rights reserved.

Journal Pre-proof

Supplementary Figure 13: Increased collagen gel contraction in *Grem1*-overexpressing YH2 cells.

(A, B) Collagen gel contraction assay using GFP-, *Grem1*- and *Islr*-overexpressing YH2 cells.

(A) Representative pictures. Collagen gel areas are outlined by dotted yellow lines. Scale bars, 5 mm.

(B) Quantification of collagen gel areas.

Collagen gel areas were evaluated 12 hours after seeding cells. n = 4 each. Data are represented as mean ± s.e.m.. Statistical analysis was performed using one-way ANOVA with Tukey's post-hoc multiple comparisons.

Journal Pre-proof

Downloaded for Anonymous User (n/a) at The University of Adelaide from ClinicalKey.com.au by Elsevier on February 19, 2021.
For personal use only. No other uses without permission. Copyright ©2021. Elsevier Inc. All rights reserved.

Journal Pre-proof

Supplementary Figure 14: ScRNA-seq from human CRC tissues reveals that *GREM1* identifies a myofibroblastic CAF subpopulation that is distinct from *ISLR*$^{+}$ CAFs.

(A, B) Spearman correlation analyses of gene expression levels in scRNA-seq data from human CRC tissues (GSE132465)[22]. **(A)** *GREM1* transcript levels are inversely correlated with *ISLR* expression in human CRC CAFs. **(B)** *GREM1*, but not *ISLR*, transcripts are positively correlated with *ACTA2* transcripts. In a total of 1501 CAFs, 1156 human CRC CAFs that express *GREM1* or *ISLR* transcripts were analyzed. Spearman r and p-values are reported in the figure. Solid pink line, linear regression.

(C, D) Violin plots depicting *GREM1* and *ISLR* expression (C) and BMP7 expression (D) in four different CRC CAF subclusters[22]. Myo, Myofibroblasts; S1, Stromal 1 fibroblasts; S2, Stromal 2 fibroblasts; S3, Stromal 3 fibroblasts. n = 1146 (Myofibroblasts), 73 (S1 fibroblasts), 158 (S2 fibroblasts), and 124 cells (S3 fibroblasts).

Kruskal-Wallis test followed by Dunn's post-hoc multiple comparisons.

****, P < 0.0001; ***, P = 0.0005; **, P = 0.0098; ns, P = 0.1375. Solid black lines, median; Dotted black lines, quartiles.

Journal Pre-proof

Downloaded for Anonymous User (n/a) at The University of Adelaide from ClinicalKey.com.au by Elsevier on February 19, 2021.
For personal use only. No other uses without permission. Copyright ©2021. Elsevier Inc. All rights reserved.

Journal Pre-proof

Supplementary Figure 15: *GREM1*$^+$ CAFs shows higher positivity for *FOXL1* in human CRC than *ISLR*$^+$ CAFs.

(A, B) Dual smFISH for *GREM1/FOXL1* (upper panel in A) and *ISLR/FOXL1* (lower panel in A) in human CRC samples. **(A)** Representative pictures. Yellow and green arrowheads denote *GREM1*$^+$*FOXL1*$^+$ cells and *ISLR*$^+$*FOXL1*$^-$ cells, respectively. The boxed areas are magnified in the adjacent panels. **(B)** Semi-quantification of *FOXL1* positivity in *GREM1*$^+$ cells and *ISLR*$^+$ cells. 3 HPFs/patient, 3 patients.

Mean ± s.e.m.. Mann-Whitney U-test. Scale bars, 50 μm.

Journal Pre-proof

Downloaded for Anonymous User (n/a) at The University of Adelaide from ClinicalKey.com.au by Elsevier on February 19, 2021.
For personal use only. No other uses without permission. Copyright ©2021. Elsevier Inc. All rights reserved.

Supplementary Figure 16: Generation of *Apc*$^{\Delta/\Delta}$, *Trp53*$^{\Delta/\Delta}$ organoids (AP tumoroids) and *Smad4-mutant* AP tumoroids (APS tumoroids)

(A) Schematic illustration of the CRISPR/Cas9-mediated sequential engineering of AP tumoroids and APS tumoroids from normal colon organoids isolated from a Rosa26-Cas9 mouse. Correctly targeted clones were enriched by selection medium as indicated. Monoclonal lines were handpicked after each transduction step. sg, single guide RNA.

(B) *Apc* and *Trp53* DNA sequence verification of biallelic insertion/deletion mutations, which result in prematurely truncated proteins.

fs, frameshift mutation; Ter, translation termination (stop) codon; PAM, Protospacer adjacent motif.

(C) Decreased SMAD4 protein expression in APS tumoroids was validated by Western blotting (WB).

(D) *Smad4* DNA sequence verification of biallelic mutations, resulting in disruption of the sequence of L1 loop protein, which is involved in the formation of SMAD protein complex formation[32].

sg*Smad4* was designed to target the genomic sequence corresponding to *SMAD4* mutation hotspot regions in human CRC[32], which were mapped to the L1 loop and its adjacent region[32].

To simplify graphical presentation, the following mutations were not shown in the schematics in (D). *Smad4* allele 1, c.1005A>G (Silent mutation in Exon 9)；*Smad4* allele2, c.953-831A>T (Mutation in an intron; Orange bar) and c.953-805_953-804insAAAAAATAAATAAAAAAAATAAAT (Mutation in an intron; Magenta bar).

Changes to proteins are reported according to the Human Genome Variation Society nomenclature. Reference sequences are as follows. *Apc*, NM_001360980.1; *Trp53*, NM_011640.3; *Smad4*, NM_008540.3.

Downloaded for Anonymous User (n/a) at The University of Adelaide from ClinicalKey.com.au by Elsevier on February 19, 2021.
For personal use only. No other uses without permission. Copyright ©2021. Elsevier Inc. All rights reserved.

Supplementary Figure 17: Conditioned medium transfer from *Grem1*-overexpressing YH2 cells decreases BMP signaling and accelerates organoid growth in AP tumoroids, but not in APS tumoroids.

(A) Experimental schematic depicting conditioned medium transfer from *Grem1*-overexpressing YH2 cells or GFP-overexpressing YH2 cells to AP (*Apc*$^{\Delta/\Delta}$, *Trp53*$^{\Delta/\Delta}$) tumoroids or APS (*Apc*$^{\Delta/\Delta}$, *Trp53*$^{\Delta/\Delta}$, *Smad4*$^{\Delta/\Delta}$) tumoroids.

(B) qRT-PCR for BMP target genes in AP and APS tumoroids (n = 3). A.U., Arbitrary Units.

(C) Luciferase signals from AP tumoroids and APS tumoroids (n ≥ 8).

(D) qRT-PCR for *Krt20* in AP tumoroids and APS tumoroids (n = 3).

Note that data normalization was performed within the AP and APS tumoroid groups separately **(B-D)**.

Statistical analyses were performed using two-tailed unpaired Student's t-test (B and D) and two-way ANOVA with Tukey's post-hoc multiple comparisons (C). Data are represented as mean ± s.e.m..

Journal Pre-proof

Downloaded for Anonymous User (n/a) at The University of Adelaide from ClinicalKey.com.au by Elsevier on February 19, 2021.
For personal use only. No other uses without permission. Copyright ©2021. Elsevier Inc. All rights reserved.

Supplementary Figure 18: Treatment with a GREM1-neutralizing antibody blocks GREM1-mediated inhibition of BMP2 signaling *in vitro*.

(A, B) Validation of the GREM1-neutralizing antibody using YH2 cells. **(A)** Experimental schematic. YH2 cells were serum-starved for 2 hours before treating with the indicated proteins for 3 hours. **(B)** qRT-PCR of *Id2* in YH2 cells was performed to confirm the effect of the GREM1-neutralizing antibody in neutralizing recombinant GREM1 and restoring BMP signaling. n = 3 each.

Data are represented as mean ± s.e.m.. Statistical analyses were performed using one-way ANOVA with Tukey's post-hoc multiple comparisons (B).

Journal Pre-proof

Downloaded for Anonymous User (n/a) at The University of Adelaide from ClinicalKey.com.au by Elsevier on February 19, 2021.
For personal use only. No other uses without permission. Copyright ©2021. Elsevier Inc. All rights reserved.

Supplementary Figure 19: Treatment with a GREM1-neutralizing antibody or conditioned medium from *Islr*-overexpressing intestinal fibroblasts attenuates tumoroid growth as assessed by tumoroid area.

(A) Treatment with a GREM1-neutralizing antibody reduces AP tumoroid areas. n = 790, 522, 3571, and 3494 tumoroids (left to right) from 6 (AP tumoroids) and 9 independent replicates (APS tumoroids). Note that AP tumoroid and APS tumoroids were evaluated 8 and 12 days after being plated. In this experimental condition, APS tumoroids generated smaller tumoroid areas than AP tumoroids when treated with an IgG isotype ($P < 0.0001$, Mann-Whitney U-test). CM, Conditioned Medium.

(B) Conditioned medium transfer from *Islr*-overexpressing YH2 cells decreases AP tumoroid areas. n = 1873 (GFP-YH2 cells) and 1713 tumoroids (*Islr*-YH2 cells) from 9 independent replicates. The AP tumoroids were evaluated 7 days after being plated.

Tumoroid areas were assessed by Image J. Mean ± s.e.m., Mann-Whitney U-test (A and B).

Journal Pre-proof

Downloaded for Anonymous User (n/a) at The University of Adelaide from ClinicalKey.com.au by Elsevier on February 19, 2021.
For personal use only. No other uses without permission. Copyright ©2021. Elsevier Inc. All rights reserved.

Supplementary Figure 20: A GREM1-neutralizing antibody-treated group showed enhanced BMP signaling and a trend toward prolonged survival in a mouse model of CRC liver metastasis.

(A) Experimental scheme for portal vein injection of AP tumoroids and subsequent GREM1-neutralizing antibody administration. The GREM1-neutralizing antibody was subcutaneously administered 1 week after portal vein injection of AP tumoroids until mice reach humane endpoints. Yellow dotted lines outline the portal vein. Scale bar, 200 μm.

(B) ISH for *Grem1* in the mouse CRC liver metastasis. *Grem1* was expressed by the fibroblastic cells in the liver metastasis mesenchyme (M), but not in the normal liver (N). Yellow dotted lines demarcate the normal liver (N) and CRC liver metastasis (M). Green arrowheads indicate *Grem1* expression. V, blood vessel. n = 3 mice. Scale bar, 50 μm.

(C, D) Immunohistochemistry (IHC) for pSmad1/5/8 in the liver metastases developed in IgG isotype-treated or GREM1-neutralizing antibody-treated mice. **(C)** Representative pictures. Scale bar, 50 μm. **(D)** Quantification of 3,3'-Diaminobenzidine (DAB) intensity by ImageJ. 4 HPFs/mouse, 5 mice each. A.U., arbitrary unit.

(E) Kaplan-Meier survival curves. n = 19 (IgG isotype) and 19 mice (GREM1-neutralizing antibody). Hazard ratio (HR) and 95% confidence interval of the hazard ratio are shown (Log-rank method).

(F) Growth kinetics of CRC hepatic metastases was assessed during the survival analysis in (E). AP tumoroid-derived luciferase signals were evaluated using an *in vivo* imaging system (IVIS).

Mean ± s.e.m.. Mann-Whitney U-test (D), Log-rank test (E), and two-way repeated-measures ANOVA (F). In (F), in order to exclude the effect of loss of samples during the experiment, statistical analysis was performed using IVIS signal values before Week 10, when the first mouse reached a humane endpoint.

Note that the same pictures were used in Figure 6A and Supplementary Figure 20A in order to show the procedure of portal vein injection.

Downloaded for Anonymous User (n/a) at The University of Adelaide from ClinicalKey.com.au by Elsevier on February 19, 2021.
For personal use only. No other uses without permission. Copyright ©2021. Elsevier Inc. All rights reserved.

Supplementary Figure 21: AAV-*Islr* treatment augments BMP signaling in the normal mouse liver.

(A, B) Immunohistochemistry (IHC) for pSmad1/5/8 in the normal liver from AAV-*Islr*-treated or AAV-mRuby2-treated mice. **(A)** Representative pictures. Scale bar, 50 μm. V, central vein; H, hepatocytes. **(B)** Quantification of 3,3'-Diaminobenzidine (DAB) intensity by ImageJ. 5 HPFs/mouse, 4 mice each. A.U., arbitrary unit.

(C) qRT-PCR for BMP target genes using normal liver tissue lysates. n = 3 mice each.

Mice were harvested 5-6 weeks after tail vein injection (3-4 weeks after tumor injection) (A-C). Mean ± s.e.m.. Mann-Whitney U-test (B) and two-tailed unpaired Student's t-test (C).

Journal Pre-proof

Downloaded for Anonymous User (n/a) at The University of Adelaide from ClinicalKey.com.au by Elsevier on February 19, 2021.
For personal use only. No other uses without permission. Copyright ©2021. Elsevier Inc. All rights reserved.

Supplementary Figure 22: No liver injury was apparent in mice administered AAV8-*Islr* via histological analysis.

(A) Fluorescent microscopy image showing expression of a red fluorescence protein (mRuby2) in the liver of mice harvested two weeks after tail vein injection of AAV8-mRuby2 and AAV8-*Islr*. White dotted lines indicate the edges of the livers. Yellow scale bar, 500 µm.

(B) Hematoxylin and eosin (H&E) staining of the liver section from mice harvested two weeks after tail vein injection of AAV8-mRuby2 and AAV8-*Islr*. n = 3 mice each.

A, hepatic artery (arrows); B, bile duct; P, portal vein. Scale bar, 100 µm.

Journal Pre-proof

Downloaded for Anonymous User (n/a) at The University of Adelaide from ClinicalKey.com.au by Elsevier on February 19, 2021.
For personal use only. No other uses without permission. Copyright ©2021. Elsevier Inc. All rights reserved.

Supplementary Figure 23: Mice administered AAV8-*Islr* show reduced fibrosis in CRC liver metastases.

(A, B) Immunohistochemistry (IHC) for αSMA using CRC liver metastases in mice administered AAV8-*Islr* or AAV8-mRuby2. **(A)** Representative pictures. **(B)** Quantification of 3,3'-Diaminobenzidine $(DAB)^+$ areas by ImageJ. 5 HPFs/mouse, 4 mice each.

(C, D) Picro-Sirius red staining for collagen using the CRC liver metastasis sections. **(C)** Representative pictures. **(D)** Quantification of Picro-Sirius-red-positive areas by ImageJ. 5 HPFs/mouse, 4 mice each.

Mean ± s.e.m.. Mann-Whitney U-test (B and D). Scale bars, 50 μm.

Journal Pre-proof

Downloaded for Anonymous User (n/a) at The University of Adelaide from ClinicalKey.com.au by Elsevier on February 19, 2021.
For personal use only. No other uses without permission. Copyright ©2021. Elsevier Inc. All rights reserved.

Journal Pre-proof

Supplementary Figure 24: *Grem1*$^{+}$ cells in the small intestine show lower *Foxl1* positivity than those in the colon.

(A, B) Single-molecule fluorescent ISH (smFISH) for *Foxl1* and immunofluorescence (IF) for tdtomato in the small intestine from *Grem1*-CreERT2; Rosa26-tdtomato mice. **(A)** Representative picture. Red and green arrowheads denote *Grem1*$^{+}$*Foxl1*$^{-}$ cells and *Grem1*$^{-}$*Foxl1*$^{+}$ cells, respectively. The boxed areas are magnified in the insets. **(B)** *Foxl1* positivity in the *Grem1*$^{+}$ cells in the small intestine (blue). For statistical comparison, the result with the colon from Figure 3D is shown on the right (red).

4 HPFs (400x)/mouse, 3 mice each. Two-tailed unpaired Student's t-test. Scale bars, 50 µm.

Journal Pre-proof

Downloaded for Anonymous User (n/a) at The University of Adelaide from ClinicalKey.com.au by Elsevier on February 19, 2021.
For personal use only. No other uses without permission. Copyright ©2021. Elsevier Inc. All rights reserved.

Supplementary References

1. Fornes O, Castro-Mondragon JA, Khan A, et al. JASPAR 2020: update of the open-access database of transcription factor binding profiles. Nucleic Acids Res 2019.
2. Mizutani Y, Kobayashi H, Iida T, et al. Meflin-Positive Cancer-Associated Fibroblasts Inhibit Pancreatic Carcinogenesis. Cancer Res 2019;79:5367-5381.
3. Maeda K, Enomoto A, Hara A, et al. Identification of Meflin as a Potential Marker for Mesenchymal Stromal Cells. Sci Rep 2016;6:22288.
4. Persons DA, Mehaffey MG, Kaleko M, et al. An improved method for generating retroviral producer clones for vectors lacking a selectable marker gene. Blood Cells Mol Dis 1998;24:167-82.
5. Hirokawa Y, Yip KH, Tan CW, et al. Colonic myofibroblast cell line stimulates colonoid formation. Am J Physiol Gastrointest Liver Physiol 2014;306:G547-56.
6. Khalil H, Nie W, Edwards RA, et al. Isolation of primary myofibroblasts from mouse and human colon tissue. J Vis Exp 2013.
7. Ran FA, Hsu PD, Wright J, et al. Genome engineering using the CRISPR-Cas9 system. Nat Protoc 2013;8:2281-2308.
8. Platt RJ, Chen S, Zhou Y, et al. CRISPR-Cas9 knockin mice for genome editing and cancer modeling. Cell 2014;159:440-55.
9. Doench JG, Fusi N, Sullender M, et al. Optimized sgRNA design to maximize activity and minimize off-target effects of CRISPR-Cas9. Nat Biotechnol 2016;34:184-191.
10. Ponomarev V, Doubrovin M, Serganova I, et al. A novel triple-modality reporter gene for whole-body fluorescent, bioluminescent, and nuclear noninvasive imaging. Eur J Nucl Med Mol Imaging 2004;31:740-51.
11. Aubrey BJ, Kelly GL, Kueh AJ, et al. An inducible lentiviral guide RNA platform enables the identification of tumor-essential genes and tumor-promoting mutations in vivo. Cell Rep 2015;10:1422-32.

Downloaded for Anonymous User (n/a) at The University of Adelaide from ClinicalKey.com.au by Elsevier on February 19, 2021.
For personal use only. No other uses without permission. Copyright ©2021. Elsevier Inc. All rights reserved.

12. Schneider CA, Rasband WS, Eliceiri KW. NIH Image to ImageJ: 25 years of image analysis. Nat Methods 2012;9:671-5.

13. Ye J, Coulouris G, Zaretskaya I, et al. Primer-BLAST: a tool to design target-specific primers for polymerase chain reaction. BMC Bioinformatics 2012;13:134.

14. Calon A, Espinet E, Palomo-Ponce S, et al. Dependency of colorectal cancer on a TGF-beta-driven program in stromal cells for metastasis initiation. Cancer Cell 2012;22:571-84.

15. Phipson B, Lee S, Majewski IJ, et al. Robust Hyperparameter Estimation Protects against Hypervariable Genes and Improves Power to Detect Differential Expression. Ann Appl Stat 2016;10:946-963.

16. Sheffer M, Bacolod MD, Zuk O, et al. Association of survival and disease progression with chromosomal instability: a genomic exploration of colorectal cancer. Proc Natl Acad Sci U S A 2009;106:7131-6.

17. Marisa L, de Reynies A, Duval A, et al. Gene expression classification of colon cancer into molecular subtypes: characterization, validation, and prognostic value. PLoS Med 2013;10:e1001453.

18. Smith JJ, Deane NG, Wu F, et al. Experimentally derived metastasis gene expression profile predicts recurrence and death in patients with colon cancer. Gastroenterology 2010;138:958-68.

19. Camp RL, Dolled-Filhart M, Rimm DL. X-tile: a new bio-informatics tool for biomarker assessment and outcome-based cut-point optimization. Clin Cancer Res 2004;10:7252-9.

20. Guinney J, Dienstmann R, Wang X, et al. The consensus molecular subtypes of colorectal cancer. Nat Med 2015;21:1350-6.

21. Cancer Genome Atlas N. Comprehensive molecular characterization of human colon and rectal cancer. Nature 2012;487:330-7.

22. Lee HO, Hong Y, Etlioglu HE, et al. Lineage-dependent gene expression programs influence

Downloaded for Anonymous User (n/a) at The University of Adelaide from ClinicalKey.com.au by Elsevier on February 19, 2021.
For personal use only. No other uses without permission. Copyright ©2021. Elsevier Inc. All rights reserved.

the immune landscape of colorectal cancer. Nat Genet 2020.

23. Li H, Courtois ET, Sengupta D, et al. Reference component analysis of single-cell transcriptomes elucidates cellular heterogeneity in human colorectal tumors. Nat Genet 2017;49:708-718.

24. Neufert C, Becker C, Neurath MF. An inducible mouse model of colon carcinogenesis for the analysis of sporadic and inflammation-driven tumor progression. Nat Protoc 2007;2:1998-2004.

25. Xiao X, Li J, Samulski RJ. Production of high-titer recombinant adeno-associated virus vectors in the absence of helper adenovirus. J Virol 1998;72:2224-32.

26. Parmiani G. Immunological approach to gene therapy of human cancer: improvements through the understanding of mechanism(s). Gene Ther 1998;5:863-4.

27. Strobel B, Miller FD, Rist W, et al. Comparative Analysis of Cesium Chloride- and Iodixanol-Based Purification of Recombinant Adeno-Associated Viral Vectors for Preclinical Applications. Hum Gene Ther Methods 2015;26:147-57.

28. Wang Q, Dong B, Firrman J, et al. Efficient production of dual recombinant adeno-associated viral vectors for factor VIII delivery. Hum Gene Ther Methods 2014;25:261-8.

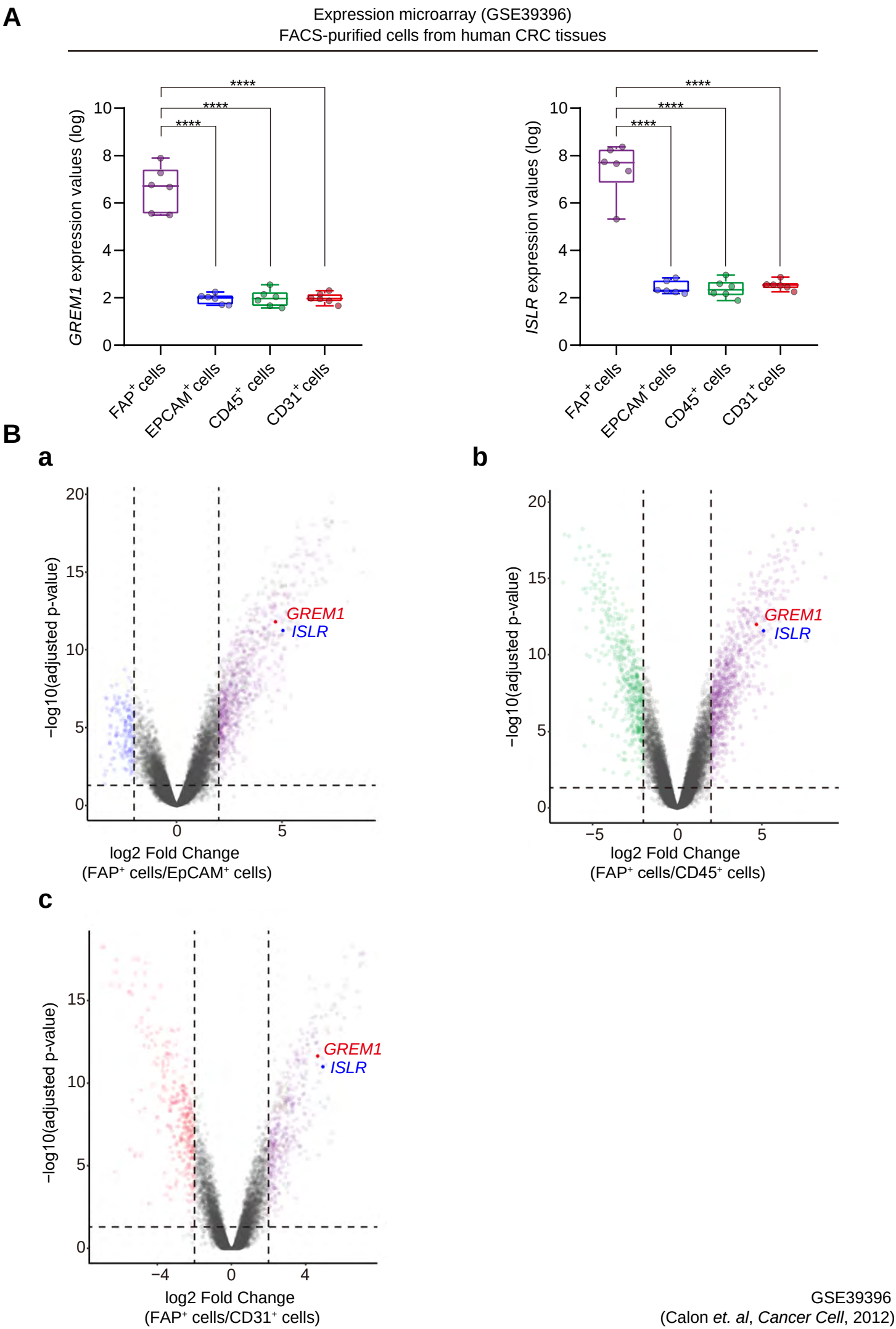
29. Gilles JF, Dos Santos M, Boudier T, et al. DiAna, an ImageJ tool for object-based 3D co-localization and distance analysis. Methods 2017;115:55-64.

30. Jackstadt R, van Hooff SR, Leach JD, et al. Epithelial NOTCH Signaling Rewires the Tumor Microenvironment of Colorectal Cancer to Drive Poor-Prognosis Subtypes and Metastasis. Cancer Cell 2019;36:319-336 e7.

31. Lugli A, Kirsch R, Ajioka Y, et al. Recommendations for reporting tumor budding in colorectal cancer based on the International Tumor Budding Consensus Conference (ITBCC) 2016. Mod Pathol 2017;30:1299-1311.

32. Fleming NI, Jorissen RN, Mouradov D, et al. SMAD2, SMAD3 and SMAD4 mutations in colorectal cancer. Cancer Res 2013;73:725-35.

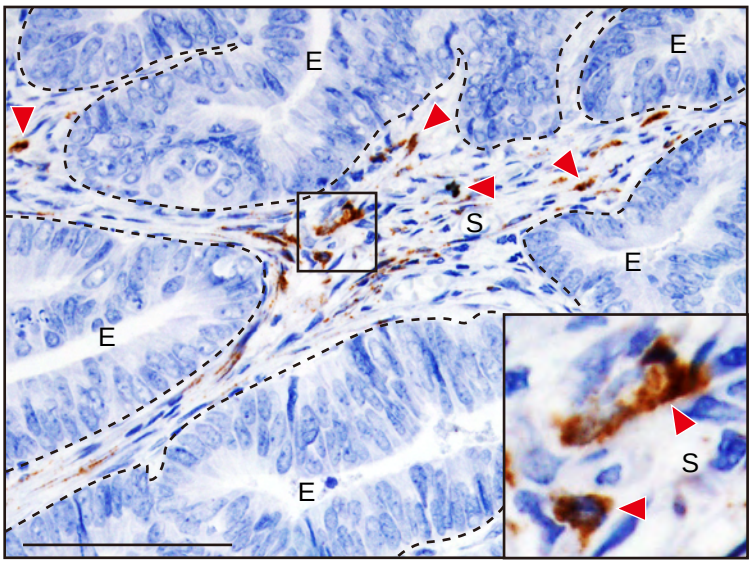
Downloaded for Anonymous User (n/a) at The University of Adelaide from ClinicalKey.com.au by Elsevier on February 19, 2021.
For personal use only. No other uses without permission. Copyright ©2021. Elsevier Inc. All rights reserved.



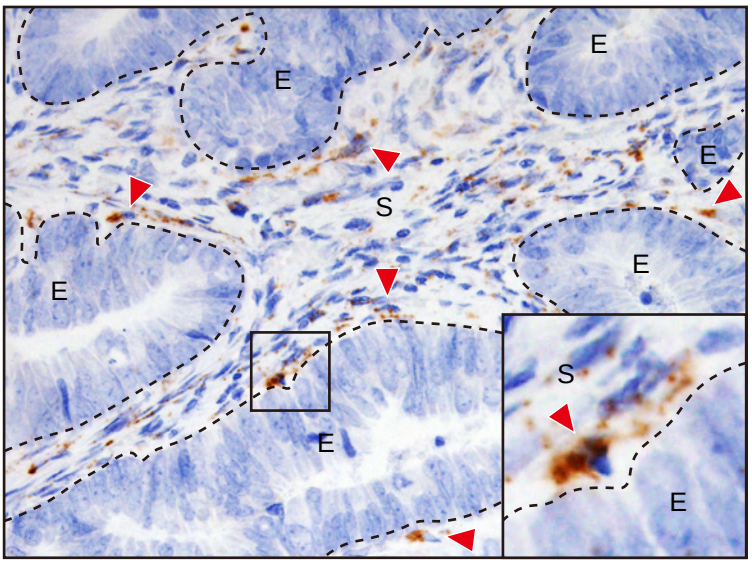
Kobayashi *et al*. Supplementary Figure 1

Downloaded for Anonymous User (n/a) at The University of Adelaide from ClinicalKey.com.au by Elsevier on February 19, 2021.
For personal use only. No other uses without permission. Copyright ©2021. Elsevier Inc. All rights reserved.

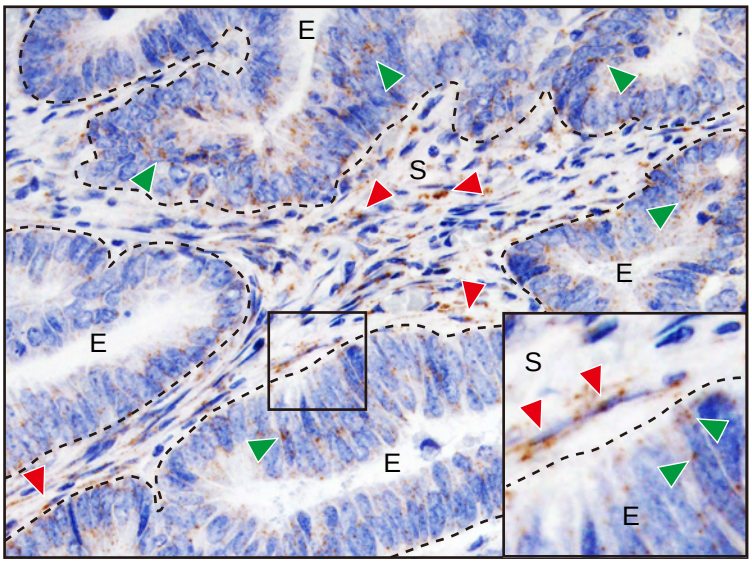
GREM1 probe



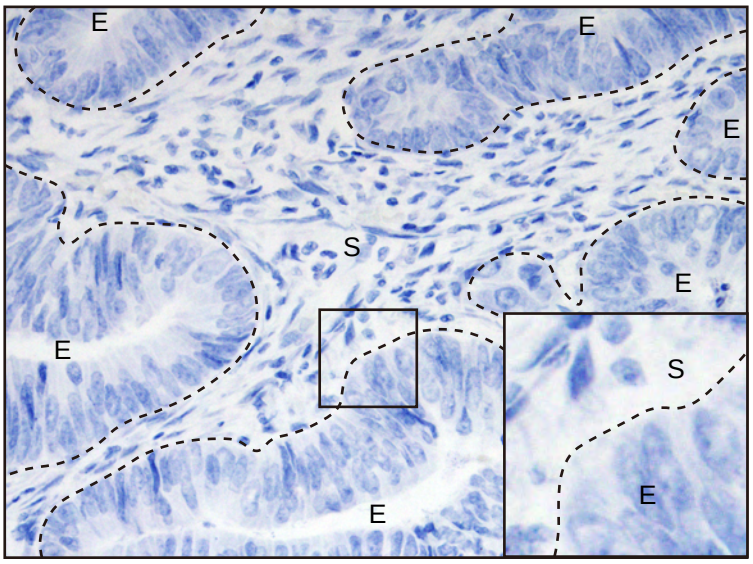
ISLR probe



Positive control probe (*PPIB*)

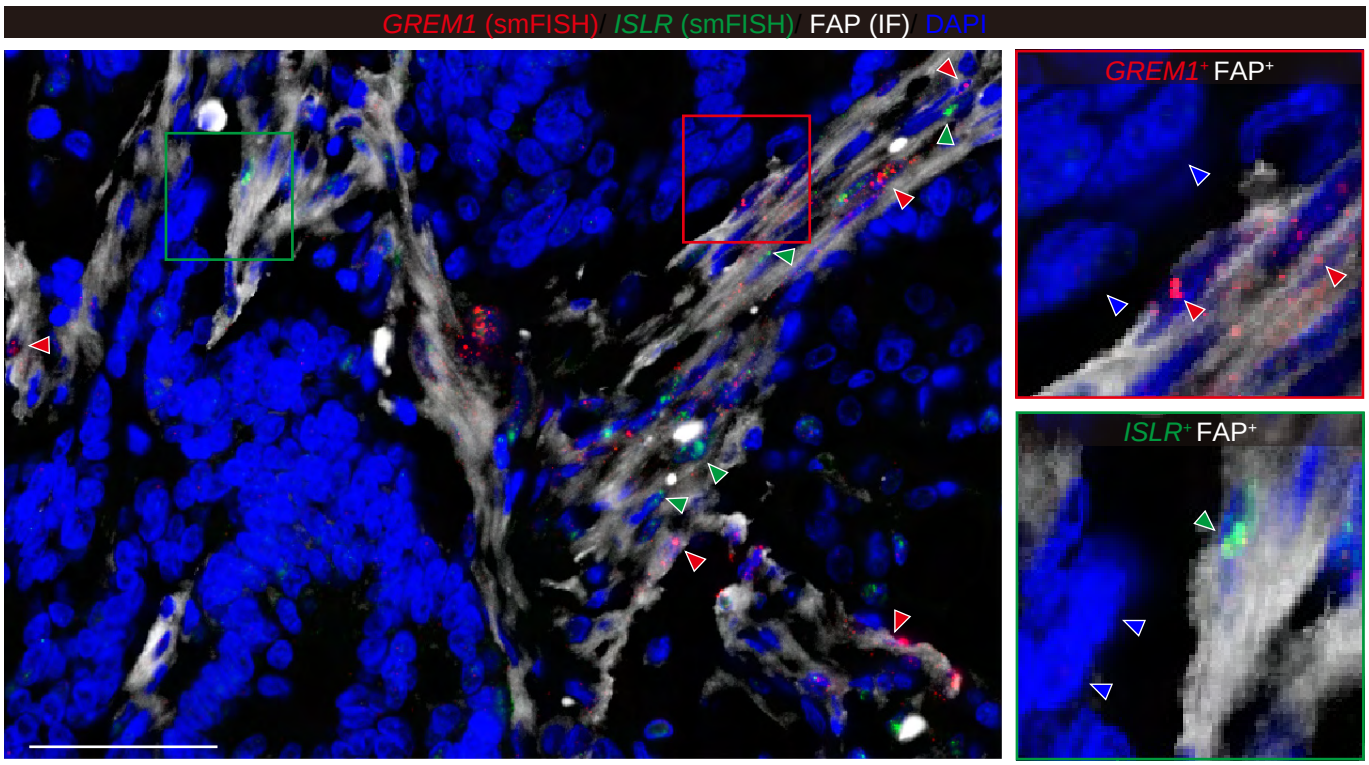


Negative control probe (*DapB*)



Kobayashi *et al.*, Supplementary Figure 2.

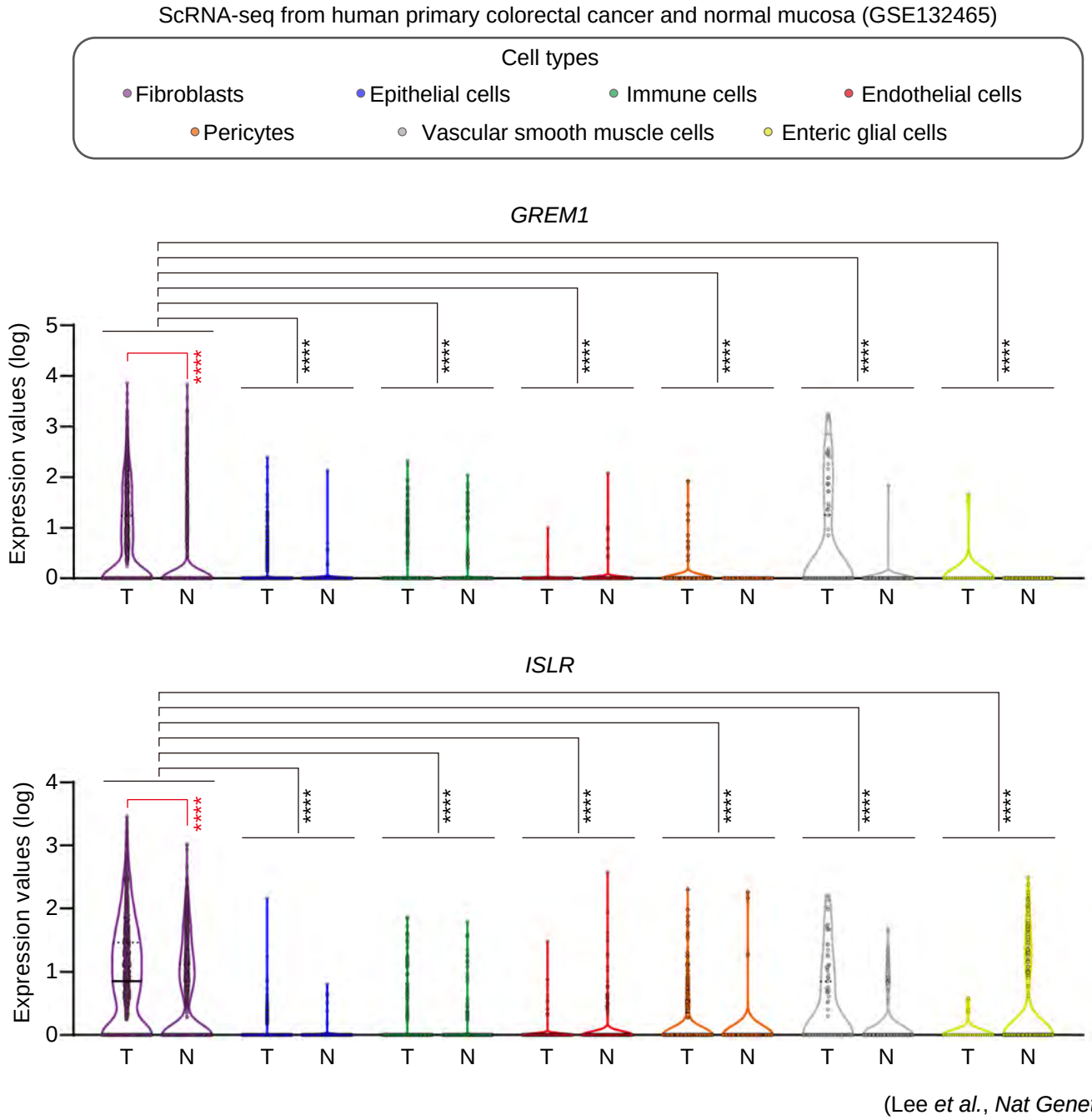
Downloaded for Anonymous User (n/a) at Griffith University from ClinicalKey.com.au by Elsevier on February 19, 2021.
For personal use only. No other uses without permission. Copyright ©2021. Elsevier Inc. All rights reserved.



Kobayashi *et al*., Supplementary Figure 3

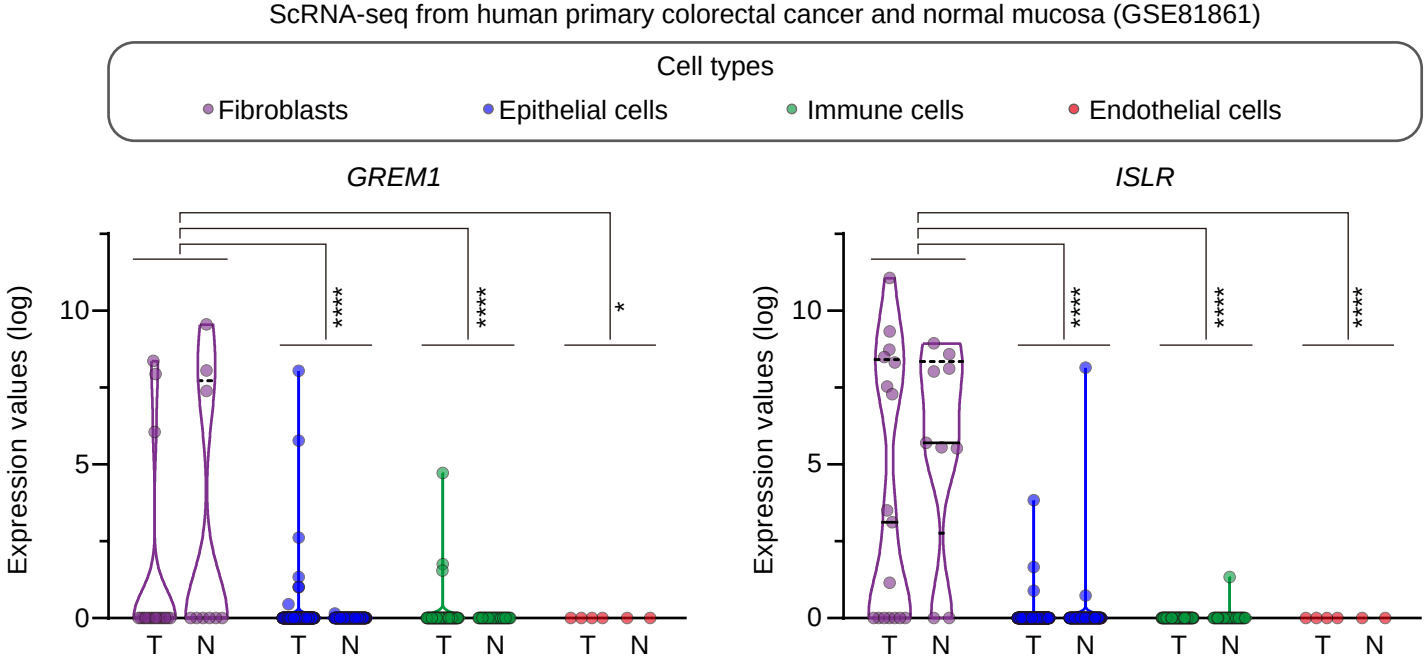
Downloaded for Anonymous User (n/a) at The University of Adelaide from ClinicalKey.com.au by Elsevier on February 19, 2021.
For personal use only. No other uses without permission. Copyright ©2021. Elsevier Inc. All rights reserved.

A



(Lee *et al.*, *Nat Genet*, 2020)

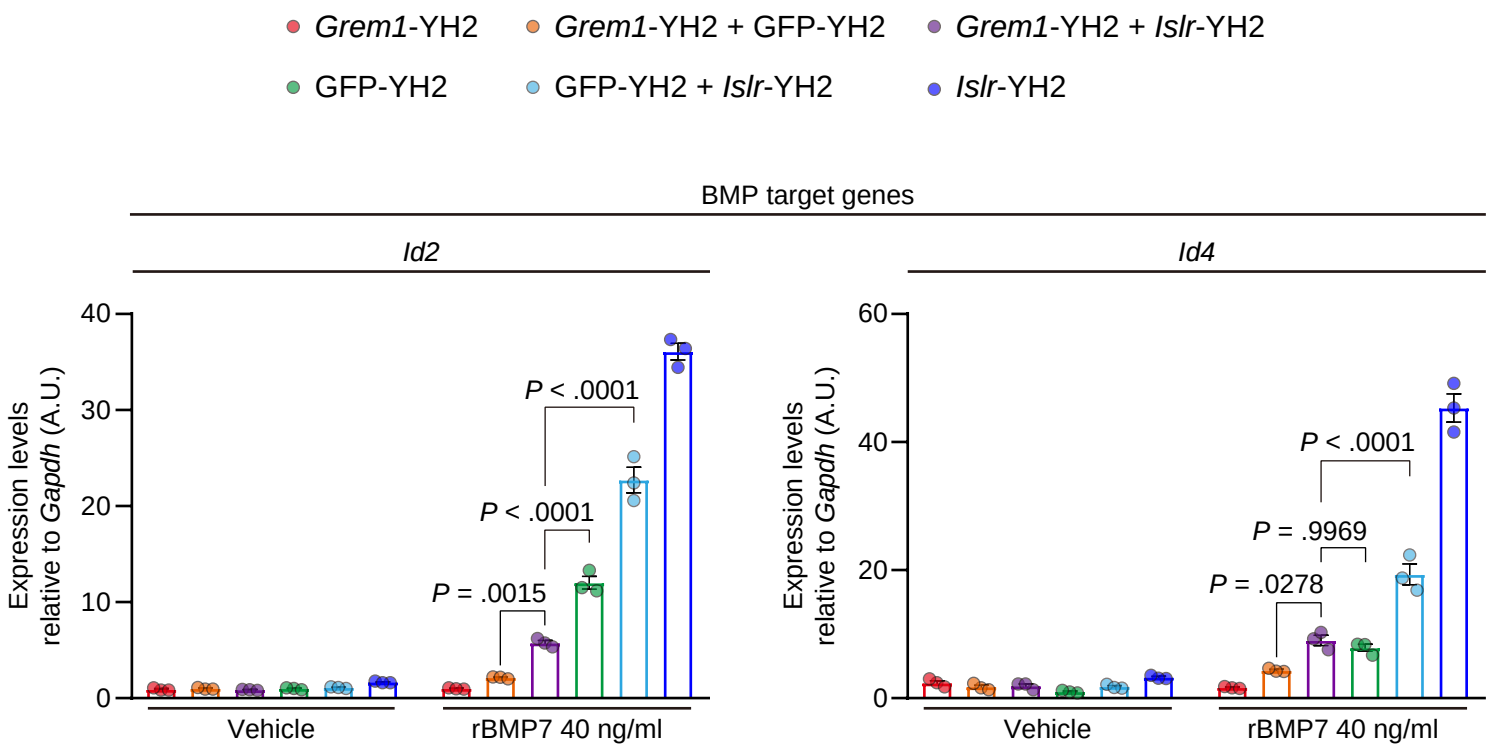
B



(Li *et al.*, *Nat Genet*, 2017)

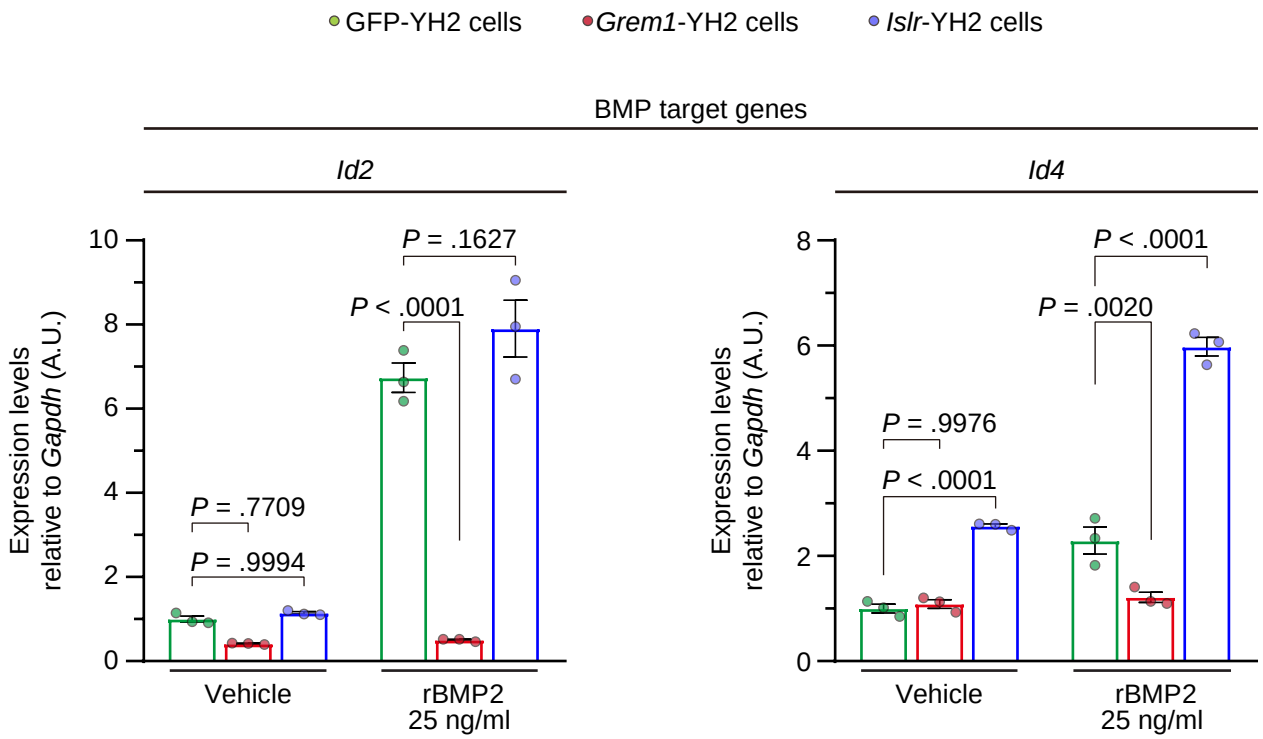
Kobayashi *et al.*, Supplementary Figure 4.

Downloaded for Anonymous User (n/a) at Universite de Montpellier from ClinicalKey.com.au by Elsevier on February 10, 2021.
For personal use only. No other uses without permission. Copyright ©2021. Elsevier Inc. All rights reserved.



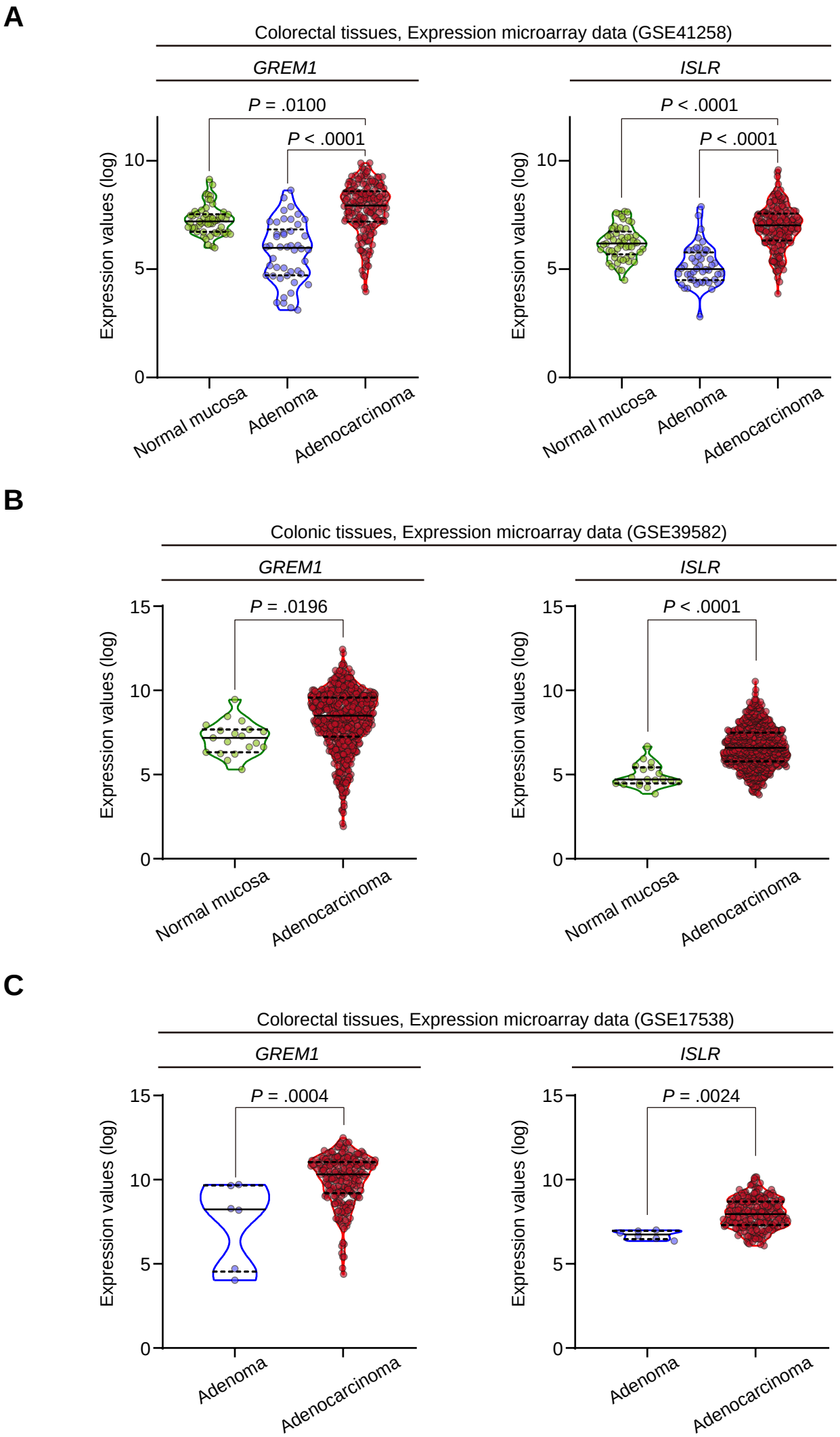
Kobayashi *et al.*, Supplementary Figure 5.

Downloaded for personal use only. Curtin University Library Article from ClinicalKey.com.au by Elsevier on February 19, 2021.
For personal use only. No other uses without permission. Copyright ©2021. Elsevier Inc. All rights reserved.



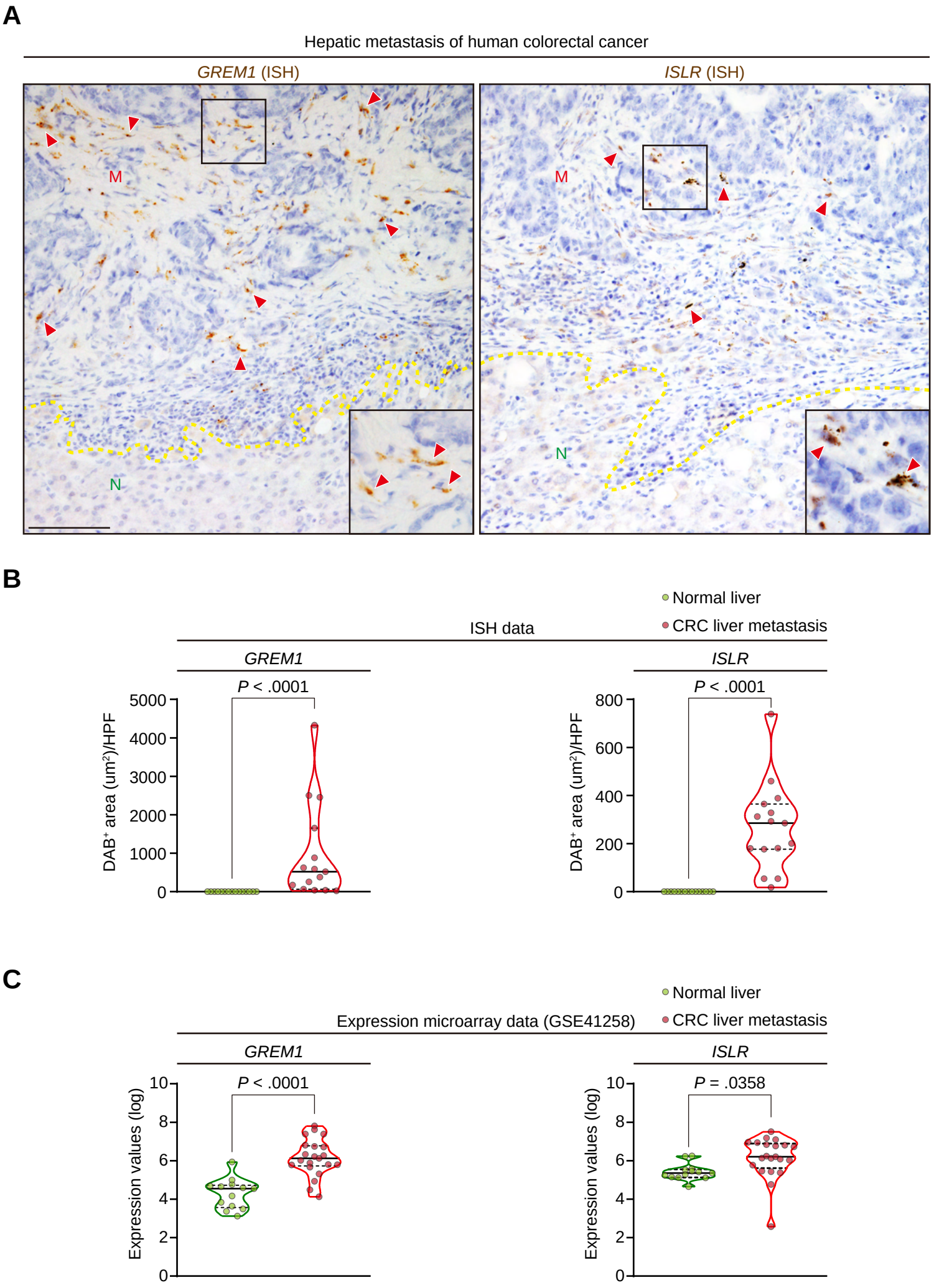
Kobayashi *et al*., Supplementary Figure 6

Downloaded for Anonymous User (n/a) at The University of Adelaide from ClinicalKey.com.au by Elsevier on February 19, 2021.
For personal use only. No other uses without permission. Copyright ©2021. Elsevier Inc. All rights reserved.



Kobayashi *et al.*, Supplementary Figure 7.

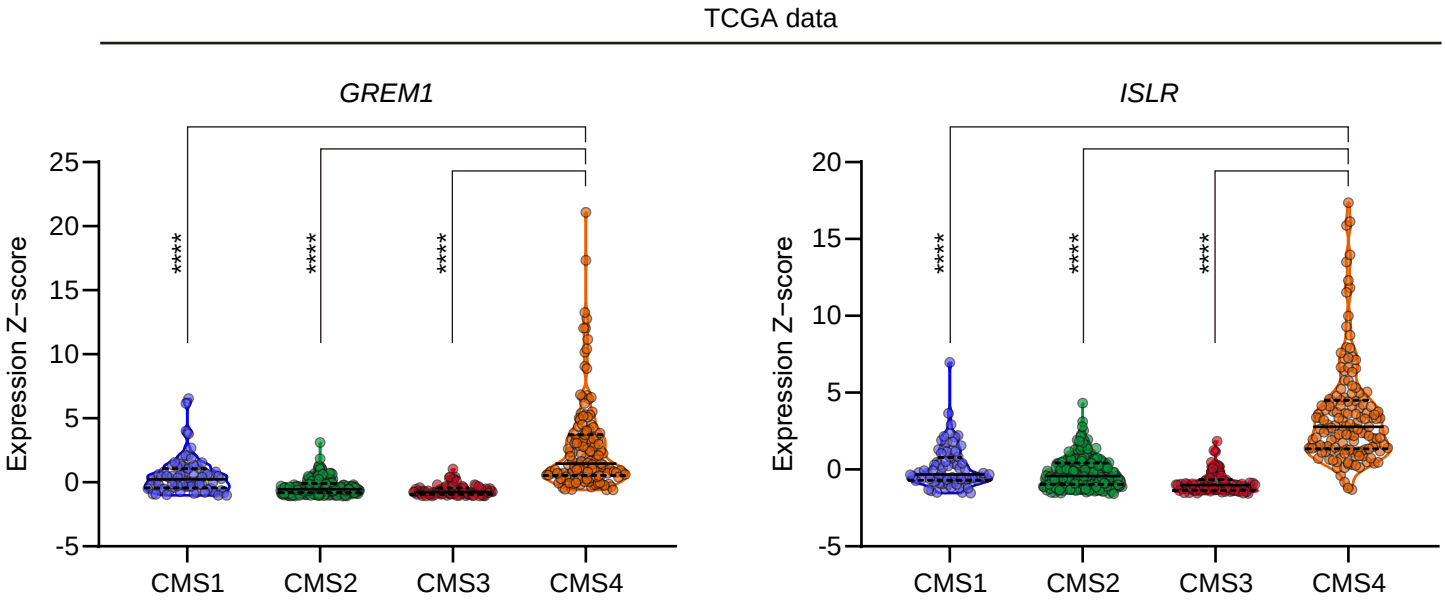
Downloaded for Anonymous User (n/a) at University of Melbourne from ClinicalKey.com.au by Elsevier on February 19, 2021.
For personal use only. No other uses without permission. Copyright ©2021. Elsevier Inc. All rights reserved.



Kobayashi *et al*. Supplementary Figure 8.

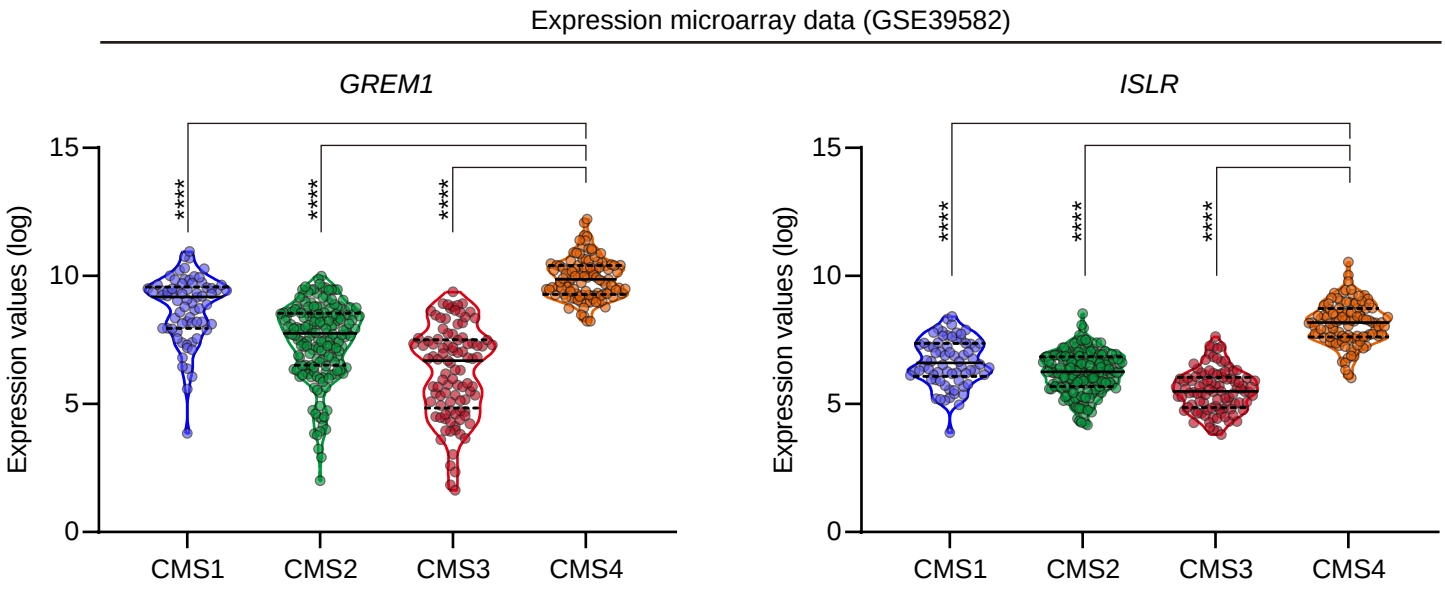
Downloaded for Anonymous User (n/a) at The University of Adelaide from ClinicalKey.com.au by Elsevier on February 19, 2021.
For personal use only. No other uses without permission. Copyright ©2021. Elsevier Inc. All rights reserved.

A



(The Cancer Genome Atlas Network, *Nature*, 2012
; Guinney *et al., Nat Med,* 2015)

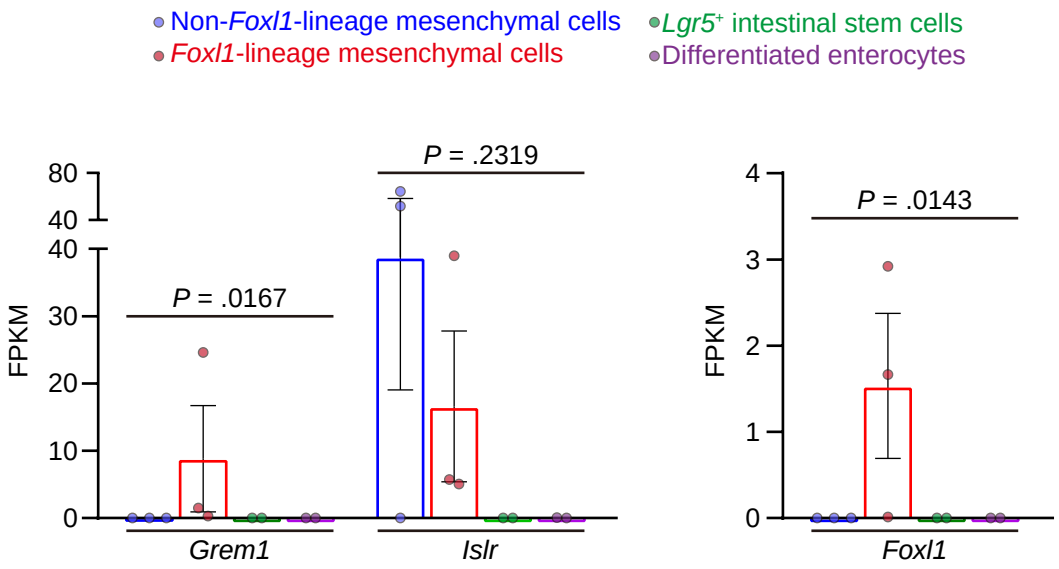
B



(Marisa *et al., PLoS Med,* 2013)

Kobayashi *et al.*, Supplementary Figure 9.

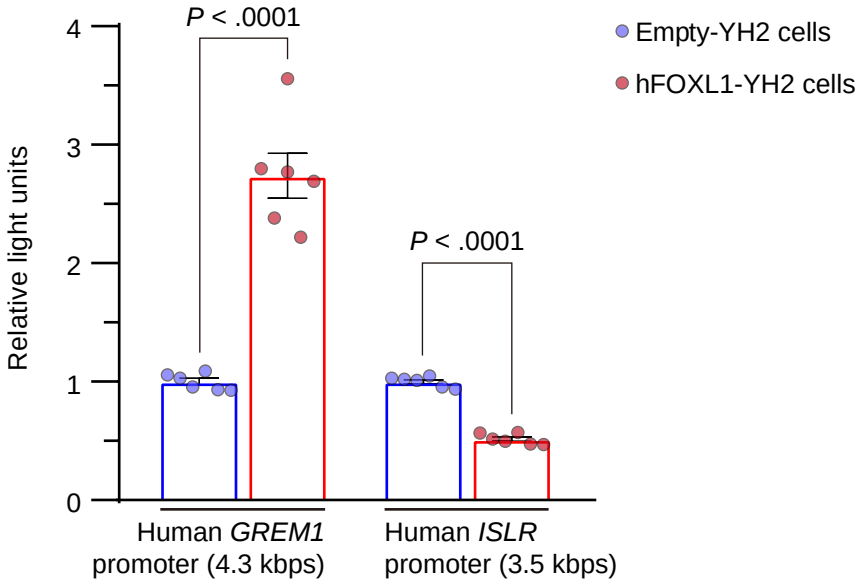
Downloaded for Duke University (duke) at Duke University from ClinicalKey.com.au by Elsevier on February 19, 2021.
For personal use only. No other uses without permission. Copyright ©2021. Elsevier Inc. All rights reserved.



(GSE94072; Shoshkes-Carmel *et al., Nature*, 2018)

Kobayashi *et al*., Supplementary Figure 10.

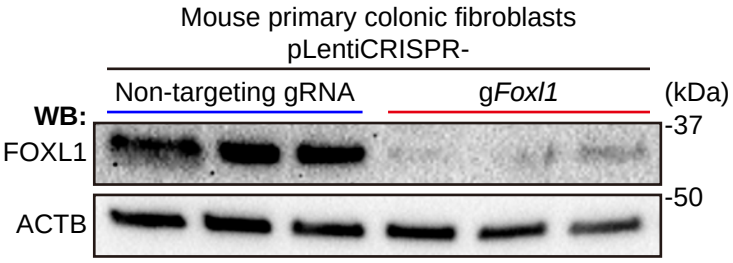
Downloaded for Anonymous User (n/a) at The University of Adelaide from ClinicalKey.com.au by Elsevier on February 19, 2021.
For personal use only. No other uses without permission. Copyright ©2021. Elsevier Inc. All rights reserved.



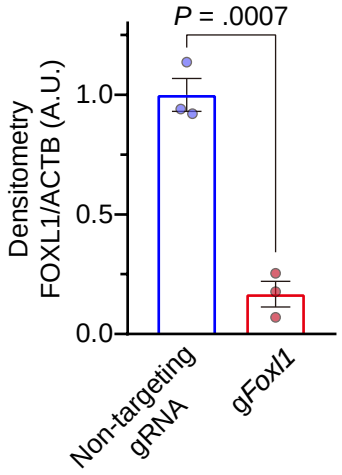
Kobayashi *et al*., Supplementary Figure 11.

Downloaded for Anonymous User (n/a) at The University of Adelaide from ClinicalKey.com.au by Elsevier on February 19, 2021.
For personal use only. No other uses without permission. Copyright ©2021. Elsevier Inc. All rights reserved.

A



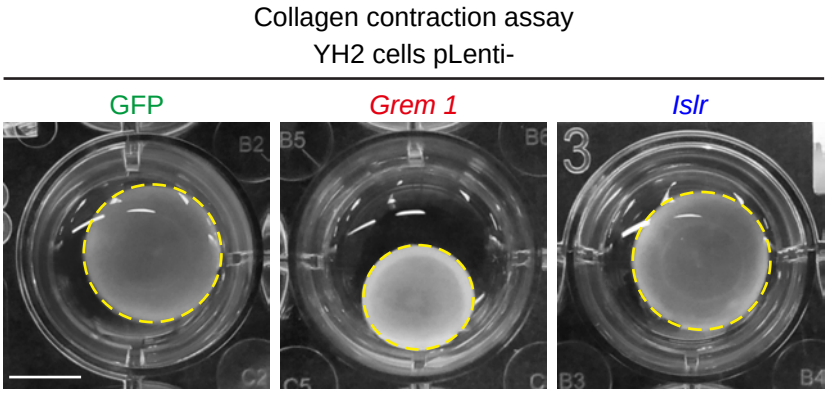
B



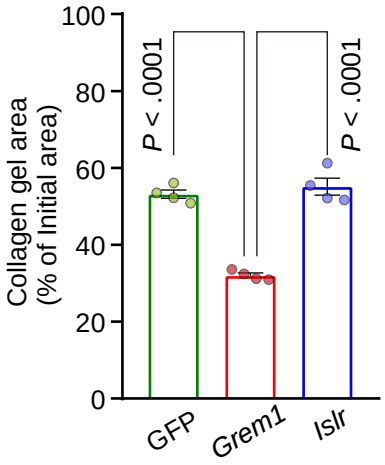
Kobayashi *et al*., Supplementary Figure 12.

Downloaded for Anonymous User (n/a) at The University of Adelaide from ClinicalKey.com.au by Elsevier on February 19, 2021.
For personal use only. No other uses without permission. Copyright ©2021. Elsevier Inc. All rights reserved.

A

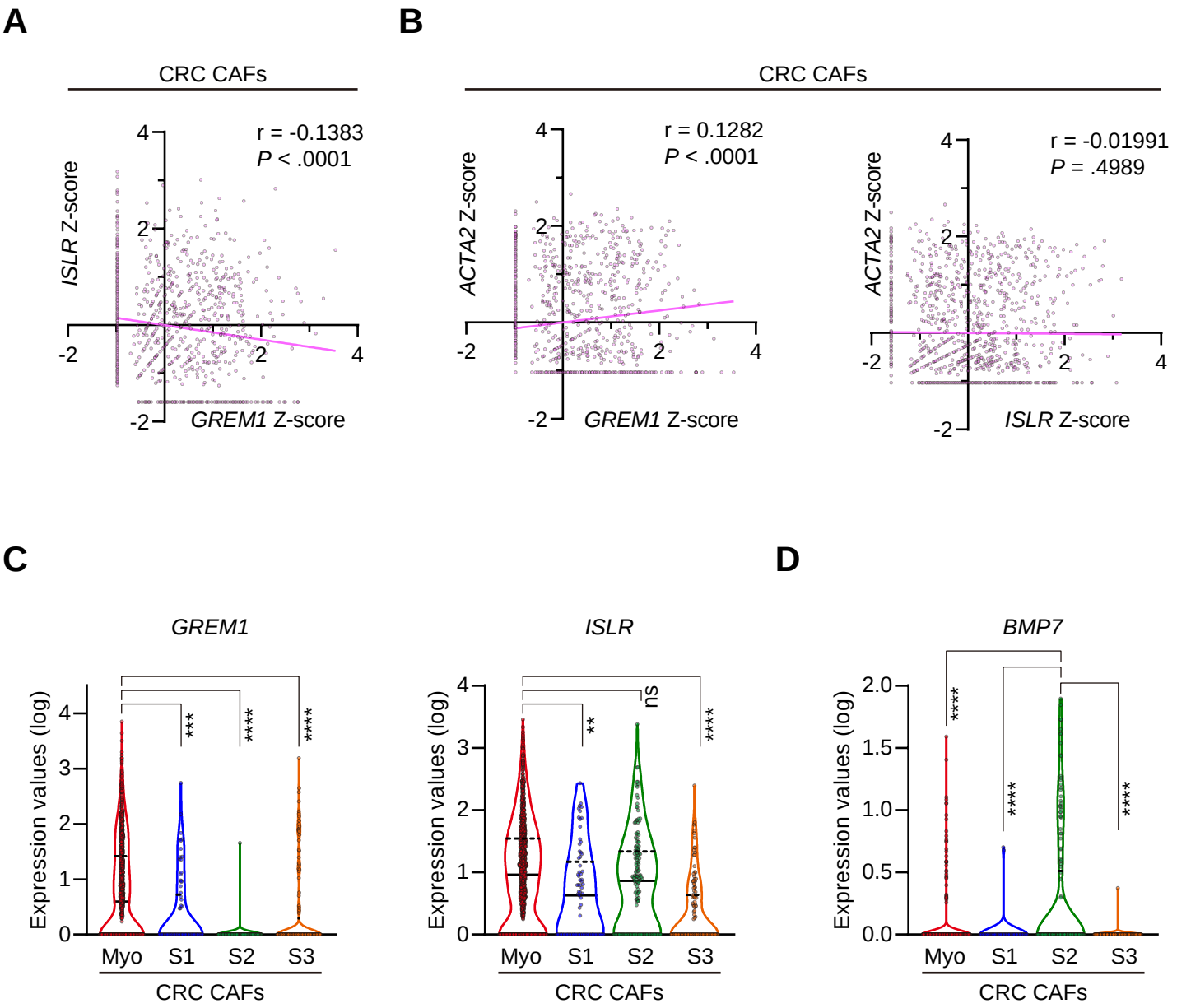


B



Kobayashi *et al*., Supplementary Figure 13.

Downloaded for Anonymous User (n/a) at The University of Adelaide from ClinicalKey.com.au by Elsevier on February 19, 2021.
For personal use only. No other uses without permission. Copyright ©2021. Elsevier Inc. All rights reserved.

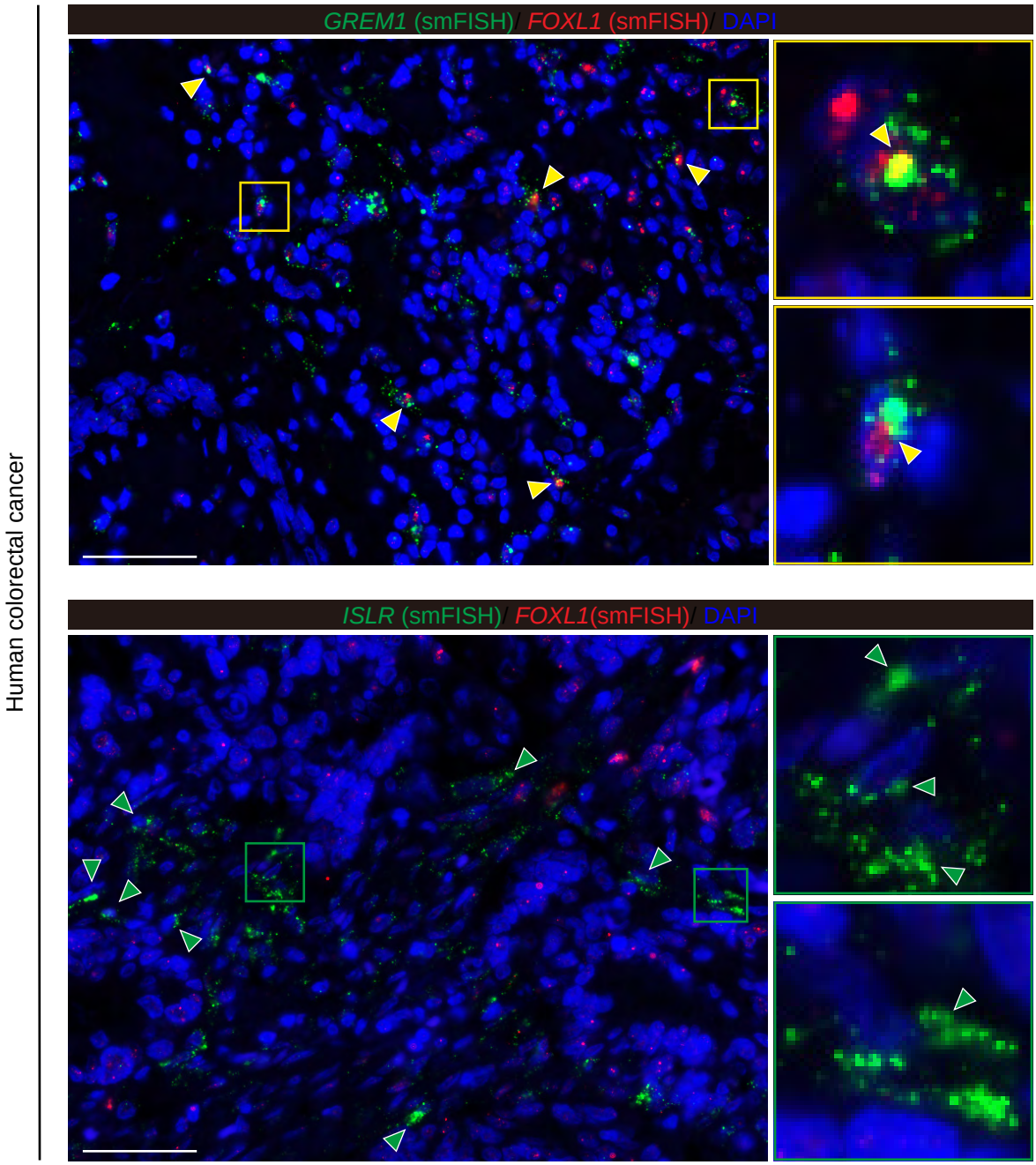


(Lee *et al.*, *Nat Genet*, 2020)

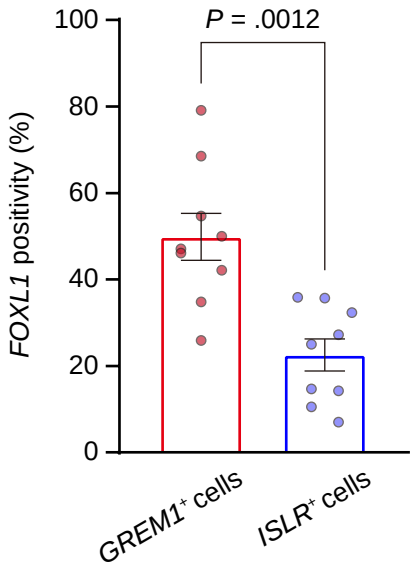
Kobayashi *et al.*, Supplementary Figure 14.

Downloaded for Anonymous User (n/a) at Monash University Caulfield from ClinicalKey.com.au by Elsevier on February 19, 2021.
For personal use only. No other uses without permission. Copyright ©2021. Elsevier Inc. All rights reserved.

A

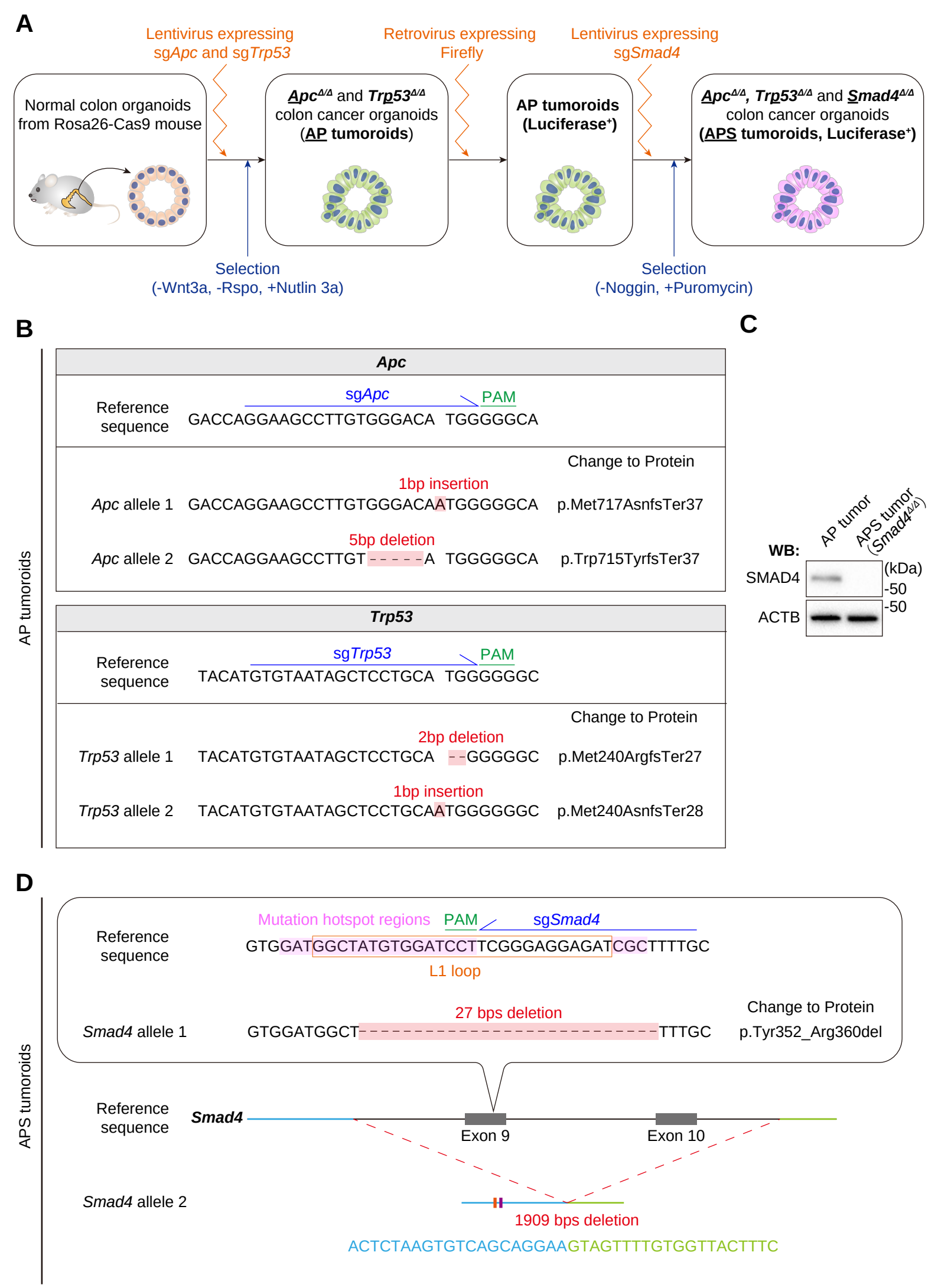


B



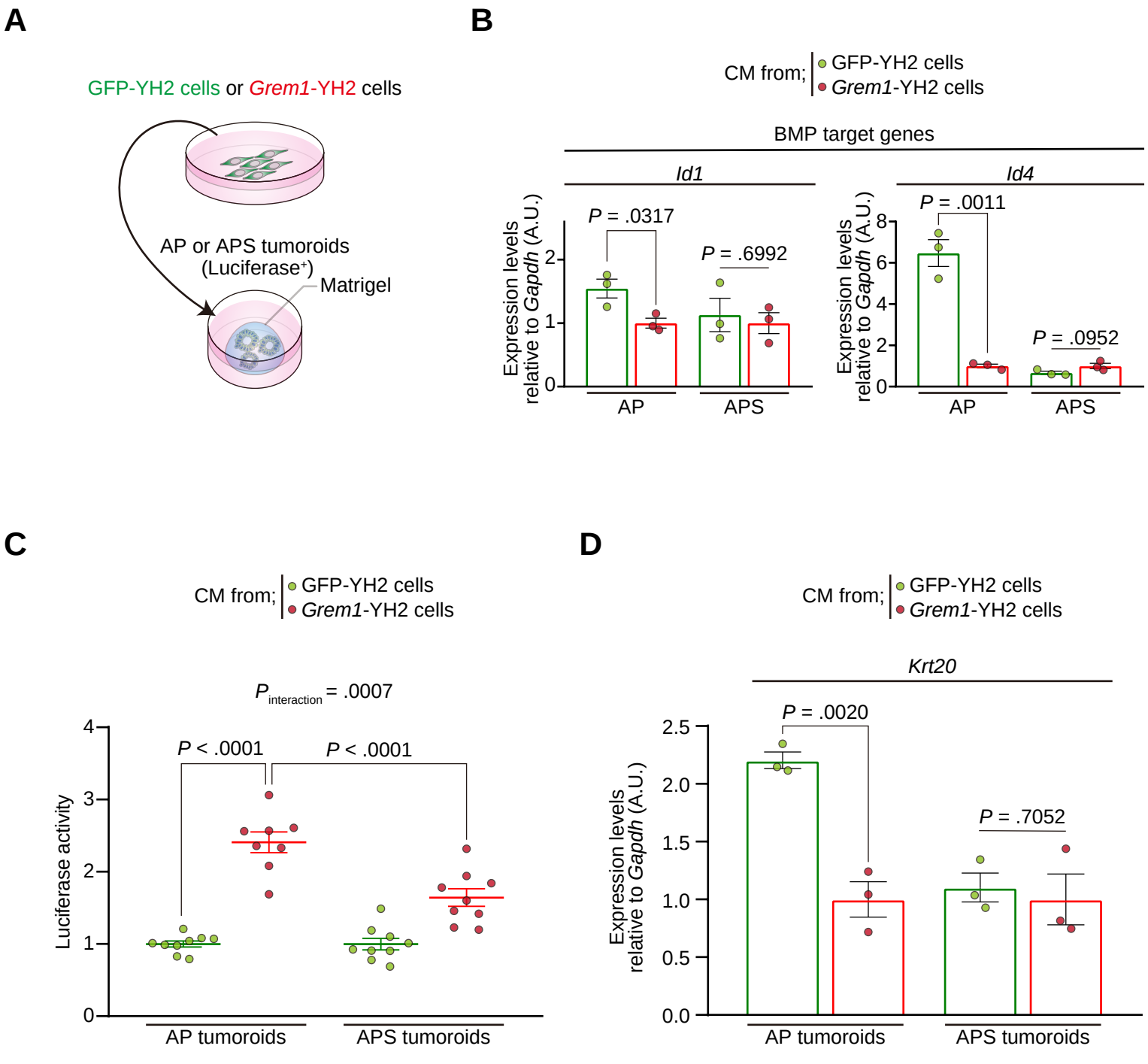
Kobayashi *et al.*, Supplementary Figure 15.

Downloaded for Anonymous User (n/a) at The University of Adelaide from ClinicalKey.com.au by Elsevier on February 19, 2021.
For personal use only. No other uses without permission. Copyright ©2021. Elsevier Inc. All rights reserved.



Kobayashi *et al.*, Supplementary Figure 16.

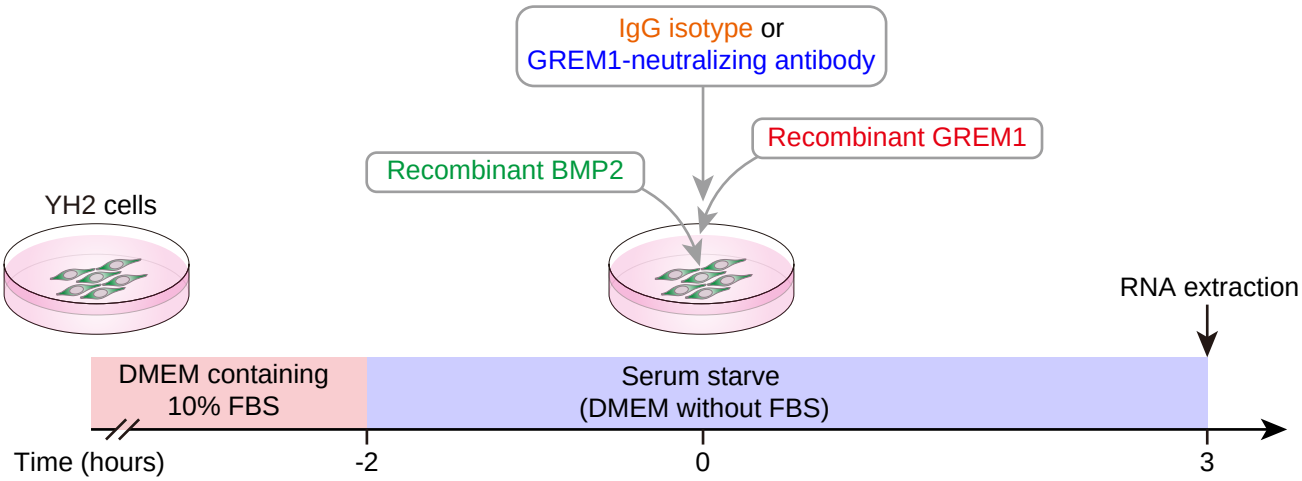
Downloaded for Anonymous User (n/a) at Monash University Library from ClinicalKey.com.au by Elsevier on February 19, 2021.
For personal use only. No other uses without permission. Copyright ©2021. Elsevier Inc. All rights reserved.



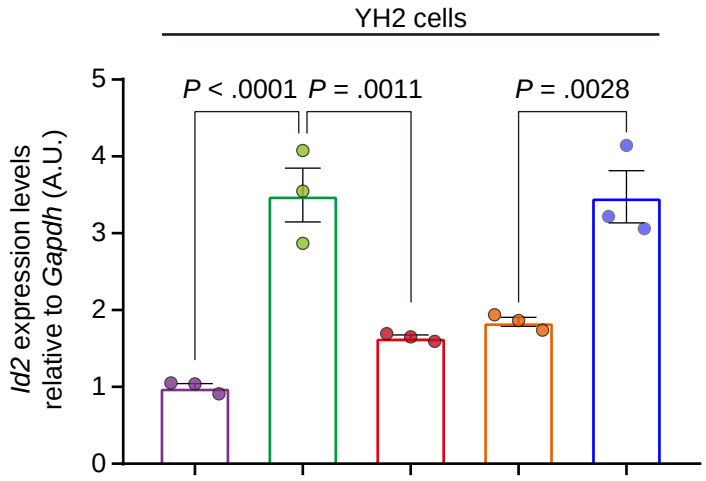
Kobayashi *et al*., Supplementary Figure 17.

Downloaded for Anonymous User (n/a) at The University of Adelaide from ClinicalKey.com.au by Elsevier on February 19, 2021.
For personal use only. No other uses without permission. Copyright ©2021. Elsevier Inc. All rights reserved.

A



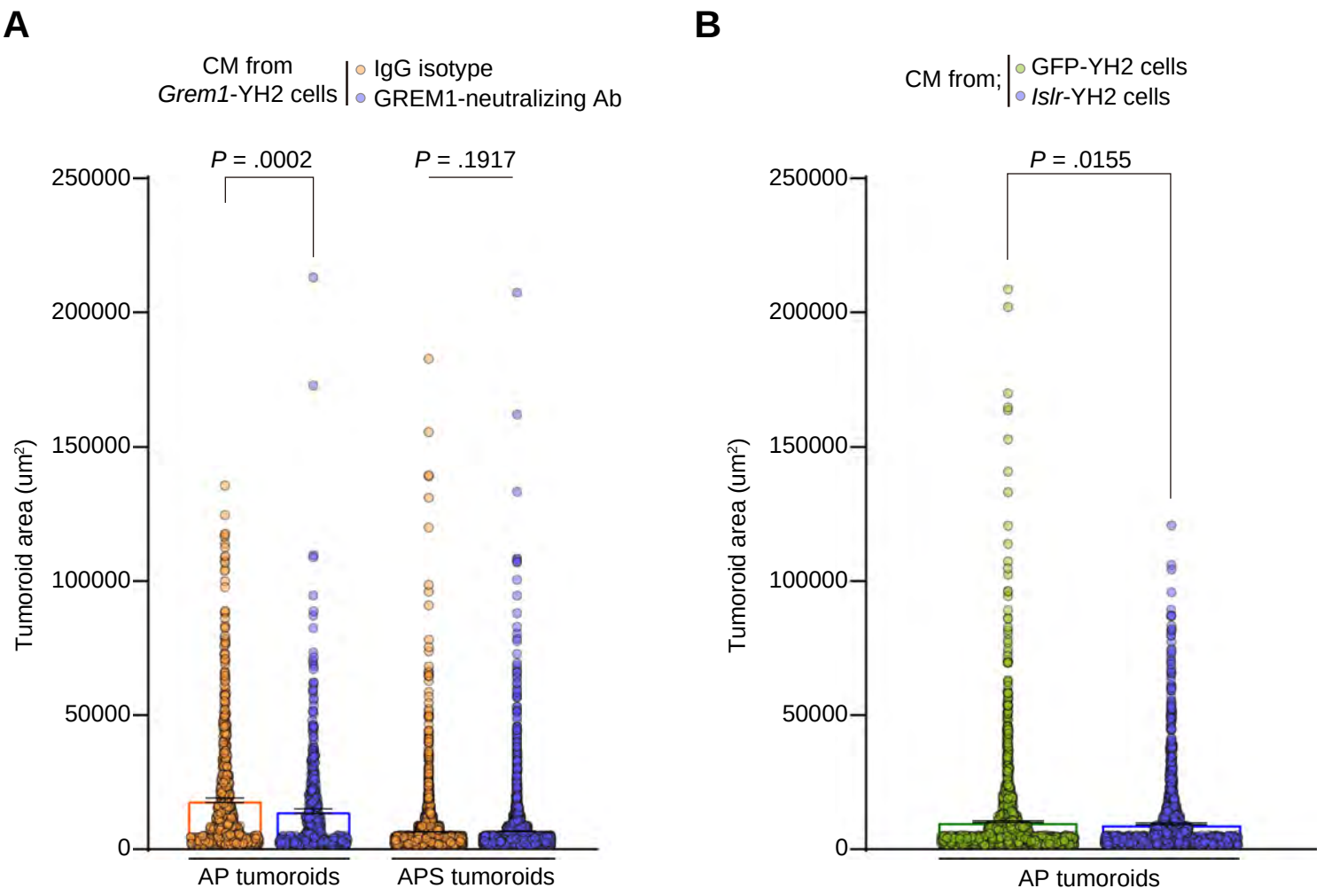
B



Recombinant BMP2 (100 ng/ml)	-	+	+	+	+
Recombinant GREM1 (200 ng/ml)	-	-	+	+	+
Isotype IgG (20 ug/ml)	-	-	-	+	-
GREM1-neutralizing antibody (20 ug/ml)	-	-	-	-	+

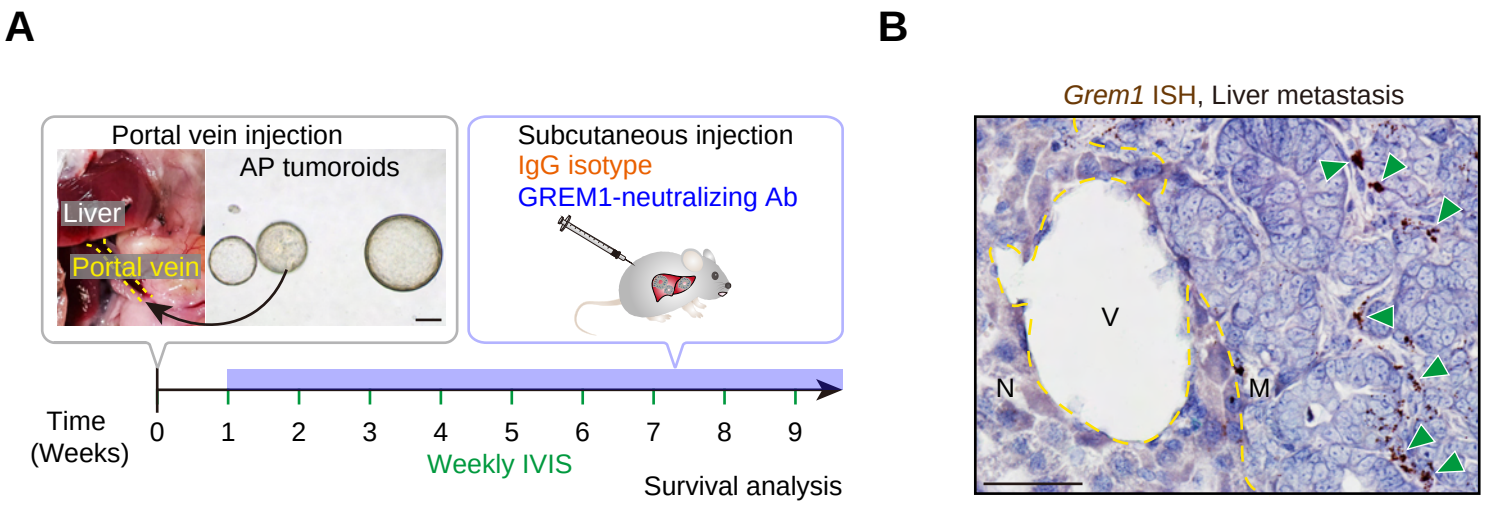
Kobayashi *et al.*, Supplementary Figure 18

Downloaded for Anonymous User (n/a) at The University of Adelaide from ClinicalKey.com.au by Elsevier on February 19, 2021.
For personal use only. No other uses without permission. Copyright ©2021. Elsevier Inc. All rights reserved.



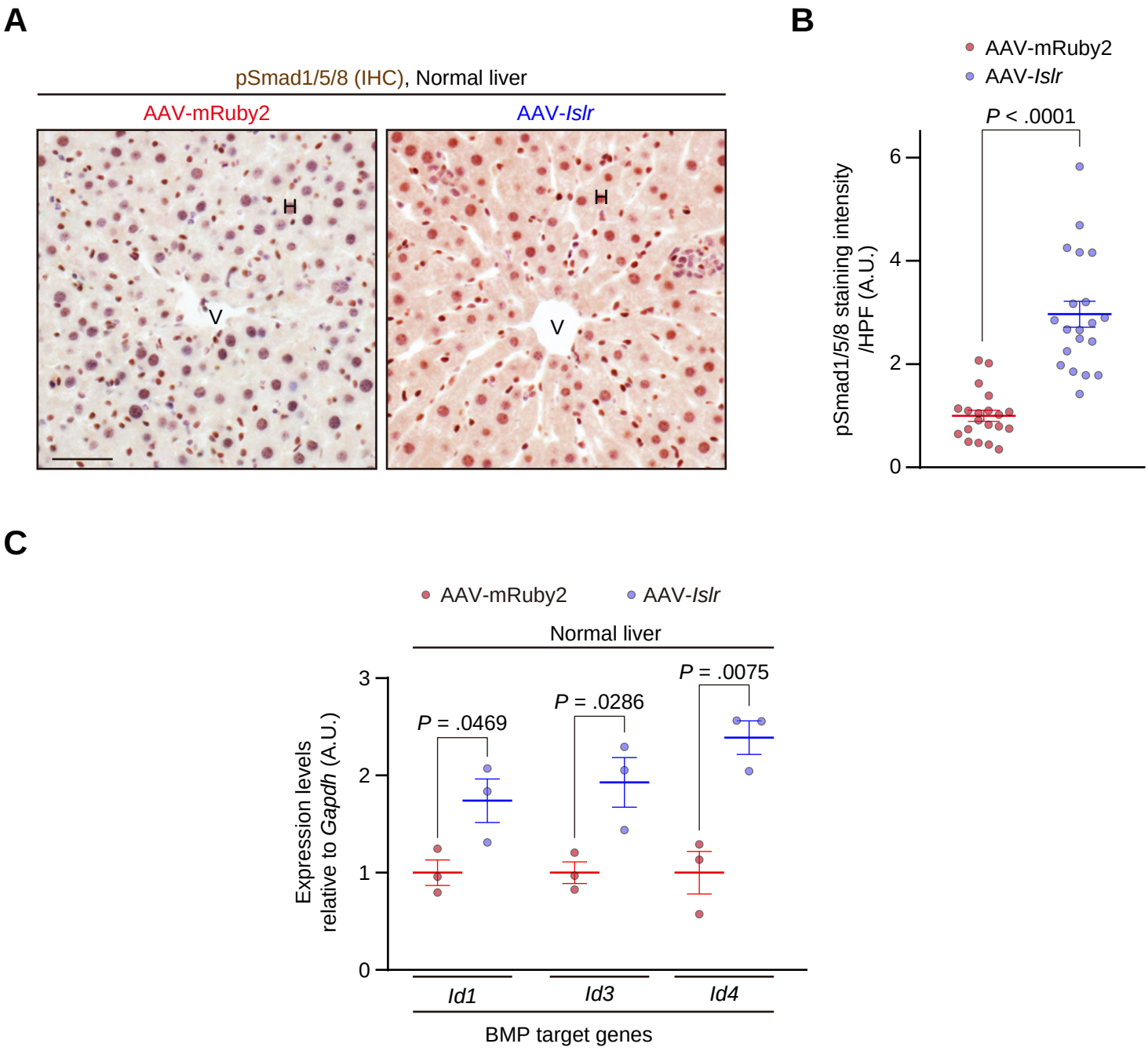
Kobayashi *et al*., Supplementary Figure 19.

Downloaded for Anonymous User (n/a) at The University of Adelaide from ClinicalKey.com.au by Elsevier on February 19, 2021.
For personal use only. No other uses without permission. Copyright ©2021. Elsevier Inc. All rights reserved.



Kobayashi *et al.*, Supplementary Figure 20

Downloaded for Anonymous User (n/a) at The University of Adelaide from ClinicalKey.com.au by Elsevier on February 19, 2021.
For personal use only. No other uses without permission. Copyright ©2021. Elsevier Inc. All rights reserved.

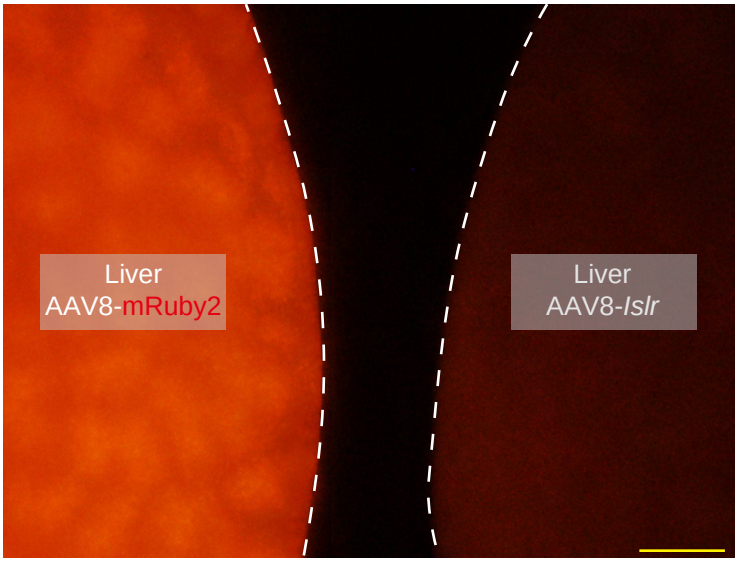


Kobayashi *et al.*, Supplementary Figure 21.

Downloaded for Anonymous User (n/a) at The University of Adelaide from ClinicalKey.com.au by Elsevier on February 19, 2021.
For personal use only. No other uses without permission. Copyright ©2021. Elsevier Inc. All rights reserved.

A

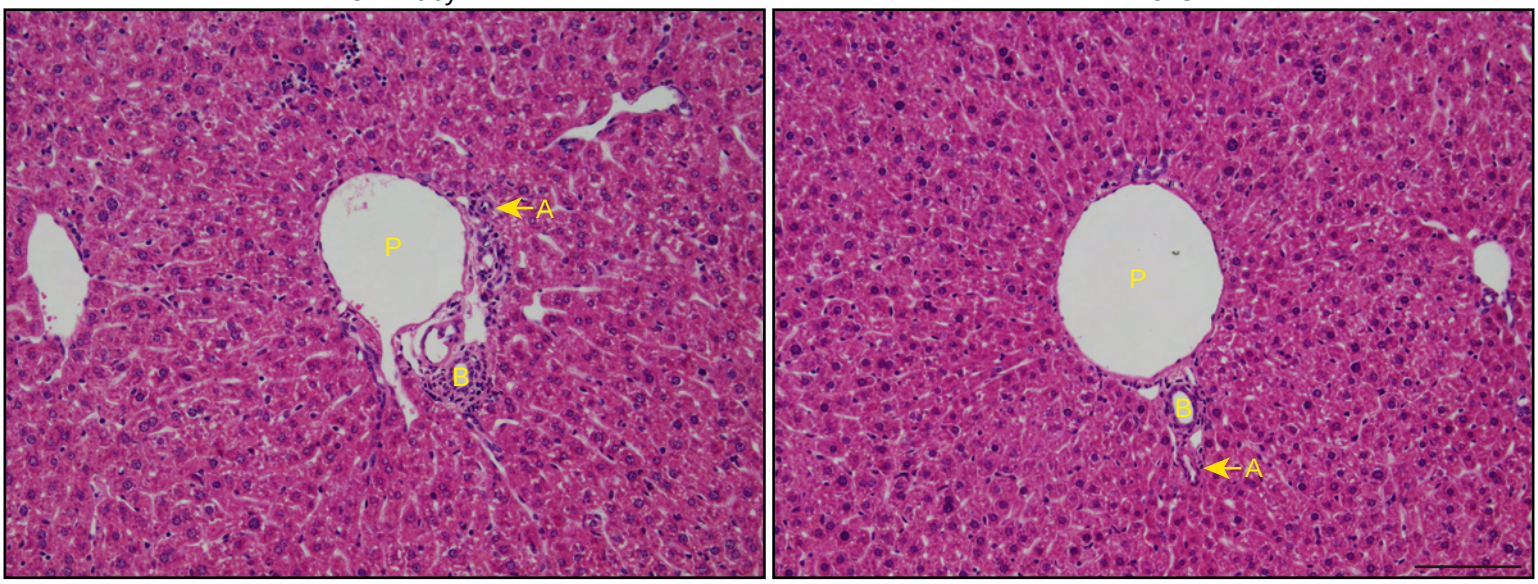
Fluorescence microscopy, Liver
2 weeks after tail vein injection of AAV8



B

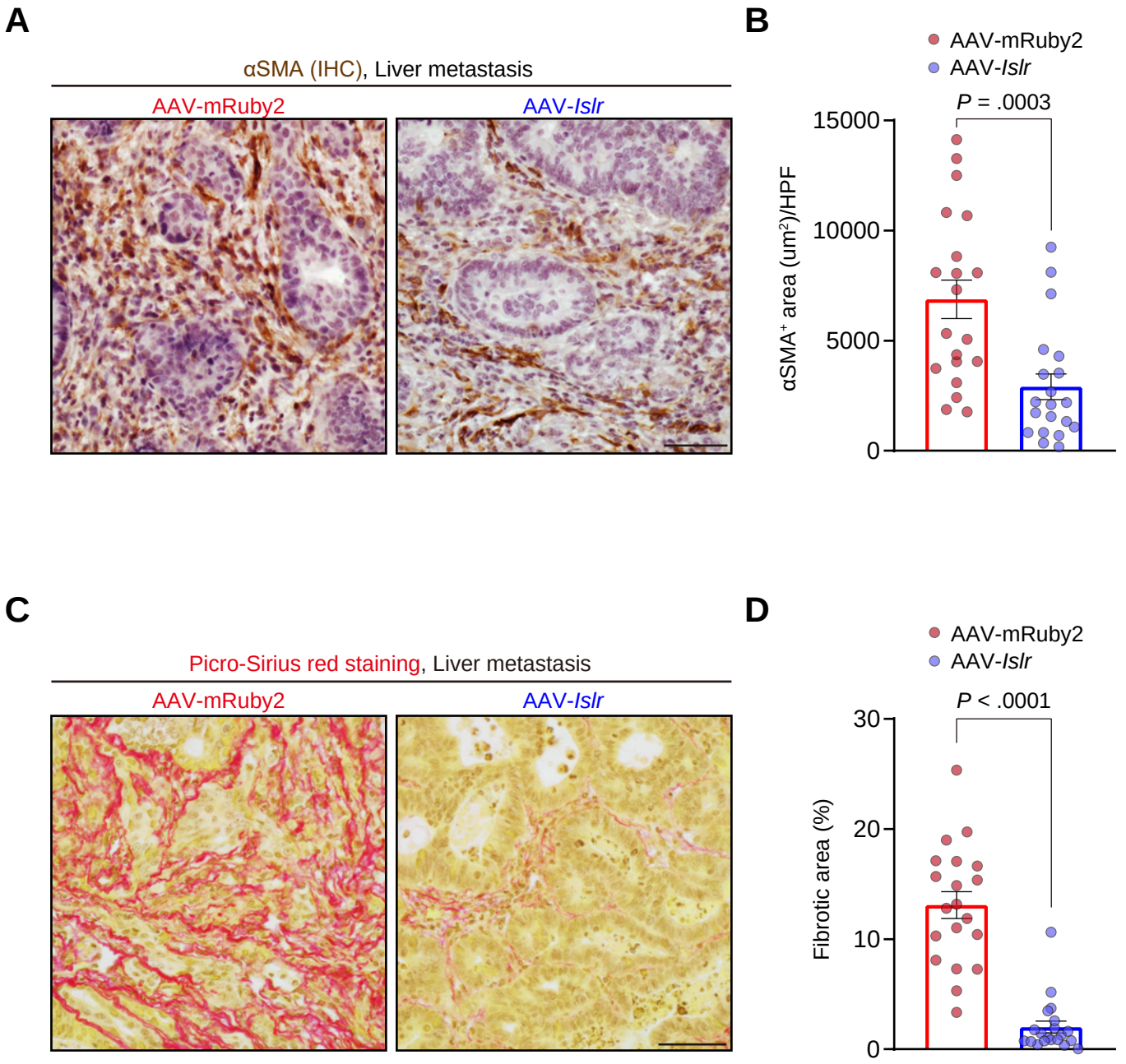
H&E staining, Liver, 2 weeks after tail vein injection

AAV8-mRuby2 | AAV8-*Islr*



Kobayashi *et al*., Supplementary Figure 22.

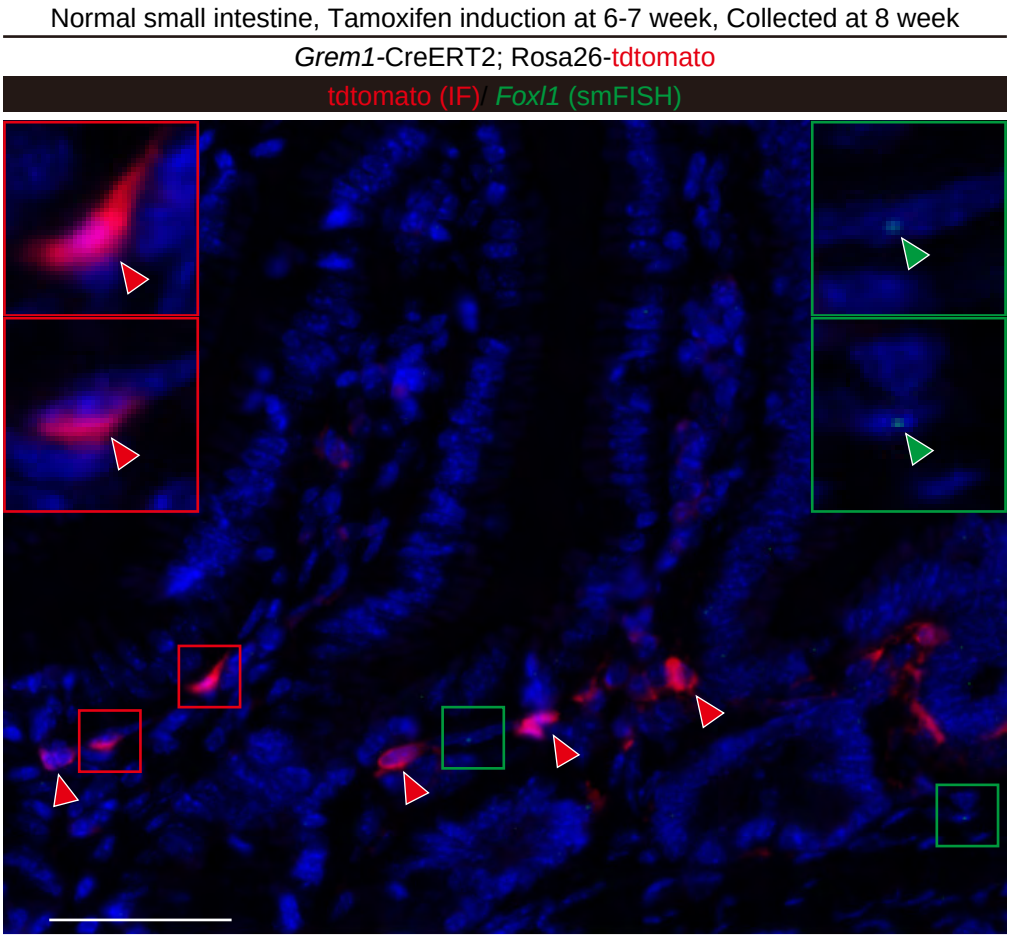
Downloaded for Anonymous User (n/a) at The University of Adelaide from ClinicalKey.com.au by Elsevier on February 19, 2021.
For personal use only. No other uses without permission. Copyright ©2021. Elsevier Inc. All rights reserved.



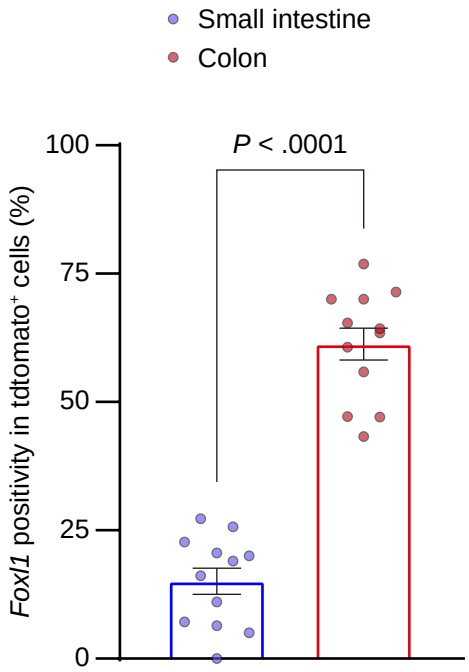
Kobayashi *et al*., Supplementary Figure 23

Downloaded for Anonymous User (n/a) at The University of Adelaide from ClinicalKey.com.au by Elsevier on February 19, 2021.
For personal use only. No other uses without permission. Copyright ©2021. Elsevier Inc. All rights reserved.

A



B



Kobayashi *et al*., Supplementary Figure 24.

Downloaded for Anonymous User (n/a) at The University of Adelaide from ClinicalKey.com.au by Elsevier on February 19, 2021.
For personal use only. No other uses without permission. Copyright ©2021. Elsevier Inc. All rights reserved.

Supplementary Table 1

List of 34 genes upregulated specifically in CRC CAFs

ADAMTS2	*COL1A1*	*CTSK*	*NOTCH3*
AEBP1	*COL1A2*	*CXCL14*	*PALLD*
ANTXR1	*COL3A1*	*CYGB*	*POSTN*
C11orf96	*COL5A1*	*DCN*	*SDC2*
C1R	*COL5A2*	*GREM1*	*TAGLN*
C1S	*COL6A1*	*ISLR*	*THBS2*
C3	*COL6A3*	*LUM*	*VCAN*
CDR1	*COL8A1*	*MEG3*	
COL12A1	*CRISPLD2*	*MXRA5*	

(GSE39396)

This list of 34 genes (corresponding to 63 transcripts in the microarray data) represents an intersection of the Venn diagram in **Figure 1A**.

GREM1 and *ISLR* are highlighted in red.

Downloaded for Anonymous User (n/a) at The University of Adelaide from ClinicalKey.com.au by Elsevier on February 19, 2021.
For personal use only. No other uses without permission. Copyright ©2021. Elsevier Inc. All rights reserved.

Supplementary Table 2

Clinicopathological characteristics of rectal cancer patients analyzed by *GREM1* and *ISLR* ISH.

	All	*GREM1* low	*GREM1* high	P values	*ISLR* low	*ISLR* high	P values
Number of patients	53	30	23		24	29	
Median age at diagnosis (range), years	64 (28-89)	65 (38-88)	64 (28-89)		66 (36-89)	63 (28-82)	
Median disease-free survival months (range)	40 (1-104)	53 (6-104)	29 (1-77)		22 (1-86)	52 (6-104)	
Age, n (%)				0.775			0.780
< 60	19 (35.8%)	10 (33.3%)	9 (39.1%)		8 (33.3%)	11 (37.9%)	
≥ 60	34 (64.2%)	20 (66.7%)	14 (60.9%)		16 (66.7%)	18 (62.1%)	
Sex, n (%)				1.000			0.762
Male	38 (71.7%)	21 (70.0%)	17 (73.9%)		18 (75.0%)	20 (69.0%)	
Female	15 (28.3%)	9 (30.0%)	6 (26.1%)		6 (25.0%)	9 (31.0%)	
pT status, n (%)				0.512			0.284
pCR	1 (1.9%)	1 (3.3%)	0 (0.0%)		1 (4.2%)	0 (0.0%)	
Tis	1 (1.9%)	1 (3.3%)	0 (0.0%)		0 (0.0%)	1 (3.4%)	
T1	3 (5.7%)	2 (6.7%)	1 (4.3%)		1 (4.2%)	2 (6.9%)	
T2	13 (24.5%)	8 (26.7%)	5 (21.7%)		4 (16.7%)	9 (31.0%)	
T3	27 (50.9%)	12 (40.0%)	15 (65.2%)		12 (50.0%)	15 (51.7%)	
T4	8 (15.1 %)	6 (20.0%)	2 (8.7%)		6 (25.0%)	2 (6.9%)	
pN status, n (%)				**0.031**			**0.010**
N0	38 (71.7%)	21 (70.0%)	17 (73.9%)		13 (54.2%)	25 (86.2%)	
N1	9 (17.0%)	7 (23.3%)	2 (8.7%)		8 (33.3%)	1 (3.4%)	
N2	4 (7.5%)	0 (0.0%)	4 (17.4%)		2 (8.3%)	2 (6.9%)	
N3	2 (3.8%)	2 (6.7%)	0 (0.0%)		1 (4.2%)	1 (3.4%)	
pM status, n (%)				1.000			0.453
M0	52 (98.1%)	29 (96.7%)	23 (100.0%)		23 (95.8%)	29 (100.0%)	
M1	1 (1.9%)	1 (3.3%)	0 (0.0%)		1 (4.2%)	0 (0.0%)	
pTNM stage, n (%)				0.978			**0.004**
pCR	1 (1.9%)	1 (3.3%)	0 (0.0%)		1 (4.2%)	0 (0.0%)	
Stage 0 (Tis)	1 (1.9%)	1 (3.3%)	0 (0.0%)		0 (0.0%)	1 (3.4%)	
Stage I	12 (22.6%)	7 (23.3%)	5 (21.7%)		1 (4.2%)	11 (37.9%)	
Stage II	24 (45.3%)	12 (40.0%)	12 (52.2%)		11 (45.8%)	13 (44.8%)	
Stage III	14 (26.4%)	8 (26.7%)	6 (26.1%)		10 (41.7%)	4 (13.8%)	
Stage IV	1 (1.9%)	1 (3.3%)	0 (0.0%)		1 (4.2%)	0 (0.0%)	
Differentiation, n (%)				1.000			**0.035**
Well	6 (11.3%)	4 (13.3%)	2 (8.7%)		0 (0.0%)	6 (20.7%)	
Moderate	41 (77.4%)	23 (76.7%)	18 (78.3%)		20 (83.3%)	21 (72.4%)	
Poor	4 (7.5%)	2 (6.7%)	2 (8.7%)		2 (8.3%)	2 (6.9%)	
Mucinous	2 (3.8%)	1 (3.3%)	1 (4.3%)		2 (8.3%)	0 (0.0%)	
Neoadjuvant treatment, n (%)				0.266			**0.029**
No	24 (45.3%)	16 (53.3%)	8 (34.8%)		15 (62.5%)	9 (31.0%)	
Chemotherapy	29 (54.7%)	14 (46.7%)	15 (65.2%)		9 (37.5%)	20 (69.0%)	
ISLR expression, n (%)				0.579			
Low	24 (45.3%)	15 (50%)	9 (39.1%)				
High	29 (54.7%)	15 (50%)	14 (60.9%)				

P value less than 0.05 is shown in bold characters (Fisher's exact test).

Downloaded for Anonymous User (n/a) at The University of Adelaide from ClinicalKey.com.au by Elsevier on February 19, 2021.
For personal use only. No other uses without permission. Copyright ©2021. Elsevier Inc. All rights reserved.

Supplementary Table 3

Univariate and multivariate Cox regression analysis of *GREM1* and *ISLR* expression levels and disease-free survival of rectal cancer patients

	Disease-free survival			
	Univariate analysis		Multivariate analysis	
Variable	**HR (95% CI)**	**P Value**	**HR (95% CI)**	**P Value**
GREM1		**0.0025**		**0.0001**
Low	1.000		1.000	
High	4.882 (1.748-13.631)		8.74 (2.864-26.675)	
ISLR		**0.0032**		**0.0013**
Low	1.000		1.000	
High	0.213 (0.076-0.596)		0.124 (0.034-0.444)	
Age		0.9768		
< 60	1.000			
≥ 60	0.986 (0.388-2.507)			
Sex		0.6791		
Female	1.000			
Male	0.815 (0.310-2.146)			
pTNM Stage		**0.0401**		0.8158
pCR and Stage 0, I, II	1.000		1.000	
Stage III,IV	2.609 (1.044-6.520)		0.869 (0.267-2.833)	
Differentiation		**0.0210**		0.1391
Well and Moderate	1.000		1.000	
Poor and Mucinous	3.770 (1.221-11.637)		2.742 (0.72-10.435)	
Neoadjuvant treatment		0.7506		
No	1.000			
Chemotherapy	0.863 (0.348-2.138)			

P values less than 0.05 are shown in bold characters.

Downloaded for Anonymous User (n/a) at The University of Adelaide from ClinicalKey.com.au by Elsevier on February 19, 2021.
For personal use only. No other uses without permission. Copyright ©2021. Elsevier Inc. All rights reserved.

Supplementary Table 4

Univariate and multivariate Cox regression analysis of
GREM1 and *ISLR* expression levels and overall survival of colon cancer patients.

	Overall survival			
	Univariate analysis		Multivariate analysis	
Variable	**HR (95% CI)**	**P Value**	**HR (95% CI)**	**P Value**
GREM1		**0.0190**		**0.0132**
Low (n = 506)	1.000		1.000	
High (n = 49)	1.704 (1.092-2.660)		1.768 (1.127-2.775)	
ISLR		**0.0222**		**0.0132**
Low (n = 56)	1.000		1.000	
High (n = 499)	0.606 (0.394-0.931)		0.577 (0.373-0.891)	
Age		0.0758		0.1226
< 60 (n = 150)	1.000		1.000	
≥ 60 (n = 405)	1.369 (0.968-1.937)		1.315 (0.929-1.862)	
Sex		0.0589		0.0648
Female (n = 249)	1.000		1.000	
Male (n = 306)	1.327 (0.989-1.779)		1.319 (0.983-1.768)	

(GSE39582)

P values less than 0.05 are shown in bold characters.
Note that one patient whose age at diagnosis was unknown (Sample ID: GSM972293)
was excluded from the univariate and multivariate Cox regression analysis.

Downloaded for Anonymous User (n/a) at The University of Adelaide from ClinicalKey.com.au by Elsevier on February 19, 2021.
For personal use only. No other uses without permission. Copyright ©2021. Elsevier Inc. All rights reserved.

Supplementary Table 5

No overlap between *GREM1*^{high} patients and *ISLR*^{low} patients in the colon cancer patient dataset (GSE39582).

	ISLR low	*ISLR* high	Total
GREM1 low	56 (11.1%)	450 (88.9%)	506 (100.0%)
GREM1 high	0 (0.0%)	50 (100.0%)	50 (100.0%)
Total	56	500	556

P = 0.005863 (Fisher's exact test)

Number of cases and the percentage within *GREM1*-low (upper row) or *GREM1*-high cases (lower row) are shown.

Downloaded for Anonymous User (n/a) at The University of Adelaide from ClinicalKey.com.au by Elsevier on February 19, 2021.
For personal use only. No other uses without permission. Copyright ©2021. Elsevier Inc. All rights reserved.

Bibliography

1. Australian Institute of Health and Welfare. Cancer data in Australia. 2020 [cited 2020 2 November 2020]. Available from: https://www.aihw.gov.au/reports/cancer/cancer-data-in-australia
2. Fearon ER, Vogelstein B. A genetic model for colorectal tumorigenesis. Cell. 1990;61(5):759-67.
3. Bettington M, Walker N, Clouston A, Brown I, Leggett B, Whitehall V. The serrated pathway to colorectal carcinoma: current concepts and challenges. Histopathology. 2013 Feb;62(3):367-86. DOI: 10.1111/his.12055.
4. Weisenberger DJ, Siegmund KD, Campan M, Young J, Long TI, Faasse MA, et al. CpG island methylator phenotype underlies sporadic microsatellite instability and is tightly associated with BRAF mutation in colorectal cancer. Nat Genet. 2006 Jul;38(7):787-93. DOI: 10.1038/ng1834.
5. Jess T, Rungoe C, Peyrin-Biroulet L. Risk of colorectal cancer in patients with ulcerative colitis: a meta-analysis of population-based cohort studies. Clin Gastroenterol Hepatol. 2012 Jun;10(6):639-45. DOI: 10.1016/j.cgh.2012.01.010.
6. Zhen Y, Luo C, Zhang H. Early detection of ulcerative colitis-associated colorectal cancer. Gastroenterol Rep (Oxf). 2018 May;6(2):83-92. DOI: 10.1093/gastro/goy010.
7. de Gramont A, Figer A, Seymour M, Homerin M, Hmissi A, Cassidy J, et al. Leucovorin and fluorouracil with or without oxaliplatin as first-line treatment in advanced colorectal cancer. J Clin Oncol. 2000;18(16):2938-47. DOI: 10.1200/JCO.2000.18.16.2938.
8. Barker N. Adult intestinal stem cells: critical drivers of epithelial homeostasis and regeneration. Nat Rev Mol Cell Biol. 2014;15(1):19-33.
9. Sato T, Vries RG, Snippert HJ, van de Wetering M, Barker N, Stange DE, et al. Single Lgr5 stem cells build crypt-villus structures in vitro without a mesenchymal niche. Nature. 2009 May 14;459(7244):262-5. DOI: 10.1038/nature07935.
10. Date S, Sato T. Mini-gut organoids: reconstitution of the stem cell niche. Annu Rev Cell Dev Biol. 2015;31:269-89. DOI: 10.1146/annurev-cellbio-100814-125218.
11. Middendorp S, Schneeberger K, Wiegerinck CL, Mokry M, Akkerman RD, van Wijngaarden S, et al. Adult stem cells in the small intestine are intrinsically programmed with their location-specific function. Stem cells. 2014 May;32(5):1083-91. DOI: 10.1002/stem.1655.
12. van de Wetering M, Francies HE, Francis JM, Bounova G, Iorio F, Pronk A, et al. Prospective derivation of a living organoid biobank of colorectal cancer patients. Cell. 2015 May 7;161(4):933-45. DOI: 10.1016/j.cell.2015.03.053.

13. Ran FA, Hsu PD, Wright J, Agarwala V, Scott DA, Zhang F. Genome engineering using the CRISPR-Cas9 system. Nat Protoc. 2013 Nov;8(11):2281-308. DOI: 10.1038/nprot.2013.143.
14. de Sousa e Melo F, Kurtova AV, Harnoss JM, Kljavin N, Hoeck JD, Hung J, et al. A distinct role for Lgr5(+) stem cells in primary and metastatic colon cancer. Nature. 2017 Mar 29;543(7647):676-80. DOI: 10.1038/nature21713.
15. Drost J, van Jaarsveld RH, Ponsioen B, Zimberlin C, van Boxtel R, Buijs A, et al. Sequential cancer mutations in cultured human intestinal stem cells. Nature. 2015 May 7;521(7550):43-7. DOI: 10.1038/nature14415.
16. Fumagalli A, Drost J, Suijkerbuijk SJ, van Boxtel R, de Ligt J, Offerhaus GJ, et al. Genetic dissection of colorectal cancer progression by orthotopic transplantation of engineered cancer organoids. Proc Natl Acad Sci U S A. 2017 Mar 21;114(12):E2357-E64. DOI: 10.1073/pnas.1701219114.
17. Lannagan TRM, Lee YK, Wang T, Roper J, Bettington ML, Fennell L, et al. Genetic editing of colonic organoids provides a molecularly distinct and orthotopic preclinical model of serrated carcinogenesis. Gut. 2019 Apr;68(4):684-92. DOI: 10.1136/gutjnl-2017-315920.
18. Matano M, Date S, Shimokawa M, Takano A, Fujii M, Ohta Y, et al. Modeling colorectal cancer using CRISPR-Cas9-mediated engineering of human intestinal organoids. Nat Med. 2015 Mar;21(3):256-62. DOI: 10.1038/nm.3802.
19. O'Rourke KP, Loizou E, Livshits G, Schatoff EM, Baslan T, Manchado E, et al. Transplantation of engineered organoids enables rapid generation of metastatic mouse models of colorectal cancer. Nat Biotechnol. 2017 Jun;35(6):577-82. DOI: 10.1038/nbt.3837.
20. Roper J, Tammela T, Cetinbas NM, Akkad A, Roghanian A, Rickelt S, et al. In vivo genome editing and organoid transplantation models of colorectal cancer and metastasis. Nat Biotechnol. 2017 Jun;35(6):569-76. DOI: 10.1038/nbt.3836.
21. Koliaraki V, Pallangyo CK, Greten FR, Kollias G. Mesenchymal Cells in Colon Cancer. Gastroenterology. 2017 Apr;152(5):964-79. DOI: 10.1053/j.gastro.2016.11.049.
22. Powell DW, Pinchuk IV, Saada JI, Chen X, Mifflin RC. Mesenchymal cells of the intestinal lamina propria. Annu Rev Physiol. 2011;73:213-37. DOI: 10.1146/annurev.physiol.70.113006.100646.
23. Worthley DL, Churchill M, Compton JT, Tailor Y, Rao M, Si Y, et al. Gremlin 1 identifies a skeletal stem cell with bone, cartilage, and reticular stromal potential. Cell. 2015 Jan 15;160(1-2):269-84. DOI: 10.1016/j.cell.2014.11.042.
24. Kalluri R. The biology and function of fibroblasts in cancer. Nat Rev Cancer. 2016 Aug 23;16(9):582-98. DOI: 10.1038/nrc.2016.73.
25. Coussens LM, Werb Z. Inflammation and cancer. Nature. 2001;420:860-7.

26. Dvorak HF. Tumors: wounds that do not heal. Similarities between tumor stroma generation and wound healing. New England Journal of Medicine. 1986;315(26):1650-9.
27. Calon A, Lonardo E, Berenguer-Llergo A, Espinet E, Hernando-Momblona X, Iglesias M, et al. Stromal gene expression defines poor-prognosis subtypes in colorectal cancer. Nat Genet. 2015;47(4):320-9.
28. Isella C, Terrasi A, Bellomo SE, Petti C, Galatola G, Muratore A, et al. Stromal contribution to the colorectal cancer transcriptome. Nat Genet. 2015 Apr;47(4):312-9. DOI: 10.1038/ng.3224.
29. Guinney J, Dienstmann R, Wang X, de Reynies A, Schlicker A, Soneson C, et al. The consensus molecular subtypes of colorectal cancer. Nat Med. 2015 Nov;21(11):1350-6. DOI: 10.1038/nm.3967.
30. Gieniec KA, Butler LM, Worthley DL, Woods SL. Cancer-associated fibroblasts-heroes or villains? Br J Cancer. 2019 Aug;121(4):293-302. DOI: 10.1038/s41416-019-0509-3.
31. Kobayashi H, Enomoto A, Woods SL, Burt AD, Takahashi M, Worthley DL. Cancer-associated fibroblasts in gastrointestinal cancer. Nat Rev Gastroenterol Hepatol. 2019 May;16(5):282-95. DOI: 10.1038/s41575-019-0115-0.
32. Sahai E, Astsaturov I, Cukierman E, DeNardo DG, Egeblad M, Evans RM, et al. A framework for advancing our understanding of cancer-associated fibroblasts. Nat Rev Cancer. 2020 Mar;20(3):174-86. DOI: 10.1038/s41568-019-0238-1.
33. Ozdemir BC, Pentcheva-Hoang T, Carstens JL, Zheng X, Wu CC, Simpson TR, et al. Depletion of carcinoma-associated fibroblasts and fibrosis induces immunosuppression and accelerates pancreas cancer with reduced survival. Cancer Cell. 2014;25(6):719-34.
34. Becker LM, O'Connell JT, Vo AP, Cain MP, Tampe D, Bizarro L, et al. Epigenetic Reprogramming of Cancer-Associated Fibroblasts Deregulates Glucose Metabolism and Facilitates Progression of Breast Cancer. Cell Rep. 2020 Jun 2;31(9):107701. DOI: 10.1016/j.celrep.2020.107701.
35. Sugimoto H, Mundel TM, Kieran MW, Kalluri R. Identification of fibroblast heterogeneity in the tumor microenvironment. Cancer Biol Ther. 2006 Dec;5(12):1640-6. DOI: 10.4161/cbt.5.12.3354.
36. Li H, Courtois ET, Sengupta D, Tan Y, Chen KH, Goh JJL, et al. Reference component analysis of single-cell transcriptomes elucidates cellular heterogeneity in human colorectal tumors. Nat Genet. 2017 May;49(5):708-18. DOI: 10.1038/ng.3818.
37. Son GM, Kwon MS, Shin DH, Shin N, Ryu D, Kang CD. Comparisons of cancer-associated fibroblasts in the intratumoral stroma and invasive front in colorectal cancer. Medicine (Baltimore). 2019 May;98(18):e15164. DOI: 10.1097/MD.0000000000015164.
38. Zhou Y, Bian S, Zhou X, Cui Y, Wang W, Wen L, et al. Single-Cell Multiomics Sequencing Reveals Prevalent Genomic Alterations in Tumor Stromal Cells of Human Colorectal Cancer. Cancer Cell. 2020 Oct 14. DOI: 10.1016/j.ccell.2020.09.015.

39. Karagiannis GS, Berk A, Dimitromanolakis A, Diamandis EP. Enrichment map profiling of the cancer invasion front suggests regulation of colorectal cancer progression by the bone morphogenetic protein antagonist, gremlin-1. Mol Oncol. 2013 Aug;7(4):826-39. DOI: 10.1016/j.molonc.2013.04.002.
40. Bardin N, Francès V, Combes V, Sampol J, Dignat-George F. CD146: biosynthesis and production of a soluble form in human cultured endothelial cells. FEBS Lett. 1998;421(1):12-4.
41. Bardin N, Blot-Chabaud M, Despoix N, Kebir A, Harhouri K, Arsanto JP, et al. CD146 and its soluble form regulate monocyte transendothelial migration. Arterioscler Thromb Vasc Biol. 2009 May;29(5):746-53. DOI: 10.1161/ATVBAHA.108.183251.
42. Harhouri K, Kebir A, Guillet B, Foucault-Bertaud A, Voytenko S, Piercecchi-Marti MD, et al. Soluble CD146 displays angiogenic properties and promotes neovascularization in experimental hind-limb ischemia. Blood. 2010 May 6;115(18):3843-51. DOI: 10.1182/blood-2009-06-229591.
43. Bardin N, Francès V, Lesaule G, Horschowski N, George F, Sampol J. Identification of the S-Endo 1 endothelial-associated antigen. Biochem Biophys Res Commun. 1996;218(1):210-6.
44. Chen J, Luo Y, Hui H, Cai T, Huang H, Yang F, et al. CD146 coordinates brain endothelial cell-pericyte communication for blood-brain barrier development. Proc Natl Acad Sci U S A. 2017 Sep 5;114(36):E7622-E31. DOI: 10.1073/pnas.1710848114.
45. Jin HJ, Kwon JH, Kim M, Bae YK, Choi SJ, Oh W, et al. Downregulation of Melanoma Cell Adhesion Molecule (MCAM/CD146) Accelerates Cellular Senescence in Human Umbilical Cord Blood-Derived Mesenchymal Stem Cells. Stem Cells Transl Med. 2016 Apr;5(4):427-39. DOI: 10.5966/sctm.2015-0109.
46. Sorrentino A, Ferracin M, Castelli G, Biffoni M, Tomaselli G, Baiocchi M, et al. Isolation and characterization of CD146+ multipotent mesenchymal stromal cells. Exp Hematol. 2008 Aug;36(8):1035-46. DOI: 10.1016/j.exphem.2008.03.004.
47. Wu CC, Liu FL, Sytwu HK, Tsai CY, Chang DM. CD146+ mesenchymal stem cells display greater therapeutic potential than CD146- cells for treating collagen-induced arthritis in mice. Stem Cell Res Ther. 2016 Feb 3;7:23. DOI: 10.1186/s13287-016-0285-4.
48. Sacchetti B, Funari A, Michienzi S, Di Cesare S, Piersanti S, Saggio I, et al. Self-renewing osteoprogenitors in bone marrow sinusoids can organize a hematopoietic microenvironment. Cell. 2007 Oct 19;131(2):324-36. DOI: 10.1016/j.cell.2007.08.025.
49. Dagur PK, McCoy JP, Jr. Endothelial-binding, proinflammatory T cells identified by MCAM (CD146) expression: Characterization and role in human autoimmune diseases. Autoimmun Rev. 2015 May;14(5):415-22. DOI: 10.1016/j.autrev.2015.01.003.

50. Flanagan K, Fitzgerald K, Baker J, Regnstrom K, Gardai S, Bard F, et al. Laminin-411 is a vascular ligand for MCAM and facilitates TH17 cell entry into the CNS. PLoS One. 2012;7(7):e40443. DOI: 10.1371/journal.pone.0040443.
51. Brechbuhl HM, Finlay-Schultz J, Yamamoto TM, Gillen AE, Cittelly DM, Tan AC, et al. Fibroblast Subtypes Regulate Responsiveness of Luminal Breast Cancer to Estrogen. Clin Cancer Res. 2017 Apr 1;23(7):1710-21. DOI: 10.1158/1078-0432.CCR-15-2851.
52. Li Q, Yu Y, Bischoff J, Mulliken JB, Olsen BR. Differential expression of CD146 in tissues and endothelial cells derived from infantile haemangioma and normal human skin. J Pathol. 2003 Oct;201(2):296-302. DOI: 10.1002/path.1443.
53. Wu SZ, Roden DL, Wang C, Holliday H, Harvey K, Cazet AS, et al. Stromal cell diversity associated with immune evasion in human triple-negative breast cancer. EMBO J. 2020 Oct 1;39(19):e104063. DOI: 10.15252/embj.2019104063.
54. Bartoschek M, Oskolkov N, Bocci M, Lovrot J, Larsson C, Sommarin M, et al. Spatially and functionally distinct subclasses of breast cancer-associated fibroblasts revealed by single cell RNA sequencing. Nat Commun. 2018 Dec 4;9(1):5150. DOI: 10.1038/s41467-018-07582-3.
55. Costa A, Kieffer Y, Scholer-Dahirel A, Pelon F, Bourachot B, Cardon M, et al. Fibroblast Heterogeneity and Immunosuppressive Environment in Human Breast Cancer. Cancer Cell. 2018 Mar 12;33(3):463-79 e10. DOI: 10.1016/j.ccell.2018.01.011.
56. Dominguez CX, Muller S, Keerthivasan S, Koeppen H, Hung J, Gierke S, et al. Single-Cell RNA Sequencing Reveals Stromal Evolution into LRRC15(+) Myofibroblasts as a Determinant of Patient Response to Cancer Immunotherapy. Cancer Discov. 2020 Feb;10(2):232-53. DOI: 10.1158/2159-8290.CD-19-0644.
57. Chen Y, Sumardika IW, Tomonobu N, Kinoshita R, Inoue Y, Iioka H, et al. Critical role of the MCAM-ETV4 axis triggered by extracellular S100A8/A9 in breast cancer aggressiveness. Neoplasia. 2019 Jul;21(7):627-40. DOI: 10.1016/j.neo.2019.04.006.
58. Jiang G, Zhang L, Zhu Q, Bai D, Zhang C, Wang X. CD146 promotes metastasis and predicts poor prognosis of hepatocellular carcinoma. J Exp Clin Cancer Res. 2016 Feb 29;35:38. DOI: 10.1186/s13046-016-0313-3.
59. Johnson JP, Bar-Eli M, Jansen B, Markhof E. Melanoma progression–associated glycoprotein MUC18/MCAM mediates homotypic cell adhesion through interaction with a heterophilic ligand. International Journal of Cancer. 1997;73(5):769-74.
60. Luo Y, Zheng C, Zhang J, Lu D, Zhuang J, Xing S, et al. Recognition of CD146 as an ERM-binding protein offers novel mechanisms for melanoma cell migration. Oncogene. 2012 Jan 19;31(3):306-21. DOI: 10.1038/onc.2011.244.
61. Mills L, Tellez C, Huang S, Baker C, Mccarty M, Green L, et al. Fully human antibodies to MCAM/MUC18 inhibit tumor growth and metastasis of human melanoma. Cancer Res. 2002;62(17):5106-14.

62. Nodomi S, Umeda K, Saida S, Kinehara T, Hamabata T, Daifu T, et al. CD146 is a novel marker for highly tumorigenic cells and a potential therapeutic target in malignant rhabdoid tumor. Oncogene. 2016 Oct 6;35(40):5317-27. DOI: 10.1038/onc.2016.72.
63. Staquicini FI, Tandle A, Libutti SK, Sun J, Zigler M, Bar-Eli M, et al. A subset of host B lymphocytes controls melanoma metastasis through a melanoma cell adhesion molecule/MUC18-dependent interaction: evidence from mice and humans. Cancer Res. 2008 Oct 15;68(20):8419-28. DOI: 10.1158/0008-5472.CAN-08-1242.
64. Wei Q, Tang YJ, Voisin V, Sato S, Hirata M, Whetstone H, et al. Identification of CD146 as a marker enriched for tumor-propagating capacity reveals targetable pathways in primary human sarcoma. Oncotarget. 2015;6(37):40283-94.
65. Xie S, Luca M, Huang S, Gutman M, Reich R, Johnson JP, et al. Expression of MCAM/MUC18 by human melanoma cells leads to increased tumor growth and metastasis. Cancer Res. 1997;57(11):2295-303.
66. Zeng Q, Li W, Lu D, Wu Z, Duan H, Luo Y, et al. CD146, an epithelial-mesenchymal transition inducer, is associated with triple-negative breast cancer. Proc Natl Acad Sci U S A. 2012 Jan 24;109(4):1127-32. DOI: 10.1073/pnas.1111053108.
67. Zigler M, Villares GJ, Dobroff AS, Wang H, Huang L, Braeuer RR, et al. Expression of Id-1 is regulated by MCAM/MUC18: a missing link in melanoma progression. Cancer Res. 2011 May 15;71(10):3494-504. DOI: 10.1158/0008-5472.CAN-10-3555.
68. Ma Y, Zhang H, Xiong C, Liu Z, Xu Q, Feng J, et al. CD146 mediates an E-cadherin-to-N-cadherin switch during TGF-beta signaling-induced epithelial-mesenchymal transition. Cancer Lett. 2018 Aug 28;430:201-14. DOI: 10.1016/j.canlet.2018.05.016.
69. Zheng B, Ohuchida K, Chijiiwa Y, Zhao M, Mizuuchi Y, Cui L, et al. CD146 attenuation in cancer-associated fibroblasts promotes pancreatic cancer progression. Mol Carcinog. 2016 Nov;55(11):1560-72. DOI: 10.1002/mc.22409.
70. Wragg JW, Finnity JP, Anderson JA, Ferguson HJ, Porfiri E, Bhatt RI, et al. MCAM and LAMA4 Are Highly Enriched in Tumor Blood Vessels of Renal Cell Carcinoma and Predict Patient Outcome. Cancer Res. 2016 Apr 15;76(8):2314-26. DOI: 10.1158/0008-5472.CAN-15-1364.
71. Xing S, Luo Y, Liu Z, Bu P, Duan H, Liu D, et al. Targeting endothelial CD146 attenuates colitis and prevents colitis-associated carcinogenesis. Am J Pathol. 2014 May;184(5):1604-16. DOI: 10.1016/j.ajpath.2014.01.031.
72. Li G, Kalabis J, Xu X, Meier F, Oka M, Bogenrieder T, et al. Reciprocal regulation of MelCAM and AKT in human melanoma. Oncogene. 2003 Oct 9;22(44):6891-9. DOI: 10.1038/sj.onc.1206819.
73. Rummel MM, Sers C, Johnson JP. Phorbol ester and cyclic AMP-mediated regulation of the melanoma-associated cell adhesion molecule MUC18/MCAM. Cancer Res. 1996;56(9):2218-23.

74. Ueno K, Hirata H, Majid S, Tabatabai ZL, Hinoda Y, Dahiya R. IGFBP-4 activates the Wnt/beta-catenin signaling pathway and induces M-CAM expression in human renal cell carcinoma. Int J Cancer. 2011 Nov 15;129(10):2360-9. DOI: 10.1002/ijc.25899.
75. Corselli M, Chin CJ, Parekh C, Sahaghian A, Wang W, Ge S, et al. Perivascular support of human hematopoietic stem/progenitor cells. Blood. 2013 Apr 11;121(15):2891-901. DOI: 10.1182/blood-2012-08-451864.
76. Crisan M, Yap S, Casteilla L, Chen CW, Corselli M, Park TS, et al. A perivascular origin for mesenchymal stem cells in multiple human organs. Cell Stem Cell. 2008 Sep 11;3(3):301-13. DOI: 10.1016/j.stem.2008.07.003.
77. Jiang T, Zhuang J, Duan H, Luo Y, Zeng Q, Fan K, et al. CD146 is a coreceptor for VEGFR-2 in tumor angiogenesis. Blood. 2012 Sep 13;120(11):2330-9. DOI: 10.1182/blood-2012-01-406108.
78. Kang Y, Wang F, Feng J, Yang D, Yang X, Yan X. Knockdown of CD146 reduces the migration and proliferation of human endothelial cells. Cell Res. 2006 Mar;16(3):313-8. DOI: 10.1038/sj.cr.7310039.
79. Tu T, Zhang C, Yan H, Luo Y, Kong R, Wen P, et al. CD146 acts as a novel receptor for netrin-1 in promoting angiogenesis and vascular development. Cell Res. 2015 Mar;25(3):275-87. DOI: 10.1038/cr.2015.15.
80. Xu W, Hua H, Chiu YH, Li G, Zhi H, Yu Z, et al. CD146 Regulates Growth Factor-Induced mTORC2 Activity Independent of the PI3K and mTORC1 Pathways. Cell Rep. 2019 Oct 29;29(5):1311-22 e5. DOI: 10.1016/j.celrep.2019.09.047.
81. Ye Z, Zhang C, Tu T, Sun M, Liu D, Lu D, et al. Wnt5a uses CD146 as a receptor to regulate cell motility and convergent extension. Nat Commun. 2013;4:2803. DOI: 10.1038/ncomms3803.
82. Tung HH, Lee SL. Physical Binding of Endothelial MCAM and Neural Transmembrane Protease Matriptase-Novel Cell Adhesion in Neural Stem cell Vascular Niche. Sci Rep. 2017 Jul 10;7(1):4946. DOI: 10.1038/s41598-017-05131-4.
83. Nakai T, Sakai D, Nakamura Y, Nukaga T, Grad S, Li Z, et al. CD146 defines commitment of cultured annulus fibrosus cells to express a contractile phenotype. J Orthop Res. 2016 Aug;34(8):1361-72. DOI: 10.1002/jor.23326.
84. Yan X, Lin Y, Yang D, Shen Y, Yuan M, Zhang Z, et al. A novel anti-CD146 monoclonal antibody, AA98, inhibits angiogenesis and tumor growth. Blood. 2003 Jul 1;102(1):184-91. DOI: 10.1182/blood-2002-04-1004.
85. Bu P, Gao L, Zhuang J, Feng J, Yang D, Yan X. Anti-CD146 monoclonal antibody AA98 inhibits angiogenesis via suppression of nuclear factor-kappaB activation. Mol Cancer Ther. 2006 Nov;5(11):2872-8. DOI: 10.1158/1535-7163.MCT-06-0260.
86. Zheng C, Qiu Y, Zeng Q, Zhang Y, Lu D, Yang D, et al. Endothelial CD146 is required for in vitro tumor-induced angiogenesis: the role of a disulfide bond in signaling and

dimerization. Int J Biochem Cell Biol. 2009 Nov;41(11):2163-72. DOI: 10.1016/j.biocel.2009.03.014.

87. Duan H, Xing S, Luo Y, Feng L, Gramaglia I, Zhang Y, et al. Targeting endothelial CD146 attenuates neuroinflammation by limiting lymphocyte extravasation to the CNS. Sci Rep. 2013;3:1687. DOI: 10.1038/srep01687.

88. Flanagan K, Tam SJ, Li L, Dolan PJ, Barbour RM, Higaki JN, et al. Anti-Mcam Monoclonal Antibody PRX003 Inhibits the Unique Migratory Potential of Pathogenic IL-17–Producing T Cells. Journal of Allergy and Clinical Immunology. 2016;137(2). DOI: 10.1016/j.jaci.2015.12.753.

89. Koller M, Flanagan K, Skov M, Goldblum R, Griffith SG, Barbour RM, et al. Clinical and preclinical assessment of the anti-MCAM monoclonal antibody PRX003, a potential novel treatment for Th17-mediated inflammatory diseases. Annals of the Rheumatic Diseases. 2016;75:134. DOI: 10.1136/annrheumdis-2016-eular.2447.

90. Kinney GG, Flanagan K, Skov M, Goldblum R, Griffith S, Barbour RM, et al. Clinical assessment of the monoclonal anitbody, PRX003, a potential novel treatment for Th17-mediated inflammatory disease [abstract]. Arthritis Rheumatol. 2016;68.

91. Aldovini D, Demichelis F, Doglioni C, Di Vizio D, Galligioni E, Brugnara S, et al. M-CAM expression as marker of poor prognosis in epithelial ovarian cancer. Int J Cancer. 2006 Oct 15;119(8):1920-6. DOI: 10.1002/ijc.22082.

92. Li Y, Yu J, Zhan X, Liu L, Jin N, Zhang Y. Correlation of CD146 expression and clinicopathological characteristics in esophageal squamous cell carcinoma. Oncol Lett. 2014;8(2):859-63.

93. Liu WF, Ji SR, Sun JJ, Zhang Y, Liu ZY, Liang AB, et al. CD146 expression correlates with epithelial-mesenchymal transition markers and a poor prognosis in gastric cancer. Int J Mol Sci. 2012;13(5):6399-406. DOI: 10.3390/ijms13056399.

94. Oka S, Uramoto H, Chikaishi Y, Tanaka F. The expression of CD146 predicts a poor overall survival in patients with adenocarcinoma of the lung. Anticancer Res. 2012;32(3):861-4.

95. Tian B, Zhang Y, Li N. CD146 protein as a marker to predict postoperative liver metastasis in colorectal cancer. Cancer Biother Radiopharm. 2013 Jul-Aug;28(6):466-70. DOI: 10.1089/cbr.2012.1426.

96. Zhang X, Wang Z, Kang Y, Li X, Ma X, Ma L. MCAM expression is associated with poor prognosis in non-small cell lung cancer. Clin Transl Oncol. 2014 Feb;16(2):178-83. DOI: 10.1007/s12094-013-1057-6.

97. Leslie MC, Zhao YJ, Lachman LB, Hwu P, Wu GJ, Bar-Eli M. Immunization against MUC18/MCAM, a novel antigen that drives melanoma invasion and metastasis. Gene Ther. 2007 Feb;14(4):316-23. DOI: 10.1038/sj.gt.3302864.

98. Stalin J, Nollet M, Garigue P, Fernandez S, Vivancos L, Essaadi A, et al. Targeting soluble CD146 with a neutralizing antibody inhibits vascularization, growth and survival of CD146-positive tumors. Oncogene. 2016 Oct 20;35(42):5489-500. DOI: 10.1038/onc.2016.83.
99. McGary EC, Heimberger A, Mills L, Weber K, Thomas GW, Shtivelband M, et al. A fully human antimelanoma cellular adhesion molecule/MUC18 antibody inhibits spontaneous pulmonary metastasis of osteosarcoma cells in vivo. Clin Cancer Res. 2003;9(17):6560-6.
100. Zoni E, Astrologo L, Ng CKY, Piscuoglio S, Melsen J, Grosjean J, et al. Therapeutic Targeting of CD146/MCAM Reduces Bone Metastasis in Prostate Cancer. Mol Cancer Res. 2019 May;17(5):1049-62. DOI: 10.1158/1541-7786.MCR-18-1220.
101. Chen C, Duckworth CA, Zhao Q, Pritchard DM, Rhodes JM, Yu LG. Increased circulation of galectin-3 in cancer induces secretion of metastasis-promoting cytokines from blood vascular endothelium. Clin Cancer Res. 2013 Apr 1;19(7):1693-704. DOI: 10.1158/1078-0432.CCR-12-2940.
102. Colomb F, Wang W, Simpson D, Zafar M, Beynon R, Rhodes JM, et al. Galectin-3 interacts with the cell-surface glycoprotein CD146 (MCAM, MUC18) and induces secretion of metastasis-promoting cytokines from vascular endothelial cells. J Biol Chem. 2017 May 19;292(20):8381-9. DOI: 10.1074/jbc.M117.783431.
103. Jouve N, Despoix N, Espeli M, Gauthier L, Cypowyj S, Fallague K, et al. The involvement of CD146 and its novel ligand Galectin-1 in apoptotic regulation of endothelial cells. J Biol Chem. 2013 Jan 25;288(4):2571-9. DOI: 10.1074/jbc.M112.418848.
104. Guezguez B, Vigneron P, Lamerant N, Kieda C, Jaffredo T, Dunon D. Dual role of melanoma cell adhesion molecule (MCAM)/CD146 in lymphocyte endothelium interaction: MCAM/CD146 promotes rolling via microvilli induction in lymphocyte and is an endothelial adhesion receptor. J Immunol. 2007;179(10):6673-85.
105. Bu P, Zhuang J, Feng J, Yang D, Shen X, Yan X. Visualization of CD146 dimerization and its regulation in living cells. Biochim Biophys Acta. 2007 Apr;1773(4):513-20. DOI: 10.1016/j.bbamcr.2007.01.009.
106. Anfosso F, Bardin N, Francès V, Vivier E, Camoin-Jau L, Sampol J, et al. Activation of human endothelial cells via S-endo-1 antigen (CD146) stimulates the tyrosine phosphorylation of focal adhesion kinase p125(FAK). J Biol Chem. 1998;273(41):26852-6.
107. Anfosso F, Bardin N, Vivier E, Sabatier F, Sampol J, Dignat-George F. Outside-in signaling pathway linked to CD146 engagement in human endothelial cells. J Biol Chem. 2001 Jan 12;276(2):1564-9. DOI: 10.1074/jbc.M007065200.
108. Hsu DR, Economides AN, Wang X, Eimon PM, Harland RM. The Xenopus dorsalizing factor Gremlin identifies a novel family of secreted proteins that antagonize BMP activities. Molecular Cell. 1998;1:673-83.

109. Ouahoud S, Hardwick JCH, Hawinkels L. Extracellular BMP Antagonists, Multifaceted Orchestrators in the Tumor and Its Microenvironment. Int J Mol Sci. 2020 May 29;21(11). DOI: 10.3390/ijms21113888.
110. Khokha MK, Hsu D, Brunet LJ, Dionne MS, Harland RM. Gremlin is the BMP antagonist required for maintenance of Shh and Fgf signals during limb patterning. Nat Genet. 2003;34(3):303-7.
111. Michos O, Panman L, Vintersten K, Beier K, Zeller R, Zuniga A. Gremlin-mediated BMP antagonism induces the epithelial-mesenchymal feedback signaling controlling metanephric kidney and limb organogenesis. Development. 2004 Jul;131(14):3401-10. DOI: 10.1242/dev.01251.
112. Davis H, Irshad S, Bansal M, Rafferty H, Boitsova T, Bardella C, et al. Aberrant epithelial GREM1 expression initiates colonic tumorigenesis from cells outside the stem cell niche. Nat Med. 2015 Jan;21(1):62-70. DOI: 10.1038/nm.3750.
113. Hardwick JC, Van Den Brink GR, Bleuming SA, Ballester I, Van Den Brande JM, Keller JJ, et al. Bone morphogenetic protein 2 is expressed by, and acts upon, mature epithelial cells in the colon. Gastroenterology. 2004 Jan;126(1):111-21. DOI: 10.1053/j.gastro.2003.10.067.
114. Vermeulen L, De Sousa EMF, van der Heijden M, Cameron K, de Jong JH, Borovski T, et al. Wnt activity defines colon cancer stem cells and is regulated by the microenvironment. Nat Cell Biol. [Research Support, Non-U.S. Gov't]. 2010 May;12(5):468-76. DOI: 10.1038/ncb2048.
115. Dutton LR, Hoare OP, Mccorry AMB, Redmond KL, Adam NE, Canamara S, et al. Fibroblast-derived Gremlin1 localises to epithelial cells at the base of the intestinal crypt. Oncotarget. 2019;10(45):4630-9.
116. Scoville DH, Sato T, He XC, Li L. Current view: intestinal stem cells and signaling. Gastroenterology. 2008 Mar;134(3):849-64. DOI: 10.1053/j.gastro.2008.01.079.
117. Mitola S, Ravelli C, Moroni E, Salvi V, Leali D, Ballmer-Hofer K, et al. Gremlin is a novel agonist of the major proangiogenic receptor VEGFR2. Blood. 2010;116(18):3677-80.
118. Ravelli C, Mitola S, Corsini M, Presta M. Involvement of alphavbeta3 integrin in gremlin-induced angiogenesis. Angiogenesis. 2013 Jan;16(1):235-43. DOI: 10.1007/s10456-012-9309-6.
119. Grillo E, Ravelli C, Corsini M, Ballmer-Hofer K, Zammataro L, Oreste P, et al. Monomeric gremlin is a novel vascular endothelial growth factor receptor-2 antagonist. Oncotarget. 2016;7(23):35353-68.
120. Yu Y, Cheng L, Yan B, Zhou C, Qian W, Xiao Y, et al. Overexpression of Gremlin 1 by sonic hedgehog signaling promotes pancreatic cancer progression. Int J Oncol. 2018 Dec;53(6):2445-57. DOI: 10.3892/ijo.2018.4573.

121. Ren J, Smid M, Iaria J, Salvatori DCF, van Dam H, Zhu HJ, et al. Cancer-associated fibroblast-derived Gremlin 1 promotes breast cancer progression. Breast Cancer Res. 2019 Sep 18;21(1):109. DOI: 10.1186/s13058-019-1194-0.
122. Rodrigues-Diez R, Lavoz C, Carvajal G, Rayego-Mateos S, Rodrigues Diez RR, Ortiz A, et al. Gremlin is a downstream profibrotic mediator of transforming growth factor-beta in cultured renal cells. Nephron Exp Nephrol. 2012;122(1-2):62-74. DOI: 10.1159/000346575.
123. Neckmann U, Wolowczyk C, Hall M, Almaas E, Ren J, Zhao S, et al. GREM1 is associated with metastasis and predicts poor prognosis in ER-negative breast cancer patients. Cell Commun Signal. 2019 Nov 6;17(1):140. DOI: 10.1186/s12964-019-0467-7.
124. Yan K, Wu Q, Yan DH, Lee CH, Rahim N, Tritschler I, et al. Glioma cancer stem cells secrete Gremlin1 to promote their maintenance within the tumor hierarchy. Genes Dev. 2014 May 15;28(10):1085-100. DOI: 10.1101/gad.235515.113.
125. Sung NJ, Kim NH, Bae NY, Jo HS, Park SA. DHA inhibits Gremlin-1-induced epithelial-to-mesenchymal transition via ERK suppression in human breast cancer cells. Biosci Rep. 2020 Mar 27;40(3). DOI: 10.1042/BSR20200164.
126. Tamminen JA, Parviainen V, Ronty M, Wohl AP, Murray L, Joenvaara S, et al. Gremlin-1 associates with fibrillin microfibrils in vivo and regulates mesothelioma cell survival through transcription factor slug. Oncogenesis. 2013 Aug 26;2:e66. DOI: 10.1038/oncsis.2013.29.
127. Yin M, Tissari M, Tamminen J, Ylivinkka I, Rönty M, Von Nandelstadh P, et al. Gremlin-1 is a key regulator of the invasive cell phenotype in mesothelioma. Oncotarget. 2017;8(58):98280-97.
128. Liu Y, Li Y, Hou R, Shu Z. Knockdown GREM1 suppresses cell growth, angiogenesis, and epithelial-mesenchymal transition in colon cancer. J Cell Biochem. 2019 Apr;120(4):5583-96. DOI: 10.1002/jcb.27842.
129. Jaeger E, Leedham S, Lewis A, Segditsas S, Becker M, Cuadrado PR, et al. Hereditary mixed polyposis syndrome is caused by a 40-kb upstream duplication that leads to increased and ectopic expression of the BMP antagonist GREM1. Nat Genet. 2012 May 6;44(6):699-703. DOI: 10.1038/ng.2263.
130. Sneddon JB, Zhen HH, Montgomery K, van de Rijn M, Tward AD, West R, et al. Bone morphogenetic protein antagonist gremlin 1 is widely expressed by cancer-associated stromal cells and can promote tumor cell proliferation. Proc Natl Acad Sci U S A. 2006;103(40):14842-7.
131. Hong D, Liu T, Huang W, Liao Y, Wang L, Zhang Z, et al. Gremlin1 delivered by mesenchymal stromal cells promoted epithelial-mesenchymal transition in human esophageal squamous cell carcinoma. Cell Physiol Biochem. 2018;47(5):1785-99. DOI: 10.1159/000491060.

132. Clark KC, Hewett DR, Panagopoulos V, Plakhova N, Opperman KS, Bradey AL, et al. Targeted Disruption of Bone Marrow Stromal Cell-Derived Gremlin1 Limits Multiple Myeloma Disease Progression In Vivo. Cancers. 2020;12(8). DOI: 10.3390/cancers12082149.
133. Davis JM, Cheng B, Drake MM, Yu Q, Yang B, Li, et al. Pancreatic stromal Gremlin 1 expression during pancreatic tumorigenesis. Genes & Diseases. 2020. DOI: 10.1016/j.gendis.2020.05.001.
134. Khalil H, Nie W, Edwards RA, Yoo J. Isolation of primary myofibroblasts from mouse and human colon tissue. J Vis Exp. 2013 Oct 12(80). DOI: 10.3791/50611.
135. Ponomarev V, Doubrovin M, Serganova I, Vider J, Shavrin A, Beresten T, et al. A novel triple-modality reporter gene for whole-body fluorescent, bioluminescent, and nuclear noninvasive imaging. Eur J Nucl Med Mol Imaging. 2004 May;31(5):740-51. DOI: 10.1007/s00259-003-1441-5.
136. Kobayashi H, Gieniec KA, Wright JA, Wang T, Asai N, Mizutani Y, et al. The balance of stromal BMP signaling mediated by GREM1 and ISLR drives colorectal carcinogenesis. Gastroenterology. 2020. DOI: 10.1053/j.gastro.2020.11.011.
137. Ye J, Coulouris G, Zaretskaya I, Cutcutache I, Rozen S, Madden TL. Primer-BLAST: A tool to design target-specific primers for polymerase chain reaction. BMC Bioinformatics. 2012;13(134). DOI: 10.1186/1471-2105-13-134.
138. Liang CC, Park AY, Guan JL. In vitro scratch assay: a convenient and inexpensive method for analysis of cell migration in vitro. Nat Protoc. 2007;2(2):329-33. DOI: 10.1038/nprot.2007.30.
139. Becker C, Fantini MC, Neurath MF. High resolution colonoscopy in live mice. Nat Protoc. 2006;1(6):2900-4. DOI: 10.1038/nprot.2006.446.
140. Goddard ET, Fischer J, Schedin P. A Portal Vein Injection Model to Study Liver Metastasis of Breast Cancer. J Vis Exp. 2016 Dec 26(118). DOI: 10.3791/54903.
141. Di Cesare Mannelli L, Maresca M, Micheli L, Farina C, Scherz MW, Ghelardini C. A rat model of FOLFOX-induced neuropathy: effects of oral dimiracetam in comparison with duloxetine and pregabalin. Cancer Chemother Pharmacol. 2017 Dec;80(6):1091-103. DOI: 10.1007/s00280-017-3449-8.
142. Robinson SM, Mann DA, Manas DM, Oakley F, Mann J, White SA. The potential contribution of tumour-related factors to the development of FOLFOX-induced sinusoidal obstruction syndrome. Br J Cancer. 2013 Oct 29;109(9):2396-403. DOI: 10.1038/bjc.2013.604.
143. Robinson SM, Mann J, Vasilaki A, Mathers J, Burt AD, Oakley F, et al. Pathogenesis of FOLFOX induced sinusoidal obstruction syndrome in a murine chemotherapy model. J Hepatol. 2013 Aug;59(2):318-26. DOI: 10.1016/j.jhep.2013.04.014.

144. Zhu G, Zhao M, Han Q, Tan Y, Sun Y, Bouvet M, et al. Temozolomide and Pazopanib Combined with FOLFOX Regressed a Primary Colorectal Cancer in a Patient-derived Orthotopic Xenograft Mouse Model. Transl Oncol. 2020 Mar;13(3):100739. DOI: 10.1016/j.tranon.2019.12.011.
145. Tanaka T, Kohno H, Suzuki R, Yamada Y, Sugie S, Mori H. A novel inflammation-related mouse colon carcinogenesis model induced by azoxymethane and dextran sodium sulfate. Cancer Sci. 2003;94(11):965-73.
146. Wirtz S, Neufert C, Weigmann B, Neurath MF. Chemically induced mouse models of intestinal inflammation. Nat Protoc. 2007;2(3):541-6. DOI: 10.1038/nprot.2007.41.
147. Takahashi M, Wakabayashi K. Gene mutations and altered gene expression in azoxymethane-induced colon carcinogenesis in rodents. Cancer Sci. 2004;95(6):475-80.
148. Zigmond E, Halpern Z, Elinav E, Brazowski E, Jung S, Varol C. Utilization of murine colonoscopy for orthotopic implantation of colorectal cancer. PLoS One. 2011;6(12):e28858. DOI: 10.1371/journal.pone.0028858.
149. Riihimaki M, Hemminki A, Sundquist J, Hemminki K. Patterns of metastasis in colon and rectal cancer. Sci Rep. 2016 Jul 15;6:29765. DOI: 10.1038/srep29765.
150. Franks LM, Hemmings VJ. A cell line from an induced carcinoma of mouse rectum. J Pathol. 1978;124(1):35-8.
151. Sakuma K, Sasaki E, Kimura K, Komori K, Shimizu Y, Yatabe Y, et al. HNRNPLL, a newly identified colorectal cancer metastasis suppressor, modulates alternative splicing of CD44 during epithelial-mesenchymal transition. Gut. 2018 Jun;67(6):1103-11. DOI: 10.1136/gutjnl-2016-312927.
152. Corbett TH, Griswold DP, Roberts BJ, Peckham JC, Schabel FM. Tumor induction relationships in development of transplantable cancers of the colon in mice for chemotherapy assays, with a note on carcinogen structure. Cancer Res. 1975;35(9):2434-9.
153. Tan MH, Holyoke ED, Goldrosen MH. Murine colon adenocarcinomas: methods for selective culture in vitro. J Natl Cancer Inst. 1976;56(4):871-3.
154. Zhang L, Shay JW. Multiple Roles of APC and its Therapeutic Implications in Colorectal Cancer. J Natl Cancer Inst. 2017 Aug 1;109(8). DOI: 10.1093/jnci/djw332.
155. Markman B, Javier Ramos F, Capdevila J, Tabernero J. EGFR and KRAS in Colorectal Cancer. 2010. p. 71-119.
156. Vassilev LT, Vu BT, Graves B, Carvajal D, Podlaski F, Filipovic Z, et al. In vivo activation of the p53 pathway by small-molecule antagonists of MDM2. Science. 2004;303(5659):844-8.
157. Nakayama M, Oshima M. Mutant p53 in colon cancer. J Mol Cell Biol. 2019 Apr 1;11(4):267-76. DOI: 10.1093/jmcb/mjy075.
158. Baklaushev VP, Kilpelainen A, Petkov S, Abakumov MA, Grinenko NF, Yusubalieva GM, et al. Luciferase Expression Allows Bioluminescence Imaging But Imposes Limitations on

the Orthotopic Mouse (4T1) Model of Breast Cancer. Sci Rep. 2017 Aug 10;7(1):7715. DOI: 10.1038/s41598-017-07851-z.

159. Limberis MP, Bell CL, Wilson JM. Identification of the murine firefly luciferase-specific CD8 T-cell epitopes. Gene Ther. 2009 Mar;16(3):441-7. DOI: 10.1038/gt.2008.177.
160. Roper J, Tammela T, Akkad A, Almeqdadi M, Santos SB, Jacks T, et al. Colonoscopy-based colorectal cancer modeling in mice with CRISPR-Cas9 genome editing and organoid transplantation. Nat Protoc. 2018 Feb;13(2):217-34. DOI: 10.1038/nprot.2017.136.
161. Moser AR, Pitot HC, Dove WF. A dominant mutation that predisposes to multiple intestinal neoplasia in the mouse. Science. 1990;247(4940):322-4.
162. Bilger A, Shoemaker AR, Gould KA, Dove WF. Manipulation of the mouse germline in the study of Min-induced neoplasia. Semin Cancer Biol. 1996;7(5):249-60.
163. Washington K, Zemper AED. Apc-related models of intestinal neoplasia: a brief review for pathologists. Surgical and Experimental Pathology. 2019;2(1). DOI: 10.1186/s42047-019-0036-9.
164. Gomez D, Dalal Z, Raw E, Roberts C, Lyndon PJ. Anatomical distribution of colorectal cancer over a 10 year period in a district general hospital: is there a true "rightward shift"? Postgrad Med J. 2004 Nov;80(949):667-9. DOI: 10.1136/pgmj.2004.020198.
165. Yadav M, Jhunjhunwala S, Phung QT, Lupardus P, Tanguay J, Bumbaca S, et al. Predicting immunogenic tumour mutations by combining mass spectrometry and exome sequencing. Nature. 2014 Nov 27;515(7528):572-6. DOI: 10.1038/nature14001.
166. Efremova M, Rieder D, Klepsch V, Charoentong P, Finotello F, Hackl H, et al. Targeting immune checkpoints potentiates immunoediting and changes the dynamics of tumor evolution. Nat Commun. 2018 Jan 2;9(1):32. DOI: 10.1038/s41467-017-02424-0.
167. Juneja VR, McGuire KA, Manguso RT, LaFleur MW, Collins N, Haining WN, et al. PD-L1 on tumor cells is sufficient for immune evasion in immunogenic tumors and inhibits CD8 T cell cytotoxicity. J Exp Med. 2017 Apr 3;214(4):895-904. DOI: 10.1084/jem.20160801.
168. Lau J, Cheung J, Navarro A, Lianoglou S, Haley B, Totpal K, et al. Tumour and host cell PD-L1 is required to mediate suppression of anti-tumour immunity in mice. Nat Commun. 2017 Feb 21;8:14572. DOI: 10.1038/ncomms14572.
169. Zhang JY, Yan YY, Li JJ, Adhikari R, Fu LW. PD-1/PD-L1 Based Combinational Cancer Therapy: Icing on the Cake. Front Pharmacol. 2020;11:722. DOI: 10.3389/fphar.2020.00722.
170. Ferlitsch M, Reinhart K, Pramhas S, Wiener C, Gal O, Bannert C, et al. Sex-specific prevalence of adenomas, advanced adenomas, and colorectal cancer in individuals undergoing screening colonoscopy. JAMA. 2011;306(12):1352-8.
171. Eichwald EJ, Silmser CR, Weissman IL. Sex-linked rejection of normal and neoplastic tissue. I. Distribution and specificity. J Natl Cancer Inst. 1958;20(3):563-75.

172. Tan JC, Wadia PP, Coram M, Grumet FC, Kambham N, Miller K, et al. H-Y antibody development associates with acute rejection in female patients with male kidney transplants. Transplantation. 2008 Jul 15;86(1):75-81. DOI: 10.1097/TP.0b013e31817352b9.
173. Popli R, Sahaf B, Nakasone H, Lee JY, Miklos DB. Clinical impact of H-Y alloimmunity. Immunol Res. 2014 May;58(2-3):249-58. DOI: 10.1007/s12026-014-8514-3.
174. Spierings E. Minor histocompatibility antigens: past, present, and future. Tissue Antigens. 2014 Oct;84(4):374-60. DOI: 10.1111/tan.12445.
175. Chew WL, Tabebordbar M, Cheng JK, Mali P, Wu EY, Ng AH, et al. A multifunctional AAV-CRISPR-Cas9 and its host response. Nat Methods. 2016 Oct;13(10):868-74. DOI: 10.1038/nmeth.3993.
176. Han WG, Unger WW, Wauben MH. Identification of the immunodominant CTL epitope of EGFP in C57BL/6 mice. Gene Ther. 2008 May;15(9):700-1. DOI: 10.1038/sj.gt.3303104.
177. Wang D, Mou H, Li S, Li Y, Hough S, Tran K, et al. Adenovirus-Mediated Somatic Genome Editing of Pten by CRISPR/Cas9 in Mouse Liver in Spite of Cas9-Specific Immune Responses. Hum Gene Ther. 2015 Jul;26(7):432-42. DOI: 10.1089/hum.2015.087.
178. Ajina R, Zamalin D, Zuo A, Moussa M, Catalfamo M, Jablonski SA, et al. SpCas9-expression by tumor cells can cause T cell-dependent tumor rejection in immunocompetent mice. Oncoimmunology. 2019;8(5):e1577127. DOI: 10.1080/2162402X.2019.1577127.
179. Gambotto A, Dworacki G, Cicinnati V, Kenniston T, Steitz J, Tüting T, et al. Immunogenicity of enhanced green fluorescent protein (EGFP) in BALB/c mice: identification of an H2-Kd-restricted CTL epitope. Gene Ther. 2000;7(23):2036-40.
180. Hu J, Schokrpur S, Archang M, Hermann K, Sharrow AC, Khanna P, et al. A Non-integrating Lentiviral Approach Overcomes Cas9-Induced Immune Rejection to Establish an Immunocompetent Metastatic Renal Cancer Model. Mol Ther Methods Clin Dev. 2018 Jun 15;9:203-10. DOI: 10.1016/j.omtm.2018.02.009.
181. Stripecke R, del Carmen Villacres M, Skelton DC, Satake N, Halene S, Kohn DB. Immune response to green fluorescent protein: implications for gene therapy. Gene Ther. 1999;6(7):1305-12.
182. Charlesworth CT, Deshpande PS, Dever DP, Camarena J, Lemgart VT, Cromer MK, et al. Identification of preexisting adaptive immunity to Cas9 proteins in humans. Nat Med. 2019 Feb;25(2):249-54. DOI: 10.1038/s41591-018-0326-x.
183. Ferdosi SR, Ewaisha R, Moghadam F, Krishna S, Park JG, Ebrahimkhani MR, et al. Multifunctional CRISPR-Cas9 with engineered immunosilenced human T cell epitopes. Nat Commun. 2019 Apr 23;10(1):1842. DOI: 10.1038/s41467-019-09693-x.
184. Moreno AM, Palmer N, Aleman F, Chen G, Pla A, Jiang N, et al. Immune-orthogonal orthologues of AAV capsids and of Cas9 circumvent the immune response to the

administration of gene therapy. Nat Biomed Eng. 2019 Oct;3(10):806-16. DOI: 10.1038/s41551-019-0431-2.

185. Wagner DL, Amini L, Wendering DJ, Burkhardt LM, Akyuz L, Reinke P, et al. High prevalence of Streptococcus pyogenes Cas9-reactive T cells within the adult human population. Nat Med. 2019 Feb;25(2):242-8. DOI: 10.1038/s41591-018-0204-6.
186. Denaro M, Oldmixon B, Patience C, Andersson G, Down J. EGFP-transduced EL-4 cells from tumors in C57BL/6 mice. Gene Ther. 2002;8(23):1814-5.
187. Skelton D, Satake N, Kohn DB. The enhanced green fluorescent protein (eGFP) is minimally immunogenic in C57BL/6 mice. Gene Ther. 2002;8(23):1813-4.
188. Ma Y, Zhang P, Wang F, Yang J, Yang Z, Qin H. The relationship between early embryo development and tumourigenesis. J Cell Mol Med. 2010 Dec;14(12):2697-701. DOI: 10.1111/j.1582-4934.2010.01191.x.
189. Reichert M, Takano S, von Burstin J, Kim SB, Lee JS, Ihida-Stansbury K, et al. The Prrx1 homeodomain transcription factor plays a central role in pancreatic regeneration and carcinogenesis. Genes Dev. 2013 Feb 1;27(3):288-300. DOI: 10.1101/gad.204453.112.
190. Sancho E, Batlle E, Clevers H. Signaling pathways in intestinal development and cancer. Annu Rev Cell Dev Biol. 2004;20:695-723.
191. Uhlen M, Fagerberg L, Hallstrom BM, Lindskog C, Oksvold P, Mardinoglu A, et al. Proteomics. Tissue-based map of the human proteome. Science. 2015 Jan 23;347(6220):1260419. DOI: 10.1126/science.1260419.
192. Chen H, Liu H, Qing G. Targeting oncogenic Myc as a strategy for cancer treatment. Signal Transduct Target Ther. 2018;3:5. DOI: 10.1038/s41392-018-0008-7.
193. Yan W, Wu X, Zhou W, Fong MY, Cao M, Liu J, et al. Cancer-cell-secreted exosomal miR-105 promotes tumour growth through the MYC-dependent metabolic reprogramming of stromal cells. Nat Cell Biol. 2018 May;20(5):597-609. DOI: 10.1038/s41556-018-0083-6.
194. Wolfer A, Wittner BS, Irimia D, Flavin RJ, Lupien M, Gunawardane RN, et al. MYC regulation of a "poor-prognosis" metastatic cancer cell state. Proc Natl Acad Sci U S A. 2010 Feb 23;107(8):3698-703. DOI: 10.1073/pnas.0914203107.
195. Arango D, Mariadason JM, Wilson AJ, Yang W, Corner GA, Nicholas C, et al. c-Myc overexpression sensitises colon cancer cells to camptothecin-induced apoptosis. Br J Cancer. 2003 Nov 3;89(9):1757-65. DOI: 10.1038/sj.bjc.6601338.
196. Green AR, Aleskandarany MA, Agarwal D, Elsheikh S, Nolan CC, Diez-Rodriguez M, et al. MYC functions are specific in biological subtypes of breast cancer and confers resistance to endocrine therapy in luminal tumours. Br J Cancer. 2016 Apr 12;114(8):917-28. DOI: 10.1038/bjc.2016.46.

197. Zhang HL, Wang P, Lu MZ, Zhang SD, Zheng L. c-Myc maintains the self-renewal and chemoresistance properties of colon cancer stem cells. Oncol Lett. 2019 May;17(5):4487-93. DOI: 10.3892/ol.2019.10081.
198. Xu J, Chen Y, Olopade OI. MYC and Breast Cancer. Genes Cancer. 2010 Jun;1(6):629-40. DOI: 10.1177/1947601910378691.
199. Zhou Y, Zhu Y, Fan X, Zhang C, Wang Y, Zhang L, et al. NID1, a new regulator of EMT required for metastasis and chemoresistance of ovarian cancer cells. Oncotarget. 2017;8(20):33110-21.
200. Aleckovic M, Wei Y, LeRoy G, Sidoli S, Liu DD, Garcia BA, et al. Identification of Nidogen 1 as a lung metastasis protein through secretome analysis. Genes Dev. 2017 Jul 15;31(14):1439-55. DOI: 10.1101/gad.301937.117.
201. Rokavec M, Bouznad N, Hermeking H. Paracrine Induction of Epithelial-Mesenchymal Transition Between Colorectal Cancer Cells and its Suppression by a p53/miR-192/215/NID1 Axis. Cell Mol Gastroenterol Hepatol. 2019;7(4):783-802. DOI: 10.1016/j.jcmgh.2019.02.003.
202. Ulazzi L, Sabbioni S, Miotto E, Veronese A, Angusti A, Gafa R, et al. Nidogen 1 and 2 gene promoters are aberrantly methylated in human gastrointestinal cancer. Mol Cancer. 2007 Feb 28;6:17. DOI: 10.1186/1476-4598-6-17.
203. Willumsen N, Bager CL, Leeming DJ, Bay-Jensen AC, Karsdal MA. Nidogen-1 Degraded by Cathepsin S can be Quantified in Serum and is Associated with Non-Small Cell Lung Cancer. Neoplasia. 2017 Apr;19(4):271-8. DOI: 10.1016/j.neo.2017.01.008.
204. Eilken HM, Dieguez-Hurtado R, Schmidt I, Nakayama M, Jeong HW, Arf H, et al. Pericytes regulate VEGF-induced endothelial sprouting through VEGFR1. Nat Commun. 2017 Nov 17;8(1):1574. DOI: 10.1038/s41467-017-01738-3.
205. Magnusson PU, Looman C, Ahgren A, Wu Y, Claesson-Welsh L, Heuchel RL. Platelet-derived growth factor receptor-beta constitutive activity promotes angiogenesis in vivo and in vitro. Arterioscler Thromb Vasc Biol. 2007 Oct;27(10):2142-9. DOI: 10.1161/01.ATV.0000282198.60701.94.
206. Sennino B, Falcon BL, McCauley D, Le T, McCauley T, Kurz JC, et al. Sequential loss of tumor vessel pericytes and endothelial cells after inhibition of platelet-derived growth factor B by selective aptamer AX102. Cancer Res. 2007 Aug 1;67(15):7358-67. DOI: 10.1158/0008-5472.CAN-07-0293.
207. Kim Y, Kim E, Wu Q, Guryanova O, Hitomi M, Lathia JD, et al. Platelet-derived growth factor receptors differentially inform intertumoral and intratumoral heterogeneity. Genes Dev. 2012 Jun 1;26(11):1247-62. DOI: 10.1101/gad.193565.112.
208. Melaiu O, Catalano C, De Santi C, Cipollini M, Figlioli G, Pellè L, et al. Inhibition of the platelet-derived growth factor receptor beta (PDGFRB) using gene silencing, crenolanib

besylate, or imatinib mesylate hampers the malignant phenotype of mesothelioma cell lines. Genes Cancer. 2017;8(1-2):438-52. DOI: 10.18632/genesandcancer.129.

209. Steller EJ, Raats DA, Koster J, Rutten B, Govaert KM, Emmink BL, et al. PDGFRB promotes liver metastasis formation of mesenchymal-like colorectal tumor cells. Neoplasia. 2013 Feb;15(2):204-17. DOI: 10.1593/neo.121726.

210. Fujino S, Miyoshi N, Ohue M, Takahashi Y, Yasui M, Hata T, et al. Plateletderived growth factor receptorbeta gene expression relates to recurrence in colorectal cancer. Oncol Rep. 2018 May;39(5):2178-84. DOI: 10.3892/or.2018.6290.

211. Nordby Y, Richardsen E, Rakaee M, Ness N, Donnem T, Patel HR, et al. High expression of PDGFR-beta in prostate cancer stroma is independently associated with clinical and biochemical prostate cancer recurrence. Sci Rep. 2017 Feb 24;7:43378. DOI: 10.1038/srep43378.

212. Frodin M, Mezheyeuski A, Corvigno S, Harmenberg U, Sandstrom P, Egevad L, et al. Perivascular PDGFR-beta is an independent marker for prognosis in renal cell carcinoma. Br J Cancer. 2017 Jan 17;116(2):195-201. DOI: 10.1038/bjc.2016.407.

213. Corvigno S, Wisman GBA, Mezheyeuski A, Van Der Zee AGJ, Nijman HW, Åvall-Lundqvist E, et al. Markers of fibroblast-rich tumor stroma and perivascular cells in serous ovarian cancer: Inter- and intra-patient heterogeneity and impact on survival. Oncotarget. 2016;7(14):18573-84.

214. Gonzalez-Gonzalez L, Alonso J. Periostin: A Matricellular Protein With Multiple Functions in Cancer Development and Progression. Front Oncol. 2018;8:225. DOI: 10.3389/fonc.2018.00225.

215. Kazanskaya O, Glinka A, del Barco Barrantes I, Stannek P, Niehrs C, Wu W. R-Spondin2 is a secreted activator of Wnt/beta-catenin signaling and is required for Xenopus myogenesis. Dev Cell. 2004 Oct;7(4):525-34. DOI: 10.1016/j.devcel.2004.07.019.

216. Szenker-Ravi E, Altunoglu U, Leushacke M, Bosso-Lefevre C, Khatoo M, Thi Tran H, et al. RSPO2 inhibition of RNF43 and ZNRF3 governs limb development independently of LGR4/5/6. Nature. 2018 May;557(7706):564-9. DOI: 10.1038/s41586-018-0118-y.

217. Reis AH, Sokol SY. Rspo2 antagonizes FGF signaling during vertebrate mesoderm formation and patterning. Development. 2020 May 27;147(10). DOI: 10.1242/dev.189324.

218. Nagano K. R-spondin signaling as a pivotal regulator of tissue development and homeostasis. Jpn Dent Sci Rev. 2019 Nov;55(1):80-7. DOI: 10.1016/j.jdsr.2019.03.001.

219. Conboy CB, Velez-Reyes GL, Tschida BR, Hu H, Kaufmann G, Koes N, et al. R-spondin 2 Drives Liver Tumor Development in a Yes-Associated Protein-Dependent Manner. Hepatol Commun. 2019 Nov;3(11):1496-509. DOI: 10.1002/hep4.1422.

220. Ilmer M, Boiles AR, Regel I, Yokoi K, Michalski CW, Wistuba, II, et al. RSPO2 Enhances Canonical Wnt Signaling to Confer Stemness-Associated Traits to Susceptible Pancreatic

Cancer Cells. Cancer Res. 2015 May 1;75(9):1883-96. DOI: 10.1158/0008-5472.CAN-14-1327.

221. Zhang L, Song Y, Ling Z, Li Y, Ren X, Yang J, et al. R-spondin 2-LGR4 system regulates growth, migration and invasion, epithelial-mesenchymal transition and stem-like properties of tongue squamous cell carcinoma via Wnt/beta-catenin signaling. EBioMedicine. 2019 Jun;44:275-88. DOI: 10.1016/j.ebiom.2019.03.076.
222. Dong X, Liao W, Zhang L, Tu X, Hu J, Chen T, et al. RSPO2 suppresses colorectal cancer metastasis by counteracting the Wnt5a/Fzd7-driven noncanonical Wnt pathway. Cancer Lett. 2017 Aug 28;402:153-65. DOI: 10.1016/j.canlet.2017.05.024.
223. Wu C, Qiu S, Lu L, Zou J, Li WF, Wang O, et al. RSPO2-LGR5 signaling has tumour-suppressive activity in colorectal cancer. Nat Commun. 2014;5:3149. DOI: 10.1038/ncomms4149.
224. Coussy F, Lallemand F, Vacher S, Schnitzler A, Chemlali W, Caly M, et al. Clinical value of R-spondins in triple-negative and metaplastic breast cancers. Br J Cancer. 2017 Jun 6;116(12):1595-603. DOI: 10.1038/bjc.2017.131.
225. Wu L, Zhang W, Qian J, Wu J, Jiang L, Ling C. R-spondin family members as novel biomarkers and prognostic factors in lung cancer. Oncol Lett. 2019 Oct;18(4):4008-15. DOI: 10.3892/ol.2019.10778.
226. Aburjania Z, Jang S, Whitt J, Jaskula-Stzul R, Chen H, Rose JB. The Role of Notch3 in Cancer. Oncologist. 2018 Aug;23(8):900-11. DOI: 10.1634/theoncologist.2017-0677.
227. Novak D, Huser L, Elton JJ, Umansky V, Altevogt P, Utikal J. SOX2 in development and cancer biology. Semin Cancer Biol. 2019 Aug 11. DOI: 10.1016/j.semcancer.2019.08.007.
228. Ozawa T, Kazama S, Akiyoshi T, Murono K, Yoneyama S, Tanaka T, et al. Nuclear Notch3 expression is associated with tumor recurrence in patients with stage II and III colorectal cancer. Ann Surg Oncol. 2014 Aug;21(8):2650-8. DOI: 10.1245/s10434-014-3659-9.
229. Serafin V, Persano L, Moserle L, Esposito G, Ghisi M, Curtarello M, et al. Notch3 signalling promotes tumour growth in colorectal cancer. J Pathol. 2011 Aug;224(4):448-60. DOI: 10.1002/path.2895.
230. Zheng J, Xu L, Pan Y, Yu S, Wang H, Kennedy D, et al. Sox2 modulates motility and enhances progression of colorectal cancer via the Rho-ROCK signaling pathway. Oncotarget. 2017;8(58):98635-45.
231. Papatsoris AG, Liolitsa D, Deliveliotis C. Manipulation of the nerve growth factor network in prostate cancer. Expert Opin Investig Drugs. 2007 Mar;16(3):303-9. DOI: 10.1517/13543784.16.3.303.
232. Reis-Filho JS, Steele D, Di Palma S, Jones RL, Savage K, James M, et al. Distribution and significance of nerve growth factor receptor (NGFR/p75NTR) in normal, benign and

malignant breast tissue. Mod Pathol. 2006 Feb;19(2):307-19. DOI: 10.1038/modpathol.3800542.

233. Yang Z, Chen H, Huo L, Yang Z, Bai Y, Fan X, et al. Epigenetic inactivation and tumor-suppressor behavior of NGFR in human colorectal cancer. Mol Cancer Res. 2015 Jan;13(1):107-19. DOI: 10.1158/1541-7786.MCR-13-0247.

234. Chen C, Shin JH, Eggold JT, Chung MK, Zhang LH, Lee J, et al. ESM1 mediates NGFR-induced invasion and metastasis in murine oral squamous cell carcinoma. Oncotarget. 2016;7(43):70738-49.

235. Jiang L, Huang S, Wang J, Zhang Y, Xiong Y, Zeng SX, et al. Inactivating p53 is essential for nerve growth factor receptor to promote melanoma-initiating cell-stemmed tumorigenesis. Cell Death Dis. 2020 Jul 20;11(7):550. DOI: 10.1038/s41419-020-02758-6.

236. Zhou X, Hao Q, Liao P, Luo S, Zhang M, Hu G, et al. Nerve growth factor receptor negates the tumor suppressor p53 as a feedback regulator. Elife. 2016 Jun 10;5. DOI: 10.7554/eLife.15099.

237. Sun F, Zhuo R, Ma W, Yang D, Su T, Ye L, et al. From clinic to mechanism: Proteomics-based assessment of angiogenesis in adrenal pheochromocytoma. J Cell Physiol. 2019 Dec;234(12):22057-70. DOI: 10.1002/jcp.28769.

238. Haghjoo N, Moeini A, Masoudi-Nejad A. Introducing a panel for early detection of lung adenocarcinoma by using data integration of genomics, epigenomics, transcriptomics and proteomics. Exp Mol Pathol. 2020 Feb;112:104360. DOI: 10.1016/j.yexmp.2019.104360.

239. Morel S, Burnier L, Roatti A, Chassot A, Roth I, Sutter E, et al. Unexpected role for the human Cx37 C1019T polymorphism in tumour cell proliferation. Carcinogenesis. 2010 Nov;31(11):1922-31. DOI: 10.1093/carcin/bgq170.

240. Jonas O, Duschl C. Force propagation and force generation in cells. Cytoskeleton (Hoboken). 2010 Sep;67(9):555-63. DOI: 10.1002/cm.20466.

241. Artym VV, Swatkoski S, Matsumoto K, Campbell CB, Petrie RJ, Dimitriadis EK, et al. Dense fibrillar collagen is a potent inducer of invadopodia via a specific signaling network. J Cell Biol. 2015 Feb 2;208(3):331-50. DOI: 10.1083/jcb.201405099.

242. Provenzano PP, Inman DR, Eliceiri KW, Knittel JG, Yan L, Rueden CT, et al. Collagen density promotes mammary tumor initiation and progression. BMC Med. 2008 Apr 28;6:11. DOI: 10.1186/1741-7015-6-11.

243. Bougherara H, Mansuet-Lupo A, Alifano M, Ngo C, Damotte D, Le Frere-Belda MA, et al. Real-Time Imaging of Resident T Cells in Human Lung and Ovarian Carcinomas Reveals How Different Tumor Microenvironments Control T Lymphocyte Migration. Front Immunol. 2015;6:500. DOI: 10.3389/fimmu.2015.00500.

244. Kuczek DE, Larsen AMH, Thorseth ML, Carretta M, Kalvisa A, Siersbaek MS, et al. Collagen density regulates the activity of tumor-infiltrating T cells. J Immunother Cancer. 2019 Mar 12;7(1):68. DOI: 10.1186/s40425-019-0556-6.

245. Salmon H, Franciszkiewicz K, Damotte D, Dieu-Nosjean MC, Validire P, Trautmann A, et al. Matrix architecture defines the preferential localization and migration of T cells into the stroma of human lung tumors. J Clin Invest. 2012 Mar;122(3):899-910. DOI: 10.1172/JCI45817.
246. Whittington CF, Yoder MC, Voytik-Harbin SL. Collagen-polymer guidance of vessel network formation and stabilization by endothelial colony forming cells in vitro. Macromol Biosci. 2013 Sep;13(9):1135-49. DOI: 10.1002/mabi.201300128.
247. Ishimoto T, Miyake K, Nandi T, Yashiro M, Onishi N, Huang KK, et al. Activation of Transforming Growth Factor Beta 1 Signaling in Gastric Cancer-associated Fibroblasts Increases Their Motility, via Expression of Rhomboid 5 Homolog 2, and Ability to Induce Invasiveness of Gastric Cancer Cells. Gastroenterology. 2017 Jul;153(1):191-204 e16. DOI: 10.1053/j.gastro.2017.03.046.
248. Gaggioli C, Hooper S, Hidalgo-Carcedo C, Grosse R, Marshall JF, Harrington K, et al. Fibroblast-led collective invasion of carcinoma cells with differing roles for RhoGTPases in leading and following cells. Nat Cell Biol. 2007 Dec;9(12):1392-400. DOI: 10.1038/ncb1658.
249. Labernadie A, Kato T, Brugues A, Serra-Picamal X, Derzsi S, Arwert E, et al. A mechanically active heterotypic E-cadherin/N-cadherin adhesion enables fibroblasts to drive cancer cell invasion. Nat Cell Biol. 2017 Mar;19(3):224-37. DOI: 10.1038/ncb3478.
250. Miyazaki K, Oyanagi J, Hoshino D, Togo S, Kumagai H, Miyagi Y. Cancer cell migration on elongate protrusions of fibroblasts in collagen matrix. Sci Rep. 2019 Jan 22;9(1):292. DOI: 10.1038/s41598-018-36646-z.
251. Kim DJ, Dunleavey JM, Xiao L, Ollila DW, Troester MA, Otey CA, et al. Suppression of TGFbeta-mediated conversion of endothelial cells and fibroblasts into cancer associated (myo)fibroblasts via HDAC inhibition. Br J Cancer. 2018 May;118(10):1359-68. DOI: 10.1038/s41416-018-0072-3.
252. Hirokawa Y, Yip KH, Tan CW, Burgess AW. Colonic myofibroblast cell line stimulates colonoid formation. Am J Physiol Gastrointest Liver Physiol. 2014 Apr 1;306(7):G547-56. DOI: 10.1152/ajpgi.00267.2013.
253. Djurec M, Grana O, Lee A, Troule K, Espinet E, Cabras L, et al. Saa3 is a key mediator of the protumorigenic properties of cancer-associated fibroblasts in pancreatic tumors. Proc Natl Acad Sci U S A. 2018 Feb 6;115(6):E1147-E56. DOI: 10.1073/pnas.1717802115.
254. Dotto GP, Weinberg RA, Ariza A. Malignant transformation of mouse primary keratinocytes by Harvey sarcoma virus and its modulation by surrounding normal cells. Proc Natl Acad Sci U S A. 1988;85(17):6389-93.
255. Lim PK, Bliss SA, Patel SA, Taborga M, Dave MA, Gregory LA, et al. Gap junction-mediated import of microRNA from bone marrow stromal cells can elicit cell cycle

quiescence in breast cancer cells. Cancer Res. 2011 Mar 1;71(5):1550-60. DOI: 10.1158/0008-5472.CAN-10-2372.

256. Madar S, Brosh R, Buganim Y, Ezra O, Goldstein I, Solomon H, et al. Modulated expression of WFDC1 during carcinogenesis and cellular senescence. Carcinogenesis. 2009 Jan;30(1):20-7. DOI: 10.1093/carcin/bgn232.

257. Mintz B, Illmensee K. Normal genetically mosaic mice produced from malignant teratocarcinoma cells. Proc Natl Acad Sci U S A. 1975;72(9):3585-9.

258. Stoker MG, Shearer M, O'Neill C. Growth inhibition of polyoma-transformed cells by contact with static normal fibroblasts. J Cell Sci. 1966;1(3):297-310.

259. Carreras CW, Santi DV. The catalytic mechanism and structure of thymidylate synthase. Annu Rev Biochem. 1995;64:721-62.

260. Longley DB, Harkin DP, Johnston PG. 5-fluorouracil: mechanisms of action and clinical strategies. Nat Rev Cancer. 2003 May;3(5):330-8. DOI: 10.1038/nrc1074.

261. Johnston PG, Kaye S. Capecitabine: a novel agent for the treatment of solid tumors. Anti-Cancer Drugs. 2001;12(8):639-46.

262. Project ACCM-A. Modulation of fluorouracil by leucovorin in patients with advanced colorectal cancer: evidence in terms of response rate. J Clin Oncol. 1992;10(6):896-903. DOI: 10.1200/JCO.1992.10.6.896.

263. Kweekel DM, Gelderblom H, Guchelaar HJ. Pharmacology of oxaliplatin and the use of pharmacogenomics to individualize therapy. Cancer Treat Rev. 2005 Apr;31(2):90-105. DOI: 10.1016/j.ctrv.2004.12.006.

264. Giacchetti S, Perpoint B, Zidani R, Le Bail N, Faggiuolo R, Focan C, et al. Phase III multicenter randomized trial of oxaliplatin added to chronomodulated fluorouracil-leucovorin as first-line treatment of metastatic colorectal cancer. J Clin Oncol. 2000;18(1):136-47. DOI: 10.1200/JCO.2000.18.1.136.

265. Diasio RB, Harris BE. Clinical pharmacology of 5-fluorouracil. Clin Pharmacokinet. 1989;16(4):215-37. DOI: 10.2165/00003088-198916040-00002.

266. Amin MB. AJCC cancer staging manual; Eighth edition. Eighth ed. Edge SB, editor. New York: Springer; 2017.

267. Ikemura M, Hashida T. Effect of Hyperglycemia on Antitumor Activity and Survival in Tumor-bearing Mice Receiving Oxaliplatin and Fluorouracil. Anticancer Res. 2017 Oct;37(10):5463-8. DOI: 10.21873/anticanres.11975.

268. Goldstein D, Mitchell P, Michael M, Beale P, Friedlander M, Zalcberg J, et al. Australian experience of a modified schedule of FOLFOX with high activity and tolerability and improved convenience in untreated metastatic colorectal cancer patients. Br J Cancer. 2005 Mar 14;92(5):832-7. DOI: 10.1038/sj.bjc.6602426.

269. Park SH, Sung JY, Han SH, Baek JH, Oh JH, Bang SM, et al. Oxaliplatin, folinic acid and 5-fluorouracil (FOLFOX-4) combination chemotherapy as second-line treatment in

advanced colorectal cancer patients with irinotecan failure: a Korean single-center experience. Jpn J Clin Oncol. 2005 Sep;35(9):531-5. DOI: 10.1093/jjco/hyi140.

270. Deng Y, Wang L, Tan S, Kim GP, Dou R, Chen D, et al. KRAS as a predictor of poor prognosis and benefit from postoperative FOLFOX chemotherapy in patients with stage II and III colorectal cancer. Mol Oncol. 2015 Aug;9(7):1341-7. DOI: 10.1016/j.molonc.2015.03.006.

271. Fransen F, van Beek AA, Borghuis T, Meijer B, Hugenholtz F, van der Gaast-de Jongh C, et al. The Impact of Gut Microbiota on Gender-Specific Differences in Immunity. Front Immunol. 2017;8:754. DOI: 10.3389/fimmu.2017.00754.

272. Klein SL, Flanagan KL. Sex differences in immune responses. Nat Rev Immunol. 2016 Oct;16(10):626-38. DOI: 10.1038/nri.2016.90.

273. Sherman MH, Yu RT, Engle DD, Ding N, Atkins AR, Tiriac H, et al. Vitamin D receptor-mediated stromal reprogramming suppresses pancreatitis and enhances pancreatic cancer therapy. Cell. 2014 Sep 25;159(1):80-93. DOI: 10.1016/j.cell.2014.08.007.

274. Al-Harbi B, Hendrayani S, Silva G, Aboussekhra A. Let-7b inhibits cancer-promoting effects of breast cancerassociated fibroblasts through IL-8 repression. Oncotarget. 2018;9(25):17825-38.

275. Melling GE, Flannery SE, Abidin SA, Clemmens H, Prajapati P, Hinsley EE, et al. A miRNA-145/TGF-beta1 negative feedback loop regulates the cancer-associated fibroblast phenotype. Carcinogenesis. 2018 May 28;39(6):798-807. DOI: 10.1093/carcin/bgy032.

276. Albrengues J, Bertero T, Grasset E, Bonan S, Maiel M, Bourget I, et al. Epigenetic switch drives the conversion of fibroblasts into proinvasive cancer-associated fibroblasts. Nat Commun. 2015 Dec 15;6:10204. DOI: 10.1038/ncomms10204.

277. Chen J, Luo Y, Huang H, Wu S, Feng J, Zhang J, et al. CD146 is essential for PDGFRbeta-induced pericyte recruitment. Protein Cell. 2018 Aug;9(8):743-7. DOI: 10.1007/s13238-017-0484-5.

278. Luo Y, Teng X, Zhang L, Chen J, Liu Z, Chen X, et al. CD146-HIF-1alpha hypoxic reprogramming drives vascular remodeling and pulmonary arterial hypertension. Nat Commun. 2019 Aug 7;10(1):3551. DOI: 10.1038/s41467-019-11500-6.

279. Witze ES, Litman ES, Argast GM, Moon RT, Ahn NG. Wnt5a control of cell polarity and directional movement by polarized redistribution of adhesion receptors. Science. 2008;320(5874):365-9.

280. Liu D, Du L, Chen D, Ye Z, Duan H, Tu T, et al. Reduced CD146 expression promotes tumorigenesis and cancer stemness in colorectal cancer through activating Wnt/β-catenin signaling. Oncotarget. 2016;7(26):40704-18.